Proceedings

INTERNATIONAL CONFERENCE ON FAN NOISE, AERODYNAMICS, APPLICATIONS AND SYSTEMS



9 to 11 APRIL 2025
ANTIBES - JUAN-LES-PINS, FRANCE

Organized by

cetiat
ensemble, innover et valider

CETIM

www.fan2025.org

Copyright © 2025 Technical Center Industries Aérauliques Et Thermiques (Cetiat)

Published by
Sigel Press
8187 Camp Road
Homerville, Ohio, USA

Visit us on the WorldWideWeb at: www.sigelpress.com

The rights of Dr A.G. Sheard, identified as editor of this work, have been asserted by him in accordance with the Copyright, Designs and Patents Act 1988.

All rights reserved. No part of this publication may be reproduced, stored in a retrieval system, or transmitted in any means, electronic, mechanical, photocopying, recording, or otherwise without prior written permission of the publisher.

Internal Design: Professional Book Compositors, Lorain, Ohio, USA
Cover Design: Francois Bessac
Cover Images: Cetiat

ISBN 978-1-905941-32-2

Typeset in Times Roman

The publisher's to use paper manufactured from sustainable forests.



Proceedings of FAN 2025

8th International Conference on Fan Noise, Aerodynamics, Applications and Systems, 9 to 11 April 2025, Antibes, Juan-les-Pines, France.

1. Fan Noise 1992: Senlis, France, 1-3 September 1992.
2. Fan Noise 2003: Senlis, France, 23–25 September 2003.
3. Fan Noise 2007: Lyon, France, 17-19 September 2007.
4. Fan 2012: Senlis, France, 18-20 April 2022.
5. Fan 2015: Lyon, France, 15-17 April 2015.
6. Fan 2018: Darmstadt, Germany, 18-20 April 2018.
7. Fan 2022: Senlis, France, 27-29 June 2022.

Organizers

CETIAT
Centre Technique des Industries Aérauliques et Thermiques
Domaine Scientifique de la Doua,
25 avenue des Arts, BP 52042
69603 Villeurbanne Cedex - France
Phone: +33 472 44 49 00
E-mail: commercial@cetiat.fr
www.cetiat.fr

CETIM
Technical Centre for Mechanical Industries
52 Avenue Félix Louat, BP 80067
60304 Senlis - France
Phone: +33 (0)6 70 01 53 17
E-mail: marc-olivier.sinanian@cetim.fr www.
cetim-engineering.com

Welcome

Following on from the FAN 2012, 2015, 2018 and 2022 conferences, the next in the series is FAN 2025. One of only a few truly international technical forums for the Fan Industry, the former event attracted three hundred attendees from thirty countries. Feedback states these events are unique in providing the opportunity to network with companies and academic institutions from across the globe.

Conference Theme

The landscape of fan design is rapidly evolving to meet the escalating demands for higher efficiency, reduced noise levels, and increased availability. Moreover, with many fans now serving safety-related applications, the need for innovation has never been more pressing. The advent of connectivity and digital services is catalyzing the emergence of novel business models, while the prevalence of variable speed introduces new design challenges for plant upgrades.

In this dynamic environment, numerical simulation techniques are becoming indispensable tools in aerodynamic design processes.

Fan 2025 is a unique platform for fan and system designers, manufacturers, and operators to come together and advance our understanding of fans and their intricate system interactions. This conference is a forum for fan and system designers, manufacturers, and operators, with the aim of improving our understanding of fans and their system interaction. Fan 2025 follows a three-track format. Each track is separate, but complimentary.

Geoff Sheard

Conference Chairman



Supporters


CidB
Centre d'information
sur le Bruit


ebmpapst
engineering a better life


Università
degli Studi
di Padova


dtg
Dipartimento di
Tecnica e Gestione
dei sistemi industriali
Università di Padova


amca
INTERNATIONAL


EUROVENT
EUROPEAN INDUSTRY ASSOCIATION


Sfa
Société
Française
d'Acoustique


fan2025

Sponsers

Platinum sponsor – Gala Dinner

ebmpapst

Delegate bags

turbo designsuite
by Advanced Design Technology

Badges

CFturbo

Lanyards

DASSAULT SYSTEMES

Bottles

amca INTERNATIONAL

Journal Issue

ZIEHL-ABEGG

Book of abstracts

NEU-JKF Fevi

fan2025

Organizing Committee

- Geoff SHEARD (AGS Consulting LLC, USA) – Conference Chairman
- Jürgen SCHÖNE (ebm-papst, Germany) – Conference Vice-Chairman
- Ossian KAGHAD (CETIAT, France) – Fan Noise Track Co-Chair
- Michel BESOMBES (Cetim, France) – Fan Noise Track Co-Chair
- Thomas CAROLUS (Siegen University, Germany) – Fan Aerodynamics Track Co- Chair
- Massimo MASI (University of Padua, Italy) - Fan Aerodynamics Track Co-Chair
- Stefan JACOB (Physikalisch-Technische Bundesanstalt, Germany) – Fan Applications and Systems Track Chair
- Michael IVANOVICH (AMCA, USA) – Fan Applications and Systems Track Co-Chair
- François BESSAC (CETIAT, France) – Website & papers management
- Caroline CUCCA (CETIAT, France) – Communication
- Séverine VASELLI (Cetim, France) - Communication
- Thierry GUERMONPREZ (CEYZ, France) – Local organizer

Scientific Advisory Committee

The Fan 2025 Organizing Committee relies on the expertise of a Scientific Advisory Committee to offer insights and direction regarding the scope and structure of the conference. Scientific Advisor Committee members comprise the most senior engineers and academics working in and with the air movement fan community.

- Mats ÅBOM (KTH – The Marcus Wallenberg Laboratory, Sweden)
- Niklas ANDERSSON (Chalmers Univ. of Technology, Sweden)
- Stefan BECKER (IPAT, FAU Erlangen, Germany)
- Martin BÖHLE (SAM Kaiserslautern, Germany)
- Tony BREEN (Nuaire, UK)
- Dario BRIVIO (Nicotra, Italy)
- Daniel CONRAD (ebm-papst, Germany)
- Piero DANIELI (University of Padua, Italy)
- Tamer ELNADY (Ain Shams University, Egypt)
- Sassan ETEMAD (Volvo Technology, Sweden)
- Alain GUÉDEL (France)
- Csaba HORVÁTH (Budapest University of Technology and Economics, Hungary)
- Lixi HUANG (Hong Kong University, Hong Kong)
- Hanbo JIANG (Eastern Institute of Technology (EIT), China)
- Mikael KARLSSON (KTH Royal Institute of Technology, Sweden)
- Phil KIRKHAM (Elta Group, UK)
- Geoff LOCKWOOD (ebm-papst, UK)
- Frieder LÖRCHER (Ziehl-Abegg SE, Germany)
- Alan MACKLIN (ELTA Group, UK)
- Stéphane MOREAU (University of Sherbrooke, Canada)
- Alex NING CHU (Zhejiang University, China)
- Peter PELZ (TU Darmstadt, Germany)
- Balazs PRITZ (Institut für Thermische Strömungsmaschinen, KIT, Germany)
- Erik REICHERT (ebm-Papst Mulfingen GmbH & Co. KG, Germany)
- Jeff ROBINSON (Halifax Fan, UK)
- Michel ROGER (Ecole Centrale de Lyon, France)
- Mats SÁNDOR (Systemair, Sweden)
- Marlène SANJOSÉ (Ecole de Technologie Supérieure, Montréal, Canada)
- Georg SCHEUERER (ISimQ, München, Germany)
- Wolfgang SCHRÖDER (Institut der RWTH Aachen, Germany)
- Lorenzo TIEGHI (Sapienza University of Rome, Italy)
- Johan VAN DER SPUY (Stellenbosch University, South Africa)
- Zhiping WANG (Morrison Product Inc., USA)
- Henrik WITT (Germany)

Table of Contents

A1 Advancements in Fan Performance Prediction 1

Paper # Title

08 **Numerical and Experimental Results for an Axial Fan Concept with Two Sequentially Arranged Impellers of Different External Diameter** 3

F. Lörcher and F. Herrlich

35 **Assessment of the Numerical Prediction Accuracy of Discharge Flow Features of a Rotor-Only Low-Pressure Axial Fan** 13

H. Witte and C. Bode

57 **Numerical Investigation of Scaling Effects on the Performance Characteristics of Large-Scale Axial Flows Fans** 23

T.O. Le Roux, C. Meyer and S.J. van der Spuy

60 **Design of Forward-Inclined Blades for a 0.5 Hub-to-Tip Ratio Tube-Axial Fan** 33

M. Masi, P. Danieli and S. Rech

A2 Tip Gap Noise of Axial Fans 43

Paper # Title

36 **Effects of Blade Tip Design Revisions on Airborne Noise of an Axial Fan** 45

I.B. ÖZENEN and E. ŞIMŞEK

42 **Numerical Investigation of Different Wing Tip Geometries on the Acoustics of an Airfoil With Tip Gap in a Wind Tunnel** 53

P. Dietrich, S.R. Mallu and F. Lex

76 **BTGNX: An Acoustic Benchmark Wind Tunnel Experiment for Tip-Gap Noise** 63

F. Reuschling, L. Liberson, M. Pott-Pollenske, J.W. Delfs and D. Ernst

80 **BTGNX: A MEMS Microphone Array for the Acoustic Benchmark Wind Tunnel Experiment for Tip-Gap Noise** 73

D. Ernst, C. Spehr, F. Reuschling and M. Schneider

A3 Fan System Effect 81

Paper # Title

04 **Co-simulation of an Axial Flow Cooling Fan and a Supercritical CO_2 Air-Cooled Heat Exchanger** 83

F.D. Boshoff, S.J. van der Spuy, J.P. Pretorius and R. Laubscher

09 **Optimising Ventilation System Preplanning: Duct Sizing and Fan Layout using Mixed-Integer Programming** 97

J.H.P. Breuer and P.F. Pelz

84 **Advanced Computational Approaches to Fan Performance and Installation Conditions** 109

U.M. Lakamana, M. Facca and A. Ahuja

B1 Design For Low-Noise Fans 119

Paper # Title

15 **Bringing NASA's Fan Noise Research Down to Earth** 121

L.D. Koch

18 **Additively Manufactured (PBF-LB) Modular Fan Blades with Structured Porosity for Noise Reduction in Turbulent Inflow Conditions** 135

D. Grützner, G. Schultheiß, F. Czwielong, M. Merkel and S. Becker

62 **Aeroacoustic Prediction and Optimization of Unevenly Spaced Blades in Axial Fans** 147

S. Assaf, T. Gras and J. Ferhat

B2 Installation Effects and Unsteady Phenomena 157

Paper # Title

22 **Effect of Installation Space on the Performance of a Centrifugal Fan** 159

M. Ottersten

40 **Modal Analysis of Tip Gap Flow in a Rectilinear Cascade of Compressor Blades at Off-Design Operating Conditions** 169

M. Sanjosé, and A.B. Drame

61 **Fan Mass Flow Determination In Open Wind Tunnel Setups** 179

P. Brunow, M. Maximilian, J. Grubert and J. Friedrichs

73 **Detection of Vortical Structures in the Leakage Flow of a Low-Speed Axial Fan** 189

B. Nyári, K.A. Kovács and E. Balla

B3 Specialized Fans For Niche Applications 197

Paper # Title

06 **Design of a Mixed-Flow Fan for Hair Dryer Application: Acoustic and Fluid Dynamic Improvement** 199

M. Piovan, N. Aldi, M. Pinelli, F. Pompoli, A. Suman, N. Zanini and E. Verzè

56 **Endless Fiber Reinforced Composite Impeller: Modular Design for Different Performance Classes** 211

S. Spitzer, J. Kluger, R. Konig, L. Schroder, A. Dargel, E. Kunze, C. Ebert and M. Gude

C1 Artificial Intelligence & Machine Learning 221

Paper # Title

11 **AI Based Prediction of Noise Emission of Protective Grilles in Axial Fan Assemblies** 223

A. Lucius, M. Schneider, L. Dsilva and T. Geyer

38 **Broadband Noise Prediction of a Low-Pressure Fan Based on Machine Learning** 233

S. Sasaki and T Hosoi

67 **Data-Driven Prediction of Fan Broadband Noise** 243

Z. Zhou, A. Arroyo Ramo , R.K. Pouhe Hiol, S. Pargal, S. Moreau and M. Sanjosé

C2 Psychoacoustics & Sound Quality 255

Paper # Title

30 **Sound Quality Evaluation of Small Fan Noise by TTNR/TPR and Determination of Those Thresholds for Annoyance** 257

T. Nakano and G. Minorikawa

58 **Improving the Psychoacoustic Assessment of Automotive Fan-Systems** 267

D. Scouarnec, S. Bennouna, T. Vicente, A. Pelat, N. Chouard, A. Godart and A. Compain

63 **Impact of Distorted Inlet Flow on Axial Fan Psychoacoustics** 275

M. Vourakis, E. Zea, S. Etemad, M. Karlsson and N. Andersson

D1 Numerical Methods For Design and Performance Analysis 287

Paper # Title

82 **The Role of Computational Fluid Dynamic (CFD) Analysis in Creating DOE Compliant Fan and Blower Product Range Performance Data** 289

A.G. Sheard, A. Demeulenaere and S. Edwards

86 **Mesh Sensitivities for the RANS Simulation of Low-Reynolds Number Propellers** 301

J. Santamaria, A. Bierrenbach-Lima and M. Sanjosé

D2 Optimization of Fan Installation To Reduce Noise 313

Paper # Title

07 **Numerical and Experimental Investigations of the Sound Generation and Possible Optimization Techniques of Wires for Fan Guard Grills** 315

S. Hub and F. Lörcher

32 **ADVentAGe: Scalable Hybrid Noise Control Systems for Fans** 325

V. Mees and D. Goecke

41 **Experimental and Numerical Study of Aerodynamic Noise of Small-Size High-Speed Centrifugal Impeller** 337

Z. Yu, Y. Huang, W. Yang, B. Li, P. Yu, H. Ouyang and Y. Wu

E1 Artificial Intelligence and Optimization Techniques 347

Paper # Title

50 **Redesign and Optimisation of a Large Axial Fan Using 3D Inverse Design Method** 349

W. Angelis, P. Wang, M. Zhang, L. Liu, Q. Zhao and M. Zangeneh

E2 Experimental Methods For Characterizing Noise Sources 357

Paper # Title

72 **Slit Tube Probe and Multi-Port Method for the Acoustical Characterisation of Ducted Axial Fans** 359

J. Riedel, S. Becker and S. Jacob

F1 Noise Prediction By Analytical / Numerical Models 371

Paper # Title

16 **Validation of the Hybrid Fan Noise Simulation Techniques on EAA Axial Benchmark Fan** 373

K. Kucukcoskun and L. Erbig

39 **Assessing Sound Propagation Models for a Low-Speed Axial Fan** 381

V. Ravi, S. Le Bras, L. Erbig and K. Kucukcoskun

65 **On the Effect of Tip Flow on the Noise of a Ducted Rotor** 393

J. Rendón-Arredondo and S. Moreau

F2 Case Studies 403

Paper # Title

29 **Assessing the Influence of Cooling Fans on Fire Risk Mitigation in Domestic Tumble Dryers** 405

P. Danieli, E. Bregolin and M. Masi

45 **Experimental Validation of a CFD procedure for the Analysis of an Industrial Cyclone Separator** 419

E. Bregolin, P. Danieli and M. Masi

G1A Prediction and Optimization of Cooling Fan Noise 431

Paper # Title

44 **Noise Prediction in Automotive Cooling Fans: A Lattice Boltzmann Based Simulation Approach and Experimental Validation** 433

A.S. Sivaramkrishnan, M. Bleiziffer, M. Zangeneh and A. Rodosti

78 **Characterization of the Installation Effects on the Aeroacoustics Sources of the Automotive Cooling Module Using the Lattice-Boltzmann Method** 445

T. Akhtar, S. Tebib, S. Moreau, B. Demory and M. Henner

G1B Fluid-Structure-Acoustic Interactions 457

Paper # Title

13 **An Enclosed Centrifugal Fan as a Benchmark Case for Fluid-Structure-Acoustic-Interaction: An Overview** 459

F. Czwielong, P. Heidegger, M. Lauber, C. Heigl, A. Wurzinger, M. Fritzsche, S. Schoder, M. Kaltenbacher, and S. Becker

26 **1-way FSI Simulation Approach to Assess Low-pressure Axial Fan Aerodynamic and Aeroacoustics Performance Variation** 469

J.D. Laguna, E. Antoniou, F. Quintero, M. Pesce, F. Czwielong and S. Schoder

H1 Fan Integration and Noise Prediction 479

Paper # Title

14 **HVAC Noise Prediction Combining Power and Wave Based Methods** 481

M. Åbom, M.W. Nashed, T. Elnady, and A. Khamis

37 **Aeroacoustics Analysis of Radiator Installation Effects in a Pulling Engine Cooling Module** 491

F. Bellelli, R. Arina, S. Moreau and F. Avallone

66 **Aeroacoustic Investigation of a Charging Cabinet for Electrical Vehicles** 501

S. Tebib, S. Moreau and C. Luzzato

74 **Evaluation of Hybrid Computational Aeroacoustic Methods Applied to Automotive Cooling-Fans** 513

D. Ghosh, M. Vourakis, A. Boström, N. Andersson, A. Roy and S. Etemad

Author Index 525

A1 Advancements in fan performance prediction

9 April - 11:00 - Auditorium

Chairmen: Sassan Etemad, Zhiping Wang

List of papers

Numerical and Experimental Results for an Axial Fan Concept with Two Sequentially Arranged Impellers of Different External Diameter

- Frieder LÖRCHER – ZIEHL-ABEGG SE (Germany)
- Ferdinand HERRLICH – ZIEHL-ABEGG SE (Germany)

Assessment of the Numerical Prediction Accuracy of Discharge Flow Features of a Rotor-Only Low-Pressure Axial Fan

- Hauke WITTE – Institute of Jet Propulsion and Turbomachinery, Technische Universität Braunschweig (Germany)
- Christoph BODE – Institute of Jet Propulsion and Turbomachinery, Technische Universität Braunschweig (Germany)

Numerical Investigation of Scaling Effects on the Performance Characteristics of Large-Scale Axial Flows Fans

- Tristan Oliver LE ROUX – Stellenbosch University (South Africa)
- Chris MEYER – Stellenbosch University (South Africa)
- Sybrand Johannes VAN DER SPUY – Stellenbosch University (South Africa)

Design of Forward-Inclined Blades for a 0.5 Hub-to-Tip Ratio Tube-Axial Fan

- Massimo MASI – University of Padova - Department of Management and Engineering (Italy)
- Piero DANIELI – University of Padova - Department of Management and Engineering (Italy)
- Sergio RECH – University of Padova - Department of Industrial Engineering (Italy)



NUMERICAL AND EXPERIMENTAL RESULTS FOR AN AXIAL FAN CONCEPT WITH TWO SEQUENTIALLY ARRANGED IMPELLERS OF DIFFERENT EXTERNAL DIAMETERS

Frieder LÖRCHER[1], Ferdinand HERRLICH[2]

[1]*ZIEHL-ABEGG SE, Pre-Development Aerodynamics & Acoustics, Heinz-Ziehl-Straße, 74653 Künzelsau, Germany*

[2]*Karlsruher Institut für Technologie (KIT), Kaiserstraße 12, 76131 Karlsruhe, Germany*

SUMMARY

The efficiency of axial fans with low hub ratio is generally limited by flow blockage or even backflow in near-hub regions of the impeller. Even though the use of adapted guide vanes can reduce the negative impact thereof, the power transfer to the fluid near the hub is still limited due to the low local relative speed of the impeller. The present investigation aims to overcome this problem at least partially by use of an additional serially arranged impeller locally in a near hub region whilst not increasing too much the noise generation. For a given baseline fan with guide vanes, some prototypes of a secondary impeller have been generated using CFD and are analysed experimentally. The baseline fan and the prototypes are briefly described, the methodology explained, and the test results discussed regarding the operating points, the efficiency curves as well as the sound power curves.

INTRODUCTION

In the development of low-pressure axial fans for applications such as data centre cooling, refrigeration, ventilation, or energy generation, energy efficiency plays, besides noise level reduction, a key role recently. The reasons for that are growing energy costs and the need to reduce CO_2 emissions. Axial fans with low hub ratio $\nu = D_{hub}/D = [0.2, \dots, 0.5]$ are widely used, as high air flow rates are required at low pressure head. However, it is known from literature [1,2,3,4], that for such fans a phenomenon called hub dead water can occur, meaning the existence of a near-hub blocking or recirculating flow region not contributing to the effective fluid transport from inlet to outlet, leading to significantly reduced stall reserve or achievable total-to-static efficiency η_{stat}. The main reason is the lower power transmission potential to the fluid in this flow region, where the local relative speed of the impeller blade is comparatively low. Whereas downstream guide vane design often may not overcome these disadvantages with low hub ratio [5,6], in [12] a promising guide vane was presented enhancing the achievable efficiency by modifying the streamline curvature in the hub

region and limiting the extent of the backflow region. A further improvement with respect to noise generation for such guide vanes is discussed in [13] in which a central guide vane section significantly reduces all swirl components in the flow. Anyhow, no additional power transfer can be affected by downstream guide vanes, so that they cannot remedy on the principal drawback of the low hub ratio axial fans. In [14], upstream guide vanes are used to increase the pressure rise capability of an induced draft axial fan increasing the transferred power by generating a pre-swirl. In the present paper, the achievable improvement by a second, locally in a near-hub region operating and independently rotating impeller situated downstream of a primary impeller is investigated. A further challenge in developing a fan concept using a secondary impeller is fan noise, which is not neglectable for today's fan industry. Bianchi et al. [15] reviewed available passive noise control technology and concluded that it's not possible to design a fan, and then optimize the design to minimize fan noise, but that designers must optimize aerodynamic and acoustic performance simultaneously. The paper follows this approach, so both aerodynamical and aeroacoustical performances are analysed and incorporated in the development process simultaneously. As baseline fan, the fan with zonal guide vane already presented in [13] is used, as its substantial swirl reduction in the near-hub zone makes it well suited for this purpose. In the Appendix, a definition of used variables and its units is given for better legibility.

DESCRIPTION OF METHODOLOGY

Baseline Fan

As baseline fan, a state-of-the-art axial fan of diameter $D = D_{duct} = 960\ mm$ (duct diameter at main impeller position) with guide vane unit is used (*Figure 1*).

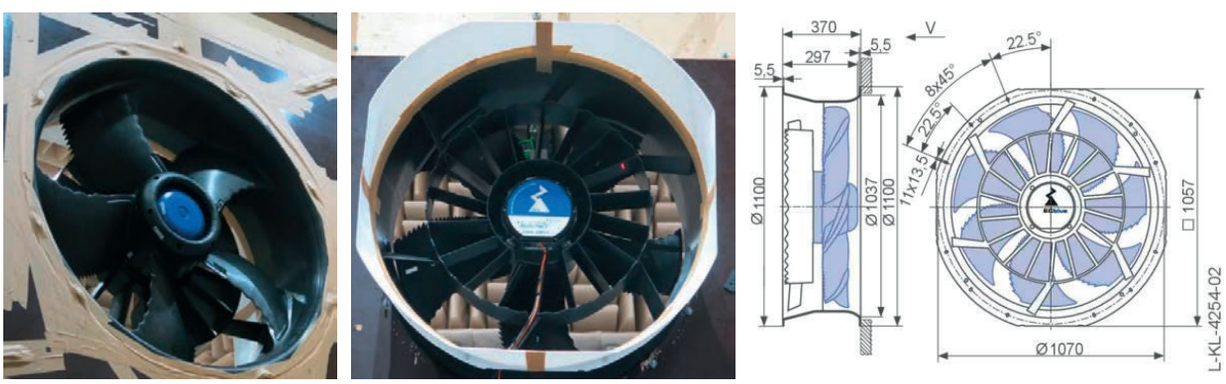


Figure 1: Baseline fan: front view (left), back view (middle), drawing (left)

Downstream the main impeller with 5 blades, the fan has a guide vane with two zones in radial direction separated by a slightly conically divergent split wall at an average diameter of $D_{split} = 700\ mm$. The hub diameter is $D_{Hub} = 329mm$ leading to a hub ratio of $\nu = 0.34$. The central zone of the guide vane consists of 18 stator vanes with axial height of about $l_{Vane} = 108\ mm$ and a trailing edge angle of 0° to the fan axis, highly reducing the swirl components in this region. This fan is used for the reference measurements and is used as baseline fan for the measurements with a secondary impeller fitted downstream the primary impeller and the inner guide vane zone. The experimental data (pressure rise curves, efficiency curves and sound power curves) are presented in the comparative graphs with the secondary impeller measurements in the Section Experimental results.

Numerical setup

Different secondary impellers have been designed with help of a CFD based optimization, for different framework conditions (assumptions) such as the choice of the diameter D_{sec} or the rotation speed n_{sec} of the

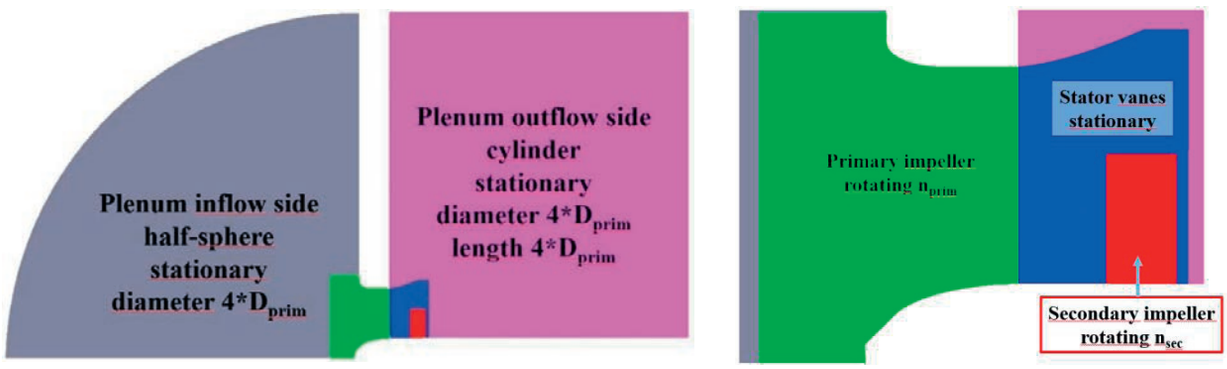


Figure 3: Meridional scheme of domain decomposition for the CFD simulations, global view (left) and detail (right)

secondary impeller. Main optimization criterium of the numerical work was the maximization of the total-to-static efficiency η_{stat}, whilst the acoustical results were obtained experimentally with a subset of promising designs manufactured as physical prototypes. The numerical tool used is ANSYS CFX. In *Figure* 2, the domains decomposition for the simulations is shown schematically in a self-explaining way. The simulations were incompressible steady state RANS simulations. Only one blade passage was modelled for each of the rotors, and the stator was divided into 6 circumferential segments using periodical boundary conditions. At wall boundaries, prism layers were applied (using 9 prism layers), where a value of Y^+in the range of 15-25 was realized. As turbulence model, the 2-equation SST-model, described in [11], was used, and wall functions have been applied. At the inlet, different mass flows and a turbulence intensity of 5 % are specified (a load curve with six load points is simulated). At the outlet, the average static pressure was prescribed. Between domains with different rotating frames, a mixing plane (called "stage interface" in CFX) was applied. For the CFD model, about 4 million unstructured elements were used for a simulation without secondary impeller and about 5 million with secondary impeller. The mesh resolution was chosen such that the computational time of one simulation (duty point) takes a wall time of about 2 hours (and not more) using 128 cores in parallel, to be able to evaluate a sufficiently high number of versions of the secondary impeller in a reasonable time. Using this setup, the duty curve of the available experimental data for the baseline fan was matched with a deviance in static efficiency $\eta_{stat} = (Q_V \cdot \Delta p_{stat})/P_{tot}$ of not more than 2% to the experimental data for the considered duty points. A posteriori, comparing with the prototype measurements of newly developed fans with the secondary impellers, the error of the simulations with secondary impeller was somewhat enhanced, up 4% in static efficiency. A mesh convergence study was not performed.



Figure 2: Inlet plenum of test facility (left) and 3-D printed prototype of secondary impeller installed at the fan system in the test facility (right)

Experimental setup

The baseline fan presented in *Figure 1* was installed in the ZIEHL-ABEGG anechoic facility with experimental fan testing according to ISO 5801 [16] which consists of two large anechoic rooms separated by a partition wall. The fan was attached with its inlet nozzle to the partition wall between an upstream and a downstream plenum. Both the inlet plenum (*Figure 3, left*) and the outlet plenum have non-reflective walls down to $100\,Hz$ and have dimensions of $9\,m\,x\,9\,m\,x\,9\,m$. The baseline fan is a commercial product with aerodynamic parts made of glass fibre reinforced polypropylene. The different secondary impellers were made from ABS using a 3-D printer. Via the secondary electrical drive, the secondary impellers were fixed to the stator structure (*example depicted in Figure 3, right*). The rotations speed of the primary impeller was held constant to $n_{prim} = 1100\,rpm$, whereas the rotation speed of the secondary impeller n_{sec} was varied independently in the experiments.

Using this experimental setup, the baseline fan and fan systems with different secondary impellers have been analysed. The volume flow rate Q_V, the static pressure rise Δp_{stat} between the plenums and the shaft input powers P_{prim}, P_{sec} yielding $P_{tot} = P_{prim} + P_{sec}$ were recorded for different duty points, as well as the A-rated specific sound power levels L_W5 and L_W6 on the suction and pressure side, respectively, with the hull surface method.

PROTOTYPES AND RESULTS

History of prototypes

The different secondary impeller designs have been optimized by use of CFD simulations, using different framework conditions, which evolved depending on experimental results, particularly the respective sound power results. In the CFD simulations, a total-to-static efficiency $\eta_{stat} = (Q_V \cdot \Delta p_{stat})/P_{tot}$ of nearby 70% could be achieved in the optimization process for most of the later prototyped impellers. A detailed list of the prototypes is given in *Table 1*. A visual impression of the impellers is provided as indicated in the table.

Table 1: List of prototyped secondary impellers

index	Rotation dir. (Counter/ Co)	topology	Blade count	Diameter (mm)	Rot. speed CFD (rpm)	η_{stat}(CFD) max (%)	Figure
1	Counter	Free tip (Winglet)	4	700	1000	69	*Figure 4 upper left*
2	Co	Free tip (Winglet)	4	700	1000	68	*Figure 4 upper left*
3	Co	Cover Ring	7	570	850	69	*Figure 4 upper mid left*
4	Co	Grid-Like	21/35/42	570	825	67	*Figure 4 upper mid right*
5	Co	Grid-Like	35/42	490	825	66	*Figure 4 upper right*
6	Co	Loop Design	4/8	570	850	69	*Figure 4 lower left*
7	Co	Loop Design	4/8	500	850	68	*Figure 4 lower middle*
8	Co	Free tip (Peak)	7	589	825	69	*Figure 4 lower right*

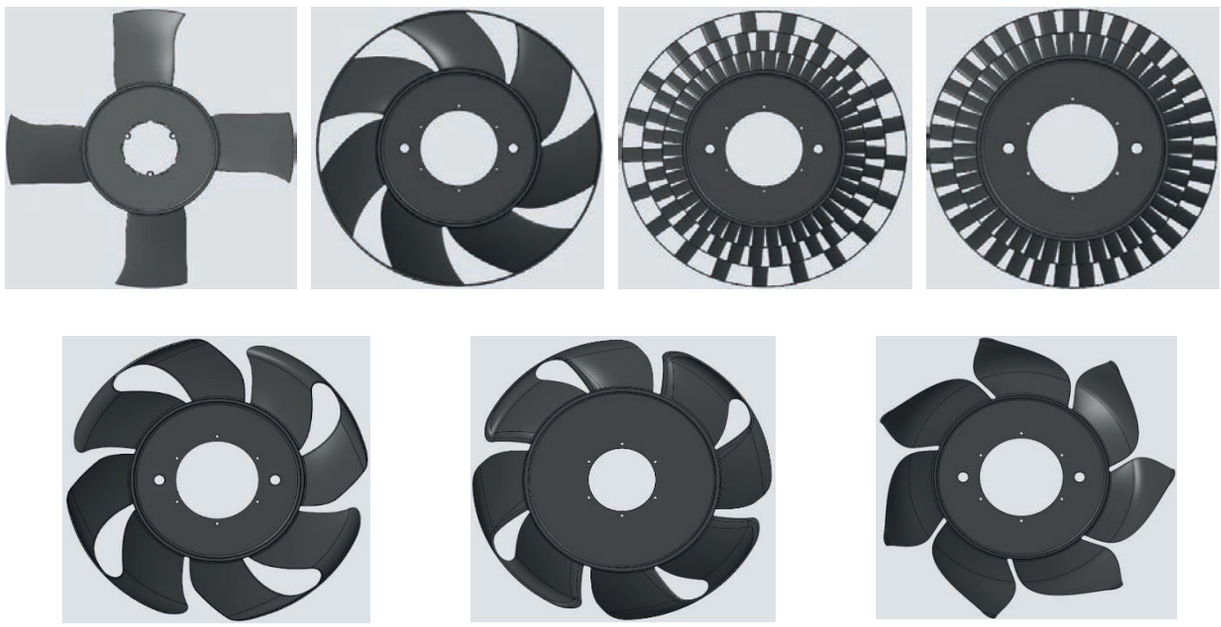


Figure 4: Manufactured prototypes for secondary impellers

The table represents the chronological emergence of the developed prototypes; so later ones incorporate experimental results from previous ones triggered especially by acoustical results, as will get clearer in the section Experimental Results.

The diameter of the first prototypes (index 1 and 2) corresponds to the downstream diameter of the split wall of the guide vane. A cylindrical extension of this split wall was used where the impeller could operate in with a small tip gap of 5 mm. Later designs do not respect any more this split wall diameter and operate freely from any stationary sidewall, but they may incorporate such outer sidewalls in the rotating part, as for design index 3-5 or partially index 6-7.

Experimental Results

In *Figure 5*, experimental results, namely duty curves and total-to-static efficiency curves, for the counter rotating secondary impeller index 1 is shown. The rotation speed of the primary impeller is constant at $n_{prim} = 1100\,rpm$. The peak efficiency is $\eta_{stat,peak} = 68.5\%$ occurs at a peak-efficiency-optimum secondary impeller speed of $n_{sec,opt} = 900\,rpm$ (these two main results are indicated for all prototypes in *Table 2*).

The secondary speed gaining best efficiency is in this case lower compared to the design speed $n_{sec} = 1000\,rpm$ used in the CFD based design of the secondary impeller (*Table 1)*. For lower and higher n_{sec}, the maximum efficiency decreases. It can be observed anyhow, that depending on the duty point, the ideal n_{sec} considering efficiency varies in the course of the duty point curve.

The duty curve gets steeper for growing secondary impeller speeds, meaning that for fixed air flow rates Q_V, the pressure rise Δp_{stat}increases with increasing n_{sec}.

In *Figure 6,*as representative measure for the loudness of the fan, the specific and A-rated sound power emitted on the downstream side of the fan $Lw6$ is indicated. In this paper, only the specific sound power is used, which is computed according for example to Eck [9]. For all measured n_{sec} in this case, the A-rated specific sound power $Lw6$ is increasing with the secondary impeller rotation speed n_{sec}. Note therefore, that the ideal n_{sec} regarding efficiency differs from the ideal speed regarding sound emissions. In a dynamic operation mode, n_{sec} could be adapted as function of dynamic requirements.

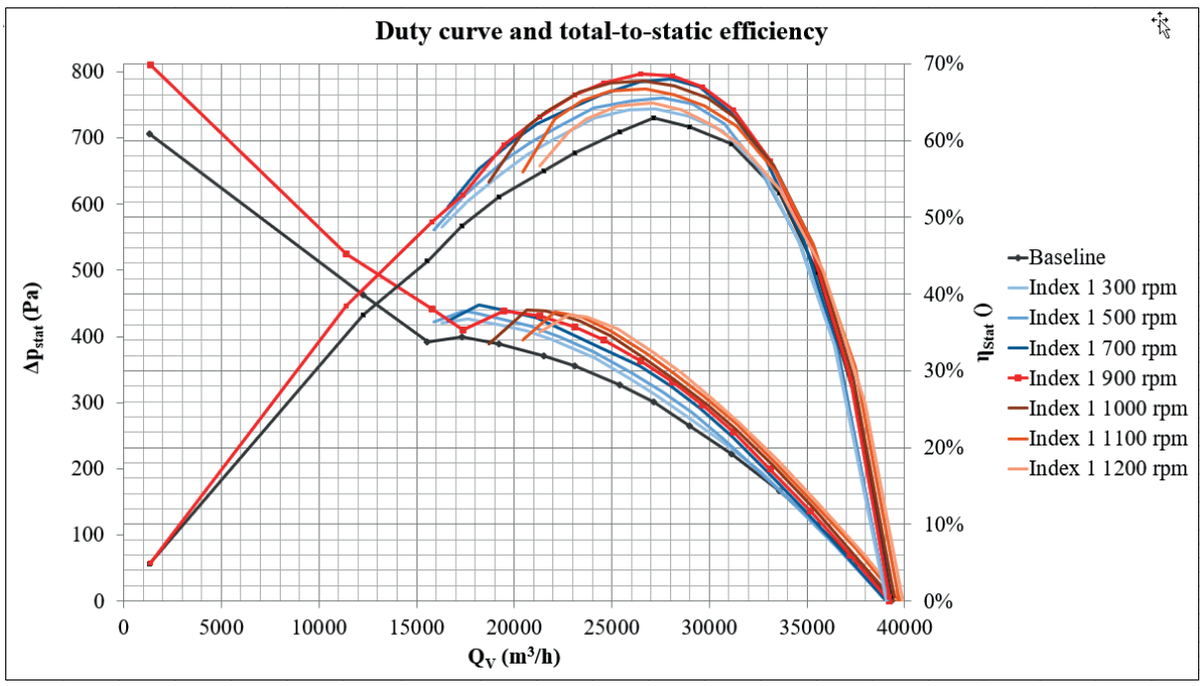


Figure 5: Duty curve and total-to-static efficiency for secondary impeller index 1

The sound power supplement $\Delta L_W 6$ at the peak efficiency point caused by the secondary fan (example: red curve in *Figure 6* for $n_{sec} = 900\,rpm\ @\ Q_V = 27000\,m^3/h$ has a sound supplement caused by the secondary impeller of $\Delta Lw6 = 10dB(A)$), which is proposed as an indicator value for the loudness of a prototype, is also given for all prototypes in *Table 2*.

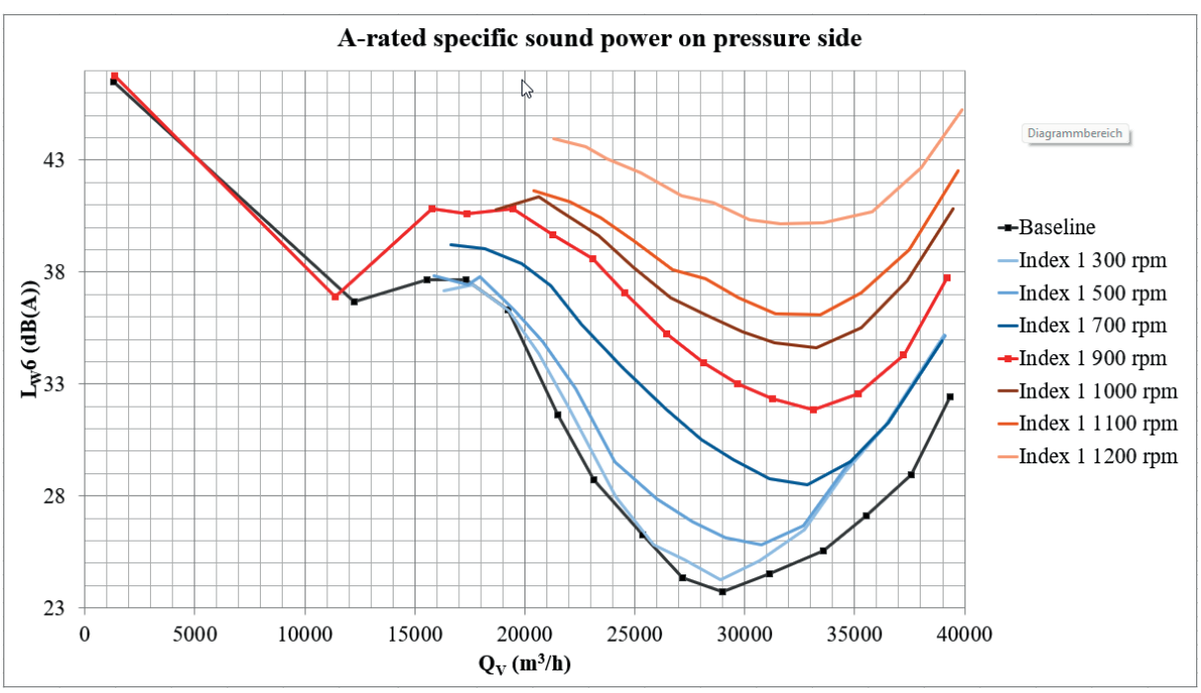


Figure 6: A-rated specific sound power on pressure side for secondary impeller index 1

Table 2: Main result parameters of experimental measurements

index	Rotation dir. (Counter/ Co)	topology	Blade count z_{sec}	D_{sec} (mm)	$n_{sec,opt}$@ max. η_{stat} (rpm)	$\eta_{stat,peak}$ (%)	$\Delta L_W 6$ @ $\eta_{stat,peak}$ (dB)	P_{sec}/P_{tot} @ $\eta_{stat,peak}$ (%)
1	Counter	Free tip (Winglet)	4	700	900	68.5	*11.0*	*10.5*
2	Co	Free tip (Winglet)	4	700	900	70.3	9.5	10.2
3	Co	Cover Ring	7	570	900	69	*3.6*	*7.4*
4	Co	Grid-Like	21/35/42	570	900	69.3	*7.9*	*7.7*
5	Co	Grid-Like	35/42	490	900	69.7	*6.3*	*6.2*
6	Co	Loop Design	4/8	570	900	70.0	*3.0*	*6.5*
7	Co	Loop Design	4/8	500	900	70.0	*2.2*	*5.1*
8	Co	Free tip (Peak)	7	589	900	70.0	*5.5*	*5.4*

The main experimental results for all manufactured prototypes of the secondary impeller are summarized in *Table 2*. Interestingly, the peak efficiency $\eta_{stat,peak}$ (maximum value for η_{stat}) always occurs at $n_{sec} = 900\,rpm$, but this may be due to a somewhat coarse resolution of the rotational speed variation of the secondary impeller in the experiments (next lower speed for n_{sec} was in the most cases in the experiment $700\,rpm$). The peak efficiency $\eta_{stat,peak}$ is for the most prototypes about 70% or slightly below – this confirms the CFD results, in most cases there is a slight upward deviation in the experiment. Of particular interest are the acoustical results, presented here as overhead specific sound power $\Delta L_W 6$ of the best efficiency operating state compared to the baseline fan at the same air flow rate. The prototypes differ significantly. Comparing index 1 and index 2, which have highest overheads $\Delta L_W 6$ as well as the highest secondary impeller diameters D_{sec}, the co-rotating variant is favourable. Reducing D_{sec} (for example, in comparison of index 4 and index 5) seems to be favourable in terms of sound generation as far as the efficiency gain can be maintained. Free tip design (index 8) has significant disadvantage compared to the design with cover ring (index 3) or the loop designs (index 6 and index 7). The grid-like designs (index 4 and index 5), anyhow, turn out to be less favourable, potential explanations are the big impeller surface and the high numbers of edges and corners, also the comparatively high blockage rate.

In addition, the power ratio of the input power for the secondary impeller to the total input power $P_{sec}/P_{tot} = P_{sec}/(P_{prim} + P_{sec})$ is given in the last column of *Table 2* as an indicator of the required driving power for the secondary impeller. The values of about 10% and below that down to 5% confirm that only a small portion of the total input power is provided by the secondary impeller to transfer additional power to a locally limited flow portion in the near hub region. This power transferred can pay off over-proportionally as it contributes to a flow stabilization and to an avoidance of flow blockage or backflow in the hub region.

Summing up the research

In *Figure 7*, a neat overview of the results is given in a $\eta_{stat,peak}$ against $L_W 6$ @ $\eta_{stat,peak}$- diagram.

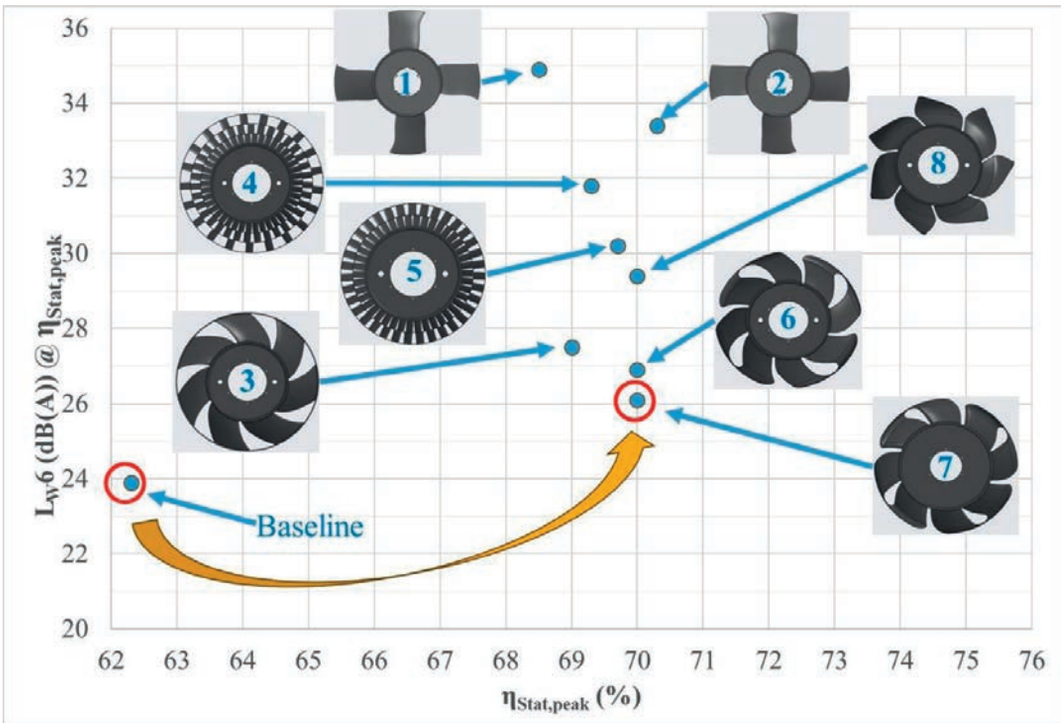


Figure 7: Graphical comparison of the results in a peak efficiency ($\eta_{stat,peak}$) against specific sound power (L_W6 @ $\eta_{stat,peak}$) diagram

Clearly, the best result is achieved with the secondary impeller index 7, enhancing the peak static efficiency $\eta_{stat,peak}$ of the baseline fan by about 7.5 %-points corresponding to a relative improvement of 12 %, at a cost of 2 $dB(A)$ in A-rated specific sound power increase, which is, in the authors estimation, an attractive trade-off for energy intensive fan applications, bearing in mind increasing energy costs. Considering the overall sustainability, it is stated, that the annual energy consumption of the baseline fan in typical applications can easily exceed 10,000 kWh which could be reduced by at least 1,000 kWh. The investment in an electrical drive with additional installed power of $P_{sec} = 800\ W$ and an impeller of diameter $D_{sec} = 500\ mm$ may be justified, depending on the specific application case.

CONCLUDING REMARKS

For a low-pressure axial baseline fan with low hub ratio $\nu = D_{hub}/D$, the approach of applying a serially arranged secondary impeller locally in a hub-near region to counteract the negative impact of hub blockage or hub backflow and to increase the total-to-static efficiency was investigated. The secondary impeller was, for the present work, installed downstream a guide vane structure and had independently adjustable rotation direction and rotation speed.

Different secondary impellers have been designed with the help of efficiency targeted CFD optimization for different framework parameters such as outer diameter, nominal rotation speed or topology. The favourite designs have been manufactured with additive prototyping techniques, build up on an anechoic fan test rig and analysed in terms of duty curve, efficiency, and sound power. Results for different rotation speeds of the secondary impeller have been recorded, and they are presented in a comparative manner with those of the baseline fan.

The main result is a significative improvement of the total-to-static efficiency from about $\eta_{stat} = 60\%$ for the baseline fan to about $\eta_{stat} = 70\%$ for fan systems with secondary impeller applied to the baseline fan. The specific sound power (A-rated) is for some designs enhanced significantly and can be influenced by different design parameters for the secondary fan.

To limit the specific sound power, it can be concluded, that low rotation speeds and low diameters of the secondary fan are helpful, whilst keeping the efficiency improvement at a maximum. Best results are achieved with co-rotating secondary impellers, being made possible by the swirl-neutralizing guide vane between the two impellers. Further, the impeller topology with a cover ring is beneficial, and, even more, a topology with loop-formed blades. In contrast, an impeller design as a grid-like fan was not interesting in terms of noise generation. Also, the design with a free peaked tip was acoustically not of interest.

The twin fan design with a secondary impeller is interesting for multiple aspects. The achievable enhancement of total-to-static efficiency $\eta_{stat,peak}$ by more than 10 % can justify the installation of the more complex twin fan design. The ratio of the rotation speeds between the two impellers can be used to optimize in real time for varying target functions such as efficiency, low sound power, or others making it a prototype of an intelligent fan system.

BIBLIOGRAPHY

[1] Strscheletzky M.: *Gleichgewichtsformen der rotationssymmetrischen Strömungen mit konstantem Drall in geraden zylindexrischen Hohlräumen.* Voith Forschung und Konstruktion, Book 5, Essay 1, **1959**

[2] Strscheletzky M.: *Zur Berechnung der Gleichgewichtsformen von rotationssymmetrischen Strömungen mit konstantem Drall in langen zylindrischen Hohlräumen.* Voith Forschung und Konstruktion, Book 8, Essay 7, **1962**

[3] Lindemann, T. B.: Optimale Niederdruckaxialventilatoren - *Optimale Niederdruck-Axialventilatoren für den Einsatz bei kleinen Reynoldszahlen.* Forschungsvereinigung Luft- und Trocknungstechnik e.V. (FLT), **2010**

[4] Lindemann, T. B.; Friedrichs; J., Stark, U.: *Development of a New Design Method for High Efficiency Swept Low Pressure Axial Fans with Small Hub/Tip Ratio.* In: ASME Turbo Expo 16-20. June **2014**

[5] Bakir, F.; Rey, R.; Moreau, S.: *Latest Developments in Automotive Engine Cooling Fan Systems Rotor-Stator Interactions.* Proceedings of the 3rd ASME, JSME Joint Fluids Engineering Conference, July 18-23, 1999, San Francisco, California, 4, pp. 487-496, American Society of Mechanical Engineers, **1999**

[6] Bakir, F.; Moreau, S.; Rey, R.; Henner, M; Borg, V.: *Experimental Aeroacoustical analysis of efficient automotive engine cooling systems.* Proceedings of Fan 2012 Symposium, Senlis, **2012**

[7] Bohl, W.: *Technische Strömungslehre.* 12. Edition, Vogel-Fachbuch, Würzburg, **2002**

[8] Laux, H.: *Beitrag zur experimentellen Untersuchung von Drallströmungen im kreiszylindrischen Rohr.* Dissertation, Berlin, **1961**

[9] Eck, B.: *Ventilatoren.* 6. Edition, Springer Verlag, **1991**

[10] Lewis, R.I.: *Turbomachinery Performance Analysis.* Book, Elsevier, **1996**

[11] Menter, F. R.: *Two-Equation Eddy-Viscosity Turbulence Models for Engineering Applications.* AIAA Journal, Vol. 32, No. 8 (1994), pp. 1598-1605, **1994**

[12] Angelis, W., Lörcher, F.: *Fan Unit with Compact Guide Vane Designed for Low Hub Ratio Axial Fans,* Proceedings of Fan 2018 Conference, Darmstadt, 18 - 20 April **2018**

[13] Lörcher, F., Hub, S.: *Effizientes und schallarmes Axialventilatorsystem mit neuartigem zonal optimiertem Nachleitrad,* Proceedings of DAGA 2023, Hamburg, 6 - 9 March **2023**

[14] Sheard, A.G.: *The Effects of Inlet Box Aerodynamics on the Mechanical Performance of a Variable Pitch in Motion Fan,* Advances in Acoustics and Vibration, vol. 2012, Hindawi Publishing Corporation, **2012,** doi:10.1155/2012/278082

[15] Bianchi, S., Corsini, A., Sheard, A.G.: *A Critical Review of Passive Noise Control Techniques in Industrial Fans,* Transactions of the ASME, Journal of Engineering for Gas Turbines & Power, vol. 136(4), paper no. 044001, pp. 1–10, **2014**

[16] ISO 5801:2017, **2017**, *Industrial Fans: Performance Testing Using Standardised Airways.*

ANNEXES / APPENDIXES

Variable Symbols, Units, Definitions

D	(m)	inner diameter of the fan housing
D_{hub}	(m)	hub diameter of the baseline fan impeller
Q_V	(m^3/h)	volume flow rate
Δp_{stat}	(Pa)	static pressure rise of the fan
$P_{prim}, P_{sec}, P_{tot}$	(W)	shaft power for primary impeller, secondary impeller, and total sum
$n_{prim},\ n_{sec}$	(rpm)	rotation speed of primary and secondary impeller
$D_{prim},\ D_{sec}$	(m)	maximum diameter of primary and secondary impeller
$\eta_{stat} = (Q_V \cdot \Delta p_{stat})/P_{tot}$	$(.)$	total to static efficiency
L_W5, L_W6	$(dB(A))$	A-rated specific sound power emitted to the suction and pressure side



ASSESSMENT OF THE NUMERICAL PREDICTION ACCURACY OF DISCHARGE FLOW FEATURES OF A ROTOR-ONLY LOW-PRESSURE AXIAL FAN

Hauke WITTE[1], Christoph BODE[1]

[1] *Instute of Jet Propulsion and Turbomachinery, Technische Universität Braunschweig,*
Hermann-Blenk-Str. 37, 38108 Braunschweig, Germany

SUMMARY

The static pressure recovery in the discharge of rotor-only low-pressure axial fans has a significant impact on their overall total-static efficiency and is driven by quantities that are difficult to measure, such as streamline curvature. Consequently, its investigation relies on numerical simulations. In this paper, a Delayed Detached Eddy Simulation (DDES) is validated against operating point and hot-wire measurements and is compared to (U)-RANS simulations. Although the RANS already deviates from the measured operating point, it is still sufficiently accurate in this regard given its computational efficiency. However, a decomposition of the pressure recovery further emphasizes the weaknesses of the RANS and justifies the higher computational effort of the DDES.

INTRODUCTION

Rotor-only low-pressure axial fans are used in a wide range of applications to provide high airflow at low pressure ratios. Examples include forced convection in cooling or heating applications and ventilation systems.

Typically, such fans discharge a swirling jet flow directly into a free atmosphere without the use of outlet guide vanes. Inside of this jet flow, a static pressure recovery occurs, partially converting kinetic energy back into potential energy, as shown first by Marcinowski in [1]. Although this static pressure recovery is neglected in most existing fan efficiency optimization studies - see, for example, Bamberger and Carolus [2] or Wang and Kruyt [3] -, it must be taken into account when evaluating the entire energy conversion process of the machine.

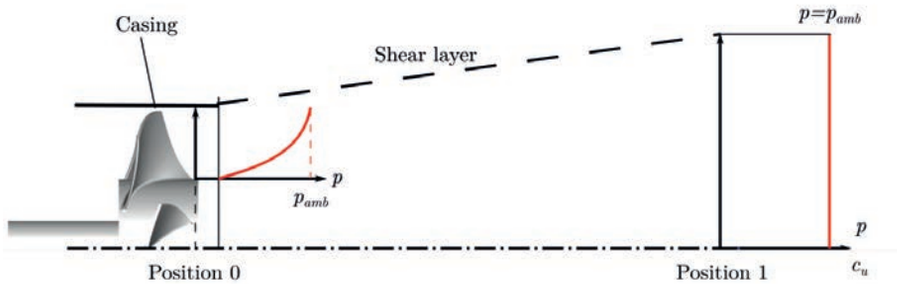


Figure 1: Schematic visualization of the static pressure recovery in the discharge flow of the fan

A fundamental description of the static pressure recovery can be derived from a momentum balance, i.e. the Navier-Stokes equations. Since time-averaged values are of interest, it is convenient to use the Reynolds-averaged Navier-Stokes (RANS) equations. In addition, due to the axisymmetry of the time-averaged flow field, a cylindrical coordinate system is used and incompressibility is assumed. Under these assumptions, the radial component of the RANS equations in an integral formulation defines the relationship between the static pressure and the velocity field as:

$$p(r) = \int_r^{r_{tip}} \rho c_x \frac{\partial c_r}{\partial x} dr + \int_r^{r_{tip}} \rho c_r dc_r - \int_r^{r_{tip}} \rho \frac{c_u^2}{r} dr + \int_r^{r_{tip}} f_v dr + \int_r^{r_{tip}} f_t dr + p(r_{tip}) \tag{1}$$

where f_v denotes all viscous forces and f_t denotes all turbulent effects (i.e. the Reynolds stresses). The static pressure recovery p_{rec} can be assessed by evaluating and averaging equation 1 at both position 0 and position 1 marked in figure 1:

$$p_{rec} = \overline{p_{s,1}(r)} - \overline{p_{s,0}(r)} = p_{amb} - \overline{p_{0,s}(r)}. \tag{2}$$

The bar denotes a mass flow weighted average. At position 1, the average pressure is equal to the ambient pressure. Replacing the static pressure at position 0 $\overline{p_{0,s}(r)}$ by equation 1 yields:

$$\begin{aligned} p_{rec} &= -\overline{\int_r^{r_{tip}} \rho c_x \frac{\partial c_r}{\partial x} dr} - \overline{\int_r^{r_{tip}} \rho c_r dc_r} + \overline{\int_r^{r_{tip}} \rho \frac{c_u^2}{r} dr} - \overline{\int_r^{r_{tip}} f_v dr} - \overline{\int_r^{r_{tip}} f_t dr} + p_{amb} - p(r_{tip}) \\ &= -\overline{p_{slc}(r)} - \overline{p_{rad}(r)} + \overline{p_{inertial}(r)} - \overline{p_v(r)} - \overline{p_t(r)} + p_{amb} - p(r_{tip}). \end{aligned} \tag{3}$$

From this equation, six contributors to the static pressure recovery can be identified: $\overline{p_{slc}(r)}$ summarizes the impact of streamline curvature at position 0, $\overline{p_{rad}(r)}$ is connected to a radial momentum transport, $\overline{p_{inertial}(r)}$ incorporates the inertial forces due to a swirl component in the discharge flow, $\overline{p_v(r)}$ and $\overline{p_t(r)}$ include all viscous / turbulent effects and the pressure imprinted at the casing $p(r_{tip})$ effects the overall level of the pressure profile at position 0. The value of $p(r_{tip})$ might differ from the ambient pressure due to a diffuser at the fan outlet.

According to ISO 5801, the total-static efficiency η_{ts} is defined by the total-static fan pressure calculated with the ambient pressure and can be expressed as

$$\eta_{ts} = \frac{\dot{V}\Delta p_{ts}}{P_R} = \frac{\dot{V}\left(p_{amb} - p_{t,in}\right)}{P_R} = \frac{\dot{V}\left(\Delta p_t - \overline{p_{dyn,0}(r)} + p_{rec}\right)}{P_R} \tag{4}$$

$$= \eta_i + \Delta\eta_{exit} + \Delta\eta_{rec}, \tag{5}$$

where Δp_t is the total pressure increase over the fan, $p_{dyn,0}(r)$ is the dynamic pressure at position 0 and P_R is the mechanical power delivered to the fan. When using this definition, η_i is the inner

efficiency of the fan, $\Delta\eta_{exit}$ summarizes the kinetic energy lost in the discharge (note that $\Delta\eta_{exit}$ is negative), and $\Delta\eta_{rec}$ represents the effect of the static pressure recovery. Using the decomposition of the static pressure recovery from equation 3, this can be extended to

$$\eta_{ts} = \eta_i + \Delta\eta_{exit} + \frac{\dot{V}}{P_R}\left(-\overline{p_{slc}(r)} - \overline{p_{rad}(r)} + \overline{p_{inertial}(r)} - \overline{p_v(r)} - \overline{p_t(r)} + p_{amb} - p(r_{tip})\right) \tag{6}$$

$$= \eta_i + \Delta\eta_{exit} + \Delta\eta_{slc} + \Delta\eta_{rad} + \Delta\eta_{inertial} + \Delta\eta_v + \Delta\eta_t + \Delta\eta_{diffuser}. \tag{7}$$

This directly gives the effect of each component of the static pressure at position 0 on the total-static efficiency.

Of the above mentioned components of the static pressure recovery, the inertial forces are the most significant. In addition, they are a function of the velocity profiles only and therefore of the fan vortex design, not the velocity gradients. This makes it possible to investigate their fundamental sensitivities analytically as was done in Witte et al. in [4]. From the investigated vortex designs, a slight shift of work towards the casing showed an optimal static pressure recovery through inertial forces. Additionally, small hub-to-tip ratios generally yield higher pressure recoveries. However, the competing trend of decreasing hydraulic efficiency of the fan with decreasing the hub-to-tip ratio due to high aerodynamic blade loadings at the hub can compensate this effect.

In [5], the authors used a delayed detached eddy simulation (DDES) analogous to the one used in this paper to demonstrate that static pressure recovery accounts for up to 8%-points of the total-static efficiency. However, this study also revealed, that the impact of the streamline curvature and viscous forces is significant and - in contrast to the inertial forces - hard to estimate in the preliminary stages of the fan design, making further investigations necessary.

However, since both the streamline curvature as well as the viscous forces are difficult to measure, further investigations rely heavily on numerical simulations. In [6] it was shown, that standard RANS-based simulations with turbulence models using eddy-viscosity approaches are not capable of correctly depicting even the time averaged integral and local flow quantities of the swirling jet flow such as velocity and pressure distributions in the free atmosphere. In the same study however, the DDES matched the available experimental data (time-averaged PIV- and five-hole-probe-measurements) well.

In this work the validation of the simulations is extended by comparing the numerical results to experimental measurements of the operating point and hotwire data. Additionally, the impact of the individual components from equation 3 on the static pressure recovery is evaluated for the investigated numerical methods.

METHODOLOGY

Fan design method

The design methodology of the fan investigated in this work is described in [5]. It is based upon the design method developed by Lindemann et al. in [7] and is extended to incorporate the isentropic simple radial equilibrium, allowing for a well defined variation of the fan vortex design. The aerodynamic and geometric boundary conditions of the fan are shown in table 1.

Numerical setup

A cross section of the computational domain visualizing its dimensions and the numerical boundary conditions as well as the hotwire measurement positions (MP) is shown in figure 2, with the instantaneous axial velocity component as contour. The simulation includes only a 72° portion of the full 360° domain utilizing the symmetry.

Table 1: Boundary conditions of the fan design

Parameter	Value
Flow coefficient	0.215
Total-total work coefficient	0.300
Tip radius	0.2485 m
Rotational speed n	22.5 Hz
Hub-to-tip ratio	0.5
Tip gap	0.0015 m
Number of blades z	5

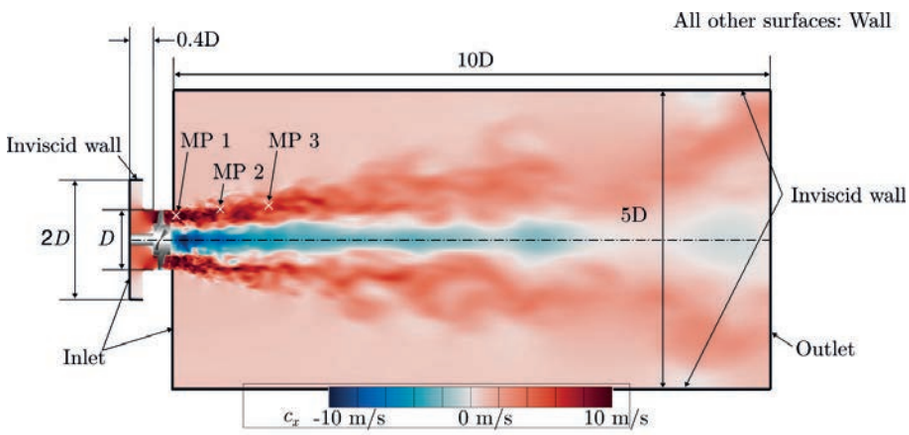


Figure 2: Computational domain with boundary conditions and hotwire measurement positions (MP) (after [5])

Three different numerical setups are investigated in this paper: A steady RANS setup, an unsteady RANS setup (URANS), both with eddy viscosity turbulence modeling and a non-zonal DDES. Both the RANS and the URANS setup use the well known k-ω-SST turbulence model developed by Menter et al. ([8]). The set of governing equations for the DDES follows the works of Strelets ([9]) and Gritskevitch et al. ([10]). This approach is also based on the k-ω-SST turbulence model. However, the destruction term of the modeled turbulent kinetic energy is adjusted to

$$D_{k,DDES} = \frac{\rho k^{\frac{3}{2}}}{l_{RANS} - f_d \max\left(0, l_{RANS} - C_{DES}\Delta_{DES}\right)}, \tag{8}$$

such that the active length scale in the denominator determines whether the simulation is in RANS- or LES-mode. When l_{RANS} is small (which is desired for example in attached boundary layers), it is the active length scale, and the model works as the original RANS-formulation. Otherwise, when l_{RANS} growths and $C_{DES}\Delta_{DES}$ is sufficiently small, the destruction terms growths and the modeled turbulence kinetic energy vanishes - the simulation is in LES-mode. The shielding function f_d further delays the onset of the LES-mode (thus delayed DES) to prevent the premature onset of the LES-mode. The computation of the subgrid length scale Δ_{DES} uses a formulation based on the local vorticity vector and the cell size developed by Shur et al. [11]. For both setups, the γ-model formulated by Menter et al. in [12] is used to account for the laminar-turbulent transition of boundary layers. The resulting set of equations is discretized with a finite volume method and a spatial accuracy of second order and an Euler-backwarts temporal discretization of second order accuracy and the CFL number is between 50 and 100. The flow solver TRACE developed by the German Aerospace Center is used (see [13]). The numerical grid - which is the same for all three setups - consists of approximately $5.70 \cdot 10^6$ cells. To properly resolve the boundary layer, a prism layers are used at the viscous walls and the dimension of the first cell is chosen, such that the nondimensional wall coordinate y^+ is less than or equal to one

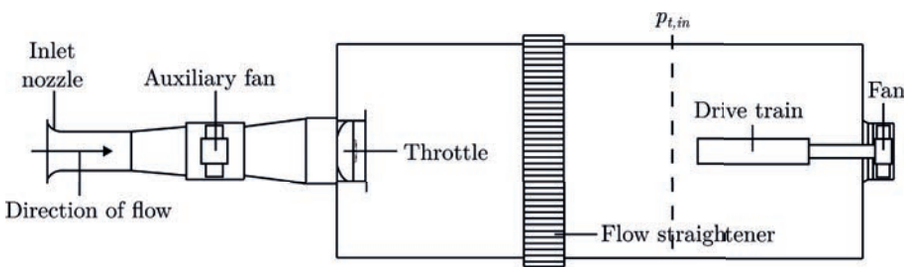


Figure 3: Schematic representation of the test bench

throughout the domain. The number of cells is the result of a grid convergence study in accordance with Roache [14] performed with the RANS-setup. The grid convergence index of the mesh used in this paper is $7.2 \cdot 10^{-4}$. The size of the physical time step per iteration for the URANS and the DDES was set to 1/100th of the blade passing frequency as in

$$t_{iter} = \frac{1}{z \cdot n \cdot 100} = \frac{1}{5 \cdot 22.5\ \text{Hz} \cdot 100} = 8.89 \cdot 10^{-5}\ \text{s}. \tag{9}$$

The resulting computational effort for the DDES exceeds the effort for the RANS by a factor of approximately 4.5 to 8.

Experimental setup

The blades are manufactured in a stereolithography 3D-printing process and the assembled fan is investigated in an inlet-side test chamber test bench for performance measurement in a free inlet free outlet configuration according to ISO 5801 type A [15]. Prior to the experimental campaign, a FEM analysis of the blade geometry was performed to ensure that the deformation of the blades during rotation is acceptable.

Figure 3 schematically shows the test bench with the location of the total inlet pressure measurement ($p_{t,in}$). The volumetric flow rate is measured at the inlet nozzle and the ambient pressure is recorded in the lab building outside of the fan discharge. The combination of the auxiliary fan and the throttle allows for the operating point to be adjusted along a characteristic line. The non-dimensional quantities defining the operating point are the flow coefficient φ and the total-static work coefficient ψ_{ts}:

$$\varphi = \frac{\dot{V}}{\pi \cdot \left(r_{casing}^2 - r_{hub}^2\right) \cdot u_{tip}}, \tag{10}$$

$$\psi_{ts} = \frac{2\left(p_{amb} - p_{t,in}\right)}{\rho \cdot u_{tip}^2} \text{ and} \tag{11}$$

The hotwire measurements were done with a CTA system from Dantec Dynamics using a single wire probe aligned normal to the average flow direction at the measurement planes. The average flow direction at each measurement plane was measured with a five-hole-probe prior to the hot-wire measurement. The sampling frequency f_s was set to 125 kHz and a number of $n_s = 250{,}000$ samples were recorded per measurement, resulting in a signal length of 2 s.

RESULTS AND DISCUSSION

Characteristic line and operating point

Figure 4 shows the experimental and numerical non-dimensional characteristic line of the investigated fan. The detail view shows the proximity of the design flow coefficient of $\varphi = 0.215$. A comparison of the RANS and URANS results shows that URANS does not improve the results over RANS.

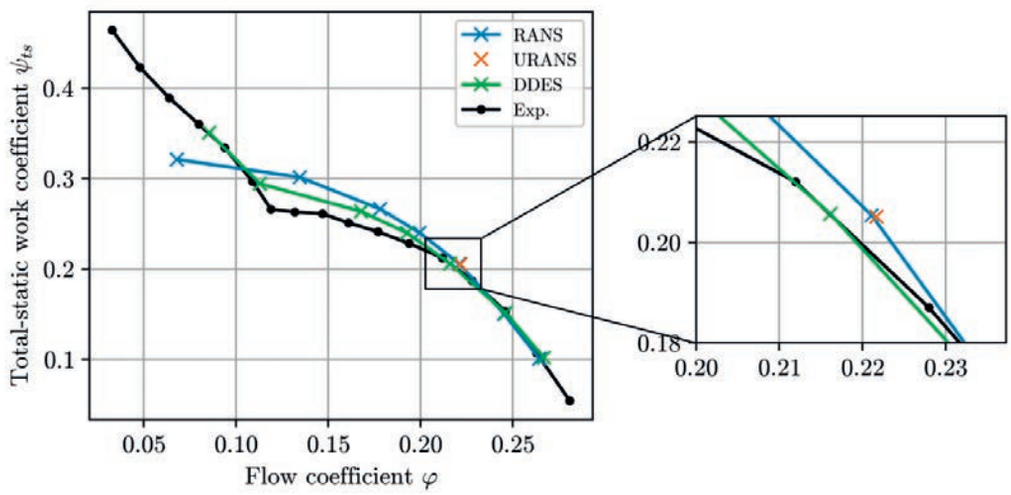


Figure 4: Characteristic line of the investigated fan and numerical results

Therefore, the URANS simulations were performed only for the design operating point and not for the full characteristic line. However, when the RANS and the DDES results are compared, significant differences are found. The DDES almost exactly matches the experimental results at the design operating point, while the RANS slightly overestimates the mass flow. Towards higher flow coefficients, both the RANS and the DDES agree well with the experimental data. The most significant deviations between the two are observed with decreasing flow coefficients. Here, the RANS curve is above the DDES results. For a given work coefficient (i.e. a given fan pressure rise) the RANS increasingly overestimates the mass flow. An exception is when the flow coefficient is less than 0.1, since the RANS does not show the distinctive kink in the characteristic line observed in the experimental and DDES results. Except for the overestimation of the work coefficient between the kink in the characteristic line and the design operating point, the DDES is in good agreement with the experimental data.

Breakdown of the static pressure recovery

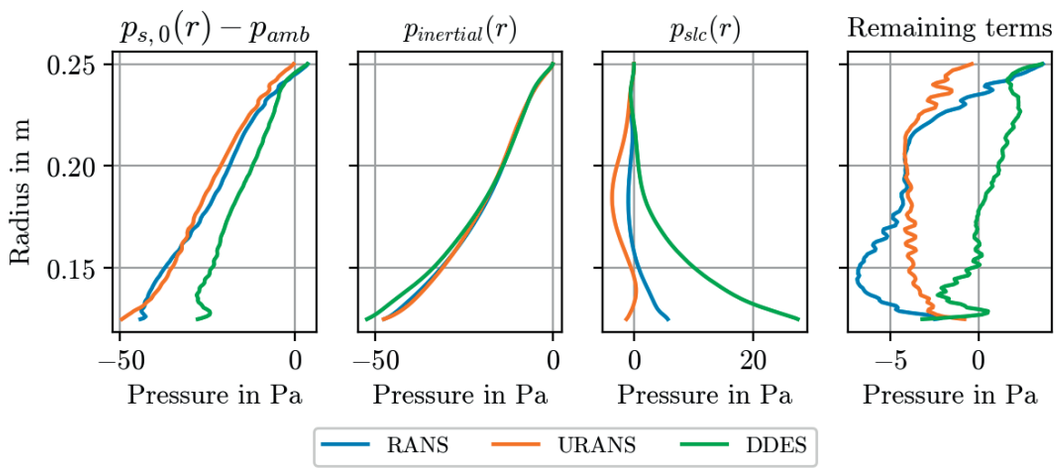


Figure 5: Circumferential and time-averaged radial profiles of the static pressure and its components at position 0

Figure 5 shows numerical results of the static pressure profile at position 0 $p_{s,0}(r)$ (left) relative to the ambient pressure and its components due to inertial forces $p_{inertial}(r)$ (center left), streamline

curvature $p_{slc}(r)$ (center right) and the remaining terms of equation 3 for the simulations at design conditions. Due to the formulation of equation 3, the sum of the profiles shown in the three right profiles gives the profile shown in the left plot, whose negative mass flow weighted average gives the static pressure recovery. Note the different ranges of the x-axis for all plots. The breakdown of the static pressure recovery confirms previous findings: Inertial forces have the largest effect. Furthermore, it can be seen that the streamline curvature has the opposite sign to the inertial forces and thus has a negative effect: It reduces the static pressure recovery and thus directly reduces the total-static efficiency. In addition, it is the streamline curvature, where the results of the different numerical models differ the most: The DDES shows a much stronger overall effect of the streamline curvature. The remaining terms in the momentum balance (i.e., the radial momentum transport, the viscous and the turbulent forces) have a small overall effect on the static pressure recovery. Differences in the static pressure profile at position 0 and its components resulting from the flow field are also visible in the circumferential and time-averaged meridional contour (S2 plane) of the axial velocity c_x shown in figure 6. For the DDES, the axial velocity near the hub at the fan outlet is reduced compared to the RANS/URANS results, implying a shift of the mass flow toward the core of the annulus, resulting in an increase in streamline curvature.

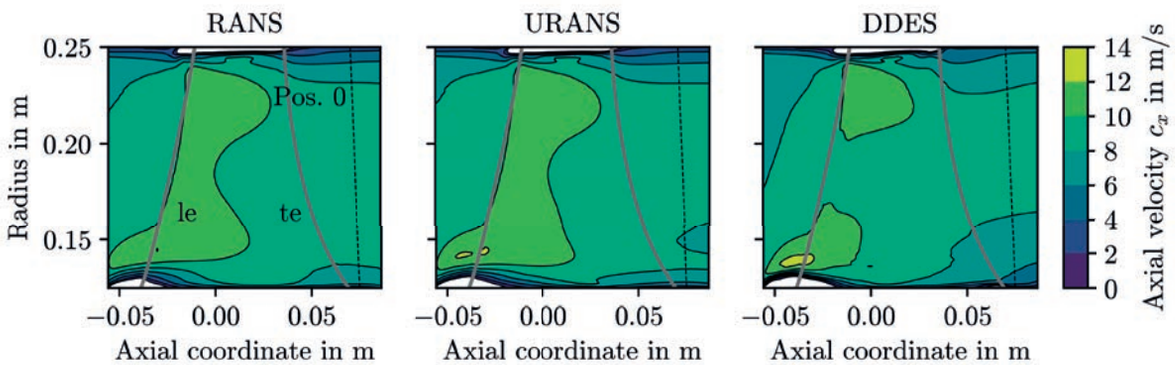


Figure 6: Circumferential and time-averaged contour of the axial velocity c_x in the meridional (S2) plane. The leading (le) and trailing (te) edges of the fan blade are shown in gray, and position 0 is marked with a dashed line.

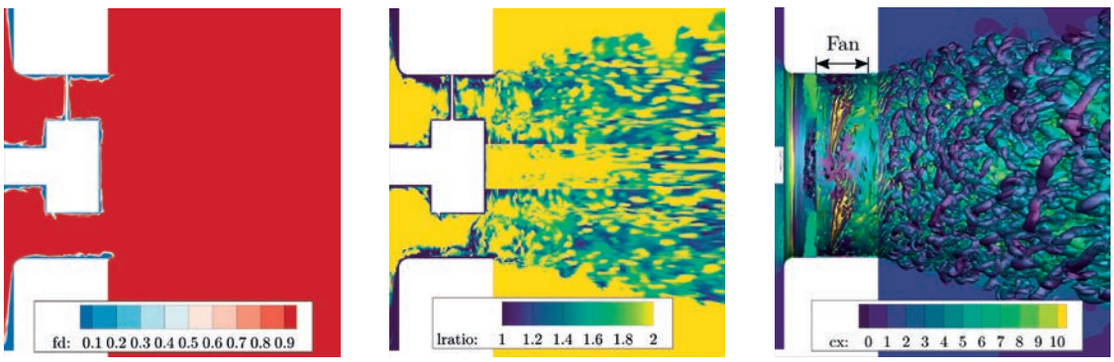
Table 2 shows the effect of the static pressure recovery and its components on the total-static efficiency as defined by equation 7. The results vary widely: While the RANS predicts an increase in the total static efficiency of 8.7 %-points from the static pressure recovery, the URANS predicts 9.5 %-points and the DDES only 5.5 %-points. These differences are due equally to the streamline curvature and the remaining components (i.e. $\Delta\eta_{rad}$, $\Delta\eta_{v}$, $\Delta\eta_{t}$, $\Delta\eta_{diffuser}$), while the effect of the inertial forces is similar for all methods.

Table 2: Breakdown of the effect of the static pressure recovery on the total-static efficiency

	Total $\Delta\eta_{rec}$	$\Delta\eta_{inertial}$	$\Delta\eta_{slc}$	Remaining
RANS	0.087	0.074	0.000	0.012
URANS	0.095	0.074	0.007	0.014
DDES	0.055	0.070	-0.012	-0.001

Resolution of turbulent structures in the DDES

To further assess the quality of the DDES, figure 7 shows the relevant model quantities and iso-surfaces of the Q-criterion Q_{crit} of an instantaneous solution. Figure 7a shows the shielding function. Values of $f_d = 1$ allow for the simulation to run in LES mode, while $f_d = 0$ ensures RANS mode.



(a) DDES shielding function f_d (see equation 8) *(b) Length scale ratio l_{ratio} as defined in equation 12* *(c) Iso-surfaces of $Q_{crit} = 10^5$. Contour is the axial velocity*

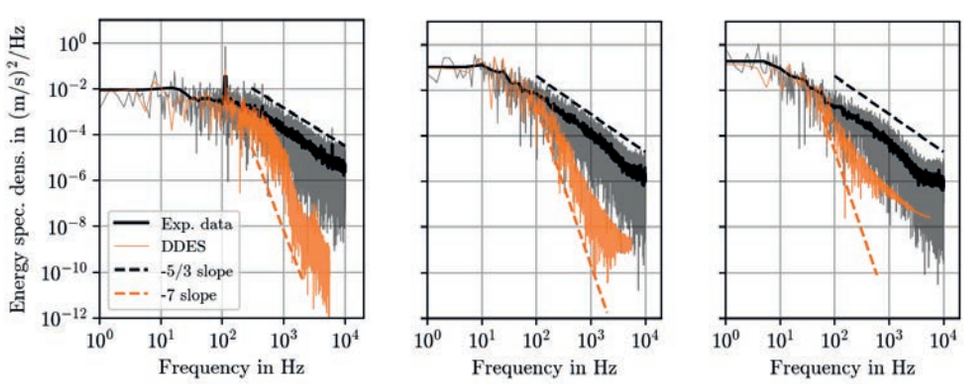
Figure 7: Meridional slice through the instantaneous solution of the DDES

As intended, f_d prevents the onset of the LES mode only in the boundary layers around the viscous walls. When $f_d = 1$, the ratio between the RANS turbulent length scale and the DDES length scale l_{ratio} defined as

$$l_{ratio} = \frac{l_{RANS}}{l_{RANS} - f_d \max\left(0, l_{RANS} - C_{DES}\Delta_{DES}\right)} \tag{12}$$

distinguishes between RANS- and LES-mode: For $l_{ratio} > 1$, the effective length scale of the destruction term of the turbulent kinetic energy falls below l_{RANS} and the modeled turbulent kinetic energy is reduced. From figure 7b, is it apparent, that in large parts of the fan discharge l_{ratio} is in fact exceeding unity, although low values are present in regions of high vorticity due to the resolved structures. The resolved turbulent structures of the DDES are made visible by iso-surfaces of $Q_{crit} = 10^4$ in figure 7c.

Turbulent energy cascade



(a) MP 1 *(b) MP 2* *(c) MP 3*

Figure 8: Comparison of the experimental (black) and numerical (orange) energy density spectra

The time signals of the velocity $c(t)$ from the hotwire measurements and the DDES are transformed into the frequency domain through a discrete Fourier transformation (DFT) and are expressed as energy spectral density $E(f)$ through

$$E(f) = \frac{|\mathrm{DFT}(c(t))|^2}{f_s \cdot n_s}, \tag{13}$$

with the sampling frequency f_s (inverse of the time step for the DDES) and the number of samples n_s (see for example [16]). The results for MP 1, MP 2 and MP 3 are shown in figure 8. Additionally the

slopes of an inertial subrange according to Kolmogorov ($E(f) \sim f^{-5/3}$) and a dissipative subrange according to Heisenberg ($E(f) \sim f^{-7}$) are depicted. A first observation is, that the asymptotic value of the energy spectrum for $f \to 0$ agrees well between experiment and simulation. This can be interpreted - under the assumption of a homogeneous and isotropic turbulence (see Roach [17]) - that the macro scale of the turbulent structures is correctly resolved in the simulation. However, the agreement between experiment and simulation deteriorates with increasing frequencies. The experimental data shows a broad inertial subrange for all measurement positions, while a dissipative subrange cannot be observed. The authors assume this is due to the dissipation occurring at amplitudes below the noise level of the signal, since the turbulent Reynolds number of the flow is high. Apparently, the present DDES is not capable of resolving the inertial subrange: The energy spectral density drops significantly below the experimental data for increasing frequencies and this premature drop of $E(f)$ has the slope of a dissipative subrange. For higher frequencies, the numerical simulation seems to be too dissipative. It is not clear to authors whether the excessive numerical dissipation is due to the grid spacing, the anisotropy of the grid (as described for example by Shur et al. in [11]) or due to the spatial and temporal discretization scheme. However, similar observations have been made in the available literature for example by Fischer et al. [18] or Odier et al. [19].

CONCLUSIONS

Increasing the fidelity of the numerical model from RANS / URANS to DDES increases the prediction accuracy with respect to the operating point especially for off-design conditions. Since RANS is already in good agreement with the experimental results at design conditions, the improvement here is rather small. However, when the effect of the static pressure recovery on fan efficiency is evaluated and broken down into its components, larger deviations are found. Especially the prediction of the streamline curvature differs between RANS / URANS and DDES.

While the presented DDES agrees well with the measured operating point, the turbulent energy cascade does not match the experimental data as good. Excessive numerical dissipation for high frequency ranges was observed in the present simulation. However, further investigation is needed to understand the origin of this spurious dissipation and whether the flow field and the static pressure recovery would differ significantly if the full spectrum were resolved in the simulation.

REFERENCES

[1] H. Marcinowski, "Optimalprobleme bei Axialventilatoren," German, Ph.D. dissertation, Technische Hochschule Karlsruhe, Karlsruhe, Germany, **1956**.

[2] K. Bamberger and T. Carolus, *Efficiency limits of fans*, en, Proceedings of the Institution of Mechanical Engineers, Part A: Journal of Power and Energy vol. 234, no. 5, pp. 739–748, **2020**, ISSN: 0957-6509, 2041-2967. DOI: 10.1177/0957650919876838. (visited on 10/18/2022).

[3] J. Wang and N. P. Kruyt, *Design for High Efficiency of Low-Pressure Axial Fans With Small Hub-to-Tip Diameter Ratio by the Vortex Distribution Method*, en, Journal of Fluids Engineering vol. 144, no. 8, p. 081 201, **2022**, ISSN: 0098-2202, 1528-901X. DOI: 10.1115/1.4053555. (visited on 05/17/2023).

[4] H. Witte, C. Bode, and J. Friedrichs, *Potential of static pressure recovery of rotor-only low-pressure axial fans*, International Journal of Turbomachinery, Propulsion and Power vol. 8, no. 3, **2023**. DOI: 10.3390/ijtpp8030033.

[5] H. Witte and C. Bode, *Impact of Blade Design on Static Pressure Recovery of Rotor-Only Low-Pressure Axial Fans*, in *Proceedings of the ASME 2024 Fluids Engineering Division Sum-*

mer Meeting FEDSM2024, Anaheim, California, USA: American Society of Mechanical Engineers, **2024**. DOI: 10.1115/FEDSM2024-123826.

[6] H. Witte and C. Bode, *Experimental and Numerical Characterization of the Discharge Flow of Low-Pressure Rotor-Only Axial Fans*, in *Proceedings of the The 9th European Congress on Computational Methods in Applied Sciences and Engineering ECCOMAS Congress*, Lisboa, Portugal, **2024**. DOI: 10.23967/eccomas.2024.126.

[7] T. B. Lindemann, J. Friedrichs, and U. Stark, *Development of a New Design Method for High Efficiency Swept Low Pressure Axial Fans With Small Hub/Tip Ratio*, in *Volume 1A: Aircraft Engine; Fans and Blowers*, Düsseldorf, Germany: American Society of Mechanical Engineers, **2014**. DOI: 10.1115/GT2014-25932.

[8] F. R. Menter, M. Kuntz, and R. Langtry, *Ten Years of Industrial Experience with the SST Turbulence Model*, Heat and Mass Transfer vol. 4, **2003**.

[9] M. Strelets, *Detached eddy simulation of massively separated flows*, in *39th Aerospace Sciences Meeting and Exhibit*, Reno,NV,U.S.A.: American Institute of Aeronautics and Astronautics, **2001**. DOI: 10.2514/6.2001-879.

[10] M. S. Gritskevich, A. V. Garbaruk, J. Schütze, and F. R. Menter, *Development of DDES and IDDES Formulations for the k-ω Shear Stress Transport Model*, Flow, Turbulence and Combustion vol. 88, no. 3, **2012**. DOI: 10.1007/s10494-011-9378-4.

[11] M. L. Shur, P. R. Spalart, M. K. Strelets, and A. K. Travin, *An Enhanced Version of DES with Rapid Transition from RANS to LES in Separated Flows*, Flow, Turbulence and Combustion vol. 95, no. 4, **2015**. DOI: 10.1007/s10494-015-9618-0.

[12] F. R. Menter, P. E. Smirnov, T. Liu, and R. Avancha, *A One-Equation Local Correlation-Based Transition Model*, Flow, Turbulence and Combustion vol. 95, no. 4, **2015**. DOI: 10.1007/s10494-015-9622-4.

[13] Institute of Propulsion Technology, *Trace user guide*, URL https://www.trace-portal.de/userguide accessed on 17.11.2024, German Aerospace Center (DLR), **2024**.

[14] P. J. Roache, *Verification of Codes and Calculations*, en, AIAA Journal vol. 36, no. 5, pp. 696–702, **1998**, ISSN: 0001-1452, 1533-385X. DOI: 10.2514/2.457. [Online]. Available: https://arc.aiaa.org/doi/10.2514/2.457 (visited on 10/18/2022).

[15] ISO, *5801:2017; Fans - Performance testing using standardized airways*, de. Geneva, Switzerland: International Organization for Standardization, **2018**.

[16] L. A. El-Gabry, D. R. Thurman, and P. E. Poinsatte, *Procedure for Determining Turbulence Length Scales Using Hotwire Anemometry*, in *Technical Memorandum GRC-E-DAA-TN4063 of the Glenn Research Center*, NASA, **2014**.

[17] P. Roach, *The generation of nearly isotropic turbulence by means of grids*, International Journal of Heat and Fluid Flow vol. 8, no. 2, pp. 82–92, **1987**. DOI: 10.1016/0142-727X(87)90001-4.

[18] L. Fischer, M. Straußwald, and M. Pfitzner, *Analysis of Large Eddy Simulations and 1D Hot-Wire Data to Determine Actively Generated Main Flow Turbulence in a Film Cooling Test Rig*, Journal of Turbomachinery vol. 144, no. 11, p. 111 003, **2022**. DOI: 10.1115/1.4054778. (visited on 11/14/2024).

[19] N. Odier, F. Duchaine, L. Gicquel, *et al.*, *Evaluation of Integral Turbulence Scale Through the Fan Stage of a Turbofan Using Hot Wire Anemometry and Large Eddy Simulation*, in *Volume 2C: Turbomachinery*, Oslo, Norway: American Society of Mechanical Engineers, **2018**, V02CT42A021. DOI: 10.1115/GT2018-75741.



NUMERICAL INVESTIGATION OF SCALING EFFECTS ON THE PERFORMANCE CHARACTERISTICS OF LARGE-SCALE AXIAL FLOWS FANS

Tristan Oliver LE ROUX, Chris MEYER,
Sybrand Johannes VAN DER SPUY

Stellenbosch University, The Department of Mechanical and Mechatronic Engineering, Joubert Street, POB 7602, Stellenbosch, South Africa

SUMMARY

Large diameter Axial flow fans are predominantly used for cooling purposes, such as in air-cooled heat exchangers. Since it is difficult to experimentally test large-scale fans in the controlled environments provided by fan test facilities, smaller scaled-down versions of the fans are tested instead. Scaling laws (affinity laws) are then used to determine the performance characteristics of the large-scale fan.

The size difference between two scaled fans means that it is not possible to match their Reynolds numbers when testing with the same test fluid.

A comparison is conducted using experimental results and four numerical models for two different fans, which are scaled to different fan sizes: 0.63 m, 1.542 m, 3.6576 m and 7.3152 m, to determine the effect of the Reynolds number on the performance characteristics of an axial flow fan. The numerical geometries are based on the M- and B2a-fan, and are tested in the A-type experimental setup fan test facility at Stellenbosch University, which is used to obtain the experimental results.

It was found that as the fan size increases, and thus the Reynolds number increases, the performance characteristics improve and tend toward their performance limits, which correlates with the Reynolds number effect on the lift and drag properties of aerofoils.

INTRODUCTION

Axial flow fans are predominantly used for cooling purposes. One such application is within air-cooled heat exchangers. Since wet-cooled alternatives require a considerable amount of water to operate, air-cooled systems reduce the water consumption while still providing a cost-effective substitute [1]. Thus, in regions with dry climates where water is scarce, air-cooled heat exchangers are a preferable alternative to wet-cooled systems. Air-cooled heat exchangers are therefore very convenient for use in concentrated solar power (CSP) plants, as these are typically located within deserts or arid regions with high solar potential but limited water resources [2].

Air-cooled heat exchangers operate by using an array of axial flow fans, which move large amounts of air through heat exchanger bundles. This allows for the rejection of energy to the environment in the form of heat using convection. Since it is difficult to experimentally test large-scale fans in the controlled environments provided by fan test facilities, smaller scaled-down versions of the fans are tested instead. Scaling laws (affinity laws) are then used to determine the performance characteristics of the large-scale fan. The size difference between two scaled fans means that it is not possible to match their Reynolds numbers when testing with the same test fluid. Since the Reynolds number describes the relationship between inertial and viscous forces, a difference in Reynolds number between two fans of different sizes leads to non-identical behaviour of the boundary layers on the fan blades, which produce different performance characteristics. It is therefore important to determine and quantify the effect that the Reynolds number has on the accuracy of predicting the performance characteristics of scaled-down axial flow fans.

Pelz et al. [3] conducted research on a new scaling method aimed at omitting empirical functions in scaling to develop a universal, physically-based scaling method. The scaling method is a modification of the scaling formulation derived by Pelz and Hess [4], based on the assumption that inertia losses in the model consist of two parts: scaling the efficiency and subsequently the flow coefficient. However, a shortcoming of Pelz et al.'s [3] work is that it does not extend to the large diameters of fans typically considered for cooling applications.

FAN SPECIFICATIONS

The axial flow fan used in this paper is the M-fan designed by Wilkinson [5] and B2a-fan by Bruneau [6]. Four different diameter versions of the each fan are used, namely 7.3152 m, 3.6576 m, 1.542 m, and 0.63 m. Therefore, it is important to scale down the operating conditions from the 7.315 m diameter fan to match those of the 3.6576 m, 1.542 m, and 0.63 m version. It was decided to scale the fans down using the shroud diameter instead of the rotor diameter; however, the tip gap was kept constant at 0.259% of the shroud diameter. The following table details the operating specifications of the M- and B2a-fan at a diameter of 1.542 m.

Table 1: Fan Operating Specifications

	Units	M-Fan	B2a-Fan
Number of Blades	–	8	8
Hub-to-Tip Ratio	–	0.289	0.4
Casing Diameter	m	1.542	1.542
Volume Flow rate	m^3/s	14.797	16
Fan Static Pressure Rise	Pa	116.7	210
Blade Tip Speed	m/s	58	60.55
Rotational Speed	rpm	718.36	750
Shaft Power	W	2812	6000
Fan Static Efficiency	%	61.4	56
Density	kg/m^3	1.209	1.209

EXPERIMENTAL TESTING

The performance of the M-fan was evaluated by experimentally measuring the pressure rise, efficiency, and power consumption characteristics as a function of the volumetric flow rate. This experimental analysis is required to validate the analytical and numerical models. The experimental testing is conducted within a type A (free inlet and outlet) 1.542 m diameter wind tunnel at the Mechanical and Mechatronic Engineering Department at Stellenbosch University. The procedure is performed according to the ISO 5801 standards [7], which deals with performance testing of fans using standardized airways.

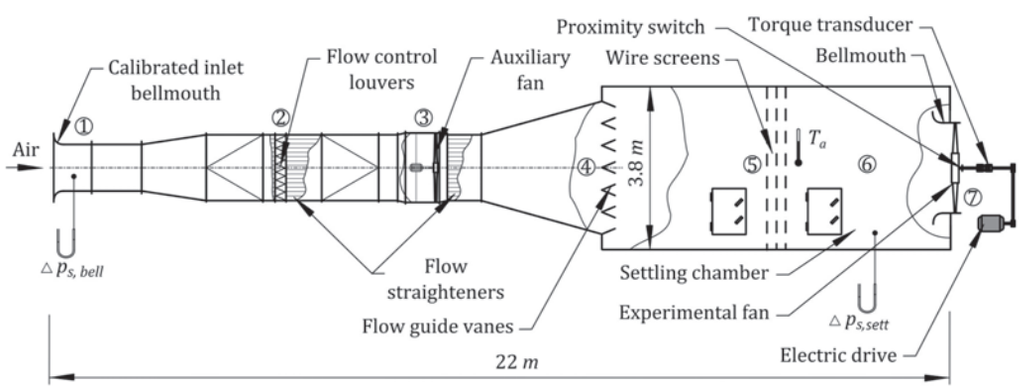


Figure 1: Stellenbosch University BS 848, Type A Fan Test Facility ([8])

NUMERICAL MODEL

The performance characteristics of the M-fan and B2a-fan is modeled at a range of flow rates and blade setting angles to verify and quantify the performance characteristics of the M-fan.

Computational Domain

The P3DM computational domain consists of three sub-domains, the inlet, outlet, and rotor subdomain, with two sets of non-conformal periodic interfaces coupling the inlet and outlet meshes to

the rotor mesh. Having three individual subdomains allows for flexible grid resolution based on localized pressure gradients while also saving on computational processing where necessary [9]. All three meshes are constructed using poly-hexcore cells, which combine octree hexahedrons (for bulk regions), poly-prisms (for boundary layers), and polyhedra (for interfaces between octree hexahedrons and poly-prism cells) to create a mesh within Ansys Fluent Mesher. Each subdomain contains a periodic pair and is configured with a rotational matching periodic boundary condition at an angle of 45°.

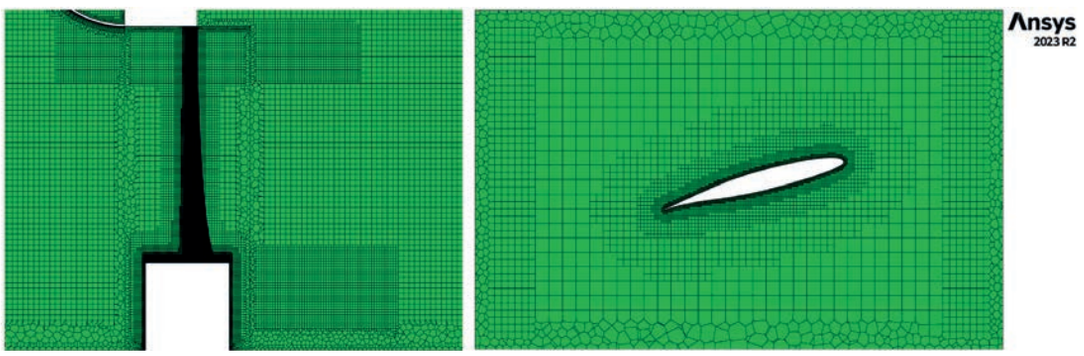


Figure 2: P3DM Rotor Mesh

The method used to model the flow through the three subdomains is the Multiple Reference Frame Model (MRF) model. The MRF model is a steady-state approximation in which individual domains rotate around different axes and/or rotational speeds. Each sub-domain is solved by calculating the relative flow in its chosen reference frame. Special treatment of the interfaces between the different sub-domains is required to allow for the boundary conditions to have the correct reference frame.

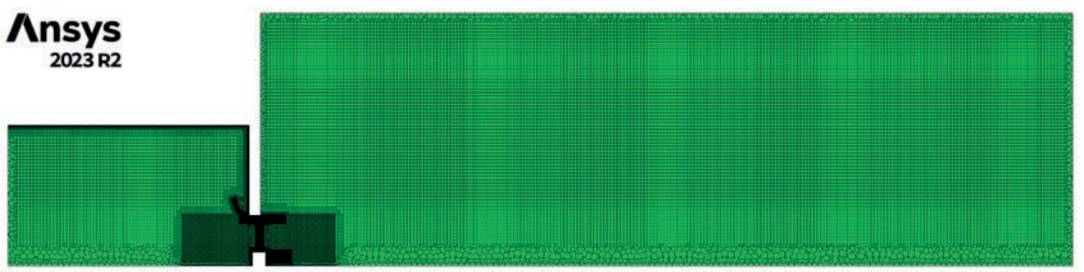


Figure 3: P3DM Computational Domain

The rotor sub-domain is composed of an angular segment that encloses the blade profile and hub and is situated between the inlet and outlet sub-domain. An inflation layer is applied to the blade, shroud, hub, and bellmouth to constrain the y^+ values along the blade length to accommodate the different turbulent models y^+ requirement. A grid independence study was conducted, and it was determined that a cell count of approximately 8.8×10^6 was sufficient for convergence for all three fan diameters. The inlet and outlet sub-domain boundary lengths are determined through a sensitivity analysis. To achieve sufficient convergence, the lengths are set to $z_i = 2.406 d_c$ and $z_o = 8 d_c$, respectively.

Boundary Conditions

Since the P3DM consists of a one-eighth segment of the M-fan and B2a-fan, each sub-domain contains a periodic pair and is configured with a rotational matching periodic boundary condition at an angle of 45°. When combining the three sub-domains into one computational domain, two non-conformal periodic repeats mesh interfaces are created to join the rotor sub-domain to the inlet and

outlet sub-domains. A non-conformal interface applies an interpolation scheme between the two surfaces, allowing all relevant properties to transfer from one sub-domain to the other.

The inlet is defined as a velocity inlet, with flow entering the domain normal to the boundary in the negative z-direction. This allows for a constant flow distribution at the inlet of the domain. The outlet is defined as a zero gauge static pressure outlet, while the backflow is set normal to the boundary with a static pressure specification. The flow turbulence is specified to enter the inlet and leave the outlet with an intensity of 3%, while the length scale is shown in Table 2:

Table 2: M-Fan Turbulence Length Scale

Casing Diameter	7.315 m	3.657 m	1.542 m	0.63 m
Length Scale	0.047 m	0.024 m	0.01 m	0.004 m

The inlet and outlet sub-domains are specified as having a stationary reference frame, while the rotor sub-domain is specified as having a rotational reference frame with a rotational speed about the negative z-axis in the absolute coordinate scheme.

All surfaces in the three sub-domains are specified to have a no-slip wall boundary condition. The shroud in the rotor sub-domain functions as a moving wall, with zero rotational speed in the absolute reference frame. The two blades, three hubs, and two shroud surfaces in the inlet and outlet sub-domains are designated as stationary walls, as they remain stationary relative to the flow's rotation.

Turbulence Modelling

Several turbulence models were compared using the base M-fan, and it was found that the Realizable $k-\omega$ model provided the most accurate results across the following y^+ ranges on the rotor for the four fan diameters:

Table 3: M- and B2a-Fan Y^+ *Ranges*

Casing Diameter	7.315 m	3.657 m	1.542 m	0.63 m
Minimum y^+	1.821	1.157	0.707	0.523
Maximum y^+	109.1	53.05	53.12	40.6
Initial Layer Height	0.95 mm	0.4 mm	0.4 mm	0.2942 mm
Cell Count	$8.76x10^6$	$8.85x10^6$	$8.17x10^6$	$8.32x10^6$

Solver Settings

The discretization schemes and solver settings are shown in Table 4 and are selected based on work done by Wilkinson [5] and Louw [8]. Table 4 represents the solver settings for the Realizable k-ε model with enhanced wall functions.

Table 4: P3DM Solver Settings

Pressure-Velocity Coupling	SIMPLE
Flux Type	Rhie-Chow: Momentum Based
Discretization Scheme (Gradient)	Least Squares Cell Based
Discretization Scheme (Pressure)	PRESTO!
Discretization Scheme (Momentum)	QUICK
Turbulent Kinetic Energy	QUICK
Specific Dissipation Rate	QUICK
Pseudo Time Method	Off
Warped-Face Gradient Correction	On

Warped-face gradient correction was enabled, which improves gradient accuracy by addressing high aspect ratios, non-flat-faced cells in boundary layers, and highly deformed cells. However, it was found to have no effect on the simulation results, although it increased the rate of convergence. All under-relaxation factors were kept to their default values proposed by Ansys [10], while all residual convergence limits are set to 1e-5.

RESULTANT EFFECTS ON FAN SCALING

From the numerical results, the influence of the fan diameter on fan behavior is investigated for a range of volume flow rates ($12-19 m^3/s$). These effects are compared using the total-to-static pressure rise, shaft power, and total-to-static efficiency. The experimental results are displayed both as raw data and poly-fitted curves from several sets of experimental data for the fan's pressure, power, and efficiency curves. The performance characteristics of the M-Fan and B2a-Fan with a 0.259% (4 mm for the 1.542 m fan) tip gap at their design hub angles are discussed to determine the accuracy of the P3DM.

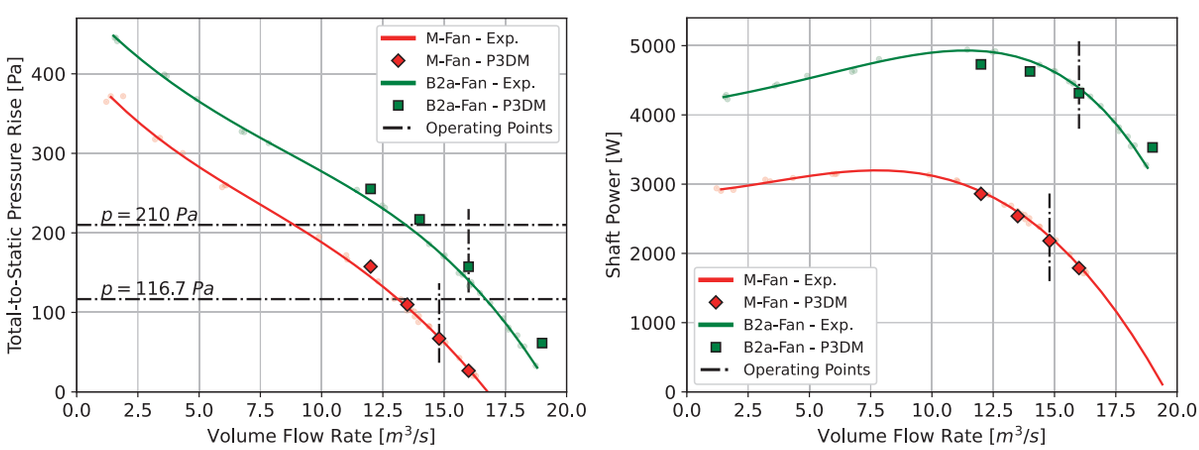


Figure 4: M-Fan and B2a-Fan Performance Characteristics

Comparing the experimental pressure rise of the M-Fan to the P3DM for the 1.542 m fan shows a strong correlation across the full range of simulated volume flow rates, while the numerical results of the B2a-Fan overpredict the pressure rise by an average of 8.66%. The comparison between the experimental and numerical shaft power for the M-Fan shows a strong correlation, while the B2a-Fan

underpredicts power at flow rates lower than the design and overpredicts it at higher flow rates.

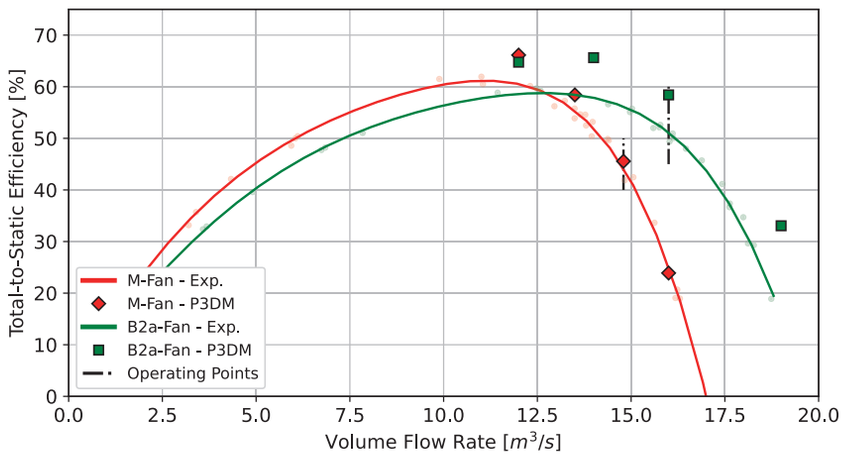


Figure 5: Total-to-Static Efficiency

The total-to-static efficiency depends on the pressure and power characteristics of the fan. As such, the trends and errors seen in Figure 4 are carried over to the efficiency and are visible in Figure 5. As seen in Figure 5, due to the underprediction of shaft power and the overprediction of the pressure rise, the P3DM overpredicts the efficiency of the B2a-Fan. Meanwhile, the P3DM accurately predicts the total-to-static efficiency of the M-Fan across the full range of flow rates.

The performance characteristics at the design flow rate versus Reynolds number at the blade tip for the M- and B2a-fan are shown in Figure 6 and Figure 7. The pressure rise for all four fan diameters were scaled to 1.542 m and then normalized by the pressure rise of the 1.542 m fan. The same method was applied to the shaft power and efficiency. This was done to compare the change in pressure rise, power, and efficiency relative to each other, since the M-fan and B2a-fan have vastly different pressure rise and power consumption values.

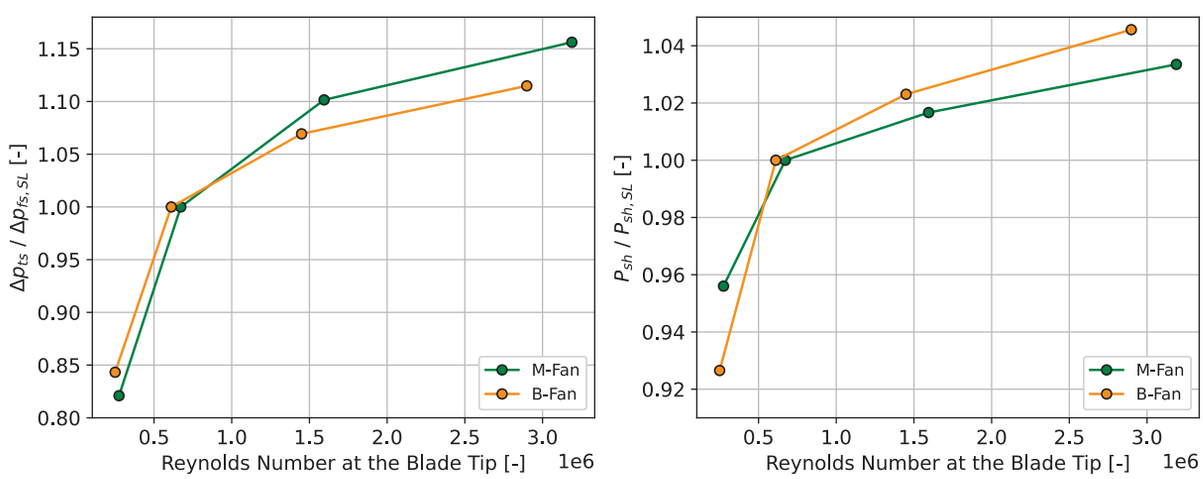


Figure 6: Effect of Reynolds Number on the Performance Characteristics

For both fans, there is a general increase in fan static pressure, power, and efficiency with an increase in fan size and thus Reynolds number, at constant flow rates. However, as fan size and Reynolds number increase, the improvement in fan performance characteristics diminishes. The performance characteristics are then said to be independent of the Reynolds number.

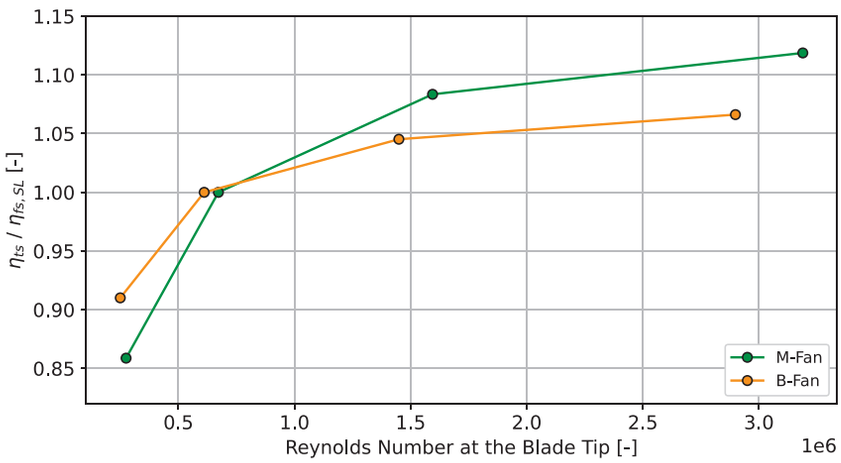


Figure 7: Effect of Reynolds Number on the Fan Efficiency

According to the affinity laws, the efficiency of the different-sized fans should be equal. In reality, this is not the case, since the affinity laws neglect viscous effects and changes in Reynolds number. As the Reynolds number increases, the effect of viscous losses, such as surface friction, decreases. In turn, inertia losses, such as tip clearance losses, dominate. This results in the logarithmic trend of Reynolds number on fan performance characteristics, as seen in the figures above.

The following aerofoil properties for the NASA 0413 were obtained from XFoil by Drela and Youngren [11] with an N_{crit} value of 0.1, as it has been proven to give improved results for low angles of attack below the stall point [5]. The following figures show the effect that the Reynolds number has on the lift at the hub of the M-Fan, which has an angle of attack of 2.85°, for the 7.315 m ($Re_{hub} = 9.5 \times 10^5$) and 0.63 m ($Re_{hub} = 8.14 \times 10^4$) diameter fans. There is a 15.16% drop in lift and an 84.62% increase in drag at the hub of the fan when reducing the fan diameter from 7.3152 m to 0.63 m. For the tip, which has a Reynolds number of 3.19×10^6 for 7.3152 m fan and 2.75×10^5 for 0.63 m fan, there is a 2.78% drop in lift and a 61.08% increase in drag at an angle of attack of 0.67°.

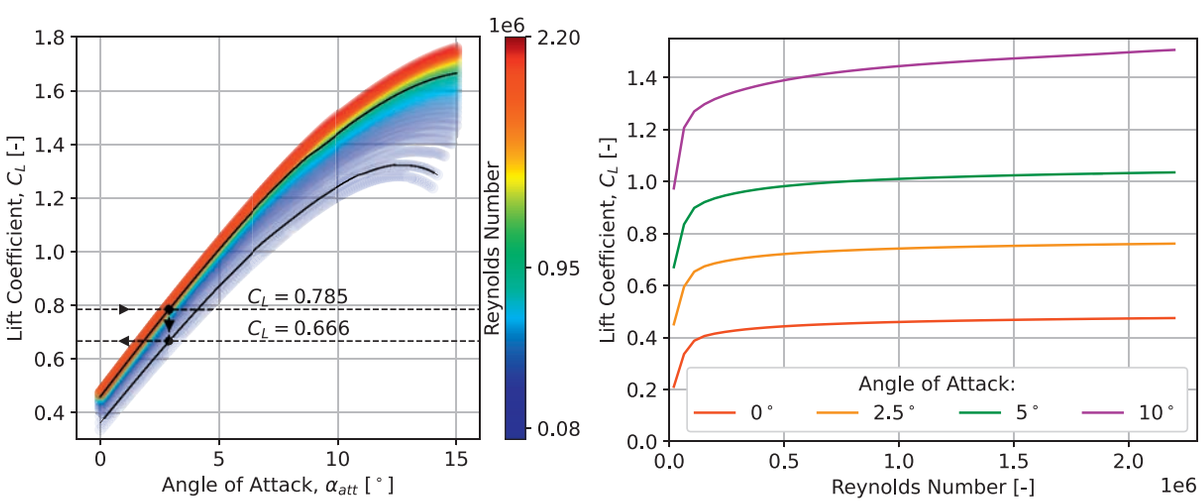


Figure 8: Reynolds Number Effects on the Lift Coefficient

As the Reynolds number increases, the lift tends to follow the same characteristic curve, as seen in Figure 8. Lift, not drag, is the primary contributor to both pressure rise and power, and, in conjunction, they define efficiency. This shows that, as the fan diameter increases, the effect of an increase in

Reynolds number on the fan decreases, which was observed with the performance characteristics of the M-Fan and B2a-Fan at different fan diameters.

CONCLUSION

Fan performance over a range of flow rates for 0.63 m, 1.542 m, 3.6576 m and 7.3152 m diameter M- and B2a-fans was assessed to determine the effect that fan size and Reynolds number have on an axial flow fan. It was found that the trends observed between the two different types of fans are consistent and show that an increase in pressure rise, power consumption, and total-to-static efficiency occurs with an increase in fan size and subsequently Reynolds number. As the diameter increases, and thus Reynolds number increases, the performance characteristics tend to approach their performance limits. Similar trends are observed in the effect that Reynolds number has on the lift and drag characteristics of aerofoil profiles.

REFERENCES

[1] D. G. Kröger, *Air-cooled Heat Exchangers and Cooling Towers*. Department of Mechanical Engineering, Stellenbosch University: Self Published, **2004**.

[2] T. O. Meyer, "Design of a tip appendage for the control of tip leakage vortices in axial flow fans," Ph.D. dissertation, Mechanical Engineering, Stellenbosch University, South Africa, **2021**.

[3] P. F. Pelz, S. Stonjek, and B. Matyschok, *The influence of reynolds number and roughness on the efficiency of axial and centrifugal fans.* Journal of Engineering for Gas Turbines and Power vol. 135, **2012**.

[4] P. F. Pelz and M. Hess, *Scaling friction and inertia losses for the performance prediction of turbomachines.* 13th International Symposium on Transport Phenomena and Dynamics of Rotating Machinery (ISROMAC-13) vol. 122, **2010**.

[5] M. B. Wilkinson, "The design of an axial flow fan for air-cooled heat exchanger applications," M.S. thesis, Mechanical Engineering, Stellenbosch University, South Africa, **2017**.

[6] P. R. P. Bruneau, "The design of a single rotor axial flow fan for a cooling tower application," M.S. thesis, Mechanical Engineering, Stellenbosch University, South Africa, **1994**.

[7] *Industrial fans - performance testing using standardized airways*, 2nd ed., International Standard, **2007**.

[8] F. G. Louw, "Investigation of the flow field in the vicinity of an axial flow fan during low flow rates," Ph.D. dissertation, Mechanical Engineering, Stellenbosch University, South Africa, **2015**.

[9] J. N. Rohwer, "Blade surface pressure measurements of an axial flow fan," M.S. thesis, Mechanical Engineering, Stellenbosch University, South Africa, **2019**.

[10] *Ansys fluent user's guide*, Release 18.1, **2017**.

[11] M. Drela and H. Youngren, *Xfoil 6.94 user guide*, **2001**.

DESIGN OF FORWARD-INCLINED BLADES FOR A 0.5 HUB-TO-TIP RATIO TUBE-AXIAL FAN

Massimo MASI[1], Piero DANIELI[1], Sergio RECH[2]

[1] *University of Padova, Department of Management and Engineering – DTG, stradella S. Nicola 3, 36100 Vicenza, Italy*

[2] *University of Padova, Department of Industrial Engineering – DII, via Venezia 1, 35131 Padova, Italy*

SUMMARY

The paper deals with the design of forward-inclined blades, where "forward-inclination" is intended as the design-dependent amount of forward sweep to be incorporated in non-free-vortex blades to restore a quasi-2D flow behaviour within the rotor passages. The aim of the work is to assess the effectiveness of this design modification in a 0.5 hub-to-tip ratio fan with radially stacked blades that induce a roughly constant-swirl velocity at the rotor exit. To this end, the original blade has been modified by incorporation of a forward sweep amount that translates into a forward-inclined design, defined in accordance with a method suggested by the authors. The forward-inclined design demonstrated experimentally to improve pressure rise and efficiency of the original fan in the whole operation range with ca 10% gain at design operation.

INTRODUCTION

Forward sweep is a well-acknowledged means to reduce the noise emissions and improve both the stall margin and efficiency at design operation of low-speed axial fans with radially stacked blade rotors [1]. These advantages are generally counteracted by some decrease of the fan pressure rise at design operation [2]. According to the simplified theory of forward sweep for low-speed axial-fans suggested by the authors ten years ago [3], each blade of a rotating annular cascade made of radially stacked aerofoils behaves aerodynamically as a backward-swept wing when it is designed to leave a spanwise constant swirl component downstream of the trailing edge. This is because the radial shift of the meridional flow induced in the annular cascade passages by the non-free-vortex blade aerodynamic loading mimics the slide of the free-stream along the wingspan induced by backward sweeping the wing axis. Since the lift reduction associated with backward sweeping of aeronautical wings axis has its low-speed axial-fans counterpart in the pressure rise reduction associated with the obliquity of the meridional flow (relative to the fan blade axis), rotor blades forward sweep allows to increase the fan pressure up to a maximum level, theoretically achieved when the obliquity of the meridional flow relative to the blade axis is eliminated. In this case, the geometrical forward-sweeping should be more appropriately defined as forward-inclining, as stated in [4]. True forward sweep and related effects expected on the fan performance [5] are achieved only when the radially stacked design is swept more forward than the forward-inclined design. In [6] the authors demonstrated by experiments that the two good-

aerodynamic-design fans with hub-to-tip ratios equal to 0.28 and 0.4 and radially stacked aerofoil blades presented in [7] can increase further their performance by incorporation of a blade forward sweep angle equal to the obliquity of the conical surface that approximates the most oblique bulk-flow stream surface within the blade passage. On the other hand, the different quantity and type of aerodynamic performance improvement achieved by the two fan designs (either an efficiency increase with no pressure rise modification at design– or a pressure rise increase with approximately no efficiency modification), led to suppose that the amount of forward sweep needed to nullify the meridional flow obliquity relative to the blade axis also depends on the tip clearance magnitude, due to the role the latter plays on the meridional flow obliquity. Accordingly, an updated version of the criterion to estimate the meridional flow obliquity has been proposed in [8], and therein successfully applied to design a 0.5 hub-to-tip ratio tube-axial fan with constant-swirl blade loading. However, both the validity of the forward-swept blades design method – first formalised in [6] and successively slightly revised in [4] – and the effectiveness of the criterion to estimate the meridional flow obliquity – as updated in [8] – have not yet been assessed for tube-axial fan design with hub-to-tip ratio higher than 0.4.

In the present paper, the tube-axial fan with constant-swirl blade loading obtained by radial stacking of 2D aerofoil sections – whose aerodynamic design and experimentally-assessed-good-performance have been documented in [8] – has been taken as benchmark fan for the design of its forward-inclined variant. The preliminary CFD predictions of the aerodynamic performance of the two designs have been compared with the experimental tests performed on two 315mm diameter prototypes manufactured by 3D-printing. The final aim is to assess the effectiveness of the forward-inclined blade design in a 0.5 hub-to-tip ratio fan with constant-swirl blade loading.

The paper is organised in 6 sections. The first one briefly overviews the major characteristics of the CFD model used for the preliminary assessment of the fan aerodynamic performance and the test rig used for the experimental assessment. The second presents the geometric features and aerodynamic performance of the 0.5 hub-to-tip ratio tube-axial fan taken as benchmark for this work. The third section recalls the method proposed to incorporate blade forward sweep in constant-swirl design and the revised criterion for the quantification of the sweep angle. The fourth section shows the application of the design method, the forward-inclined design variant, and compares the performance predicted by CFD with those simulated for the benchmark fan. The fifth section compares the experimental data collected for the two designs and critically discusses the obtained results. Finally, the last section concludes the paper reporting the major findings of this work.

INSTRUMENTS AND TOOLS

This section briefly summarises the major features of the CFD model and the experimental test rig used in this work. For the sake of generality, the fan pressure (p_f as defined by ISO 5801), total -to-static pressure rise (p_{fs}), and flow rate (q_v), at any specified operating condition, are combined in terms of dimensionless performance parameters, and namely: the flow rate coefficient ($\Phi = q_v/(\omega D^3)$), the pressure coefficient ($\Psi = p_f/(\rho \omega^2 D^2)$), the aeraulic efficiency ($\eta_{aer} = q_v p_f/(T\omega)$), and the total-to-static efficiency ($\eta_{TS} = q_v p_{fs}/(T\omega)$), where T, ω and ρ are the shaft torque, the fan rotational speed, and the air mass density, in that order.

CFD model

The preliminary assessment of the fans aerodynamic performance has been performed using a reduced-domain single-channel steady-state incompressible-flow CFD model solved with the STAR CCM+ CFD software. The domain has been discretised using a fully structured grid counting approximately 250k cells and including a near-wall grid refinement that permit achieving $1<y^+<13$ on the blade surfaces. The blade tip gap has been discretised with 10 cells in spanwise direction. All computations have been performed using the k-ε realizable turbulence model and the "all y^+ wall treatment". The top-left and middle frames in Fig.1 show the meridional and perspective view of the geometrical domain surface grid, respectively. The details of the model and the grid independence study are thoroughly documented in [8].

Test rig

The fan aerodynamic performance tests were performed using an inlet-chamber fan test rig coupled with a multi-nozzle system for flow-rate measurements. The rig (see right frame of Fig.1) is suited to test free-inlet free-outlet fan installations and complies with the ISO 5801:2008 standard, where it is classified as type A installation rig. its design and manufacturing process is documented in detail in [9]. All pressure data required

by the simplified test procedure provided in the standard have been measured using Betz micro-manometers, whereas the high frequency sampling of the torque sensor signal have been used to derive the mechanical power at the shaft as reported in [10]. The whole instrumentation setup and measurements accuracy are reported in [10] and other papers therein referenced.

THE CONSTANT SWIRL BENCHMARK FAN

The Constant Swirl (CS) design is a 0.5 hub-to-tip ratio (ν) fan with 12 blades featuring 1.72 aspect-ratio (AR). The fan rotor was designed to induce a spanwise constant value of the absolute velocity swirl component. Each rotor blade is obtained by envelope of 8 radially stacked FSeries aerofoil sections with 3.8% camber, 10% thickness to chord ratio, and 3% nose droop, wrapped around cylindrical surfaces coaxial with the rotor axis. Solidity (σ) and stagger (ξ) at each cylindrical surface with dimensionless radius ($x=r/R_{casing}$) are listed in Tab.1. The design process of the CS fan is described in detail in [8] as well as the practical engineering motivations that imposed a tip clearance to blade height ratio (tc/B) equal to 1.7%. The left-bottom frame of Fig.1 shows the fan geometrical model and a picture of the 3D-printed rotor.

Table 1: Geometric parameters of the CS fan rotor blading.

Parameters	**Values**							
Section ID	1 (root)	2	3	4	5	6	7	8 (casing)
Dimensionless radius x	0.5	0.549	0.598	0.647	0.697	0.746	0.869	1
Solidity σ	1.11	1.01	0.93	0.86	0.8	0.74	0.64	0.56
Stagger ξ	57.8°	59.9°	61.7°	63.2°	64.5°	65.6°	67.7°	69.4°

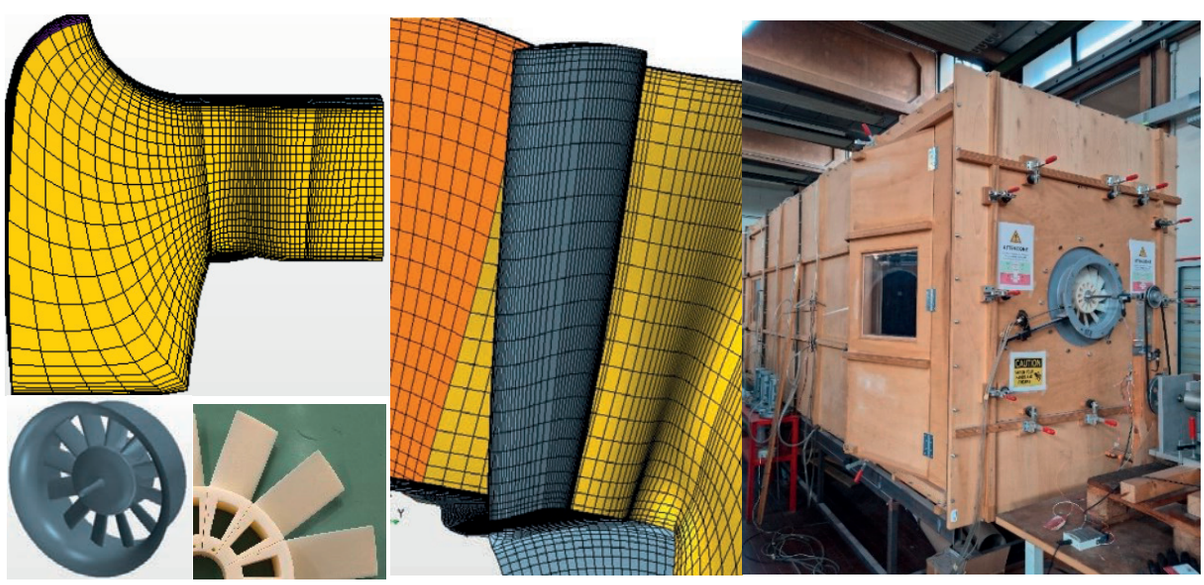


Figure 1: meridional (top left) and perspective (bottom left) views of the CFD model surface grid (taken from [8]); ISO 5801 Type A rig used for the aerodynamic performance tests (middle); geometrical model (top right) and 3D-printed rotor (bottom right) of the CS benchmark fan (taken from [8]).

Figure 2 compares the global aerodynamic performance of the CS fan design as predicted by the CFD model with the experimental data measured at the type A test rig. The CFD model overestimates to some extent the experimental performance but reproduces the trend of the corresponding curves well. Thus, the experimental data validate only in terms of qualitative trends the reliability of the CFD model that was validated in [8] from the numerical point of view. More on this subject will be dealt with in the fourth and fifth sections.

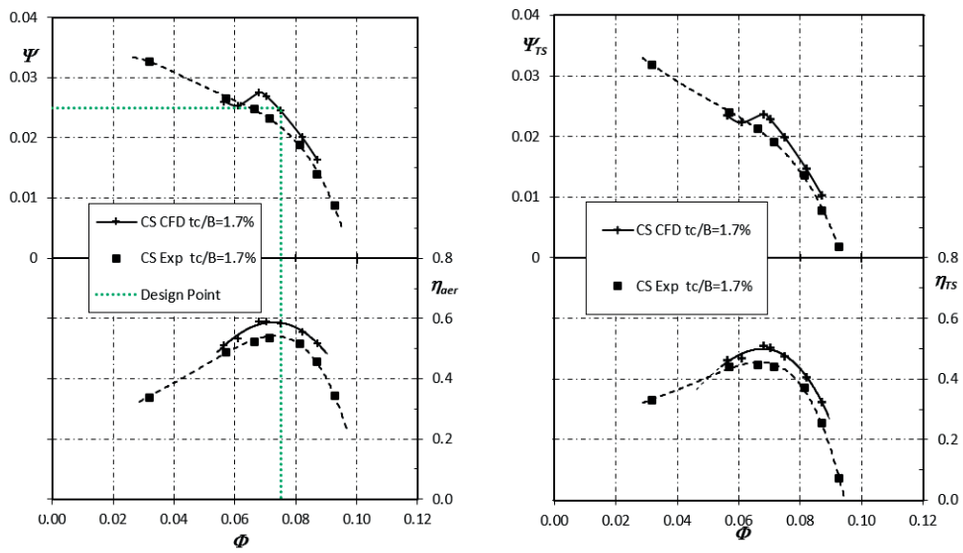


Figure 2: CS fan aerodynamic performance. CFD predictions (cross markers) and experimental data (square markers). Design point flow rate and pressure coefficients are indicated by the green point vertical and horizontal lines, respectively. Diagrams on the left and right side refer to the data with and without inclusion of ISO dynamic pressure.

Figure 3 shows the local absolute velocity components predicted by the CFD model (markers) for the CS fan in each cell crossed by the exit reference plane (arbitrarily placed 0.036 fan diameters downstream of the blade axis) and the corresponding velocity distributions expected by design (continuous lines). In the figure, each velocity component has been made dimensionless through division by the average axial velocity in the blade annulus. Thus, the tangential, radial and axial velocity distributions are reported in the form of their dimensionless counterparts, i.e. the swirl coefficient (ε_S), radial velocity ratio (ε_r) and axial velocity ratio (ε_A), in that order.

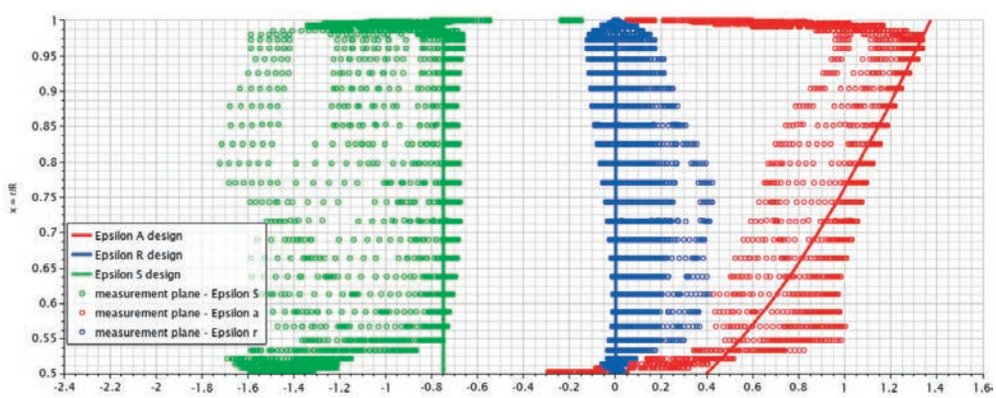


Figure 3: Dimensionless velocity ratios at design operation (Φ_D=0.075) of the CS fan as expected by design (continuous lines) and predicted by CFD in each cell cut by the reference plane downstream of the rotor exit (markers).

It is worth noting that the ε_S distribution finely approximates the design distribution except for the near hub region close to the rotor hub where also the ε_A distribution departs from the design expectations, showing a very slight negative velocity component as result of a hub flow separation that occurs at flow rates moderately higher than those expected by design.

METHOD

The analogy presented in [3] to support the formalisation of the simplified theory of forward sweep in fan rotor blades, is graphically summarised in Fig. 4, where the left-side sketches refer to the blade-to-blade (top) and meridional (bottom) views of a tube-axial fan, and the right-side sketches refer to the side (top) and top (bottom) views of an airplane with swept wings. As shown by the sketch in the bottom-left side of the figure, the circulation gradient along the rotor blade axis associated with a non-free-vortex blade loading distributions

induces a velocity component aligned with the blade axis, which translates into an oblique path of the meridional flow that crosses the rotor far from the end-walls. The local obliquity (γ) of the meridional flow is defined as the angle between the local meridional velocity vector and the rotor axis. In order to replicate a similar flow relative to the airplane wing showed on the bottom-right of the figure, the axis of the prismatic wing lifting the airplane that is flying at the same velocity as the rotor throughflow (and opposite direction) must be locally swept backward by an angle λ, equal to γ, with respect to the original wing axis.

This analogy explains why some moderately forward-swept fan rotors with non-free-vortex design documented in the literature were able to achieve a pressure rise higher than their unswept counterpart and, in doing so, seemed to contradict the well-known $\cos(\lambda)$ rule valid for the aeronautical wings. In fact, according to the analogy, the aeronautical counterpart of non-free-vortex radially stacked rotor blades is a swept wing, and not the wing with axis that forms with the airplane axis the same right angle as that included between the blade and the rotor axes, as it would be expected based only on geometrical arguments.

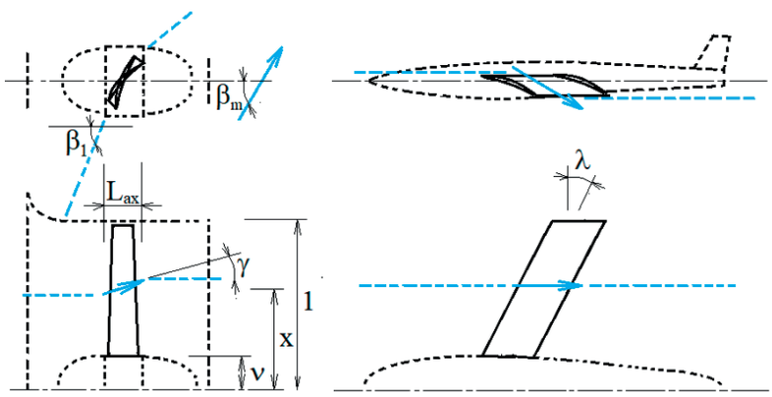


Figure 4: Graphical representation of the analogy between fan blades implementing the constant-swirl blade loading concept and Busemann's swept wing (taken from [4]).

Thus, as reported in the Introduction, according to the analogy, it is possible to achieve the maximum fan pressure increase from a radially stacked non-free-vortex fan rotor by incorporation on the blade of a sweep amount appropriate to reset around each blade aerofoil the same 2D flow as expected by design. Such a blade design is "geometrically swept" but "aerodynamically unswept" and should be referred to as "inclined" [4].

From the application point of view, fan rotors implementing the constant-swirl blade loading concept are particularly attractive. According to the analogy, and neglecting the end-walls effect, a constant-swirl blade design realised by means of a unique aerofoil section with constant chord-length and constant local incidence angle all along the blade span translates in the untwisted rectangular wing. In fact, the twist of the fan blade is merely a geometrical transformation required to replicate within the rotor reference frame the same relative flow as the untwisted wing. Furthermore, any forward or backward tilt of the rotor's rectangular blade induces changes in the local incidence at the blade leading edge and in the aerofoil shape effective-for-lift that depend only on the amount of tilt regardless of the radial coordinate of each blade leading edge point, similarly to any backward or forward tilt of an aeronautical rectangular wing. Thus, as far as the forward-inclined blade design is concerned, the conceptual difficulty of sweep incorporation reduces to the estimate of an average value for the meridional obliquity Γ of the bulk-flow crossing the rotor, being the other sweep implementation issues simply a matter of geometrical transformations, once the sweep magnitude λ has been quantified (equal to Γ).

Obviously, the higher σ and the lower AR of the fan rotor are, the weaker the validity of the analogy with the isolated infinite-AR rectangular wing is. This argument has been considered in simplified form within the criterion to estimate Γ, recently updated in [8] as reported in eq.(1), where γ_{max} and γ_{MW} are the maximum and mass-flow-averaged obliquities along the whole blade span.

$$\Gamma = \begin{cases} \gamma_{MW} = \dfrac{\int_{\nu}^{1} \gamma(x)\varepsilon_A(x)\, x\, dx}{\int_{\nu}^{1} \varepsilon_A(x)\, x\, dx} & if\ {}^{tc}/_{B} \le 0.0025 \\ \gamma_{MW}\dfrac{0.025-{}^{tc}/_{B}}{0.0225} + \gamma_{max}\dfrac{{}^{tc}/_{B}-0.0025}{0.0225} & if\ 0.0025 < {}^{tc}/_{B} < 0.025 \\ \gamma_{max} = max[\gamma(x)]_{\nu}^{1} & if\ {}^{tc}/_{B} \ge 0.025 \end{cases} \quad (1)$$

According to eq.(1), Γ (i.e., λ of forward-inclined designs) depends on: the aerodynamic load of the blade (that defines $\varepsilon_A(x)$ through the solution of the radial equilibrium equation at the rotor exit for a fixed ε_S); the blade *AR* (that defines $\gamma(x)$ through the fulfilment of the continuity constraint imposed to any stream tube crossing the blade span from the rotor entrance to its exit – conventionally placed one blade root axial chord-length downstream of the entrance); the *tc/B* magnitude (that blends the maximum obliquity value expected at high *tc/B* with the minimum obliquity value expected at low *tc/B*, when *tc/B* is in between such two extrema).

FORWARD-INCLINED FAN DESIGN AND CFD MODEL RESULTS

The 50I23_12 fan design, hereafter referred to as FI (Forward-Inclined), was obtained by incorporating in the CS design a forward-sweep amount quantified by the method summarised in the previous section as appropriate for the achievement of a forward-inclined design. Table 2 reports the kinematic parameters derived from the solution of the radial equilibrium equation at the rotor exit and the imposition of the continuity constraint across the rotor for the 8 cylindrical surfaces (IDs) used to wrap the blade skeleton aerofoil sections in the CS design. Since the CS blade was designed to achieve a spanwise constant ε_S =0.75 and fulfill all other requirements for the validity of the simplified forward-sweep theory, Tab. 2 could be used to estimate Γ by discrete approximation of the continuous functions included in eq.(1). According to Tab.2 data, γ_{max} =26.6°, and the discretised counterpart of eq.(1) yields γ_{MW} = 12.7° and Γ = 21.6°, when *tc/B* = 1.7%. Such estimates are very good approximations of the numerically calculated γ_{max} =26.6°, γ_{MW} = 16.6°, and Γ = 23°.

Table 2: Geometric parameters of the CS fan rotor blading.

Parameters	**Values**							
Section ID	1 (root)	2	3	4	5	6	7	8 (casing)
Dimensionless radius *x*	0.5	0.549	0.598	0.647	0.697	0.746	0.869	1
Axial velocity ratio $\varepsilon_A(x)$	0.394	0.544	0.668	0.777	0.876	0.968	1.175	1.371
Meridional obliquity $\gamma(x)$	0°	18.9°	24.8°	26.6°	26.2°	24.4°	15.3°	0°

To obtain the forward-inclined design, each aerofoil section ID defined as skeleton of the CS blade is therefore: (i), rotated around the tangent to the ID cylindrical surface that intersects the radial stacking line at 90° with respect to the rotor axis, up to achieve a meridional obliquity Γ = 23°; (ii), shifted along the helicoidal path corresponding to the conformal mapping of the aerofoil chord onto the ID cylindrical surface, up to achieve a local angle $\lambda = \Gamma$ between the stacking lines of new blade and the CS blade designs. Figure 5 shows two views of the FI fan, as extracted from its geometrical model and two pictures of the FI 3D-printed prototype mounted on the test rig.

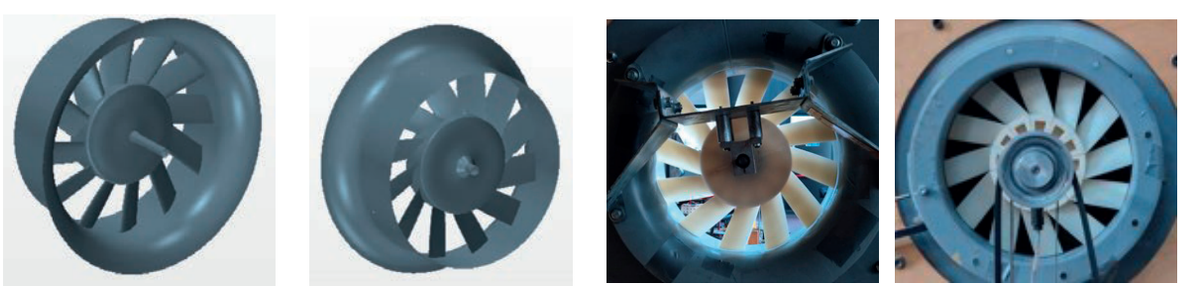


Figure 5: perspective front (left) and rear (middle-left) views of the FI fan, as extracted from its geometrical model, and front (middle-right) and rear (right) views of the FI 3D-printed prototype mounted on the ISO 5801 type A test rig.

Figure 6 compares the global aerodynamic performance predicted by CFD for the FI design with those predicted for the CS fan (already shown in Fig. 2). According to the CFD results, the FI design copies the CS fan performance at design but can improve the CS pressure coefficients and efficiencies at flow rate coefficients higher than design. This improvement at the higher flow rates is counteracted by a moderate performance decrease at flow rates lower than design and a slight reduction of the stall margin.

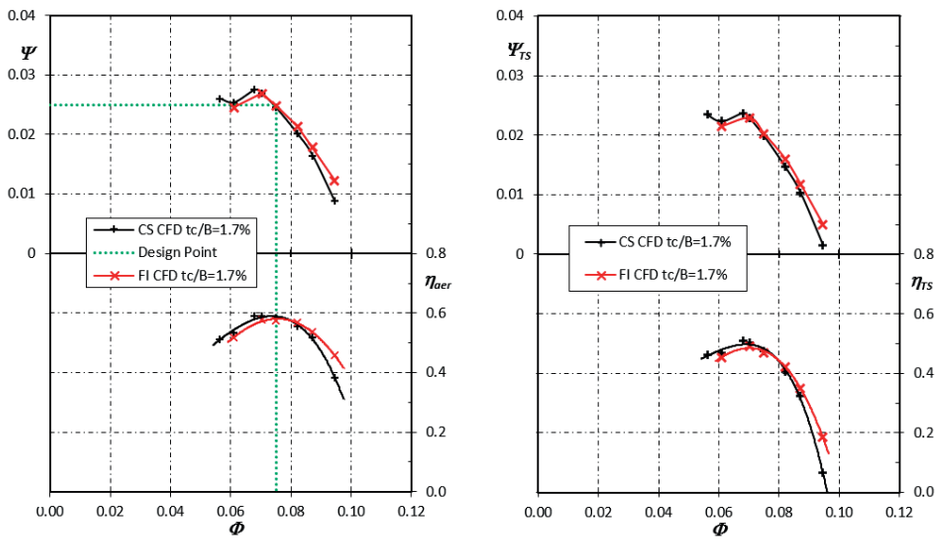


Figure 6: aerodynamic performance predicted by CFD for the FI (red) and CS (black) design. Design point flow rate and pressure coefficients are indicated by the green point vertical and horizontal lines, respectively. Diagrams on the left and right side refer to the data with and without inclusion of ISO dynamic pressure.

Figure 7 shows the dimensionless velocity ratios at the exit reference plane and the design expectations. On the whole, it can be stated that the velocity triangles predicted by CFD for the FI variant fit the design requirements to the same good extent as for the CS design (Fig.3). However, a more detailed observation of the dimensionless velocity ratios predicted by CFD for the two designs discloses some not negligible differences. First, the two distributions of the tangential velocity ratio (green markers in Figs. 3 and 7) indicate that the exit swirl velocity of the FI design is slightly higher than that of the CS design in the majority of the blade span. Second, the comparison between axial velocity ratios (red markers) suggests that FI blades moderate the radial flow migration occurring far from the end-walls in the CS design (see both blade span ranges $0.6< x < 0.8$). These two observations should translate into the expectation of a higher work transfer (and theorical pressure rise) for the FI design, that is not confirmed by the approximately equal performance predicted by CFD at design operation for the two fans. This incongruence between local flow field observations and global performance data would be solved if, for example, higher flow losses were suffered by the FI design.

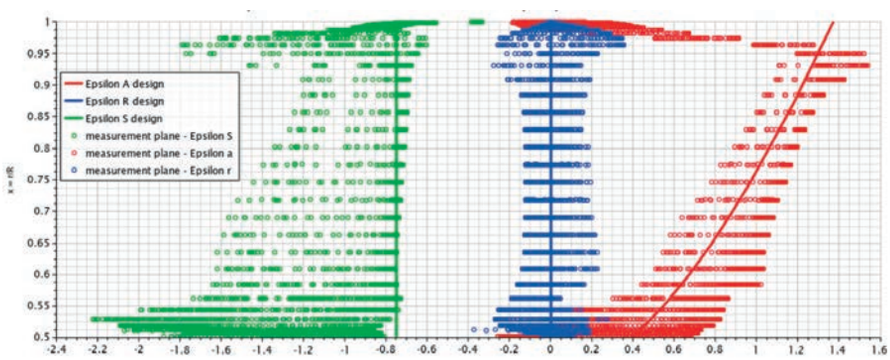


Figure 7: Dimensionless velocity ratios at design operation (Φ_D=0.075) of the FI fan as expected by design (continuous lines) and predicted by CFD (markers) in each cell cut by the reference plane downstream of the rotor exit.

However, the search for a definite addressing of this issue was not performed in this research context for two main reasons. First, of practical engineering relevance, this research can rely on experimental data to make the comparison between the global aerodynamic performance of the two designs. Second, of scientific relevance, the recently published work [11] demonstrates that fans global aerodynamic performance predicted by CFD models exploiting single-channel steady-state calculations on idealised annular domains are remarkably affected by the location of the exit reference plane downstream of the rotor. In the present case, looking at the axial velocity ratio distribution in the outermost region of the FI blade span (red markers close to the blade tip), it clearly emerges how the average velocity is remarkably lower than the corresponding velocity predicted for the CS blade, and how the FI radial velocity ratio is nearly zero (on average, see blue markers in Fig.7),

differently from the CS design, where an outward radial flow component is still present in at the exit reference plane (blue markers in Fig.3). Such two occurrences suggest that the radial equilibrium condition has not yet been fully achieved at the exit reference plane of the CS design. Thus, in spite of the numerical validation stated in [8] for the CFD model used here, it is deemed as more appropriate for the present research to limit the comparison between CFD results to the evaluation of different designs in term of local flow features and compare the global performance of the two design only on an experimental basis. This also because [11] demonstrated that single-channel calculations performed on idealised annular domains overestimate the fan aerodynamic performance experimentally measured on type A test rigs, regardless of the axial extension of the domain.

EXPERIMENTAL ASSESSMENT AND DISCUSSION OF THE RESULTS

The global aerodynamic performance experimentally measured for the FI design variant are compared in fig. 8 to those already shown in Fig.2 for the CS design. The generalised improvement achieved in both pressure and efficiency curves by the FI variant over the CS design is apparent.

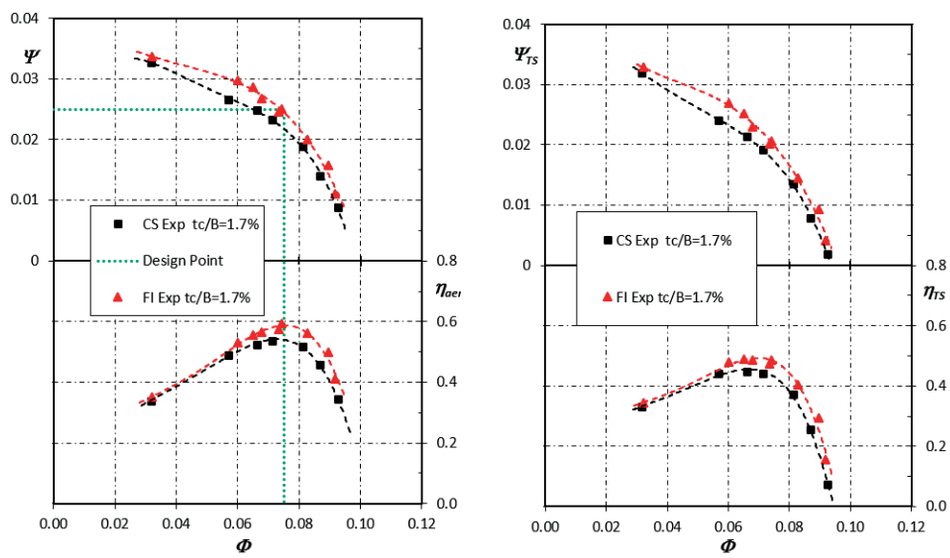


Figure 8: aerodynamic performance measured at the ISO 5801 Type A test rig for the FI (red) and CS (black) design. Design point flow rate and pressure coefficients are indicated by the green vertical and horizontal point lines, respectively. Diagrams on the left and right side refer to the data with and without inclusion of ISO dynamic pressure.

In particular, the improvements in Ψ and Ψ_{TS} achieved by the FI design range from 2.5% at low Φ to more than 20% at high Φ for the former and from 2.5% (at low Φ) to approximately 40% (at high Φ) for the latter. At peak efficiency, Ψ and Ψ_{TS} gains are approximately equal to 10% and 15%, respectively. With regard to the corresponding efficiency improvements, η_{aer} is improved from approximately 2% to 9% up to 15% moving from low Φ to peak efficiency to high Φ operations, whereas η_{TS} is improved from a minimum, approximately 2%, to 10%, up to 33%, in the same Φ range. These significant improvements confirm that the CFD predictions of global aerodynamic performance achieved by a fan on an ISO 5801 type A test rig are not highly reliable when derived from steady-state single-channel computations performed on idealised annular domains. Moreover, the range of performance difference found in [11] for CFD simulations of a fan in operation in either an annular domain or an ISO 5801 type A test rig are confirmed by the present comparison between annular domain CFD results and ISO 5801 type A experiments. Nonetheless, useful information on the differences existing between the internal flow fields of the two fan designs can be extracted from the CFD results by comparing the internal flow for the two fans in operation where CFD predicts performance difference comparable with those obtained by experiments. Thus, Fig. 9 compares the dimensionless velocity ratios at the reference exit plane for fans operation at Φ=0.0944. The higher ε_S achieved by the FI design is apparent and justifies the higher Ψ such design is able to assure. Another interesting point to note is that, at the reference exit plane, FI design shows lower amplitude of the velocity ratios spread and lower radial velocity magnitude than the CS design. Both occurrences suggest that the FI design allows for an earlier achievement of the radial equilibrium condition downstream of the rotor in comparison with the CS design.

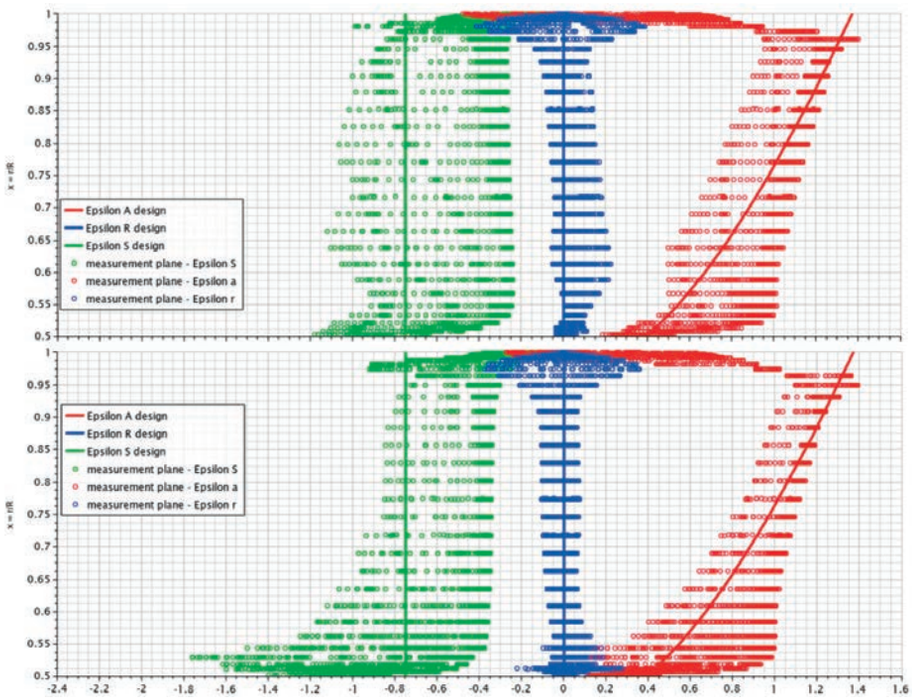


Figure 9: Dimensionless velocity ratios at Φ=0.0944 for the CS (top) and FI (bottom) fans as expected by design (continuous lines) and predicted by CFD (markers) in each cell cut by the reference plane downstream of the rotor exit.

Finally, Fig. 10 compares the pressure contours on the pressure and suction sides of the CS and FI blade surfaces. As expected for constant swirl blade loading designs, the minimum pressure on the suction side and maximum pressure on the pressure side of the blade are both located towards the blade tip. In the FI design these maximum and minimum absolute values are both higher than the corresponding values in the CS design. Moreover, FI isobars are generally more aligned with the blade axis than CS isobars, especially in the zone close to the blade leading edge. This alignment translates in a spanwise inwards extension of the minimum and maximum pressure zones on the suction and pressure sides of the blade surface, respectively. As underlined in [5], the addition of forward sweep (actually, forward inclination in the present case) to controlled vortex design blades with positive spanwise circulation gradient shortens the flow path on the blade suction side further away from the end-walls. This moderates the effect of the skin friction and contributes to the efficiency gain obtained here by the FI design.

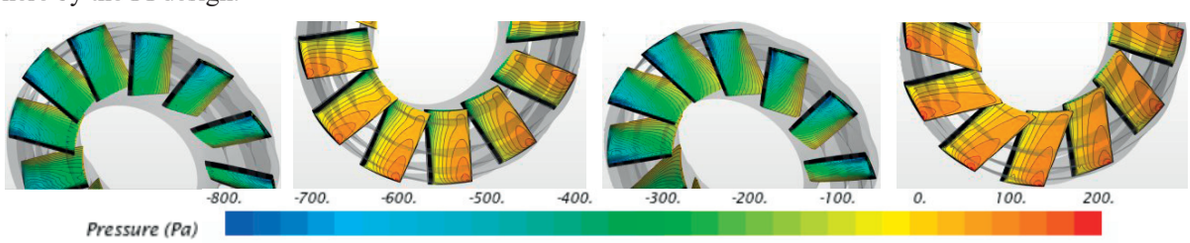


Figure 10: pressure contours on the blades' suction and pressure side for the CS (left and middle-left frames) and FI (middle-right and right frames) fans at Φ=0.0944. Gray surfaces are the 5%, 30%, 55%, and 80% stream-surfaces.

CONCLUSIONS

It was proven by experiments that the modification of a 0.5 hub-to-tip ratio fan by forward inclination of its blades designed to induce a roughly constant-swirl velocity at the rotor exit remarkably improves the pressure and efficiency curves in the entire fan operation range with approximately 10% gain at design operation.

This result confirms the validity of the forward swept blades design method suggested by the authors in obtaining forward-inclined blade designs and demonstrates that the updated criterion to estimate the meridional flow obliquity required to apply the amount of sweep necessary to obtain forward-inclined blades is effective for tube-axial fan designs with hub-to-tip ratio equal to 0.5.

BIBLIOGRAPHY

[1] M. G. Beiler, T. H. Carolus – *Computation and measurement of the flow in axial flow fans with skewed blades.* ASME J. Turbomachinery, 121, 59-66, **1999**

[2] J. Vad – *Aerodynamic effects of blade sweep and skew in low-speed axial flow rotors at the design flow rate: an overview*. Proc. IMechE, Part A: J. Power and Energy, 222, 69-85, **2008**

[3] M. Masi, A. Lazzaretto – *A simplified theory to justify forward sweep in low hub-to-tip ratio axial fan.* ASME paper GT2015-43029, **2015**

[4] M. Masi, A. Lazzaretto – *The design of tube-axial fans with forward inclined blades – Part II*. (In Italian). La Termotecnica, October, 68-72, **2021**

[5] J. Vad –*Forward blade sweep applied to low-speed axial fan rotors of controlled vortex design: an overview*. J. Eng. Gas Turbines Power, 135, 1-9, **2013**

[6] M. Masi, A. Lazzaretto – *A New Practical Approach to the Design of Industrial Axial Fans: Part II — Forward-Swept Blades with Low Hub-to-Tip Ratio.* ASME paper GT2019-91532, **2019**

[7] M. Masi, A. Lazzaretto – *A new practical approach to the design of industrial axial fans: tube-axial fans with very low hub-to-tip ratio*. J. Eng. Gas Turbines Power, 141, 101003-1/10, **2019**

[8] M. Masi, P. Danieli, E. Dal Cin, E. Bregolin – *Effects of different blade loading strategies applied to low-speed tube-axial fans*. Journal of the Global Power and Propulsion Society, 9, in press., **2025**

[9] S. Castegnaro, M. Masi, A. Lazzaretto – *Design and testing of an ISO 5801 inlet chamber test rig and related issues with the Standard*. Proceedings of Fan 2018 Conference, Darmstadt, Germany, **2018**

[10] M. Masi, A. Lazzaretto, P. Danieli, C. Bettanini – *Design of a small axial-flow fan with 0.2hub-to-tip ratio*. Proceedings of Fan 2022 Conference, Senlis, France, **2022**

[11] F. D. Boshoff, S. J. van der Spuy, J. P. Pretorious, C. J. Meyer – *Investigation into the predicted performance of a cooling fan for an sCO2 concentrated solar power plant*. Proc. IMechE, Part A: J. Power and Energy, 238(5), 788-799, **2024**

A2 Tip Gap Noise of Axial Fans

9 April - 11:00 - - Room 1 Fitzgerald

Chairmen: SStefan Becker, Taner Elnady

List of papers

Effects of Blade Tip Design Revisions on Airborne Noise of an Axial Fan

- İmge B engisu ÖZENEN – ANOVA R&D Technologies (Turkey)
- Ekincan ŞIMŞEK – ANOVA R&D Technologies (Turkey)

Numerical Investigation of Different Wing Tip Geometries on the Acoustics of an Airfoil With Tip Gap in a Wind Tunnel

- Philipp DIETRICH – ebm-papst Mulfingen GmbH & Co. KG (Germany)
- Shivaprasad Reddy MALLU – ebm-papst Mulfingen GmbH & Co. KG (Germany)
- Florian LEX – ebm-papst Mulfingen GmbH & Co. KG (Germany)

BTGNX: An Acoustic Benchmark Wind Tunnel Experiment for Tip-Gap Noise

- Fabian REUSCHLING – DLR e.V. (Germany)
- Lev LIBERSON – DLR e.V. (Germany)
- Michael POTT-POLLENSKE – DLR e.V. (Germany)
- Jan Werner DELFS – DLR e.V. (Germany)
- Daniel ERNST – DLR e.V. (Germany)

BTGNX: A MEMS Microphone Array for the Acoustic Benchmark Wind Tunnel Experiment for Tip-Gap Noise

- Daniel ERNST – DLR (Germany)
- Carsten SPEHR – DLR (Germany)
- Fabian REUSCHLING – DLR (Germany)
- Marc SCHNEIDER – ebm-papst (Germany)

EFFECTS OF BLADE TIP DESIGN REVISIONS ON AIRBORNE NOISE OF AN AXIAL FAN

İmge Bengisu ÖZENEN, Ekincan ŞİMŞEK

ANOVA R&D, Dumlupınar Boulevard 2082. St, 06510 Ankara, Turkey

SUMMARY

Military axial fans are designed to offer high durability and high performance; hence they have increased noise levels. However, they are expected to have lower noise levels to enhance comfort in human-occupied areas and to ensure operational discretion. Sound power level of the sample fan is measured as 86.3 dB(A). Fan speed reduction and design revisions has been considered to prevent airborne noise. Design revisions of the fan blades has been performed which includes notched trailing edge and bevelled blade tip design variations. In this study, analysis and tests results of both aerodynamic and acoustics of the fan are shared to present the effect of the fan speed reduction and design revisions on the performance and sound power level of the fan.

INTRODUCTION

Military axial fans are mostly used in aerospace and defence industry due to the fact that they are specifically designed pursuant to military standards. Military standards requires axial fans to pass such as sand and dust, durability and EMI&EMC tests. Another point to consider is that axial fans shall supply high performance, since they are generally used in HVAC systems of aircrafts and military vehicles. HVAC systems are generally used for air conditioning in human-occupied areas such as cockpit and for cooling the equipment inside such as electronic devices that generate high amount of heat. Furthermore, they are required to have low noise for the purpose of maintaining operating discretion and improving comfort in places occupied by people.

The aim of the study is to reduce the noise level of a military axial fan that works at 6000 rpm. The main source is determined as airflow induced noise according to results of acoustic measurement, since noise level peaks occur at blade passing frequency of the fan. Thus, rework design that may improve aeroacoustics features of the fan is considered to reduce the noise level.

Different solution methods and model designs that have been studied in the past to prevent and improve air flow-induced noise in axial fans have been investigated in the literature. By examining wing designs in the literature, knowledge was created for future studies. Novakovic et al.[1] studied nine different blade models on an axial fan based on previous studies in literature. In these model studies, modifications were made on the wing, at the hood end of the wing and at the wing edge,

and the effect of this modification on the aerodynamic and acoustic properties of the fan was shown with test results and compared with the main model. It was observed that the sound level decreased in all changes except for the modification in which a fin was added to the wing and the modification in which a ring was added to the end of the hood. Among the fans that were improved, the aerodynamic performance of the fans that only had flaps added to the wing tip and deep teeth added to the leading edge of the wing did not decrease. Qingyi et al.[2] conducted a study on improvement of the design of the trailing edge of an axial fan blade. The trailing edge of the axial fan is flat, and it is designed to be radial in three different radii in order to reduce the airborne noise level of the fan. In this study, sound pressure levels at blade passing frequency (BPF) of the fan is mentioned in order to compare airborne noise reduction of prototypes. Acoustic tests have shown that blade designs with radial trailing edges reduce the sound level by considering the first and second harmonics of its BPF.

In this study, notched trailing edge and bevelled blade tip design variations are designed to apply rework on the sample fans. Acoustic and aerodynamic performance of the fan are compared both numerically and experimentally.

DESIGN STUDY

The sample fan is a five-blade axial fan that rotates at 6000 rpm with 28 V. Hub diameter and shroud diameter of the fan are 75 mm and 146 mm respectively. The model of the fan is shown in Figure 1.

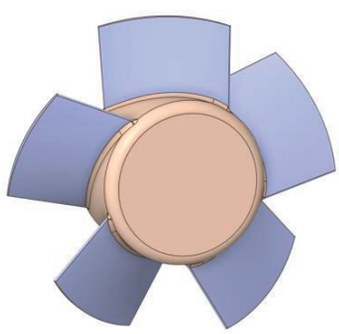


Figure 1: Model of the sample fan

The sample fan can supply up to 460 CFM (781.5 m^3/h) volumetric flow rate at open air as shown in its performance curve that given in its datasheet shown in Figure 2. Performance curve of the fan is determined by performance curve tests according to AMCA 210-2007. Performance tests are explained in Aerodynamic Tests section.

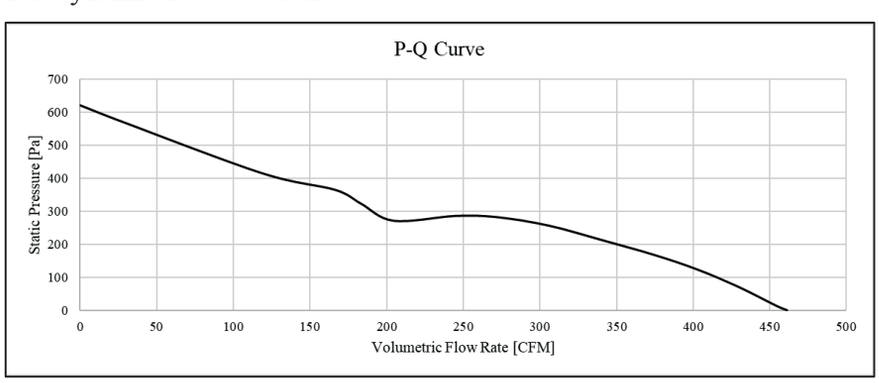


Figure 2: Performance curve of the fan

The total sound power level of the fan is measured as 86.3 dB(A). Besides, sound pressure level is measured at 3-feet (0.91 m) at the inlet of the fan in order to determine the noise level of the fan, since it is the noise level value given in the datasheet. Frequency spectrum of the sound pressure level is given in Figure 3. Frequency spectrum is determined by using Fast Fourier Transform (FFT) of the acoustic measurement in fully anechoic room that complies with ISO 3744-2010. Peaks on the frequency spectrum are checked with the aim of determining the main source of the noise, and it is observed that peaks occur at 500 Hz and its harmonics. The blade passing frequency of the fan is calculated as 500 Hz as given in Equation 1. That shows that the main noise source of the fan is airborne noise.

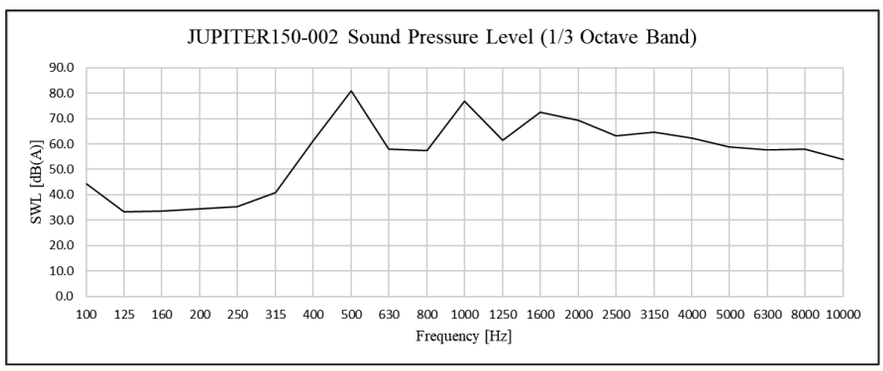


Figure 3: Sound pressure level of the sample fan at 0.91 m

$$\mathrm{BPF}_{\mathrm{Sample}} = \frac{6000 \cdot 5}{60} = 500 \text{ Hz} \tag{1}$$

Two new models of fan blades are designed to lower airborne noise level by reducing vortexes at the tip of the blade as the result of literature research. Rework design are considered and prioritized to keep performance curve as reducing the noise, and additionally, to get production process fast and easier. Thus, two new fans are designed directly on the same blade model of the sample fan. Revised designs of the fan are given in Figure 4, which blades have notched trailing edge (A) and bevelled tip added on notched trailing edge (B).

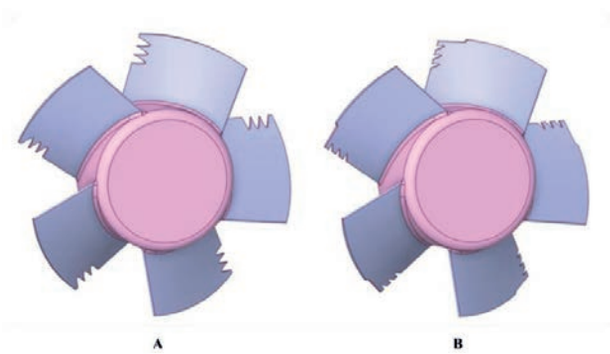


Figure 4: Revised blade models

PERFORMANCE AND ACOUSTIC ANALYSIS

Analysis of sample fan and revised models are conducted at steady state using shear stress transport on CFX. Mass flow at inlet and static pressure at outlet of the fan are defined under normal conditions. Aerodynamic analyses are performed at operating points which are above stall region of the sample fan which is in 250-460 CFM (424.8-781.5 m^3/h). Twenty harmonics of blade passing frequency is considered to calculate total sound power level in order to determine the frequency range up to 10 kHz, so that, results can be compared to the acoustics tests.

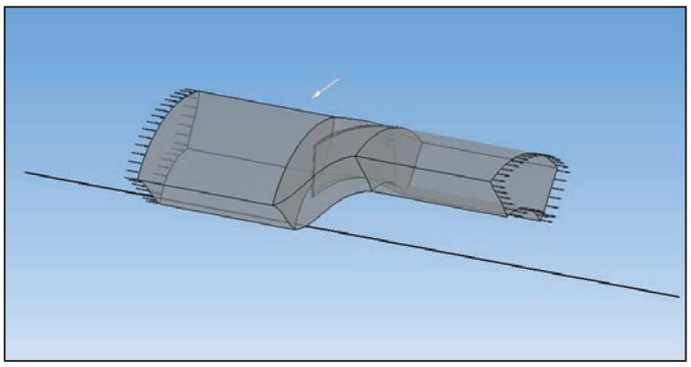


Figure 5: Flow domain

Performance curves of the sample fan and revised design are shown in Figure 6. Average static pressure at outlet of the fan is considered as performance criterion to compare three fans in determined flow rate region. It is noted that the sample fan has higher performance at analysis result than its performance curve on datasheet, yet overall characteristic of the curve is resulted similar. Overall performance in operating region of Model A and Model B are observed to be lower with average of %3 and %16 than the sample fan respectively.

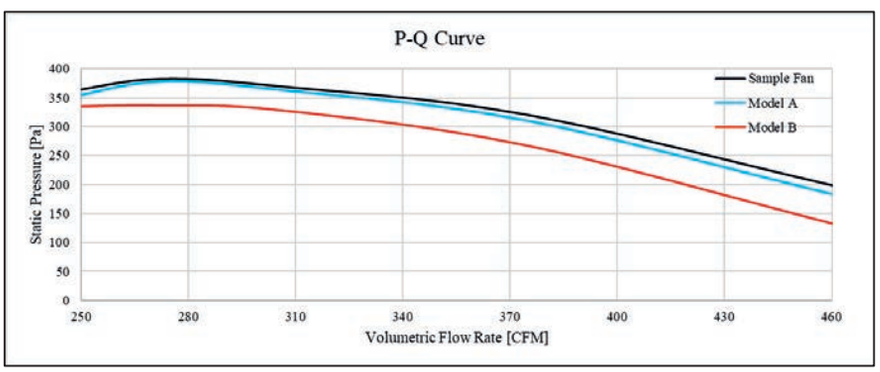


Figure 6: Performance Results of Analyses

Sound power levels and sound pressure levels at 0.91 m of three fans are given in Table 1. Total sound power level of twenty harmonics of the sample fan is turned out to be 84.3 dB. Design revisions on Model A decreases the sound power level by 0.7 dB with marginal performance loss. The sound power level of Model B is 3.1 dB lower than the sample fan, however, its performance curve is considerably lower.

Table 1: Sound Level Results of Analyses

Model	Sound Power Level [dB]	Sound Pressure Level [dB]
Sample	84.3	74.1
A	83.6	73.4
B	81.2	71.0

PERFORMANCE AND ACOUSTIC TESTS

Aerodynamic Tests

Performance tests of the fans are conducted on a test set-up that is designed according to AMCA 210-2007 that is showed in Figure 7 and Figure 8. Fan is mounted on the inlet of the test set-up at point 1. Static pressure value is measured at point 2 right after the inlet. Volumetric flow rate is

calculated by using pressure difference at nozzles on point 3. Air exits the test set-up at point 4 where a blower is placed to set different pressure points in order to determine the performance curve.

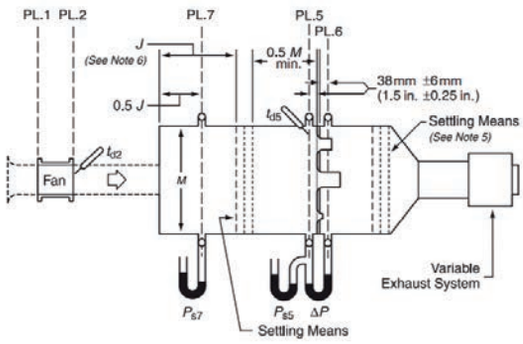


Figure 7: Outlet chamber Setup - Multiple Nozzles In Chamber (AMCA210-007)

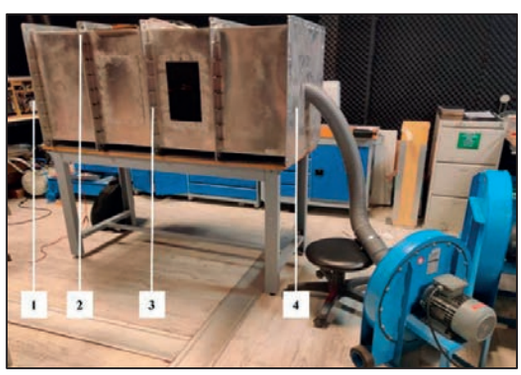


Figure 8: Set-up of performance tests

The performance of the fans are determined by conducting test on their operating regions. The sample fan is also tested with revised models in order to prevent any inconvenience caused by external effects. It is important to note that the stall region of the fans is kept exceptional and not tested, since it is not an optimal operational condition.

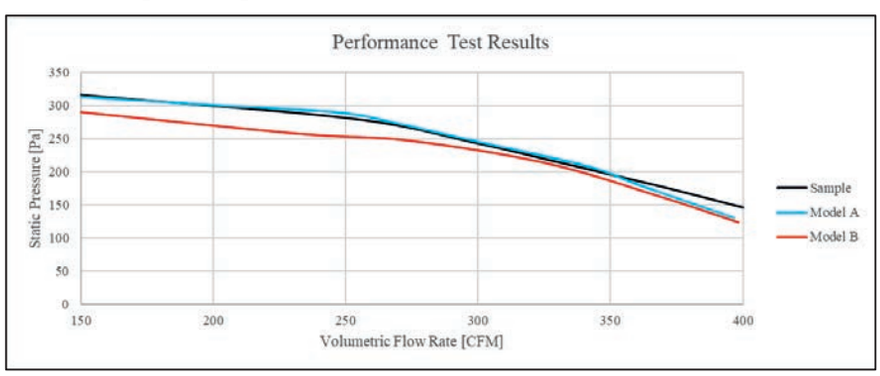


Figure 9: Performance comparison of fans

Comparison of the performance of the fans are determined by comparing static pressure at the same flow rate. It is observed that Model A has 2% performance loss at overall curve where Model B has 7% performance loss in Figure 9. Performance of Model A and Model B are getting closer as volumetric flow rate increases.

Acoustic Tests

Acoustic tests of the fans are conducted in a fully anechoic room according to ISO 3744-2010. Test set-up contains 11 microphones which are 10 microphones for measurement of sound power level and one microphone for measurement of sound pressure level at 3-feet (0.91 m) distance. Ten microphones are located spherically around the fan and the radius of the semi-sphere is 2 m as shown in Figure 10. The eleventh microphone is located at the inlet (suction side) of the fan. Fan is fixed on a tripod and placed in the middle of the anechoic room. Acoustic measurements are conducted for 60 seconds for each fan. In this study, sound pressure levels of the fans are considered to observe the noise reduction on blade passing frequencies. However, sound power levels are also mentioned to compare overall noise levels. Both sound pressure level and sound power level results are given with A-weighted frequency filter.

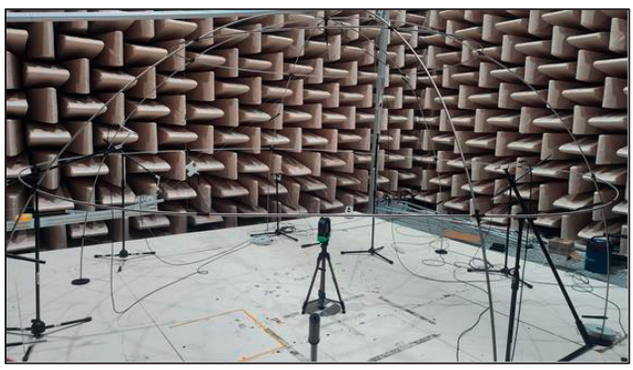


Figure 10: Test set-up of acoustic measurements

Frequency spectrum of sound pressure level of fans are shown in Figure 11. It is observed that sound pressure level of revised design models are lower at blade passing frequency and its harmonics. Especially, decrease in the sound pressure levels of Model A and Model B reaches up to 1.8 dB(A) and 2 dB(A) in the third harmonics respectively.

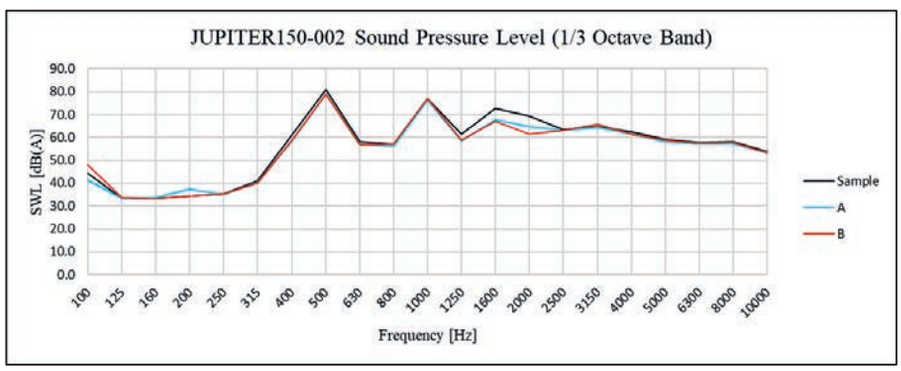
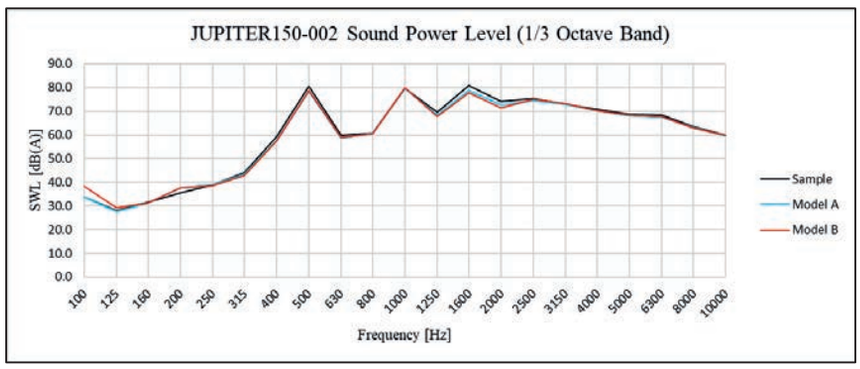


Figure 11: Sound pressure level comparison of fans

Frequency spectrum and overall total of sound power level is given in . The overall sound power level of Model A and Model B are both 85.1 dB(A) which is 1.2 dB lower than the sample fan. Additionally, sound power level decrease is distinct on the third harmonic of the blade passing frequency.



CONCLUSION AND FUTURE WORK

According to aerodynamic analyses, Model B has the lowest sound power level, however, Model B is expected to have lower performance than both the sample fan and Model A. Model A and Model B have similar results of both aerodynamic and acoustic tests. That may be mentioned that bevelled tip and notched edge designs have similar effects on the aerodynamic features of the axial fan. Contrary to analysis results, the reduction in sound power level of both Model A and Model B has the same as 1.2 dB(A) as given in Table 2. Even though Model A and Model B have acceptable loss in performance according to test results, the reduction in noise level is not sufficient to consider.

Table 2: Comparison of Sound Power Level between Tests and Analyses

	Sound Power Level [dB(A)]	
Model	**Test Result**	**Analysis Result**
Sample	86.3	84.3
A	85.1	83.6
B	85.1	81.2

In the future work, a new fan design shall be created to have lower sound power level at present performance level. Number of blades can be increased to reduce the speed of fan, so that, sound power level due to high speed may be decreased and blade passing frequency is shifted. New blade tip design and swept blade design can be worked on the blade number increased fan. Notched edge and bevelled tip designs that are studied in this paper can also be applied on the new fan to maximize the reduction in sound power level.

BIBLIOGRAPHY

[1] Novaković, Tadej, et al. *"Impact of geometric modifications of small axial fans on psychoacoustic metrics."* Applied Acoustics, vol. 218, **2024**.
[2] Qingyi, Sai, et al. *"Experimental and numerical study on a new noise reduction design for a small axial fan."* Applied Acoustics, vol. 211, **2023.**
[3] Rossing, Thomas D. "23.2.7 Noise From Stationary Sources" *Handbook of Acoustics*. Springer, **2007**.
[4] *"Laboratory Methods of Testing Fans for Certified Aerodynamic Performance Rating."* ANSI/AMCA 210-07. Air Movement and Control Association International, **2007**.

NUMERICAL INVESTIGATION OF DIFFERENT WING TIP GEOMETRIES ON THE ACOUSTICS OF AN AIRFOIL WITH TIP GAP IN A WIND TUNNEL

Philipp DIETRICH, Shivaprasad Reddy MALLU, Florian LEX

ebm-papst Mulfingen GmbH & Co. KG, Bachmühle 2, 74673 Mulfingen, Germany

SUMMARY

The acoustics of axial fans is significantly influenced by the tip gap region. Even minor alterations in the fan blade geometry can impact the emitted sound. The rotating geometry poses challenges for detailed measurements of the unsteady flow. At the DLR in Brunswick the BTGNX (Braunschweig Tip Gap Noise eXperiment) was conducted to investigate the effect of the tip gap on the acoustics of an airfoil. Besides the size of the tip gap clearance, the impact of the geometry of the wing tip was analysed as well. Scale resolving simulations were performed on selected configurations from this experiment to validate the simulation process and further analyse the source mechanisms responsible for the emitted acoustics.

INTRODUCTION

The emitted acoustics is of key importance in the development of new generations of fans. Especially for applications operating close to humans (e.g. kitchen hood, air conditioning, etc.) silent fans are requested. In addition to traditional tools, such as experimental investigations and aerodynamic simulations, the increased availability of computational resources has enabled the use of scale resolving simulations, such as Large Eddy Simulations (LES), to predict the emitted sound in the development process of new fans. One major influence on the acoustics of axial fans is the tip gap region. Even minor changes in the fan blade geometry can significantly influence the acoustic behaviour. This was demonstrated in an experiment at the University of Siegen, where an axial fan in a duct was investigated [1]. The measured sound power level was significantly impacted by the size of the tip gap clearance. However, detailed measurements in the vicinity of the fan blades, particularly the tip gap region, are challenging due to the rotating geometry. At the École Centrale de Lyon an experiment of an airfoil between to plates with a variable tip gap was conducted [2]. This experiment identified different sound source mechanisms, which are also relevant for the acoustics of axial fans. Recently, a similar experiment, the Braunschweig Tip Gap Noise Experiment (BTGNX), was conducted at the DLR in Brunswick [3]. This experiment focussed more on the acoustics, featuring for example sound source localization with a beamforming array. Special attention was given to the wing tip section, where four different geometries were investigated. These winglet geometries are similar to those used in axial fans.

In this work, scale resolving simulations, using the LES approach in StarCCM+ were performed on selected configurations of the BTGNX. The primary focus is to evaluate the potential of this simulation approach to reproduce the acoustic effects observed in the experiment.

This paper begins with an overview of the BTGNX. Afterwards, the simulation setup is presented. A comparison of the aerodynamic and aeroacoustic results of the simulations and the measurement is then discussed. Finally, a summary and outlook are provided.

BTGNX

The Braunschweig Tip Gap Noise Experiment (BTGNX) is based on an experiment conducted at the University of Lyon, where an airfoil with tip gap clearance between two plates was investigated [4]. Unlike the original experiment, the BTGNX focusses on the acoustics resulting from changes in the tip gap region. The experiment features a NACA 5510 airfoil with a 200 mm chord length and a maximum span width of 700 mm, which is located between two horizontal plates. The gap between the upper plate and the airfoil can be adjusted automatically allowing the investigation of different tip gap clearances. To control the flow and the boundary layer in the tip gap region, the upper plate is placed in the core flow of the wind tunnel nozzle of the Acoustic Windtunnel Braunschweig (AWB). An array of 256 MEMS microphones is installed in the upper plate, directly above the airfoil, to measure the local unsteady flow characteristics in the tip gap. The wing tip geometry itself can be exchanged, allowing the investigation of different wing tip geometries (winglet). In addition to the sharp edge of the airfoil, which was studied in the Lyon experiment, three additional winglets were analysed. These winglets are similar to those found in the tip gap region of axial fans. A picture of the experimental setup and the different winglet geometries can be found in Figure 1.

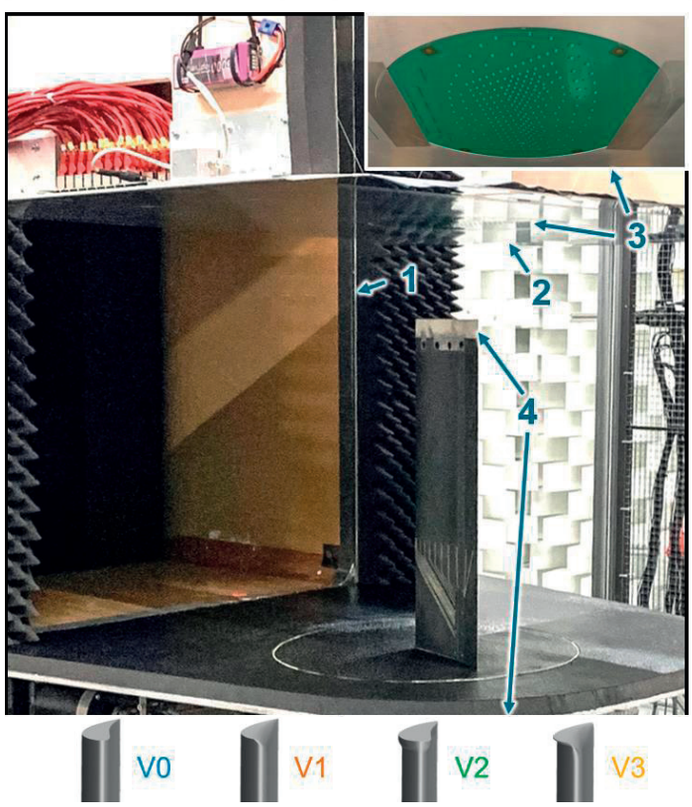


Figure 1: Overview of the experimental setup of the BTGNX in the AWB with the following features highlighted (based on [3]): 1 – nozzle exit of the AWB, 2 – upper plate to control boundary layer flow, 3 – Array of 256 MEMS-microphones above the airfoil, 4 – Exchangeable winglet versions

The larger span width of the BTGNX airfoil, compared to the experiment in Lyon, allows a more precise distinction of the sound sources at the tip gap and the foot of the airfoil. To localise the sound sources via beamforming an array of 96 microphones is used on the suction side of the airfoil. Additionally, 10 far-field microphones were installed, seven on the suction and three on the pressure

side of the airfoil. The distance of the far-field microphones and the microphone array is 1.7 m in reference to the airfoil, except for two microphones facing the suctions side, which are placed at 2.67 m. The aerodynamic performance of the airfoil is evaluated by 31 static pressure probes located at the mid-span of the airfoil. The experiment includes a variation of the tip gap clearance from 0 mm up to 200 mm, different winglet geometries, four different wind velocities (30 m/s, 40 m/s, 50 m/s and 60 m/s) as well as angles of attack (0° up to 16° in 2° increments).

SIMULATION SETUP

The aeroacoustic simulations are based on the master theses of Shivaprasad Reddy Mallu [5] and Florian Lex [6]. In this work, the reference configuration defined by the DLR Brunswick is simulated with the four different winglet configurations. This reference configuration is characterized by a wind velocity of 40 m/s, 12° angle of attack and a tip gap clearance of 10 mm. This setup, along with the expected boundary layer on the top plate, resembles the flow found in the tip gap clearance of large axial fans, as investigated in previous studies at ebm-papst [7].

A RANS (Reynolds Average Navier Stokes) investigation is conducted to determine the final setup for the aeroacoustic simulations. The simulation domain is derived from the dimensions of the wind tunnel and includes the nozzle as well as the part of the experimental setup in contact with the main flow. The support structures and the mounting bracket for the airfoil are excluded from the simulation domain. The collector at the end of the testing area in the wind tunnel is also excluded for stability reasons. However, the influence on the flow around the airfoil was found to be negligible [5]. Figure 2 shows the simulation domain with and without the collector geometry.

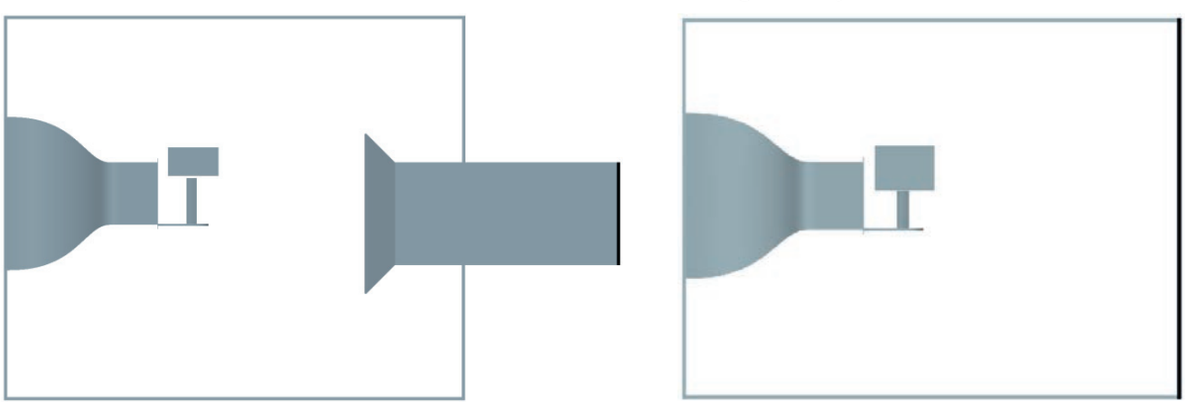


Figure 2: Simulation domain for the aeroacoustic simulations:
AWB geometry with collector (left), AWB geometry without collector (right) [5]

The walls of the wind tunnel are represented by non-reflecting boundary conditions. In order to measure the sound power level an additional 36 microphones were placed mid-span, normal to the span of the airfoil, on a circle with a radius of 1 m.

The recommended resolution for the boundary layer of scale resolving simulations, such as LES, require a Y+ value below 1 and X+ (representing the tangential direction) value below 40. These requirements result in a simulation grid with more than 500 million cells. The resulting storage and computational resources demands cannot be realized in an industrial environment. Previous investigations have shown that an X+ value below 200 can sufficiently predict the acoustics of fans, although local aerodynamic fluctuations may occasionally show differences [7]. To test the required mesh resolution the tip section of the airfoil is investigated using both the recommended resolution and the best-practice from ebm-papst. The best-practice setup results in a numerical grid with approximately 65 million cells. Refining only the upper section of the airfoil, referred to as “BigGap” (with a span width of one chord length) results in approximately 180 million cells. The positioning of the additional microphones and the subdivision of the airfoil can be seen in Figure 3.

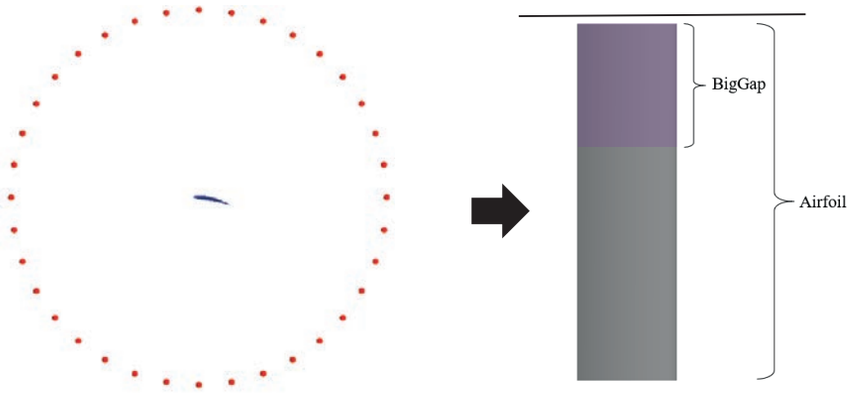


Figure 3: Setup for acoustic evaluation
36 Microphones on a 1 m circle around the mid span of the airfoil (left) [5],
Subdivision of the airfoil for resolution tests and FWH-domain (right) [6]

Aeroacoustic simulations for both configurations are performed using StarCCM+. These simulations are based on an initial RANS simulation to estimate the mean flow field. This data is then used as initial and boundary conditions for the subsequent compressible LES. The scale resolving part of the simulation is divided into three stages. First, an initial transient solution is calculated using a comparably coarse timestep of 1e-3 s for a simulated time of 0.1 s. To enhance the temporal resolution, an additional 0.05 s are simulated with a timestep of 1e-4 s. The final stage involved the acoustic evaluation, where an additional 0.05 s are calculated with a timestep of 1e-5 s, resulting in 5 000 timesteps for the aeroacoustic evaluation.

The acoustic evaluation is based on the propagation of the transient pressure fluctuations using the Ffowcs-Williams and Hawkings (FWH) method from different surfaces (Airfoil and BigGap). The sound pressure level is evaluated based on the last 4 000 timesteps for the different resolutions and two different winglets as shown in figure 5. Additionally, the aerodynamic evaluation of the boundary layer is presented in Figure 4.

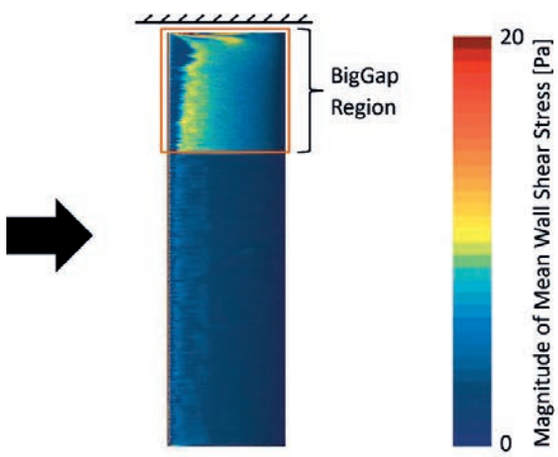


Figure 4: Mean wall shear stress on airfoil surfaces with refined tip gap region (BigGap) (based on [6])

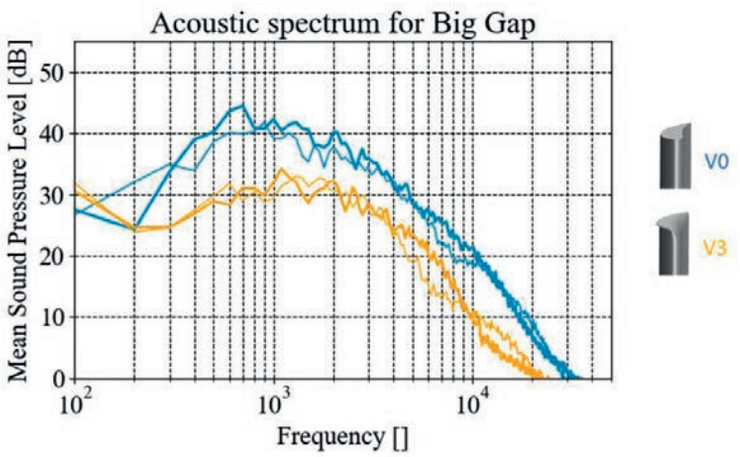


Figure 5: Acoustic sound pressure level in the tip gap section of the airfoil (BigGap) for the reference wing tip (red) and the winglet 3 (ref. Figure 1) for coarse (thin lines) and fine (thick lines) mesh resolution

Similar to previous investigations [7], a significant difference in the aerodynamic properties in the vicinity of the airfoil, based on the selected numerical refinement, can be observed (Figure 4). The acoustic spectra for the tip gap region show a similar behaviour, although slight differences can be noted due to the different resolutions. As shown in Figure 5, these differences manifest in the same frequency regions. Consequently, the best-practice approach can be used for the further investigations.

SIMULATION RESULTS

This work focusses on the influence of different tip gap geometries on the acoustics of the airfoil. The acoustic spectra obtained in the measurement as well as the spectra for the FWH propagation for the far field microphones (ref. BTGNX) can be found in figure 6.

While the shapes of the spectra differ, the same behaviour between the different winglet geometries can be observed in the measurement as well as in the simulation. The reference geometry (V0) shows the highest sound pressure level over the entire frequency range, whereas winglet version 3 (V3) shows the lowest levels. In the lower frequency range (1 000 – 2 000 Hz), winglet V2 shows a similar level to the reference (V0), while winglet version V1 shows similar levels to V3. For higher frequencies (> 3 0000 Hz) this behaviour shifts. Now winglet version V1 shows similar levels to the reference (V0), whereas version V2 behaves similarly to version V3.

A direct comparison the simulation results of winglets V0 and V3 to the measurement can be found in figure7. Here the different shape of the spectra is clearly visible. For lower frequencies (< 1 000 Hz) the differences between measurement and the simulation can be attributed to the reduced evaluation time (~0.04 s) in the simulation. Furthermore, in the simulation only the propagation directly from the airfoil is considered. In the measurement additional effect, such as the reflections at the plates and the shear layer of the nozzle flow, can influence the acoustics.

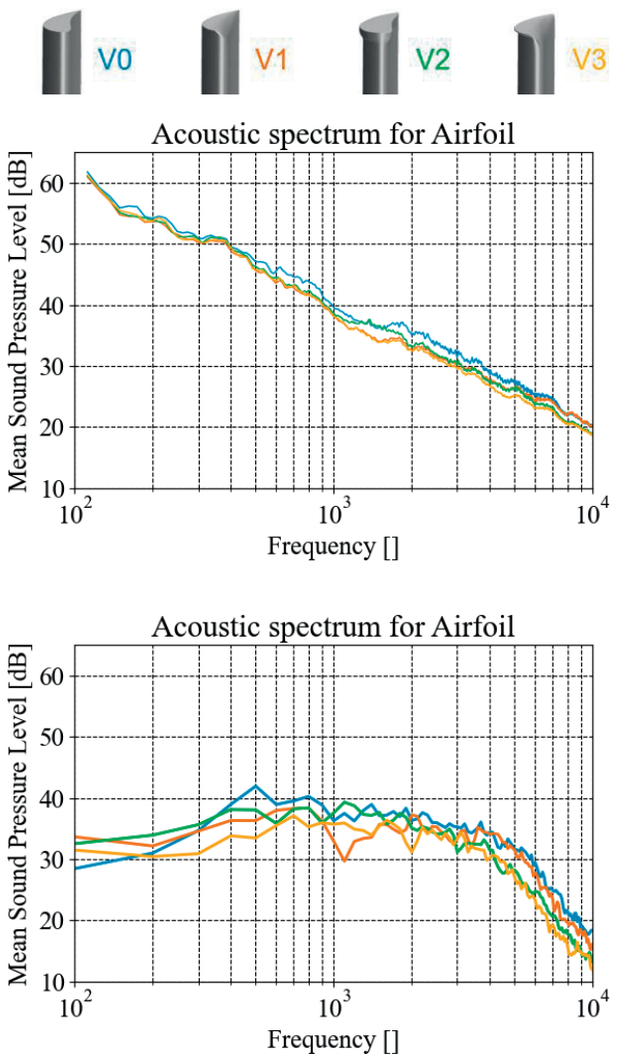


Figure 6: Mean acoustic sound pressure level for far field microphones in measurement (top) and simulation (bottom) for the different wing tip geometries

For higher frequencies (> 2 000 Hz), the elevated levels observed in the simulation are most likely caused by the mesh resolution. This behaviour can also be found for fans within this frequency range when using the best-practice boundary layer treatment presented in the previous section [7].

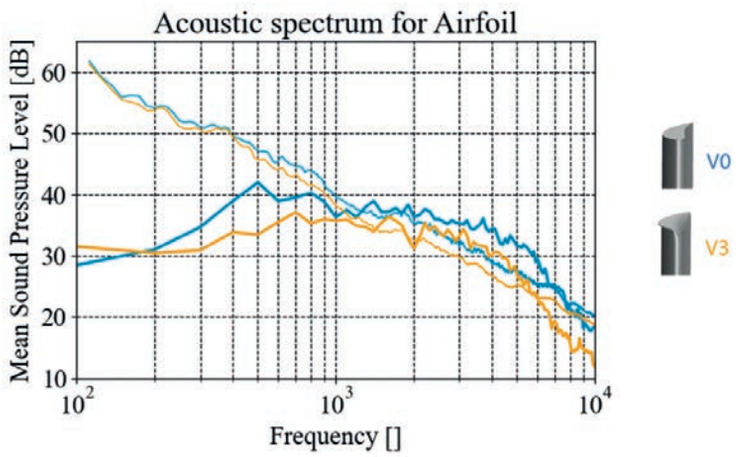


Figure 7: Comparison of winglet version V0 (reference) to V3 in simulation (thick lines) and measurement (thin lines)

The differences between the winglet configuration are also evident in the flow field within the tip gap region. The instantaneous distribution of the lambda 2 criterion and the mean trail of the vortex core are shown in Figure 8.

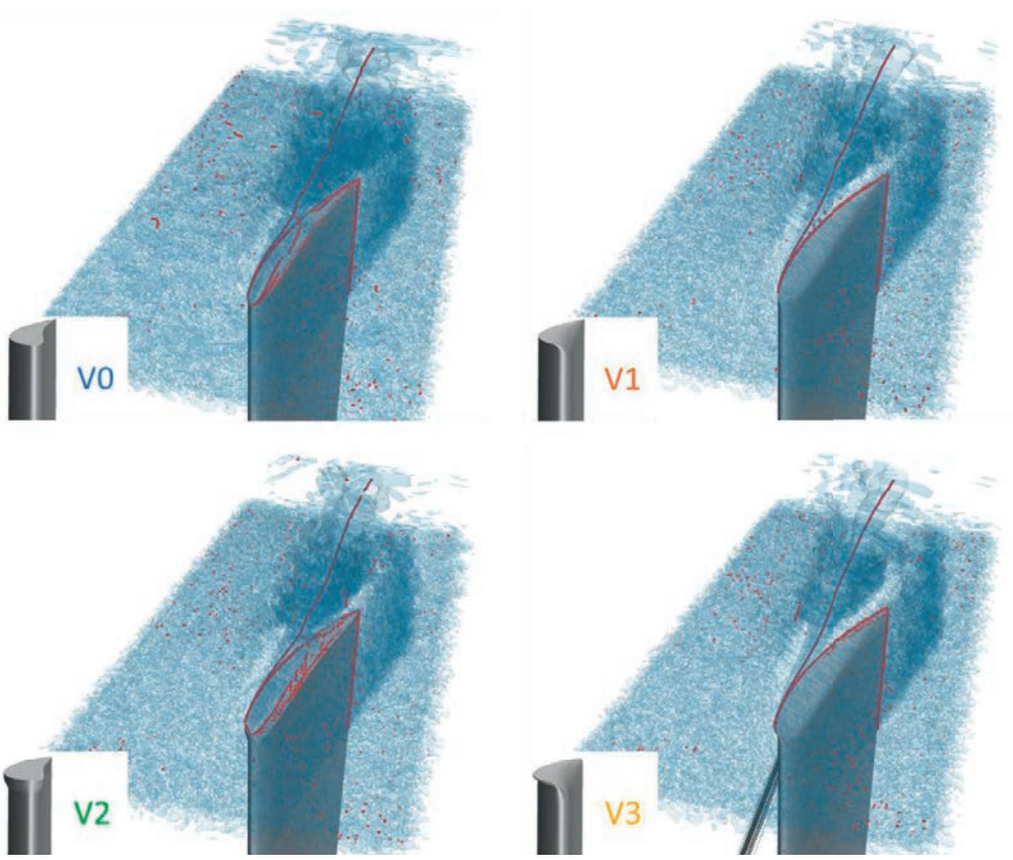


Figure 8: Isosurface of the instantaneous lambda 2 criterion (blue; 50 000 1/s) and the trail of the vortex core (red) for the different winglet versions (V0 – upper left; V1 – upper right; V2 – lower left; V3 – lower right) (artifact in flow field of V3 are due to display bug)

For all winglet versions two distinct turbulent separation regions can be identified at the trailing edge and in the tip gap region. The tip gap vortex for versions V0 and V2 show a higher intensity compared to the other versions. Furthermore, these versions show separation areas on the tip edge on the

pressure side, which are eliminated by the large radius on the pressure side for versions V1 and V3 allowing a smoother transition between the pressure side and the wing tip. These two mechanisms can be the reason for the different behaviour observed in the mid frequency range (1 000 – 2 000 Hz) shown in Figure 6. This is in agreement with the findings of Corsini and Sheard [8], who concluded, that the "bursting" of the tip gap vortex has a significant impact on the emitted acoustics. For V0 and V2 small structures in the vortex indicate such "bursting", whereas the absence of the structures leads to a more stable tip gap vortex in V1 and V3.

In addition to the far field microphones the array of MEMS microphones in the plate above the tip gap can be evaluated. The comparison of the aerodynamic pressure levels for the third octave band at 1 600 Hz can be found in Figure 9.

Despite different levels, similar patterns for the different wing tips can be observed. In the simulation the tip gap vortex consists of 2 parts. One component separates close to the leading edge whereas the other components is located mid to trailing edge of the tip gap. The separation close to the leading edge is significantly more pronounced in the simulation. As shown in Figure 8, the intensity of the separation from the mid to the trailing edge shows higher levels for versions V0 and V2. The intensity of this separation region shows a qualitative agreement to the measurements. This indicates that the higher levels in this frequency range (ref. Figure 6) are caused by this separation effect.

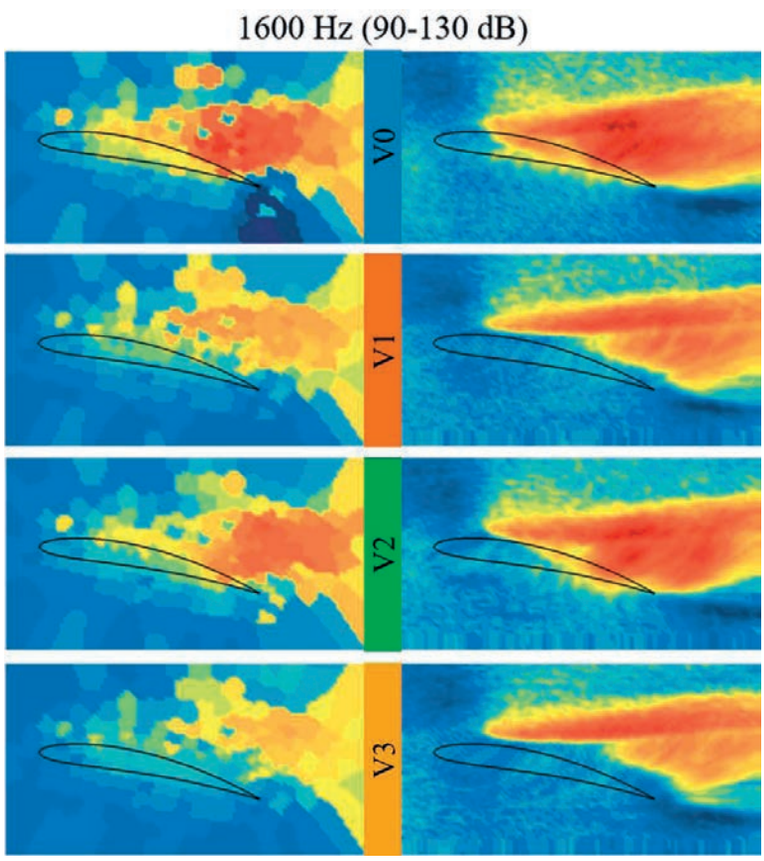


Figure 9: Third octave band levels at 1 600 Hz of the pressure fluctuations on the plate above the wing tip derived from the MEMS-array (left) and the simulation (right)

An additional comparison of the aerodynamic pressure fluctuations in this region for the third octave band at 5 000 Hz is shown in Figure 10. Higher levels are observed in the vortex separating close to the leading edge for versions V0 and V1. This indicates that this mechanism is responsible for the acoustic spectra at higher frequencies (ref. Figure 6).

FAN 2025
Antibes Juan-les-Pins (France), 9 – 11 April 2025

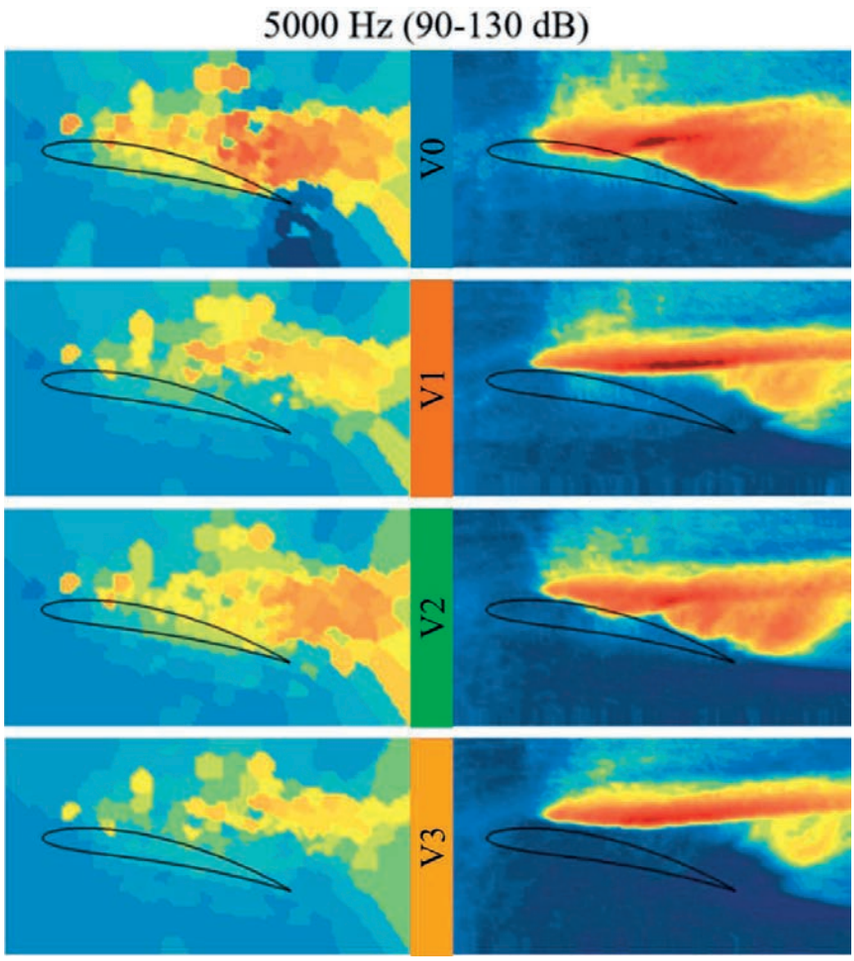


Figure 10: Third octave band levels for 5 000 Hz of the pressure fluctuations on the plate above the wing tip derived from the MEMS-array (left) and the simulation (right)

SUMMARY AND OUTLOOK

This paper investigates the impact of different wing tip geometries on the acoustics of an airfoil with tip gap clearance between two plates using scale resolving simulations. It was demonstrated that even with reduced computational effort, such as mesh resolution, the general acoustic trends, the main effects on the flow field as well as the sound generating mechanisms can be identified. This was achieved due to extensive measurement techniques, such as the MEMS-Array above the airfoil and allows the transition of the numerical investigation methods to rotating geometries such as fans.

Despite differences observed between the measurement and simulation, a good qualitative reproductions of main flow features can be found. Additionally, the same trend of the acoustic impact of the different winglet versions is visible.

Since the BTGNX experiment offers more measurements results than shown in this work, for example data from the microphone array on the suction side of the airfoil, additional investigations and comparisons can be conducted based on the available experimental and numerical data.

BIBLIOGRAPHY

[1] T. Zhu – *Akustische Nachrechnung Von Ventilatoren: Bericht Zum Zusätzlichen FLT-Eigenmittelprojekt Teilprojekt 2 Zum Hauptarbeitspaket C: Akustisches Validierungsexperiment* Project report of University of Siegen (AiF 16773 N/2) University of Siegen, Siegen, **2015**

[2] J. Grilliat – *Contribution à l'étude aéroacoustique des écoulements de jeu.* Phd thesis, Ecole Centrale de Lyon, **2009**

[3] F. Reuschling, L. Liberson, S-M. Pott-Pollenske, J.W. Delfs – *BTGNX: Windkanalexperiment zu kopfspaltströmungsinduzierter Geräuschentstehung – Teil 2: Experimentelle Untersuchung*, Proceedings of DAGA2024, Hannover, **2024A**

[4] F. Reuschling – *BTGNX Messprotokoll* Deutsches Zentrum für Luft- und Raumfahrt (DLR) Braunschweig, **2024**

[5] S. R. Mallu – *Aeroacoustic Simulation of Tip Gap Noise* Masterthesis, Technical University of Braunschweig, **2023**

[6] F. Lex – *Aeroakustische Simulation von Kopfspaltgeräuschen am Tragflügel* Masterthesis, Hochschule Aalen, **2024**

[7] A. Lucius, S. Hütter, P. Dietrich, M. Schneider, M. Lehmann, T. Geyer *Experimental and numerical investigation of axial fan aeroacoustics at disturbed inflow conditions* Proceedings of the FAN2018, Darmstadt, **2018**

[8] A. Corsini, A. G. Sheard *End-plate for noise-by-flow control in axial fans* Periodica Polytechnica Mechanical Engineering, **2013**

BTGNX: AN ACOUSTIC BENCHMARK WIND TUNNEL EXPERIMENT FOR TIP-GAP NOISE

Fabian REUSCHLING[1], Lev LIBERSON[2], Michael POTT-POLLENSKE[1], Jan W. DELFS[1], Daniel ERNST[3]

[1] *German Aerospace Center (DLR), Institute of Aerodynamics and Flow Technology, Technical Acoustics, Lilienthalplatz 7, 38108 Braunschweig, Germany*

[2] *previously: German Aerospace Center (DLR), Institute of Aerodynamics and Flow Technology, Technical Acoustics, Lilienthalplatz 7, 38108 Braunschweig, Germany*

[3] *German Aerospace Center (DLR), Institute of Aerodynamics and Flow Technology, Experimental Methods, Bunsenstrasse 10, 37073 Göttingen, Germany*

SUMMARY

Within a current cooperation between the fan manufacturer ebm-papst and the department of Technical Acoustics at the DLR-Institute of Aerodynamics and Flow Technology, an optimisation workflow for a fan blade side edge geometry to minimise tip-gap noise is being developed. For validation of this approach, an acoustics-focused wind tunnel experiment was performed. It employs extensive near- and far-field acoustic measurement techniques and is intended to serve as a benchmark experiment for future tip-gap noise research.

INTRODUCTION

With the reduction of other noise sources in housed fans, the tip-gap noise originating from the gap between a fan blade's side edge and the fan housing has become increasingly relevant for the overall sound radiated by a fan. The analysis of this noise source and development of sound reduction measures is the topic of a current cooperation between the fan manufacturer ebm-papst and the department of Technical Acoustics at the DLR-Institute of Aerodynamics and Flow Technology. The ultimate goal is the development of a numerical optimisation workflow for the geometry of the fan blade's side edge (for details see [1]). For this purpose, the simulations have to be able to accurately determine the relative difference in sound radiated by two different side edge geometries. Literature data to be used for validation of this approach is scarce, however. Therefore, the Braunschweig Tip-Gap-Noise eXperiment (BTGNX) was developed within the cooperation

with the aim of providing a broad database that can be used not only for validation of the optimisation workflow, but also serve as a benchmark for future tip-gap noise research.

EXPERIMENTAL SET-UP

For the set-up of the validation experiment, cues were drawn from previous tip-gap noise experiments (e.g. [2], [3]). Representative for these is a thorough – aerodynamics focused – investigation carried out at the University of Lyon [4]. This used a static wing with a NACA 5510 aerofoil and 200 mm chord, mounted vertically between two plates extending the wind tunnel nozzle. The tip-gap is created between the wing side edge and one of the plates. These experiments usually have several shortcomings from an aeroacoustic perspective. The most significant one being the use of relatively small wind tunnels leading to a small wing span – in case of the experiment performed in Lyon 200 mm in the no-gap configuration – and potential influences of the mounting on the opposite side of the tip-gap on the measured far-field spectra. The small span also makes sound source localization using phased microphone arrays difficult.

The goal of the Braunschweig Tip-Gap-Noise eXperiment was to address these shortcomings. It was set-up in the Acoustic Wind tunnel Braunschweig (AWB) featuring an 800 mm wide and 1200 mm tall nozzle exit surface. While the basic set-up, the used aerofoil, and chord are identical to the experiment carried out at the University of Lyon, the wing span was extended to 700 mm in the no-gap configuration. The tip-gap (height h) is created between the wing's side edge and a flat plate mounted horizontally in the wind tunnel (see Figure 1). The last 30 mm of the wing span were made interchangeable to study the effect of different wing tip geometries. Four different winglets were manufactured using Stereolithography (SLA) 3D-printing: A simple extension of the wing's aerofoil as reference winglet (0), a winglet rounded off from the pressure to the suction side (1), a winglet where this rounding extends beyond the suction side edge (2) and a winglet with extensions on the suction and the pressure side creating the shape of a "T" (3). The rotation point of the wing was placed 30 mm (0.15 chord) downstream of the leading edge on the camber line. This position ensures that the tip vortex system remains at the same position throughout all measured angles of attack and was determined from PIV measurements performed in the experiment at the University of Lyon. The flow on the bottom side of the plate was tripped directly after the leading edge. The flow on the wing was not tripped. This set-up better separates the noise generated in the tip-gap and from the mounting of the wing compared to previous experiments in small wind tunnels.

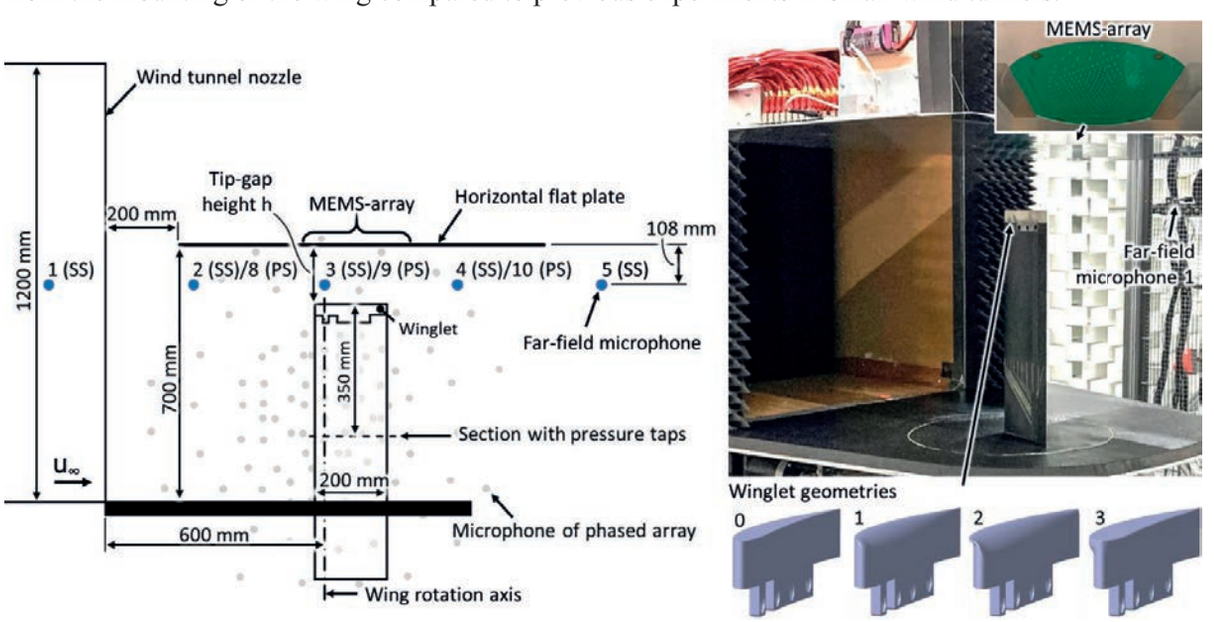


Figure 1: Set-up of the Braunschweig Tip-Gap-Noise eXperiment

The wing was equipped with 31 static pressure taps along the mid-span section (i.e. at 350 mm from the side edge) and two Kulites type LQ-062 behind 0.5 mm pinholes, one in the Pressure Side (PS) at 0.25 chord and one in the Suction Side (SS) at 0.9 chord, both at 33 mm from the wing side edge. A further two Kulites type XCQ-093 were integrated into the side edge of the reference wingtip on the camber line at 0.03 chord and 0.775 chord. To capture the far-field acoustics, ten ¼" microphones (type GRAS 46BF-1) were placed 108 mm below the flat plate, spaced at an angle of 12° relative to rotation point of the wing. Seven of the microphones were located on the suction side, starting with an angle of -24° measured towards a line perpendicular to the primary flow direction. The remaining three microphones were placed on the pressure side directly opposite to the microphone positions 2, 3 and 4 (-12°, 0°, 12°) on the suction side. The microphones had a distance of 1.7 m to the middle plane of the wind tunnel nozzle, except for the last two microphones on the suction side (at 36° and 48°) which had a distance of 2.67 m. A phased microphone array with 96 ½" microphones was placed on the suction side in a distance of 1.7 m from the nozzle middle plane. The middle was located 473 mm below the flat plate and at the same distance from the nozzle as the wing rotation point. Finally, an array consisting of 256 MEMS microphones (MEMS = Micro Electro-Mechanical System) was integrated into the flat plate opposite the wing's side edge. A detailed description of this array and measurement results are reported in [5].

In the measurement campaign, 22 gap heights between 0 mm (no gap) and 200 mm (presumed to be equivalent to a free side edge) and nine geometric angles of attack between 0° and 16° in 2° intervals were measured. The reference winglet was measured at inflow velocities of 30 m/s, 40 m/s, 50 m/s and 60 m/s. The other three winglets were measured at velocities of 40 m/s and 60 m/s. The microphone data were recorded at a sample rate of 51 kHz over a period of 30 seconds.

RESULTS AND DISCUSSION

While the primary purpose of the dataset is to be post-processed for validation of the simulations, an analysis of the measured spectra for the reference configuration – 40 m/s inflow velocity (u_∞) and 12° geometric angle of attack (α_{geo}, equalling about 5.9° aerodynamic angle of attack) – is still conducted for far-field microphone 4 (located at a 90° angle to the chord) to gain an understanding of the occurring effects. The two most important parameter variations in this regard are the variation of the gap height to identify the most relevant frequency bands and the comparison between the four winglet geometries to draw conclusions about the prevalent sound generation mechanisms. All presented Sound Pressure Levels (SPLs) are normalised to a distance of 1.7 mm from the wing's rotation axis.

Gap height variation

The far-field sound pressure spectra for the most relevant gap heights (h) at the reference configuration are presented in Figure 2. Additionally, a measurement for the same set-up except for the wing is included as background noise. The spectra for all measured gap heights can be found in Figure 6 in the Annex.

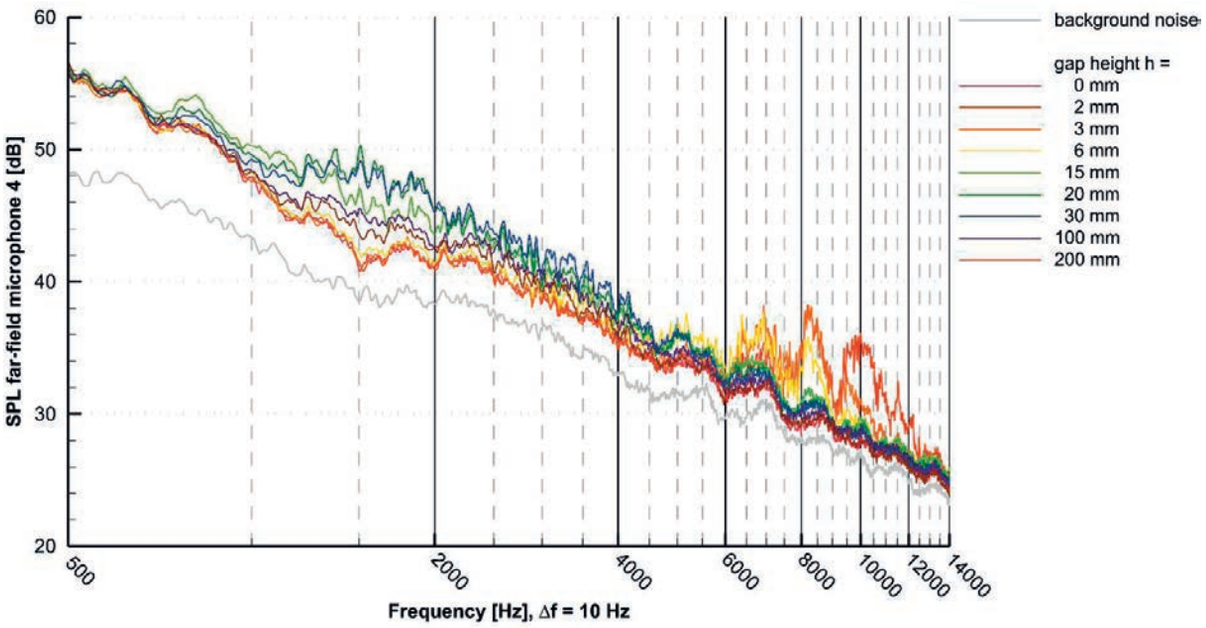


Figure 2: SPL for far-field microphone 4 at selected gap heights (reference winglet, u_∞ = 40 m/s, α_{geo} = 12°)

From the spectra, two frequency bands can be distinguished where a change in gap height leads to a change in the recorded sound pressure level: The first is between 1 kHz and 3 kHz where the spectra fan out and the second is between 6 kHz and 12 kHz where three broadband peaks are observed. In the first frequency band, the lowest SPLs are measured for gap heights up to 6 mm, thereafter gradually increasing by 9 dB in total to the maximum at 20 mm gap height. This is followed by a reduction that levels out 4 dB above the lowest SPLs at 100 mm gap height. Consequently, the spectra at gap heights above 100 mm can be considered not to be influenced by the tip-gap noise source any more, confirming the presumption of a free side edge at 200 mm gap height. The minimal difference in sound pressure level between gap heights up to 6 mm coincides with the boundary layer thickness at this location on the flat plate, which was measured to be 8 mm at 40 m/s inflow velocity. When the gap height is equivalent to the boundary layer thickness the measured SPL is equivalent to that of the free side edge (see Figure 6). This indicates that the tip-gap noise source is suppressed when the wing's side edge is within the boundary layer of the flat plate. The observation is confirmed by the sound source localization using the phased microphone array that primarily shows secondary sound sources at 2 mm gap height (in this case the mounting of the wing in the bottom side plate) whereas a clear source in the tip-gap region is visible for 20 mm gap height (see Figure 3).

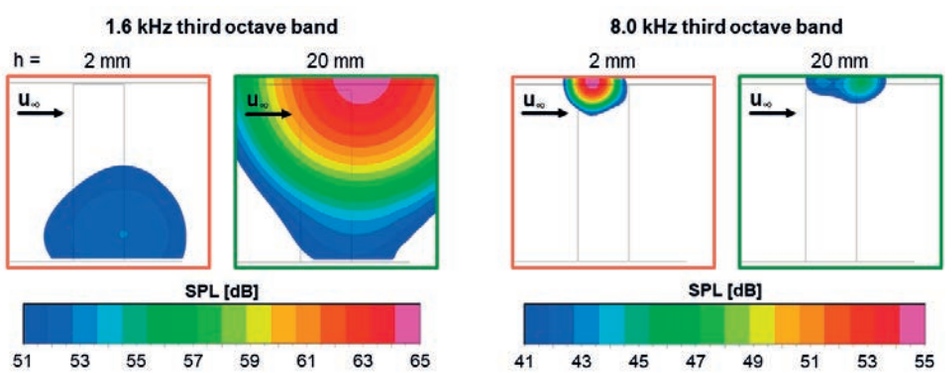


Figure 3: Sound source localization in 1.6 kHz and 8.0 kHz third octave bands (reference winglet, u_∞ = 40 m/s, α_{geo} = 12°, conventional beamforming)

In the second frequency band between 6 kHz and 12 kHz on the contrary, the tip-gap noise is the strongest at small gap heights with the maximum being 8 dB above the free side edge at h = 2 mm. The following decline in measured sound pressure level is the largest at the third peak around 10 kHz and less strong and occurs at larger gaps heights at the other two peaks around 7 kHz and 8 kHz. At 20 mm gap height, the SPL is close to that of the free side edge. Until this gap height, the source localization places the primary source in the tip-gap near the leading edge of the wing. At larger gap heights, the primary source shifts to the tip of the trailing edge indicating a non-tip-gap-related sound generation mechanism (see Figure 3). The sound source at 0 mm and 1 mm gap height is also placed in the tip-gap, albeit the SPL being at the level of the free side edge. This is likely due to how these two gap heights were measured: In order to prevent scratching along the MEMS-array, measurements at 0 mm gap height (direct contact) and 1 mm gap height were taken separately, while all other gap heights were measured in one motion starting at h = 2 mm.

Winglet variation

To draw more detailed conclusions about the sound generation mechanisms present in the two identified frequency bands, it is helpful to compare the sound pressure levels for the four winglet geometries at gap heights of 2 mm, 6 mm, 20 mm and 100 mm. The respective spectra for the reference configuration and far-field microphone 4 are presented in Figure 4. Each of the winglets with geometry modifications compared to the reference winglet was designed to reduce one of the tip-gap noise generation mechanisms known from literature [6]: The winglet rounded off from the pressure to the suctions side aims at weakening the Tip Separation Vortex (TSV) typically rolling up on the wing's side edge, the T-shaped winglet aims to push the Tip Leakage Vortex (TLV) further from the wing's suction side to reduce the noise generated as it convects past the trailing edge, and the winglet where the rounding extends past the suction side combines both approaches.

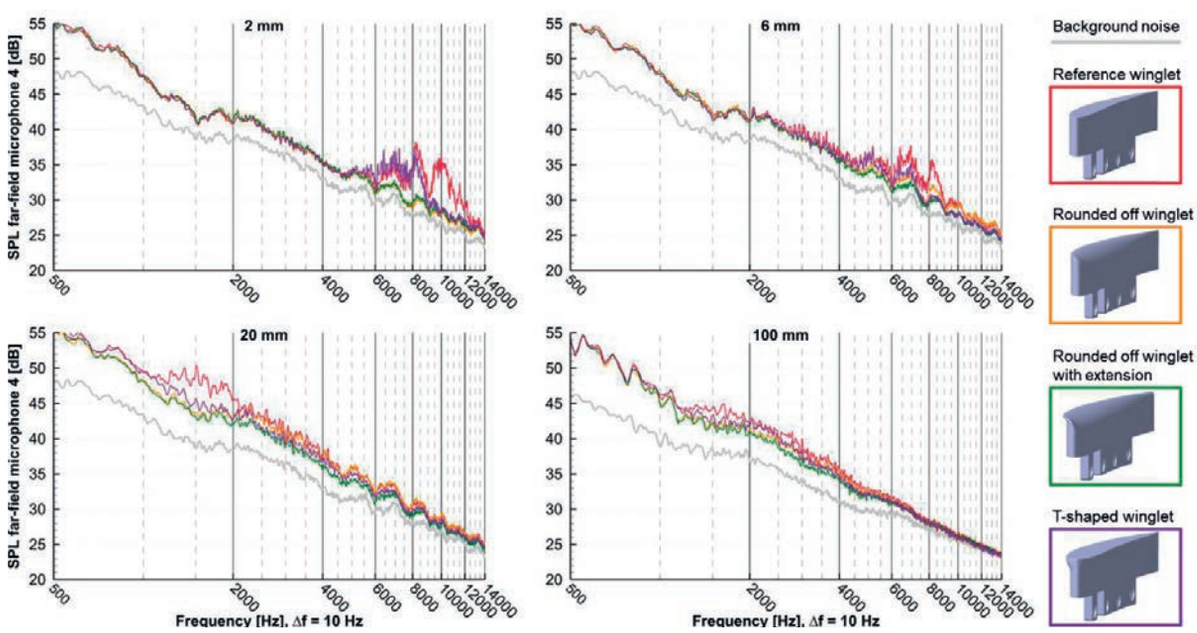


Figure 4: SPL for far-field microphone 4 for different winglet geometries (u_∞ = 40 m/s, α_{geo} = 12°)

In the first frequency band between 1 kHz and 3 kHz, no effect of the winglet geometry on the measured sound pressure level is observed at gap heights below the boundary layer thickness (2 mm and 6 mm). This is in line with the previously drawn conclusion that the tip-gap noise source is suppressed if the wing's side edge is within the boundary layer. At 20 mm gap height, all modified winglet geometries lead to a SPL reduction – up to 7 dB for the two rounded off winglets and 5 dB for the T-winglet – compared to the reference winglet. This difference gradually becomes smaller towards larger gap heights. It is not clear which sound generation mechanism is prevalent in this

frequency band, as all geometry modifications lead to a reduction in radiated sound. It can be suspected that the primary cause of sound is the TSV since both winglets rounded off from the pressure to the suctions side (preventing the roll up of the tip separation vortex) lead to similar SPL reductions. However, it is unclear then why the T-shaped winglet also causes a reduction in radiated sound compared to the reference winglet. One possible explanation is the larger TSV-reattachment zone (see [7]) due to the wider side edge. Confirmation might be achieved from the analysis of the surface pressures measured with the MEMS-array that are not considered in this work.

Between 6 kHz and 12 kHz, the largest differences between the winglets are found for 2 mm gap height, as is expected from the analysis of the gap height variation. The three broadband peaks at 7 kHz, 8 kHz, and 10 kHz are only observed for the reference winglet. The spectrum of the T-winglet includes the first two peaks, while no clear peak is found in the spectra of the rounded off winglets. The recorded sound pressure levels for these winglets are roughly equal and up to 7 dB below those of the reference and the T-winglet. At 6 mm gap height, this difference narrows and the spectrum of the T-winglet shifts towards the one for the rounded off winglet with extension. The opposite behaviour is observed for the spectrum of the rounded off winglet that moves closer to that of the reference winglet. This trend continues towards larger gap heights. From 20 mm gap height, the spectra of the reference and the rounded off winglets overlay, as do those of the T-winglet and the rounded off winglet with extension. This shift indicates two different sound generation mechanisms in the second frequency band: At gap heights up to 6 mm, the primary cause is the tip separation vortex scraping off the pressure side edge which is not observed for the two rounded off winglets. The sound source localisation near the leading edge (discussed in the analysis of the gap height variation) coincides well with where the TSV starts forming according to literature [8]. Towards larger gap heights, the main cause becomes the tip leakage vortex interacting with the trailing edge. As the rounded off winglet with extension and the T-winglet push the TLV further from the wing, the radiated sound is reduced compared to the other two winglets. This conclusion also fits the previously discussed sound source localisation.

POST-PROCESSING FOR COMPARISON WITH NUMERICS

As stated previously, the goal of the numerical investigations running in parallel is to accurately predict the relative differences between the noise generated by the winglets to facilitate a geometry optimisation (for results see [1] and [9]). Part of the optimisation workflow is the calculation of an acoustic metric that is used to place the investigated winglet geometries in a sequence from loudest to quietest. To validate this step of the workflow, the measured data are post-processed in a similar way yielding one sequence of winglets for each combination of inflow velocity, gap height and angle of attack (“configuration”).

The processing is performed automatically for the entire dataset of far-field microphone measurements on the basis of third octave bands. In a first step, the background noise is subtracted from the sound pressure level in each frequency band. Then, the resulting SPLs are summed up over the two frequency ranges determined from the gap height variation (1 - 3 kHz and 6 - 12 kHz) and the entire range from 1 kHz to 12 kHz. Subsequently, the sequence of winglets is determined from the summed-up SPLs. Both, the subtraction of the background noise and the summation of the SPLs is done with arithmetic subtraction/addition as well as energetically to investigate the robustness of the approach.

The resulting number of occurrences of each sequence of winglets per far-field microphone is plotted in Figure 5. Each row corresponds to one calculation scheme (arithmetic/energetic subtraction/addition) in the three frequency ranges while each column represents one sequence of winglets (from loudest to quietest). The cells are coloured according to the number of occurrences of the respective sequence in the entire measurement dataset. In total, 103 configurations with valid data for all four winglets were found.

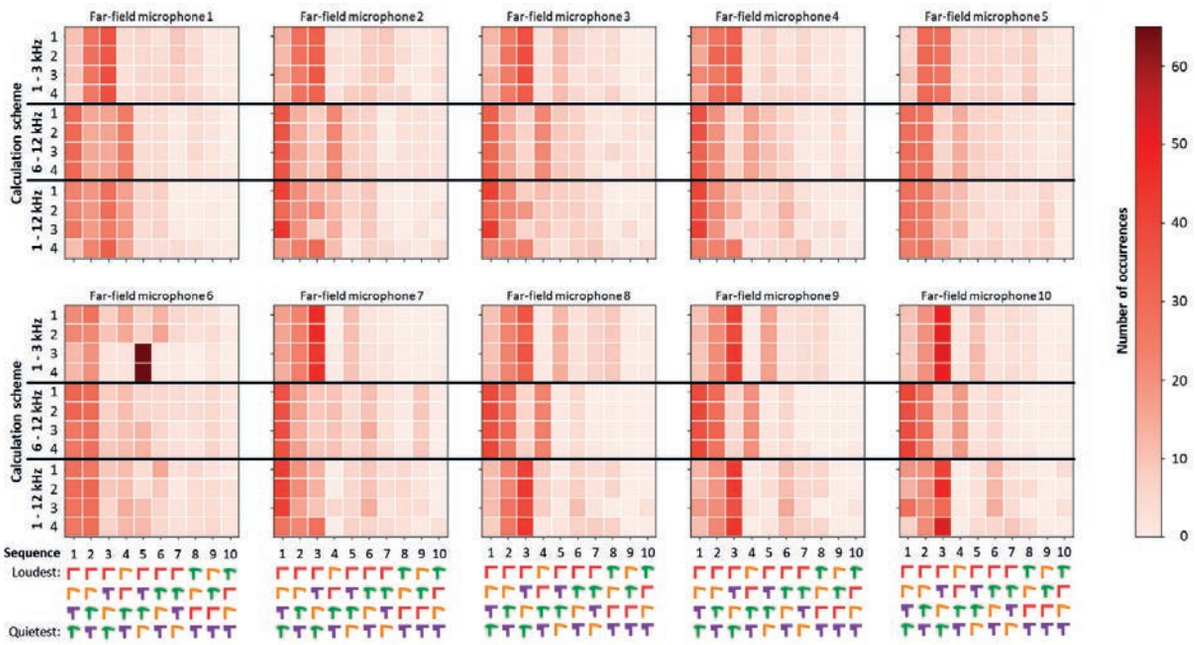


Figure 5: Occurrences of winglet sequences
Calculation schemes: 1 – arithmetic subtraction of background noise, arithmetic summation; 2 – arithmetic subtraction, energetic addition; 3 – energetic subtraction, arithmetic summation; 4 – energetic subtraction, energetic summation

For the two frequency bands from 1 kHz to 3 kHz and from 6 kHz to 12 kHz, there generally is good agreement between the different calculation schemes. The sole exception is found for far-field microphone 6. This, however, is due to significant noise in the microphone's spectra masking the tip-gap noise. When the combined frequency range is used, the most common sequence strongly depends on the calculation scheme. This is explained by the different effects and trends previously found for the two frequency bands, preventing the determination of a common sequence and underlining the importance of considering both frequency bands independently. Overall, the sequence calculation is found to be robust and independent from how the single value used to sort the winglets is calculated.

Analysing the found sequences, the previously discovered distinction between the two frequency bands is visible: Between 1 kHz and 3 kHz, the two most common sequences place the reference winglet as loudest, followed by the rounded off, the rounded off with extension and the T-winglet (sequence 2) or the T-winglet, the rounded off and the rounded off with extension (sequence 3). Between 6 kHz and 12 kHz, the most common sequence also starts with the reference winglet and the rounded off winglet, but is then followed by the T-winglet and the rounded off with extension as quietest winglet (sequence 1). This sequence is rarely found in the first frequency band. The other two often observed sequences in the second frequency band are sequence 2 – already detected between 1 kHz and 3 kHz – and the rounded off winglet as loudest, followed by the reference winglet, the rounded off with extension and the T-winglet (sequence 4). For both frequency bands, a directivity can be observed. Between 1 kHz and 3 kHz, sequence 3 is more commonly observed than sequence 2 the further downstream the microphone is placed on the suction and the pressure side (i.e. the rounded off winglet with extension being the quietest instead of the T-winglet). In the second frequency band (6 – 12 kHz), a shift from sequence 2 to sequence 1 (i.e. also from the T-winglet to the rounded off with extension as the quietest winglet) is observed, but less clearly and only on the suction side.

Comparing the calculated sequences to those found in analysing the winglet variation, many similarities are found. In the first frequency band, sequence 3 is clearly observed starting with a gap

height of 20 mm, while it can be suspected that sequence 2 is deduced from small gap heights where there is little difference in the SPL of the four winglet geometries. Between 6 kHz and 12 kHz, the winglet sequence found for gap heights larger than 20 mm – reference and rounded off winglets at about the same level and rounded off with extension and T-winglet at lower SPLs – is mirrored in sequences 1 and 2. However, the winglet sequence found for gap heights below 20 mm (equivalating to sequence 3 or sequence 5 with the last two winglets switching places) is rarely observed in the calculated sequences, while sequence 4 cannot be seen in the winglet variation analysed previously. A closer inspection reveals that sequences 3 and 5 are only prevalent among gap heights below 20 mm at inflow velocities of 40 m/s. At inflow velocities of 60 m/s, the spectra in this frequency band are closer together and sequence 4 more commonly observed. Consequently, the sequence found for the first frequency band in the previous section is less important when the entire dataset is considered.

In summary, the post-processing approach is well suited to validate the numerical optimisation workflow. The trends and winglet sequences present in the measured data are captured and can easily be compared to those deduced from the acoustic metric. Moreover, analysis of the sequences leads to a better understanding of the measured data and can be used to place observations made for one particular configuration into context. The same post-processing approach was used to find common gap height sequences, generally confirming the conclusions drawn from the gap height variation studied herein.

CONCLUSION AND OUTLOOK

In this work, the set-up of a benchmark experiment for tip-gap noise and far-field results for a tip-gap height and wing side edge variation were presented. The design is based on previous tip-gap noise experiments using a vertically mounted non-rotating wing, but incorporates modifications to limit the influence of secondary noise source enabling a better separation of the tip-gap noise source. From the sound pressure levels measured for the gap height variation, two distinct frequency bands were identified in which the tip-gap noise source is active. In the first band between 1 kHz and 3 kHz, the noise source is suppressed at gap heights below the boundary layer thickness and strongest at 20 mm gap height. From comparison of the wing side edge modifications, it is suspected that the sound generated by the tip separation vortex when scraping off the pressure side edge and reattaching on the wing side edge is dominating in this frequency band. However, further investigation using the surface pressures recorded with a MEMS-array installed in the tip-gap opposite of the wing's side edge (reported in [5]) is necessary. In the second frequency band between 6 kHz and 12 kHz, the strongest contribution of the tip-gap noise source to the far-field was recorded for 2 mm gap height. Analysis of the side edge modifications revealed the separation of the TSV as the primary noise source at gap heights below the boundary layer thickness. At larger gap heights, the interaction of the tip leakage vortex was identified as the prevalent noise source.

Finally, the wing side edge modifications were sequenced from loudest to quietest for all measured configurations (i.e. combinations of inflow velocity, gap height and angle of attack). This revealed the reference side edge (straight continuation of the aerofoil) to be the loudest in both frequency bands. In the first band, it is followed by the T-shaped side edge and the side edges rounded off from the pressure to the suction side. In the second band, the rounded off side edge is louder than the T-shaped side edge followed by the rounded off side edge extending slightly beyond the suction side. The results confirmed that the effects observed in the spectra for the reference configuration (u_∞ = 40 m/s, α_{geo} = 12°) are also present in the other measured configurations. Besides giving a concise overview of all measured data, the sequences can be used to evaluate the numerical optimization workflow that is based on the prediction of relative differences between different side edge geometries.

Future work will focus on correlating the acoustic effects measured in this experiment with the aerodynamic data reported for other tip-gap noise experiments (e.g. the research performed at the University of Lyon, extensively reported in [4]). Furthermore, a detailed analysis of other measured configurations will be performed, attempting to link the conclusions drawn to findings reported in literature, in particular a recently published research by Awasthi et al. [10] investigating the radiated sound at different ratios of gap height to boundary layer thickness. This was found to be a major obstacle for comparison with previous research as the boundary layer thickness usually was much larger than the largest gap height investigated.

ACKNOWLEDGEMENTS

The authors would like to thank the cooperation partners at ebm-papst for the fruitful cooperation, helpful input, and support throughout the project.

BIBLIOGRAPHY

[1] L. Liberson, F. Reuschling, R. Ewert, M. Pott-Pollenske, J. W. Delfs – *BTGNX: Windkanalexperiment zu kopfspaltströmungsinduzierter Geräuschentstehung – Teil 1: Numerische Ergebnisse*. Fortschritte der Akustik – DAGA 2024, **2024**

[2] M. C. Jacob, J. Grilliat, R. Camussi, G. Caputi Gennaro – *Aeroacoustic investigation of a single airfoil tip leakage flow*. International Journal of aeroacoustics, volume 9, number 3, **2010**

[3] I. Saraceno, S. Palleja-Cabre, C. Paruchuri, B. Ganapathisubramani – *Influence of non-dimensional parameters on the tip leakage noise*. AIAA Aviation Forum 2023, **2023**

[4] J. Grillant– *Contribution à l'étude aéroacoustique des écoulements de jeu.* PhD Thesis, **2009**

[5] D. Ernst, C. Spehr, F. Reuschling, M. Schneider – *BTGNX: A MEMS microphone array for the acoustic benchmark wind tunnel experiment for tip-gap noise.* Proceedings of Fan Noise 2025 Symposium, **2025**

[6] R. Koch, M. Sanjosé, S. Moreau – *Large-Eddy Simulation of a Single Airfoil Tip-Leakage Flow*. AIAA Journal, volume 59, number 7, **2021**

[7] J. D. Denton – *Loss mechanisms in Turbomachines.* Proceedings of the ASME 1993 International Gas Turbine and Aeroengine Congress and Exposition, volume 2, **1993**

[8] S. Kang, C. H. Hirsch – *Experimental study on the three-dimensional flow within a compressor cascade with tip clearance: Part II—the tip leakage vortex.* ASME Journal of Turbomachinery, **1993**

[9] P. Dietrich, S. R. Mallu, F. Lex – N*umerical investigation of different wing tip geometries on the acoustics of an airfoil with tip gap in a wind tunnel.* Proceedings of Fan Noise 2025 Symposium, **2025**

[10] M. Awasthi, A. O. Wills, D. Moreau, P. Croaker, P. Dylejko – *A Parametric Study of Far-Field Sound Radiated by an Idealised Tip Leakage Flow.* 30th AIAA/CEAS Aeroacoustics Conference, **2024**

ANNEX

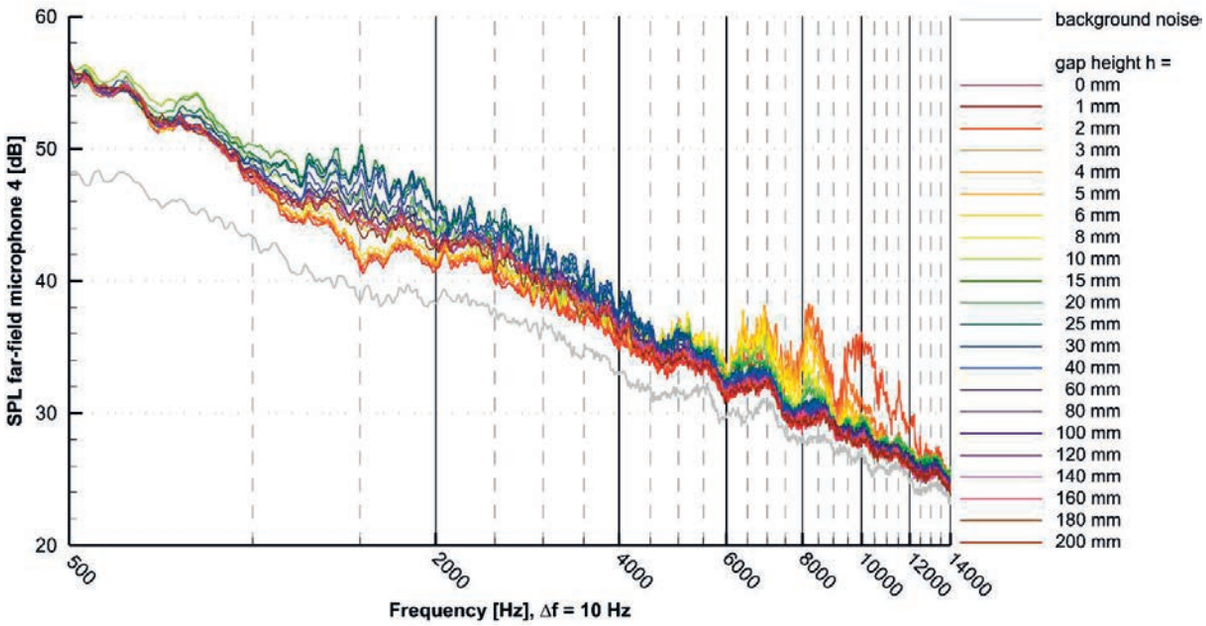


Figure 6: SPL for far-field microphone 4 at all measured gap heights (reference winglet, u_∞ = 40 m/s, α_{geo} = 12°)



BTGNX: A MEMS MICROPHONE ARRAY FOR THE ACOUSTIC BENCHMARK WIND TUNNEL EXPERIMENT FOR TIP-GAP NOISE

Daniel ERNST[1], Carsten SPEHR[1],
Fabian REUSCHLING[2], Marc SCHNEIDER[3]

[1] *German Aerospace Center (DLR), Institute of Aerodynamics and Flow Technology, Experimental Methods, Bunsenstrasse 10, 37073 Göttingen, Germany*

[2] *German Aerospace Center (DLR), Institute of Aerodynamics and Flow Technology, Technical Acoustics, Lilienthalplatz 7, 38108 Braunschweig, Germany*

[3] *ebm-papst Mulfingen GmbH Co. KG, Bachmühle 2, 74673 Mulfingen, Germany*

SUMMARY

A generic experiment has been carried out to investigate the tip leakage flow between a flat plate and a non- rotating airfoil. The measurements were carried out in the open test section of the acoustic wind tunnel at DLR Braunschweig (AWB) and the experiment is called the "Braunschweig Tip-Gap-Noise Experiment" (BTGNX). The experimental setup consists of a microphone array for the acoustic source localization from the acoustic far field, static pressure measurements to determine the wing lift distribution and the MEMS microphone sensors integrated into the flat casing plate to record the fluctuating surface pressures distribution in the near field of the acoustic source region. The presentation focusses on the experimental setup of the microphone array integrated into the plate which consists of 256 MEMS microphones. This MEMS array allows the determination of the fluctuation pressure distribution in dependency of the various experimental parameter such as free flow velocity, angle of attack and the gap between flat plate and wing tip. Furthermore, the analysis of the MEMS microphone data gives inside into the surface flow distribution as well as the near field acoustic pressure field to locate and identify the main sound source mechanism.

FAN 2025
Antibes - Juan-les-Pins (France), 9 - 10 April 2025

INTRODUCTION

The tip-gap noise has become a significant contributor to overall sound of in housed fans due to the reduction of other contributing noise sources. To address this, ebm-papst and the DLR-Institute of Aerodynamics and Flow Technology are collaborating to develop a numerical optimization workflow for fan blade side edge geometry. The goal is to accurately determine the difference in sound radiated by different side edge geometries. To support this, the Braunschweig Tip-Gap-Noise eXperiment (BTGNX) was created to provide a comprehensive database for validation and benchmarking.
The experiment in general is described in more detail and was performed by Reuschling et al. [1] and corresponding numerical results are shown by Dietrich et al. [2]. Similar work was done by Malkki et al. [3] and Al-Am et al. [4].
This paper is focused on the MEMS microphone array measurements and results (see 1).

EXPERIMENTAL SET-UP

The experiment was set up in the Acoustic Wind tunnel Braunschweig (AWB) with a nozzle size of 800 x 1200 mm. Four different 3D-printed winglets were placed on a wing with a chord length of approx. 200 mm and a wind span of approx. 700 mm. The gap between the winglet and the top plate where varied between 0 mm and 200 mm. The geometric angle of attack is varied between 0° to 16° and the flow speed from 30 m/s to 60 m/s.

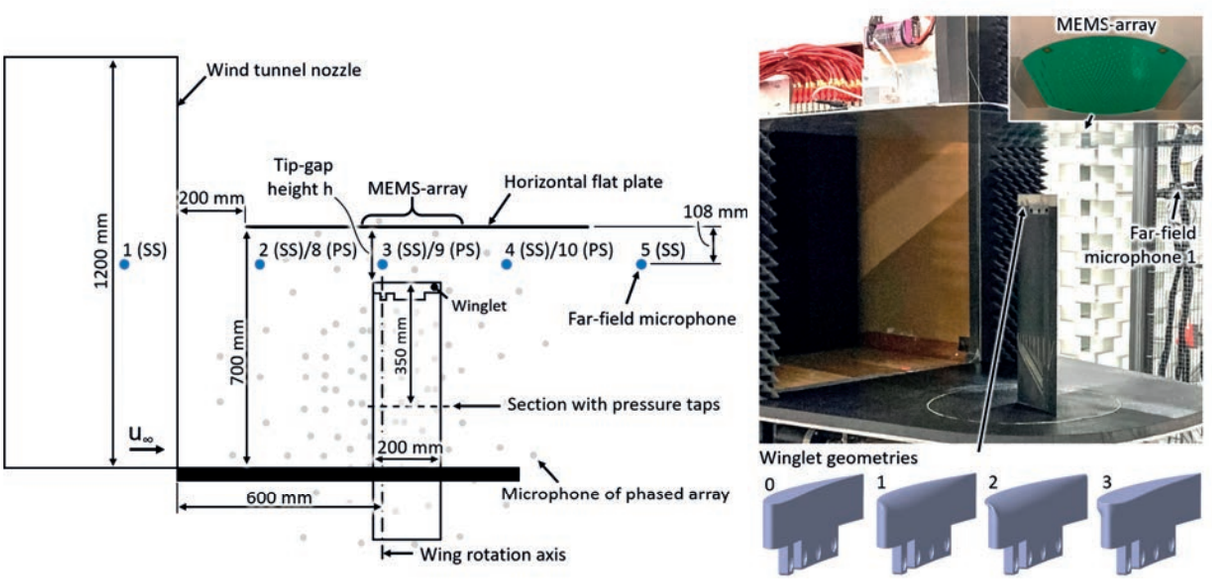


Figure 1: Set-up of the Braunschweig Tip-Gap-Noise eXperiment. Figure made by Reuschling [1]

A static pressure tap line of 31 sensors was placed 350 mm spanwise from the winglet, to measure the aerodynamic performance of the wing unfluenced by the winglet. Four Kulites are placed inside the winglet. Out of flow, ten far field microphones and a microphone array of 96 microphones are placed to measure the radiated sound from tip gap.
In the plane above the winglet a MEMS microphone array was placed containing 256 sensors. In total 366 instationary pressure sensors were measured synchronised at 51 kHz sampling frequency, allowing to evaluate in detail near- and farfield correlations.

The 256 MEMS microphones of type Vesper VM2020 are distributed over a circular disk of diameter

FAN 2025
Antibes - Juan-les-Pins (France), 9 - 10 April 2025

320 mm and follow in general the expected contour of turbulence footprint predicted by CFD simulations for a mean angle of attack. While the wing was rotated and moved up and down to adjust the gap height, the MEMS microphone was fixed in position inside the top plate. All holes and vias on the pcb (=printed circuit board), except the 0.4 mm diameter sound ports of the MEMS microphones and a hole of 4 mm diameter at $x = y = 0$ mm, were filled or taped to assure minimal influence on the flow by the array itself.

RESULTS AND DISCUSSION

In this section, the acoustic results obtained from the MEMS microphone array data are presented in a detailed manner. The data is analyzed as averaged surface pressure fluctuations in the frequency domain and as beamforming visualizations on the winglet. These representations are essential for understanding the noise characteristics and turbulence structures around the winglet configurations. For all results presented, a single experimental parameter is varied while all other parameters are held constant to ensure the reliability and comparability of the findings. Specifically, the free-stream velocity is fixed at 40 m/s throughout the study. The varied parameters include the angle of attack (AoA), the gap height between the winglet and the top plate (Gap), and the type of winglet employed in the setup (refer to Figure 1 for a detailed schematic of the configuration).

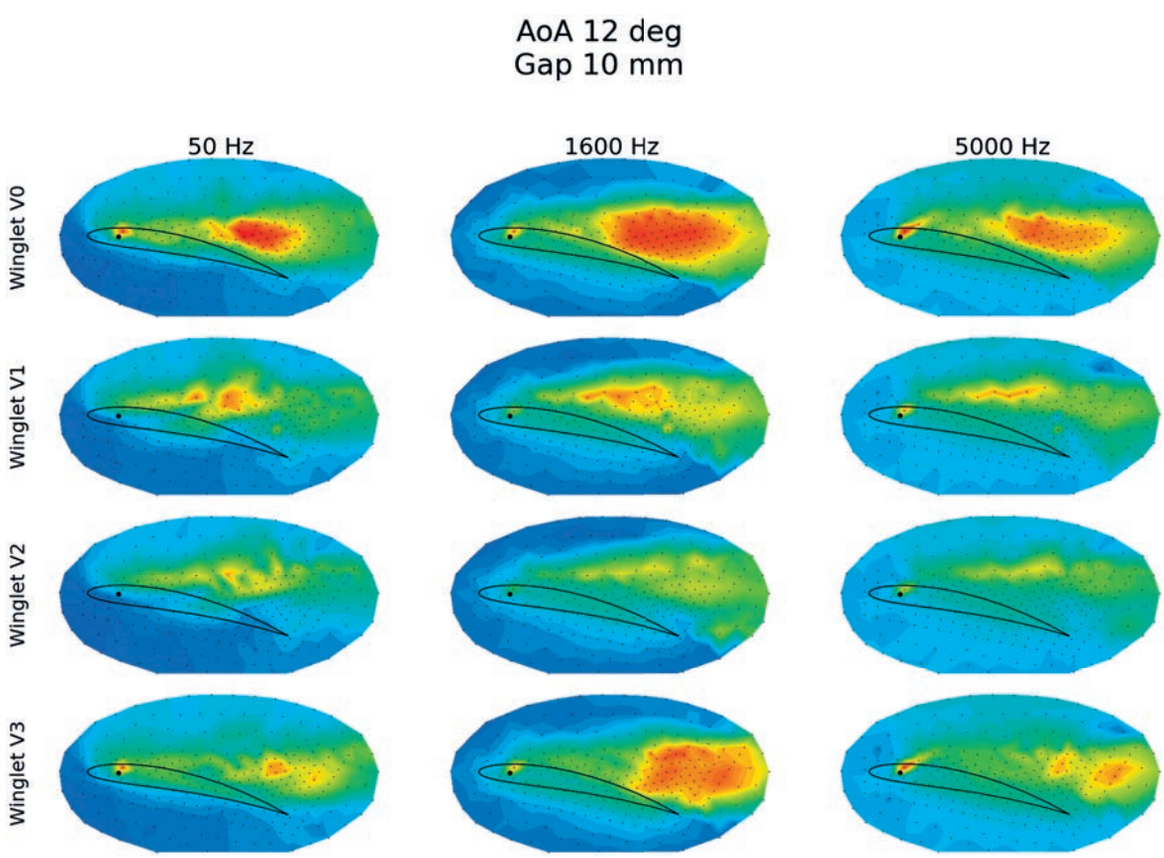


Figure 2: Third Octave surface pressure from MEMS array with color range from 90 to 130 dB. Angle of Attack 12 deg and gap height of 10 mm.

To facilitate a meaningful comparison with the results reported by [2], three specific 1/3 octave band frequencies are selected for analysis: 50 Hz, 1600 Hz, and 5000 Hz. Small dots indicate the position of each MEMS microphone in the following surface pressure plots.

The reference case, characterized by an angle of attack of 12 degrees and a gap height of 10 mm, is illustrated in Figure 2. This configuration serves as a baseline for comparing the effects of the different winglet designs. Notably, the winglet labeled as V0, which features sharp edges, exhibits a more extensive turbulence footprint on the wall compared to all other winglet configurations. This behavior is consistent across all analyzed frequencies. In the visualizations, a black dot is used to indicate the position and accurate size (4 mm in diameter) of an open hole on the printed circuit board (PCB) that was not sealed during the experiments. This unsealed hole significantly influences the flow behavior, particularly for winglet designs V0 and V3, where a direct wake originating from the hole is clearly discernible.

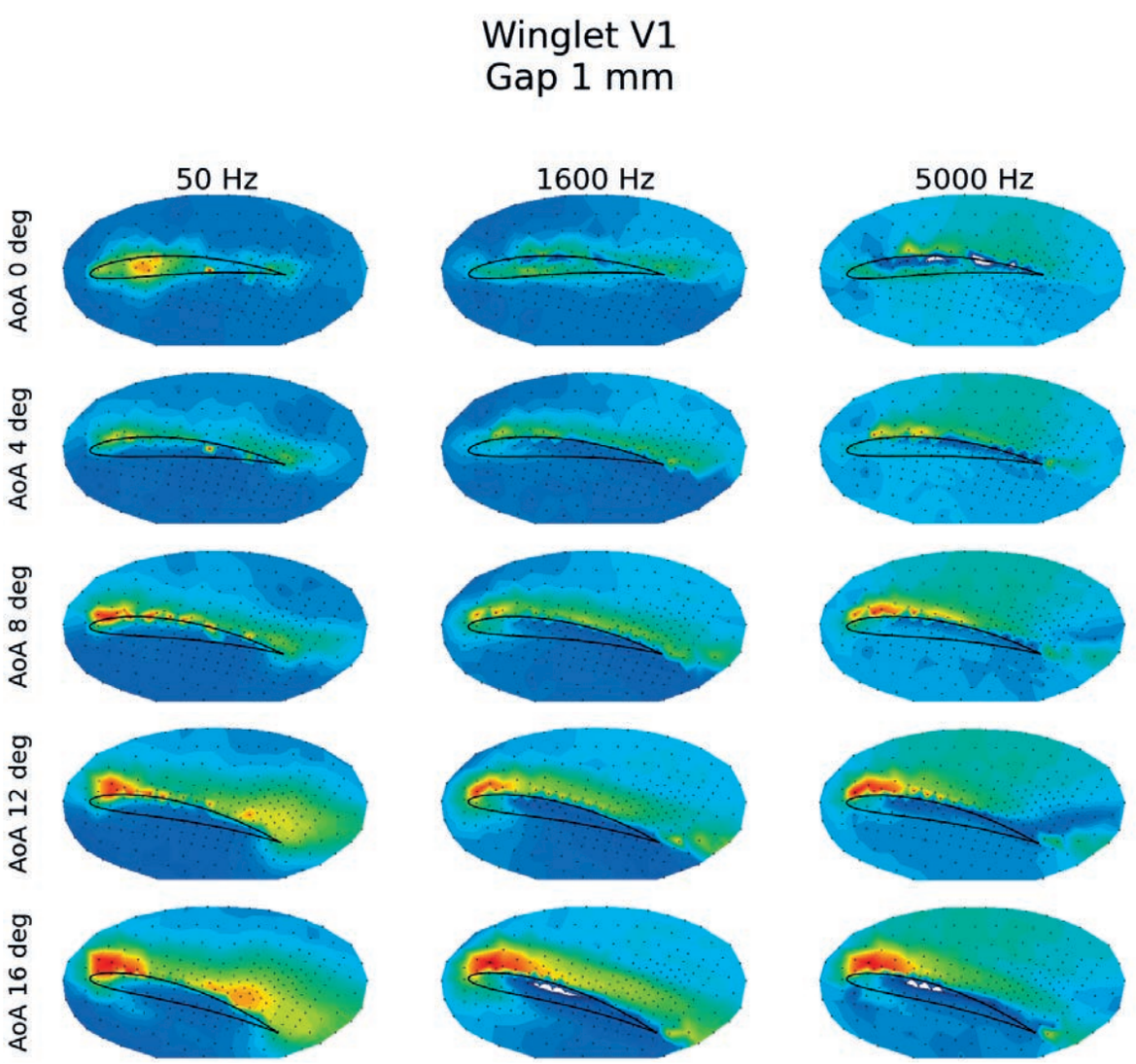


Figure 3: Third Octave surface pressure from MEMS array with color range from 90 to 130 dB. Winglet V1 and gap height of 1 mm.

For the winglets designated as V1 and V2, a more complex wake structure is observed at the low frequency of 50 Hz. Specifically, three distinct wakes appear at approximately 10%, 70%, and 100% of the chord length. This intricate wake pattern highlights the sensitivity of these winglet designs to low-frequency turbulence. At higher frequencies, such as 1600 Hz and 5000 Hz, these wakes become indistinguishable.

A comparison with the simulation results reported by [2] reveals a notable discrepancy in the turbu-

FAN 2025
Antibes - Juan-les-Pins (France), 9 - 10 April 2025

lence characteristics within the tip gap region for all winglet designs. The experimental data consistently show significantly higher levels of turbulence in this region.

As anticipated, the turbulence intensity exhibits a clear increase with higher angles of attack, as shown in Figure 3. Notably, the small gap height of 1 mm plays a significant role in shaping the observed flow characteristics. Due to the minimal separation distance between the winglet and the top plate, no secondary wakes are discernible in the results. This absence suggests that the limited gap suppresses the formation of additional flow structures, effectively simplifying the wake pattern downstream of the winglet.

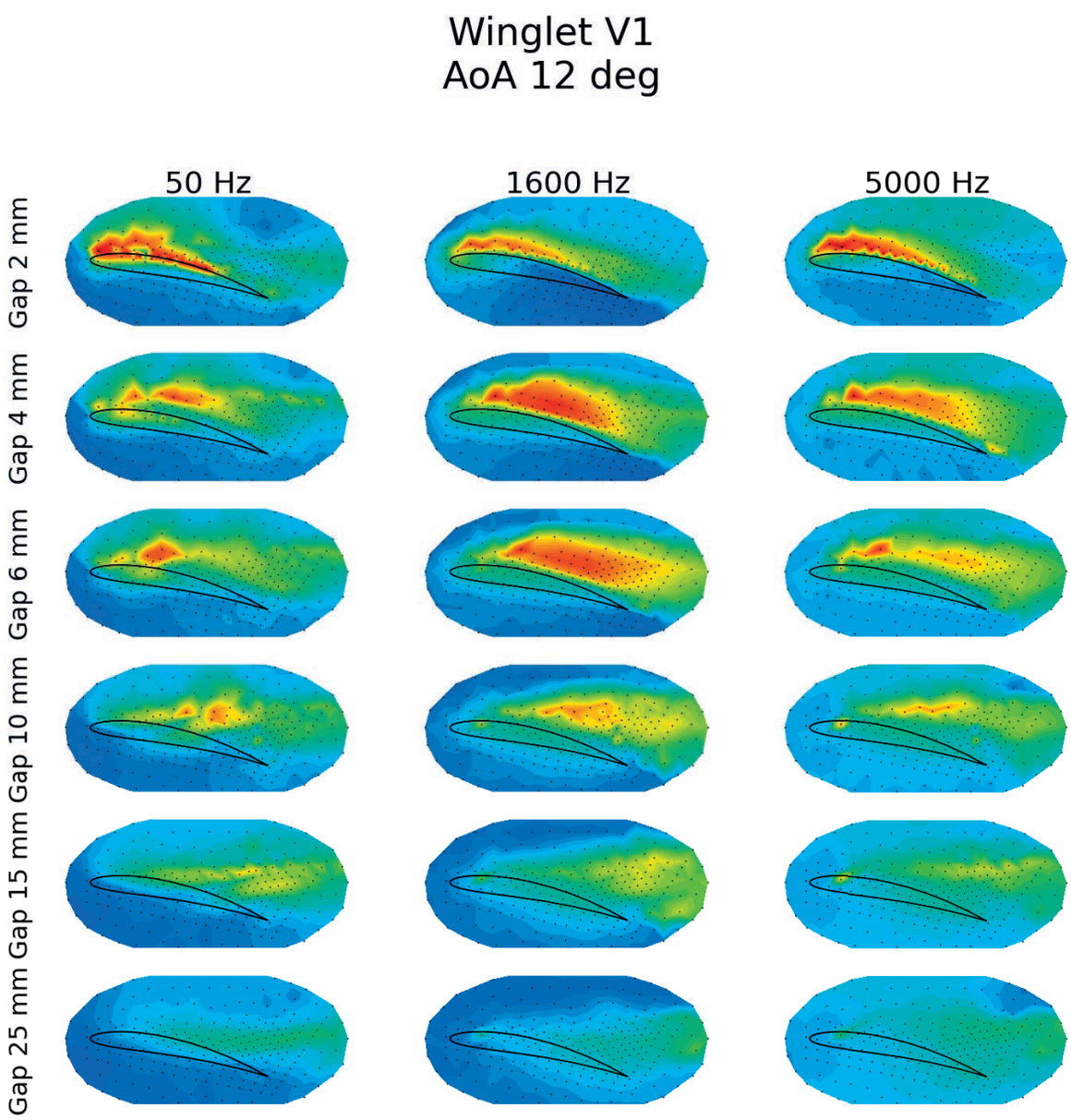


Figure 4: Third Octave surface pressure from MEMS array with color range from 90 to 130 dB. Winglet V1 and angle of attack of 12 deg.

With increasing gap size, as illustrated in Figure 4, a notable decrease in surface pressure levels is observed. This reduction is accompanied by the emergence of distinct wake patterns at the leading edge, center chord position, and trailing edge, particularly at a frequency of 50 Hz. For gap sizes of 10 mm and 15 mm, these wakes are clearly distinguishable, indicating a significant effect of gap size

on the flow dynamics. The results suggest that larger gaps allow for more complex wake structures to develop across the chord, likely due to increased flow interaction between the winglet and the surrounding surfaces.

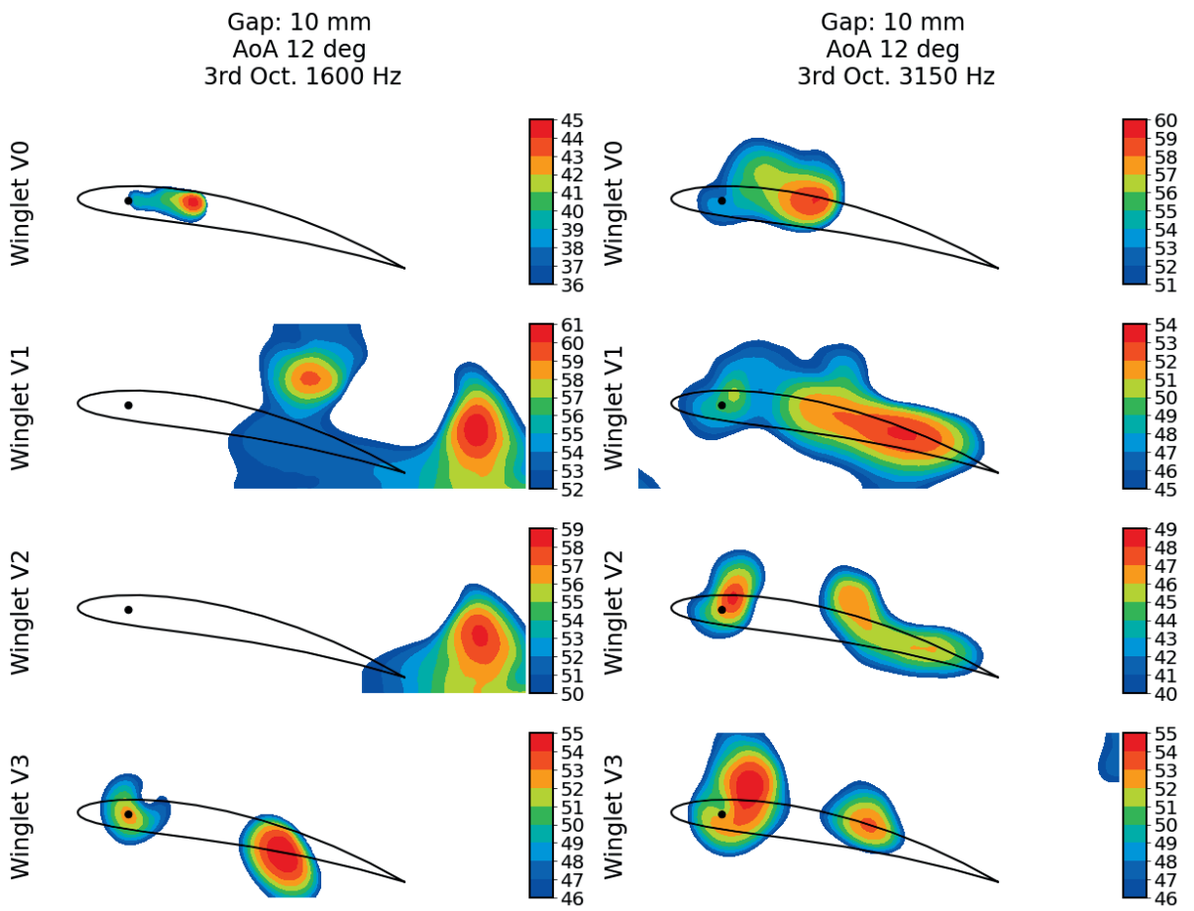


Figure 5: Conventional beamforming result from MEMS microphone array.

Thanks to the high channel count of pressure fluctuation sensors distributed around the wing tip, beamforming analysis with a focus on the winglet tip is feasible. This capability enables the separation of turbulence-induced footprints from sound radiation, providing deeper insight into the flow-acoustic interaction. Figure 5 illustrates the beamforming results for the 3rd octave bands centered at 1600 Hz and 3150 Hz.

The analysis reveals that the hole located at x = y = 0 mm acts as an acoustic source; however, it is not a dominant contributor. At 1600 Hz, the most prominent acoustic sources are generated by the turbulence wake impinging on the top plate downstream of the trailing edge. These sources are markedly louder for winglets V1 and V2 compared to winglets V0 and V3, which contradicts the observation of lower surface pressure fluctuations downstream of V1 and V2.

At 3150 Hz, the dominant acoustic source shifts to approximately 40% chord length on winglet V0. For winglet V2, the acoustic emissions are approximately 10 dB quieter, with the dominant source localized near the open hole. Winglets V1 and V3 exhibit a quieter profile, approximately 5 dB lower than V0, with dominant source locations identified at 80% and 20% chord length, respectively.

CONCLUSION

This study investigates the acoustic and aerodynamic behavior of various winglet configurations using data from a high-resolution MEMS microphone array. By analyzing surface pressure fluctuations and applying beamforming techniques, we explored the impact of angle of attack, gap size, and winglet type on turbulence and acoustic emissions. Key findings are summarized as follows:

Angle of Attack (AoA): Turbulence intensity increases with higher AoA. For a minimal gap height of 1 mm, secondary wakes are absent, suggesting simplified flow dynamics in tightly confined configurations.

Gap Size: Larger gap sizes reduce surface pressure levels but induce distinct wakes at specific chord locations (leading edge, mid-chord, and trailing edge) at low frequencies (50 Hz). This highlights the role of gap size in shaping wake structures and their acoustic footprints.

Winglet Design: The sharp edges of winglet V0 produce a larger turbulence footprint across all frequencies, while other designs exhibit more localized effects. Beamforming analysis reveals that acoustic sources shift with frequency and winglet type, with turbulence wakes downstream and near-chord locations dominating the sound radiation. Winglets V1 and V3 generally exhibit quieter profiles compared to V0.

Comparison with Simulations: Experimental results show higher turbulence levels in the tip gap compared to simulations, particularly for high-frequency acoustic sources, emphasizing the importance of empirical validation.

Overall, the findings underscore the complex interplay between aerodynamic parameters and acoustic behavior, offering valuable insights for optimizing winglet designs in aeroacoustic applications.

ACKNOWLEDGEMENTS

The authors would like to thank the cooperation partners at ebm-papst for the fruitful cooperation throughout the project.

REFERENCES

[1] F. Reuschling, L. Liberson, M. Pott-Pollenske, J. Delfs, and D. Ernst, *BTGNX: An acoustic benchmark wind tunnel experiment for tip-gap noise*, in *Fan 2025, Antibes Juan-les-Pins (France), 9 – 11 April*, **2025**.

[2] P. Dietrich, S. R. Mallu, and F. Lex, *Numerical investigation of different wing tip geometries on the acoustics of an airfoil with tip gap in a wind*, in *Fan 2025, Antibes Juan-les-Pins (France), 9 – 11 April*, **2025**.

[3] J. Malkki, Y. Yauwenas, C. Doolan, and D. Moreau, *Comparison of small rotor tonal and random noise decomposition methods*, en, Acoust. Aust. vol. 52, no. 3, pp. 323–337, **2024**.

[4] J. Al-Am, V. Clair, A. Giauque, J. Boudet, and F. Gea-Aguilera, *Aeroacoustic analysis of the tip-leakage flow of an ultrahigh bypass ratio fan stage*, en, Phys. Fluids (1994) vol. 35, no. 4, **2023**.

A3 Fan System Effect

9 April - 11:00 - Room 2 Miles Davis

Chairmen: Stefan Jacob, Joe Brooks

List of papers

Co-simulation of an Axial Flow Cooling Fan and a Supercritical CO2 Air-Cooled Heat Exchanger

- Francois BOSHOFF – Stellenbosch University (South Africa)
- Sybrand Johan VAN DER SPUY – Stellenbosch University (South Africa)
- Johannes PRETORIUS – Stellenbosch University (South Africa)
- Ryno LAUBSCHER – Stellenbosch University (South Africa)

Optimising Ventilation System Preplanning: Duct Sizing and Fan Layout using Mixed-Integer Programming

- Julius BREUER – Chairmen of Fluid Systems, Technische Universität Darmstadt (Germany)
- Peter F. PELZ – Chairmen of Fluid Systems, Technische Universität Darmstadt (Germany)

Advanced Computational Approaches to Fan Performance and Installation Conditions

- Uma Mahesh LAKAMANA – MAICO GULF LLC (UAE)
- Massimo FACCA – MAICO GULF LLC (UAE)
- Amit AHUJA – MAICO GULF LLC (UAE)



CO-SIMULATION OF AN AXIAL FLOW COOLING FAN AND A SUPERCRITICAL CO_2 AIR-COOLED HEAT EXCHANGER

Francois D. Boshoff, Sybrand J. van der Spuy,
Johannes P. Pretorius, Ryno Laubscher

Stellenbosch University, South Africa

SUMMARY

An axial flow fan has been designed for the air-cooled heat exchanger (ACHE) of a concentrated solar power plant, based on a supercritical carbon dioxide (sCO_2) Brayton cycle. This paper presents a high-fidelity co-simulation method, which simultaneously solves the air- and sCO_2-side flows through the ACHE and fan. The air-side flow is modelled using three-dimensional computational fluid dynamics, while the sCO_2 flow is solved using a one-dimensional thermofluid network model. The co-simulation is used to determine the thermal performance of the ACHE and to investigate the effects of non-uniform air flows on the behaviour of the sCO_2 in the tube bundle.

INTRODUCTION

Supercritical carbon dioxide (sCO_2) Brayton cycles for power generation is a new technology, that promises many improvements over steam Rankine cycles. These include increased plant thermal efficiencies [1], compact turbomachinery [2], and the fact that fluids at ambient conditions, such as air and water, function well as coolants for sCO_2 [3]. These benefits have caused research into the sCO_2 Brayton cycle to increase over the last two decades, including its application to a range of energy sources such as nuclear, geothermal and concentrated solar power (CSP).

The use of sCO_2 as working fluid complicates the design and control of such plants. Firstly, CO_2 must remain above its critical temperature and pressure, at 30.98°C and 7.38 MPa respectively, to remain supercritical. If the temperature or pressure drops below these values, the fluid could experience drastic changes in its fluid properties, leading to a decreased cycle efficiency, unpredictable behaviour or even damage to downstream components [2]. The fluid properties of sCO_2 are also very sensitive to temperature and pressure variations, particularly near the critical point, and are therefore difficult to predict accurately.

Various models of sCO_2 Brayton cycles have been reported in the literature which discretises the sCO_2 flow path to account for local variations in fluid properties [2, 4, 5, 6]. While these provide a

good understanding of the overall power cycle performance, it gives very little practical information on the performance of individual components, such as turbomachinery and heat exchangers. There are also very few experimental models of sCO_2 power cycles reported in the literature.

The work of Deshmukh et al. [2] investigates a 100 MW CSP plant based on the sCO_2 Brayton cycle, which uses an air-cooled heat exchanger (ACHE) for cooling. In particular, this work considers the transient effects of air temperature changes on the sCO_2 in the finned-tube bundle, which begins to provides more detail on how such a system would behave. To build on this understanding of ACHE units for sCO_2-based CSP plants, and to provide a practical example, Boshoff et al. [7, 8, 9] develops a detailed ACHE design for a similar CSP plant.

In their work, Boshoff et al. designs a bespoke axial flow cooling fan, specifically for use in this ACHE [7]. The resulting design features an unusual configuration for an axial flow fan, with a large hub-to-tip ratio of 0.51, and blades with very little twist. The performance of the fan is evaluated using both Computational Fluid Dynamics (CFD) and experimental tests of a 1:4.78 scale model of the fan [8]. The aerodynamic interaction between the fan and the finned-tube bundle is also investigated using CFD, assuming isothermal flow [9]. This model assumes that the heat transferred from the sCO_2 to air has no effect on the air-side flow, and can therefore be neglected. Based on the results, Boshoff et al. finds that the overall cooling air flow rate is only 3.6% below the required operating point, but the distribution of this cooling air throughout the bundle is highly non-uniform.

Considering the sensitivity of sCO_2 to temperature changes near the critical point, it is unclear what the effect of this non-uniform cooling air distribution will be on the overall thermal performance of the ACHE, and on the sCO_2 within the tubes. It is also possible that the non-uniform cooling could cause the sCO_2 in some tubes to be cooled excessively, to below the critical point, leading to drastic changes in fluid properties. Therefore, in the current work, a co-simulation model is developed which simultaneously solves the air-side flow field using three-dimensional CFD, implemented in ANSYS Fluent, and the sCO_2-side flow field using a one-dimensional thermofluid network method, implemented in a Python script. Communication between these models is managed by the *PyFluent* module. This co-simulation approach allows for the estimation of the overall thermal performance of the ACHE, and demonstrates the effect of the fan's non-uniform cooling air distribution on the sCO_2 flow in the finned-tube bundle.

AIR-SIDE MODEL

The ACHE's finned-tube bundle consists of 1160 finned tubes positioned above six fans. Each tube is bent to obtain eight vertical passes, with each pass spanning across the same two fans, as shown in Figure 1. The computational domain is defined by dividing the entire ACHE into thirds, each of which contains two fan units and roughly 386.7 tubes, with the assumption being that flow in each of these segments of the ACHE is identical. Both the air- and sCO_2-side flow fields are discretised, but uses different discretisation resolutions and methods.

The air-side flow through the two fan units is modelled using a three-dimensional CFD method, implemented in ANSYS Fluent. Each fan unit is split into five sub-domains: an inlet, fan rotor, plenum chamber, tube bundle and outlet. A hexahedral mesh is generated for the fan rotor sub-domain using ANSYS Turbogrid. Tetrahedral meshes are generated for the inlet, plenum and outlet sub-domains, using ANSYS Meshing, which are converted to polyhedral meshes after importing into ANSYS Fluent. Finally, a hexahedral mesh is generated for the tube bundle sub-domain. The assembled mesh is shown in Figure 1.

To simplify the air-side flow field solution, the complex geometry of the finned-tube bundle is neglected. Instead, the tube bundle effects are modelled using three distinct methods: Firstly, the flow

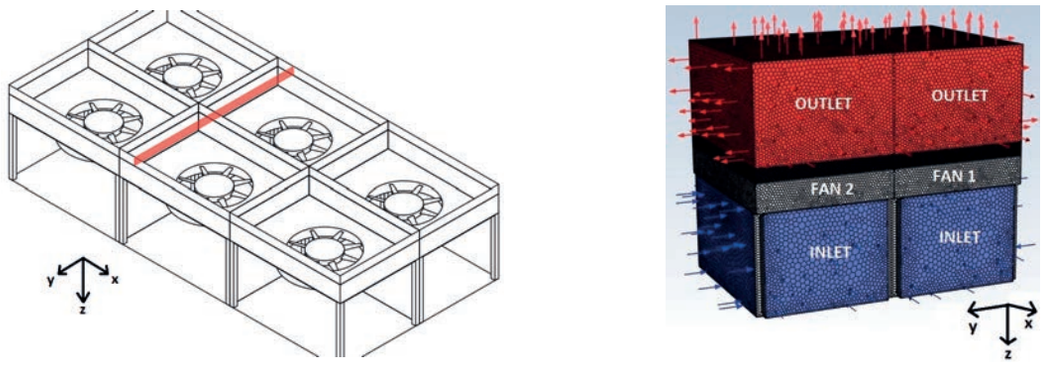


Figure 1: Position of a tube above two fans in the ACHE (left) and the assembled air-side CFD mesh containing two fan units (right)

straightening effect of the tube bundle is modelled using a Porous Media Model, with the x- and y-direction inertial resistance factors given a value of 1000. This high inertial resistance results in air flowing directly upwards (negative z-diretion) through the bundle.

Secondly, the static pressure drop of the air flowing through the tube bundle is modelled using z-direction momentum source terms. The value of these source terms are calculated using a User Defined Function (UDF). For each cell, the static pressure drop is calculated using the empirical correlation by Ganguli [10], expressed as:

$$\Delta p = \frac{2N_r G_{crit}}{\rho} \left[1 + \frac{2e^{-\frac{P_t - d_f}{4d_o}}}{1 + \frac{P_t - d_f}{d_o}} \right] \left[0.021 + 13.6 \frac{d_f - d_o}{Re(P_f - t_f)} + 0.252 \left(\frac{d_f - d_o}{Re(P_f - t_f)} \right)^{0.2} \right] \quad (1)$$

The pressure drop values for each cell are then converted to an equivalent force by multiplying with the bundle frontal area, and further to a momentum source term by dividing by the bundle volume.

Thirdly, the heat transferred to the air flowing through the tube bundle is modelled using an energy source term. The heat transferred between the sCO_2 and air for each sCO_2-side element is calculated by the Python script, which then writes these values to a text file in a specific order. The Python script uses *PyFluent* to instruct ANSYS Fluent to run another UDF. This UDF reads the heat transfer values from the text file and converts them to an energy source term by dividing by the volume of the sCO_2-side element. The UDF then assigns these energy source term values to the corresponding air-side mesh cells.

To simplify the air-side flow field solution further, the fan is modelled using the Frozen Rotor approach. This approach effectively fixes the tangential position of the two fan rotors during the simulation. A local reference frame is defined for each rotor sub-domain, which is specified to be rotating at the same speed and the same rotation origin as the fans, allowing flow to be approximated as steady.

With these simplifications in mind, the RANS equations are solved in the CFD model, with flow being considered compressible and steady in the relative frame of reference. The equation for energy conservation is also solved. Air is modelled as a real gas to account for fluid properties changes as the temperature increases through the bundle, using the NIST Real Gas option in ANSYS Fluent. Turbulence is modelled using the realizable k-epsilon model and enhanced wall treatment. The operating pressure is set to a value of 100000 Pa (1 bar).

All wall surfaces are set to no-slip wall boundary conditions. The interfacing surfaces between all mesh sub-domains, and between the two fan units, are connected using standard mesh interfaces. The remaining surfaces in the two inlet sub-domains are specified as pressure inlet boundary conditions, with the gauge total pressure set to 0 Pa and temperature to 15°C. For the two outlet sub-domains, the

remaining surfaces are set to pressure outlet boundary conditions, with the backflow gauge pressure set to 0 Pa and temperature to 15°C.

The SIMPLE pressure-velocity coupling scheme is used. For spatial discretisation, Least Squares Cell Based is used for gradient, PRESTO! for pressure, and QUICK for momentum, turbulent kinetic energy, turbulent dissipation rate and energy. The under-relaxation factors are set to 0.175 for momentum and 0.25 for energy. All other under-relaxation values are set to the default values suggested by ANSYS Fluent.

To validate the air-side setup, a simplified computational domain is used. Table 1 compares the temperature rise of the air in this simplified computational domain to that specified by Deshmukh et al. [2], with the air being modelled both with constant fluid properties and as a real gas. The close correlation between the results demonstrates that the modelling of the heat transferred to the air works as intended.

Table 1 also compares the static pressure drop of the air in this simplified domain to that predicted by the empirical correlation of Ganguli [10]. The good agreement between the constant fluid properties variant and Ganguli's correlation demonstrates that the modelling of the pressure drop also works as intended. However, the real gas variant predicts a significantly higher static pressure drop compared to the model using constant properties. This is due to the density of the air being reduced as it is heated, which accelerates the flow and leads to higher frictional losses.

Table 1: Comparison of air-side static pressure drop and temperature rise through the tube bundle

Model	Δp (Pa)	ΔT (°C)
Ganguli [10], Deshmukh et al. [2]	115.1	81.20
Simplified model with constant fluid properties	115.1	81.27
Simplified model with real gas properties	136.6	81.19

sCO_2-SIDE MODEL

The sCO_2 flow inside the tube bundle is modelled using the Thermofluid Network Method (TNM) of Laubscher et al. [6], implemented in a Python script. Flow is assumed to be incompressible, since Mach numbers well below 0.3 are expected. The TNM firstly discretises the sCO_2 flow path into one-dimensional elements, which are control volumes with only one inlet and outlet, and zero-dimensional nodes, which represent connections between the elements and can have multiple inlets and outlets.

Figure 2 illustrates how the flow is discretised in the y- and z-directions, along the length of an individual tube. To discretise the bundle in the x-direction, the bundle is divided into "blocks of tubes", each of which contains an equal number of tubes. It is then assumed that the sCO_2 flow inside of all tubes contained within a particular block are identical. Figure 2 gives an example of the resulting thermofluid network, with the bundle divided into five tube blocks.

The TNM applies the principles of conservation of mass and energy at each node, and conservation of linear momentum to each element, which defines three sets of equations. The TNM then solves the mass flow rates in each element, the stagnation pressures at each node, and the stagnation enthalpies at each node which simultaneously satisfies all three sets of equations. To achieve this, the solution procedure makes an initial guess of the sCO_2 flow field parameters, after which it continuously loops through a set of functions. Each function updates a portion of the flow field parameters. The Python script evaluates whether the required residuals have been achieved after each loop, allowing the sCO_2-side solution procedure to stop only upon meeting these criteria.

The first sCO_2 solution function updates the sCO_2 fluid properties at each node, as follows: the

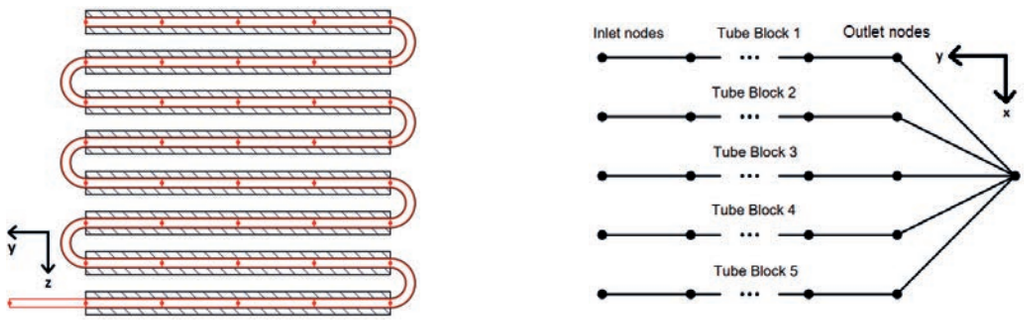


Figure 2: Thermofluid network model layout of sCO_2 flow in the tube bundle (not to scale)

entropy (s), velocity (u), static enthalpy (h), static pressure (p) and density (ρ) of the sCO_2 at a particular node is determined using:

$$s = f(h_0, p_0) \qquad u = \frac{\dot{m}_{per\,tube}}{\rho A_i} \qquad h = h_0 - \frac{u^2}{2} \qquad p = f(s,h) \qquad \rho = f(h,p) \tag{2}$$

where f indicates that the *CoolProp* module is used with the inputs given in brackets. The Python script uses the *fsolve* function to solve these equations simultaneously. The dynamic viscosity (μ), thermal conductivity (k) and specific heat capacity (c_p) of the sCO_2 at a particular node can then be calculated with the *CoolProp* module, using:

$$\mu = f(h,p) \qquad k = f(h,p) \qquad c_p = f(h,p) \tag{3}$$

The second sCO_2 solution function updates the sCO_2 friction factors in each element. For this purpose, the Reynolds number in each element is calculated using:

$$Re = \frac{\rho d_i u}{\mu} \tag{4}$$

The Darcy friction factor is then calculated using the Blasius correlation [5], expressed as:

$$f_D = 0.316 Re^{-\frac{1}{4}} \; for\; Re < 20000 \quad or \quad f_D = 0.184 Re^{-\frac{1}{5}} \; for\; Re > 20000 \tag{5}$$

The third sCO_2 solution function updates the sCO_2 mass flow rate in each element and the stagnation pressure at each node. Since the set of nodal mass balance equations alone does not have a singular, unique solution, the nodal mass and elemental momentum balance equations must be solved simultaneously (coupled solution). For each node along a tube length, the mass balance equation is defined as:

$$\dot{m}_{out} - \dot{m}_{in} = 0 \tag{6}$$

For the final outlet node in the bundle, which receives the flow leaving all tube blocks, the mass balance equation is expressed as:

$$\sum \dot{m}_{tube\,block\,outlets} - \dot{m}_{BC} = 0 \tag{7}$$

where $\dot{m}_{BC}$ is a boundary condition representing the mixed, uniform flow leaving the tube bundle. This boundary condition is always set to a value of 203.9 kg/s, which is the design point sCO_2 mass flow rate specified by Deshmukh et al. [2] for this ACHE, divided by three to account for the computational domain being only a third of the bundle. For each element along a tube length, the momentum balance equation is given by:

$$p_{0,out} - p_{0,in} + f_D u^2 \frac{\rho}{2} \frac{l}{d} = 0 \tag{8}$$

Finally, at each inlet node, a stagnation pressure boundary condition is defined, using:

$$p_{0,tube\ block\ inlet} - p_{BC} = 0 \tag{9}$$

where p_{BC} is always set to a value of 7.653 MPa, which is the design point sCO_2 pressure at the tube bundle inlet specified by Deshmukh et al. [2]. With the mass and momentum balance equations defined, the *fsolve* function is used to solve the equations simultaneously.

The fourth sCO_2 solution function updates the stagnation enthalpy at each node by solving the energy balance equations. For each node along a tube length, the energy balance equation is represented by:

$$(\dot{m}h_0)_{out} - (\dot{m}h_0)_{in} - \dot{Q} = 0 \tag{10}$$

where the calculation of the heat transfer rate ($\dot{Q}$) is discussed later in the paper. For the final outlet node in the bundle, which receives the flow leaving all tube blocks, the energy balance equation is formulated as:

$$\sum (\dot{m}h_0)_{tube\ block\ outlets} - \dot{m}_{BC}\, h_{0,mixed\ outlet} = 0 \tag{11}$$

At each inlet node, a stagnation enthalpy boundary condition is applied, using:

$$h_{0,tube\ inlet} - h_{BC} = 0 \tag{12}$$

where h_{BC} is set to the enthalpy corresponding to the design point temperature and pressure at the tube bundle inlet from Deshmuhk et al. [2], given as 111.2°C and 7.653 MPa. Since the enthalpy values are known at the inlet of each tube block, and the mass flow rate and heat transfer rate in each element have been calculated above, this set of energy balance equations can be solved simply by calculating the enthalpies from the inlet to the outlet nodes. The corresponding temperature values can then be found using the *CoolProp* module.

To validate the sCO_2-side model, the results are compared with that of a similar model in the Flownex Simulation Environment. The tube bundle is split into three tube blocks, with a different arbitrary heat transfer rate assigned to each. The results are compared in Table 2. The strong correlation seen between the two models demonstrate that the sCO_2 flow model works as intended.

Table 2: Comparison of sCO_2 results for Python TNM and Flownex model

Model/Block	$\dot{Q}$ (MW)	$\dot{m}$ (kg/s)	p_{out} (MPa)	T_{out} (°C)
Current/Block 1	0	60.98	7.473	110.2
Current/Block 2	5.822	67.89	7.473	52.40
Current/Block 3	11.64	75.00	7.473	32.81
Flownex/Block 1	0	60.97	7.474	110.2
Flownex/Block 2	5.822	67.86	7.474	52.38
Flownex/Block 3	11.64	75.04	7.474	32.83

HEAT TRANSFER MODEL

As noted before, the tube bundle is split into a number of elements. For the sCO_2-side, these elements are control volumes which represent the flow inside the tubes of a particular tube block. For the air-side, these elements are control volumes which represent the flow around the outside of the tubes in the tube block. The heat transferred between the two fluids in each element is solved using an iterative procedure, implemented in the Python script.

Accessing the required sCO_2 flow field parameters is simple, since the Python script stores these values in lists which are updated as the solution continues. To access the required air-side flow parameters, however, the values must be obtained from the ANSYS Fluent CFD simulation. The *PyFluent* module is therefore used to define a set of points in the CFD simulation, with each point representing the centre of a tube bundle element. When required, *PyFluent* is used to read the air-side conditions at each of these points, which are then stored in Python lists.

The heat transfer rate in each element is then calculated using the method by Kröger [11], as follows: The Prandtl number, Nusselt number and heat transfer coefficient of the sCO_2 in each element is calculated using the Gnielinski correlation [2, 5, 12], and Reynolds numbers from Equation 4:

$$Pr = \frac{c_p \mu}{k} \qquad Nu = \frac{(f_D/8)\,(Re-1000)\,Pr}{1+12.7\,(f_D/8)^{0.5}\left(Pr^{2/3}-1\right)} \qquad h_{sCO_2} = \frac{Nu\,k}{d_i} \tag{13}$$

After the air-side conditions have been obtained using *PyFluent*, the Reynolds number for the air in each tube bundle element is calculated using:

$$Re = \frac{\rho\, v_{crit}\, d_o}{\mu} \qquad v_{crit} = v_{free}\frac{A_{free}}{A_{crit}} \tag{14}$$

where v_{free} is the air velocity obtained from ANSYS Fluent, A_{free} is the tube bundle frontal area, and A_{crit} is the critical (minimum) flow area through the bundle. The air-side Prandtl number, Nusselt number and heat transfer coefficient in each element are then calculated using the correlation by Briggs and Young [13]:

$$Pr = \frac{c_p \mu}{k} \quad Nu = 0.134 Pr^{0.33} Re^{0.681}\left[\frac{2(P_f - t_f)}{d_f - d_r}\right]^{0.2}\left[\frac{P_f - t_f}{t_f}\right]^{0.1134} \qquad h_{air} = \frac{Nu\,k}{d_o} \tag{15}$$

Next, the geometric parameters must be calculated. The air- and sCO_2-side surface areas for each element are calculated using:

$$A_{air} = \left[\pi d_o\left(P_f - t_f\right) + 2\times\frac{\pi}{4}\left(d_f^2 - d_o^2\right) + \pi d_f t_f\right]\frac{L_{Element}}{P_f} \qquad A_{sCO_2} = \pi d_i L_{element} \tag{16}$$

The fin efficiency is calculated using the correlation by Schmidt and Zeller [5]:

$$\eta_f = \frac{\tanh\left(\frac{b\,d_o\,\phi}{2}\right)}{\frac{b\,d_o\,\phi}{2}} \qquad b = \left(\frac{2h_{air}}{k_{aluminium} t_f}\right)^{0.5} \qquad \phi = \left(\frac{d_f}{d_o} - 1\right)\left[1 + 0.35\ln\left(\frac{d_f}{d_o}\right)\right] \tag{17}$$

The finned surface effectiveness can then be calculated using the correlation by Kröger [11]:

$$\varepsilon_{surface} = 1 - \left(1 - \eta_f\right)\left(\frac{A_{fin}}{A_{fin} + A_{root}}\right) \tag{18}$$

The overall heat transfer coefficient and heat transfer rate for each element can be found using:

$$UA = \left(\frac{1}{h_{sCO_2} A_{sCO_2}} + \frac{\ln\left(\frac{d_o}{d_i}\right)}{2\pi k_{steel} L_{element}} + \frac{1}{h_{air} A_{air} \varepsilon_{surface}}\right)^{-1} \tag{19}$$

$$\dot{Q} = UA(T_{sCO_2} - T_{air}) \times N_{Tubes/Block} \tag{20}$$

Finally, once the heat transfer rates for all elements have been calculated, they are written to the text file, as mentioned in the air-side model section above.

CO-SIMULATION PROCEDURE

The Python co-simulation script starts by reading the initialised air-side case and data files from ANSYS Fluent. The heat transfer rates in all elements are initially set to zero, and the sCO_2-side flow field is solved. With both sides of the co-simulation initialized, the overall co-simulation procedure starts, which loops through the following steps until the solution has converged: *PyFluent* accesses the air-side conditions in each element from ANSYS Fluent; the heat transfer rates in each element are calculated and written to a text file; the sCO_2-side flow field is solved; *PyFluent* instructs ANSYS Fluent to use the UDF, which reads the heat transfer rate text file, converts them to energy source terms, and assigns them to the air-side mesh cells; *PyFluent* instructs ANSYS Fluent to run a number of air-side solution iterations.

RESULTS

For the full thermal ACHE co-simulation, the computational domain is split into twelve tube blocks, and each tube pass is split into sixteen sections. The air-side mesh uses 19.16×10^6 cells. These results were compared with two coarser co-simulations, which produces similar results. Therefore, the results are not sensitive to the selected discretisation resolution.

Overall performance

Table 3 provides the main ACHE thermal performance results, and compares these values to the design point values specified by Deshmukh et al. [2]. The overall heat transfer rate is seen to be significantly below the design point value. Consequently, the average sCO_2 outlet temperature is higher than the required value.

Table 4 compares the fan performance values for both fans within the co-simulation to that of the isothermal model of Boshoff et al. [9]. The cooling air flow rates obtained are below that of the isothermal model, which is likely due to the current model accounting for the heat transferred to the air. As demonstrated in Table 1, this results in an increase in static pressure drop through the bundle. As a result, the fans operate further from their design point flow rate of 175.7 m^3/s, which reduces their efficiency. The reduced cooling air flow rate also contributes to the low heat transfer rate seen in Table 3.

Table 3: ACHE overall thermal performance results

Method	$\dot{Q}_{ACHE}$ (MW)	$T_{sCO_2,out}$ (°C)
Design point	104.8	32.10
Co-simulation	83.34	35.61

Table 4: Fan aerodynamic performance results

Method	$\dot{V}_F$ (m^3/s)	Δp_{ts} (Pa)	P_F (kW)	η_{ts} (%)
Design point	175.7	-	-	-
Isothermal model [9]	169.4	110.5	31.91	58.66
Co-simulation, Fan 1	157.3	117.0	33.13	55.55
Co-simulation, Fan 2	157.2	117.1	33.10	55.61

sCO_2 conditions in each tube block

An investigation of the results for the individual tube blocks demonstrates that the sCO_2 mass flow rates and outlet temperatures are distributed in a symmetrical pattern. This is due to the non-uniform cooling air velocity profile provided by the two fans, which results in higher heat transfer rates over tubes directly downstream of the fan blades, and lower heat transfer rates behind the fan hubs and towards the sides of the bundle. The sCO_2 mass flow rates are therefore seen to range from 16.83 kg/s for the tube blocks downstream of the hub, to 17.15 kg/s for tube blocks downstream of the blades.

Flow conditions along the tube length

Figure 3 illustrates the distributions of heat transfer rate and sCO_2 temperature in each tube block. The results for each tube block are coloured based on their distance from the x-axis origin (at the centre of the fans). The heat transfer rates are seen to vary between blocks, with the tube blocks closer to the centre achieving higher heat transfer rates. This is caused by the higher air velocities downstream of the fan. Note that, since the sCO_2 pressures at the inlet and outlet of each tube block are identical, the sCO_2 pressure distributions in each tube block are also nearly identical, regardless of the non-uniform cooling.

The resulting temperature distributions, however, are seen to differ between blocks, with tube blocks close to the centre having lower outlet temperatures. As a result, the sCO_2 leaving the central tube blocks are closer to the critical point. Due to the overall heat transfer rate achieved being below the design value, the sCO_2 in all tube blocks remains well above the critical temperature, meaning there is no risk of the sCO_2 ceing cooled below the critical point.

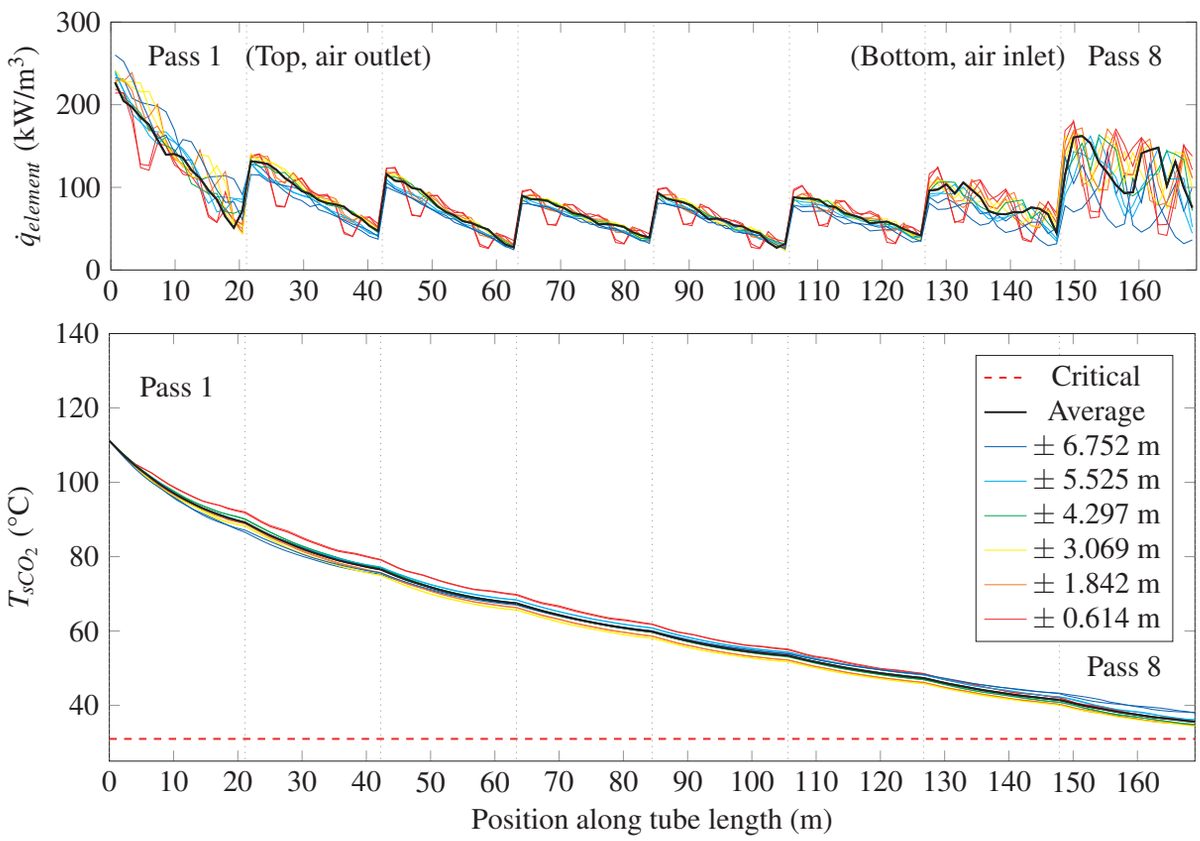


Figure 3: Heat transfer rate and sCO_2 temperatures in each tube block

CONCLUSIONS AND RECOMMENDATIONS

The co-simulation demonstrates that the heating of the air significantly increases the air's static pressure drop through the finned-tube bundle. Since this effect was not accounted for by the fan design procedure, the operating point flow rate achieved by each fan is 18.5 m^3/s (10.5%) below the required value. Further, the co-simulation predicts that the overall heat transfer rate achieved by the ACHE is 21.5 MW (20.5%) below the required value, partly due to the low cooling air flow rate. As a result of the low heat transfer rate, the sCO_2 leaving the tube bundle and entering the compressor is further from the critical point than intended, and therefore less dense. This will most likely result in the power cycle's efficiency being reduced.

The results indicate that the sCO_2 in tubes downstream of the high velocity air leaving the fan blades are at a lower temperature. Due to the low overall heat transfer rate achieved however, the sCO_2 temperature is still well above the critical point. If the overall heat transfer rate achieved was closer to the design value, and was applied non-uniformly, the sCO_2 in some tubes could very well be cooled below the critical point. To avoid this, the uniformity of the cooling air distribution provided by the fans could be improved. However, since the sCO_2 leaving all tubes are mixed, the sCO_2 should return to the supercritical state before leaving the ACHE. The effect of non-uniform cooling on the entire power cycle is therefore not as significant. Instead, it is important to ensure that the overall heat transfer rate does not exceed the design point value significantly, as this could result in the overall outlet conditions being sub-critical, which would most likely cause a large reduction in the power cycle's efficiency.

ACKNOWLEDGEMENTS

The authors would like to acknowledge the following groups and individuals for their contribution towards the completion of this work: The Solar Thermal Energy Research Group at Stellenbosch University for their ongoing support. Prof Alessandro Corsini, Prof Giovanni Delibra and Dr Lorenzo Tieghi from Sapienza University of Rome, for their guidance during the early stages of the work, and the Centre for High Performance Computing, South Africa, for providing computational resources to this research project. This work is based on the research supported in part by the National Research Foundation of South Africa (grant no KIC240821261750).

REFERENCES

[1] V. Dostal, P. Hejzlar, and M. J. Driscoll, "High-performance supercritical carbon dioxide cycle for next-generation nuclear reactors," *Nuclear Technology*, vol. 154, no. 3, 2006.

[2] A. Deshmukh, J. Kapat, and A. Khadse, "Transient thermodynamic modeling of air cooler in supercritical CO2 Brayton cycle for solar molten salt application," in *Proceedings of the ASME Turbo Expo 2019: Turbomachinery Technical Conference and Exposition*, (Phoenix, Arizona), 2019.

[3] K. Brun, P. Friedman, and R. Dennis, *Fundamentals and applications of supercritical carbon dioxide (sCO2) based power cycles*. Cambridge: Elsevier Science & Technology, 2017.

[4] A. Moisseytsev, Q. Lv, and J. J. Sienicki, "Dry Air Cooler Modeling for Supercritical Carbon Dioxide Brayton Cycle Analysis," tech. rep., Argonne National Laboratory - Nuclear Engineering Division, 2016.

[5] A. Lock, K. Hooman, and Z. Guan, "A detailed model of direct dry-cooling for the supercritical carbon dioxide Brayton power cycle," *Applied Thermal Engineering*, vol. 163, 2019.

[6] R. Laubscher, P. Rousseau, J. Van der Spuy, C. Du Sart, and J. Pretorius, "Development of a 1D network-based momentum equation incorporating pseudo advection terms for real gas sCO2 centrifugal compressors which addresses the influence of the polytropic path shape," *Thermal Science and Engineering Progress*, vol. 55, no. October, pp. 1–13, 2024.

[7] F. D. Boshoff, S. J. Van der Spuy, J. P. Pretorius, and C. J. Meyer, "Design of an axial flow fan for a unique cooling application," in *Proceedings of the ASME Turbo Expo 2022: Turbomachinery Technical Conference and Exposition*, (Rotterdam, Netherlands), 2022.

[8] F. D. Boshoff, S. J. Van der Spuy, J. P. Pretorius, and C. J. Meyer, "Investigation into the predicted performance of a cooling fan for an sCO2 concentrated solar power plant," *Proceedings of the Institution of Mechanical Engineers, Part A: Journal of Power and Energy*, vol. 238, no. 5, 2024.

[9] F. D. Boshoff, S. J. Van der Spuy, and J. P. Pretorius, "Axial Flow Fan Performance in a Forced Draught Air-Cooled Heat Exchanger for a Supercritical Carbon Dioxide Brayton Cycle," *Journal of Engineering for Gas Turbines and Power*, vol. 147, no. 1, 2025.

[10] A. T. Ganguli, "Parametric study of air-cooled heat exchanger finned tubed geometry," *American Institute of Chemical Engineers Symposium Series*, vol. 81, no. 245, pp. 122–128, 1985.

[11] D. G. Kröger, *Air-cooled heat exchangers and cooling towers*. Tulsa, Okla: Penwell Corp., 2004.

[12] L. Abrahams, C. Du Sart, and R. Laubscher, "Design of an air-cooled heat rejection system for a sCO2 concentrated solar power plant," in *16th International Conference on Heat Transfer, Fluid Mechanics and Thermodynamics*, (Virtual), 2022.

[13] D. E. Briggs and E. H. Young, "Convection heat transfer and pressure drop of air flowing across triangular pitch banks of finned tubes," *Chemical Engineering Progress Symposium Series*, vol. 59, no. 41, pp. 1–10, 1963.

NOMENCLATURE

Abbreviations

ACHE	Air-cooled heat exchanger
CFD	Computational fluid dynamics
CSP	Concentrated solar power
RANS	Reynolds-averaged Navier-Stokes
sCO_2	Supercritical carbon dioxide
TNM	Thermofluid network model
UDF	User defined function

Variables

A	Area (m^2)
b	Placeholder
d	Diameter (m)

f	Friction factor, function
G	Mass velocity (kg/s·m^2)
H	Height (m)
h	Heat transfer coefficient (W/m^2·K), specific enthalpy (J/kg)
k	Thermal conductivity (W/m·K)
L	Length (m)
$\dot{m}$	Mass flow rate (kg/s)
N	Number of
P	Pitch (m), power (W)
p	Pressure (Pa)
$\dot{Q}$	Heat transfer rate (W)
$\dot{q}$	Heat transfer rate per unit volume (W/m^3), per unit length (W/m)
S	Source term
s	Specific entropy (J/kg·K)
T	Temperature (°C or K)
t	Thickness (m)
UA	Overall heat conductance (W/K)
V	Volume (m^3)
$\dot{V}$	Volumetric flow rate (m^3/s)
v	Velocity (m/s)
W	Width (m)
Δ	Change in
ε	Effectiveness
η	Efficiency (%)
μ	Dynamic viscosity (kg/s·m)
ρ	Density (kg/m^3)
ϕ	Placeholder

Subscripts

0	Stagnation
ACHE	Entire air-cooled heat exchanger
air	Air-side
aluminium	For aluminium
BC	Boundary condition
crit	Critical
D	Darcy
element	Element

F	Fan
f	Fin
fin	Fin
$free$	Free
fr	Frontal
i	Inner
in	Inlet
l	Longitudinal
o	Outer
out	Outlet
p	Constant pressure
t	Transverse
r	Rows
$root$	Root
$steel$	For steel
$surface$	Surface
ts	Total-to-static
z	z-component

Dimensionless numbers

Eu	Euler number
Nu	Nusselt number
Pr	Prandtl number
Re	Reynolds number



OPTIMISING VENTILATION SYSTEM PREPLANNING: DUCT SIZING AND FAN LAYOUT USING MIXED-INTEGER PROGRAMMING

Julius H.P. BREUER[1], Peter F. PELZ[1]

[1] *Technische Universität Darmstadt, Chair of Fluid Systems, Otto-Berndt-Straße 2, 64287 Darmstadt, Germany*

SUMMARY

The sizing of ducts is traditionally done by balancing pressure losses in all branches. As a subsequent step, fans are laid out for the resulting system. For distributed fans in the central duct network, this approach does no longer work. In order to plan the topology of a ventilation system, the placement of distributed fans and the duct sizing should thus be performed in a single step. This paper presents a methodology that exploits the non-linear and non-convex problem's structure, yielding a holistic Mixed-Integer Linear Program which solves for minimal life-cycle costs, including ducts, fans and volume flow controllers accounting for multiple load cases.

INTRODUCTION

In the European Union, fans account for approximately 12.3% of the total electrical energy demand [1]. Mechanical ventilation systems, which rely on fans to ventilate buildings, have the potential to reduce overall energy consumption. This reduction is achievable when these systems incorporate heat recovery mechanisms and are paired with highly insulated building designs. However, this energy saving potential depends on the fans themselves having a low energy demand [2].

The question arises of how to decrease the fans' power demand. The electrical power demand of a system with multiple fans is the sum of the individual fan's power demands po^{el}, which can be calculated by

$$po^{\mathrm{el}} = \frac{\Delta p q}{\eta}, \tag{1}$$

with the fan's pressure increase Δp, volume flow q and efficiency η. The total electrical power demand of a system thus can be reduced by (i) decreasing the volume flows, (ii) decreasing the pressure losses

in the system or (iii) increasing the efficiency. The volume flows (i) can be reduced to the actual demand, with variable volume flow systems, this is state-of-the-art and thus assumed given. The pressure losses (ii) depend on the system topology. In a central system, a fan – or multiple parallel fans – have to provide the maximal pressure loss of all branches. However, distributed systems can decrease the central pressure increase by incorporating distributed fans in the central fan duct, leading to a reduced hydraulic power demand. This approach is gaining increased attention with researchers at University of Kassel demonstrating the potential and showing the practical applications [3], [4] as well as Müller et al. and Breuer et al. using mathematical optimisation to optimally plan distributed fan systems [5], [6]. The pressure increase can also be reduced by having wider ducts in the network, thus decreasing the pressure loss of the system. Lastly, the efficiency (iii) can be increased by making sure that fans and volume flow controllers (VFCs) operate efficiently, i.e. optimally coordinating the components in the system.

To account for all three factors is very hard for human planners, thus normally heuristics are applied. In the literature, duct sizing is often approached by balancing pressure losses across all branches [7]. However, this approach does not incorporate the trade-off between electrical energy costs and investment costs. Even more importantly, this approach is invalid in presence of distributed fans. New methods explore alternative strategies with optimisation approaches but do not incorporate detailed fan characteristics [8].

The earliest stage of building planning is the preplanning. Preplanning refers to the first design stage of a building. For the ventilation system in this early stage, the duct network should be laid out and sized and the location and number of components should be defined. Typically, the planning procedure is separated into two tasks: Dimensioning of the duct network and a subsequent definition of location and number of fans, VFCs, etc. This separation is due to the complexity of the planning and the interaction with other building trades during the early-stage design.

In this paper, we optimise the ventilation system's topology in terms of fan placements – potentially incorporating distributed fans – and duct sizing using methods from mathematical optimisation. Using methods from discrete mathematics, the planning complexity can be handled using algorithms and thus a holistic optimisation becomes possible. This allows us to address the trade-off between using wider ducts to reduce pressure losses and placing distributed fans in high-loss branches to minimise total energy demand. To obtain simple models, fan characteristic curves as well as pressure loss models are efficiently linearised. This results in a Mixed-Integer Linear Program (MILP) that combines duct dimensioning and (distributed) fan placement.

Given the need for coordination with other construction trades, defining the duct network topology in the optimisation is impractical, as it depends heavily on decisions made by other trades. Therefore, the topology of the duct network is assumed to be predefined in the optimisation, while the dimensions (width and height) of the ducts are the optimisation problem's variables.

A key aspect of our approach is the integration of detailed fan models to accurately reflect power consumption and multiple load cases to capture real-world variability. The optimisation extends beyond preplanning requirements, providing insights into which fans to purchase and how to operate them across different load cases. However, given the inherent uncertainties of early-stage design, the model prioritises simplicity and computational efficiency. Through extensive linearisation, the proposed method ensures that optimal solutions can be computed within seconds, making it highly practical for preplanning.

The primary objective of this work is to develop a novel methodology for ventilation building planning. While the approach has potential for broader adoption, this paper emphasises methodological advancements rather than software deployment.

FAN 2025
Antibes - Juan-les-Pins (France), 9 - 10 April 2025

METHOD

The following section introduces the system model, the fan model, and the duct model in detail.

System model

The supply and exhaust air systems are modelled separately, and the ventilation system can be represented as a mathematical tree-like graph $\mathscr{G}(\mathscr{V},\mathscr{E})$, where the nodes are $v \in \mathscr{V}$ and the edges are $(i,j) \in \mathscr{E}$. The ventilation system model is formulated as a Mixed-Integer Linear Program (MILP). This model includes the objective function, the mathematical graph representation of the system, the component models (see following subsections), the load cases $\mathscr{S}$, topology constraints, and conservation equations. The fans, VFCs and ducts are defined on the edges $(i,j) \in \mathscr{E}$.

The mathematical optimisation problem is structured into two stages:

1. Determining a cost-effective purchase decision for the components.
2. Operating a subset of the purchased components for each load case $s \in \mathscr{S}$ within the specified load profile, ensuring that the system meets the demand while maximising efficiency.

The load cases differ in volume flow demand for each room. This formulation results in a 2-stage stochastic MILP. The system model is not given in detail, refer to [6] section 2.3 for the model.

The objective of the optimisation is to minimise the life-cycle costs, consisting of:
(i) **Investment costs**, including costs for fans (fan-type dependent $f \in$ fans: C_f^{fan}), VFCs (C^{vfc}), and ducts ($c_{i,j}^{\text{duct}}$, see eq. (10)) and
(ii) **Operating costs**, determined by the load case frequency H_s, electrical energy cost C^{el} in €/kWh, the ventilation system's entire operation time in hours T^{op} and the energy consumption of the fans $po_{s,i,j}^{\text{el}}$.

The investment costs are calculated according to the annuity method described in [9]. With these costs, the objective function can be expressed as:

$$\min \underbrace{\sum_{(i,j)\in\text{fan edges}} \sum_{f\in\text{fans}} C_f^{\text{fan}} x_{i,j,f} + \sum_{(i,j)\in\text{VFC edges}} C_{i,j}^{\text{vfc}} x_{i,j} + \sum_{(i,j)\in\text{duct edges}} c_{i,j}^{\text{duct}}}_{\text{investment costs}} \tag{2}$$

$$+ \underbrace{T^{\text{op}} C^{\text{el}} \sum_{s\in\mathscr{S}} H_s \sum_{(i,j)\in\text{fan edges}} po_{s,i,j}^{\text{el}}}_{\text{operating costs}}. \tag{3}$$

For improved clarity, this paper uses capital letters to denote parameters of the optimisation model and lowercase letters to represent variables.

Fan, VFC, and pressure loss models for ducts and fittings complete the system model. The VFCs are modelled to allow a variable pressure loss when purchased. The remaining models are presented in the following.

Fan station model

A fan's operation is described by its rotational speed n, volume flow q, pressure increase Δp and its electrical energy consumption po^{el}. Only two variables are independent, typically the two character-

istic curves $\Delta p(q,n)$ and $po^{\mathrm{el}}(q,n)$ are used:

$$\Delta p(q,n) = \alpha_0 q^2 + \alpha_1 qn + \alpha_2 n^2 \tag{4}$$

$$po^{\mathrm{el}}(q,n) = \beta_0 q^3 + \beta_1 q^2 n + \beta_2 qn^2 + \beta_3 n^3 + \beta_4, \tag{5}$$

where α_i ($i \in \{0,...,2\}$) and β_i ($i \in \{0,...,4\}$) are fan-specific constants derived from fitting manufacturer data.

To operate multiple fans in parallel, their pressure increase is set identical and only their volume flow may be different. As shown by Groß et al., in case of identical parallel fans, maximum efficiency is achieved when the fans operate identically [10]. This is modelled with additional constraints. Fans can be purchased at the cost C_f^{fan}, and only a purchased fan can be activated in the load cases.

The fan characteristic curves are non-linear and non-convex. Thus, they present a serious challenge to the optimisation solver. Common techniques to handle the complexity are linearisation approaches using piecewise linear approximations. These however introduce a huge number of binary variables and thus the solving times are still extensive, compare [11]. Another approach from the field of discrete optimisation is to approximate the non-convex characteristic curves using convex functions. These convex functions can be linear hyperplanes. To obtain linear models a certain procedure is performed. Due to the page limit of this paper, the detailed procedure is not included here. However, the main idea for obtaining linear fan models is as follows:

1. Fan power consumption is expressed as a function of $po^{\mathrm{el}}(q,\Delta p)$. Therefore eq. (4) is solved for the rotational speed, the result is plugged into eq. (5).

2. For multiple parallel fans, the total electrical power consumption is split into a hydraulic power term, ΔpQ with Q known a-priori, and the power loss $po^{\mathrm{loss}}(q,\Delta p)$: $po^{\mathrm{el}} = \Delta p + po^{\mathrm{loss}}$. Now, the hydraulic power can be written as a linear term (as the volume flow over the edge is known, but not that of the individual fans). The power loss function has a smaller locally non-convex region than the original power consumption function.

3. The power loss model per fan is linearised using supporting hyperplanes, i.e. Outer Polyhedral Approximation. For a given operating point (n,q), the power loss can be approximated by underestimating the actual curve with tangent hyperplanes. Because the objective function favours smaller electrical powers, solutions will lie on these tangents.

4. As the rotational speed is no longer part of the model, its value has to be bounded to not exceed 100 %. Therefore, a convex hull based on tangents is introduced that constraints the electrical power to be lower than the rotational speed 100 %, as shown in fig. 1.

For a single fan on an edge, the procedure simplifies as the volume flow through the fan is known.

This linearisation enables highly efficient computation, as it does not require the introduction of binary variables, unlike piecewise linearisation techniques. Yet, in non-convex regions of the power loss model, the approximation is deviating visibly from the exact curves, see fig. 1. Due to the underestimation in step 3, the optimised system's power consumption represents a lower limit compared to the exact solution. Any exact system's power consumption cannot be lower than this limit. By calculating the exact power consumption of the solution – reverting the approximations based on the pressure increase and volume flow – an upper limit of the power consumption can be established. Consequently, any system with minimal life-cycle costs must fall within the range defined by the approximated system and its exact counterpart. This solution bounding approach enables to assess how much better the optimisation of the exact system can get.

FAN 2025
Antibes - Juan-les-Pins (France), 9 - 10 April 2025

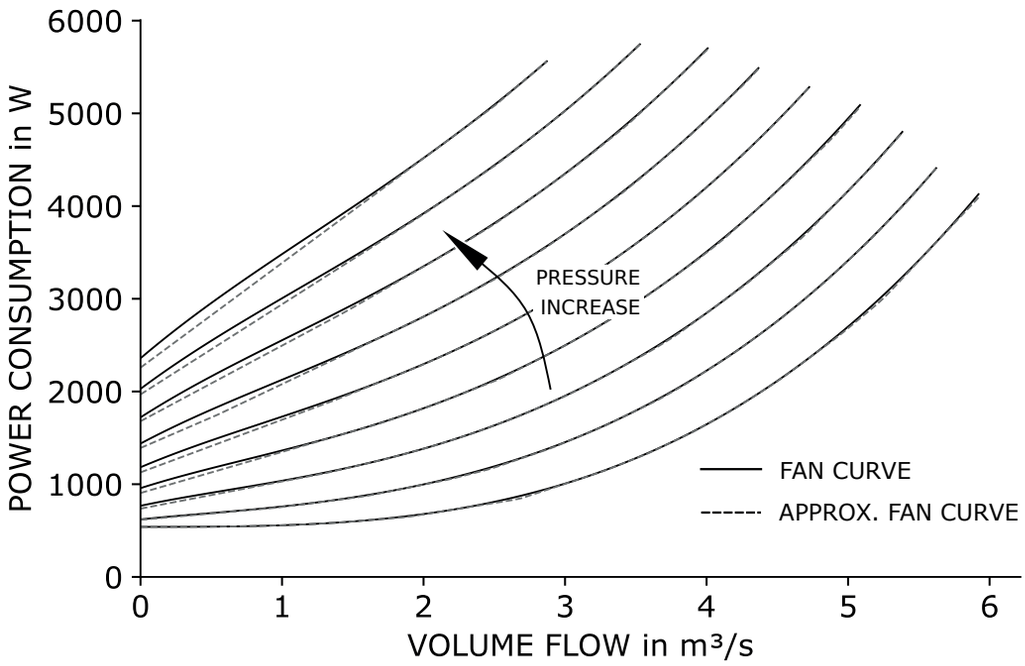


Figure 1: Approximation of an example fan curve: The dashed lines represent approximations of the solid lines representing non-linear fan curves. At low volume flows and high pressure losses, the electric power is visibly underestimated, while at high volume flows, the approximation error is minimal.

Pressure losses

The pressure losses are present on every edge of the graph that represents the duct network or auxiliary components other than fan stations. As the duct topology is fixed, each duct's length L as well as the volume flow Q through the ducts and auxiliary components are known beforehand. Given the volume flows, the auxiliary components' pressure losses are calculated a priori and are thus not part of the optimisation. Concerning the ducting, the design variables are only the width w and the height h. The pressure loss is described by

$$\Delta p = \zeta \frac{\rho}{2} \frac{Q^2}{(wh)^2}, \tag{6}$$

with density ρ and resistance coefficient ζ.

For duct friction, ζ can be calculated using the Darcy-Weisbach equation:

$$\zeta = \frac{L}{d_\mathrm{h}} \lambda(k^+, \mathrm{Re}), \tag{7}$$

with $\lambda(k^+, \mathrm{Re})$ being the friction factor dependent on the relative roughness k^+ and the Reynolds number Re. For simplicity λ is assumed to be constant. $d_\mathrm{h} = 2wh/(h+b)$ is the hydraulic diameter of a rectangular cross-section. Plugging eq. (7) into eq. (6) and reformulating, one obtains

$$\Delta p = \frac{\rho}{4} \frac{Q^2}{(wh)^2} \frac{L(w+h)}{wh} \lambda(k^+, \mathrm{Re}) \tag{8}$$

$$= \frac{\rho}{4} Q^2 L \frac{w+h}{(wh)^3} \lambda(k^+, \mathrm{Re}), \tag{9}$$

For fittings, the pressure loss depends on geometrical and/or flow factors. The fitting-dependent resistance coefficient ζ is calculated according to VDI standard 3803 part 6 [12]. For most fittings it is feasible to approximate a fixed value that can be calculate a-priori. For a branch, the pressure loss strongly depends on the ratio of velocities in the branches. To simplify, too small velocity ratios are excluded in the optimisation as these result in exponentially growing pressure losses.

The equations presented above are highly non-linear. To fulfil the goal of simple models that are easy to calculate, linearisation is needed. For the pressure loss model, it can be shown, that the general pressure loss formula eq. (6) as well as the duct friction formula eq. (9) are convex functions w.r.t. width w and height h. This is proofed in section 8.1. As the optimisation favours smaller pressure losses for given w, h, again Polyhedral Outer Approximation can be used to linearise the equations.

The investment costs of a duct depend on the surface area of the duct walls, this can be expressed as

$$c_{i,j}^{\text{ducts}} = 2L_{i,j}(w_{i,j} + h_{i,j})C^{\text{ducts}}, \tag{10}$$

with C^{ducts} being the duct costs in €/m^2.

CASE STUDY

In this case study, the same building and load cases as in Breuer [6] are optimised, see fig. 2. Only the supply air system is optimised. The system is planned to operate for 12 years. The duct network layout is predefined; however, the width w and height h of each section remain to be determined as part of the optimization process. The dimensions of the ducts range between 0.2 m and 0.6 m, except for the central duct, where the maximum dimension is 1.5 m.

The central fan station can accommodate up to three fans, selected from two product lines with two different diameters. Each individual fan type can be installed up to three times. Additionally, in front of each room and in front of each branch up to three fans – chosen from the same set of fans as those used centrally – and/or a VFC can be installed. The case where both, fans and a VFC, are purchased would result in a parallel arrangement where either one or the other component is active.

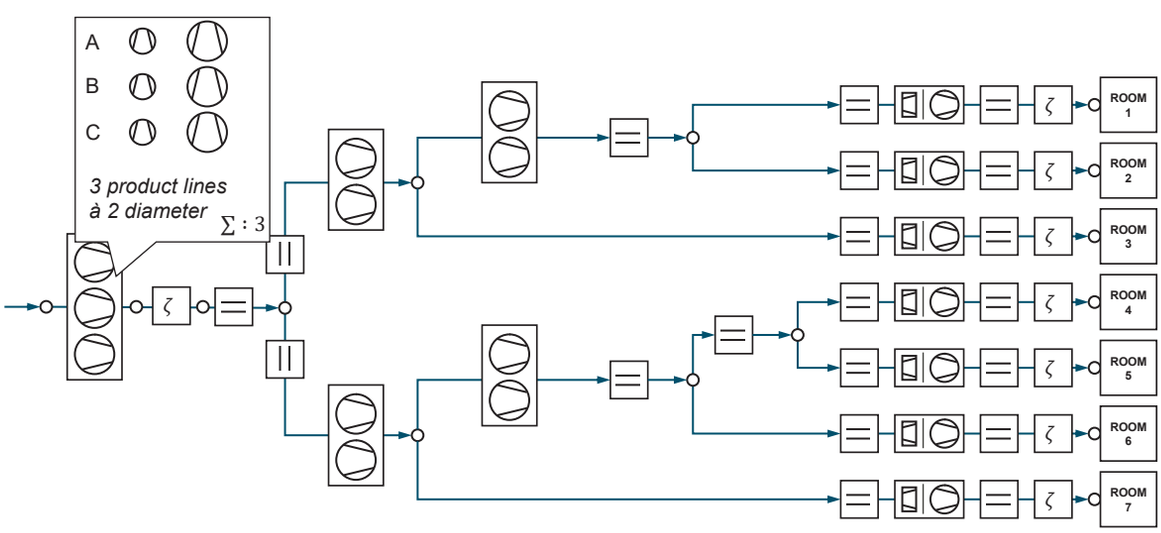


Figure 2: The case study building's ventilation system supplies outdoor air to seven rooms. The blocks represent system components: in addition to the fan and VFC blocks, there is a ζ-value block with a prescribed ζ-value. The blocks with two horizontal parallel lines represent duct sections that require dimensioning. When distributed fans are present, the branches require shut-off dampers, which are not shown in this diagram.

RESULTS

The mathematical models are implemented in Python using the PYOMO [13] modelling language and solved using Gurobi 12.0.1 [14]. Gurobi employs a branch-and-bound algorithm to solve the problem. The computations were carried out on a Ubuntu Workstation with Ubuntu 24.04 operating system, 80 GB of RAM, and two AMD EPYC 7313 32-core processors and a maximum clock speed of 3.7 GHz.

The resulting ventilation system is shown in fig. 3. A single fan is purchased centrally, no fan is purchased in front of a branch and in front of each room one or two fans but no VFCs are purchased – the optimal topology is distributed. In comparison to the optimal central solution (which is not shown here), the system has decreased life-cycle costs. Counter-intuitevly, this does not stem from decreased energy costs but from the fact that the cheapest fans are cheaper than the cheapest VFCs.

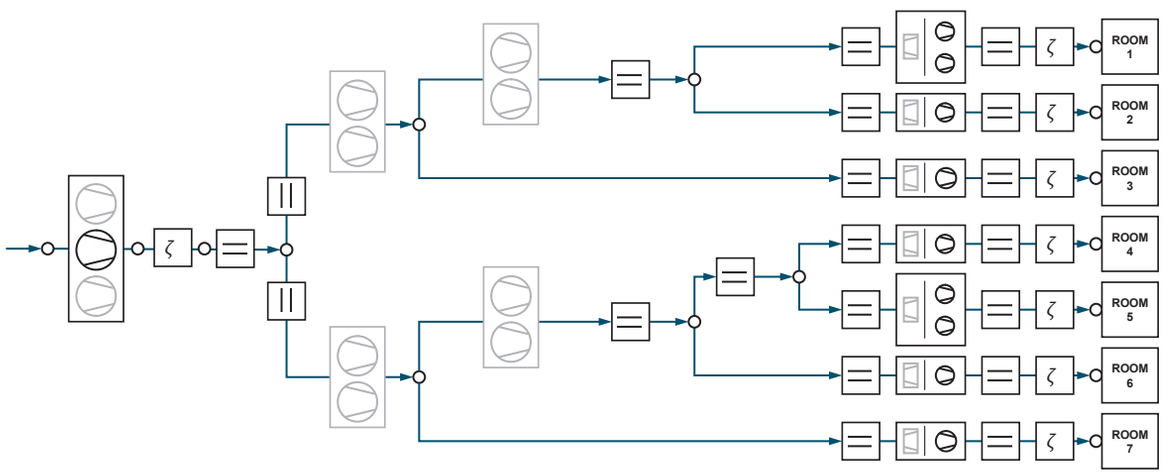


Figure 3: The optimal configuration of the case study building's ventilation system. A single fan is purchased centrally. In front of the rooms one or two fans are purchased.

The life-cycle costs of the system are 49 255 €. The cost distribution is given in fig. 4. The largest cost factor, at 41 %, is the duct investment costs, followed by the fan electric energy costs with 30 %. The fan investment cost is just below that.

As multiple approximations are employed, it is important to evaluate the approximation errors. Using the known operating points, the fan's exact electrical power consumption can be calculated. Similarly, with the known duct dimensions, the exact friction pressure loss per duct can also be determined. The approximated values are then compared to the exact values, as shown in fig. 5. Overall, the approximation demonstrates good agreement with the exact values. Using the solution bounding approach, it is made sure that any optimisation performed using exact fan characteristic curves will yield results that lie between the approximated and the exact problem. In other words, optimising the topology with exact fan characteristic curves could, at best, achieve up to 1.4 % lower electrical power consumption compared to the current approximated topology.

DISCUSSION AND CONCLUSION

This paper introduces a novel methodology that enables a systematic trade-off between larger duct dimensions and distributed fans. By utilising mathematical optimisation, the approach provides valuable insights into the optimal design and behaviour of ventilation systems, balancing investment costs

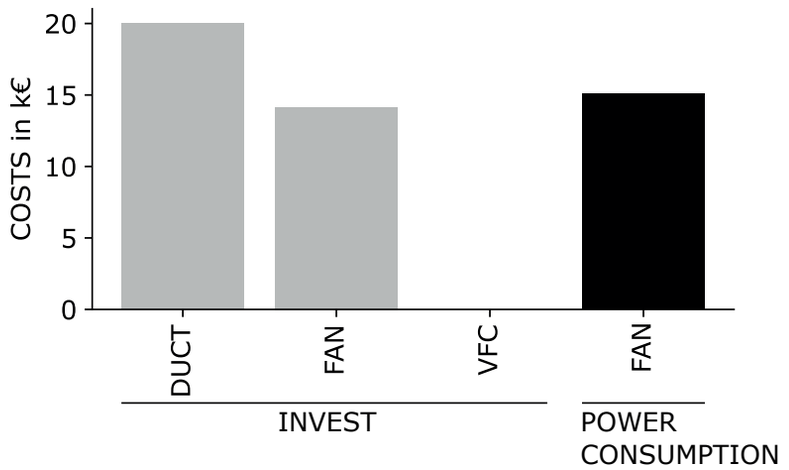


Figure 4: Cost distribution of optimal solution. Duct investment costs are the biggest cost factor.

and operational efficiency.

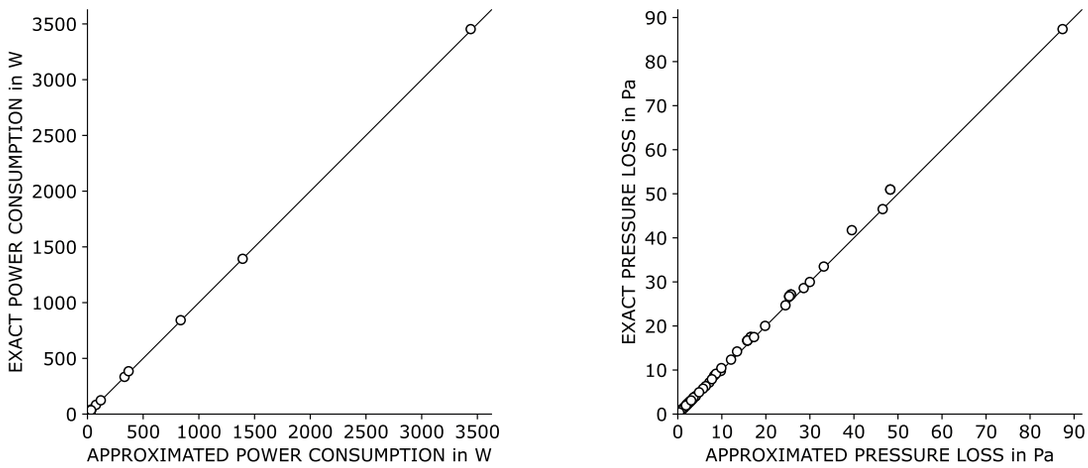
The results of the presented case study demonstrate the capability of the methodology to solve complex preplanning tasks within seconds. This efficiency stems from the linear nature of the problem formulation, which ensures very low computational times. For comparison, solving the same problem using the original non-linear fan models (eqs. (4) and (5)) takes multiple hours, whereas the linearized model solves within 2.5 min.

The results further show that the approximated fan power and pressure losses align closely with exact values. The observed deviation of up to 1.4 % from the exact power consumption is a reasonably small error given the significant reduction in solving times. This trade-off between accuracy and computational efficiency makes the methodology particularly suitable for the preplanning stage. In the preplanning stage, planners typically try many different topologies. Using the method shown in this paper, the planners can optimise different duct network topologies within seconds and compare their results. The solution bounding approach even allows statements of the non-approximated system's optimal life-cycle costs.

In the case study, duct width and height were treated as independent parameters, allowing them to vary within identical ranges. However, this approach may not fully align with practical applications, as the optimisation naturally leads to symmetric duct dimensions for maximum efficiency. In real-world planning, dimensions are often influenced by constraints imposed by other building trades, particularly limitations on duct height. Such constraints can be directly incorporated into the optimisation process by setting upper limits on duct height or allowing only specific width-to-height ratios. Additionally, due to the iterative nature of the planning process and interactions with other trades, spatial limitations frequently arise. For example, it is often not feasible to increase duct dimensions beyond a certain height simply because there is not enough available space.

The findings of this case study should not be generalised. A larger-scale investigation involving multiple buildings with more complex ventilation systems is needed to better identify scenarios where distributed fans provide significant value. Yet, first results on a larger building with more distributed fans and more fan product lines show that the methodology's computational efficiency scales well and solves within a few minutes. In contrast, solving the non-linear formulation takes multiple days. The accuracy of the larger building's solution is even better than in this case study.

Further research could also include integrating heat demands and respective components into the



(a) fan power consumption. The plot shows the one purchased fan in three different load cases, the fits are always underestimating but the error is reasonably small.

(b) duct friction pressure losses. The fit contains only a minor error from the true pressure loss.

Figure 5: comparisons of true values and those approximated using outer polyhedral approximation. The line with unit slope represents exact similarity between true and approximated values.

optimisation framework. This extension would enable an even more comprehensive evaluation of system performance and energy efficiency, further broadening the applicability of the methodology.

ACKNOWLEDGEMENTS

The presented results were obtained within the research project “Algorithmic System Planning of Air Handling Units”, Project No. 22289 N/1, funded by the program for promoting the Industrial Collective Research (IGF) of the German Ministry of Economic Affairs and Climate Action (BMWK), approved by the Deutsches Zentrum für Luft- und Raumfahrt (DLR). We want to thank all the participants of the working group for the constructive collaboration.

REFERENCES

[1] *Commission Regulation (EU) No 327/2011 of 30 March 2011 implementing Directive 2009/125/EC of the European Parliament and of the Council with regard to ecodesign requirements for fans driven by motors with an electric input power between 125 W and 500 kW*, Multiple languages, `http://data.europa.eu/eli/reg/2011/327/oj`, Text with EEA relevance. OJ L 90, 6.4.2011, p. 8–21. In force. Current consolidated version: 09/01/2017, **2011**.

[2] Federal Ministry for Economic Affairs and Energy, *Energy efficiency strategy for buildings: Methods for achieving a virtually climate-neutral building stock*, BMWi, Ed., Berlin, **2015**.

[3] N. Alsen, T. Klimmt, J. Knissel, and M. Giesen, *Einsatz dezentraler ventilatoren zur luftförderung in zentralen rlt-anlagen insbesondere bei nicht-wohngebäuden*, **2018**.

[4] Jens Knissel, Max Giesen, Tobias Klimmt, *Planungsleitfaden semizentrale lüftung – dezentrale ventilatoren in zentralen rlt-anlagen*, kassel university press, Ed., **2018**.

[5] T. M. Müller, M. Sachs, J. H. Breuer, and P. F. Pelz, *Planning of distributed ventilation systems for energy-efficient buildings by discrete optimisation*, Journal of Building Engineering vol. 68, p. 106 205, **2023**.

[6] J. H. Breuer and P. F. Pelz, *Algorithmic planning of ventilation systems: Optimising for life-cycle costs and acoustic comfort*, Journal of Building Engineering, p. 111 547, **2024**, ISSN: 2352-7102. DOI: https://doi.org/10.1016/j.jobe.2024.111547. [Online]. Available: https://www.sciencedirect.com/science/article/pii/S2352710224031152.

[7] Z. Kabbara, S. Jorens, E. Ahmadian, and I. Verhaert, *Improving hvac ductwork designs while considering fittings at an early stage*, Building and Environment vol. 237, p. 110 272, **2023**, ISSN: 03601323. DOI: 10.1016/j.buildenv.2023.110272.

[8] S. Jorens, K. Sörensen, I. Verhaert, and A. de Corte, *Air distribution system design optimization in non-residential buildings: Problem formulation and generation of test networks*, Journal of Building Engineering vol. 12, pp. 60–67, **2017**, ISSN: 23527102. DOI: 10.1016/j.jobe.2017.05.006.

[9] Verein Deutscher Ingenieure, *VDI 2067: Economic efficiency of building installations – fundamentals and economic calculation*, **2012**.

[10] T. Groß, P. Pöttgen, and P. F. Pelz, *Analytical approach for the optimal operation of pumps in booster systems*, Journal of Water Resources Planning and Management vol. 143, no. 8, p. 04 017 029, **2017**.

[11] T. M. Müller, P. Leise, I.-S. Lorenz, L. C. Altherr, and P. F. Pelz, *Optimization and validation of pumping system design and operation for water supply in high-rise buildings*, Optimization and Engineering vol. 22, pp. 643–686, **2021**.

[12] Verein Deutscher Ingenieure, *VDI 3803 Blatt 6 - Luftleitsysteme druckverluste und wärmetechnische berechnungen*, **2023**.

[13] W. E. Hart, J.-P. Watson, and D. L. Woodruff, *Pyomo: Modeling and solving mathematical programs in python*, Mathematical Programming Computation vol. 3, pp. 219–260, **2011**.

[14] Gurobi Optimization, LLC, *Gurobi Optimizer Reference Manual*, **2023**. [Online]. Available: https://www.gurobi.com.

APPENDIX

CONVEXITY

To show that the general pressure loss formula eq. (6) as well as the duct friction formula eq. (9) are convex functions w.r.t. width w and height h, we show that their curvature is always positive. As these functions are multivariate, their Hessian must thus be positive semi-definite.

To show this, first the general pressure loss formula eq. (6) is simplified by removing its constant factors.

$$f(w,h) = \frac{1}{(wh)^2} \tag{11}$$

Now, we calculate the Hessian

$$H_f = \begin{bmatrix} \frac{\partial^2 f}{\partial w^2} & \frac{\partial^2 f}{\partial w \partial h} \\ \frac{\partial^2 f}{\partial h \partial w} & \frac{\partial^2 f}{\partial h^2} \end{bmatrix} = \begin{bmatrix} \frac{6}{w^4 h^2} & \frac{4}{w^3 h^3} \\ \frac{4}{w^3 h^3} & \frac{6}{w^2 h^4} \end{bmatrix} \tag{12}$$

FAN 2025
Antibes - Juan-les-Pins (France), 9 - 10 April 2025

and thus, the principal minors are non-negative:

$$H_{f(w,w)} = \frac{6}{w^4 h^2} \geq 0 \tag{13}$$

$$H_{f(h,h)} = \frac{6}{w^2 h^4} \geq 0 \tag{14}$$

$$\det(H_f) = \frac{20}{w^6 h^6} \geq 0. \tag{15}$$

Similarly, the principal minors of the duct friction eq. (9) are also non-negative and thus the duct friction is convex.

ADVANCED COMPUTATIONAL APPROACHES TO FAN PERFORMANCE AND INSTALLATION CONDITIONS

Uma Maheswararao LAKAMANA, Massimo FACCA, Amit AHUJA

MAICO Gulf LLC, Ras Al Khaimah, United Arab Emirates

SUMMARY

This paper investigates advanced computational methods to improve fan performance and ensure accurate installation conditions, with a focus on HVAC system manufacturing. The primary aim is to analyze system losses in current HVAC designs and to validate these systems using computational approaches. The case study presented examines the System Effect Factor (SEF) and External System design validation. Centrifugal fans, commonly used in ventilation applications to supply or extract air, often face performance issues when installed in conditions different from those specified in ISO/AMCA testing standards. This mismatch leads to system effect losses. Using Computational Fluid Dynamics (CFD), this paper demonstrates how SEF impacts fan performance and shows that incorporating an Effective Duct Length (EDL) upstream of the fan can enhance efficiency by 5 %.

INTRODUCTION

Centrifugal fans play a key role in industrial applications and modern HVAC systems, where maintaining proper airflow and pressure is essential for efficiency. However, real-world installations often differ from ideal design conditions, leading to performance challenges. One major issue is the System Effect Factor (SEF), which occurs due to non-ideal inlet and outlet configurations, such as elbows, ducts, or obstructions near the fan. These improper connections disrupt the fan's aerodynamics, causing performance to fall short of catalog ratings, even if system pressure losses are accurately calculated. The term "system effect" refers to this drop in fan performance caused by installation factors.

System designers commonly incorporate safety factors into calculated system resistance to address unforeseen circumstances. These safety factors can sometimes compensate for unaccounted resistance losses, enabling the actual system to deliver the intended airflow. However, if the actual system resistance is lower than the design resistance, including the safety factors, the fan may produce excessive airflow. This outcome might be undesirable, as the fan could operate at a less efficient point on its performance curve, consuming more power than necessary. To optimize performance under such conditions, it may be necessary to adjust the fan's operation. This can be achieved by reducing the fan speed, modifying the variable inlet vane (VIV) if available, or adjusting the inlet damper.

The System Effect Factor (SEF) represents the impact of unfavorable installation conditions on fan performance within an air system. The inlet or outlet system effect (denoted as SE in the equations below) and air velocity (V) can be calculated for specific configurations. Air velocity (V) is the average flow

velocity at the fan inlet (if there's an obstacle at the inlet) or at the fan outlet (if there's an obstacle at the outlet).

Equations: System Effect factor calculation as below:

$$SE = C \times P_{fd} \tag{1}$$

and

$$Pfd = \left(\frac{V}{1.414}\right)^2 \rho \quad SI \tag{2}$$

and

$$V = Q/A \tag{3}$$

with

C = the dynamic pressure loss coefficient (also called the system effect coefficient).
P_{fd} = the velocity pressure (or dynamic pressure) at the fan inlet or outlet, Pa
V = the air velocity at fan Inlet or outlet, m/s
Q = the airflow at the fan inlet or outlet, m^3/s
A = the fan area at the inlet or outlet, m^2

Figure 1 graphically illustrates the system effects from the above equations. By entering the chart at the appropriate air velocity (on the abscissa), it is possible to read across from any curve (to the ordinate) to find the SEF in Pa for a particular configuration.

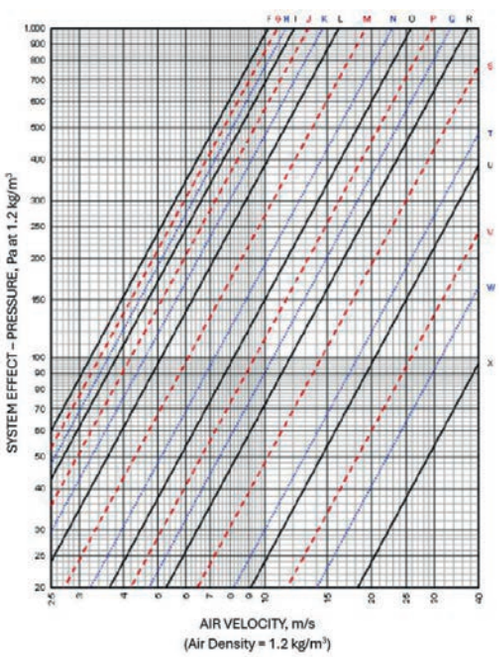


Figure 1: System Effect Curves

To validate the SEF at the fan inlet and outlet under non-ideal conditions, the fan is analyzed with various inlet and outlet configurations. Since maintaining the effective duct length is often not feasible in real-world installations, CFD analysis provides reliable and quantifiable results to account for site-specific conditions.

The case study explores the implications of SEF on centrifugal fan performance through advanced CFD analysis by using ANSYS Software. Using a centrifugal fan equipped with a backward-curved impeller, key performance parameters—flow rate, aerodynamic power, total pressure (TP), and efficiency—are evaluated under varying installation conditions. The findings reveal critical issues, including increased impeller load and efficiency drops caused by high-velocity regions and flow disturbances at elbows.

METHODOLOY OF COMPUTATIONAL STUDY

The methodology of Computational Fluid Dynamics (CFD) analysis involves using numerical techniques and computational tools to simulate and analyze fluid flow, heat transfer, and other related physical phenomena. Here's a step-by-step explanation of the CFD methodology.

- Problem Definition
- Geometry creation and Domain Setup
- Mesh generation
- Physics Setup
- Solver Setup
- Solution process
- Post processing

SEF STUDY ON SINGLE WIDTH SINGLE INLET (SWSI) BACKWARD BLOWER

The performance of a fan can significantly deviate from its tested values when installed under conditions different from those used in standardized testing. These deviations are attributed to system effects, which arise when the fan is not installed in accordance with ISO 5801 and AMCA 210 test standards. These standards outline four specific test configurations:

- Type A – Free Inlet, Free Outlet
- Type B – Free Inlet, Ducted Outlet
- Type C – Ducted Inlet, Free Outlet
- Type D – Ducted Inlet, Ducted Outlet

This study focuses on a Single Width Single Inlet (SWSI) backward-curved blower to analyze the System Effect Factor (SEF). The objective is to evaluate how system effects influence the blower's performance when it is installed in real-world conditions where airflow disturbances occur upstream and downstream of the fan. The key goals of the study are as follows:

- Calculate the SEF for the SWSI blower under non-standard installation conditions.
- Compare these results with the baseline performance data from a Type D (Ducted Inlet, Ducted Outlet) configuration.
- Utilize Computational Fluid Dynamics (CFD) simulations to quantify the pressure drop caused by system effects at both the upstream and downstream ends of the fan.

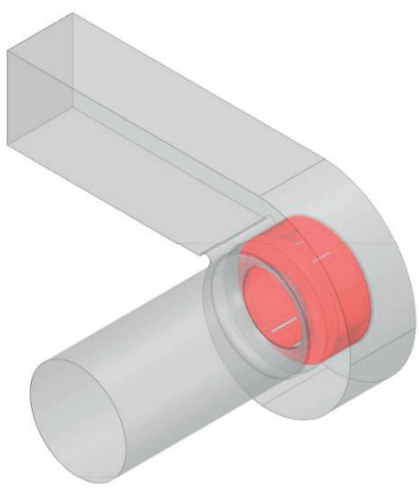


Figure 2: SWSI Blowe Type D Configuration

The geometry of the SWSI blower was meticulously designed following the fundamental principles of component design, focusing on impeller and volute configurations to achieve the desired flow and pressure coefficients. To create a precise and watertight 3D model, SpaceClaim software was employed to design the 3D model with 100 % effective duct length at fan inlet & outlet, as illustrated in Figure 2.

To calculate 100 % duct length, assume a minimum of 2½ duct diameters for 12.7 m/s or less. Add 1 duct diameter for each additional 5.08 m/s. The basic model includes inlet and outlet ducts that replicate the test configurations outlined in the ISO 5801 and AMCA 210 standards. This setup ensures that the simulation conditions align closely with the standardized test environment, enabling accurate analysis and validation of the blower's performance.

Meshing is a crucial step in the simulation process within ANSYS, as it defines the quality and accuracy of the computational results. Meshing is the process of dividing a complex geometry into smaller, simpler elements called **mesh elements** for numerical simulation in software like ANSYS FLUENT. These elements form a discrete representation of geometry, which enables mathematical approximation of physical phenomena (e.g., fluid flow, heat transfer, structural deformation). In this case study, the patch conforming tetrahedron meshing method selected to all geometries and include three level of inflation layers near the walls to capture the boundary layer effects accurately as shown in Figure 3 & 4.

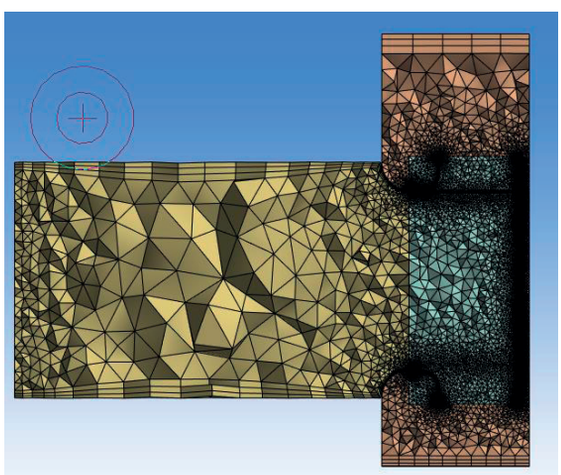


Figure 3: SWSI Blower – Patch conforming tetrahedron & Inflation layer near walls

The boundary layer is a thin region of fluid near a solid surface (wall) where viscous effects dominate. Properly resolving the boundary layer is crucial in simulations, especially in CFD, to accurately predict flow characteristics like frictional drag, and separation points.

Equation: Wall Distance (y+) Calculation

To capture the boundary layer effects in CFD, the y+ value is used to determine the first cell height near the wall.

y+ is a dimensionless wall distance defined as:

$$y+ = \frac{\rho u_t y}{\mu} \tag{4}$$

u_t = Friction velocity ($u_t = \sqrt{\tau_w / \rho}$), where τ_w is the wall shear stress

y = Distance from the wall to the first cell center

μ = Dynamic viscosity

In ANSYS FLUENT, the meshing tool automatically calculates the boundary layer heights based on the specified number of inflation layers and the selected faces in the geometry. In our case, the selected faces include the inlet duct shroud, the casing wall, and the impeller wall. The total mesh elements are 0.8 million with mesh quality skewness less than 0.9.

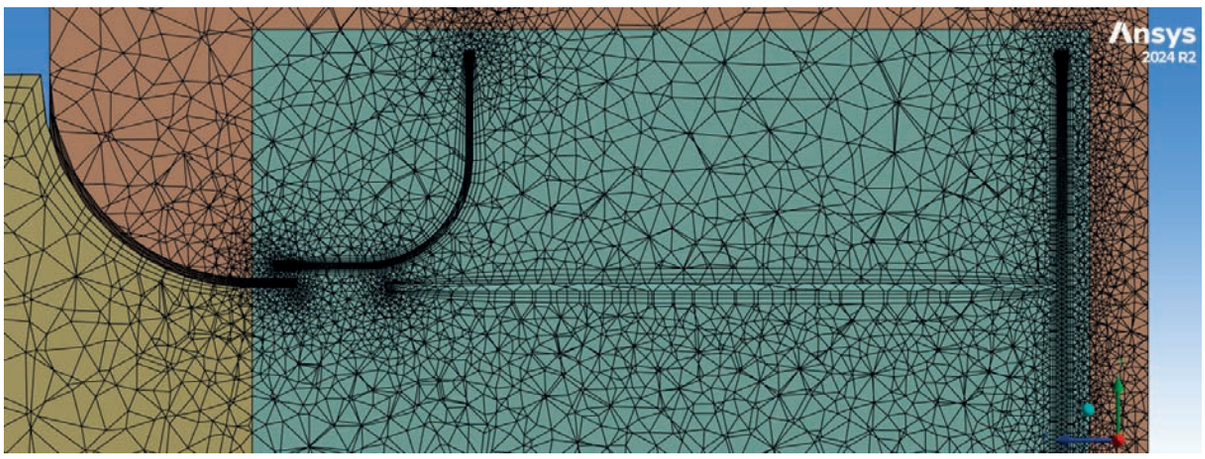


Figure 4: SWSI Blower – Patch conforming tetrahedron & Inflation layer near Impeller Cone & Blades

In the physics setup, the selection of turbulence model based on Raynolds number and Reynolds number (Re) is a dimensionless quantity used in fluid mechanics to predict and characterize the nature of fluid flow. It represents the ratio of inertial forces to viscous forces in a fluid system and helps determine whether the flow is laminar, turbulent, or in transition.

Equation: Reynolds Number Formula

$$R_e = \frac{U.L}{\nu} = \frac{15 \times 1.25}{1.516 \times 10^{-5}} = 1.2 \times 10^6 > 4000 \qquad (5)$$

U = Characteristic velocity of the flow (m/s) = Fan outlet velocity = 15 m/s

L = Characteristic length (e.g., diameter, chord length) (m) = approx. duct length = 1m (100% EDL)

ν = Kinematic viscosity of the fluid (ν=μ/ρ) (m²/s) = 1.516 × 10^{-5} m²/s at standard air density 1.2 kg/m^3

Low Reynolds Number (Re < 2,000): Flow is laminar, smooth, and orderly, with fluid layers moving in parallel.

High Reynolds Number (Re > 4,000): Flow is turbulent, chaotic, and dominated by eddies and vortices.

For this case study, the k-ε turbulence model was selected due to the Reynolds number exceeding 4000. The k−ϵ turbulence model is one of the most widely used two-equation turbulence models in computational fluid dynamics (CFD). It is designed to solve the transport equations for turbulent kinetic energy (k) and its dissipation rate (ϵ) to model turbulence.

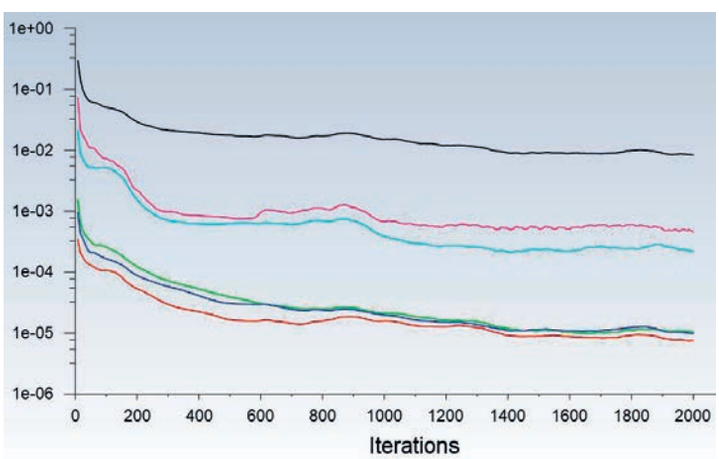


Figure 5: SWSI Blower – Residual convergence at 1300 iterations

The boundary conditions for the problem are defined as follows: pressure inlet and outlet conditions at the fan inlet and outlet, respectively. Additionally, the Moving Reference Frame (MRF) method was applied to the impeller domain, with a rotational speed of 1205 rpm.

The Standard Initialization defines values for velocity, pressure, and temperature and set-up initial values for solver. Set residuals convergence criteria as 10^{-3} for continuity, velocity, turbulence, and energy and the solution converged after 2000 iteration as illustrated in Figure 5.

To develop the fan performance curve in the Fluent simulation setup, it is essential to apply back pressure boundary conditions at the fan outlet to replicate the test conditions. The performance values for each static pressure are then obtained, as shown as flow vs pressure curve in Figure 6.

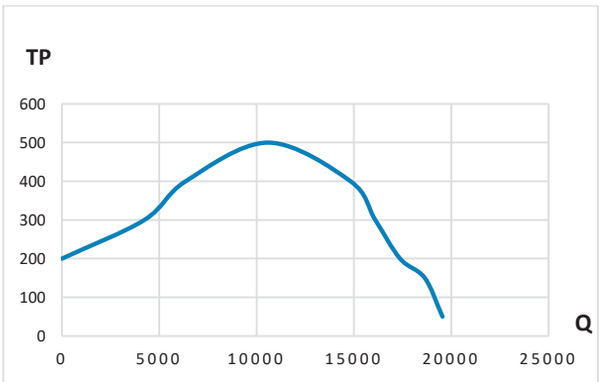


Figure 6: SWSI Blower – performance Curve at 1205 rev/min

CFD-Post is ANSYS's dedicated post-processing tool for analyzing and visualizing results from CFD simulations, including those run in ANSYS Fluent. It provides a robust environment to interpret and display simulation data, helping engineers understand flow behavior, assess design performance, and make informed decisions. The below contour displays scalar quantity such as velocity, Figure 7.

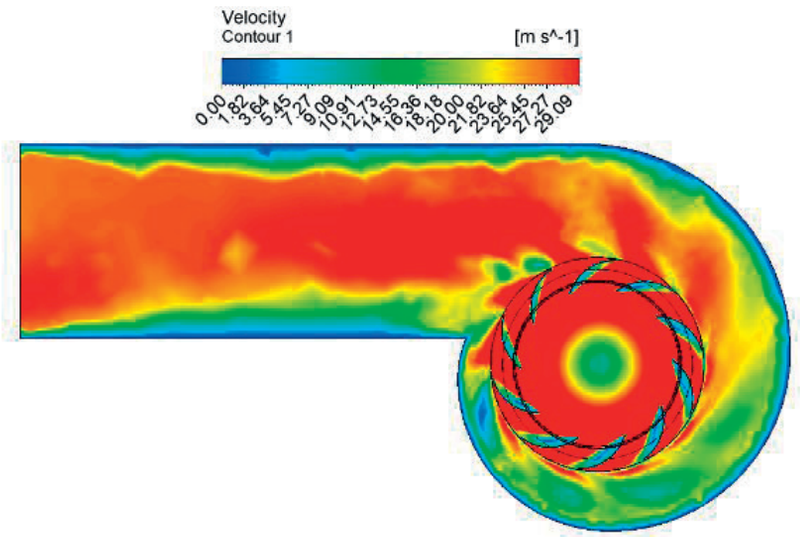


Figure 7: SWSI Blower – Velocity Contour at 1205 rev/min

The performance of an SWSI blower can be significantly influenced by site conditions that deviate from the tested conditions. To evaluate the System Effect Factor (SEF) in such cases, the design illustrated in Figure 7 incorporates inlet and outlet systems with ducts fitted with bends. Fan performance is highly sensitive to nonuniform or swirling inlet flows, which can substantially impact its efficiency.

Fan ratings and catalog performance data are typically based on unobstructed inlet conditions. Any disruption to the inlet airflow—such as restrictions caused by walls, obstructions, or plenums—can reduce fan performance. Similarly, restricted inlets positioned close to walls or cabinets can adversely affect performance. Additionally, centrifugal fans are sometimes installed with suboptimal outlet duct configurations. If a full-length outlet duct cannot be used, the outlet SEF must be added to the inlet SEF to account for the overall system losses.



Figure 7: SWSI Blower – Inlet & Outlet SEF

To better understand the performance of an SWSI blower in such installations, the same computational methodology is applied to evaluate the SEF with both inlet and outlet system effects for a centrifugal fan.

Non-uniform airflow into a fan inlet is a common cause of deficient fan performance. An elbow located at or in close proximity to the fan inlet will not allow the air to enter the impeller uniformly. The result is less than cataloged air performance as shown in Figure 8.

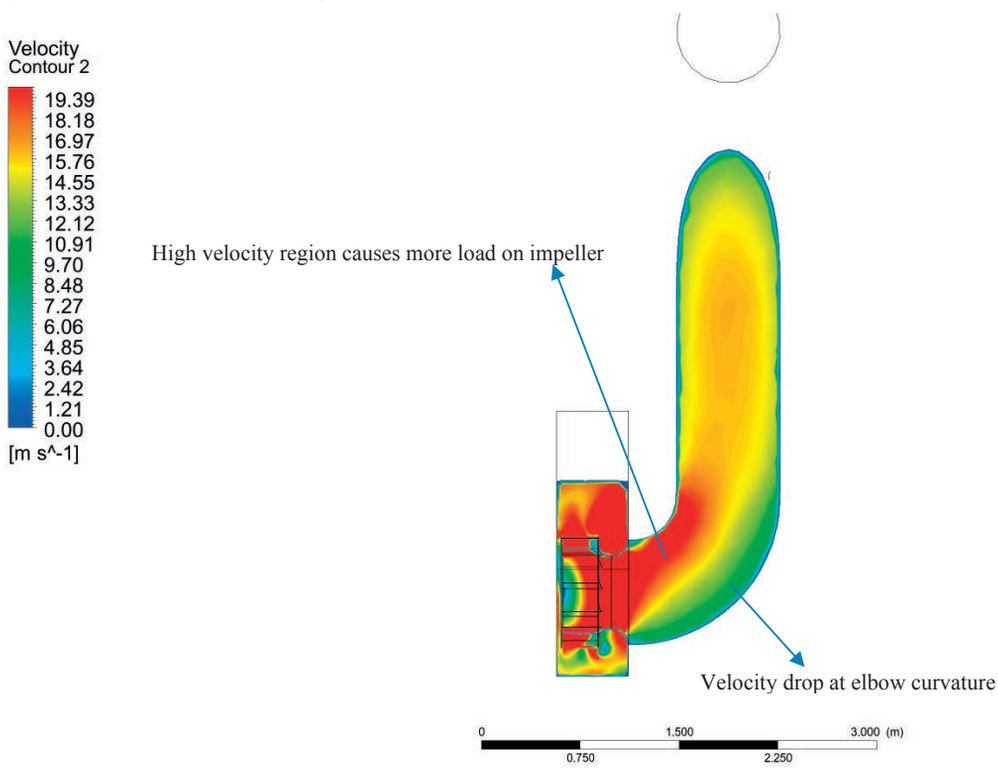


Figure 8: SWSI Blower – Inlet & Outlet SEF

differently from the CS design, where an outward radial flow component is still present in at the exit reference plane (blue markers in Fig.3). Such two occurrences suggest that the radial equilibrium condition has not yet been fully achieved at the exit reference plane of the CS design. Thus, in spite of the numerical validation stated in [8] for the CFD model used here, it is deemed as more appropriate for the present research to limit the comparison between CFD results to the evaluation of different designs in term of local flow features and compare the global performance of the two design only on an experimental basis. This also because [11] demonstrated that single-channel calculations performed on idealised annular domains overestimate the fan aerodynamic performance experimentally measured on type A test rigs, regardless of the axial extension of the domain.

EXPERIMENTAL ASSESSMENT AND DISCUSSION OF THE RESULTS

The global aerodynamic performance experimentally measured for the FI design variant are compared in fig. 8 to those already shown in Fig.2 for the CS design. The generalised improvement achieved in both pressure and efficiency curves by the FI variant over the CS design is apparent.

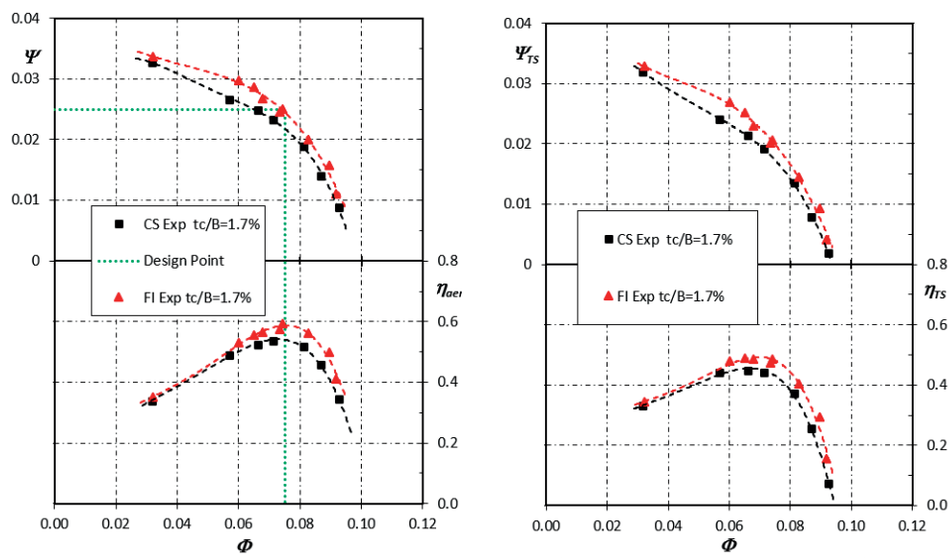


Figure 8: aerodynamic performance measured at the ISO 5801 Type A test rig for the FI (red) and CS (black) design. Design point flow rate and pressure coefficients are indicated by the green vertical and horizontal point lines, respectively. Diagrams on the left and right side refer to the data with and without inclusion of ISO dynamic pressure.

In particular, the improvements in Ψ and Ψ_{TS} achieved by the FI design range from 2.5% at low Φ to more than 20% at high Φ for the former and from 2.5% (at low Φ) to approximately 40% (at high Φ) for the latter. At peak efficiency, Ψ and Ψ_{TS} gains are approximately equal to 10% and 15%, respectively. With regard to the corresponding efficiency improvements, η_{aer} is improved from approximately 2% to 9% up to 15% moving from low Φ to peak efficiency to high Φ operations, whereas η_{TS} is improved from a minimum, approximately 2%, to 10%, up to 33%, in the same Φ range. These significant improvements confirm that the CFD predictions of global aerodynamic performance achieved by a fan on an ISO 5801 type A test rig are not highly reliable when derived from steady-state single-channel computations performed on idealised annular domains. Moreover, the range of performance difference found in [11] for CFD simulations of a fan in operation in either an annular domain or an ISO 5801 type A test rig are confirmed by the present comparison between annular domain CFD results and ISO 5801 type A experiments. Nonetheless, useful information on the differences existing between the internal flow fields of the two fan designs can be extracted from the CFD results by comparing the internal flow for the two fans in operation where CFD predicts performance difference comparable with those obtained by experiments. Thus, Fig. 9 compares the dimensionless velocity ratios at the reference exit plane for fans operation at Φ=0.0944. The higher ε_S achieved by the FI design is apparent and justifies the higher Ψ such design is able to assure. Another interesting point to note is that, at the reference exit plane, FI design shows lower amplitude of the velocity ratios spread and lower radial velocity magnitude than the CS design. Both occurrences suggest that the FI design allows for an earlier achievement of the radial equilibrium condition downstream of the rotor in comparison with the CS design.

A summary of the performance metrics under various conditions is provided in Table 1.

Table 1: Performance metrics

S. No	Parameter	As tested	With SEF	Design Change
1	Flow out (m³/s)	9	7.5	8
2	Velocity (m/s)	25	21	32
3	Aero Efficiency (%)	72	60	65

CONCLUSION

This study highlights the critical role of advanced computational techniques, such as CFD, in addressing the challenges associated with fan performance and installation conditions in HVAC systems. The results underscore the importance of accounting for System Effect Factors (SEF) and optimizing installation parameters to enhance fan efficiency. The analysis demonstrates that incorporating design modifications, such as turning vanes, can mitigate performance losses and improve efficiency by up to 5 %. Adherence to established standards, including ISO 5801 and AMCA guidelines, is essential for achieving accurate performance predictions and reducing operational costs. These findings provide a robust framework for optimizing fan design and installation in real-world applications.

BIBLIOGRAPHY

[1] ISO 5801: **2017 -** Fans – Performance testing using standardized airways.

[2] ANSI/AMCA Standard 210-16 / ASHRAE 51-16 – Laboratory Methods of Testing Fans for Certified Aerodynamic Performance Rating.

[3] ANSI/AMCA Standard 208-18 – Calculation of the Fan Energy Index.

[4] AMCA Publication 201-23 – Fans and Systems.

[5] AMCA Publication 202-17 – Troubleshooting.

[6] AMCA Publication 203-90 (R**2011**) – Field Performance Measurement of Fan Systems.

[7] AMCA Publication 801-01 (R**2008**) – Specification Guidelines.

[8] ANSI/AMCA Standard 207-17 – Fan System Efficiency and Fan System Input Power.

[9] ANSI/ASHRAE Standard 62.1-**2022** – Ventilation and Acceptable Indoor Air Quality.

[10] SMACNA – HVAC Duct Construction Standards - Metal and Flexible, 4th Edition.

[11] BS EN 13779:**2007** – Ventilation for non-residential buildings. Performance requirements for ventilation and room-conditioning systems.

[12] ASCE/SEI 7-16 – Minimum Design Loads and Associated Criteria for Buildings and Other Structures.

[13] ANSI/SPRI WD-1 **2020** –Wind Design Standard Practice for Roofing Assemblies.

[14] Fan Handbook: Selection, Application, and Design, 1st edition by BLEIER

B1 Design For Low-Noise Fans

9 April - 15:45 - Auditorium

Chairman: Dario Brivio

List of papers

Bringing NASA's Fan Noise Research Down to Earth

- Lisa Danielle KOCH – NASA Glenn Research Center (USA)

Additively Manufactured (PBF-LB) Modular Fan Blades with Structured Porosity for Noise Reduction in Turbulent Inflow Conditions

- Dominik GRÜTZNER – Institute of Fluid Mechanics (LSTM), Universität Erlangen (Germany)
- Garvin SCHULTHEIß – Institute for Virtual Product Development, Aalen University (Germany)
- Felix CZWIELONG – Institute of Fluid Mechanics (LSTM), Universität Erlangen (Germany)
- Markus MERKEL – Institute for Virtual Product Development, Aalen University (Germany)
- Stefan BECKER – Institute of Fluid Mechanics (LSTM), Universität Erlangen (Germany

Aeroacoustic Prediction and Optimization of Unevenly Spaced Blades in Axial Fans

- Samir ASSAF – CETIM (France
- Thibaut GRAS – CETIM (France)
- Jacques FERHAT – CETIM (France)



BRINGING NASA'S FAN NOISE RESEARCH DOWN TO EARTH

L. Danielle KOCH

NASA Glenn Research Center, Acoustics Branch, 21000 Brookpark Road,[1]
Cleveland, Ohio 44135, United States

SUMMARY

NASA performs research on a variety of fans for spacecraft and aircraft and transfers technology broadly so that others can improve the performance of fans used in many industrial, architectural, automotive, and marine applications. In this article, fan aerodynamic and acoustic research at the NASA Glenn Research Center is highlighted, noting collaborations with NASA Johnson Space Center and NASA Langley Research Center. Three examples of fan noise research for spacecraft are presented, followed by four examples of fan noise research for aircraft propulsion. Emphasis is given to fans with publicly available geometries. Selected comparisons are made between these different fans, capitalizing on the breadth of fan aerodynamic and acoustic research at NASA. NASA's efforts to disseminate new fan technology and research results, support commercialization, and raise the bar on fan performance across different industries are described since technology transfer is paramount.

INTRODUCTION

Technologists at the NASA Glenn Research Center (GRC) are performing aerodynamic and acoustic research on fans for spacecraft cabin ventilation, fans for cooling electronics onboard spacecraft, and fans for aircraft propulsion and power. In doing so, NASA GRC has demonstrated that some of the expertise, theory, software, experimental facilities, instrumentation, and techniques traditionally used for aircraft engine noise reduction can be used to reduce noise for smaller fans used on spacecraft. This introduction presents the motivation for the spacecraft fan work, followed by the motivation for the aircraft engine fan research. Section 2 presents three examples of fan research and development for spacecraft systems. Section 3 presents four examples of fan research for aircraft propulsion and power. A few comparisons between tone noise predictions for these different axial fans is included in Section 4 before concluding remarks and references are provided at this end of this article.

---

[1] **Notice for Copyrighted Information** This manuscript is a work of the United States Government authored as part of the official duties of employee(s) of the National Aeronautics and Space Administration. No copyright is claimed in the United States under Title 17, U.S. Code. All other rights are reserved by the United States Government. Any publisher accepting this manuscript for publication acknowledges that the United States Government retains a non-exclusive, irrevocable, worldwide license to prepare derivative works, publish, or reproduce the published form of this manuscript, or allow others to do so, for United States government purposes.

1.1 Motivation for spacecraft fan research at NASA

NASA is motivated to study fan performance for spacecraft cabins, and engineers at the NASA Glenn Research Center's (GRC) Acoustic Branch have been collaborating with NASA Johnson Space Center (JSC) since 2005. [1] Noise inside spacecraft cabins has been a serious problem since the beginning of the space age and poses risks to future long duration space exploration missions. Spacecraft cabin noise interrupts sleep and interferes with speech communication. Exposure to loud sounds can result in temporary or permanent hearing loss, depending upon the exposure duration. The Environmental Control and Life Support System (ECLSS) ventilation fans have been known to be dominant sources of noise onboard the Apollo Command Module, the Space Shuttle, and the International Space Station (ISS). Often, mufflers, silencers, and acoustic liners have been added to the ventilation system ductwork to try to reduce spacecraft cabin noise. These remedies have been costly and difficult and often added significant mass and volume to the spacecraft. Sometimes noisy fans in use on-orbit have been replaced with quieter fans.

Additionally, many fans are also needed for forced-air cooling of electronics onboard spacecraft, since natural convective flows in microgravity environments are also insufficient to transfer waste heat. Often these fans are placed in the vicinity of finger guards and other obstructions, causing flow around the fan to be distorted resulting in unsteady loads on the fan and noise. Fan noise specifications as a function of flow rate are often unavailable from fan manufacturers, so fan noise testing has become important for spacecraft systems developers.

1.2. Motivation for aircraft engine fan research at NASA

NASA is motivated to study fan performance for aircraft propulsion since air and noise pollution from aircraft engines is a complex and widespread problem. Pollution from aircraft contributes to climate change, is associated with serious health problems, raises social justice questions, and is linked to reductions in biodiversity. [2-7] Noise regulations on commercial aircraft takeoff and landing procedures create the conditions for international competition and collaboration, since quieter aircraft have a competitive advantage in the global market.

Innovation and intricate cooperation are needed to develop a more sustainable air transportation system accessible to a growing world population. Integrating engines into airframes while optimizing aircraft performance remains intensely challenging, since the airframe affects engine performance and vice versa as operating conditions vary during flight. Electrifying aircraft engines is being explored for a wide range of conceptual air vehicles.

NASA is motivated to cooperate with other organizations globally, and aircraft propulsion research at NASA GRC is done in collaboration with other NASA centers, industry, academia, and other governmental agencies. NASA GRC's fan performance research for aircraft propulsion is aligned with many national and international policies and regulations. These include a) the National Aeronautics Research and Development Policy, b) the National Aeronautics Science and Technology Priorities, c) the NASA Strategic Plan, d) the NASA Aeronautics Strategic Implementation Plan, e) the NASA Glenn Strategic Plan, f) International Civil Aviation Organization's Committee Aviation Environmental Protection outlook, g) FAA's United States 2021 Aviation Climate Action Plan, h) the U.S. Code of Federal Regulations, Title 14, Chapter 1, Subchapter C, Part 36 Noise Standards, and j) the U. S. Center for Disease Control Health Statistics. [8-15]

Motivated to broadly disseminate information, NASA's research results are routinely made available to the global public. A literature search performed by the author in 2021 using Google Scholar and reference manager software revealed that at least 106 people working at NASA GRC wrote at least 1760 publications related to aircraft engine noise reduction research from around 1948 to the present cited over 29,000 times, Figure 1, Table 1. Of this set, NASA GRC employees authored 325 publications are related to fan aeroacoustics research performed at NASA GRC. In 2013, Huff highlighted some of these accomplishments [16] and this paper highlights some more recent research.

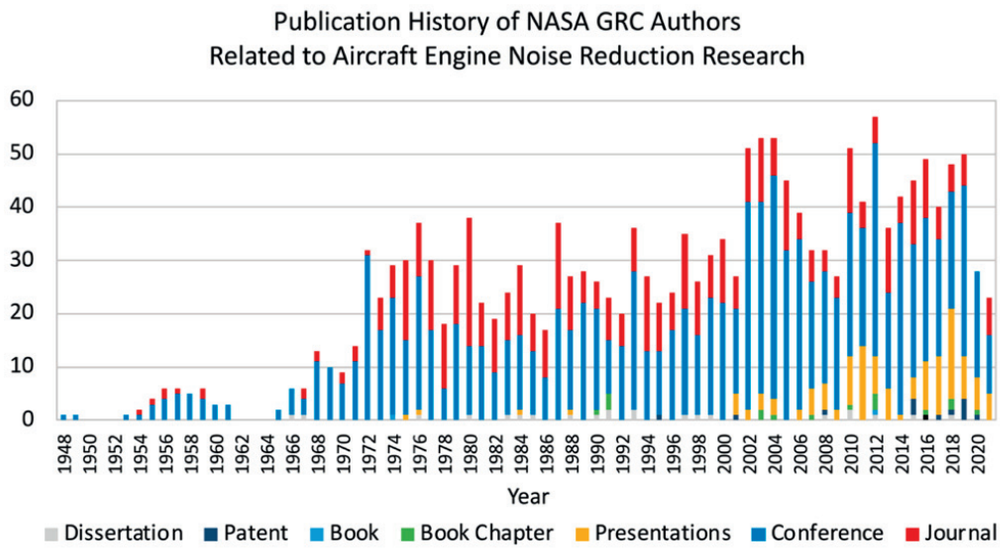


Figure 1: Publication history of the NASA GRC employees on the topic of aircraft propulsion acoustics.

Table 1: Publications of the NASA GRC employees on aircraft propulsion acoustics, 1948-2021.

Publication Type	Number	Percentage
Conference papers, NASA TM, TN, and CR series reports	1123	63.8%
Journal articles, NASA TP series reports	456	25.9%
Audiovisual materials	126	7.2%
Dissertations and theses	21	1.2%
Books, NASA SP series reports	4	0.2%
Book chapters	16	0.9%
Patents	14	0.8%
Total number of publications	1760	100%
Total number of citations in 2021	29,133	--

FAN RESEARCH AT NASA FOR SPACECRAFT SYSTEMS

Researchers at NASA GRC and JSC are performing aerodynamic and acoustic research on fans for spacecraft cabin ventilation and fans for cooling electronics onboard spacecraft. [1] Two examples of spacecraft ventilation fan research will be presented here: 1) NASA's Quiet Space Fan (QSF) and 2) a scaled version of the NASA QSF. One example of the aerodynamic and acoustic research for small fans used for electronics cooling on spacecraft is also presented in this section.

These fans are being tested in the NASA GRC Acoustical Testing Laboratory (ATL), which was constructed in 2000 so that noise emissions from equipment destined for the International Space Station could be quantified. [17] The ATL is a reconfigurable anechoic/hemi-anechoic chamber, 7.0 m (23 ft) wide, 8.2 m (27 ft) long, and 6.1 m (20 ft high). The sides of the chamber are covered in 0.86 m (34 in) fiberglass wedges protected by a fabric layer and a 53 % open area metal perforate that absorb sound down to 100 Hz. The wedges that are used to cover the floor are modular and are installed on 2 ft by 2 ft sections. Metal grating is installed over the floor wedges so that people and equipment can access the test chamber when it is in the anechoic configuration. A separate control room is adjacent to the chamber, which helps to protect people while performing the experiments in the anechoic chamber. The ATL also now features a ceiling-mounted remote-controlled traverse system, which has been used to hold microphone arrays for noise surveys.

2.1 The NASA Quiet Space Fan (QSF) for spacecraft cabin ventilation systems

NASA has made the geometry for a metal prototype of the QSF publicly available via the NASA Technical Reports Server so that the fan industry at-large can learn from this research and work independently to improve the performance of small fans. [18] The QSF was originally chosen to nominally represent an Orion spacecraft cabin ventilation fan or an intermodule ventilation fan on the International Space Station, though this version of the design is not qualified for spaceflight and is being used for ground tests only. [19] Specifications for the NASA QSF are given in Table 2, a cross section is shown in Figure 2a, predicted performance in Figure 3, and a photograph is shown in Figure 11. Using turbofan engine design practices, a low-noise blade-vane count was chosen to try to reduce rotor-stator interaction tone noise generated by this fan by cutting off tones at the first three blade passing frequency harmonics. [20]

The metal version of the NASA QSF was tested at the NASA GRC Acoustical Testing Laboratory using a duct rig inspired by several fan testing standards. Notably, a 72-channel in-duct microphone array was used to gather data to help validate the tone noise predictions used to design the fan. Also, a port was installed in the fan so that a hot wire probe could be used to measure the velocities in the rotor wake which is data that is being used to validate noise prediction algorithms, seen in Figure 4.

The fan was throttled through its operating range using, and results indicated that the measured aerodynamic and acoustic performance was in good agreement with predictions, as shown in Figures 5 to 8. In-duct microphone array measurements indicated that the most evident tones occur for frequencies of 1,800 Hz (1 BPF) and 7,200 Hz (4 BPF).

This fan was also described as a baseline geometry in the NASA Small Business Innovation Research (SBIR) program. solicitation for 2024. NASA has awarded four small businesses to develop improved versions of this spacecraft cabin ventilation fan via SBIR Phase 1 awards.

2.2 The Scaled NASA Quiet Space Fan (Scaled QSF) for spacecraft cabin ventilation systems

NASA has made the geometry for a scaled version metal prototype of the QSF publicly available via the NASA Technical Reports Server, too. [21] Using aerodynamic scaling laws, the pressure rise and the flow rate of the NASA QSF was increased by increasing the rotor tip diameter and shaft speed. The mechanical structure was then optimized using generative design for low weight. Specifications for the Scaled QSF are given in Table 2, and a cross section is shown in Figure 2b. The blade and vane count remained the same, chosen to try to reduce rotor-stator interaction tone noise generated by this fan by cutting off tones at the first three blade passing frequency harmonics. As of this writing, NASA has not yet fabricated or tested this scaled version of the QSF to validate the predictions.

2.3 Fan research for cooling electronics onboard spacecraft

NASA has made test results of a commercially available spaceflight qualified 80 mm diameter axial flow fan publicly available via reports on the NASA Technical Report Server, though the fan geometry itself is not publicly available. [22, 23] In 2006 the overall aerodynamic and acoustic performance of the fan was measured using an automated plenum in accordance with ISO 10302 in the hemi-anechoic chamber of NASA Glenn's Acoustical Testing Laboratory. Additional aerodynamic measurements of the inlet, exhaust, and rotor wake regions of the fan using Particle Image Velocimetry (PIV) and hot-wire probes. The fan setup for PIV tests is shown in Figure 9.

Pressure rise was measured for different flow rates as the fan was throttled through its operating range at a constant rotational speed of 3,300 rpm with and without a simple inlet duct 80 mm in length. The A-weighted overall sound power level for each of the throttled conditions was plotted as a function of flow rate. Comparisons of the fan with and without the short inlet duct fan at design speed indicated that the addition of the duct increased pressure rise by 22%, increased the flow rate by 11%, and reduced the overall A-weighted sound power level by 1 dBA, as shown in Figure 10.

Table 2: Specifications of the NASA Quiet Space Fan and the scaled version of the NASA Quiet Space Fan

	The NASA Quiet Space Fan	**The Scaled NASA Quiet Space Fan**
Rotor LE Tip Radius	4.23 cm (1.667 in)	4.84 cm (1.91 in)
Internal Duct Diameter	8.9 cm (3.5 in)	10.2 cm (4.0 in)
Rotor design speed	12,000 rpm	14,300 rpm
Overall length	20 cm (8.0 in)	23 cm (9.0 in)
Design Flow Rate	0.0709 m^3/s (150 CFM)	0.118 m^3/s (250 CFM)
Design Pressure Rise	904 Pa (3.64 in H_20)	1,742 (7.0 in H_20)
Design Pressure	101 kPa (14.7 psia)	101 kPa (14.7 psia)
Design Temperature	21°C (70°F)	21°C (70°F)
Number of rotor blades	9	9
Number of stator vanes	11	11

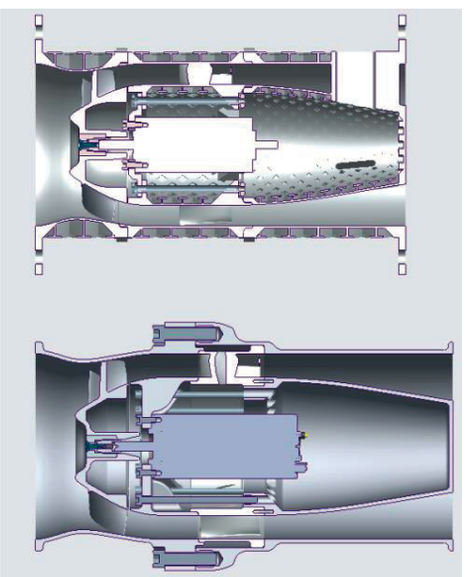


Figure 2: Cut-away views of the of a) NASA Quiet Space Fan (2022 version) and b) Scaled NASA Quiet Space Fan (2024 version).

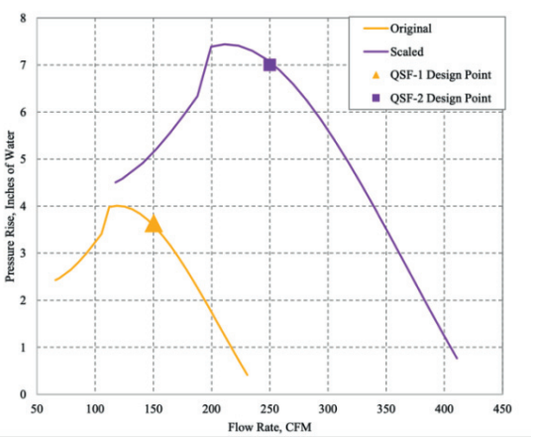


Figure 3: The predicted performance of the scaled version of the NASA Quiet Space Fan compared to the original design of the NASA Quiet Space Fan.

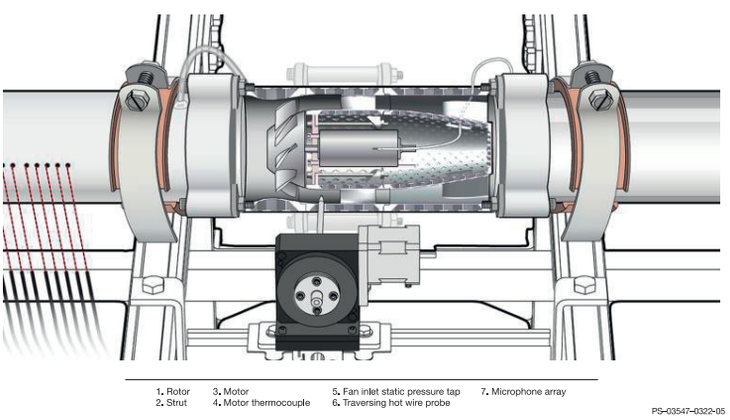


Figure 2: Cross-section of the metal version of the NASA Quiet Space Fan instrumented for aeroacoustic tests.

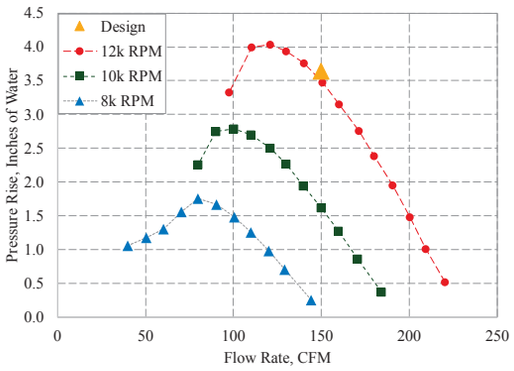


Figure 5: Pressure rise versus flow rate for three speed settings of the NASA Quiet Space Fan.

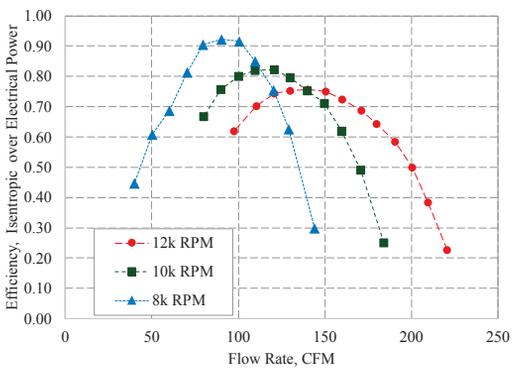


Figure 6: Efficiency versus flow rate for three speed settings of the NASA Quiet Space Fan.

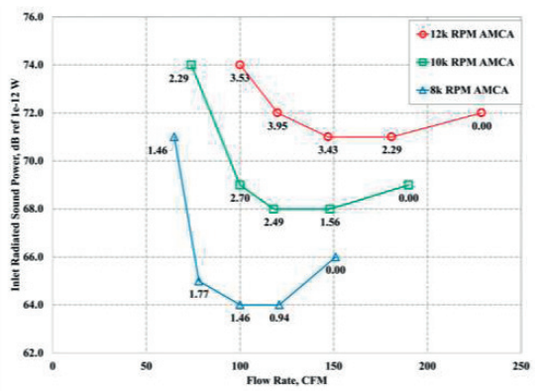


Figure 7: Inlet radiated sound power versus flow rate for three speed settings of the NASA Quiet Space Fan.

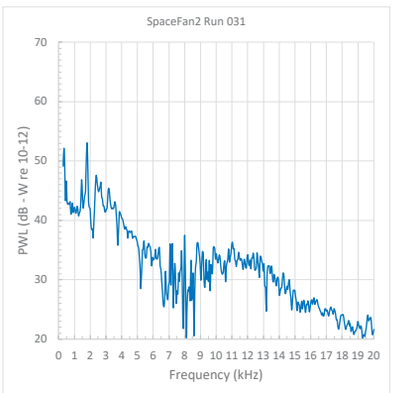


Figure 8: Sound power level spectra computed from the measurements of the 72-channel in-duct microphone array installed upstream of the NASA Quiet Space Fan.

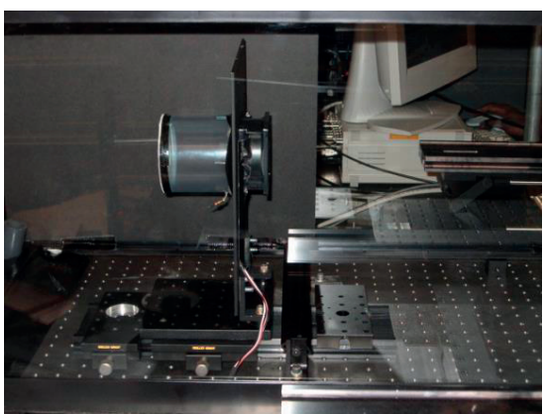


Figure 9: A commercially available spaceflight-qualified 80-mm diameter fan with an 80-mm inlet duct prepared for Particle Image Velocity measurements of the inlet and exhaust regions.

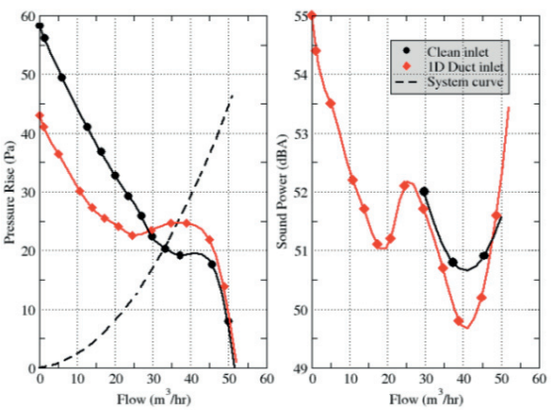


Figure 10: Measured aerodynamic and acoustic performance maps for a commercially available spaceflight-qualified 80 mm diameter fan.

FAN 2025
Antibes Juan-les-Pins (France), 9 – 11 April 2025

FAN RESEARCH AT NASA FOR AIRCRAFT PROPULSION

NASA has made the geometry for several fans used for aircraft engine noise reduction research publicly available, too. Three examples are given: 1) the Advanced Noise Control Fan (ANCF), 2) the Source Diagnostics Test (SDT) Fan, and 3) the Computationally Optimized Proprotor (COPR-4). Additionally, the DGEN 380 Aerospace Research Turbofan (DART) at NASA GRC is a versatile engine test rig used to explore new fans and components for the next generation of aircraft propulsion systems. Specifications are given in Table 3 for the ANCF and SDT. [24, 25]

The ANCF and the DART have been tested in the NASA Aero-Acoustic Propulsion Laboratory (AAPL). The AAPL is a dual-purpose 65-foot radius geodesic dome used to reduce community noise and perform aeroacoustic tests of aircraft engines and engine components. Built in 1993, it was the first-known free-standing geodesic dome to include materials to reduce transmission of sound through the walls and absorb sound within it. [26] The test area inside the AAPL can be configured as a hemi-anechoic or anechoic chamber. Approximately 17,000 custom-designed 2-ft thick fiberglass wedges are mounted to the inside surface of the dome walls and placed on the floor and around test rigs to absorb sound and prevent sound reflections. Specialized rigs and instrumentation such as microphone arrays and particle image velocimetry have been used to characterize the aerodynamic performance of fans, nozzles, and aircraft engines in the AAPL.

The SDT was tested in the NASA GRC 9- by 15-ft Low Speed Wind Tunnel (LSWT). [27] Built in 1968, the 9- by 15' LSWT is the most utilized low-speed continuous flow propulsion acoustic facility in the world, and the test section is 2.7 m (9.0 ft) high, 4.6 m (15 ft) wide, and 10 m (33 ft) long. Takeoff and landing conditions (Mach 0 to 0.21) can be simulated, and the tunnel is used to characterize the aerodynamic and acoustic performance of fans, nozzles, inlets, and propellers. Major upgrades to the tunnel were completed in 2019 to reduce the background noise levels by ~10 dB over a wide frequency range. Acoustic treatment was added to the turning vanes, diffuser, and test section and serpentine baffles were installed. Additionally, the pressure measurement system was upgraded a new traversing microphone rake was installed. [28, 29] There are several air-turbine drives rigs used to power single-rotation or counter-rotating experimental fans in the 9- by 15' LSWT. Hughes describes that the SDT rotor was driven by the NASA GRC Ultra High Bypass Drive Rig, capable of generating up to 3,728 kW (5,000 hp) at shaft speeds up to 16,875 rpm.

The COPR-4 propeller has been tested in the NASA GRC Icing Research Tunnel (IRT), since icing is a safety concern for propellers on electric Vertical Takeoff and Landing (eVOTL) Advanced Air Mobility (AAM) vehicles. The NASA GRC IRT completed its first test in 1944 and is the longest running icing tunnel in the world and one of the largest. The test section of the closed return tunnel is 1.8 m (6.0 ft) high by 2.7 m (9.0 ft) wide and 6.1 m (20 ft) long. An array of water spray nozzles can form a cloud of supercooled water droplets between 15 and 275 microns in diameter. Airspeeds range from 50 to 325 knots and the minimum controllable temperature in the test section is -35°C (-31°F) year-round. Details from a recent calibration of the tunnel are given in Reference 31.

Table 3: Selected specifications for two NASA research fans.

Parameter	ANCF	SDT
Fan diameter	1.2 m (48 in)	0.56 m (22 in)
Corrected tip speed	122 m/s (~400 ft/s)	370 m/s (1,215 (ft/s))
Stage pressure ratio	~1.05	1.47
Rotor hub-to-tip radius ratio	0.375	0.30
Bypass ratio	N/A	8.9
Corrected weight flow	(~130 (lbm/ft^{2}s))	100.5 (lbm/ft^2-s)
Rotor blade count	16	22
Bypass duct stator vane count	13, 14, 15, 26, 28,30	54
Rotor hub radius	9 in	3.30 in
Rotor speed, design, corrected	1,886 RPMc	12,657 RPMc

3.1 Advanced Noise Control Fan (ANCF)

NASA has made the geometry of the ANCF publicly available, and requests for this fan can be made by contacting the NASA GRC Acoustics Branch. A literature search conducted with Google Scholar and reference manager software in 2025 indicates that there are at least 230 publications referencing the ANCF from 1996 to 2025. A photograph of the ANCF appears in Figure 13, and specifications are given in Table 3. The ANCF was tested inside the NASA GRC Aero-Acoustic Propulsion Laboratory (AAPL) for over 20 years, and a retrospective was published by Sutliff. [32] The ANCF, with a 1.2 m (48 in) diameter rotor, driven by a 149 kW (200 hp) electric motor, is a low-speed, reconfigurable fan rig used to measure and understand how fans generate noise and how that noise propagates through the ducts and into the far field. The ANCF is no longer tested in the NASA GRC AAPL, and has been operated by the University of Notre Dame Turbomachinery Laboratory in Indiana, USA since 2017. [33]

3.2 Source Diagnostics Test (SDT) Fan

NASA has also made the geometry of the SDT publicly available, and requests for this fan can be made by contacting the NASA GRC Acoustics Branch. A literature search conducted with Google Scholar and reference manager software in 2025 indicate that there are over 340 publications referencing the SDT Fan. A photograph of the SDT Fan appears in Figure 15 and specifications given in Table 3. [25] As the name implies, this fan was used in experiments to diagnose the dominant sources of noise generated by a turbofan engine bypass fan and outlet guide vane. As summarized by Huff [16], a key finding of the SDT experiments was that inlet radiated noise was generated mostly by the rotor and aft generated noise was dominated by the interaction of the rotor wakes on the outlet guide vanes.

Huff [16] also reported that results of the SDT Fan tests were presented at the 2002 American Institute of Aeronautics and Astronautics' (AIAA) Aeroacoustics Conference. Since then, the SDT Fan was used as a case study in a series of Fan Broadband Noise Prediction Workshops offered as part of the AIAA Aeroacoustics Conferences. The Fan Broadband Noise Prediction Workshop, facilitated by Edmane Envia from NASA GRC, were held every year between 2014 and 2018. The Fan Broadband Noise Prediction Workshops typically featured between three and six presentations. Many of these presentations were also papers submitted to the AIAA Aeroacoustics Conferences or later submitted as articles in various journals.

3.3 The Computationally Optimized Proprotor (COPR-4)

Motivated to study propulsors for electric Vertical Takeoff and Landing (eVTOL) vehicles NASA has made the geometry for a Computationally Optimized Proprotor, the COPR-4, publicly available, as well. Requests for the COPR-4 geometry can be made by contacting the NASA GRC Acoustics Branch. This fan was recently tested in the NASA GRC IRT. A photograph of a COPR-4 propeller in the NASA GRC IRT is shown in Figure 17, and ice is evident on the blades. [34, 35]

The COPR-4 geometry features a NACA 0012 airfoil, and the chord and twist angle distributions are given in Reference 35. By geometrically scaling the COPR-4 design, three carbon fiber propellers of different diameters were built and tested: 0.610 m, 0.711 m, and 0.914 m (24, 28, and 36 inches). A variable pitch hub was used to adjust the blade pitch setting. The target operating speed of the COPR-4 was 1,516 rpm. The COPR-4 was driven by an EMRAX 188 permanent magnet synchronous motor with a continuous power rating up to 34 kW (45 hp).

An objective of the test was to measure the ice accretion on the proprotor for different simulated cloud conditions and proprotor operating conditions. Data from these tests are used to understand how ice forms on these propulsors and to validate ice prediction tools, such as the GlennICE code. Results of these studies are intended to improve the safety of new eVTOL aircraft.

3.4 The DGEN 380 Aeropropulsion Research Turbofan (DART)

Recently, the DGEN 380 Aeropropulsion Research Turbofan is a small geared turbofan engine used for aeroacoustics research at NASA GRC. [36] The DGEN 380, manufactured by Price Induction/Akira, is a main component of the DART, The DGEN 380 produces 2.5 kN (570 lbf) of thrust and he fan diameter is 36 cm (14 in). A literature search conducted with Google Scholar and reference manager software in 2025 indicate that there at least 20 publications referencing the DGEN 380 at NASA. A photograph of the DART appears in Figure 18. The DART is a currently tested inside the NASA GRC AAPL. While the fan geometry for the DGEN 380 is not publicly available, the DART is modular and reconfigurable and is being used to understand how noise generates and propagates through turbofan engines and develop new engine components. For example, the DART was instrumental for testing prototypes of a Multiple Degree of Freedom (MDOF) Perforate-Over-Honeycomb (POHC) acoustic duct liner [37] that eventually advanced to flight tests onboard the Quiet Technology Demonstrator aircraft. [38] The MDOF liner research is one example of collaborations between NASA GRC and NASA Langley Research Center (LaRC).

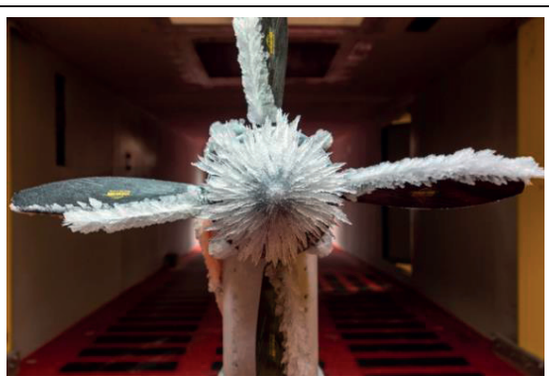


Figure 18: The NASA COPR-4 propeller installed in the NASA GRC Icing Research Wind Tunnel.



Figure 17: The NASA DART installed in the NASA GRC AAPL.

FAN TONE NOISE COMPARISONS

NASA GRC has demonstrated that some of the expertise, theory, software, experimental facilities, instrumentation, and techniques traditionally used for aircraft engine noise reduction can be used to explore and reduce noise for smaller fans used on spacecraft. Results from the small spacecraft cabin ventilation fan are compared to three other larger fans that NASA uses to for aerodynamic and acoustic research, mainly for aircraft propulsion systems: the large low-speed Advanced Noise Control Fan (ANCF), the Source Diagnostic Test (SDT) fan. Figures 12,14, and 16 show plots of frequency versus circumferential mode number for the blade passing tone harmonics. The cut-off frequency for each mode is shown by the solid line that forms a "V" in the plot. The modes generated by rotor-stator interaction, as predicted by duct theory [39] and rotor-stator interaction of Tyler and Sofrin [40] are indicated by the symbols.

A rule of thumb for the larger fans indicated that a stator with twice the number of rotor blades plus a few extra could be used to cut-off the first blade passing frequency tone. This research revealed that for the smaller spacecraft cabin ventilation fan, the first three blade passing frequency tones could be cut-off for a fan with 9 blades and 11 vanes (rather than 18 or more vanes, as the rule of thumb suggests). Theory developed by Tyler and Sofrin [41], who were motivated to reduce tone noise from aircraft engines, did prove to be useful in reducing the tone noise from the much smaller spacecraft cabin vent fan.

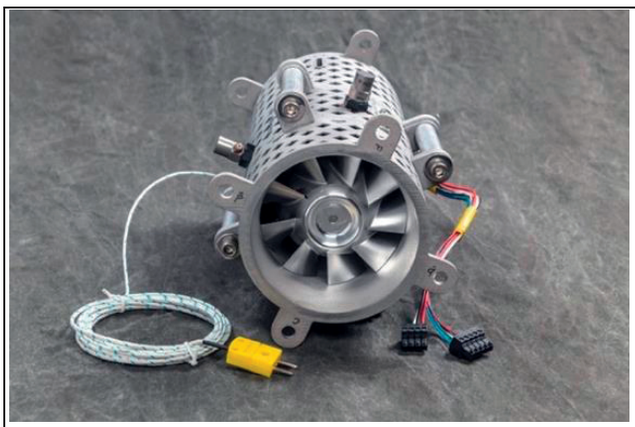


Figure 11: The metal version of NASA Quiet Space Fan designed, fabricated, and tested in 2021.

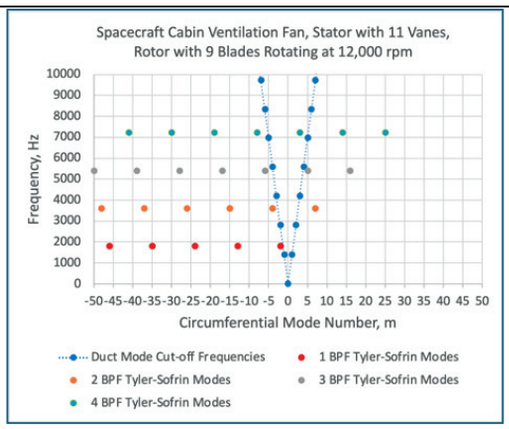


Figure 12: Cut-off frequencies for the rotor-stator interaction tones for the NASA QSF.



Figure 13: The NASA ANCF installed in the NASA GRC AAPL.

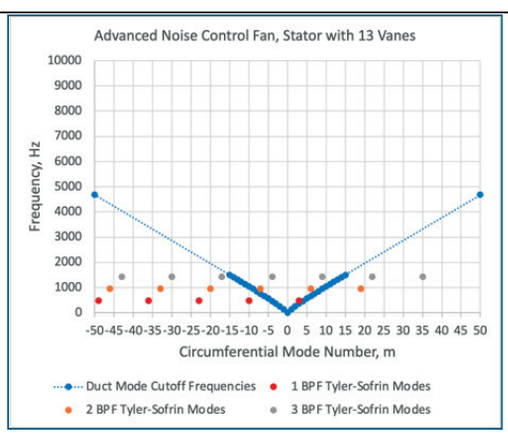


Figure 14: Cut-off frequencies for the rotor-stator interaction tones for the NASA ANCF.



Figure 15: The NASA SDT installed in the NASA GRC 9- by-15-Ft Low Speed Wind Tunnel.

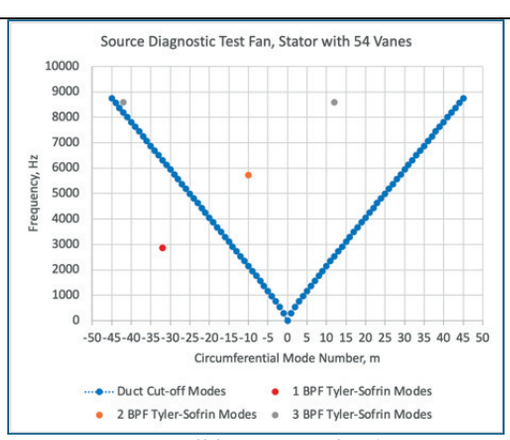


Figure 16: Cut-off frequencies for the rotor-stator interaction tones for the NASA SDT.

CONCLUSION

NASA GRC continues to perform research on fans for spacecraft ventilation, fans for cooling electronics onboard spacecraft, and fans for aircraft propulsion. This article emphasized publicly-available fan geometries. Three examples of fan noise research for spacecraft were presented: NASA's Quiet Space Fan, NASA's Scaled Quiet Space Fan, and results of aerodynamic and acoustic tests of a commercially available 80 mm diameter fan used for electronics cooling inside spacecraft. Four examples of fan noise research for aircraft propulsion were presented: NASA's Advanced Noise Control Fan, NASA's Source Diagnostic Test Fan, NASA's Computationally Optimized Proprotor, and NASA's DGEN 380 Aeropropulsion Research Turbofan. Selected comparisons were made between these different fans. Four facilities at NASA GRC were also described: the Acoustical Testing Laboratory, the AeroAcoustic Propulsion Laboratory, the 9- by 15-Ft Low Speed Wind Tunnel, and the Icing Research Tunnel. NASA routinely distributes results publicly via the NASA Technical Reports Server. NASA supports small businesses in the US via the Small Business Innovation Research Program. NASA partners with many organizations, trying to transfer technology developed for spacecraft and aircraft to benefit all.

ACKNOWLEDGEMENTS

Many people at NASA have contributed to fan research over the years. Fan research for spacecraft applications has been funded by NASA's Exploration Systems Mission Directorate's Environmental Control and Life Support/Crew Health and Performance System Capabilities Leadership Team, and the International Space Station Program. Fan research for aircraft propulsion has been funded by NASA's Aeronautics Research Mission Directorate's Advanced Air Transport Technology project.

The author also extends special thanks to several people who contributed to this article: Jonathan Goodman from NASA GRC's Mechanical Systems Design and Integration Branch; David Stephens, Daniel Sutliff, Daniel Ingraham, and Edmane Envia from the NASA GRC Acoustics Branch; John Lucero, Chief of the NASA GRC Acoustics Branch; and Christopher Allen, Head of the NASA JSC Acoustics Office.

BIBLIOGRAPHY

1. Koch, L. D., Stephens, D., Goodman, J. M., Mirhashemi, A., Buerhle, R., Sutliff, D. L.,Allen, C. S., "Spacecraft Cabin Ventilation Fan Research at NASA," AIAA-2024-3269, 2024, https://ntrs.nasa.gov/citations/20240004675
2. Lee, D. S., Fahey, D. W., Skowron, A., Allen, M. R., Burkhardt, U., Chen, Q., Doherty, S. J., Freeman, S., Forster, P. M.,Fuglestvedt, J., "The contribution of global aviation to anthropogenic climate forcing for 2000 to 2018," *Atmospheric environment*, Vol. 244, pp. 117834. 2021, https://www.sciencedirect.com/science/article/am/pii/S1352231020305689
3. World Health Organization, *Burden of disease from environmental noise: Quantification of healthy life years lost in Europe* (World Health Organization. Regional Office for Europe, 2011), https://apps.who.int/iris/handle/10665/326424
4. Collins, T. W., Nadybal, S.,Grineski, S. E., "Sonic injustice: Disparate residential exposures to transport noise from road and aviation sources in the continental United States," *Journal of Transport Geography*, Vol. 82, pp. 102604. 2020, https://doi.org/10.1016/j.jtrangeo.2019.102604
5. Cohen, J. P.,Coughlin, C. C., "Spatial hedonic models of airport noise, proximity, and housing prices," *Journal of regional science*, Vol. 48, No. 5, pp. 859-878. 2008, https://doi.org/10.1111/j.1467-9787.2008.00569.x

6. Nolte, C., “High-resolution land value maps reveal underestimation of conservation costs in the United States,” *Proceedings of the National Academy of Sciences*, 2020, https://www.pnas.org/doi/full/10.1073/pnas.2012865117
7. Barber, J. R., Crooks, K. R.,Fristrup, K. M., “The costs of chronic noise exposure for terrestrial organisms,” *Trends in Ecology and Evolution*, Vol. 25 3, pp. 180-189. 2010, https://doi.org/10.1016/j.tree.2009.08.002
8. National Science And Technology Council, “National Aeronautics Research and Development Policy,” 2006, https://obamawhitehouse.archives.gov/sites/default/files/microsites/ostp/aero-natrdpolicy-2006.pdf
9. Aeronautics Interagency Working Group of the National Science and Technology Council., “The National Aeronautics Science and Technology Priorities,” 2023, https://www.whitehouse.gov/wp-content/uploads/2023/03/032023-National-Aeronautics-ST-Priorities.pdf
10. Nasa, “NASA Glenn Research Center Strategic Action Plan,” 2022, https://nasa.sharepoint.com/sites/grc/SitePages/strategic-planning.aspx
11. NASA, “NASA Aeronautics Strategic Implementation Plan,” 2023, https://www.nasa.gov/wp-content/uploads/2021/04/sip-2023-final-508.pdf
12. International Civil Aviation Organization, “Environment Report on Aviation and the Environment: Destination Green: The Next Chapter,” 2019, https://www.icao.int/environmental-protection/Documents/ICAO-ENV-Report2019-F1-WEB%20%281%29.pdf
13. Federal Aviation Administration, “United States 2021 Aviation Climate Action Plan,” 2021, https://www.faa.gov/sites/faa.gov/files/2021-11/Aviation_Climate_Action_Plan.pdf
14. Federal Aviation Administration, “Federal Aviation Regulation (FAR) Title 14, Chapter 1, Subchapter C, Part 36: Noise Standards: Aircraft Type and Airworthiness Certification,” 2014, https://www.faa.gov/regulations_policies/advisory_circulars/index.cfm/go/document.list/parentTopicID/112
15. Blackwell, D. L., Lucas, J. W.,Clarke, T. C., “Summary health statistics for US adults: national health interview survey, 2012.,” *Vital and health statistics. Series 10, Data from the National Health Survey*, No. 260, pp. 1-161. 2014, https://www.cdc.gov/nchs/data/series/sr_10/sr10_260.pdf
16. Huff, D. L., “NASA Glenn’s Contributions to Aircraft Engine Noise Research,” *Journal of Aerospace Engineering*, Vol. 26, No. 2, 2013, https://ntrs.nasa.gov/citations/20150000139
17. Cooper, B. A., Akers, J. C.,Passe, P. J., “NASA Glenn Research Center Acoustical Testing Laboratory: Five Year Retrospective,” *The Journal of the Acoustical Society of America*, Vol. 118, No. 3, pp. 1887-1887. 2005, https://asa.scitation.org/doi/pdf/10.1121/1.4779588
18. Stephens, D., Goodman, Jonathan, Buehrle, R., Mirhashemi, A., Koch, L. D., Shook, T. D., Sutliff, D., Allen, C.,Matty, C., “NASA TM-Highlights of Aeroacoustic Tests of a Metal Spacecraft Cabin Ventilation Fan Prototype,” NASA-TM-2022-0012622, 2022, https://ntrs.nasa.gov/citations/20220012622
19. Tweedt, D. L., “Aerodynamic Design and Computational Analysis of a Spaceflight Vehicle Cabin Ventilation Fan,” NASA CR-2010-216329, 2010, https://ntrs.nasa.gov/citations/20110002741
20. Koch, L., “A Study of Preliminary Design Methods for Low Noise Fans,” *INTER-NOISE and NOISE-CON Congress and …*, 2023, https://www.ingentaconnect.com/content/ince/incecp/2023/00000266/00000002/art00017
21. Stephens, D., Koch, L. D., Goodman, J.,Allen, C. S., “Acoustics and Performance of a Scaled Spacecraft Cabin Ventilation Fan,” Proceedings of the 53rd International Conference on Environmental Systems, 2024, https://ntrs.nasa.gov/citations/20240005871

22. Van Zante, D. E., Koch, L. D., Wernet, M.,Podboy, G. G., "An Assessment of NASA Glenn's Aeroacoustic Experimental and Predictive Capabilities for Installed Cooling Fans: Part 1: Aerodynamic Performance," NASA TM-2006-214448, 2006, https://ntrs.nasa.gov/citations/20060045853
23. Koch, L. D., Van Zante, D. E., Wernet, M.,Podboy, G. G., "An Assessment of NASA Glenn's Aeroacoustic Experimental and Predictive Capabilities for Installed Cooling Fans; Part 2: Source Identification and Validation," NASA TM-2006-214450, 2006, https://ntrs.nasa.gov/citations/20060048234
24. Sutliff, D. L., "Advanced noise control fan: A 20-year retrospective of contributions to aeroacoustics research," *NASA/SP–2019-643*, 2019, https://ntrs.nasa.gov/citations/20190029278
25. Envia, E., Tweedt, D., Woodward, R., Elliott, D., Fite, E., Hughes, C., Podboy, G.,Sutliff, D., "An assessment of current fan noise prediction capability," AIAA 2008-2991, 2008, https://arc.aiaa.org/doi/pdf/10.2514/6.2008-2991
26. Cooper, B. A., "A large hemi-anechoic enclosure for community-compatible aeroacoustic testing of aircraft propulsion systems," *Noise control engineering journal*, Vol. 42, No. 1, pp. 1-7. 1994, https://pascal-francis.inist.fr/vibad/index.php?action=getRecordDetail&idt=6042084
27. Woodward, R., Hughes, C., Jeracki, R., Miller, C., "Fan Noise Source Diagnostic Test--Far-field Acoustic Results," AIAA-2002-2427, 2002, https://arc.aiaa.org/doi/pdf/10.2514/6.2002-2427
28. Stephens, D., Van Zante, D. E., Stark, D. E., "Overview of the Acoustic Improvement Program for the 9-by 15-Foot Low Speed Wind Tunnel," AIAA-2021-2969, 2021, https://arc.aiaa.org/doi/abs/10.2514/6.2021-2969
29. Dussling, J. J., "Historical Overview and Recent Improvements at the NASA Glenn Research Center 8x6 9x15 Wind Tunnel Complex," 2015, https://ntrs.nasa.gov/citations/20150000703
30. Hughes, C. E., Jeracki, R. J., Woodward, R. P.,Miller, C., J., "Fan Noise Source Diagnostic Test-Rotor Alone Aerodynamic Performance Results," AIAA-2002-2426, 2002, https://ntrs.nasa.gov/citations/20050175875
31. Timko, E. N., King-Steen, L. E., Van Zante, J. F.,Acosta, W. J., "NASA Glenn Icing Research Tunnel: 2019 Cloud Calibration Procedure and Results," NASA TM-20205009045, 2021, https://ntrs.nasa.gov/citations/20205009045
32 Sutliff, D. L., "A 20 year retrospective of the advanced noise control fan–contributions to turbofan noise research," Vol. AIAA Propulsion and Energy 2019 Forum, pp. 3824. 2019, https://arc.aiaa.org/doi/pdf/10.2514/6.2019-3824
33. Sutliff, D., "ANCF at UND Commissioning Test Highlights: GRC AAPL vs UND White Field," *Acoustics Technical Working Group Meeting*, 2019, https://ntrs.nasa.gov/citations/20190025411
34. Von Hardenberg, P. H., Flack, C. A.,Rigby, D. L., "Ice Shape Analysis of an eVTOL Propeller in Forward Flight at the NASA Glenn Icing Research Tunnel," AIAA-2024-4448, 2024, https://arc.aiaa.org/doi/10.2514/6.2024-4448
35. Zawodny, N. S., Pettingill, N. A., Lopes, L. V.,Ingraham, D. J., "Experimental Validation of an Acoustically and Aerodynamically Optimized UAM Proprotor Part 1: Test Setup and Results," NASA TM-20220015637, 2023, https://ntrs.nasa.gov/citations/20220015637
36. Sutliff, D. L., Brown, C. A., Bayon, B.,Sree, D., "Farfield acoustic characteristics of the DGEN380 turbofan engine as measured in the NASA Glenn AeroAcoustic propulsion laboratory," AIAA-2016-3006, 2016, https://arc.aiaa.org/doi/pdf/10.2514/6.2016-3006
37. Nark, D. M., Jones, M. G.,Sutliff, D. L., "Broadband inlet liner design for the DGEN aero-propulsion research turbofan,"AIAA-2018-3608, 2018, https://ntrs.nasa.gov/citations/20190027214

38. Wong, J., Nesbitt, E., Jones, M. G.,Nark, D. M., "Flight Test Methodology for NASA Advanced Inlet Liner on 737MAX-7 Test Bed (Quiet Technology Demonstrator 3)," Vol. 25th AIAA/CEAS Aeroacoustics Conference, pp. 2763. 2019, https://arc.aiaa.org/doi/pdf/10.2514/6.2019-2763
39. Morse, P. M.,Ingard, K. U., *Theoretical Acoustics* (McGraw-Hill, 1986).
40. Tyler, J. M.,Sofrin, T. G., "Axial Flow Compressor Noise Studies," *SAE Transactions*, Vol. 70, pp. 309-332. 1962.
41. Sofrin, T. G.,Mathews, D. C., "Asymmetric Stator Interaction Noise," *Journal of Aircraft*, Vol. Vol. 17, Issue 8, pp. 554-560. 1979.



ADDITIVELY MANUFACTURED (PBF-LB) MODULAR FAN BLADES WITH STRUCTURED POROSITY FOR NOISE REDUCTION IN TURBULENT INFLOW CONDITIONS

Dominik GRÜTZNER[1], Garvin SCHULTHEIß[2],
Felix CZWIELONG[1], Markus MERKEL[2], Stefan BECKER[1]

[1] *Institute of Fluid Mechanics (LSTM), Universität Erlangen, Cauerstraße 4, 91058 Erlangen, Germany*

[2] *Institute for Virtual Product Development, Aalen University, Beethovenstraße 1, 73430 Aalen, Germany*

SUMMARY

In this work, the aerodynamic and acoustic performance of axial fan blades with simplified porosity, implemented as drilled holes, was investigated. The blades were manufactured using the Laser Powder Bed Fusion (PBF-LB) process, and three distinct slot configurations: Front-to-Back (F2B), Middle-to-Middle (M2M), and Back-to-Front (B2F) were evaluated under both disturbed and undisturbed inflow conditions. The study found that the F2B configuration offered the best compromise between noise reduction and aerodynamic performance, particularly with smaller perforations (1.0 mm diameter). These results demonstrate the potential of simplified porosity designs to achieve noise mitigation in axial fans while minimizing aerodynamic penalties.

INTRODUCTION

Axial fans are essential in various applications, ranging from enhancing indoor air quality in building ventilation systems to supporting environmentally friendly heating solutions like heat pumps. However, one of the significant challenges associated with these fans is the noise they produce, particularly under turbulent inflow conditions [1], [2]. Reducing sound emissions is a critical focus for both research and industry due to its impact on user comfort, especially in noise-sensitive environments such as residential buildings. The quiet operation of these systems is vital for their broader acceptance and use.

To mitigate noise, researchers have explored various modifications to fan blades, including serrations, slots, and wavy designs [3]–[7], particularly targeting sound generated by high inflow turbulence. The advancement of additive manufacturing technologies has provided new opportunities for sound mitigation in axial fan blades, allowing undercuts and complex structures to be created. In particular, the layer-based Laser Powder Bed Fusion (PBF-LB) process facilitates the fabrication of solid components from a range of metallic materials, including the widely used casting alloy AlSi10Mg. This process combines favorable mechanical properties with significant design flexibility.

Ocker et al. have demonstrated promising results by integrating porous structures into the leading edge of axial fans and wings [8], [9]. Their study revealed a potential noise reduction of up to 1.6 dB in airfoils, particularly in the low-frequency range. Additionally, it was found that shifting porosity downstream of the leading edge can yield further benefits. These findings were subsequently applied to an axial fan, where similar noise reductions were observed; however, this came at the cost of deteriorating aerodynamic performance [7]. Furthermore, they established that a connection between the suction side and pressure side of a an airfoil is necessary to achieve noticeable acoustic improvements [8]. It presents a significant challenge to identify an appropriate design for the integrated porosity that provides aeroacoustic advantages while maintaining the fan's aerodynamic performance.

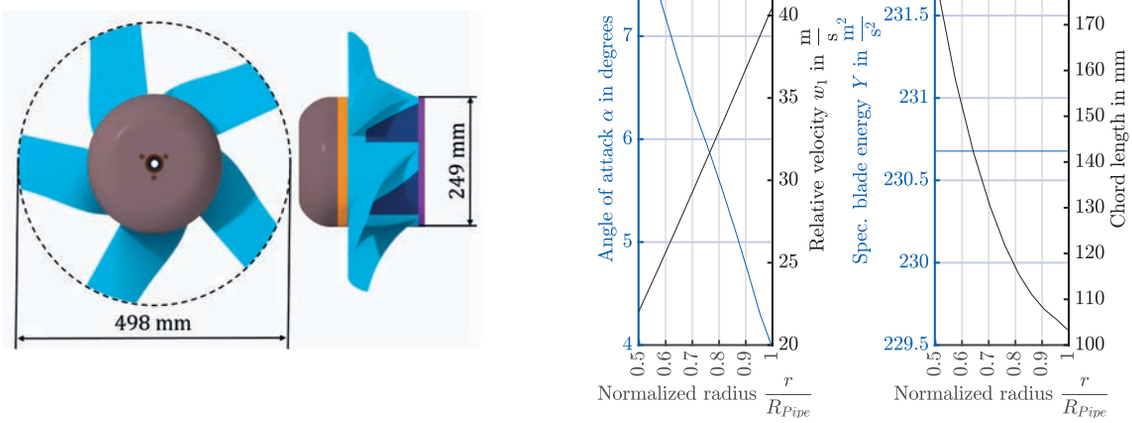
Building upon this foundation, this research aims to identify an optimal balance between aerodynamic and aeroacoustic performance by investigating three distinct slot geometries with integrated holes incorporated into a fan blade. These designs are fabricated using the Laser Powder Bed Fusion (PBF-LB) process. Holes are a simple and comparable version of creating a porosity that allows air to flow through the fan blade in a defined area. A novel fan blade design featuring a modular leading edge is introduced for this purpose. The three variations of slots are tested aerodynamically and aeroacoustically under both undisturbed and disturbed inflow conditions to determine which slot shape offers the best balance for further exploration of porous structures in sound mitigation for axial fans. All leading-edge designs are compared against an unmodified leading edge serving as a reference ventilator.

AXIAL FAN DESIGN

An unskewed axial fan was used for the investigations, designed to operate within a duct segment with a total diameter of $D_{\mathrm{hub}} = 498\,\mathrm{mm}$, resulting in a tip gap of $s_{\mathrm{tip}} = 1\,\mathrm{mm}$. The fan is integrated into a duct system, where it operates at a specified flow rate and rotational speed. The fan is designed for a volumetric flow rate of $\dot{V} = 1.4\,\frac{\mathrm{m}^3}{\mathrm{s}}$ at a rotational speed of $n_{\mathrm{fan}} = 1500\,\frac{1}{\mathrm{min}}$, and features $z = 5$ blades. The blades are based on the NACA 4510 airfoil profile and were designed using blade element theory [10], with a hub-to-tip ratio of $\nu_i = 0.5$ and an isoenergetic load distribution across the blades. A CAD model of the fan, including its dimensions, is presented in Figure 1a. The stacking line of the profile sections runs through the leading edge to facilitate the interchangeability of the leading edge, as discussed below in the paper.

Figure 1b illustrates the angle of attack α, the relative velocity w_1 at the fan inlet, the chord length c, and the specific blade energy Y_{blade} as a function of the radius. To maintain constant specific blade energy, both the chord length c and the angle of attack are reduced from the hub to the tip of the blade, where higher circumferential speeds are encountered.

FAN 2025
Antibes - Juan-les-Pins (France), 9 - 10 April 2025



(a) CAD model of the axial fan.

(b) Angle of attack, relative velocity, specific blade energy and chord length at design point.

Figure 1: (a) CAD model of the axial fan and (b) angle of attack, relative velocity, specific blade energy and chord length at design point as a function of the fan radius.

AXIAL FAN WITH INTERCHANGABLE LEADING EDGES

An SLM 280 HL (SLM Solutions, Lübeck Germany) is used to manufacture the leading edges and fan blades using the layer-based Laser Powder Bed Fusion process (PBF-LB) with the material AlSi10Mg. A 30 µm layer of gas-atomized powder is deposited onto the build plate via a rake, and the sliced geometry is then scanned with a 400 W laser using material-specific parameters to melt the geometry onto the previous layer. This process repeats until a solid build part is achieved. The geometric freedom of the process allows the introduction of porosities in selected areas of the blade through the use of different unit cells or the constructive insertion of holes, as demonstrated in this research. A novel modular fan design is introduced, which allows for the quick swapping of the leading edges of the fan blades, thus enabling the testing of different variations without the need to balance and check the clearance at each blade for each version. The process of interchanging the leading edges is schematically visualized in Figure 2.

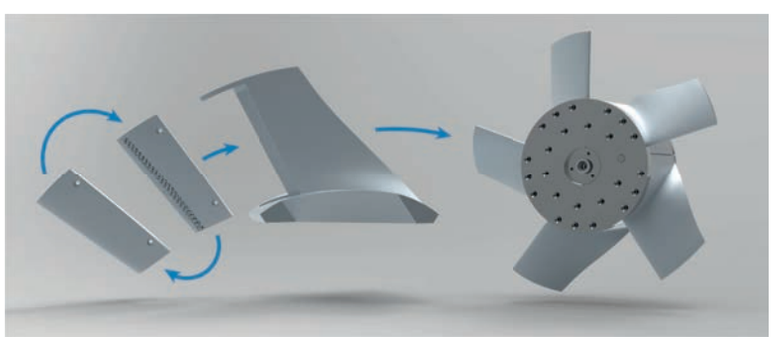


Figure 2: Schematic illustration of the axial fan with NACA 4510 profiles as blades, featuring 5 blades and demonstrating the interchangeable leading edge concept.

To achieve this, the fan blade is divided into two parts at one-third of the chord length of the tip of the fan $l_{c/3}$= 33 mm using a stepped cut. The two parts will henceforth be referred to as the "base fan blade" and "leading edge" (see Figure 3). The stepped cut facilitates lateral screw fixation of the leading edge, which can be replaced while the fan is installed on the test bench. Since the tip gap has

a significant impact on the aeroacoustic properties of a fan [11], the outer 3 mm of the leading edge are part of the base fan blade. This ensures a consistent tip gap when comparing different variants and provides a geometric barrier against the centrifugal forces that occur during operation, preventing any potential detachment of the leading edge. According to Ocker et al.[9], designing the tip of the fan blade solid could also help to prevent the amplification of unwanted subharmonic humps in the sound pressure level (SPL) spectrum of the fans.

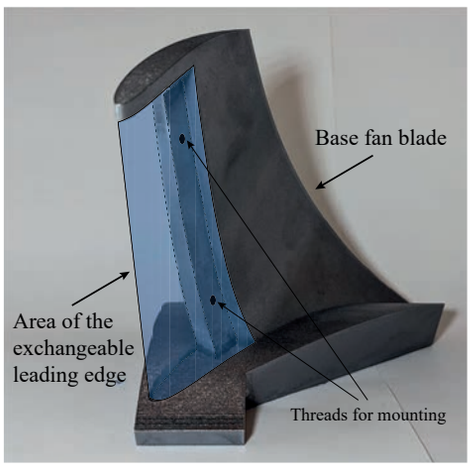


Figure 3: Depiction of the additively manufactured base blade made from AlSi10Mg and marks the area of the modular leading edge as well as the threads for the lateral mounting of the.

LEADING EDGES WITH INTEGRATED POROSITY (HOLES)

In principle, fans become quieter as the leading edge is designed to be more porous [12]. However, this acoustic benefit comes at the expense of the fan's aerodynamic efficiency. Regarding acoustic benefits, studies on airfoils have shown that making the airfoil partially porous starting from the leading edge can reduce noise. Interestingly, a similar noise reduction effect can also be achieved by introducing a row of holes downstream of the aerofoil leading edge [13]. Furthermore Ocker et al. [7] have demonstrated through airfoil studies that limiting the porous area to approximately 5 % of the chord length strikes a good balance between aerodynamic performance and acoustic advantage. In addition, they also showed that keeping the first 5 % of the leading edge solid does not only provide a similar acoustic effect but also significantly improves the aerodynamic performance compared to fully porous configurations [7].

Building on this foundation, this study examines which orientation of porosity integrated into the blade is most effective aerodynamically and acoustically. To achieve this, a slot with a width of 5 % of the chord length c will be incorporated into the leading edge of the axial fan. This slot will be filled with holes aligned along its length, acting as a simplified geometric representation of porosity. The goal is to determine how the orientation of the porous slot within the blade influences performance. Three configurations are investigated: front-to-back (F2B), where the slot is aligned with the flow direction; middle-to-middle (M2M), where the slot is oriented orthogonally to the chord, and back-to-front (B2F), where the slot is aligned against the flow direction. The three configurations and their dimensional specifications are illustrated in Figure 4. All dimensions are normalized to the chord length c and thus vary along the blade span. The inlet and outlet areas of the slots (filled with holes) remain consistent across all configurations, with a nominal cross-sectional area of $733.5 \pm 6.5\,\mathrm{mm}^2$.

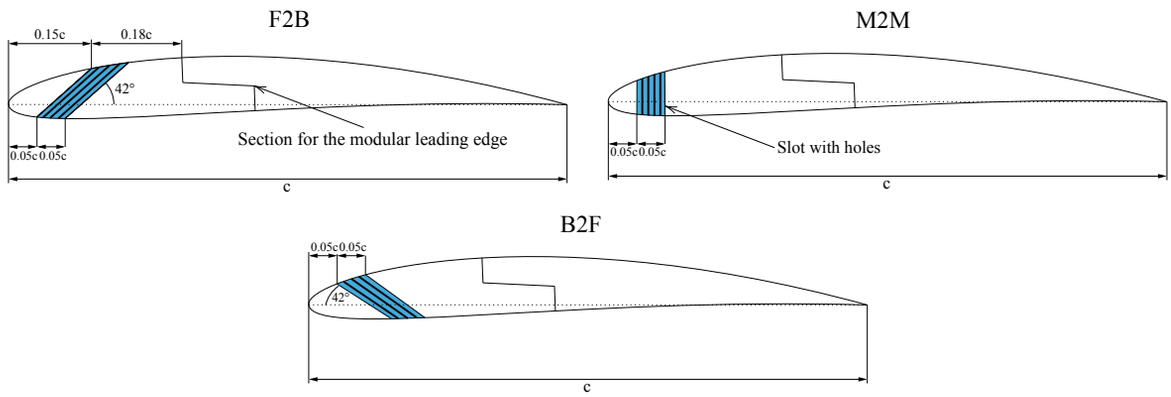


Figure 4: Sectional drawing with dimensions of the different leading edges front to back (F2B), middle to middle (M2M) and back to front (B2F).

For each slot variant, two different hole configurations are produced and examined. The first configuration features 1.5 mm holes spaced 1.8 mm apart, corresponding to an approximate relative density of 50 %, while the second configuration has 1 mm holes spaced 1.8 mm apart, corresponding to an approximate relative density of 75 %. An overview of the discussed variants is presented in Table 1.

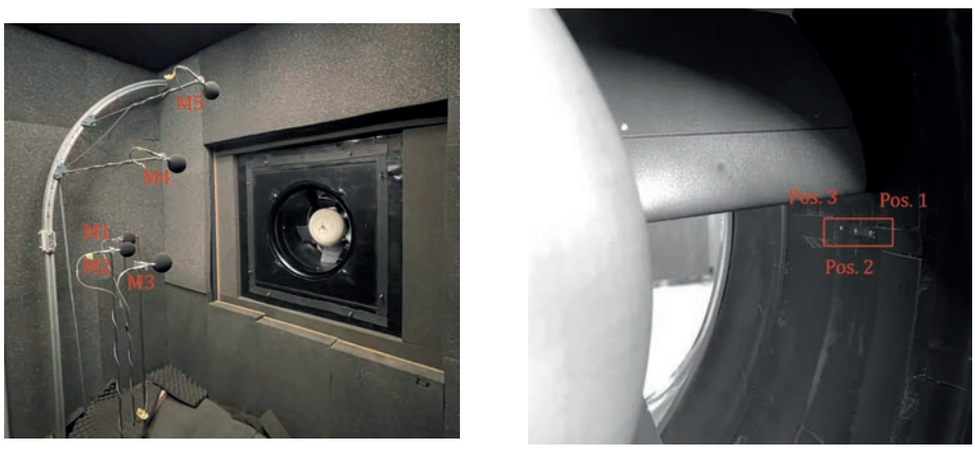
Table 1: Overview of perforated leading-edge designs and their properties.

Name	Hole Diameter (*mm*)	Hole Spacing (*mm*)	Relative Density *RD* (%)
Front2Back (FB2)	1.0	1.8	75
	1.5	1.8	50
Middle2Middle (M2M)	1.0	1.8	75
	1.5	1.8	50
Back2Front (B2F)	1.0	1.8	75
	1.5	1.8	50

EXPERIMENTAL SETUP FOR CHARACTERIZING AERODYNAMIC AND AEROACOUSTIC PERFORMANCE OF FANS

The aerodynamic and acoustic performance of the axial fans is evaluated using a standardized axial fan test rig at the LSTM Erlangen. The test rig is designed and constructed in compliance with DIN 5801 [4], [14]. It features a low-reflection chamber on the suction side of the fan, enabling the characterization of sound radiation under varying inflow conditions. Disturbed inflow conditions are created using heat exchangers [15] or, as in this study, passive turbulence grids [4] positioned upstream of the fan. Figure 5a provides a schematic representation of the test setup within the anechoic chamber of the axial fan test rig. The five free-field microphones are arranged on a spherical surface at a distance of one meter. The centre of the sphere aligns with the centre of the fan's bell mouth inlet. Microphones M1 to M3 are arranged along a parallel on the sphere's equatorial plane, while microphones M4 and M5 are positioned along a meridian passing through the equator's midpoint. The angular spacing between adjacent microphones is 22.5°. Additionally, Figure 5b illustrates the three installed Miniature Pressure Transducers of type XCS-093-1psi D (Kulite, USA), which are located in the tip gap of the fan. The sensor at position 1 is placed directly at the beginning of the tip gap at the leading edge. The sensor in position 2 is located in the middle of the fan blade, while the sensor in position 3 is positioned at the end of the tip gap near the trailing edge. The operating point of the

axial fan can be determined simultaneously with the investigation of its aeroacoustic properties on the suction side. This is achieved by measuring the pressure rise and volume flow rate. The pressure measurement is conducted using a ring pressure line integrated into the low-reflection chamber, which is connected to the external environment via a differential pressure sensor. The volume flow rate is measured using a standard volumetric flow nozzle in compliance with DIN 5801[14].



(a) Acoustic measurement setup. *(b) Pressure sensor positions in tip gap.*

Figure 5: Experimental setup for the characterization of the suction-side sound field of the axial fan.

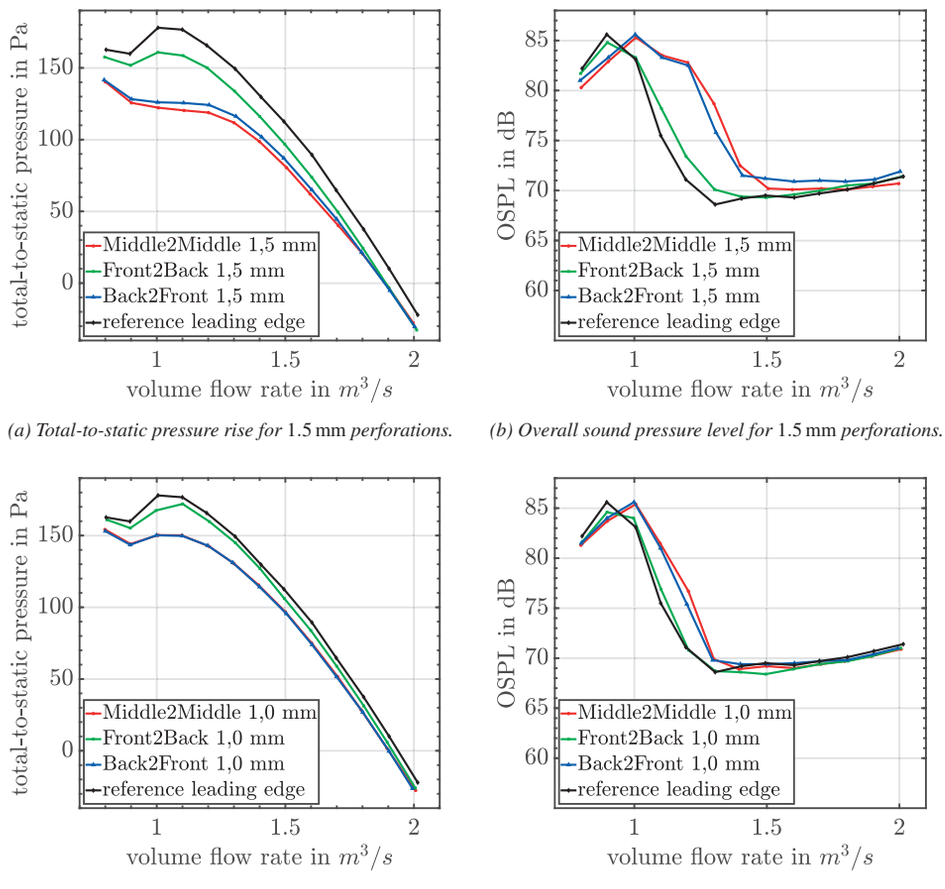
IMPACT OF PERFORATED LEADING-EDGE VARIANTS UNDER VARYING INFLOW CONDITIONS

The aerodynamic and acoustic comparison, in undisturbed inflow conditions, of the three slot variants with each 1 mm and 1.5 mm perforations relative to an unperforated reference leading edge is illustrated in Figure 6. The kinematic flow conditions where kept constant. The total-to-static pressure increases for the 1.5 mm variants are shown in Figure 6a. At the design point of 1.4 m^3/s, the F2B variant incurs a penalty of 13.6 Pa whereas the B2F and M2M variants exhibit poorer performance across the entire curve, with penalties of 27.9 Pa (B2F) and 30 Pa (M2M) at the design point.

The acoustic characteristics of the different variants 1.5 mm under undisturbed flow conditions are depicted in Figure 6b. None of the variants shows an advantage over the unperforated reference in this scenario. In particular, the M2M and B2F variants demonstrate a significant increase in SPLs in volume flow rates below the design point. In contrast, the F2B variant acoustically resembles the reference starting from 1.4 m^3/s.

In Figure 6c, the results for the total-to-static pressure for the variants with 1 mm, perforations are presented. It can be seen that the smaller diameter of the perforation leads to fewer penalties compared to the 1.5 mm version. For instance, the F2B variant is only 2.7 Pa below the unperforated reference leading edge at the design point, while the M2M and B2F variants exhibit similar aerodynamic properties with penalties of 15.6 Pa.

The acoustic properties of the 1 mm perforations are shown in Figure 6d. The M2M and B2F variants exhibit less significant acoustic performance losses compared to the reference version with smaller perforations with volume flow rates below the design point. For volume flow rates above the design point, these variants show acoustic behaviour similar to the reference version. The F2B variant, demonstrates improvement in the volume flow range from 1.4 m^3/s to 1.6 m^3/s with the largest improvement of 1.1 dB occurring at 1.5 m^3/s.



(a) Total-to-static pressure rise for 1.5 mm *perforations.*

(b) Overall sound pressure level for 1.5 mm *perforations.*

(c) Total-to-static pressure rise for 1.0 mm *perforations.*

(d) Overall sound pressure level for 1.0 mm *perforations.*

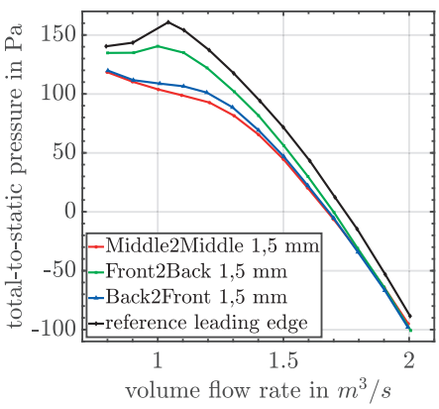
Figure 6: Comparison of the aerodynamic and acoustic performance of leading-edge modifications with 1.5 mm *perforations (a, b) and* 1.0 mm *perforations (c, d) under undisturbed inflow conditions at a constant rotational speed.*

To generate disturbed inflow conditions, a passive turbulence grid is installed upstream of the fans. The leading edge of the axial fan is located 170 mm downstream of the grid. The grid consists of bars with a width of 16 mm and a mesh size of 96 mm. The flow field downstream of the grid has been previously investigated by Zenger and Czwielong et al. [15], [16]. The mean turbulence intensity was found to be $\mathrm{Tu} = 18\,\%$, and the mean integral length scale was determined to be $\Lambda = 20\,\mathrm{mm}$.

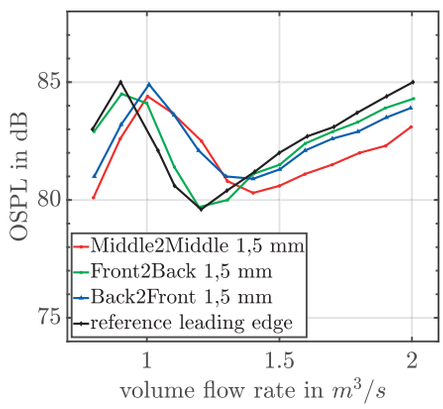
The aerodynamic properties of the three modified variants under the investigated turbulent inflow conditions are illustrated in Figure 7a. It is evident that the F2B variant exhibits the lowest aerodynamic loss, with 12.3 Pa at 1.4 m^3/s. In contrast, the B2F and M2M variants shows a reduced pressure rise of 24.7 Pa and 28.4 Pa, respectively. Larger differences are observed compared to undisturbed inflow conditions in acoustic performance, as shown in Figure 7a. Above the design point and at higher flow rates, the F2B variant achieves the smallest improvement, with 0.5 dB at 1.5 m^3/s, while the B2F variant performs slightly better with an improvement of 0.7 dB. The M2M variant demonstrates the most significant improvement, reaching 1.4 dB at 1.5 m^3/s and up to 2.0 dB at 1.7 m^3/s. Below the design point of 1.4 m^3/s, however, both the M2M and F2B variants show a noticeable deterioration in OSPL compared to the unperforated reference variant.

Finally, the results for 1 mm perforations under disturbed inflow conditions, as shown in Figure 7c and Figure 7d, are discussed. Similar to the case of undisturbed inflow, the reduction in pressure rise for the F2B variant is very low, amounting to only 1.4 Pa. The B2F and M2M variants again exhibit similar behaviour across the entire performance curve, with a penalty of approximately 13.4 Pa at

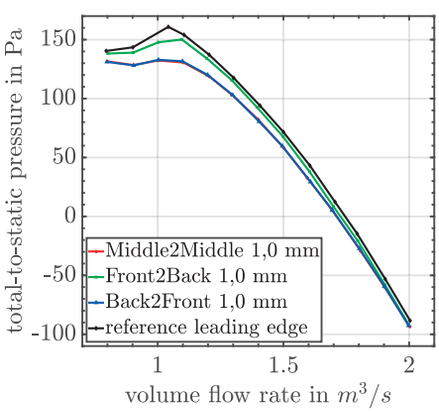
the design point. From an acoustic perspective, all three variants exhibit an improvement starting at a volume flow rate of 1.3 m^3/s. The M2M variant achieves the greatest reduction in SPL, with a decrease of 0.8 dB at a volume flow rate of 1.5 m^3/s. In comparison, the F2B and B2F variants reach a maximum reduction of 0.7 dB within the volume flow rate range of 1.4 m^3/s to 1.6 m^3/s.



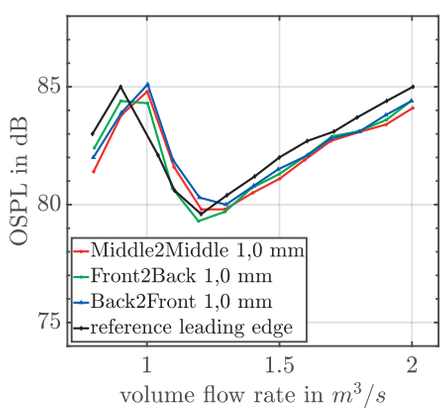
(a) Total-to-static pressure rise for 1.5 mm *perforations.*



(b) Overall sound pressure level for 1.5 mm *perforations.*



(c) Total-to-static pressure rise for 1 mm *perforations.*



(d) Overall sound pressure level for 1 mm *perforations.*

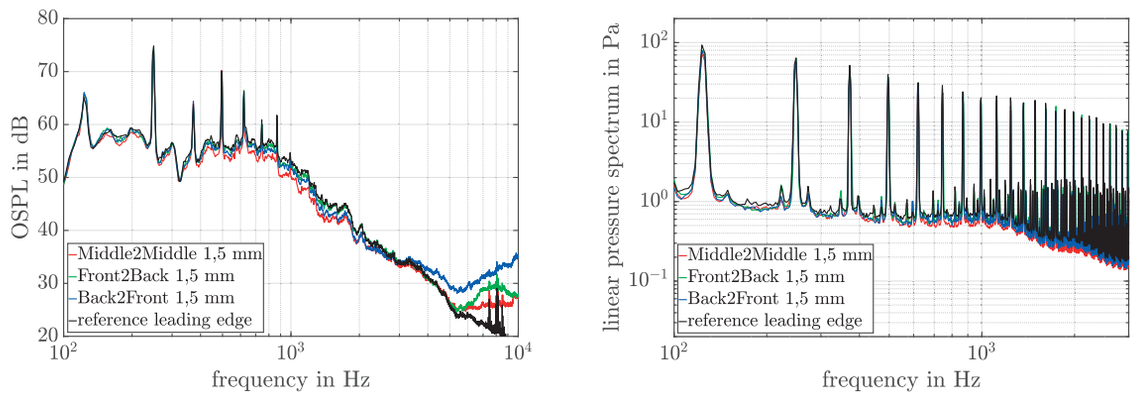
Figure 7: Comparison of the aerodynamic and acoustic performance of leading-edge modifications with 1.5 mm *perforations (a, b) and* 1.0 mm *perforations (c, d) under disturbed inflow conditions at a constant rotational speed.*

To investigate the physical mechanisms of perforated leading edges, the sound pressure spectrum is shown in Figure 8a, while the pressure spectrum in the tip gap is presented in Figure 8b. This analysis revisits the previously examined flow case with disturbed inflow conditions at 1.5 m^3/s, where the highest SPL reduction occurs. The sound pressure spectrum indicates that perforated variants do not affect the blade passing frequency. A broadband noise reduction is evident in the range $f \in [300\,\text{Hz}; 3000\,\text{Hz}]$, with the M2M variant showing the most significant reduction. This effect is likely due to an altered pressure distribution, influenced by flow penetration effects similar to those observed in porous airfoil leading edges [17]. The interaction between perforations and the boundary layer may modify the surface pressure and mitigate turbulence interaction noise [18].

At higher frequencies $f \in [5000\,\text{Hz}; 10000\,\text{Hz}]$, an increase in SPLs is observed, varying among the variants. The B2F variant exhibits the most pronounced increase. Due to the identical perforated surface area across all variants, high-frequency noise can be attributed to roughness noise [17], [18]. However, differences in high-frequency SPLs suggest an additional contributing mechanism. The B2F variant, positioned closest to the suction peak, experiences the highest pressure difference,

leading to the greatest volume flow through the perforations and, consequently, the highest flow-induced noise. The F2B variant, despite having the lowest pressure difference, is louder than M2M, likely due to boundary layer effects influenced by the outflow direction [13].

An impact on the tip gap vortex is evident in Figure 8b, particularly at position two within the tip gap. This leads to reduced broadband high-frequency pressure fluctuations, especially for the M2M variant. The noise reduction in the frequency range $f \in [300\,\text{Hz}; 3000\,\text{Hz}]$ may be attributed to decreased pressure fluctuations, as both are closely interconnected in aerodynamic noise generation [19].



(a) Sound pressure spectrum at $1.5\,\text{m}^3/\text{s}$.

(b) Pressure spectrum in tip gap (Pos.1) at $1.5\,\text{m}^3/\text{s}$.

Figure 8: Comparison of spectra of the 1 mm *perforation variants under disturbed inflow conditions at* $1.5\,\text{m}^3/\text{s}$.

CONCLUSION

This study examined the aerodynamic and acoustic performance of axial fan blades with simplified porosity designs, represented by implemented holes, manufactured using the Laser Powder Bed Fusion (PBF-LB) process. The results demonstrated that the design of the leading-edge slot, which incorporates the porosity, impacts the trade-off between noise reduction and aerodynamic efficiency. Three distinct slot configurations were evaluated: Front-to-Back (F2B), Middle-to-Middle (M2M), and Back-to-Front (B2F), under both undisturbed and disturbed inflow conditions.

The front-to-back (F2B) design, which incorporates a slot aligned with the flow direction, demonstrated the most promising overall performance. It achieved noise reduction under both inflow conditions while maintaining minimal aerodynamic losses. For instance, the F2B design with 1 mm diameter perforations incurred a loss of only 1.3 % in total-to-static pressure rise at the design point under disturbed inflow conditions, while reducing the fan's OSPL by 0.7 dB. In contrast, the B2F design exhibited poor aerodynamic performance and provided no notable acoustic advantages compared to the other designs. The M2M variant, although associated with larger aerodynamic penalties than F2B, demonstrated noise reduction potential under turbulent inflow conditions. In particular, the 1.5 mm diameter perforation version of M2M achieved noise reductions of up to 1.6 dB.

Additionally, smaller perforations (1 mm diameter) were found to offer a better balance between acoustic and aerodynamic performance compared to larger perforations (1.5 mm diameter). The results indicate that the F2B slot design is the most suitable choice for future applications, balancing effective noise reduction with aerodynamic efficiency.

ACKNOWLEDGEMENT

The authors would like to thank the German Federal Ministry for Economic Affairs and Climate Protection (BMWK), which provided financial support for the research work as part of a project in the programme Industrielle Gemeinschaftsforschung (IGF) with the funding number IGF 22627 N. The authors would also like to thank the Forschungsvereinigung fur Luft- und Trocknungstechnik (FLT e.V.) for their technical support of the project.

BIBLIOGRAPHY

[1] B. D. Mugridge, *Axial flow fan noise caused by inlet flow distortion*, Journal of Sound and Vibration vol. 40, no. 4, pp. 497–512, **1975**, ISSN: 0022460X. DOI: 10.1016/S0022-460X(75)80059-9.

[2] H. Kobayashi and J. F. Groeneweg, *Effects of inflow distortion profiles on fan tone noise*, AIAA Journal vol. 18, no. 8, pp. 899–906, **1980**, ISSN: 0001-1452. DOI: 10.2514/3.50832.

[3] F. Tong, W. Qiao, K. Xu, L. Wang, W. Chen, and X. Wang, *On the study of wavy leading-edge vanes to achieve low fan interaction noise*, Journal of Sound and Vibration vol. 419, pp. 200–226, **2018**, ISSN: 0022460X. DOI: 10.1016/j.jsv.2018.01.017.

[4] F. Krömer, *Sound emission of low-pressure axial fans under distorted inflow conditions*.

[5] B. Lyu, L. J. Ayton, and P. Chaitanya, *On the acoustic optimality of leading-edge serration profiles*, Journal of Sound and Vibration vol. 462, p. 114 923, **2019**, ISSN: 0022460X. DOI: 10.1016/j.jsv.2019.114923.

[6] T. M. Biedermann, P. Czeckay, T. F. Geyer, F. Kameier, and C. O. Paschereit, *Effect of inflow conditions on the noise reduction through leading edge serrations*, AIAA Journal vol. 57, no. 9, pp. 4104–4109, **2019**, ISSN: 0001-1452. DOI: 10.2514/1.J057831.

[7] C. Ocker, F. Czwielong, T. F. Geyer, P. Chaitanya, M. Merkel, and S. Becker, *Permeable structures for leading edge noise reduction*, in *AIAA AVIATION 2021 FORUM*, Reston, Virginia: American Institute of Aeronautics and Astronautics, **2021**, ISBN: 978-1-62410-610-1. DOI: 10.2514/6.2021-2192.

[8] F. Czwielong, B. Berchtenbreiter, C. Ocker, *et al.*, *On the application and limitations of sound-absorbing materials for axial fan blades*, **2022**. DOI: 10.26083/TUPRINTS-00021725.

[9] C. Ocker, T. F. Geyer, F. Czwielong, *et al.*, *Permeable leading edges for airfoil and fan noise reduction in disturbed inflow*, AIAA Journal vol. 59, no. 12, pp. 4969–4986, **2021**, ISSN: 0001-1452. DOI: 10.2514/1.J060396.

[10] T. Carolus, *Ventilatoren*. Wiesbaden: Vieweg+Teubner Verlag, **2013**, ISBN: 978-3-8348-2471-4. DOI: 10.1007/978-3-8348-2472-1.

[11] T. Fukano, Y. Takamatsu, and Y. Kodama, *The effects of tip clearance on the noise of low pressure axial and mixed flow fans*, Journal of Sound and Vibration vol. 105, no. 2, pp. 291–308, **1986**, ISSN: 0022460X. DOI: 10.1016/0022-460X(86)90158-6.

[12] C. Ocker, T. F. Geyer, F. Czwielong, *et al.*, *Experimental investigation of the impact of 3d-metal-printed perforated leading edges on airfoil and axial fan noise*, in *AIAA AVIATION 2020 FORUM*, Reston, Virginia: American Institute of Aeronautics and Astronautics, **2020**, ISBN: 978-1-62410-598-2. DOI: 10.2514/6.2020-2529.

[13] P. Chaitanya, P. Joseph, T. P. Chong, M. Priddin, and L. Ayton, *On the noise reduction mechanisms of porous aerofoil leading edges*, Journal of Sound and Vibration vol. 485, p. 115 574, **2020**, ISSN: 0022460X. DOI: 10.1016/j.jsv.2020.115574.

[14] Deutsche Norm DIN EN ISO 5801, International Organization for Standardization, *Industrial fans-performance testing using standardized airways*, **2007**.

[15] F. Czwielong, F. Krömer, and S. Becker, *Experimental investigations of the sound emission of axial fans under the influence of suction-side heat exchangers*, in *25th AIAA/CEAS Aeroacoustics Conference*, Reston, Virginia: American Institute of Aeronautics and Astronautics, **2019**, ISBN: 978-1-62410-588-3. DOI: 10.2514/6.2019-2618.

[16] F. Zenger, G. Herold, and S. Becker, *Acoustic characterization of forward- and backward-skewed axial fans under increased inflow turbulence*, AIAA Journal vol. 55, no. 4, pp. 1241–1250, **2017**, ISSN: 0001-1452. DOI: 10.2514/1.J055383.

[17] L. Bowen, A. Celik, M. Azarpeyvand, and C. R. Da Silva, *Porous geometry effects on the generation of turbulence interaction noise*, in *AIAA AVIATION 2021 FORUM*, Reston, Virginia: American Institute of Aeronautics and Astronautics, **2021**, ISBN: 978-1-62410-610-1. DOI: 10.2514/6.2021-2193.

[18] T. F. Geyer and E. Sarradj, *Self noise reduction and aerodynamics of airfoils with porous trailing edges*, Acoustics vol. 1, no. 2, pp. 393–409, **2019**. DOI: 10.3390/acoustics1020022.

[19] Dominic Lallier-Daniels, *Analysis of Tip Leakage Flow Noise Inception in Axial Fans*. **2019**.

AEROACOUSTIC PREDICTION AND OPTIMIZATION OF UNEVENLY SPACED BLADES IN AXIAL FANS

Samir ASSAF, Thibaut GRAS, Jacques FERHAT

CETIM, 52, avenue Félix-Louat, BP 80064. 60300 Senlis, France

SUMMARY

In this study, a hybrid analytic/numeric approach for predicting the tonal noise of fans is proposed. It is based on the acoustic interference law applied to the sound pressure generated by each blade and Computational Aero Acoustics (CAA). An optimization procedure is then implemented to minimize the prominence of tonal noise peaks where the decision variables are the blade angular positions, and the constraints are the rotor balancing and the minimum angular distance between adjacent blades. The obtained results show that the developed method may help designers to reduce tonal noise annoyance by optimizing blade spacing.

INTRODUCTION

Aerodynamic noise emitted from rotating machinery is a concern in several industrial applications in terms of comfort and regulations. In mobile machinery, the sound generated by cooling fans contributes strongly to the overall external noise level. Consequently, manufacturers aim to reduce the noise level of machines while improving sound quality. It is known that the tonal noise (TN) contribution to radiated acoustic power is the most important cause of annoyance, related to TN peaks prominence of the sound pressure level (SPL) spectrum [1]. Periodic loading fluctuations on the rotor blades often take place which cannot be suppressed and result in TN generation. One of the methods of reducing TN described in the literature consists in adjusting the tonal characteristics of the fan by unevenly spacing the blades around the hub [2] . Indeed, an evenly spaced rotating fan passes by with a frequency equal to the product of the shaft rotational frequency and the number of blades. This frequency is called the blade passage frequency or BPF. Thus, the fan generates sound pressure waves at the BPF and its harmonics. The use of Unevenly Spaced Blades (USB) distributes the tonal noise over a larger number of tones spread across a broader range of frequencies hub [3]. As a result, many peaks appear at the rotor frequency harmonics but at a lower level resulting in less perceivable TN components. If the fluid dynamics and mechanical constraints are not changed by this spacing modification, this method preserves the geometry of the propeller blades and therefore does not harm propeller performance except in extreme configurations. Thus, it is very convenient and could be used as a correction action of existing rotors.

However, the expected result is not always achieved and finding suitable spacing distribution is not an easy task [4]. For this reason, tools for aerodynamic noise prediction and reduction are necessary not only to simulate the behavior of uneven blade spacing but also to determine the optimal circumferential angular distribution. The objective of this study is to build a hybrid approach numeric/analytic, based on one hand on

the acoustic interference principle and, on the other hand, on the recent advances in aeroacoustics computation. This model predicts well the TN and allow the use of optimization procedure. Hence, in the present approach, the problem of the TN annoyance reduction becomes the one of determining an optimal blade spacing law. It overcomes the inherent limitation of analytical laws of spacing usually employed in literature which can be managed only if the number of free parameters is kept low resulting in reduced design space of possible angular distribution [5].

This paper describes first the general context of this study and the main results of the experimental campaign conducted by CETIM aiming at testing different geometric configurations of fans on an excavator [6]. The objective was to reduce tonal noise of the standard fan mounted on the machine using the uneven blade spacing technique. Then the hybrid numeric/analytic model is developed. It allows the analytical construction of the acoustic pressure spectrum of the fan from that of a single blade calculated numerically, significantly reducing computation time. The numerical model is based on a simplified Computational Fluid Dynamics (CFD) model available in commercial software STARCCM+ [7] . It computes the noise sources, due to the periodic loading fluctuations and aerodynamic perturbations by solving the unsteady flow field and uses the Ffowcs Williams-Hawkings equation to predict the far-field noise generated by a single blade [8]. An optimization procedure is then implemented to minimize the prominence of tonal noise peaks where the decision variables are the blade angular positions, and the constraints are the rotor balancing and the minimum angular distance between adjacent blades. Finally, the main results are given and discussed highlighting the specific acoustic behavior of uneven blade spacing and assessing the effectiveness of the overall proposed approach.

HYBRID NUMERIC/ANALYTIC APPROACH

Context

A study was conducted by Cetim to test USBs on an excavator that exhibits very marked tones generated by the cooling fan, particularly at blade passage frequencies [6]. The objective was to compare their acoustic performance to fans usually mounted in series on the machine using ISO 3744 standard [9]. USB prototypes were designed and manufactured using additive methods (3D printing). The tests were carried out on an Evenly Spaced Blades (ESB) similar to the original fan, as well as two USB (USB1 and USB2) configurations, see Figure 1.

The main results of the noise measurement campaign, illustrated in Figure 2, showed that regarding tonal noise, USB effectively reduced the levels of blade passage frequencies (BPF 1 and 2) but significantly increased certain harmonics of the fan's rotation frequency. The level of these harmonics sometimes reached the level of the BPF, which contradicts the desired result. This finding clearly shows the need of predictive tools to both reduce BPF levels and limit the rise of other harmonics when designing non-uniform fans.

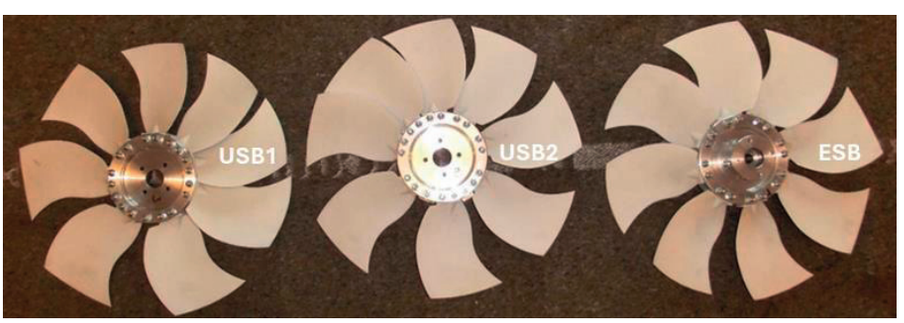


Figure 1: Tested fans, uneven USB1 and USB2, even ESB

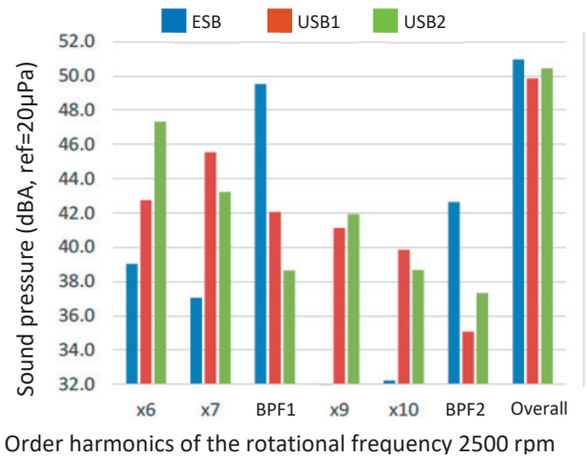


Figure 2: Sound pressure level radiated by the tested fans

Theoretical Background

The tonal noise of a fan can be considered as the superposition of the acoustic fields generated by each blade. If the receiver is in the far field, there is a phase difference in the acoustic waves arriving at the receiver due to the different locations of the circumferential distribution of the blades. Therefore, the principle of phase interference can be utilized with the following assumptions [10]:

- A rotor blade interacts with a stationary flow perturbation or generates a periodic flow perturbation resulting in periodic loading fluctuations.
- The periodic loading fluctuation results in the radiation of a periodic acoustic wave with the fundamental frequency equal to the frequency rotation of the rotor.
- The loading fluctuation associated to each blade is the same, hence each blade generates a periodic wave of same waveform.

Hence, two blades that are located at an angular distance $\Delta\theta$ generate two identical waves with a time delay of $\tau = \Delta\theta/\omega$, where ω is the angular rotation frequency. The waves sum according to the acoustic interference law assuming linear propagation. Thus, a fan composed by N blades generates N waves with a delay of $\tau_m = \theta_m/\omega$, where θ_m is the angle between m^{th} blade and first blade considered as reference (θ_1=0), see Figure 3.

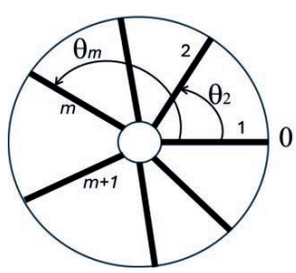


Figure 3: Schematic of blade circumferential distribution

Neglecting the broadband noise, the power spectral density (PSD) of the acoustic pressure due to one blade $S_{pp,bl}$ is related to the PSD of the whole fan by:

$$S_{pp,fan}(f_n) = |F_{int}(f_n)|^2 S_{pp,bl}(f_n) \quad (1)$$

where $f_n = \frac{n\omega}{2\pi}$ is the n^{th} harmonic of the fundamental frequency of the fan, F_{int} is the interference function jointly determined by the spatial distribution of the blades and the rotational speed [10]. The superposition of the fan's tonal noise occurs only at the rotating fundamental frequency and its harmonics. Therefore, only the interference at f_n frequencies needs to be considered:

$$F_{int}(f_n) = \sum_{m=1}^{N} \exp\left(-j\frac{2\pi f_n}{\omega}\theta_m\right) \quad (2)$$

This expression shows that, depending on the blade spacing, acoustic interference may amplify or attenuate the $S_{pp,bl}$. For an equally spaced fan, $\left|\mathrm{F}_{\mathrm{int}\,(\mathrm{f_n})}\right|^2$ assumes its extreme values which are given by:

$$|F_{int}(f_n)|^2 = N^2 \text{ if } n = kN \quad (3)$$

$$|F_{int}(f_n)|^2 = 0 \text{ if } n \neq kN \quad (4)$$

for any integer k. According to the above equations, in the equally spaced blade fan, all tones are canceled by destructive interference, but the ones at frequencies multiple of BPF = $N f_1$, which are amplified by a factor N^2. All the waves are perfectly in phase yielding high tonal noise components at those locations. In contrast, for an unequally spaced blade fan $F_{int}(f_n)$ may take any value between 0 and N^2 at any harmonic, indicating that the acoustic energy is more dispersed, and thus the interference function actually modulates the noise spectrum. Hence, a suitable choice of the spacing may lower the peaks at the BPF harmonics in the SPL spectrum and let the peaks at the other harmonics appear thus reducing the tonal annoyance of the received noise.

The SPL spectrum is defined by:

$$SPL(f_i) = 10\log_{10}\left(\frac{1}{P_{ref}^2}\int_{f_i-\Delta f/2}^{f_i+\Delta f/2} S_{pp}(f_i)\,df\right) \quad (5)$$

where P_{ref}=20 μP_a is the reference acoustic pressure, $f_i = i\Delta f$ corresponds to the i^{th} band of width Δf, which aligns with the i^{th} harmonic of the fan blade passage frequency. Taking into account of Eq. (1) and Eq. (5), the link between the SPL spectrum generated by one blade and by the whole fan is given by [5]:

$$SPL_{fan}(f_n) = SPL_{bl}(f_n) + 10\log_{10}\left(\left|F_{int}(f_n)\right|^2\right) \quad (6)$$

CFD numerical simulation

Nowadays with the rapid development of CFD and Computational Aero Acoustics (CAA) technology, numerical prediction of aerodynamic noise has become increasingly achievable. This section describes CFD calculations of the sound pressure radiated by a single blade that is used in the analytic construction of the SPL of the whole fan as given in Eq. (6).

Aeroacoustics computation of airborne noise requires highly accurate numerical approaches to deal with the complexity of phenomena involved, such as turbulent flow over solid bodies and unsteady aerodynamic loadings. Moreover, the requirements in terms of time and space resolution for the aeroacoustics as well as the identification and calculation of noise sources make the computation of aerodynamic generated and propagated sound often very time demanding. Therefore, this study proposes a simplified numerical approach that is less expensive, light, and suited for rotating blades: the Ffowcs Williams-Hawkings (FW-H) Aeroacoustics Model [7]. As usually used in the literature, the numerical computations are divided into two steps: the first step is to obtain the noise sources by solving the unsteady flow field, and in the next step, the Lighthill acoustic analogy or its special formalisms such as FW–H equation [8], are applied to predict the far-field noise [12]. This model looks particularly at two sound generation mechanisms. First is « Thickness surface noise » than can be thought of as caused by the blade displacing the air. This contribution is dependent only on the shape and motion of the blade. The second mechanism is the « Loading noise » that is aerodynamic adverse effect due to the acceleration of force distribution of the air around the fan blades. Although there is other sound generating mechanism listed by Brentner and Farassat [15], these two sound generation contributors are considered the major one in the absence of any installation effects.

The FW-H model is based on a convergent Reynolds-Averaged Navier-Stokes (URANS) approach for aerodynamic computation of fan blade loads for multiple moving reference frames. Hence, the flow field is composed of rotational domain and stationary domain. The rotating domain is applied to the region of mesh containing the blade (Figure 4). A sensitivity study has first been conducted on mesh type (hexahedral versus polyhedral) and size, on time discretization, on numerical schemes and on turbulence models, to ensure numerical convergence of the computed results. This study showed better convergence of residuals for the polyhedral mesh than the hexahedral mesh at equivalent number of cells. Different boundary layer refinement have also been tested to find the suitable mesh resolution near the surface blades and leading edges, to capture accurately the pressure fluctuations. Finally, a 2.3 million cells mesh has been used to ensure both computational accuracy and efficiency. The inlet and outlet boundary conditions of the external stationary

domain were defined as free to represent the ambient pressure (Figure 4). Applying a moving reference frame to a region generates a constant grid flux in the appropriate conservation equations. This grid flux is calculated based on the properties of the reference frame rather than the local motion of cell vertices. The thickness and loading noise obtained using the FW-H acoustics model are computed from the pressure field computation.

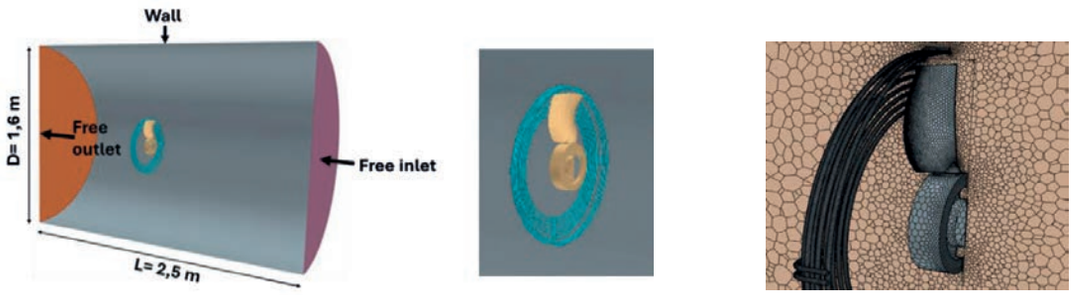


Figure 4: Computational fluid domain - fan with single blade - CFD Mesh model rotor with single blade

URANS turbulence models provide closure relations for the Reynolds-Averaged Navier-Stokes equations. The used k−ω SST turbulence model (Wilcox [16], Menter [17]) solves transport equations for the turbulent kinetic energy and the specific dissipation rate to determine the turbulent eddy viscosity. It provides a better prediction of flow separation than most URANS models. It is also the most common model used in industry given its high accuracy to cost ratio. The solver employed resolves the conservation equations for continuity, momentum, and energy in a coupled manner, deriving the velocity field directly from the momentum equations. The velocity field is obtained from the momentum equations. The pressure is calculated from the continuity equation considering the density as constant. The discretization scheme used for computing the convection flux and the turbulence model is the second-order upwind convection scheme. The radiated acoustic pressure is computed in time domain, with a time step of 10^{-4} s, and the SPL spectrum is obtained by Fourier Transform. A sensitivity study has been performed to ensure the numerical convergence of the model.

Optimization method

The optimization of the blade spacing distribution to minimize tonal noise is formulated as an optimization problem, where the objective is to determine the optimal angular positions of the fan blades. The optimization procedure begins with the calculation of a cost function that quantifies the tonal noise generated by the fan. In this approach, the tonal noise is modeled as a superposition of the acoustic fields emitted by each blade, with the resulting sound pressure spectrum depending on the phase relationships between the blades, as described above.

The first step in the optimization algorithm is the calculation of the interference function (see Eq. (2). Then, to ensure that the spacing distribution satisfies physical constraints, several conditions are incorporated into the optimization process. The first constraint is the sum of the cosine and sine components of the blade positions must be close to zero to preserve static balancing of the rotor. This is satisfied through the following constraints:

$$\sum_{m=1}^{N} \cos(\theta_m) \leq \alpha \qquad \sum_{m=1}^{N} \sin(\theta_m) \leq \alpha \tag{7}$$

where θ_m are the angular positions of the blades, N is the number of blades and α is a threshold to ensure the constraint (for example 10-4). The second constraint is the shape Factor Constraint, which measures the degree of spacing non-uniformity. It is related to the minimum angular distance between neighbouring blades as:

$$R = 1 - \frac{2\pi}{N} \min(|\theta_{m+1} - \theta_m|) \leq \beta \tag{8}$$

where β is the threshold to ensure this constraint. A smaller value of R indicates more uniform spacing. The optimization aims to keep R below a specified threshold, typically R ≤ 0.3 [18]. This allows for finding optimized configurations that are constructible while avoiding blade overlap.

Then, an objective function must be defined to perform the optimization. In this study, the maximum of the SPL generated by the fan is used as objective function (see Eq. (6)). The objective is to minimize the tonal peaks while ensuring that the angular spacing of the blades satisfies the predefined constraints. Furthermore,

to limit the instability of the algorithm, the angle values in radians are rounded to two decimal places in the cost function, which corresponds to an angular deviation of +/- 0.5 degrees. This prevents some configurations that generate performance interference for very precise angle values but are hard to perform with real blade spacings.

The optimization is carried out using Sequential Least Squares Quadratic Programming (SLSQP) [21], which is used to solve constrained optimization problems by iteratively adjusting variables to minimize or maximize an objective function while satisfying equality and inequality constraints. It iteratively adjusts the blade positions and evaluates the resulting cost function. The design space for the optimization is defined by the possible angular positions of the N-1 blades (the first one being the reference at 0 rad), bounded between 0 and 2π. SLSQP is chosen for this optimization because it efficiently handles constrained problems, which is essential for minimizing tonal noise while respecting physical constraints on the blade positions. It is particularly effective for continuous design spaces, like the angular positions of blades, and uses gradient-based methods to quickly converge towards an optimal solution. SLSQP provides a direct approach, ensuring both accuracy and reliability in finding the best blade configuration. Additionally, its simplicity in implementation and ability to work with both equality and inequality constraints make it the best choice for this problem. Multiple initial guesses for the blade positions are generated randomly within a specified range, and the optimization algorithm converges towards the configuration that minimizes the cost function. Figure 5 represents an example of optimized angle blade spacings and the values of the cost function according to iteration number. The color of the cost function represents the constraint normalized values. It represents the degree to which a set of angles meets three constraints: the sum of the cosines and sines of the angles, and a value of R that must remain below a maximum threshold. It evaluates the compliance for each constraint, normalizing them between 0 and 1, with 1 indicating full compliance. Then, it returns an average score that measures how well the solution satisfies all constraints. For this example, the function starts to converge to a value close to 48 dBA after 100 iterations, while still respecting the constraints.

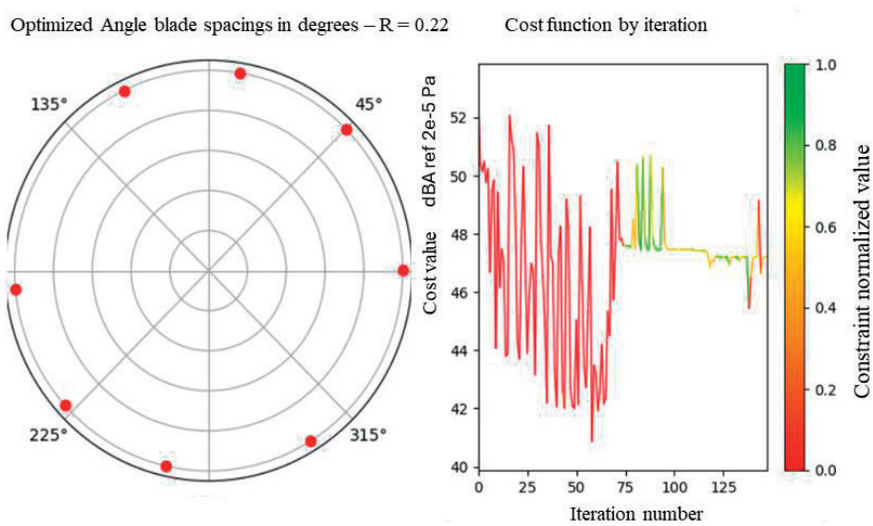


Figure 5: Optimized angle blade spacings (left). Cost function by iteration and according to constraint normalized values

The optimized spacing configuration is expected to reduce the prominence of tonal noise peaks in the SPL spectrum, thus improving the overall acoustic performance of the fan while maintaining its aerodynamic efficiency.

RESULTS AND DISCUSSION

In the following, the optimization procedure described above is applied to the previously tested even configuration ESB presented in Figure 1. In order to avoid the deterioration of the aerodynamic performance of the fan, it is necessary to ensure that the pitch between the blades is not too small. Parametric study was conducted by varying R between 0.22 and 0.35 (corresponding to minimal angular distances between 29° and 35°). Maximum sound levels are plotted according to R values in Figure 6. It is seen that convergence is reached beyond 0.29 for optimized sound levels around 42.3 dBA.

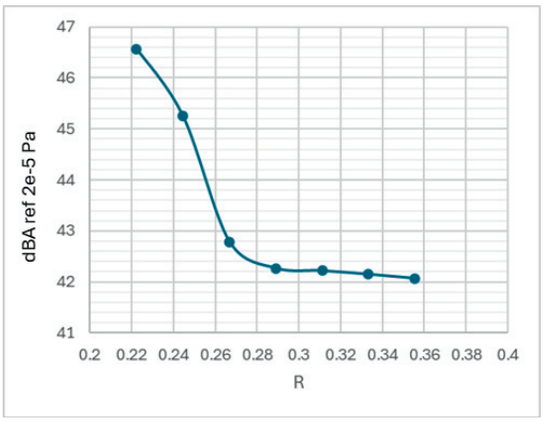


Figure 6: Convergence study of optimized sound power levels according to R values

Hence, two shape factors (Eq. 8) are selected as constraints in this study R = 0.22 and R = 0.29. The corresponding angle distribution and the fan arrangements obtained by the optimization algorithm are given in Table 1 and plotted in Figure 7.

Table 1: Spacing of optimized axial fan rotors. (Values in deg.)

Shape Factor	θ_1	θ_2	θ_3	θ_4	θ_5	θ_6	θ_7	θ_8
R = 0.22	0	34.4	68.8	143.2	177.6	212.0	257.8	315.1
R = 0.29	0	32.1	109.4	142.1	174.2	221.2	280.7	326.6

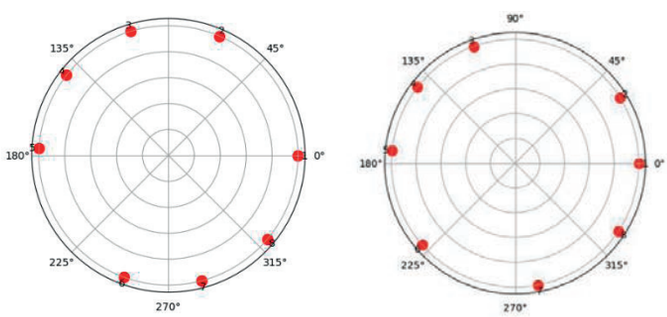


Figure 7: Optimized axial fan rotors. Schematics of the blade arrangements, left R=0.22, right R=0.29

The considered rotational speed is 2500 rpm, which corresponds to a fundamental frequency of 41.7 Hz. The observation point is located at 3 meters in front of the fan.

Figure 9 compares the resulting sound pressure level of three models:

- The developed hybrid analytic/numeric approach and the optimization procedure for the uneven configuration R=0.22 (HAN model)
- The complete CFD/CAA numerical model of the entire fan in configuration R=0.22 (Full model)
- The complete CFD/CAA numerical model of the even configuration ESB (Full model)

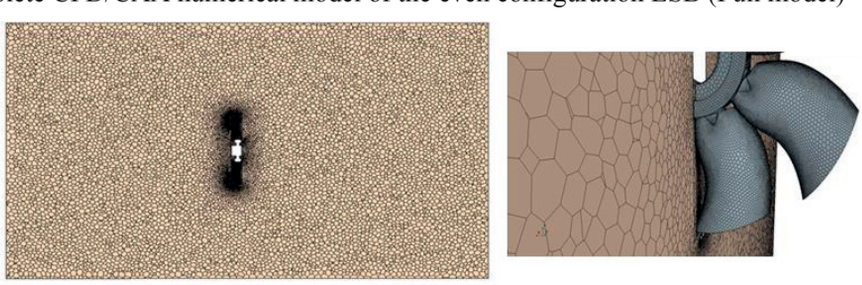


Figure 8 : CFD Mesh model of the entire fan (Full model)

The numerical procedure in Full model is the same as described in the "CFD numerical simulation" section but applied to the fan with all its blades. Figure 8 presents the mesh model of the fan and the associated computational fluid domain.

Compared to the evenly spaced configuration ESB, the theoretical curve (HAN model) given by the optimization procedure shows high reduction in the tonal level at BPFs along with distribution of the acoustic energy over other harmonics. However, new important peaks, in particular, harmonics n°12 and 20 emerge and could be explained by the coincidence phenomenon. The CFD numerical simulation of the entire fan with *R=0.22* (Full Model) confirms this result.

The coincidence phenomenon, described in the literature [4] and well observed in the experimental measurements carried out on the studied fans (Figure 2), leads to the emergence of certain unexpected frequencies corresponding to harmonics of the rotation frequency. Indeed, when the uneven distribution of *N* blades is too close to an even distribution of *M* blades in which (*N* - *M*) blades have been added, the peaks corresponding to harmonics multiple of *M* are amplified. This could explain the emergence of harmonics n°12 and n°20 which correspond to the 3rd and 5th harmonic of 4 evenly spaced blades to which 4 other blades have been added in a non-uniform manner.

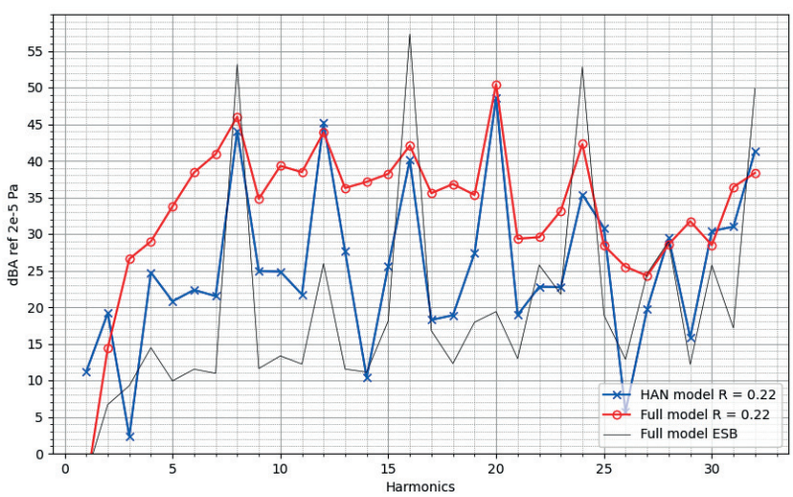


Figure 9: SPL spectra at harmonics related to even configuration ESB and uneven configuration R=0.22

Figure 10 compares the results obtained on both configurations *R=0.22* and *R=0.29*. It shows that the latter decreases and flattens the highest peaks, the maximum level is limited to 42 dBA. However, even when further reduced, harmonics 12 and 20 are still relatively high compared to the remain harmonics of the fan. This indicates that the coincidence effect is not completely eliminated despite the strong decrease of the peaks at BPFs.

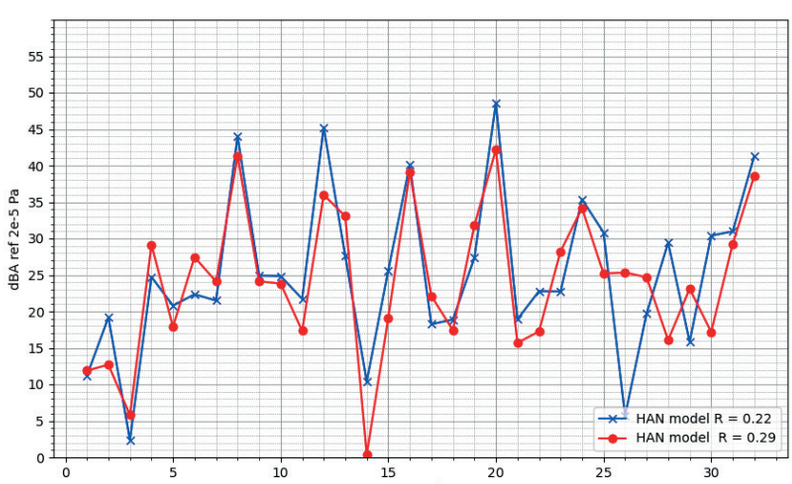


Figure 10: SPL spectra at harmonics related to uneven configuration R=0.22 and R=0.29

Concerning the effect of blade spacing variations on the aerodynamic performance of the fan, Table 2 shows that, for the studied configurations, there is no major impact as the maximum variation of the flow rate and torque does not exceed 3 %. Similar results have been reported in the literature [19].

Table 2: aerodynamic performance

Fan	Flow rate (Kg/s)	Torque (N.m)	Power (W)
ESB	1.205	2.665	697.6
$R = 0.22$	1.178	2.618	685.4
$R = 0.29$	1.177	2.591	678.4

These results show that the developed hybrid analytic/numeric model associated with the optimization procedure are effective in lowering the prominent fan tones. It may help designers to find good spacing resulting in a strong average decrease of the peaks that are the most important cause of annoyance.

CONCLUSION

An optimization method aimed at minimizing the tonal noise peaks prominence from the SPL spectrum was used to design unevenly spaced axial fans. First, a hybrid analytical/numerical approach for predicting the tonal noise was developed. It is based on the acoustic interference law applied to the sound pressure generated by each blade. This model allows the analytical construction of the acoustic pressure spectrum of the fan from that of a single blade calculated numerically. The used CFD/CAA model computes the noise sources, due to the periodic loading fluctuations and aerodynamic perturbations on the blade by solving the unsteady flow field and uses FW-H equation to predict the far-field noise. This hybrid approach was validated on even and uneven spacing configurations and the obtained results showed that it could be used effectively in predicting TN radiated by fans. Then, an optimization method to determine the optimal angular positions of the fan blades was proposed. The objective is to minimize the tonal peaks while ensuring that the angular spacing of the blades satisfies the predefined constraints. This method provides a systematic and efficient approach to blade spacing optimization, addressing both the tonal noise reduction and the physical constraints inherent in fan design, resulting in static balanced fans and limited loss of aerodynamic performance. The obtained results showed that the developed hybrid analytic/numeric model associated with the optimization procedure are effective in lowering the prominent fan tones. Hence, by leveraging numerical simulations and advanced optimization algorithms, the developed method offers a powerful tool for improving the acoustic performance of fans.

Several perspectives to this study are proposed. First, work is now underway to experimentally validate the angular distribution obtained by the optimization procedure. Two types of tests are planned. Validation with the fan set in free field conditions, thus reproducing the numerical simulation conditions (fan not connected). The objective of this test is to validate the proposed overall approach without taking into account the effects of fan installation. This ensures adherence to the underlying assumptions of acoustic interference law stated above (identical waves generated by the blades, without considering the effects of masking or reflections that actually disturb the shape and amplitude of the acoustic waves). The second test, more realistic, will simulate the fan mounting conditions and explore several fan operating conditions and their influence on the radiated noise level. The objective of this test is to validate the proposed method, which assumes a preponderant tonal behavior of the fan and therefore the validity of the superposition law even under real installation conditions. Second, the objective function could be improved, by seeking to minimize not a level associated with a harmonic but rather a level associated with bands of harmonics. The objective is to distribute the acoustic energy over many harmonics thus eliminating the coincidence effects.

Finally, this work should be completed by introducing psychoacoustic parameters that are necessary to assess the improvement of the acoustic quality. These parameters should be included in the spacing determination in order to find optimal angular distributions that reduce annoyance and enhance the perceived noise quality.

BIBLIOGRAPHY

[1] Lee J., Francis JM., Wang LM. – *How tonality and loudness of noise relate to annoyance and task performance*. Noise Control Eng. J, 65(2):71–82, **2017**

[2] Brentner KS., Edwards BD., Riley R. & Schillings J. – *Predicted Noise for a Main Rotor with Modulated Blade Spacing*. Journal of the American Helicopter Society, Vol. 50, No. 1, pp. 18–25, **2005**

[3] Kim TY. – *Reduction of Tonal Propeller Noise by Means of Uneven Blade Spacing*. PhD Thesis, University of California, Irvine, **2016**

[4] Roger M. – *Contrôle du bruit aérodynamique des machines tournantes axiales par modulation de pales*. Acustica 80:247–59, **1994**

[5] Cattanei A., Ghio R., Bongiovì A. – *Reduction of the tonal noise annoyance of axial flow fans by means of optimal blade spacing*. Appl Acoust, 68(11-12):1323–45, **2007**

[6] Bollade L., Chassaignon C. – *Performances acoustiques des ventilateurs à pales désordonnées*. CETIM, internal publication n°245437, **2021**

[7] Simcenter STAR-CCM+®, Siemens PLM Software

[8] Ffowcs Williams JE., Hawkings DL. – *Sound generation by turbulence and surfaces in arbitrary motion*. Phil. Trans. Ryo. Soc., A264, **1969**

[9] NF EN ISO 3744 - *Acoustics — Determination of sound power levels and sound energy levels of noise sources using sound pressure*", AFNOR, February **2012**

[10] Cattanei A., Zecchin FM., Di Pasquali A., Lazari A. – *Effect of the uneven blade spacing on the noise annoyance of axial-flow fans and side channel blowers*. Applied Acoustics 177, **2021**

[11] Li W., Yang L., Hu A., Wu Y. & Li G. – *Noise Reduction Design Method and Validation of Unequal-Pitch.* Processes 11, 2953, **2023**

[12] Frota J., Lempereur P. & Roger M. – *Computation of the noise of a subsonic propeller at an angle of attack*. 4th AIAA/CEAS Aeroacoustic Conference, Toulouse (France), **1998**

[13] Gennaro M. & Caridi D. – *Ffowcs Williams-Hawkings Acoustic Analogy for Simulation of NASA SR2* Propeller Noise in Transonic Cruise Condition", ECCOMAS CFD, 2010

[14] Marinus B. & Roger M. – *Truncated Method for Propeller Noise Prediction Up to Low Supersonic Helical Tip Mach Numbers*. AIAA-3330**, 2009**

[15] Brentner KS. & Farassat F. – *Analytical comparison of the acoustic analogy and Kirchhoff formulation for moving surfaces*. AIAA Journal 36(8), **1998**

[16] Wilcox DC. – *Turbulence Modeling for CFD*. 2nd edition, DCW Industries, Inc.,**1998**

[17] Menter FR. – *Two-equation eddy-viscosity turbulence modeling for engineering application*. AIAA Journal 32(8), **1994**

[18] Anghinolfi D., Canepa E., Cattanei & Paolucci M. – *Psychoacoustic Optimization of the Spacing of Propellers, Helicopter Rotors, and Axial Fan*. J Prop Power, 32(6), **2016**

[19] Dobrzynski W. – *Propeller noise reduction by means of unsymmetrical blades pacing*. J Sound Vib; 163 **1993**

[20] Boltezar M., Mesaric M., Kuhelj A. – *The influence of uneven blade spacing on the SPL and noise spectra radiated from radial fans*. J Sound Vib 216 **1998**

[21] Kraft D. – *A software package for sequential quadratic programming*. Tech. Rep. DFVLR-FB 88-28, DLR German Aerospace Center — Institute for Flight Mechanics, Koln, Germany, **1988**

B2 Installation Effects and Unsteady Phenomena

9 April - 15:45 - Room 1 Fitzgerald

Chairmen: Henrik Witt, Thomas Carolus

List of papers

Effect of Installation Space on the Performance of a Centrifugal Fan

- Martin OTTERSTEN – Swegon Operations (Sweden)

Modal Analysis of Tip Gap Flow in a Rectilinear Cascade of Compressor Blades at Off-Design Operating Conditions

- Marlène SANJOSÉ – École de Technologie Supérieure (Canada)
- Ahmadou Bamba DRAME – École de Technologie Supérieure (Canada)

Fan Mass Flow Determination In Open Wind Tunnel Setups

- Patrick BRUNOW – TU Braunschweig (Germany)
- Mennicken MAXIMILIAN – Deutsches Zentrum für Luft- und Raumfahrt (Germany)
- Jonas GRUBERT – TU Braunschweig (Germany)
- Jens FRIEDRICHS – TU Braunschweig (Germany)

Detection of Vortical Structures in the Leakage Flow of a Low-Speed Axial Fan

- Bendegúz NYÁRI – HUN-REN-BME Condensed Matter Research Group (Hungary)
- Kinga Andrea KOVÁCS – Budapest University of Technology and Economics, Faculty of Mechanical Engineering, Department of Fluid Mechanics (Hungary)
- Esztella BALLA – Budapest University of Technology and Economics, Faculty of Mechanical Engineering, Department of Fluid Mechanics (Hungary)

EFFECT OF INSTALLATION SPACE ON THE PERFORMANCE OF A CENTRIFUGAL FAN

Martin OTTERSTEN

Chalmers University of Technology, Division of Fluid Dynamics, Department of Mechanics and Maritime Science, Gothenburg, Sweden,

Swegon operations AB, Box 336, SE-40125 Gothenburg, Sweden

SUMMARY

Property owners prefer ventilation systems with smaller installation dimensions to maximize rentable space. A ventilation system typically includes a low-speed isolated centrifugal fan within an air handling unit (AHU). However, reducing the AHU's size limits space for the fan, potentially harming its performance. This study investigates the aerodynamic performance of AHUs of varying heights using improved delayed detached eddy simulation (IDDES). The results show that the AHU with the largest height significantly reduces the static pressure downstream of the fan. This reduction is attributed to the large swirling flow created in the AHU after the fan, which generates high-velocity air movement.

INTRODUCTION

Heating, ventilation, and air conditioning (HVAC) systems are essential for maintaining a comfortable indoor environment. They ensure proper airflow, temperature control, air quality, and humidity levels. However, one drawback of HVAC systems is their significant energy consumption, as approximately 40 % of total energy use in the European Union comes from the building sector, which includes HVAC systems. Of this energy, about 10 % to 15 % is specifically used to operate fans [1].

Property owners often prefer HVAC systems with smaller installation dimensions, as this allows for more rentable space. A modern HVAC system typically features a low-speed isolated centrifugal fan installed within an air handling unit (AHU). However, reducing the dimensions of the AHU limits the space available for the fan, which can negatively impact its performance. As noted in [2], placing a centrifugal fan in an AHU that is too small can lead to installation losses.

Several studies have investigated the impact of installation space on fan performance. Research, including simulations and experiments related to an AHU [3], has shown that adding a cube-shaped body downstream of an isolated centrifugal fan can enhance efficiency. This configuration reduces downstream vortices and allows for the transformation of kinetic energy into static pressure. Similar results were reported in another study [4]. Additionally, the cross-sectional aspect ratio of the AHU plays a significant role in static pressure; optimizing this ratio can result in a smaller pressure drop within the unit [5]. The dimensions of the plenum chamber, specifically its width and height, also significantly impact static pressure [6].

In a recent investigation [7], the authors found that for a voluteless centrifugal fan, the pressure at the outlet is unevenly distributed, which affects both the flow and static pressure downstream of the fan.

This study aims to explore how the height of the AHU influences fan performance. Three different cases, featuring varying AHU heights, will be tested. The numerical simulations for this study will utilize the improved delayed detached eddy simulation (IDDES) and the k-ω SST turbulence model, allowing for an accurate representation of fluctuations despite modeling sub-grid scale quantities [8].

CONFIGURATION

The voluteless centrifugal fan, along with its inlet duct and three different AHU configurations (Case 1, Case 2, and Case 3) are illustrated in Figure 1. In each AHU case, the width (w), length (l_3), and outlet diameter (d_3) remain constant. However, the height (h) of the AHU varies across the cases, with Case 1 having the smallest height and Case 3 having a larger height than Case 2. The parameters of the AHU are listed in Table 1. The same fan is used in all cases, which is the same fan analyzed in reference [9]. This fan features seven blades, and there is a clearance (inlet gap) located between the stationary inlet duct and the rotating shroud.

As shown in Figure 1a, the fan and inlet duct are situated within the AHU, which connects to the downstream duct (diameter d_3). The inlet duct connects to an upstream duct (diameter d_4). This simplified geometry layout is designed for numerical simulations, reducing the complexity of the geometry while retaining the primary flow characteristics. The upstream and downstream ducts are identical across all cases, and the parameters for the fan and ducts are listed in Table 2.

The fan rotation speed is 2400 rpm. The operation point is at the maximum efficiency, where the mass flow rate was set to 0.441 kg/s, giving a pressure rise of 500 Pa for Case 1.

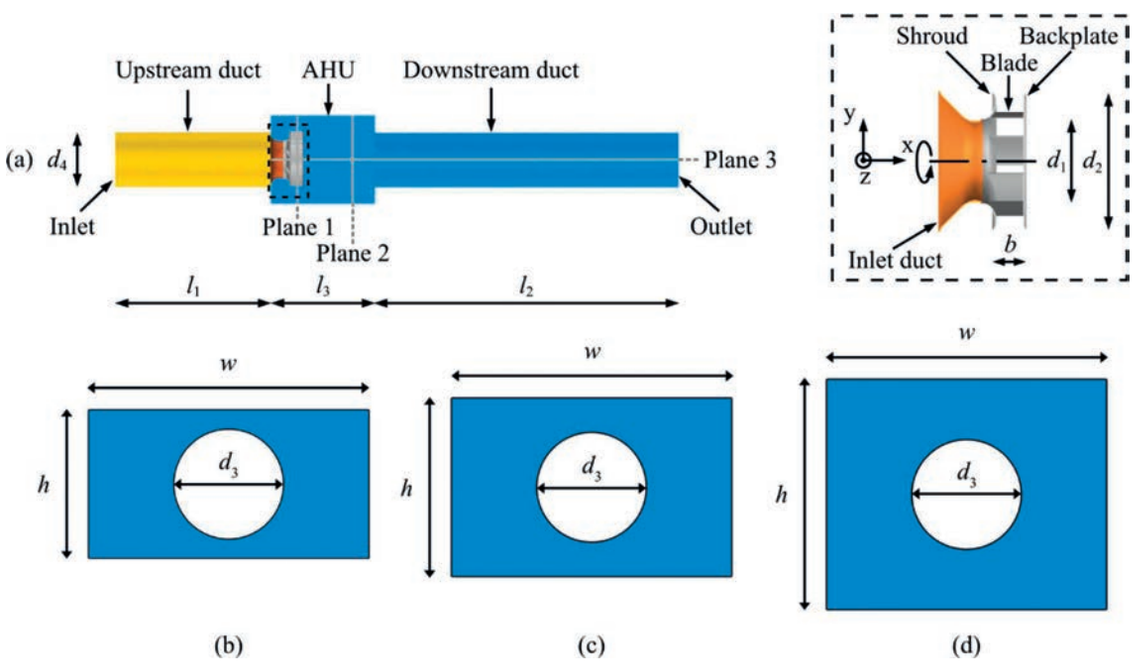


Figure 1. The fan configurations. Gray indicates the rotating fan and brown is the stationary inlet duct. a) The simple geometry layout for the numerical simulations. The rotation axis of the fan is the x-axis. Planes 1 and 2 are perpendicular to the x-axis, while Plane 3 is perpendicular to the y-axis. b) Case 1, c) Case 2, and d) Case 3

Table 1. AHU parameters

w	l_3	d_3	$h_{Case\ 1}$	$h_{Case\ 2}$	$h_{Case\ 3}$
0.71 m	0.54 m	0.28 m	0.38 m	0.45 m	0.59 m

Table 2. The fan and duct parameters

d_1	d_2	d_4	b	l_1	l_2
0.20 m	0.32 m	0.28 m	0.064 m	1.0 m	1.47 m

NUMERICAL METHODOLOGY

CFD methodology

The air is considered as an ideal gas. The flow is compressible. A finite volume method is utilized to discretize the continuity, momentum, and energy equations. The method employs a segregated flow solver accomplished with the Semi-Implicit Method for Pressure-Linked Equations (SIMPLE) algorithm. All simulations are performed using the commercial software STAR-CCM+ [10]. The turbulence is simulated using the IDDES [11] that is combined with the k-ω SST turbulence model. This setup has been tested in several studies on rotating machinery [9, 12].

Numerical settings

The entire computational domain is divided into stationary and rotating parts. The meshes of the stationary and rotary meshes are not conformable at the interfaces between them. The flux convergence of the interpolation at the interface between the two meshes has been validated in [13].

The under-relaxation factors for the velocity and pressure in the segregated flow solver are set to 0.7 and 0.4, respectively. The under-relaxation factor for the turbulence equations is 0.7.

The mass-flow boundary condition is set at the inlet with a uniform velocity distribution. The modeled turbulence intensity is set to $I = 4\,\%$ according to $I = 0.16(R_e)^{-1/8}$ [10]. The modeled turbulence length scale, ℓ, is set to 0.05 m based on $\ell = 0.7d_4$ where d_4 is the upstream duct diameter. The pressure boundary condition is set at the outlet with the static pressure of 0 Pa, and the reference pressure, p_{ref} = 101325 Pa , defined in the ambient air. The no-slip boundary condition is specified on all walls.

The time step is set to $\Delta t = 2.0 \times 10^{-5}$ s, leading to a maximum convective Courant number of around 10 in the computational domain. This value fulfills the numerical stability required for the implicit time-marching method. The maximum number of inner iterations per time step is set to 12.

MESH

The same mesh generation strategy was adopted, developed, and evaluated in [9], where the fan is the same as in this study. A polyhedral mesh generation method was used to produce prism layers near the walls and polyhedral cells in the rest of the computation domain. The use of polyhedral cells for turbomachines has been demonstrated in [13, 14]. The growth rate is set to 1.05, as suggested in [15]. The most important finding in the mesh study performed in [9], was that a local refinement has to be made at the regions extending from the gap to the BLE and along the blade to the blade trailing edge. The mesh parameters are listed in Table 2 and the volume mesh at Plane 1 is illustrated in Figure 2.

Table 3. The mesh parameters

	Case 1	**Case 2**	**Case 3**
Total number of cels	51.6×10^6	53.9×10^6	55.6×10^6
Number of cells in the fan unit	7.5×10^6	9.8×10^6	11.5×10^6
Number of cells in the rotating region	41.9×10^6	41.9×10^6	41.9×10^6
Maximum Δy^+ near blade walls	0.73	0.73	0.73

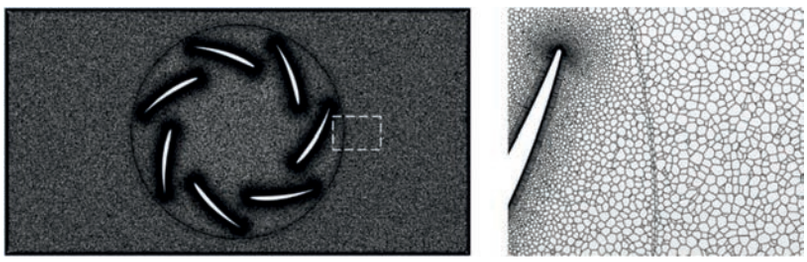


Figure 2. Volume mesh in plane 1

RESULTS AND DISCUSSION

Fan performance

For the purpose of this analysis, static pressure is defined as $p = P - p_{ref}$, where $p_{ref} = 101325$ Pa. The static pressure is presented along the axial symmetric line for three cases in Figure 3. All cases exhibit similar pressure in the upstream duct of the fan; however, differences are observed downstream. Case 1 shows the highest pressure, while Case 3 has the lowest. Since the height of the AHU is the only modification made, the difference in pressure rise downstream of the fan is attributed to the height change. Cases 2 and 3 experience significant pressure drops within the AHU as indicated in the gray zone of Figure 3. In contrast, Case 1 shows its pressure drop occurring at the transition between the AHU and the downstream duct. In the downstream duct, Cases 2 and 3 maintain static pressure. The time-averaged static pressure rise, $\Delta\bar{p}$, between the fan inlet and outlet is summarized for all cases in Table 4. This results are contrary to the results in [2]. Additionally, the fan torque remains approximately the same across all cases.

The time history of the static pressure, p, at the outlet is illustrated in Figure 4. The dashed lines represent the average value for each case, with Case 3 showing the lowest average value, as indicated in Table 4. Notably, Case 3 also experiences the highest amplitude of pressure fluctuations. Furthermore, all cases exhibit a periodic low-frequency fluctuation related to the fan rotation. For Cases 1 and 2, the low-frequency fluctuation has a time period of approximately 1.5 fan revolutions, while for Case 3, this period is approximately 2 fan revolutions. These findings suggest that a low-frequency oscillation related to the fan rotation occurs within the AHU.

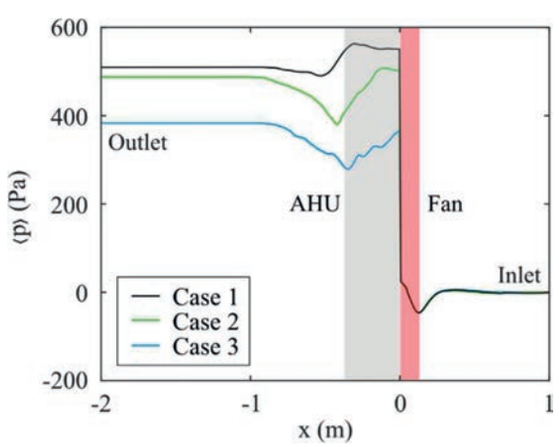


Figure 3. The pressure along the axial axis of the fan across the computational domain. Here x = −2 corresponds to the location near the outlet and x = 1 near the inlet. The fan location is marked with the red zone and the AHU location is marked with the gray zone

Table 4. Time-averaged static pressure

	Case 1	Case 2	Case 3
$\Delta\overline{p}$ **(Pa)**	500	481	380

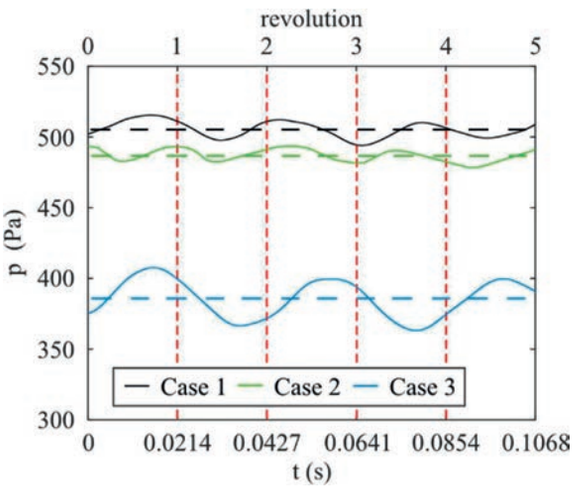


Figure 4. Time history of the static pressure (p) *at the outlet for all cases. The dashed lines indicate the average value for each case*

Comparison of static pressure

Figure 5 illustrates the instantaneous static pressure (p) in Plane 1 (refer to the plane's position in Figure 1) for all cases. All cases display unevenly distributed pressure. The average surface pressure is higher for Cases 1 and 2, which aligns with the observation in Figure 4 that Case 3 exhibits the lowest pressure.

A monitoring point, designated as P1, is positioned near the fan outlet, indicated by black dots in Figure 5. The time history of the static pressure (p) at this monitoring point is presented in Figure 6, containing a duration of 5 fan revolutions. The dashed lines represent the average values for each case. In Case 3, significant pressure fluctuations with large amplitudes and low frequencies are observed. Although fluctuations are also present in Cases 1 and 2, their amplitudes are smaller and occur at higher frequencies. The average pressures at this monitoring point are more consistent compared to the outlet (see Figure 4). This finding suggests that Case 3 experiences a greater loss of pressure within the AHU compared to the other cases, aligning with the results shown in Figure 3. Additionally, a periodic low-frequency fluctuation corresponding to the fan's rotation is evident in Case 3, with a time period of approximately one fan revolution.

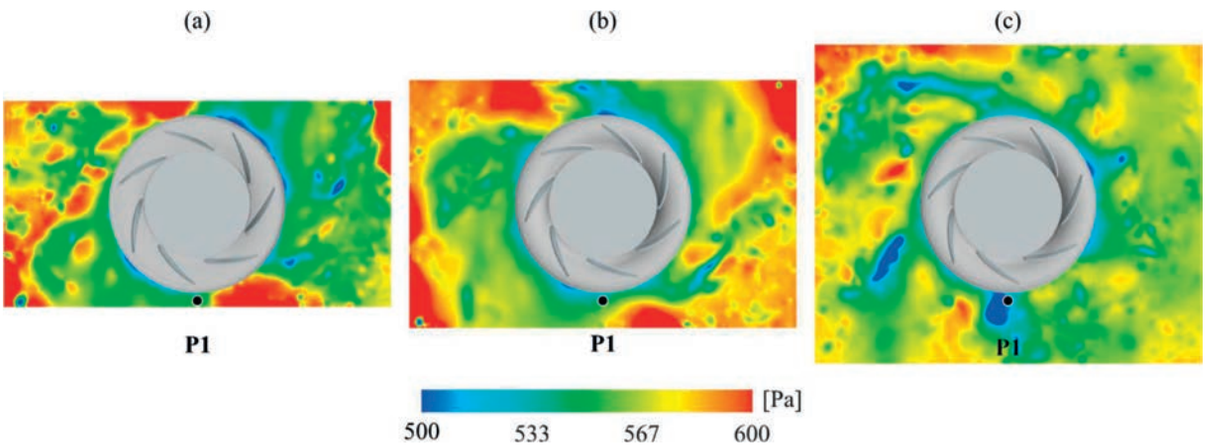


Figure 5. The instantaneous static pressure (p) *in Plane 1: a) Case 1, b) Case 2, and c) Case 3. Black dots indicate the monitoring point P1.*

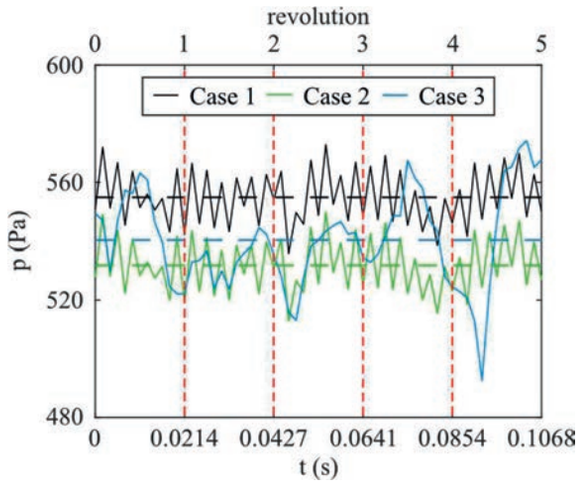


Figure 6. Time history of the static pressure (p) at the monitoring point, P1, for all cases. The dashed lines indicate the average value for each case

A snapshot of the static pressure contours (p) on Plane 3 for all cases is shown in Figure 7. Cases 2 and 3 display regions of low static pressure in the center of the AHU and the downstream duct, extending from the fan to the outlet. These regions are not present in Case 1. Among the three cases, Case 3 demonstrates the highest pressure difference within the fan unit compared to Cases 1 and 2. This observation supports the findings in Figures 4 and 6, which indicate that Case 3 experiences a greater pressure loss.

Two monitoring points, P2 and P3, are positioned to observe the pressure, marked as black dots in Figure 7. The time history of static pressure (p) at these points is displayed over five fan rotations in Figure 8. Cases 1 and 2 show minor pressure fluctuations in contrast to Case 3, while Case 1 maintains the highest pressure at both monitoring points.

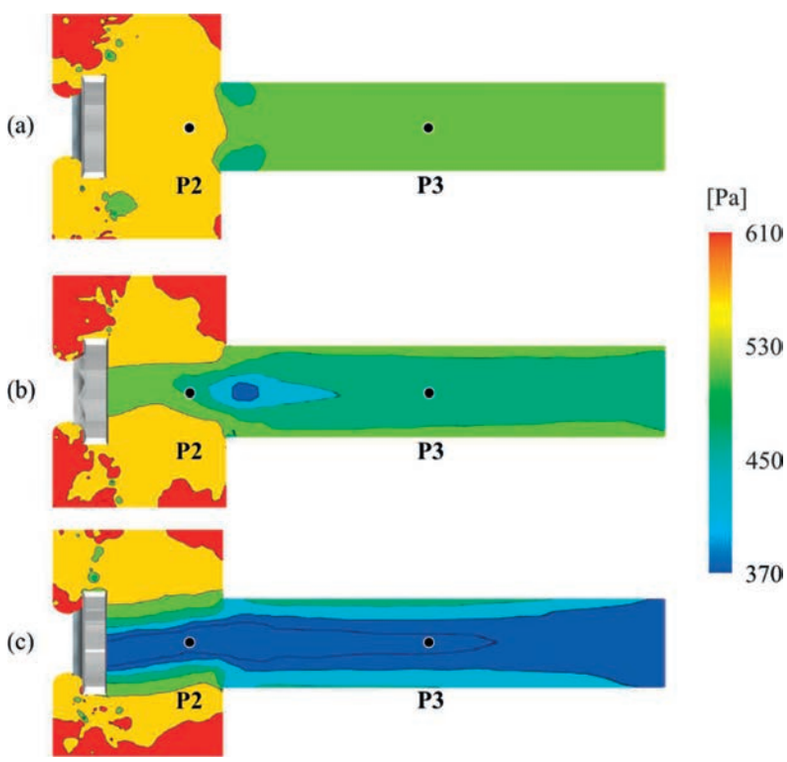


Figure 7. The instantaneous static pressure (p) in Plane 3: a) Case 1, b) Case 2, and c) Case 3. The Black dots indicate the monitoring points, P2 and P3

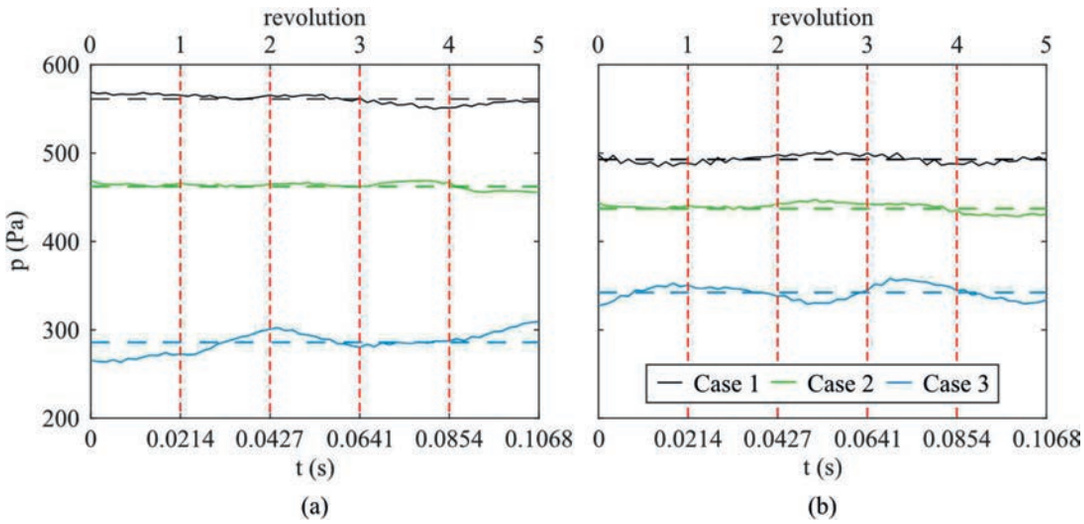


Figure 8. The time history of the static pressure, (p), in the monitor points, a) P2 and b) P3. The dashed lines indicate the average value for each case

Swirling flow

The contours of the velocity magnitude in Plane 2 and the streamlines of the velocity magnitude are shown in Figure 9 for all cases. Case 3 has the highest velocity magnitude at the center and the highest average overall velocity. Case 2 demonstrates a greater velocity compared to Case 1. The higher velocity observed at the center in Case 3 contributes to the low static pressure at monitor point P2, as shown in Figure 8a. Case 3 displays a major swirl with a high velocity at its center. In contrast, Case 1 shows no swirl at this position, and the velocity magnitude is low. Case 2 features a swirl that is smaller than that of Case 3, indicating that increasing the height of the AHU enhances the swirl downstream of the fan.

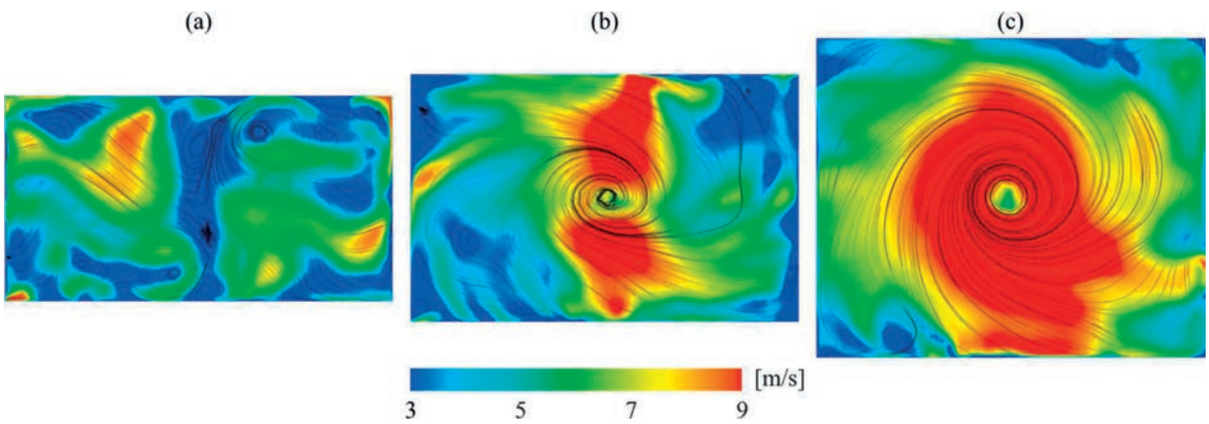


Figure 9. Instantaneous velocity magnitude visualized in Plane 2: a) Case 1, b) Case 2, and c) Case 3

The contours of the velocity magnitudes in the y-z plane are defined as $|\boldsymbol{v}_R| = \sqrt{v_y^2 + v_z^2}$ (coordinate axes defined in Figure 1) in Plane 3 are displayed for all cases in Figure 10. Please note that the axial velocity component along the fan rotation axis is not included in the velocity vectors. In Cases 2 and 3, the flow demonstrates a high rotational velocity both within the AHU and in the downstream duct. Case 3 shows the highest level of rotational flow, originating at the fan and extending to the outlet. In contrast, Case 1 exhibits only a small area of rotation at the transition between the AHU and the downstream duct. Additionally, Case 3 has the highest velocity magnitude downstream of the fan. This elevated velocity results in low static pressure, reinforcing the conclusion drawn from Figure 3-8.

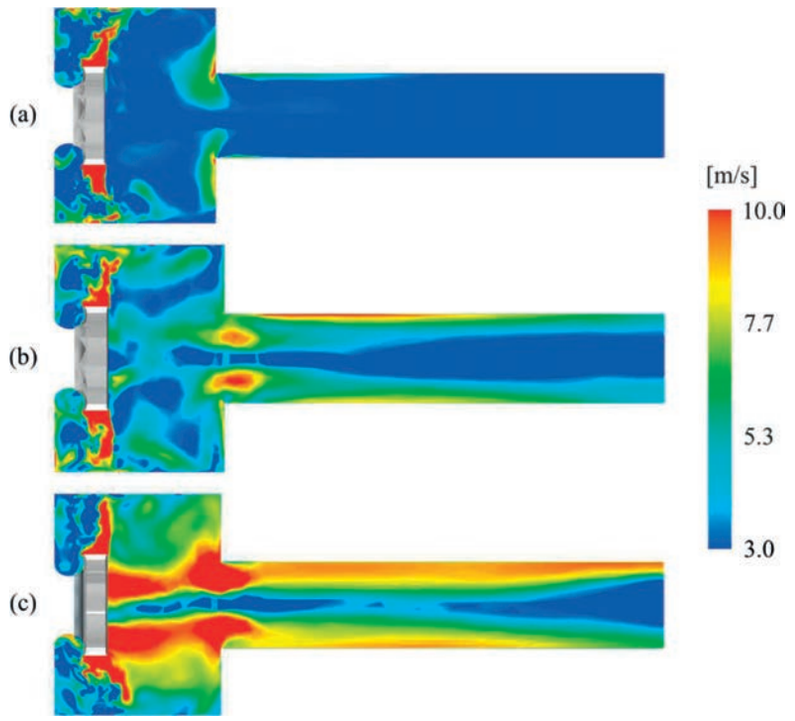


Figure 10. Instantaneous velocity magnitude $|\boldsymbol{v}_R| = \sqrt{v_y^2 + v_z^2}$ *visualized in Plane 3: a) Case 1, b) Case 2, and c) Case 3*

CONCLUSION

The aerodynamic performance of a voluteless centrifugal fan installed in an AHU was studied at different heights of the AHU. The smallest height (Case 1) resulted in the highest static pressure, while the largest height (Case 3) produced the lowest static pressure. Since the only variable changed was the height of the AHU, the differences in pressure rise downstream of the fan are therefore attributed to this alteration.Notably, the torque remained consistent regardless of the height.

There were minor differences in static pressure at the fan outlet among the various cases; however, significant differences were observed at the downstream duct outlet. This indicates that Case 3 experiences a greater loss of pressure within the AHU to the other cases. Additionally, Case 3 exhibited the highest amplitude of pressure fluctuations both near the fan outlet (P1) and at the downstream duct outlet.

In Case 3, a large swirl with a high-velocity magnitude at its center was identified, while Case 2 displayed a smaller swirl, and Case 1 showed no swirl at all. Furthermore, there was a notable region of high rotational velocity in both the AHU and the downstream duct in Case 3, compared to the other cases. These findings suggest that increasing the height of the AHU enhances the swirl downstream of the fan. The higher velocity magnitude observed at the center in Case 3 contributes to the reduced static pressure.

One reason the swirling flow increases with a higher AHU is that a larger volume of airflow in the downstream duct promotes the development of swirling flow due to reduced air resistance. Additionally, an asymmetrical AHU can obstruct the swirling flow since the swirl rotates around the central axis of rotation.

Overall, increasing the height of the AHU has a detrimental effect on its aerodynamic performance. While the torque remains constant, the static pressure decreases significantly.

Future work will involve conducting tests to validate the results presented in this study, as well as investigating the effets on aeroacoustics performance.

ACKNOWLEDGMENTS

Swegon Operation finances the present work. The simulations were performed on resources provided by the Swedish National Infrastructure for Computing (SNIC) at C3SE.

REFERENCES

[1] M. Economidou, B. Atanasiu, C. Despret, J. Maio, et al. – *Europe's buildings under the microscope. A country-by-country review of the energy performance of buildings.* Netherlands: N. p., **2011**.

[2] EBM-Papst – *Technology – Basic principles. **2015**. https://ebmpapst.se/sv/dat/media_manager/news/789/news-files/Brosch_Technologie_EN_screen.pdf*

[3] A. Azem, P. Mathis, F. Stute, M. Hoffmann et al. – *Efficiency increase of free running centrifugal fans through a pressure regain unit used in an air handling unit.* Energy and Buildings, **2018**.

[4] M. Ottersten – *Air handling unit comprising flow guiding stator disc*. US Patent 17/914,289, **2023**.

[5] W. Zhang, A. Li, M. Zhou, R. Gao et al. – *Flow characteristics and structural parametric optimisation design of rectangular plenum chambers for HVAC systems*. Energy and Buildings, **2021**.

[6] S. Song, Y. Ge, H. Zhao – *Structure optimization and numerical verification of plenum chamber for relaxation heat setting machine.* Applied Mechanics and Materials, **2012**.

[7] M. Ottersten, H.D. Yao, L. Davidson – *Inlet gap influence on low-frequency flow unsteadiness in a centrifugal fan*. Aerospace, **2022**.

[8] M. Sanjose, S, Moreau, – *Numerical simulations of a low-speed radial fan*. Int. J. Engineering Systems Modelling and Simulation, **2012**.

[9] M. Ottersten, H.D. Yao, L. Davidson – *Tonal noise of voluteless centrifugal fan generated by turbulence stemming from upstream inlet gap.* Physics of Fluids, **2021**.

[10] Siemens PLM Software – *STAR-CCM+ User Guide.* Version 2210, **2022**.

[11] S. Salunkhe, O.E Fajri, S. Bhushane, D. Thompson, D. O´Dohety, T. O´Dohety, and A. Mason-Jones – *Validation of tidal stream turbine wake predictions and analysis of wake recovery mechanism.* Journal of Marine Science and Engineering, 7, **2019**.

[12] A. Rynell, G. Efraimsson, M. Chevalier, and M. Åbom – *Inclusion of upstream turbulent inflow statistics to numerically acquire proper fan noise characteristics.* SAE Technical Paper 2016-01-1811, **2016**.

[13] M. Ottersten, H.D. Yao, L. Davidson – *Unsteady Simulation of tonal noise from isolated centrifugal fan*. Proceedings of Fan Noise 2018 Symposium, Darmstadt **2018**.

[14] O. Baris, F. Mendonça – *Automotive turbocharger compressor CFD and extension towards incorporating installation effects*. Proceedings of the ASME Turbo Expo 2011: Power for Land, Sea and Air, **2011**.

[15] H.-D. Yao, L. Davidson, and L.E. Eriksson – *Surface integral analogy approaches for predicting noise from 3D high-lift low-noise wings.* Acta Mech. Sin. 30:326-338, **2014**.



MODAL ANALYSIS OF TIP GAP FLOW IN A RECTILINEAR CASCADE OF COMPRESSOR BLADES AT OFF-DESIGN OPERATING CONDITIONS

Marlène SANJOSÉ, Ahmadou Bamba DRAME

[1] *École de Technologie Supérieure, Département de génie aérospatial,*
1100 rue Notre Dame Ouest,
Montreal, QC, H3C1K3, Canada

SUMMARY

Fan systems used for HVAC may operate at higher loads than expected, where they experience flow instabilities. The present work investigates the unsteady flow associated with the tip gap on a rectilinear cascade of compressor blades under off-design operating conditions with a hybrid RANS-LES approach (Shear Blended Eddy Simulation) available in ANSYS-CFX.

The flow at the best efficiency point (BEP), the maximum pressure rise (MPR) operating conditions are investigated using Dynamic Mode Decomposition (DMD) and Spectral Proper Orthogonal Decomposition (SPOD) techniques. The decomposition at BEP reveals natural instabilities. However, the flow in the cascade is globally stable and exhibits a broadband spectral response. At MPR, the decomposition demonstrates a dominant instability where the pressure and suction sides of the compressor blade are coupled through the early breakdown of the tip leakage vortex.

INTRODUCTION

In a rotating machine, a clearance between the blade tip and the casing wall is necessary for its proper operation. However, a leakage flow through this gap is favored by the pressure difference between the pressure and suction sides of the blade. The tip gap flow is a major source of performance deterioration for axial turbomachinery [1]. The tip gap flow strengthens and becomes more and more unstable when the flow rate across an axial compressor is decreased. The relationship between the tip gap flow instabilities such as its spiral oscillations and breakdown and the occurrence of partial stall or rotating instabilities issued from spike-inception has been long discussed in the literature [2–6].

Most of the studies involve experimental measurements or unsteady simulation based on Reynolds Averaged Navier-Stokes simulations.

With the increase in available computational resources for research and the development of advanced scale-resolving approaches, the analysis of turbulence and modal properties of the tip gap flow in isolated airfoil, cascade or low-pressure compressor have recently gained interest [7–9]. Continuing the investigation of the tip gap flow initiated by Koch *et al.* [10] of the Virginia Tech compressor cascade at design using Large Eddy Simulation, the present work will present scale-resolved simulations on the same cascade at two operating conditions. The purpose of this study is to identify the modal content of the tip gap flow and characterize the mechanisms of instability that develops at the maximum pressure rise of the cascade.

NUMERICAL METHODS

The investigated rectilinear cascade geometry includes a single blade passage from the experimental section of the Cascade Wind Tunnel operated at Virginia Tech [11]. The tip leakage flow in this configuration was widely characterized in several experimental campaigns at the BEP [12, 13]. The total tunnel height is $H = 254$ mm which also corresponds to the chord $C = 254$ mm of the extruded blade. The blade geometry corresponds to a cross-section of the GE Rotor B low speed compressor [11] which design methodology based on a modified circular meanline and a double-circular-arc thickness distribution is reported in [14]. The maximum thickness is $4\%C$ at 60% chord location and the maximum camber is $5\%C$ at 50% chord location. In the present work, the tip gap height $h = 4$ mm corresponds to 1.6% of the chord. The computational domain is shown in Fig 1. Its dimensions are $4C \times 1C \times 1.5C$ in the streamwise (X), spanwise (Y) and transverse (Z) directions respectively. The lower wall mimics the casing wall in a turbomachine. It is located at the coordinate $Y = 0$ facing the tip of the blade. The blade is staggered with an angle $\chi = 56.9°$ measured from the streamwise direction.

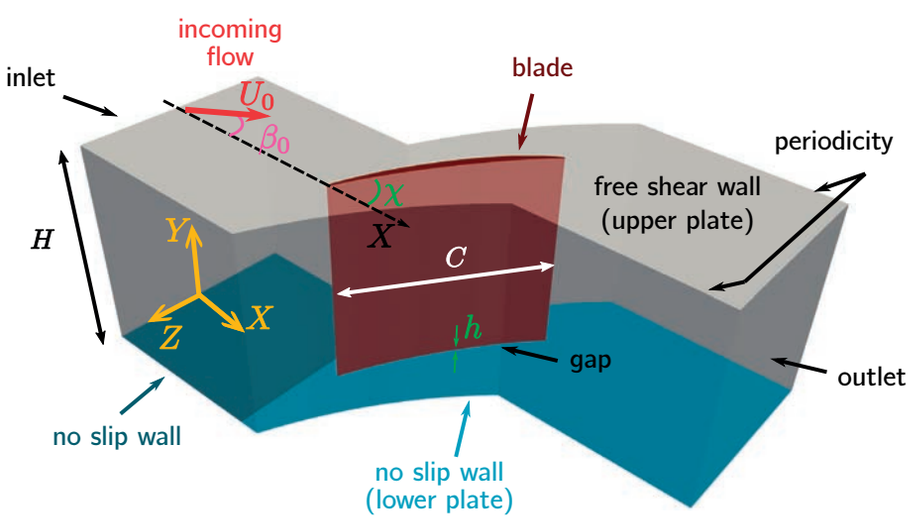


Figure 1: Numerical domain used for the computations.

The boundary conditions are identified in Fig 1. Periodic conditions are applied in the transverse direction, whereas no-slip conditions are specified everywhere except on the upper wall where no shear is applied to simplify the resolution. The uniform upstream velocity U_0 corresponds to the relative velocity of the flow as seen by the blade. The angle β_0 corresponds to the angle of the flow with respect to the machine axis (X). The flow coefficient $\phi = 1/\tan\beta_0$ is defined from the incoming velocity components. No time-resolved turbulent fluctuations are provided on the inlet condition,

only a low level of 1% turbulent kinetic energy (the model one transported by the RANS equations) is provided.

In the present work, the velocity intensity is kept at $U_0 = 25.2$ m/s. Two simulations are performed for β_0 equal to 65.1° and 69.1° i.e. for ϕ equal to 0.464 and 0.382 respectively. These operating points were carefully selected to represent the Best Efficiency Point (BEP) and the Maximum Pressure Rise (MPR) respectively. The Reynolds number based on the blade chord is therefore identical in the two simulations at $Re_c = 4.4 \times 10^5$. The Mach number is $Ma = 0.07$, which justifies the incompressible approach adopted in the simulations. The air density is set to $\rho = 1.185$ kg/m^3.

The Shear Blended Eddy Simulations (SBES) are performed with the ANSYS CFX solver 2021.R2. The $k-\omega$ SST RANS model and the WALE LES models are combined to compute the viscous stress tensor through a blending function which activates the RANS portion of the model not for the entire boundary layer, but only for the region very close to the wall. In other regions (wake, gap), the turbulence is resolved with LES approach [15].

The initial grid designed in [10] is used for the BEP. It consists of 135×10^6 cells with 10 prismatic layers on the blade surface and on the lower plate, and tetrahedrons elsewhere. This mesh is sufficiently refined near the tip gap and in the wake in order to capture the main and the small vortex structures. The wall resolution wall units (y^+) is between $1 < y^+ < 2$ on both the suction and pressure sides. For the lower flow rate, as the flow might massively separate from the walls, the initial grid is slightly modified to capture tip gap flow in the blade passage and upstream of the leading-edge, by extending refinement zones in these areas.

The calculations are performed with the "High Resolution" advection scheme [16]. The time step is fixed at 13 μs to ensure a CFL number less than one in the tip gap region. The L2-norm equation residuals are converged up to 5×10^{-5} within 3 sub-iterations by physical time step. First, for each simulation, the flow establishment in the computational domain has been carefully verified by checking the convergence of the time traces of the blade force components and verifying the convergence of the mean and standard deviation of the pressure on the blade surface [17]. The two simulations are then run for a total physical time of $10T_c$, where $T_c = C/U_0$ is the through-flow time over the blade chord C.

OVERALL PERFORMANCES

Prior to the evaluation of the unsteadiness associated with the tip leakage vortex in this configuration, the aerodynamic performance associated to the selected flow conditions is verified. In the context of an incompressible cascade flow, the pressure coefficient ψ is evaluated from the static pressure gain across the cascade, and the efficiency η is obtained from the total pressure losses as given below:

$$\psi = \frac{P_{\text{outlet}} - P_{\text{inlet}}}{\frac{1}{2}\rho U_0^2} \tag{1}$$

$$\eta_t = 1 - \frac{P_{t,\text{inlet}} - P_{t,\text{outlet}}}{\frac{1}{2}\rho U_0^2} \tag{2}$$

where P_{inlet} and P_{outlet} are mass flow averaged static pressure at inlet and outlet respectively and $P_{t,\text{inlet}}$ and $P_{t,\text{outlet}}$ are mass flow averaged total pressure at inlet and outlet respectively.

Figure 2 compares the efficiency and pressure coefficient obtained from simulations with previous RANS simulations performed on the same configuration using the $k-\omega$ SST turbulent model closure [18]. In this previous work, the RANS results at BEP were verified by comparing cascade deviation angle, pressure loading distribution at mid-span section and tip leakage vortex core trajectory with experimental measurements available for this operating condition only [11, 12]. Both

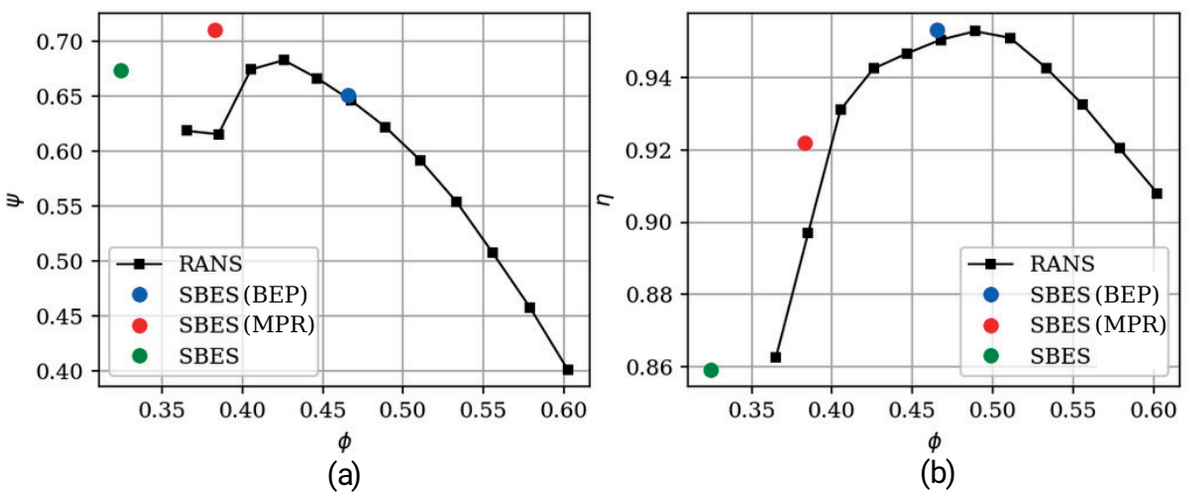


Figure 2: Comparison of RANS and SBES calculation - (a) : Static pressure rise ψ ; (b) : Efficiency η.

RANS and SBES simulations show similar performance at BEP, but significant differences arise at lower flow coefficients due to the emergence of unsteady mechanisms. Using progressive increase of the inlet flow angle, it was possible to identify the maximum pressure rise point which occurs at $\phi = 0.422$ with the RANS approach, but is delayed to $\phi = 0.381$ with the SBES approach. At this point, designated MPR, efficiency is reduced by 3% compared with BEP. The subsequent evaluations show a drop in efficiency for both approaches.

TIP GAP FLOW VISUALIZATION

To highlight the change in flow topology in the tip gap region from BEP to MPR, the coherent flow structures in the tip gap region are identified by an isosurface of Q criterion in Fig. 3. In both cases, the dominant vortex is the Tip Leakage Vortex (TLV), which forms just behind the Leading Edge (LE). At BEP, it remains attached to the leading edge until 40% of the chord. It is then pushed away toward the passage center while being surrounded by several rings of Induced Vortex (IV). At the MPR, the strong leakage flow rejoined the TLV more rapidly, which pushes the vortex structure further into the blade passage. The IV vortex rings are still visible, but much more randomly distributed and impact on a larger section of the blade suction side. The vortex structure associated to the tip gap flow at MPR is more massive than at BEP. It covers almost the full blade passage and interacts with the adjacent blade.

MODAL DECOMPOSITION

The objective of the modal decomposition is to identify the unsteady mechanisms associated to the tip gap flow features previously identified.

Decomposition techniques

In this paper, two different techniques are applied to the same data. First, a Dynamic Mode Decomposition (DMD), originally proposed by Schmid [19], is performed. The principle is to obtain an approximate linear mapping that can describe the temporal evolution of the flow field. The mapping is obtained by an economy-size QR-decomposition of the data sequence. Second, a Spectral Proper Orthogonal Decomposition (SPOD) recently popularized by Towne *et al.* [20, 21], is performed. The principle of this decomposition is to project the temporal evolution of the flow field onto an optimal spatio-temporal basis. The latter are defined as the eigenvectors of the cross-spectral density matrix

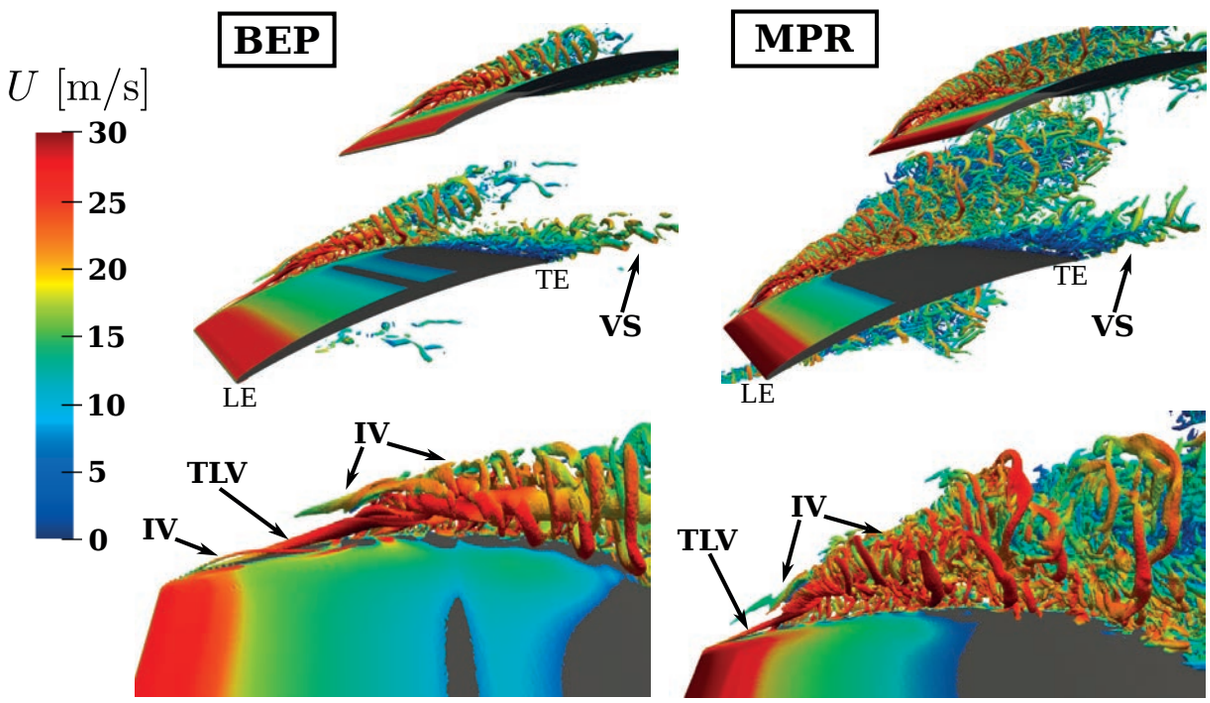


Figure 3: Isosurface of Q criterion with value $Q = 10^6\ s^{-2}$ coloured by the velocity magniture for identification of coherent structures in the tip gap flow at BEP (left) and MPR (right) operating conditions.

at each frequency. Towne *et al.* showed that the two decomposition techniques are related [20]. In the present challenging problem dominated by low frequency content, they provide different modal and frequency resolution. The modal structures at selected frequencies are compared and analyzed in section 7.

Data acquisition

The SBES simulations are continued for another 6 T_c and data are collected at a sampling frequency of 12.8 kHz on blade surfaces, planes parallel to the casing and planes perpendicular to the chord line which are shown in Fig 4. In the present work the DMD and SPOD are performed on the temporal evolution of the static pressure. A single flow quantities is selected for reduced computation. The use of pressure, which is related to velocity components through Bernoulli's equation, is believed to provide a meaningful and thorough description of the flow dynamics. For the SPOD a Welch periodogram is first applied. The time signal is divided into 15 blocks of 2 T_c allowing an overlap of 80% between the blocks. A Hanning windowing and about 20% of zero padding are applied, before a fast Fourier transform is applied to each segment. The SPOD spectrum is limited to a resolution of 60 Hz. Modal decomposition is applied independently for each plane, considering the pressure only in a first approach. For the DMD analysis, the frequency resolution is an outcome of the calculated eigenvalues [19]. Given the signal length, a resolution of about 10 to 15 Hz between consecutive eigenvalues is observed.

RESULTS

SPOD and DMD spectra

Figure 5 shows the energy distribution of the modes obtained with the DMD and SPOD decompositions for selected planes of analysis. Note that for the SPOD, only the energy associated to the first mode is shown, as it is dominant over the higher order modes. For the DMD, the pressure mode

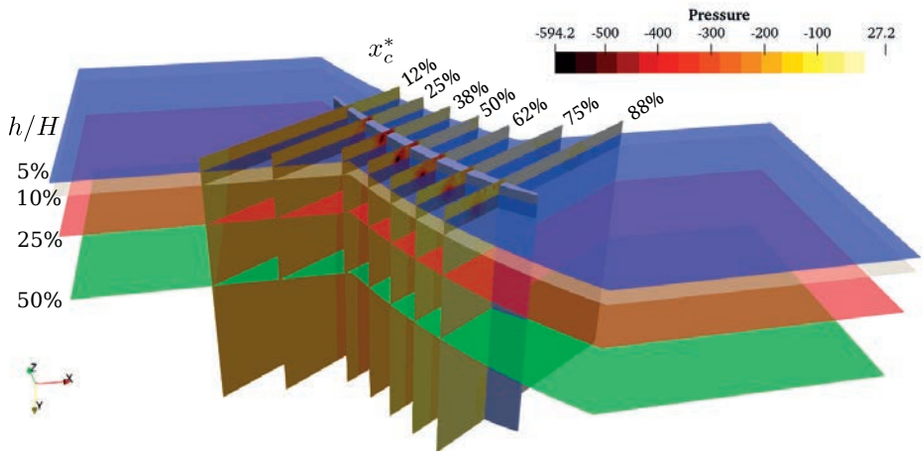


Figure 4: Location of extraction planes.

amplitude in a linear scale is shown and not its energy content. The selected plane denomination and color refer to the definitions provided in Fig. 4. The continuous and dash lines refer to the BEP and MPR cases respectively.

Both techniques identify that the MPR is strongly more unsteady than the BEP, with the former exhibiting significantly higher modal amplitude and energy. The dominant peaks or humps in the spectra appear at roughly the same frequencies with both techniques. The SPOD spectra show a better resolution of the peaks at high frequencies, this can be clearly seen in the blade-to-blade plane at $h/H = 50\%$. The dominant peaks and humps are reported in Tab. 1. At MPR, the low frequency 90 Hz and 180 Hz are visible in all planes and surfaces processed, indicating a global instability mechanism. At BEP, the dominant humps are observed at 1000 Hz and 2000 Hz far from the blade tip at $h/H = 50\%$. Only the 2000 Hz centered hump is captured on the blade surface. A hump of lower amplitude, around 100 Hz, is discernible in all spectra. Humps at 250 Hz and 500 Hz, though their predominance differs between the SPOD and DMD techniques. The analysis indicates that the BEP is undergoing local instabilities, which are stable and not amplified.

Table 1: Main frequencies of unsteadiness. The dominant one is highlighted in bold.

Operating point	**Frequencies [Hz]**
BEP	100, **1000**, 2000
MPR	90, **180**, 250-400, 700

SPOD and DMD mode identification

The modes obtained with both decomposition techniques are shown in Fig. 6 for dominant frequencies at BEP and MPR. The modal distributions shown in the planes $h/H = 5\%$ and $x_c^* = 75\%$ are very similar in terms of lobe distribution between the two techniques. In the SPOD modes, a better alignment of the lobes and clearer lobe shapes can be noticed. This is consistent with SPOD technique being able to find out the optimal mode decomposition [20]. Note that a scaling issue can be noticed in the SPOD mode reconstruction as the mesh cells can be distinguished in the visualizations. This issue will be solved in the final paper.

In terms of physics, the main unsteadiness mechanism at BEP can be attributed to the TLV breakdown and the TLV merge with the shed vortices in the airfoil wake. In the crosswise plane, these fluctuations are associated to the spiral wind-up of the IV structures around the TLV. The vortex ring structures

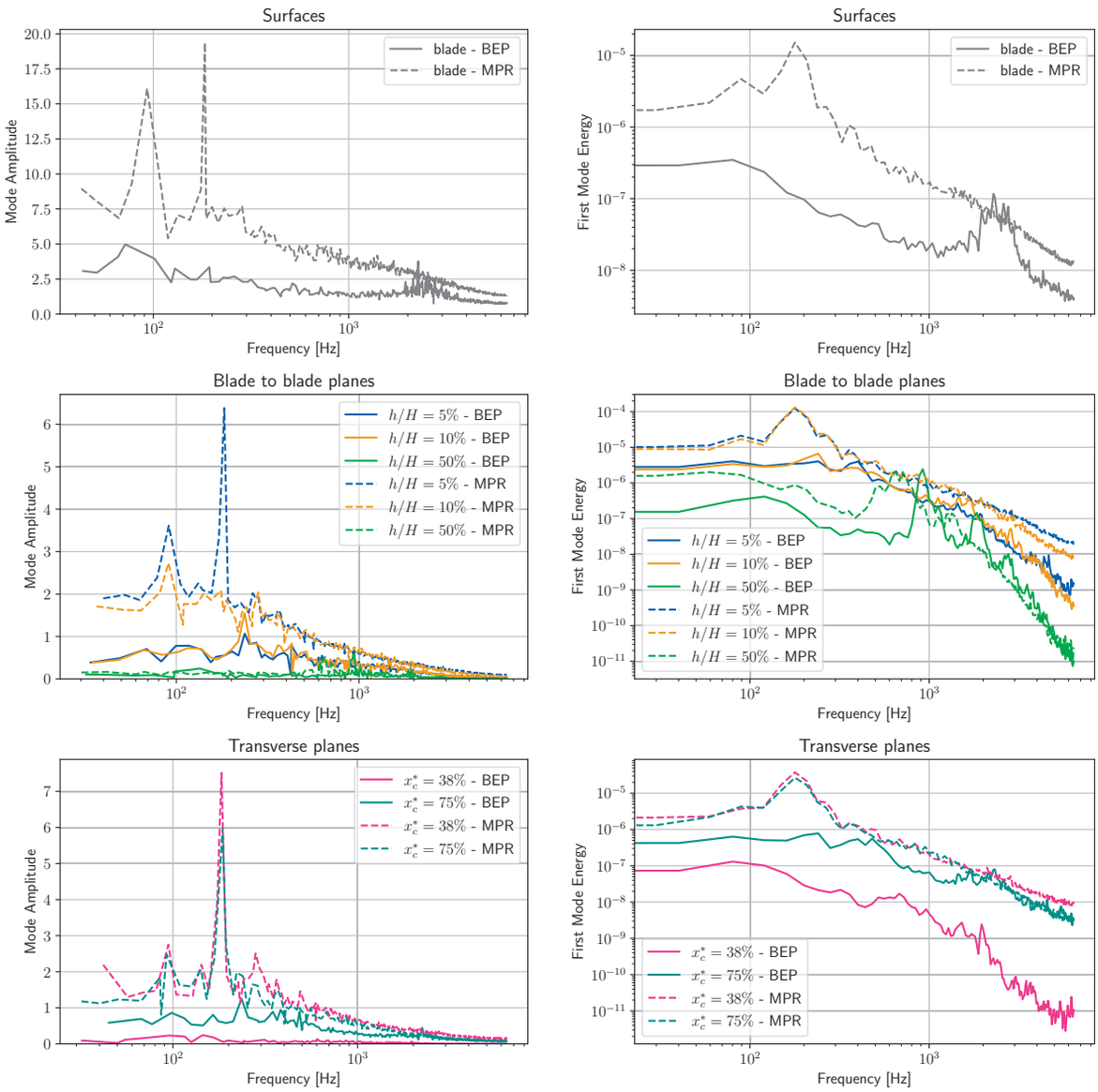


Figure 5: Spectral response of the computed modal content obtained with DMD (left) and SPOD (right).

are clearer in the SPOD reconstruction. At MPR, the instability is associated to the large lobes that develop along the pressure side of the airfoil. Phase opposition can be clearly distinguished. The lobes are translating along the blade in the time reconstructions. The lobe sign alternance is associated to the emission of vortices by the tip leakage jet, which are clearly identified on the suction side (on the right side of the blade) in the inset picture in the SPOD mode reconstruction. It can be concluded that the TLV breakdown is amplified by the pressure and suction side coupling through the clearance.

CONCLUSIONS

Numerical simulations of the compressor cascade of Virginia Tech (VT) using the hybrid Shear-Blended Eddy Simulation (SBES) approach for two different flow coefficients corresponding to the best efficiency point (BEP), the maximum pressure rise (MPR) have been performed. The overall performances between SBES and RANS are identical at BEP, but pressure rise is higher at MPR highlighting the role of unsteady flow patterns at these operating conditions. The use of a scale-

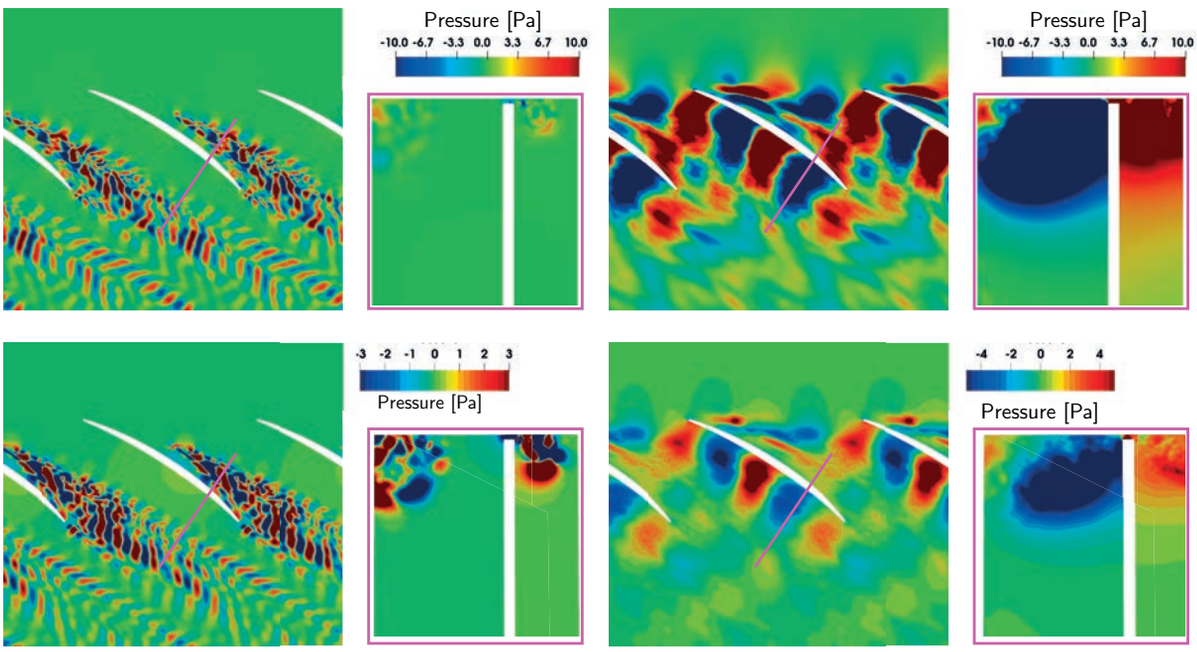


Figure 6: Pressure mode reconstruction in the $h/H = 5\%$ and $x_c^* = 75\%$ planes using DMD mode (top) and SPOD mode (bottom) for the principal frequency of 1000 Hz for BEP (left) and of 180 Hz for MPR (right).

resolved approach like SBES allows identifying the turbulent eddies associated with the tip gap flow. The well documented tip gap flow structure can be observed in this canonical configuration at BEP with great details. Induced Vortex (IV) rings wrap around the Tip Leakage Vortex (TLV) and contribute to its progressive breakdown. At MPR, the IV rings are less organized and contribute to spread vortices over the entire blade passage participating in the efficiency reduction of the cascade.

In order to characterise the unsteady mechanisms at BEP and MPR conditions, a Dynamic Modal Decomposition (DMD) and a Spectral Proper Orthogonal Decomposition (SPOD) have been performed on several planes across the configuration. It was found that these two techniques identify the same modal distribution. The DMD allows a better frequency resolution and is able to accurately capture the low-frequency modes. While the amplitude of the mode reconstruction obtained with the two techniques is not similar, both techniques identify identical flow patterns, with teh SPOD approach providing slightly better resolution in the lobe shapes of the reconstructed pressure fields. For the MPR condition, the modal decompositions allow discerning the amplification mechanism of the tip vortex breakdown at 180 Hz which is associated with a coupling of pressure and suction side through the tip gap. The SPOD technique is better suited for broadband mechanisms. In particular, for the BEP condition, SPOD is able to clearly identify the Induced Vortex (IV) rings causing the breakdown of the TLV and its merge with the wake.

ACKNOWLEDGMENTS

These simulations and their analysis were carried out on the Niagara supercomputer operated by SciNet and administered by the Digital Research Alliance of Canada. This project is funded by NSERC grant RGPIN-2020-05919.

REFERENCES

[1] S. L. Dixon and C. A. Hall, *Fluid Mechanics and Thermodynamics of Turbomachinery*, Seventh edition. Amsterdam ; Boston: Butterworth-Heinemann is an imprint of Elsevier, **2014**.

[2] F. Kameier and W. Neise, *Rotating Blade Flow Instability as a source of noise in axial turbomachines*, Journal of Sound and Vibration vol. 203, no. 5, pp. 833–853, **1997**. DOI: 10.1006/jsvi.1997.0902.

[3] K. Yamada, K. Funazaki, and H. Sasaki, *Numerical Investigation of Relation Between Unsteady Behavior of Tip Leakage Vortex and Rotating Disturbance in a Transonic Axial Compressor Rotor*, in *Volume 6: Turbomachinery, Parts A, B, and C*, Berlin, Germany: ASME, **2008**, pp. 425–436. DOI: 10.1115/GT2008-50779.

[4] H. D. Vo, *Role of Tip Clearance Flow in Rotating Instabilities and Nonsynchronous Vibrations*, Journal of Propulsion and Power vol. 26, no. 3, pp. 556–561, **2010**. DOI: 10.2514/1.26709.

[5] M. Furukawa, K. Saiki, K. Yamada, and M. Inoue, *Unsteady Flow Behavior due to Breakdown of Tip Leakage Vortex in an Axial Compressor Rotor at Near-Stall Condition*, in *ASME Turbo Expo 2000: Power for Land, Sea, and Air*, American Society of Mechanical Engineers Digital Collection, **2014**. DOI: 10.1115/2000-GT-0666.

[6] M. Hewkin-Smith, G. Pullan, S. D. Grimshaw, E. M. Greitzer, and Z. S. Spakovszky, *The Role of Tip Leakage Flow in Spike-Type Rotating Stall Inception*, Journal of Turbomachinery vol. 141, no. 6, **2019**. DOI: 10.1115/1.4042250.

[7] X. Su, X. Ren, X. Li, and C. Gu, *Unsteadiness of Tip Leakage Flow in the Detached-Eddy Simulation on a Transonic Rotor with Vortex Breakdown Phenomenon*, Energies vol. 12, no. 5, p. 954, **2019**. DOI: 10.3390/en12050954.

[8] T. Zhu, D. Lallier-Daniels, M. Sanjosé, S. Moreau, and T. Carolus, *Rotating coherent flow structures as a source for narrowband tip clearance noise from axial fans*, Journal of Sound and Vibration vol. 417, pp. 198–215, **2018**. DOI: 10.1016/j.jsv.2017.11.014.

[9] T. Zhu and T. H. Carolus, *Axial fan tip clearance noise: Experiments, Lattice–Boltzmann simulation, and mitigation measures*, International Journal of Aeroacoustics vol. 17, no. 1/2, pp. 159–183, **2018**. DOI: 10.1177/1475472X17743627.

[10] R. Koch, M. Sanjosé, and S. Moreau, *Aerodynamic investigation of a linear cascade with tip gap using Large-Eddy simulation*, Journal of the Global Power and Propulsion Society vol. 5, pp. 39–49, **2021**. DOI: 10.33737/jgpps/133601.

[11] C. Muthanna, "Flowfield Downstream of a Compressor Cascade with Tip Leakage," M.S. thesis, Virginia Tech, **1998**.

[12] C. Muthanna and W. J. Devenport, *Wake of a Compressor Cascade with Tip Gap, Part 1: Mean Flow and Turbulence Structure*, AIAA Journal vol. 42, no. 11, pp. 2320–2331, **2004**. DOI: 10.2514/1.5270.

[13] C. W. Wenger, W. J. Devenport, K. S. Wittmer, and C. Muthanna, *Wake of a Compressor Cascade with Tip Gap, Part 3: Two Point Statistics*, AIAA Journal vol. 42, no. 11, pp. 2341–2346, **2004**. DOI: 10.2514/1.842.

[14] D. C. Wisler, "Core compressor exit stage study. Volume 1: Blading design," Tech. Rep. DOC-R77AEG400-VOL-1, **1977**.

[15] F. Menter, "Stress-Blended Eddy Simulation (SBES)—A New Paradigm in Hybrid RANS-LES Modeling," in *Progress in Hybrid RANS-LES Modelling*, Y. Hoarau, S.-H. Peng, D. Schwamborn, and A. Revell, Eds., vol. 137, Cham: Springer International Publishing, **2018**, pp. 27–37. DOI: 10.1007/978-3-319-70031-1_3.

[16] ANSYS, Inc, "CFX-Solver Theory Guide," Canonsburg, PA, Documentation 2022.R2, **2022**, p. 288.

[17] A. B. Drame, "Simulation et modélisation de l'écoulement de jeu dans un compresseur axial," Ph.D. dissertation, École de technologie supérieure, Montréal, Canada, **2024**.

[18] A. B. Drame and M. Sanjosé, *Analyse et modélisation des pertes dans une grille rectiligne de compresseur avec jeu.* Transactions of the Canadian Society for Mechanical Engineering, **2024**. DOI: 10.1139/tcsme-2024-0008.

[19] P. J. Schmid, *Dynamic mode decomposition of numerical and experimental data*, Journal of Fluid Mechanics vol. 656, pp. 5–28, **2010**. DOI: 10.1017/S0022112010001217.

[20] A. Towne, O. T. Schmidt, and T. Colonius, *Spectral proper orthogonal decomposition and its relationship to dynamic mode decomposition and resolvent analysis*, Journal of Fluid Mechanics vol. 847, pp. 821–867, **2018**. DOI: 10.1017/jfm.2018.283.

[21] O. T. Schmidt and T. Colonius, *Guide to Spectral Proper Orthogonal Decomposition*, AIAA Journal vol. 58, no. 3, pp. 1023–1033, **2020**. DOI: 10.2514/1.J058809.



FAN MASS FLOW DETERMINATION IN OPEN WIND TUNNEL SETUPS

Patrick BRUNOW[1], Maximilian MENNICKEN[2],
Jonas GRUBERT[1], Jens FRIEDRICHS[1]

[1] *TU Braunschweig, Institute of Jet Propulsion and Turbomachinery (IFAS), Hermann-Blenk-Str. 37, 38108 Braunschweig, Germany*

[2] *German Aerospace Center (DLR), Institute of Propulsion Technology, Linder Höhe, 51147 Cologne, Germany*

SUMMARY

This paper aims to describe the challenges of fan mass flow determination in an experimental setup that consists of an open wind tunnel facility which houses an open fan test rig. The accuracy of the mass flow measurement in the presented setup is influenced by the short axial distance of the available measurement planes to the fan. The experimental setup as well as a corresponding CFD setup are described in detail. The latter is used as benchmark for the experimental approach and source of validation. The influence of the fan's presence on the underlying pressure measurement shows a major influence on the mass flow determination and corrupts the results. A correction for the flawed pressure measurement is presented.

INTRODUCTION

Determining mass flow in open experimental propulsor setups is a challenging task. This paper presents an innovative approach to determining the current mass flow in an open wind tunnel facility. The test setup has been designed to enable experimental evaluation of low hub-to-tip ratio (HTTR) fan stages under a variety of flow conditions, including crosswinds and low headwind velocities. It is noteworthy that the test rig incorporates a variable area nozzle (VAN), which allows for a comprehensive investigation of the compressor map of the installed fan stage. However, direct measurement of the mass flow presents a challenge due to the fact that the engine mock-up operates

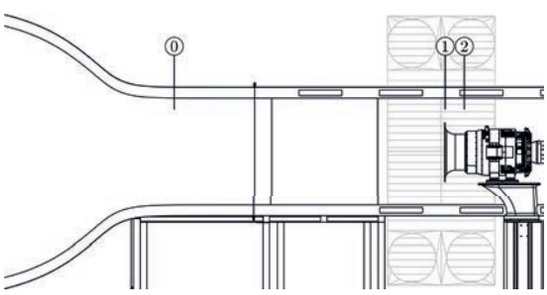
as an air-breathing engine with free stream exit flow, which simulates the bypass flow observed in modern turbofan engines. The rationale behind the design of the test rig in question is the necessity for enhanced propulsive efficiency in modern Ultra High Bypass Ratio (UHBR) jet engines, which can be achieved by increasing fan and nacelle diameters. This results in challenges such as increased aerodynamic drag and engine weight. To mitigate these issues, intake geometries are often shortened, which leads to intensified interactions between the intake and the fan. The shortening of the axial distance between the intake opening and the rotor itself introduces a potential effect of the rotor and spinner, which influences the measured static pressure in front of the rotor. This paper presents a methodology for the determination of mass flow in an open test rig environment, which makes use of Computational Fluid Dynamics (CFD) calculations in conjunction with experimental data obtained during the commissioning phase. It outlines the mass flow approach utilised with a bellmouth intake geometry and presents analytical techniques that incorporate corrections for upstream effects caused by the fan and spinner, complementing the work of *Sebourn* [1]. Bellmouth flow meters are used across a wide field of aerodynamic applications, flow velocities and mass flows [2], [3]. This provides valuable insights to optimise performance and design flexibility beyond aviation.

EXPERIMENTAL SETUP

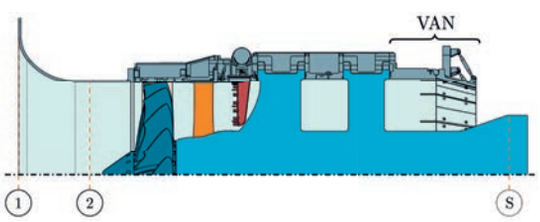
The Institute of Jet Propulsion and Turbomachinery (IFAS) operates an open wind tunnel that houses a powered modular test rig [4], [5]. The following describes the test environment with key measurement evaluation (ME) planes and measurement techniques.

WIND TUNNEL

The Propulsor Test Facility (PTF) of the IFAS is an open wind tunnel in Eiffel configuration. An array of eight blowers downstream of the test section is used for creating an inflow to the test section of $Ma_0 = 0$ to 0.2. The test section itself, as shown in Fig. 1a, has a cross section of $2.4\,\mathrm{m} \times 2.4\,\mathrm{m}$ with a length of 9 m. For powered propulsor tests, the test rig is connected to a 2 MW electrical drive. It is located in the centre of the blower array, downstream of the test section. Rig and motor are connected via a 8 m long shaft.



(a) Cross section of the wind tunnel including the fan rig and measurement locations.



(b) Fan rig with bellmouth intake, VAN and measurement locations.

Figure 1: Overview of the experimental setup.

Fan Rig

The Integrated Nacelle Fan Rig assembly (INFRa) is a novel test rig for the investigation of coupling effects between the intake and fan aerodynamics at different off-design conditions. One area of focus is the investigation of propulsion systems with short flight intakes. An actuated variable area nozzle (VAN) is used on the rig to carry out a detailed investigation of an entire compressor map [6]. The VAN enables stepless adjustment of the back pressure by regulating the outlet cross section of the rig. The investigated fan stage is a blisk with 18 rotor blades and a hub-to-tip ratio of $\nu = 0.26$. The

tip radius of the blades is 0.325 m with a tip gap of 0.5 mm for the hot geometry. The fan stage is representative of modern turbofan engines with a cruise bypass ratio (BPR) of approximately 10 to 12. However, this rig neglects the core flow into the engine and only considers the bypass flow [4]. In lieu of an actual flight intake, a bellmouth nozzle is installed for the rig's commissioning. This is illustrated in Fig. 1b. The bell mouth is used for mass flow rate (MFR) calculation and subsequent calibration of a downstream pressure measurement. This enables a mass flow estimation even after conversion to the flight intake geometry. The bellmouth is equipped with ten static pressure tappings, situated 160 mm ($L/D_{Fan} = 0.49$) upstream of the leading edge of the rotor (evaluation plane ME2). Far upstream of the rig is the measurement evaluation plane ME0. Temperature and the required averaged static pressures are measured on the walls. ME1 is not equipped with sensors. Values of interest are only accessible via fluid dynamic relations.

CFD SETUP

The numerical setup represents the test section of the PTF and is shown in Fig. 2. The cross section of the head wind tunnel is 2.4 m × 2.4 m and the length of the numerical domain is 6 m. The rotor inlet is located halfway downstream of the domain inlet. In the real setup, the mass flow through the fan stage is merged with the tunnel flow via the VAN. In the numerical domain, the merging of the two flows is neglected. Wall functions are applied to the solid surfaces of the wind tunnel, the bellmouth

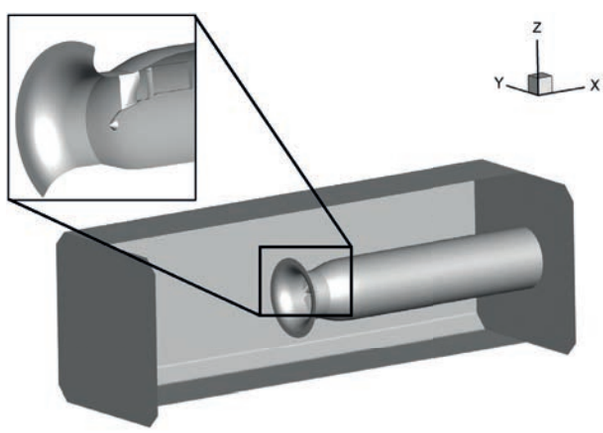


Figure 2: CFD-Domain.

and the outer casing, while the inner flow path including the fan and the OGV are meshed with a $y^+ < 1$. Consequently, the flow near the solid walls is resolved with a low Reynolds approach. The flow path of the test section and the bellmouth are considered as a full annulus with uniform inflow, while a single passage approach is taken advantage of for the fan stage. The mesh of the fan contains 752 128 cells per rotor and 406 912 per stator passage. The overall mesh features 24.36 million cells. The interfaces between the bellmouth and the rotor plane as well as the rotor and the stator interface are implemented via mixing plane approaches. The RANS-based flow solver TRACE [7] is used to calculate the compressor map data applying a steady-state mode. The flow field is assumed to be fully turbulent, and the turbulence is resolved by the two-equation $k-\omega$ SST model [8]. The extensions for stagnation anomaly fixes [9] as well as for rotational effects [10] are used.

MASS FLOW DETERMINATION

As a consequence of the aforementioned configuration, the determination of the mass flow during operation and in data post processing, with an acceptable degree of precision, represents a challenging endeavour. The aim is a robust mass flow calibration, that works without additional, invasive

measurement devices and can be used with different intake geometries. Therefore, prior to the fan rig being operated with a genuine flight intake configuration, it is necessary to commission it with a loss-optimised bellmouth intake, which ensures a uniform inflow and serves as mass flow calibration. Once the relationships between mass flow, VAN setting and a surrogate pressure, that is independent of the installed inlet, have been established over the entire compressor map, the inlet can be exchanged. The surrogate pressure is a plane-averaged static pressure measurement at the rig outlet (marked "S" in Fig. 1b). By assigning the mass flow to the current throttle state and the surrogate pressure, the mass flow can later be identified with these two input variables [5]. The bellmouth geometry is created according to the specifications of the DIN-5167 standard [11]. This standard also provides a set of equations for determining the mass flow. The following section describes the two approaches to calculating mass flow, one using DIN formulae and the other using basic fluid mechanics equations.

Mass flow via basic fluid mechanics equations

The presented set of equations is utilized to describe the current fan mass flow with the limited available measuring points and probes (cf. experimental setup). The bellmouth design is a loss optimized intake geometry, which allows for fundamental equations being used to determine the mass flow

$$\dot{m}_{basic} = c_2 \cdot \rho_2 \cdot A_2. \tag{1}$$

Isentropic compression is assumed and the measurement positions are ME0, the upstream position inside the test section, and measuring plane ME2, which is located in front of the rotor, cf. Fig. 1. The velocity c_2 is derived by applying the principle of energy conservation by using the stagnation temperature between ME0 and ME2:

$$T_0 + \frac{c_0^2}{2c_p} = T_2 + \frac{c_2^2}{2c_p}, \tag{2}$$

which allows it to be converted into:

$$c_2 = \sqrt{\left[2c_p\left(T_0 - T_2\right) + c_0^2\right]}. \tag{3}$$

As the temperature in the flow at ME2 is not directly measurable, it is calculated from the isentropic relation:

$$\frac{T_2}{T_0} = \left(\frac{p_2}{p_0}\right)^{\frac{\kappa-1}{\kappa}}. \tag{4}$$

The density at ME2 can be calculated with the same approach:

$$\rho_2 = \rho_0 \left(\frac{p_2}{p_0}\right)^{\frac{1}{\kappa}}. \tag{5}$$

The test section density ρ_0 is derived by the static pressure p_0, the temperature T_0 and the ideal gas constant R:

$$\rho_0 = \frac{p_0}{RT_0}. \tag{6}$$

This results in the velocity at the bellmouth exit of

$$c_2 = \sqrt{\left[2c_pT_0\left(1 - \left(\frac{p_2}{p_0}\right)^{\frac{\kappa-1}{\kappa}}\right)\right] + c_0^2} \tag{7}$$

and finally leads to the mass flow as a function of the measured values of p_0, p_2 and T_0. The test tunnel velocity c_0 is determined in the same way as c_2 via test tunnel nozzle far upstream of the test

rig. The values for c_p and R are taken from literature and the cross section of the bellmouth exit A_2 is known:

$$\dot{m}_{basic} = \frac{p_0}{RT_0}\left(\frac{p_2}{p_0}\right)^{\frac{1}{\kappa}}\sqrt{2c_pT_0\left(1-\left(\frac{p_2}{p_0}\right)^{\frac{\kappa-1}{\kappa}}\right)+c_0^2}\cdot A_2\cdot C_d. \tag{8}$$

In addition to Eq. 1, the discharge coefficient C_d has been added to the equation. It covers the influence of the boundary layer displacement thickness on the mass flow. Based on the Reynolds number [3] and the position of the measurement plane relative to the bellmouth radius [1], a value of $C_d = 0.99$ has been defined. This allows for the calculation of the current mass flow for any specific fan operation point.

Mass flow via DIN-5167 equations

The DIN-5167 standard [11], that defined the installed intake design, is providing a set of equations to determine the mass flow based on geometric relations and fluid parameters:

$$\dot{m}_{DIN} = \frac{C}{\sqrt{1-\beta^4}}\varepsilon\frac{\pi}{4}{D_2}^2\sqrt{2\Delta p\rho_0}. \tag{9}$$

It relies on the bellmouth discharge pressure $\Delta p = p_1 - p_2$ and the geometric ratio $\beta = {}^{D_2}/_{D_1}$ of the exit and entry cross section. Besides the geometric dependency, the empiric throughflow coefficient C is solely dependent on the Reynolds number at the bellmouth entry Re_{D1}

$$C = 0.990 - 0,2262\cdot\beta^{4.1} - \left(0.00175\cdot\beta^2 - 0.0033\cdot\beta^{4.15}\right)\left(\frac{10^6}{Re_{D1}}\right)^{1.15} \tag{10}$$

The Reynolds number of the described experiment lies in the range of $Re_{D1} = 4\times10^6$ to 6×10^6 which leads to a calculated mean value of $C = 0.9470$. This lies in the range of the tabular constant C-value of $C = 0.9462$ that is provided by the DIN for $Re_{D1} = 2\times10^6$ to 1×10^7. To reflect the compressibility of the fluid, the DIN standard introduces the expansion number ε

$$\varepsilon = \sqrt{\left(\frac{\kappa\tau^{2/\kappa}}{\kappa-1}\right)\left(\frac{1-\beta^4}{1-\beta^4\tau^{2/\kappa}}\right)\left(\frac{1-\tau^{(\kappa-1)/\kappa}}{1-\tau}\right)}. \tag{11}$$

The pressure ratio of the bellmouth is described by $\tau = {}^{p_2}/_{p_1}$.

It is important to note that the presented bellmouth design has an exit diameter of $D_2 = 650\,\text{mm}$ which falls outside the DIN applicability range of $50\,\text{mm} < D_2 < 630\,\text{mm}$. Despite the awareness of potential shortcomings, the technique is still employed to introduce a second comparative value to the presented study and to understand its limitations.

EXPERIMENT VS NUMERICAL STUDY

In order to assess the efficacy of the described mass flow approach, the experimental measurement has been replicated within the CFD results. Consequently, the same pressure tapping positions have been implemented, and the results are being compared to those of conventional CFD analysis. This serves as a benchmark for determining the accuracy of the chosen approach. The resulting plots of three speedlines (4000, 6000 and 8020 rpm) are shown in Fig. 3 (left).

The solid black lines represent the three different speed lines derived from the fully informed CFD data. Each data point on the curve represents a Fan Pressure Ratio (FPR) versus Mass Flow Ratio (MFR) relationship, where FPR is the total pressure rise behind the Outlet Guide Vanes (OGV) relative to the measurement plane in front of the fan, and MFR is the corrected mass flow rate measured

in the plane downstream of the fan stage. The dashed green lines employ the identical FPR data as the black curves, thus facilitating a comparison of the mass flows. In contrast, the MFR is calculated from the CFD data in accordance with the fundamental fluid mechanics methodology outlined in the preceding section. The dashed blue lines represent the outcomes of the DIN equations applied to the CFD data, while the red circles illustrate the actual measured values obtained through an MFR calculation based on fundamental fluid mechanics principles, as previously described, but with experimental data instead of numerical results. The FPR is measured with the measurement rakes downstream of the OGV (see Fig. 1b).

The initial conclusion drawn from the presented plot is that the method used to determine the mass flow is flawed, resulting in an overestimation of the actual mass flow compared to the values derived from the comprehensive CFD analysis. The second significant outcome is that the experimental mass flow determination aligns closely with the CFD replication, as evidenced by the red dots' precise alignment with the dashed green lines at 4000 rpm and 6000 rpm. At 8020 rpm, the experimental mass flow appears to be lower than the numerical replication of the experiment (CFD-EXP). This discrepancy seems to be related to flaws in the chosen approach, which are also responsible for the deviations at low speeds, but appear to become more dominant at high speeds. Furthermore, it can be observed that the DIN equation approach (dashed blue lines) is less accurate than the calculation via energy equation under these circumstances. In order to gain insight into the origin of the deviation, a simple difference between the benchmark MFR (solid black) and the two calculated MFRs (dashed green and blue) has been plotted in Fig. 3 (right), with the benchmark data on the x-axis. The discrepancy in mass flow between the comprehensive data set obtained from CFD and the replicated experiment based on the CFD data, which assumes homogeneous velocity and density distributions in the measurement plane, is expressed as

$$\Delta MFR = \dot{m}_{CFD-EXP} - \dot{m}_{CFD}. \tag{12}$$

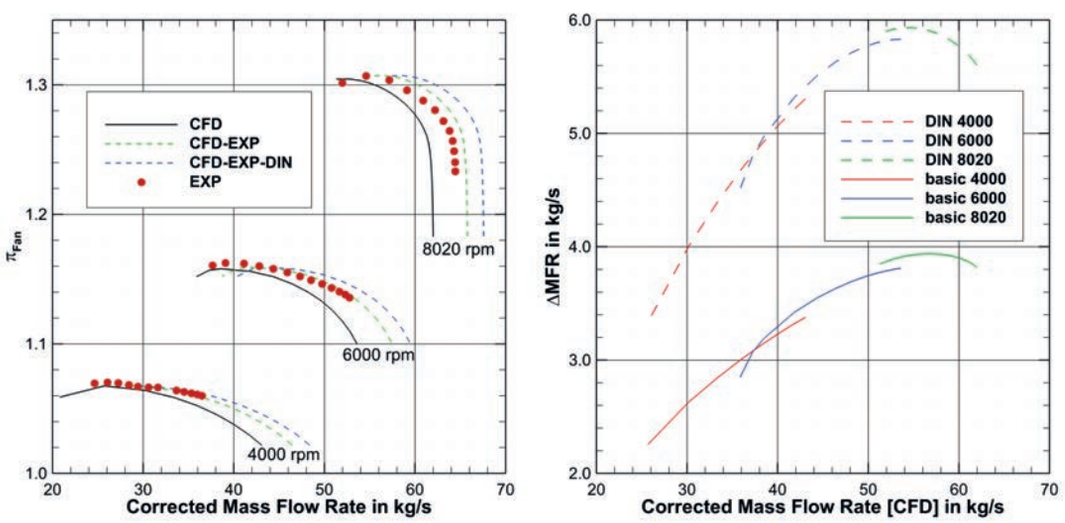


Figure 3: Compressor map of fully informed CFD, replica of the experimental measurement and real experimental data (left). Delta between CFD and CFD-Replica for "basic" and DIN equation approach (right).

In Fig. 3 (right), it can be observed that the difference at highest mass flows for the *basic* approach is roughly $4\,\mathrm{kg\,s^{-1}}$ while appearing mainly constant. At these conditions, high Mach numbers near the casing are present and fluid compressibility dominates the flow field. This leads to a high static pressure variation along the span. Therefore, the assumption of homogeneous flow conditions is violated at high mass flows. Along the highest iso-speedline, there is no monotonic increase in delta

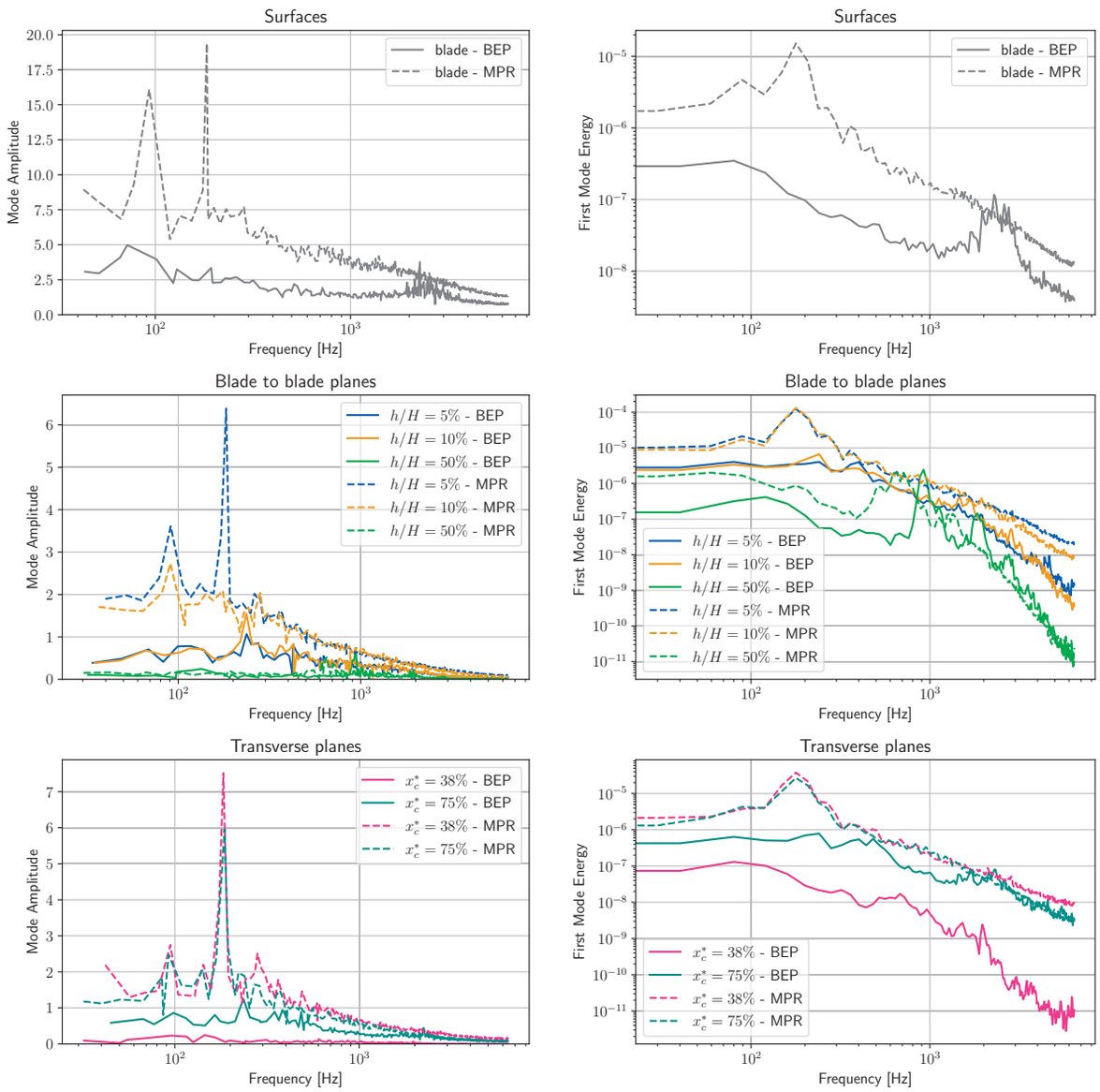


Figure 5: Spectral response of the computed modal content obtained with DMD (left) and SPOD (right).

are clearer in the SPOD reconstruction. At MPR, the instability is associated to the large lobes that develop along the pressure side of the airfoil. Phase opposition can be clearly distinguished. The lobes are translating along the blade in the time reconstructions. The lobe sign alternance is associated to the emission of vortices by the tip leakage jet, which are clearly identified on the suction side (on the right side of the blade) in the inset picture in the SPOD mode reconstruction. It can be concluded that the TLV breakdown is amplified by the pressure and suction side coupling through the clearance.

CONCLUSIONS

Numerical simulations of the compressor cascade of Virginia Tech (VT) using the hybrid Shear-Blended Eddy Simulation (SBES) approach for two different flow coefficients corresponding to the best efficiency point (BEP), the maximum pressure rise (MPR) have been performed. The overall performances between SBES and RANS are identical at BEP, but pressure rise is higher at MPR highlighting the role of unsteady flow patterns at these operating conditions. The use of a scale-

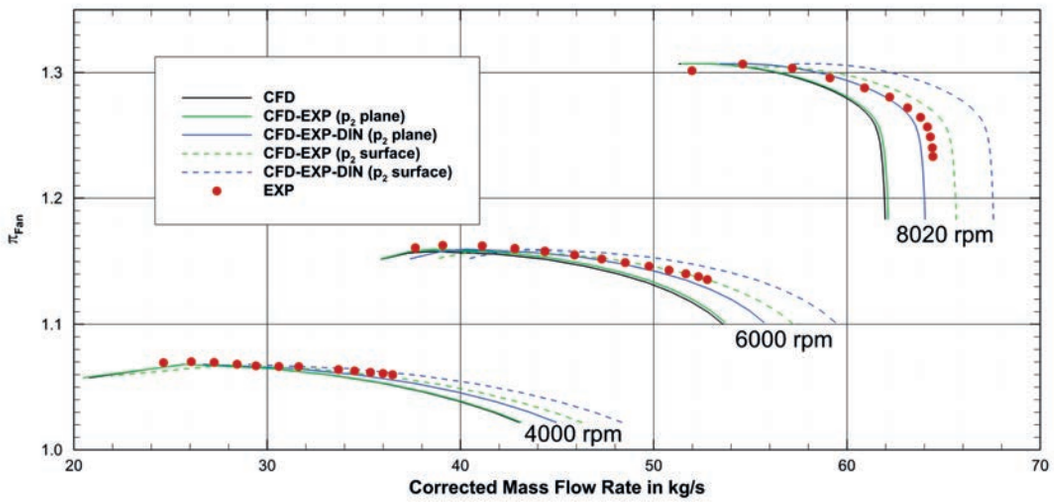


Figure 5: Compressor map of the proposed mass flow approaches using $p_{2,plane}$ versus $p_{2,surface}$.

The remaining discrepancies are a consequence of the simplifications made in the calculations of density and velocity, which directly affect the resulting mass flows. It is evident that the most effective method for enhancing the precision of the mass flow determination in this configuration would be to incorporate a longer cylindrical section between the bellmouth exit and the rotor plane, with the objective of decoupling both components and minimising fan effects. However, as the data collection cannot be replicated at this stage, it is recommended that a correction is made to the existing data set. Due to the overall weaker performance, the DIN approach is not part of the following discussion.

MASS FLOW CORRECTION

Two methods for correcting the mass flow have been identified. One promising approach involves a mathematical correction based on CFD results that adjusts the $p_{2,surface}$ measurement towards the correct value of $p_{2,plane}$. An alternative approach is to "calibrate" the empirical DIN equations using fully informed CFD results. This would yield a significantly lower through flow coefficient C and replace the given definition of C in Eq. 10. However, this is not included here as a direct p_2 correction is expected to give more favourable results with fewer assumptions. The analysis of the delta between $p_{2,surface}$ and $p_{2,plane}$ (cf. Fig. 4) might lead to the impression that the rotor and spinner influence on the static pressure probes is of non-linear nature. However, plotting the ratio $p_{2,surface}/p_{2,plane}$ against $p_{2,surface}$ in Fig. 6 shows a linearity in the flawed measurement, that is representable by a polynomial. While a 1st degree polynomial would be sufficient, a 2nd degree polynomial is preferred for increased accuracy. The corrected $p_{2,corrected}$ values are displayed in Fig. 6 (right).

The polynomial, which represents the dependency of $p_{2,plane}$ to $p_{2,surface}$ is given by

$$\frac{p_{2,surface}}{p_{2,plane}} = -5.672 \times 10^{-12} p_{2,surface}^2 + 2.782 \times 10^{-6} p_{2,surface} + 7.768 \times 10^{-1}. \tag{13}$$

The polynomial and the effect of this correction on the CFD data is illustrated in Fig. 6. Incorporating the aforementioned correction to the initial mass flow determination for the experimental data, as shown in Fig. 3, results in the orange circles in Fig. 7. It can be observed that this correction improves the mass flow in the same quality for all three speed lines. This confirms the previous statement of an increasing dominance of an impaired measurement at high speeds.

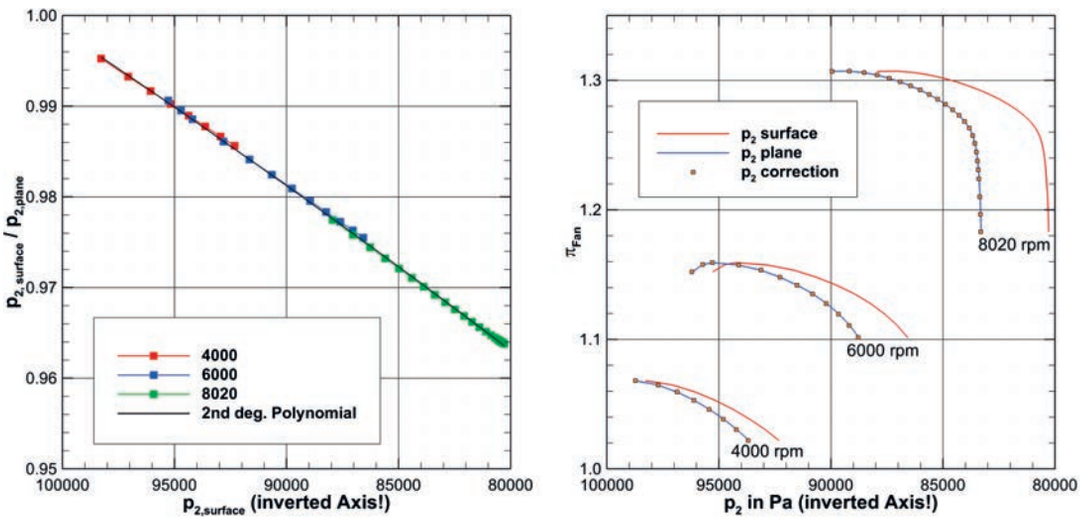


Figure 6: Correlation between $p_{2,plane}$ and $p_{2,surface}$ (left). $p_{2,surface}$-correction via 2nd degree polynomial (right).

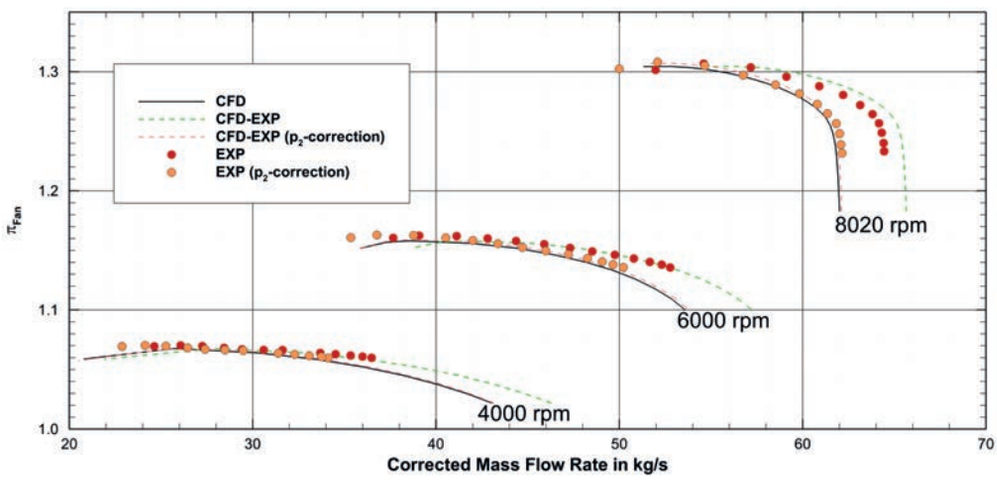


Figure 7: Compressor map with corrected p_2-measurement for the "basic"-approach.

SUMMARY AND OUTLOOK

This paper presents a methodology for mass flow determination in a challenging experimental setup. The initial results are evaluated by a comparison with the results of a representative CFD simulation. It was found that the experimental approach was flawed in this adaptation and required appropriate correction. Given the circumstances and the considerable amount of data already collected, it is preferable to make a post-processing correction rather than repeat the experimental campaign with an improved measurement. The desired improvement is achieved by analysing the factors involved and presenting a mathematical correction of the erroneous parameter. It can be seen that a satisfactory correction is possible. The total error of the approach within the whole measurement chain is the subject of ongoing analyses. A further potential for improvement lies in a more accurate calculation of the discharge coefficient. The presented mass flow determination with the described correction in CFD amounts to an average of about 0.3 %.

However, the correction presented in this exact manner is only suitable for the setup shown and is not, at this stage, applicable to other cases without taking the same steps, including a CFD replica to determine the necessary polynomial. The aim of this paper is to provide guidance for similar cases.

[17] A. B. Drame, “Simulation et modélisation de l’écoulement de jeu dans un compresseur axial,” Ph.D. dissertation, École de technologie supérieure, Montréal, Canada, **2024**.

[18] A. B. Drame and M. Sanjosé, *Analyse et modélisation des pertes dans une grille rectiligne de compresseur avec jeu.* Transactions of the Canadian Society for Mechanical Engineering, **2024**. DOI: 10.1139/tcsme-2024-0008.

[19] P. J. Schmid, *Dynamic mode decomposition of numerical and experimental data*, Journal of Fluid Mechanics vol. 656, pp. 5–28, **2010**. DOI: 10.1017/S0022112010001217.

[20] A. Towne, O. T. Schmidt, and T. Colonius, *Spectral proper orthogonal decomposition and its relationship to dynamic mode decomposition and resolvent analysis*, Journal of Fluid Mechanics vol. 847, pp. 821–867, **2018**. DOI: 10.1017/jfm.2018.283.

[21] O. T. Schmidt and T. Colonius, *Guide to Spectral Proper Orthogonal Decomposition*, AIAA Journal vol. 58, no. 3, pp. 1023–1033, **2020**. DOI: 10.2514/1.J058809.

DETECTION OF VORTICAL STRUCTURES IN THE LEAKAGE FLOW OF A LOW-SPEED AXIAL FAN

Bendegúz NYÁRI[1], Kinga Andrea KOVÁCS[2], Esztella BALLA[2]

[1] *HUN-REN-BME Condensed Matter Research Group, Budapest University of Technology and Economics, Műegyetem rkp. 3., H-1111 Budapest, Hungary*

[2] *Department of Fluid Mechanics, Faculty of Mechanical Engineering, Budapest University of Technology and Economics, Műegyetem rkp. 3., H-1111 Budapest, Hungary*

SUMMARY

This study investigates the vortices generated in the tip leakage flow of a low-speed axial fan. Particle Image Velocimetry (PIV) measurements provide detailed velocity data to describe these complex flow structures. The study utilizes the Lagrangian Averaged Vorticity Deviation (LAVD) method to objectively identify vortex regions and their centres, surpassing traditional methods such as the Q criterion that rely on subjective thresholds. This method, previously validated in numerical simulations of bluff bodies and an axial fan, is extended to experimental turbomachinery data in this research. It is found that the LAVD method adequately identifies the core and the boundary of vortices in the leakage flow.

INTRODUCTION

Low-speed axial fans are critical components in systems that directly affect human comfort and industrial efficiency, such as heating, ventilation and air conditioning systems, household appliances, and transportation devices. The noise levels of these fans is of significant concern as they often operate in environments where humans are present. Excessive noise can affect comfort, productivity, and health, emphasizing the need for quieter operation. Another important factor is energy consumption. Poor aerodynamic performance can lead to increased power usage, undermining sustainability goals and raising operational costs.

The performance of fans can be affected by the formation of vortical structures during operation which can also induce vibrations. Persistent vibrations may lead to mechanical wear, reduced lifetime, or

failure of fan components, resulting in costly repairs or replacements. In addition, vibration issues caused by unmitigated vortical activity can escalate into safety hazards in critical applications, such as in transportation or industrial machinery, where fan failure could have serious consequences. Vortices may form at different locations (e.g. downstream of the blades or supporting struts). In addition to vibration issues, vortices may also cause sound generation.

The present paper focuses on the vortices that originate in the tip leakage flow of an axial fan. Tip-leakage flow, which can roll up to form the tip-leakage vortex (TLV), is one of the most prominent noise sources of low-speed fans [1]. In many cases the TLV exhibits an unsteady phenomenon, which is called vortex wandering. For the quantitative investigation of the vortex motion it is desirable to be able to detect the vortex and its core objectively and automatically. Most of the common vortex detection methods (e.g. Q criterion) rely on arbitrarily set threshold values, which makes the evaluation time-consuming and subjective. In the present paper, the capabilities of the LAVD technique [2] for the detection of the TLV of a low-speed fan with rotating shroud are demonstrated. PIV results from measurements on a low-speed fan with rotating shroud [3], [4] are processed. The LAVD method has already been applied for various cases, like satellite-derived ocean velocity data [5], the blood flow in the human heart based on phase contrast magnetic resonance (PC-MRI) data [6]–[8], or on numerical simulations carried out on bluff bodies [9], and on a case study of an axial fan (non-identical to the fan presented herein) [10]. The benefit of the LAVD method compared to other vortex detection methods is that it is capable of determining not only the boundary of the vortex region, but also its centre. Furthermore, during the application of the method only geometrical parameters are required, and no subjective threshold values are used.

The novelty of the present paper is the application of the LAVD method to measurement data, which may be contaminated with measurement error. To the authors' best knowledge this is the first occasion that the LAVD method is applied to PIV measurements on turbomachinery. In the first part of this paper, the setup of the PIV measurements for the low-speed fan rotor is introduced. Then the LAVD vortex detection method for turbomachinery flow data, specifically for PIV measurements, is presented. Finally, the detection of vortical structures with the LAVD method is described and a brief comparison with results obtained with other methods is given.

THE SETUP OF THE PIV MEASUREMENT

Experimental facility

The PIV measurements were carried out in the aeroacoustics laboratory of DIME [3]. The measurement setup is presented briefly herein, in order to make the results interpretable. The test was carried out according to the ISO 10302 [11] standard, making it possible to carry out measurements at different operating points. The fan rotor consists of 9 blades and was manufactured from polyamid with glass fibres. The chord of the blades is 72 mm at the tip and 65 mm at the hub. The radii of the hub and the blade tip are $r_{\text{hub}} = 90.5$ mm and $r_{\text{tip}} = 227$ mm, respectively. The external diameter of the rotating shroud is 460 mm. The fan is mounted without stator vanes. Further details of the fan and the test configuration are reported in Canepa *et al.* [12], [13].

Two operational points were investigated. A first operating state, DP3000, corresponds to the design point with rotational speed $\Omega = 3000$ rpm, flow rate $Q = 1.174$ m^3/s and static pressure rise $\Delta p = p_{\text{out}} - p_0 = 388$ Pa. The flow and pressure coefficients were $\phi = Q/(u_{\text{tip}}\pi r_{\text{tip}}^2) = 0.098$ and $\Psi = \Delta p/(0.5\rho_0 u_{\text{tip}}^2) = 0.121$, respectively, where u_{tip} is the blade tip speed. A second operating point, DP2400, was also investigated, with $\Omega = 2400$ rpm. DP2400 was chosen for investigation because of a change in flow patterns between DP3000 and DP2400 (see [3]).

Measurement techniques, instrumentation and data processing

Two-dimensional PIV measurements were carried out on the flow around the fan, thus only two velocity components could be measured, data on the tangential component is absent. Two cameras were used for recording with a sampling frequency of 6 Hz, which is too low to obtain properly time resolved data of the rotating fan. However, time-averaged phenomena could still be investigated in the following manner. The instantaneous velocity vector fields were sorted into 90 phase bins per revolution with each bin representing a 4° angular window in the relative frame, resulting in 10 bins per blade passage. In order to increase the statistical reliability, the data have been ensemble averaged for the 9 blade passages, i.e. the velocity fields belonging to a given bin of each blade passage are sorted together. This results in smoother trends of the ensemble averaged velocity components, but the unresolved unsteadiness could increase.

The laser sheet has been focused on the upper side of the tip ring in a vertical meridional plane as shown in Fig. 1. The investigated area, has been set in front of the gap, ranging between $r = 200$ mm and $r = 295$ mm (i.e. $r/r_{\text{tip}} = 0.870 - 1.283$), with an axial extension of 70 mm $= 0.308 r_{\text{tip}}$. The velocity data were obtained on a square grid of 1.4 mm step.

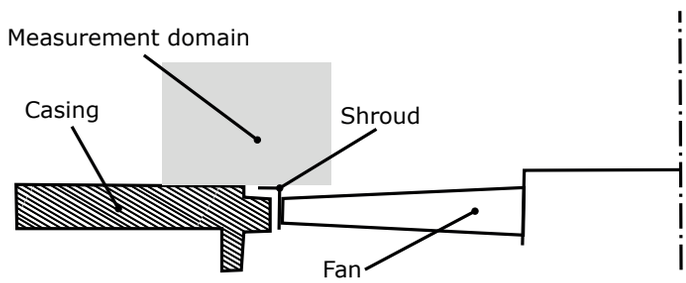


Figure 1: Position of the PIV measurement domain.

APPLIED VORTEX DETECTION METHODS

LAVD method

The Lagrangian-Averaged Vorticity Deviation (LAVD) method was proposed by Haller *et al.* [2]. The LAVD is derived from the dynamic rotation tensor, which is obtained from the dynamic polar decomposition of the deformation gradient. This provides an objective global vortex criterion which is entirely frame-invariant, and mathematically it can be expressed in the following manner, as proposed in [2] (it is the trajectory integral of the absolute difference between the vorticity and its spatial mean):

$$\text{LAVD}^{t}_{t_0}(x_0) = \int_{t_0}^{t} |\omega\left(x(s,x_0),s\right) - \overline{\omega}(s)|\,\mathrm{d}s \tag{1}$$

where t_0 [s] is the starting time instant of the integration, t [s] is the final time instant of the integration, x_0 [m] denotes the initial particle positions, $\omega(x,s)$ [s^{-1}] is the instantaneous vorticity distribution, $x(s;x_0)$ [m] denotes the instantaneous particle positions, s [s] is the variable of integration, and $\overline{\omega}(s)$[s^{-1}] is the spatial mean of the vorticity. The LAVD method does not depend on an arbitrarily chosen threshold value, and according to Haller *et al.* [2], a rotationally coherent Lagrangian vortex must satisfy the following conditions:

1. It is an evolving material domain $D(t)$ where $D(t_0)$ is filled with tubular level surfaces of

$\mathrm{LAVD}^{t}_{t_0}(x_0)$ and the LAVD values are decreasing as one moves outwards.

2. The boundary $B(t)$ of $D(t)$ is a material surface where $B(t_0)$ is the outermost tubular level surface (minimum) of $\mathrm{LAVD}^{t}_{t_0}(x_0)$ in $D(t_0)$.

3. The center $C(t)$ of $D(t)$ is a material set where $C(t_0)$ is the innermost member (maximum) of $\mathrm{LAVD}^{t}_{t_0}(x_0)$ in $D(t_0)$.

During the detection, the values of three vortex detection parameters have to be set. These parameters are the following: number of contour levels intended to be extracted (Nct), minimum perimeter of sought vortices (MinLength, %), and maximum convexity deficiency threshold (DeficiencyThresh, %). The minimum perimeter of sought vortices is expressed as a percentage of the characteristic length of the given geometry, in this case the length of the blade chord at the tip, i.e. 72 mm. This idea was proposed in [9], because originally an absolute length scale had to be set which was harder to interpret for different setups ranging from atmospheric to engineering flow case studies. The allowable deviation from an ideal convex vortex can be set with the DeficiencyThresh parameter. It is defined based on the ratio of the area of the detected vortex and its convex hull. If the deficiency is above the set DeficiencyThresh, then the detected vortex will not be considered a true vortex. The physical meaning of these parameters (Nct, MinLength, DeficiencyThresh) can be well interpreted, and they do not correspond directly to the LAVD values, thus their setting is not cosidered arbitrary. The values of these parameters were set based on the findings of previous studies [9], [10].

Q criterion

Probably one of the most widespread and well-known vortex identification methods is the Q-criterion. Hunt et al. [14] defined vortices in the following way (Q is the second invariant of G with G being the Jacobian of the velocity field):

$$Q = \frac{1}{2}(\|\Omega\|_F^2 - \|S\|_F^2) > 0 \tag{2}$$

where $S = \frac{1}{2}[G + G^{\mathrm{T}}]$ is the strain rate tensor, and $\Omega = \frac{1}{2}[G - G^{\mathrm{T}}]$ is the angular rotation rate tensor, with the Frobenius norm $\|.\|_F$.

Based on Eq. (2), a vortex exists where there is more rotation than stretching. During vortex detection the following criterion is used: $Q > Q_{\mathrm{thresh}}$, where Q_{thresh} is an individually chosen threshold value, which is not necessarily equal to zero and has to be fine-tuned. Setting the threshold too low (high) can lead to the detection or elimination of physically meaningless or meaningful vortices, respectively.

Omega-Liutex method

The Omega-Liutex method was proposed by Dong et al. [15] and is a combination of the Ω [16] and the Liutex [17] methods. The Ω-method has the advantage that it does not need an arbitrarily chosen threshold value, and the Liutex method has the advantage that it can differentiate between rotational vortices and shear layers. After the calculation of Ω_R (representing the Omega-Liutex field, presented in detail in [15] similarly to the Ω-method), $\Omega_R = 0.52$ is advised [18] to be chosen to visualize the vortex structures.

VORTEX DETECTION

All three vortex detection methods are applied to the ensemble-averaged data corresponding to the two operating conditions (DP2400 and DP3000). The three-dimensional representation of the results are shown in Fig. 2. The blue band indicates the position of the clearance between the rotating shroud

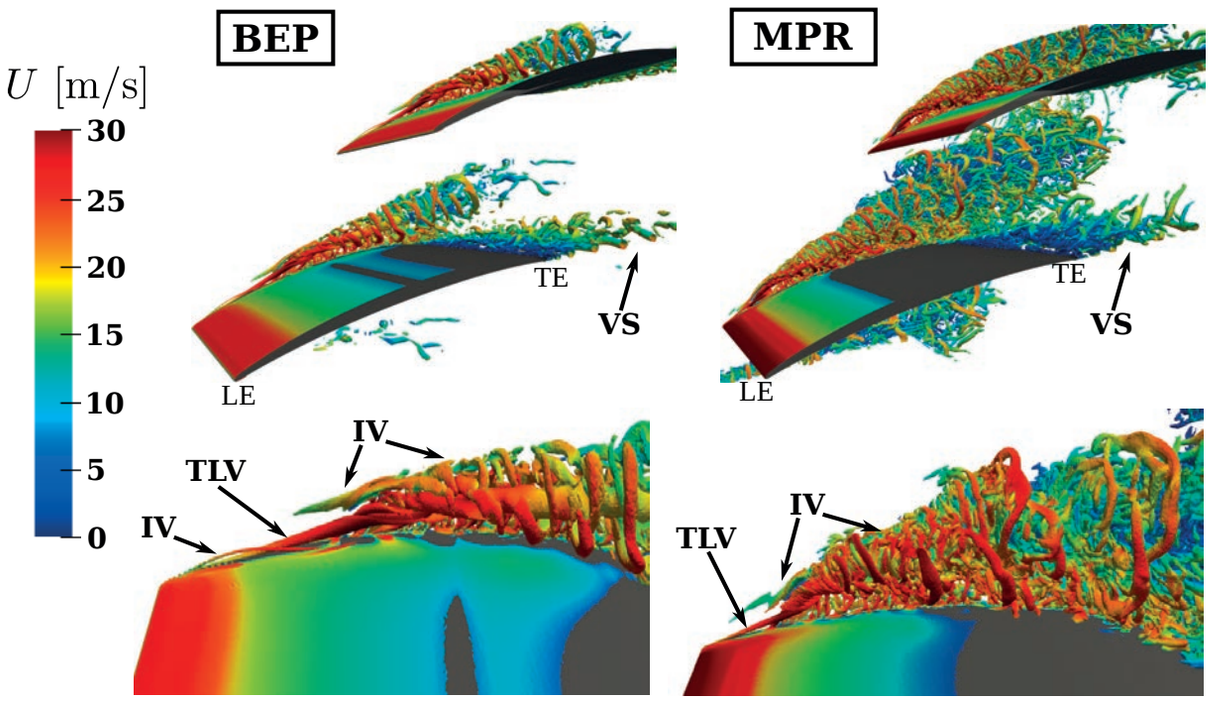


Figure 3: Isosurface of Q criterion with value $Q = 10^6\ s^{-2}$ coloured by the velocity magniture for identification of coherent structures in the tip gap flow at BEP (left) and MPR (right) operating conditions.

at each frequency. Towne *et al.* showed that the two decomposition techniques are related [20]. In the present challenging problem dominated by low frequency content, they provide different modal and frequency resolution. The modal structures at selected frequencies are compared and analyzed in section 7.

Data acquisition

The SBES simulations are continued for another 6 T_c and data are collected at a sampling frequency of 12.8 kHz on blade surfaces, planes parallel to the casing and planes perpendicular to the chord line which are shown in Fig 4. In the present work the DMD and SPOD are performed on the temporal evolution of the static pressure. A single flow quantities is selected for reduced computation. The use of pressure, which is related to velocity components through Bernoulli's equation, is believed to provide a meaningful and thorough description of the flow dynamics. For the SPOD a Welch periodogram is first applied. The time signal is divided into 15 blocks of 2 T_c allowing an overlap of 80% between the blocks. A Hanning windowing and about 20% of zero padding are applied, before a fast Fourier transform is applied to each segment. The SPOD spectrum is limited to a resolution of 60 Hz. Modal decomposition is applied independently for each plane, considering the pressure only in a first approach. For the DMD analysis, the frequency resolution is an outcome of the calculated eigenvalues [19]. Given the signal length, a resolution of about 10 to 15 Hz between consecutive eigenvalues is observed.

RESULTS

SPOD and DMD spectra

Figure 5 shows the energy distribution of the modes obtained with the DMD and SPOD decompositions for selected planes of analysis. Note that for the SPOD, only the energy associated to the first mode is shown, as it is dominant over the higher order modes. For the DMD, the pressure mode

through planes 5-2 and eventually becomes undetectable in plane 3. The vortex near the blade tip region does not appear to change its position, thus it might be a false detection, and high LAVD values may be related to the high vorticity present in the boundary layer of the rotating shroud. The vortex detected at around $r/r_{\text{tip}} = 0.97$ and 0.9 may be related to a vortex shed from the blade trailing edge.

For DP3000 the positions of the observed vortices are similar to DP2400, however their spatial extent is smaller. In this case, vortical structures move radially outwards as can be observed from Plane 4 to Plane 1, from $r/r_{\text{tip}} = 1.14$ to 1.17. The magnitude of the LAVD contour value of the radially outermost vortex decreases as it moves radially outwards, and in Plane 2 it eventually becomes undetectable. There is also a vortex pair present in the clearance which seems to have a fixed position. The vortical region detected around $r/r_{\text{tip}} = 1$ may be again related to the boundary layer forming on the shroud. The vortex detected in Plane 5 at around $r/r_{\text{tip}} = 0.94$ may be related to the trailing edge vortex of the blade.

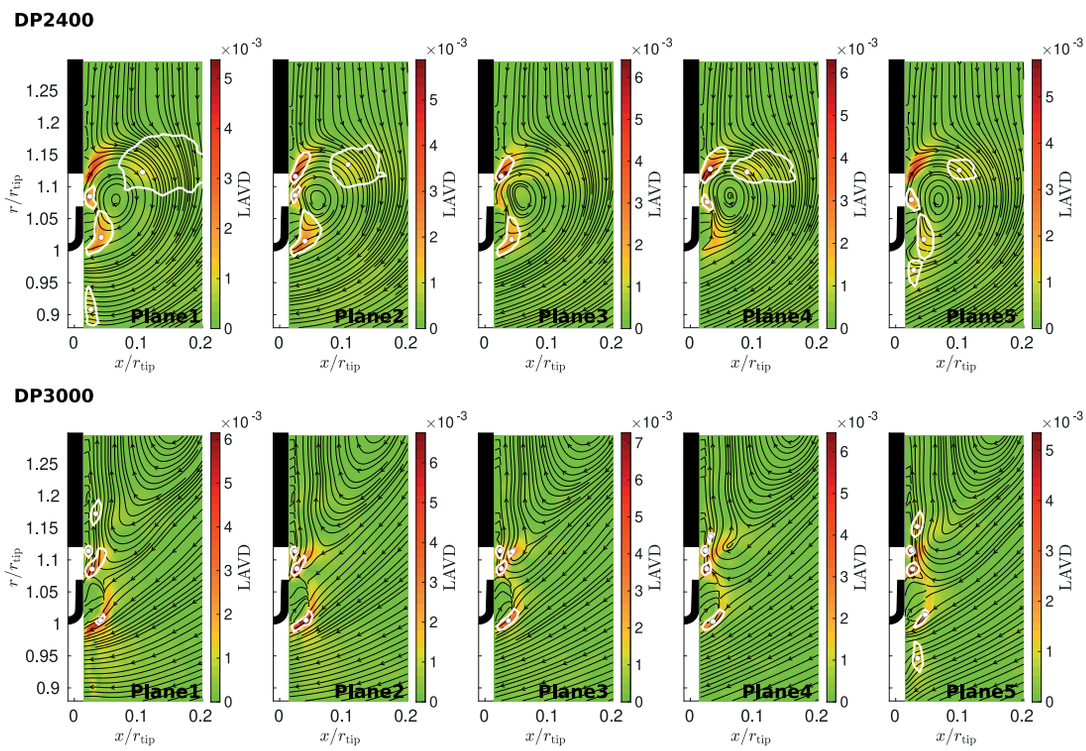


Figure 3: The LAVD field for the DP2400 and the DP3000 operation state in the different planes of the measurement.

SUMMARY AND CONCLUDING REMARKS

It is shown that the LAVD method is able to identify vortices not only in simulational data but also in PIV measurement data. The Omega-Liutex method provided highly contaminated vortex detection results, which suggests its unreliability for this specific case. The presented vortex detection results are in accordance with the findings of [3]. The LAVD method offers a convenient way for the detection of the vortex core and also for the boundary of the vortex region. Since it only requires parameters which are easy to comprehend, the setting of its parameters is more straight forward compared to the Q criterion. The parameter setting is based on physical features of the setup, e.g. the blade chord herein. The output is quantifiable (e.g. the exact position of vortex centers), which makes the detection with the LAVD technique easy to automatize. The drawbacks of the method include higher

computational time, compared to the other presented methods, which is more significant for three-dimensional cases. The computational cost is two order of magnitudes higher than for the Q and the Omega-Liutex methods.

A possible future research objective is the automatization of the detection and tracking of the vortices. This would allow an easy and convenient categorization and description of vortical structures both for experimental and simulation data available with sufficient spatial resolution.

ACKNOWLEDGMENT

The research reported in this paper is part of project no. 143204, implemented with the support provided by the Ministry of Innovation and Technology of Hungary from the National Research, Development and Innovation Fund, financed under the OTKA K 22 funding scheme and project no. TKP-6-6/PALY-2021, implemented with the support provided by the Ministry of Culture and Innovation of Hungary from the National Research, Development and Innovation Fund, financed under the TKP2021-NVA funding scheme. The work of Esztella BALLA was supported by the ”Back into the Science!” scholarship (”Vissza a Tudományba! ösztöndíj”) of the BME. The work of Kinga Andrea KOVÁCS was supported by the EKÖP-24-3-BME-194 University Research Scholarship Program of the Ministry for Culture and Innovation from the source of the National Research, Development, and Innovation Fund.

REFERENCES

[1] B. Lendvai and T. Benedek, *Experimental and numerical investigation of the blade tip-related aeroacoustic sound source mechanisms of a ducted low-speed axial flow fan*, Applied Acoustics vol. 215, **2023**.

[2] G. Haller, A. Hadjighasem, M. Farazmand and F. Huhn, *Defining coherent vortices objectively from the vorticity*, Journal of Fluid Mechanics vol. 795, pp. 136–173, **2016**.

[3] E. Canepa, A. Cattanei, F. M. Zecchin and D. Parodi, *Large-scale unsteady flow structures in the leakage flow of a low-speed axial fan with rotating shroud*, Experimental Thermal and Fluid Science vol. 102, pp. 1–19, **2019**.

[4] E. Canepa, A. Cattanei, F. M. Zecchin and D. Parodi, *Instantaneous piv data related to the leakage flow of a low-speed axial-flow fan with rotating shroud*, Data in brief vol. 24, p. 103 895, **2019**.

[5] M. Serra and G. Haller, *Forecasting long-lived lagrangian vortices from their objective eulerian footprints*, Journal of Fluid Mechanics vol. 813, pp. 436–457, **2017**.

[6] K. Yang, S. Wu, H. Zhang, D. N. Ghista, O. W. Samuel and K. K. Wong, *Lagrangian-averaged vorticity deviation of spiraling blood flow in the heart during isovolumic contraction and ejection phases*, Medical & Biological Engineering & Computing vol. 59, pp. 1417–1430, **2021**.

[7] K. Yang, S. Wu, D. N. Ghista, D. Yang and K. K. Wong, *Automated vortex identification based on lagrangian averaged vorticity deviation in analysis of blood flow in the atrium from phase contrast mri*, Computer Methods and Programs in Biomedicine vol. 216, p. 106 678, **2022**.

[8] K. Yang, S. Zeng, D. N. Ghista, X. Hu, S. Lv and K. K. Wong, *Automated cardiac vortex ring identification and characterization based on recurrent all-pairs field transforms and lagrangian averaged vorticity deviation*, Computers in Biology and Medicine vol. 179, p. 108 836, **2024**.

[9] K. A. Kovács and E. Balla, *Parameter identification of the lagrangian-averaged vorticity deviation vortex detection method through the investigation of fluid flow around solid bodies*, Periodica Polytechnica Mechanical Engineering vol. 67, no. 4, pp. 293–302, **2023**.

[10] E. Balla, K. A. Kovács and B. Lendvai, *Comparison of vortex detection methods on the numerical simulation of tip leakage flow of a low-speed axial fan*, in *Turbo Expo: Power for Land, Sea, and Air*, American Society of Mechanical Engineers, vol. 87981, **2024**, V006T10A002.

[11] ISO 10302, "Acoustics-method for Measurement of Airborne Noise Emitted by Small Air-moving Devices," International Organization for Standardization, ISO Geneva, Switzerland, Standard, **1996**.

[12] E. Canepa, A. Cattanei, F. M. Zecchin, G. Milanese and D. Parodi, *An experimental investigation on the tip leakage noise in axial-flow fans with rotating shroud*, Journal of Sound and Vibration vol. 375, pp. 115–131, **2016**.

[13] E. Canepa, A. Cattanei, F. Jafelice, F. M. Zecchin and D. Parodi, *Effect of rotor deformation and blade loading on the leakage noise in low-speed axial fans*, Journal of Sound and Vibration vol. 433, pp. 99–123, **2018**.

[14] J. C. Hunt, A. A. Wray and P. Moin, *Eddies, streams, and convergence zones in turbulent flows*, Studying turbulence using numerical simulation databases, 2. Proceedings of the 1988 summer program, **1988**.

[15] X. Dong, Y. Gao and C. Liu, *New normalized rortex/vortex identification method*, Physics of Fluids vol. 31, no. 1, **2019**.

[16] C. Liu, Y. Wang, Y. Yang and Z. Duan, *New omega vortex identification method*, Science China Physics, Mechanics & Astronomy vol. 59, pp. 1–9, **2016**.

[17] S. Tian, Y. Gao, X. Dong and C. Liu, *Definitions of vortex vector and vortex*, Journal of Fluid Mechanics vol. 849, pp. 312–339, **2018**.

[18] C. Liu, Y.-s. Gao, X.-r. Dong, *et al.*, *Third generation of vortex identification methods: Omega and liutex/rortex based systems*, Journal of Hydrodynamics vol. 31, pp. 205–223, **2019**.

[19] K. A. Kovács and E. Balla, *Quantitative comparison of vortex identification methods in three-dimensional fluid flow around cylinder geometries*, International Journal of Heat and Fluid Flow, **(Accepted)**.

B3 Specialized Fans For Niche Applications

9 April - 16:45 - Room 2 Miles Davis

Chairmen: Nazme Mohsina, Christian Taber

List of papers

Design of a Mixed-Flow Fan for Hair Dryer Application: Acoustic and Fluid Dynamic Improvement

- Mattia PIOVAN – University of Ferrara (Italy)
- Nicola ALDI – University of Ferrara (Italy)
- Michele PINELLI – University of Ferrara (Italy)
- Francesco POMPOLI – University of Ferrara (Italy)
- Alessio SUMAN – University of Ferrara (Italy)
- Nicola ZANINI – University of Ferrara (Italy)
- Emilio VERZÈ – GA.MA Srl (Italy)

Endless Fiber Reinforced Composite Impeller: Modular Design for Different Performance Classes

- Sebastian SPITZER – Technische Universität Dresden, Institute of Lightweight Engineering and Polymer Technology (Germany)
- Jonas Kluger - Technische Universität Dresden, Institute of Lightweight Engineering and Polymer Technology (Germany)
- Richarc Konig - Technische Universität Dresden, Institute of Lightweight Engineering and Polymer Technology (Germany)
- Leon Schroder - Technische Universität Dresden, Institute of Lightweight Engineering and Polymer Technology (Germany)
- Alrik DARGEL – Technische Universität Dresden, Institute of Lightweight Engineering and Polymer Technology (Germany)
- Eckart KUNZE – Technische Universität Dresden, Institute of Lightweight Engineering and Polymer Technology (Germany)
- Christoph EBERT – Technische Universität Dresden, Institute of Lightweight Engineering and Polymer Technology (Germany)
- Maik GUDE – Technische Universität Dresden, Institute of Lightweight Engineering and Polymer Technology (Germany)



DESIGN OF A MIXED-FLOW FAN FOR HAIR DRYER APPLICATION: ACOUSTIC AND FLUID DYNAMIC IMPROVEMENT

Mattia PIOVAN[1], Nicola ALDI[1], Michele PINELLI[1], Francesco POMPOLI[1], Alessio SUMAN[1], Nicola ZANINI[1], Emilio VERZÈ[2]

[1] *University of Ferrara, Via G. Saragat 1, 44122, Ferrara, Italy*

[2] *GA.MA Srl., Viale dei Rivi 4, 29020, Gossolengo, Piacenza, Italy*

SUMMARY

Annually, more than 250 million hairdryers are sold globally. The average CO_2 emissions per hairdryer are estimated to be approximately 25 kg per annum. Consequently, there is a clear need to improve the efficiency of these appliances in order to reduce the electrical power demand. Furthermore, the prolonged use of hair dryers is associated with other problems, including noise emission, particularly from the fan, and weight, which can have adverse effects on the operator's health. The weight of the device can be reduced by utilising plastic materials, while the noise emission can be minimised by optimising the design of the fan and the internal components of the device. The current work presents a methodology for the redesign of the fan in a hairdryer, with the objective of enhancing its efficiency and reducing the acoustic emissions.

INTRODUCTION

One of the most important challenges for hair dryer manufacturers is the reduction of noise emissions withou increasing the weight of their products, which is the other requirement for a professional hairdryer. Inside hairdryer, the principal sources of noise are related to the fan noise and the jet noise caused by the interactio between the airflow and frontal or rear grids, which protect the user from injury [1]. Moreover, the emitte sounds depend on the accessory, i.e. diffusers and nozzles, inserted into the hairdryer [2]. These noise source increase their intensity as the rotational speed of the fan increases due to the higher flow rate elaboratec therefore a reduction of the rotational speed is always beneficial from an acoustic point of view. The con c the reduction of the flow rate is the longer hair drying time. Therefore, a good compromise must be set betwee performance and noise emission. Another aspect that must be taken into account in the design phase of th hairdryer is the required electrical power demand. The aspect with the greatest impact is related to the powe consumption of the resistance employed to generate heat. However, the consumption of the fans should not b overlooked, as it could reach up to 20% of the overall consumption. The work focussed on redesigning th impeller and the internal parts of the hairdryer to decrease the noise emission and increase the efficiency of th fan. According to the literature, the most suitable impeller for the specific application is a mixed-flow one This type of impeller is not commonly used in the literature for two reasons. The first issue concerns th absence of general design rules for this type of turbomachine. In fact, in the literature, only a limited numbe

of works involving the design of mixed-flow fans can be found. For instance, in [3] the effects of different geometrical parameters on the performance of a mixed-flow fan used for a hairdryer application are evaluated using a DOE approach. In [4] the results of a redesign process that focused on noise emission are presented, in which a mixed-flow fan is used to replace a radial flow one. In [5] instead a design process for a Battery Electric Vehicles mixed-flow fan is presented which is finalized to replace an axial flow one to reduce the noise emission. The second issue pertains to the potential challenges associated with the realization of a mixed-flow fan, as opposed to an axial or radial one, given the distinctive shapes involved. This fact can be overcome by the realization of the fan using plastic material, or by means of 3D printing techniques. Moreover, by coupling rapid prototyping with Computational Fluid Dynamics analysis, which is very useful for estimating the performance of a fan [6, 7, 8], the cost for the realization of a prototype can be significantly reduced. As abovementioned, one of the most important noise sources inside a hair dryer is related to the fan [9], this type of acoustic emission can be divided into two components, tonal noise, and broadband noise. The first one is caused by pressure fluctuations, due to the periodic interaction between the rotating blades and the steady parts. Moreover, it is characterized by a harmonic frequency named Blade Passing Frequency, BPF, that depends on the fan number of blades and the rotational speed. The broadband noise instead is caused by the pressure fluctuations due to the turbulence. According to the literature, different strategies can be used to reduce the noise emissions of a fan. For instance, the tonal noise can be reduced by acting on the BPF, moving it to frequencies where the effect of the A-weighting correction is more effective [5] and by increasing the fluid dynamics efficiency of the fan. Regarding the broadband noise, a reduction can be achieved by adding some geometry peculiarity on the blades, i.e. LE/TE serration and LE bumps [10, 11] or by optimizing the blade shape [12].

The current work shows a fluid dynamic redesign for a hair dryer application finalized for acoustic improvement. In the first part, a comparison between experimental data and numerical ones is presented to validate the numerical simulation and to find the fundamental parameters for the redesign process. At this point, the fan is redesigned according to the literature in order to increase efficiency and reduce noise emissions. Initially, only the fan is re-designed, and the original hairdryer case is used, afterward, also the casing is shaped to reduce the flow losses that occur inside the device. In this way, it is possible to separate the effects of the casing shape to the impeller one, in both fan performances and noise emission. In the end, the optimized geometries are prototyped by means of rapid prototyping, i.e. SLS technique, and experimentally tested to assess both fluid dynamics and noise improvements. Regarding the acoustic measurements, the prototypes are tested in a semi-anechoic chamber into two different modalities, the first one is the fan at the design rotational speed while the second one is the fan at the design flow rate.

METHODOLOGY

The performances of the original hairdryer are evaluated experimentally to find the flow rate, the electrical power demand, and the noise emissions at the maximum airspeed of the device. The workflow used to redesign the impeller needs as input the total pressure rise generated by the fan. For this reason, in order to calculate this parameter, the baseline geometry is simulated by means of computational fluid dynamics, CFD. At this point, the design process is performed to increase the flow rate and efficiency at the original rotational speed. The hairdryer casing is then shaped to further enhance the performance of the device. In the end, the optimized geometries are tested experimentally to assess the real improvements in terms of noise emission, electrical power demands, and flow rate.

Experimental setup

The authors decided not to intubate the dryer, but to use an airbox system to aspirate the air surrounding the device. The outlet of the hairdryer instead, is used in free-blowing condition to represent the real operating condition. Figure 1 (left) shows a scheme of the experimental setup used for the determination of the flow rate elaborated by the hairdryer. The flow rate is calculated, in accordance with UNI EN 5801, by dividing the duct section into annular sectors and calculating the average velocity over these sectors. A pitot tube is used to estimate the air velocity. The pressure sensor with its acquisition device has been individually calibrated using a MicroCal PM200+ pressure calibrator. This instrument is the secondary standard of the internal laboratory, which is in turn calibrated against a primary laboratory standard certified by the Italian Accreditation Body (Accredia). The airbox allows the calculation of the fan's rotational speed using a strobe light. A voltage regulator is employed to modify the power supply of the electrical driver, thereby enabling the regulation of

the fan's rotational speed and, consequently, the elaborated mass flow rate. All measurements have been performed without the use of air heating as the objective is the redesign of the fan.

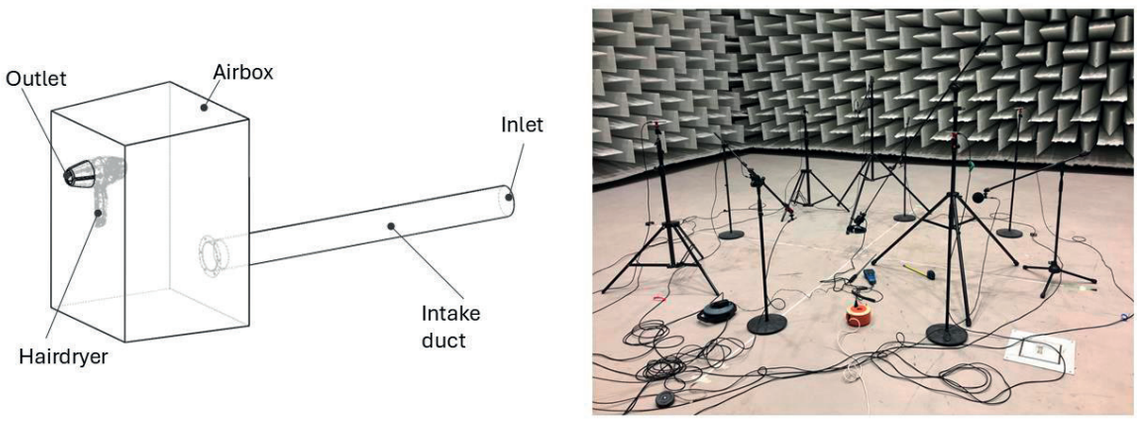


Figure 1: Experimental setup (left), anechoic chamber setup (right)

The anechoic chamber of the University of Ferrara is used in the semi-anechoic configuration, to estimate the sound power level of the hairdryer. Figure 1 (right) shows the experimental setup used for the estimation of the noise emission. The hairdryer is positioned horizontally in the centre of the semi-anechoic chamber, at a height of 25 cm from the reflective floor (measured from the impeller rotational axis). Moreover, nine omnidirectional free-field microphones, positioned according to the standard [13] are used to evaluate the sound pressure level at each microphone position. The measurements are performed for 30 seconds in order to approximate the stationary condition. At this point starting from the mean A-weighting sound pressure level over the nine microphones, the sound power level that characterizes the device is calculated. Another type of analysis, using a beamforming antenna, is performed to find the primary sources of noise inside the device. For this analysis was used the microphone array Signal Interface Group (SIG) model ACAM 100, that combines 40 digital MEMS microphones and a 5-megapixel optical camera in a planar, 40 x 40 cm array. The array is controlled with BeamformX acoustic beamforming code and presents an optimal frequency range between 1 and 20 kHz.

Numerical setup

The computational fluid dynamic, CFD, code used for all the simulations is ANSYS CFX and the used numerical domain is reported in Figure 2. To make the work as general as possible, the authors have chosen not to insert any kind of accessory at the end of the domain. The fluid domain is divided into two parts: one rotating sub-domain, which contains the impeller, and the stationary sub-domain. Concerning the stationary sub-domain, a sphere is added at the inlet of the device to approximate the suction from the environment.

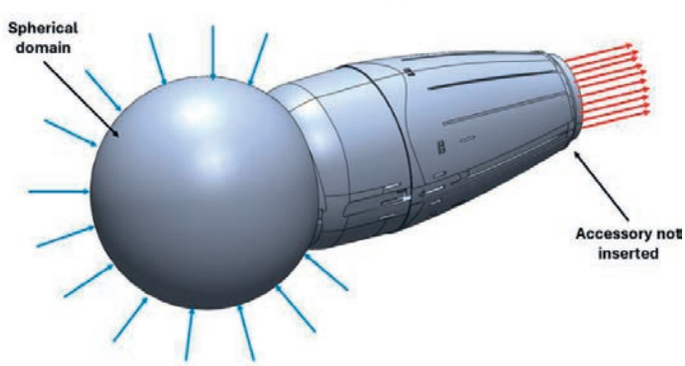


Figure 2: Numerical domain setup

The ANSYS Meshing software is used to mesh independently the two zones that constitute the numerical domain. In particular, two tetrahedral meshes using a patch-conforming method are realized, with prism boundary layer cells. Furthermore, to increase the quality of the mesh, a mesh sizing criterion is used to fix the dimensions of the elements on the impeller surfaces. A grid convergence analysis is performed by observing

the mass-flow average of the velocity at the outlet, and the torque acting on the impeller. The convergence is reached with an overall number of elements equal to about 35e6. The RANS k-epsilon turbulence model [14] with scalable wall function is selected for the specific application since it supplies, according to the literature, a good compromise between accuracy and computational effort. Moreover, a second-order scheme for both turbulence and advective terms is set, to increase the quality of the simulation. The fluid properties for the simulation, i.e. viscosity and density, have been evaluated at standard conditions, therefore a temperature of 25 °C and a reference pressure of 101325 Pa. Moreover, the fluid is considered as incompressible since the heating effect, due to the resistance, is not considered, and the Mach number within the entire domain is lower than 0.2. To represent the suction and the discharge from/to the environment, at the inlet of the domain, a zero relative total pressure is imposed while at the outlet an Opening boundary condition with relative static pressure equal to 0 Pa is set.

RESULTS AND DISCUSSION

In the first part of the work, the baseline hairdryer is experimentally tested in order to evaluate the mass flow rate elaborated by the device and to validate the numerical data. Subsequently, a numerical simulation is performed to find the total-to-total pressure rise generated by the fan, which is required as an input parameter for the redesign process. After that, the new impeller is designed taking into account different literature correlations useful to increase the efficiency and reduce the noise emission of the fan. Subsequently, the casing is redesigned with the objective of increasing performance by reducing the flow losses that occur inside the device. In the end, the optimized geometries are firstly simulated to confirm the assumption done in the preliminary design phase and therefore experimentally tested to assess the real improvement in terms of noise emission and fluid dynamics performance.

Numerical-experimental comparison of the baseline geometry

By measuring the speed in the intake duct over three circular sectors, the mass flow handled by the fan at maximum speed is calculated. For the comparison between the experimental and numerical fluid dynamic performance, two parameters are considered. The first one is the mean velocity at the outlet of the device, and the second one is the electrical power demand required by the electrical driver at the maximum rotational speed. The mean air velocity at the discharge section of the hairdryer is equal to 16.8 m/s while the electrical power demand results equal to 174 W.

Regarding the numerical results instead, a mean velocity equal to 15.4 m/s and electrical power demand equal to 184 W is predicted. The electrical power demand is calculated through the mechanical power demand calculated by means of CFD and the efficiency of the electrical driver. The numerical results are respectively 8.1 % lower and 5.7 % higher than the experimental ones. The obtained results are in agreement with the literature accuracy of a CFD simulation, especially for those applications characterized by a complex flow internal flow, as shown by the streamline plot reported in Figure 3. The efficiency of the fan results equal to 56.0 % and it is heavily influenced by tip leakage flows and the separation that occurs in the blade channel, as shown in Figure 7 by the wall shear stress contour.

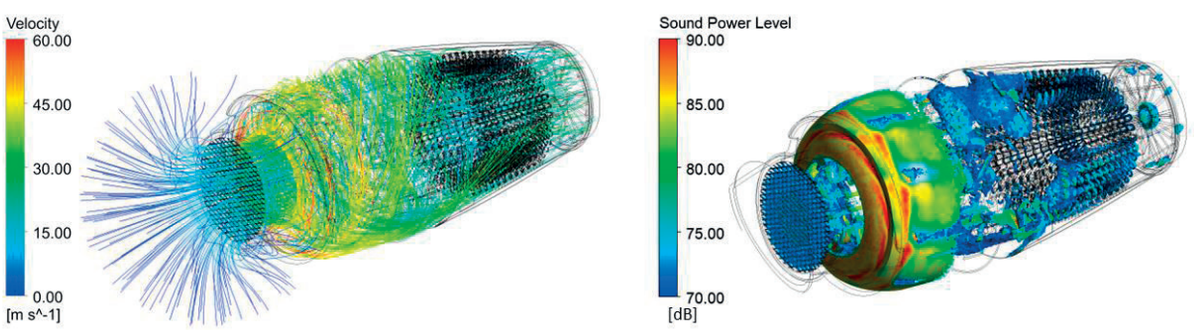


Figure 3: 3D streamlines plot (left), noise sources calculated using the Proudman criterion (right)

The experimental Overall Sound Power Level, OSPL, at the maximum rotational speed results equal to 81.6 dB(A), while the one-third octave band Sound Power Level, Lw, spectrum is reported in Figure 4. The highest noise level is obtained at a frequency of 3150 Hz, which is approximatively equal to the first harmonic

of the blade passing frequency. The beamforming antenna is therefore used to find the principal noise source inside the hairdryer. Figure 4 reports the beamforming analysis at a frequency corresponding to the maximum SPL. From this type of analysis, the main sources of noise at the frequency under consideration are found. The fan rotation and the free-blowing condition that occurs at the outlet are the main are the main noise sources. These considerations are also corroborated by the numerical results, as illustrated in Figure 3, where the Proudman formula [15] is employed to identify the noise sources within the fluid domain. The Proudman formulation, use the Lighthill's acoustic analogy [16] to estimate the broadband acoustic power generated by isotropic turbulence, this criterion is usually employed in the literature to have a fast evaluation of the noise source inside a fluid domain using a steady state simulation [17, 18]. The numerical simulation indicates that the primary source of noise is the fan and its interaction with the casing. Accordingly, the authors have selected to redesign the fan, and the relative part of casing, to reduce the noise emission of the device.

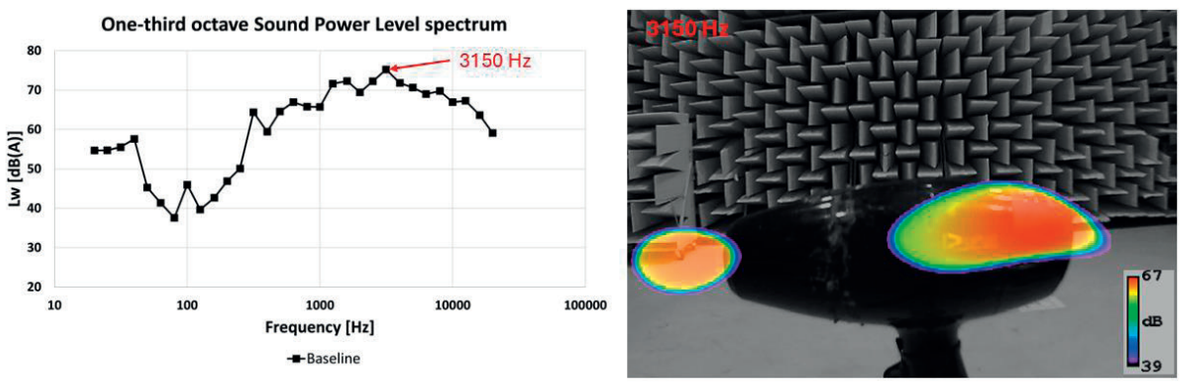


Figure 4: One-third octave band Sound Power Level spectrum (left), beamforming analysis @ 3150 Hz (right)

Development of the optimized geometry

The original impeller is a radial impeller consisting of nine extruded blades, moreover, the blade shape is truncated near the tip Trailing Edge, TE, as shown in Figure 5, to allow the positioning inside the casing. The results of the baseline numerical simulation are used to find the design mass-flow rate, rotational speed, total pressure rise of the fan, and the target efficiency of the new impeller. The Cordier diagram [19] is used to find the most suitable impeller typology for the specific application. Starting from a pressure coefficient, ψ, equal to 0.751, and a flow coefficient, φ, equal to 0.026, the specific speed is calculated and results equal to 1.2. The most suitable machine type is located between axial and centrifugal fan fields; therefore, a mixed-flow fan has been selected to be designed. The optimized impeller has been designed with the same axial dimension as the original one, thus allowing for replacement without the necessity of modifying the casing parts.

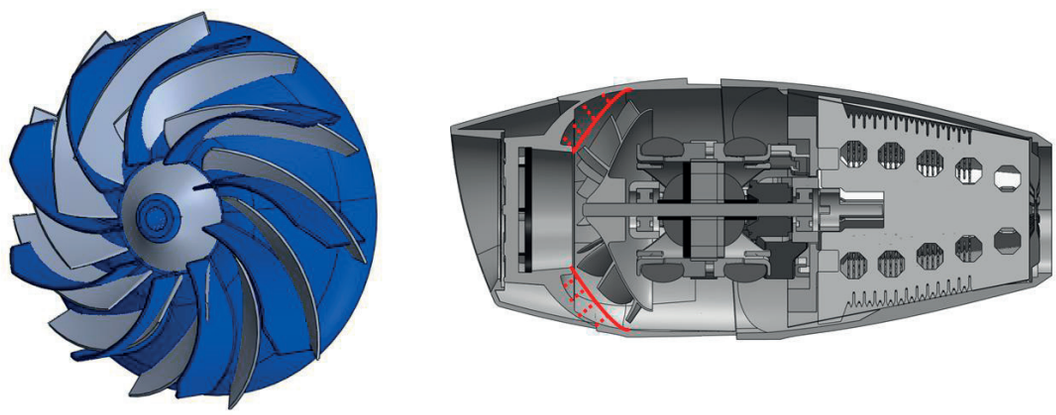


Figure 5: Impellers geometrical comparison (left), casing shape modification (right)

The conventional design methodology used for a radial fan, i.e. one-dimensional approach, is employed to determine the impeller's shape. Starting from the aforementioned non-dimensional parameters, using literature correlations, the hydraulic, volumetric, and disk-friction efficiencies of the impeller have been assumed. These

assumptions are subsequently verified and corrected by analysing the CFD simulation results. Subsequently, the correlations taken from [20, 21, 22, 23] are used to find the number of blades, Z, and the geometrical ratios b_2/D_2 and D_1/D_2 characterizing the impeller. All the considered correlations supply a number of blades between 10 and 12, therefore a number of blades equal to 11 are selected for the specific application, also for acoustic reasons. Concerning the geometrical ratios, b_2/D_2 and D_1/D_2, the resulting values are, respectively, 0.094 and 0.547. The position and the shape of the LE/TE of the blades are established by analysing the velocity distribution obtained through a 2D inviscid flow calculation of the impeller meridional channel (simulated using ANSYS Fluent). In order to ascertain the blade entry angle, a zero-incidence condition is employed. Meanwhile, the exit blade angle is adjusted to encompass the slip factor, utilising the correlation provided by Wiesner [24].

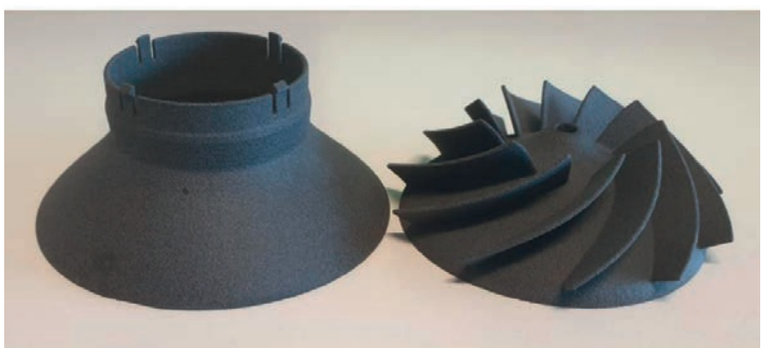


Figure 6: Casing insert (left), optimized impeller (right)

As a first attempt, only the impeller is redesigned without any type of modification to the casing. Subsequently, in order to increase the performance of the hairdryer an insert to be placed inside the hairdryer is designed to change the internal geometry of the device. Figure 5, shows the original internal geometry of the dryer, the red lines instead show the modifications applied to the casing. The optimized surface (red straight line in Figure 5) is obtained by an offset of the meridional channel outer streamline. An external view of the optimized impeller and the insert to be inserted into the casing, realized by means of Selective Laser Sintering printing techniques is reported in Figure 6.

Numerical simulation of the optimized geometries

Initially, the optimized impeller is inserted inside the baseline casing and a numerical simulation is performed to evaluate the fluid dynamic performance. The fluid dynamic efficiency results equal to 60.0 % therefore four-point percentage higher than the baseline impeller. The mean velocity at the outlet of the device results equal to 14.5 m/s, while the electrical power demand is equal to 125 W. These values are completely similar to those previously obtained with numerical simulation of the original impeller, only the efficiency is slightly improved with the new geometry.

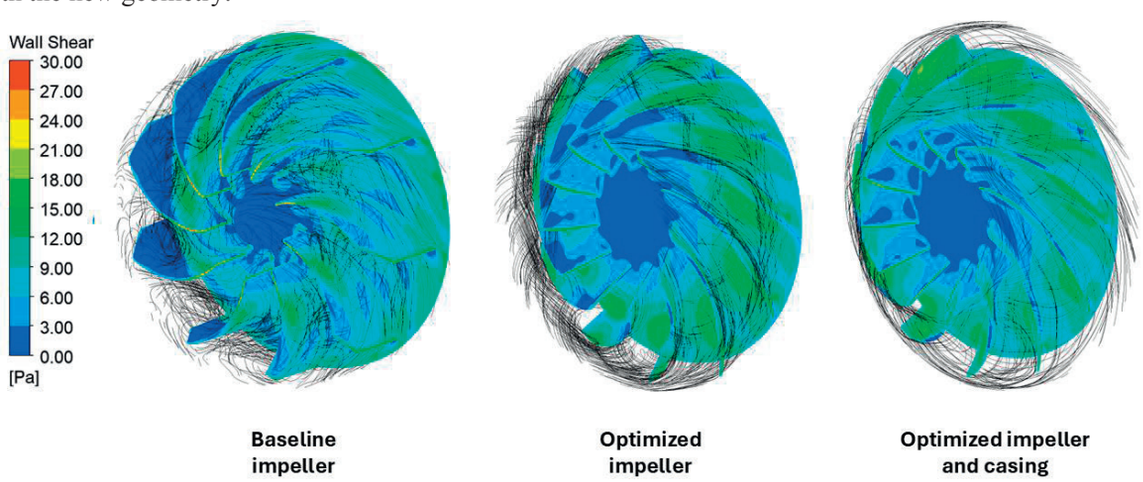


Figure 7: Impeller wall shear stress contour and streamline plot

Figure 7 highlight how the separation region has been greatly reduced using the new geometry, this is confirmed by the increase in the hydraulic efficiency to about 7 % than the original one, as reported in Table 1. Despite the significant increase in hydraulic efficiency, the fluid dynamic efficiency of the rotor is only four points percentage higher than the original one. This fact is due to the decrease in hydraulic efficiency caused by the higher tip gap width. The presence of a higher number of tip leakage flows with the new geometry can be observed by the streamline plot reported in Figure 7. At this point, the casing shape is modified to increase hydraulic efficiency and decrease the tip leakage flows. The new configuration supplies an average outlet velocity of 16.8 m/s, an electrical power demand of 156 W, and a fluid dynamics efficiency of 70.2 %. In this case, both hydraulic and volumetric efficiencies are higher than the baseline ones, therefore a reduction of the flow losses and the intensity of the tip-leakage flows is obtained, as shown in Table 1.

Table 1: Impeller fluid dynamics, volumetric, hydraulic and volumetric efficiencies

	η	η_{HDY}	η_V
Baseline	0.56	0.68	0.82
Optimized impeller	0.60	0.75	0.80
Optimized impeller and casing	0.70	0.84	0.84

Regarding the noise emission, the Proudman criterion is used to find the noise source inside the fluid domain. In particular, Figure 8 shows a comparison between the noise sources obtained with the geometries under consideration. The baseline geometry is characterized by very important noise sources that involve the separation zones and the interaction with the casing. The configuration with the optimized impeller and the original casing, have significantly lower noise sources that are localized on the blades LE, and in the tip gap region due to the higher intensity of the tip leakage flows. The last picture reported in Figure 8 referred to the configuration with the optimized casing and impeller, in this case only a few high-noise areas are highlighted in the tip gap reason, due to the reduction of the tip gap dimension. A larger noisy zone, than in the previous configuration, is detected on the impeller blades mainly due to the higher mass flow rate elaborated by the fan. In general, the results of the Proudman noise source analysis indicate that modifications to the design of the hairdryer and the impeller led to a reduction in the noise emission of the device.

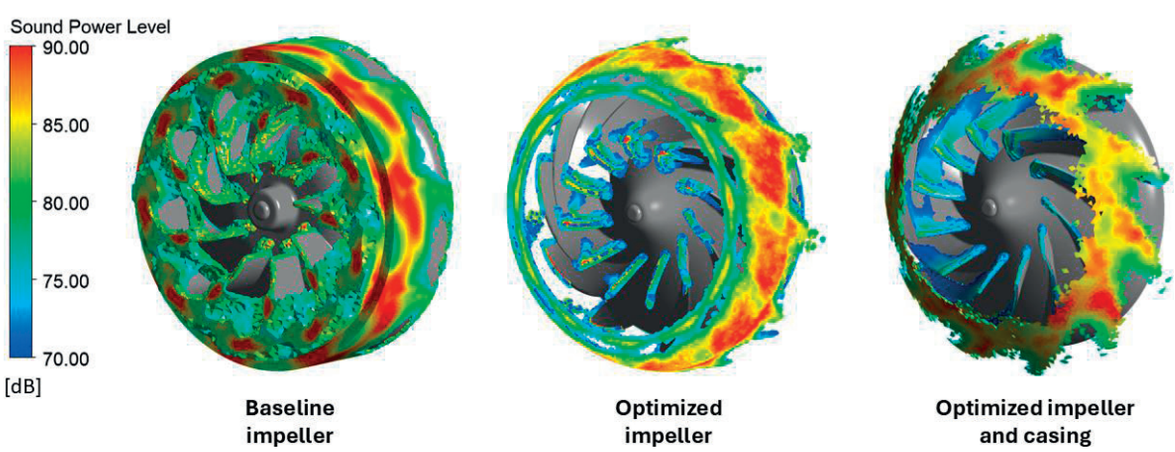


Figure 8: Noise sources calculated using the Proudman criterion

Experimental comparison between baseline and optimized hairdryer

The optimized casing insert, and impeller have been prototyped by means of Selecting Laser Sintering techniques. The Nylon material is selected for the specific application. The prototypes are inserted in the baseline hairdryer and the experimental fluid dynamic performances are evaluated, at the design rotational speed. In the optimized impeller configuration, the mean velocity at the outlet results equal to 19.6 m/s which is 16.6 % higher than the baseline one at the design rotational speed. The electrical power demand, instead, results equal to 171.4 W, therefore comparable value to the original one is obtained. Regarding the

configuration with optimized impeller and casing, a mean outlet velocity of 21.8 m/s and an electrical power demand equal to 168.2 W are detected. The findings substantiated the enhancements in the elaborated flow rate and the electrical power demand predicted by the numerical simulation of the optimized impeller-casing configuration.

The aim of the work is to optimize the geometry to supply approximately the same mass-flow rate as the target one but with lower noise emission and electrical power demand. For this reason, the optimized geometries have been also tested reducing the rotational speed to supply the same flow rate as the baseline hairdryer. Table 2 shows the results obtained by reducing the rotational speed of the new geometries. A significant electrical power demand reduction has been obtained with both the impeller-casing and impeller only optimizations. The electrical power demand results respectively 52.1 % and 29.6 % lower than the baseline one. These results confirm the improvements in the fluid dynamics efficiency obtained through the numerical calculations.

Table 2: Experimental performance comparison

	Mean outlet velocity [m/s]	**Electrical power demand [W]**	**OSPL [dB(A)]**
Baseline	16.8	173.2	82.6
Optimized impeller (design rotational speed)	19.6	171.4	82.6
Optimized impeller and casing (design rotational speed)	21.8	169.2	81.8
Optimized impeller (design flow rate)	16.8	121.9	80.4
Optimized impeller and casing (design flow rate)	16.8	82.9	77.3

In the end, the prototypes have been tested in the semi-anechoic chamber to evaluate the noise emission. The obtained Overall Sound Power Level, OSPL, is reported in Table 2, from this it is possible to notice how all the tested configurations supply lower or comparable OSPL than the original one. Moreover, the casing shaping allows a reduction of the noise emission in both design rotational speed and design flow rate operating conditions. The highest noise improvement is obtained with the optimized impeller and casing configuration at the design flow rate, with a noise reduction equal to 5.3 dB (A).

Figure 9, reports a comparison between the noise spectra obtained at the design flow rate and at the design rotational speed. The noise spectrum, relative to the improved impeller and casing, at the design flow rate, is completely below the baseline one, therefore not only the OSPL is significantly reduced but also the noise emission at each frequency. The same is true for the optimized impeller-only configuration, despite the frequency of 2000 Hz, where a slight increase in noise emission is observed in comparison to the baseline configuration. Regarding the comparison at the design rotational speed, the acoustic results are influenced by the different mass flow rates elaborated by the hairdryer. The optimized configurations supply approximately the same noise spectra at the lowest and highest frequency as the baseline one, while between 400 Hz and 4000 Hz, the optimized impeller-casing configuration supplies the lowest SPL despite for two frequencies. In general, although the optimized configurations exhibited higher flow rates, a reduction in noise emission is observed.

FAN 2025
Antibes Juan-les-Pins (France), 9 – 11 April 2025

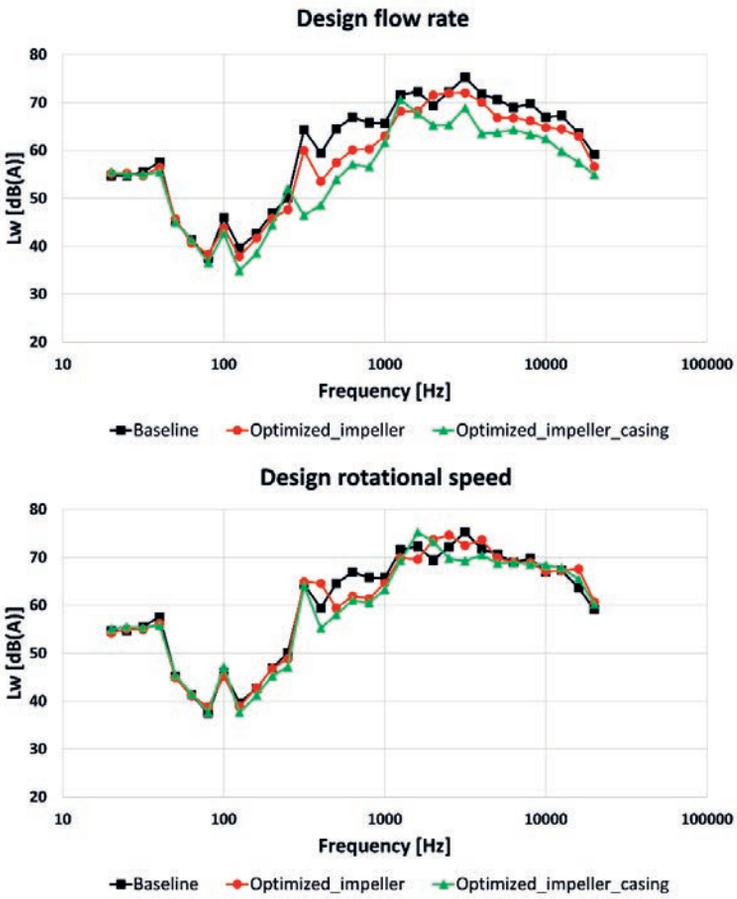


Figure 9: Experimental one-third octave band Sound Power Level spectra

CONCLUSIONS

The current work shows a redesign process of a hairdryer for efficiency and noise improvement. In the first part of the work, the baseline geometry is experimentally tested to find the target mass flow rate elaborated by the device and evaluate the noise spectra. Subsequently, a CFD simulation is performed to calculate the other parameters, i.e. efficiency and total pressure rise generated by the fan, necessary as input of the impeller redesign process. Once these parameters are calculated the most suitable fan type is selected according to the Cordier diagram. A mixed-flow impeller is chosen for the specific application. Initially, only the impeller is redesigned, and the relative CFD analysis shows a not significant improvement in the mass-flow rate elaborated by the hairdryer due to the higher tip gap width and its consequent lower volumetric efficiency. For this reason, an insert has been designed to modify the internal geometry of the hairdryer casing, to enhance the volumetric efficiency of the impeller and consequently increase the fan's flow rate. The increase in the flow rates due to the casing shape modification is also confirmed by numerical calculation, moreover a slight decrease in the electrical power demand is obtained. In the end, the optimized configurations have been experimentally tested, to assess the real performance and the noise emission into distinct operational conditions: at the design flow rate and at design rotational speed. The fluid dynamics measurements confirmed that the optimized impeller-only configuration supplies a lower flow rate than the optimized impeller-casing one, therefore confirming the numerical results at the design rotational speed. Regarding the noise improvement, a comparable OSPL to the baseline one is obtained with the optimized impeller-only configuration, while with the optimized impeller-casing configuration a reduction to about 0.8 dB(A) is obtained. However, the mass flow rate elaborated is, in both cases, significantly higher than the baseline value. In the final experimental test, the rotational speed is regulated to supply the same flow rate as the baseline one. In this case, significant noise and electrical power demand reductions have been obtained with both geometries. The optimized impeller and casing configuration yielded the most advantageous outcomes, exhibiting a notable reduction of 5.3 dB(A) in the OSPL and a substantial decrease of 90.3 W in the electrical power demand.

BIBLIOGRAPHY

[1] B. Akhmetov, S. Gupta and K. K. Ahuja, – *Noise source ranking of a hairdryer.* Proceedings of 20th AIAA/CEAS Aeroacoustics Conference, Atlanta, GA, **2014**.

[2] L. Che, H. Lee and H. P. Lee, – *Acoustical analysis and optimization design of the hair dryers.* Noise Mapping, De Gruyter, **2024**.

[3] U. Jung, J.-H. Kim, S. Kim, J.-H. Kim and Y. Choi, – *Analyzing the shape parameter effects on the performance of the mixed-flow fan using CFD & Factorial design.* Journal of Mechanical Science and Technology, **2016**.

[4] G. V. R. Seshagiri Rao, V. V. Subba Rao and C. Prabakara Rao, – *Design of mixed flow fan with rapid prototyping method for acoustics performance.* Indian Journal of Science and Technology, **2016**.

[5] N. Aldi, M. Piovan, M. Pinelli, A. Suman, N. Zanini, E. Mollica and F. Menichini, – *Numerical-experimental comparison of the performance of a mixed-flow fan designed for electric vehicles*. Proceedings of ASME Turbo Expo: Power for Land, Sea, and Air, London, UK, **2024**.

[6] N. Aldi, N. Casari, M. Pinelli, A. Suman, A. Vulpio and P. Saccenti, – *Performance modification of an erosion-damaged large-sized centrifugal fan.* Proceedings of ASME Turbo Expo: Power for Land, Sea, and Air, **2021**.

[7] N. Aldi, N. Casari, S. Oliani, M. Pinelli, E. Mollica and F. Menichini, – *Numerical Investigation of an Automotive Axial Fan: A Comparison Among Different CFD Software Packages and Experimental Validation.* Proceedings of ASME Turbo Expo: Power for Land, Sea, and Air, Rotterdam, NL, **2022**.

[8] M. Piovan, M. Pinelli, A. Suman, N. Zanini, G. Magnani and A. Zanardi, – *A re-design process of an industrial centrifugal fan through CFD and rapid prototyping.* Journal of Physics: Conference Series, **2023**.

[9] L. Lahaye, – *Hair dryer aero-acoustic study and passive solutions for noise reduction.* Master thesis, Liège, Belgique, Universitè de Liège, **2022**.

[10] S. Bianchi, A. Corsini and A. Sheard, – *A critical review of passive noise control techniques in industrial fans.* Journal of engineering for gas turbines and power, **2014**.

[11] G. Lacagnina, P. Chaitanya, J. Kim, T. Berk, P. Joseph, K. Choi, B. Ganapathisubramani, S. Hasheminejad, T. Chong, O. Stalnov, M.F. Shahab, M. Omidyeganeh and A. Pinelli, – *Leading edge serrations for the reduction of aerofoil self-noise at low angle of attack, pre-stall and post-stall conditions.* International Journal of Aeroacoustics, **2021**.

[12] N. Casari, E. S. Fadiga, M. Piovan, M. Pinelli and A. Suman, – *Low-Noise Airfoils for Turbomachinery Applications: Two Examples of Optimization.* International Journal of Turbomachinery, Propulsion and Power, **2024**.

[13] ISO-3744, – *Acoustics – Determination of sound power levels and sound energy levels of noise sources using sound pressure – Engineering methods for an essentially free field over a reflecting plane*. American National Standards Institute, **2010**.

[14] B. E. Launder and D. B. Spalding, *Lectures in mathematical models of turbulence*, Accademic Press, **1972**.

[15] I. Proudman, – *The generation of noise by isotropic turbulence.* Proceedings of the Royal Society of London. Series A, Mathematical and Physical Sciences, **1952**.

[16] M. J. Lighthill, – *On sound generated aerodynamically I. General theory.* Proceedings of the Royal Society of London. Series A. Mathematical and Physical Sciences*,* **1952**.

[17] A. Angulo, R. G. Ramirez Gustavo, W. De Oliveira, E. R. Da Silva and G. E. Niño Del Río, – *Free and non-free vortex design for axial fans with circumferential sweep through CFD techniques.* Journal of Applied Fluid Mechanics, **2022**.

[18] M. Yadegari, F. Ommi, S. K. Aliabadi and Z. and Saboohi, – *Reducing the aerodynamic noise of the axial flow fan with perforated surface.* Journal Applied Acoustics, **2024**.

[19] S. L. Dixon e C. Hall, *Fluid mechanics and thermodynamics of turbomachinery*, Butterworth-Heinemann, **2013**.

[20] T. Carolus, *Fans: aerodynamic design-noise reduction-optimization*, Springer Nature, **2022**.

[21] C. Pfleiderer, *Die Kreiselpumpen für Flüssigkeiten und Gase: Wasserpumpen, Ventilatoren, Turbogebläse Turbokompressoren*, Springer-Verlag, **2013**.

[22] B. Eck, Fans-Design and Operation of centrifugal, axial-flow and cross-flow fans, Oxford, England: Pergamont Press, **1973**.

[23] L. Bommes, *Ventilatoren*, Vulkan-Verlag GmbH, **2003**.

[24] F. Wiesner, – *A review of slip factors for centrifugal impellers.* Journal of Engineering Gas Turbine and Power*,* **1967**.



ENDLESS FIBRE REINFORCED COMPOSITE IMPELLER: MODULAR DESIGN FOR DIFFERENT PERFORMANCE CLASSES

Sebastian SPITZER, Jonas KLUGER, Richard König, Leon SCHRÖDER, Alrik DARGEL, Eckart KUNZE, Christoph EBERT, Maik GUDE

Dresden University of Technology,
Institute of Lightweight Engineering and Polymer Technology,
Holbeinstrasse 3, 01307 Dresden, Germany

SUMMARY

A modular high performance composite impeller made of fiber reinforced plastic (FRP) has previously been designed to reach maximum mechanical performance, using simplified geometry, numerical models, manufactured with simple tools and experimentally validated up to 538 m/s circumferential speed to burst point. In this study, the design is adapted in terms of aerodynamic performance, a robust and reproducible manufacturing process for fans in medium, high and highest power profiles, with targeted operating speeds of 225, 381 and 440 m/s under different conditions (ambient and elevated temperatures, humidity). The various designs incorporate glass and carbon tailored fiber placed preforms. The elaboration of the designs was supported by advanced numerical models. An improved manufacturing chain was used during implementation. The failure modes were determined by centrifugal tests.

INTRODUCTION

The performance and efficiency of future and existing blowers can be improved by using innovative high-performance centrifugal impellers made of fiber-reinforced composite materials [1, 2]. These materials offer exceptional mechanical properties in relation to their density, enabling a significant increase in operating speed. Mihalache et al. present a method for the development of a semi-open CFRP impeller using a multi-stage prepreg autoclave process for manufacturing [3]. Based on numerical investigations of the structural behavior and aerodynamic considerations, experimental investigations of the damping behavior were carried out. However, these do not allow any statements to be made about the maximum achievable circumferential speed or the failure behavior. Other publications on FRP impellers often focus on numerical analyses of various single-stage machines [4, 5, 6, 7].

This work examines the question of whether the modular design is suitable to be adapted in terms of performance and application in different performance classes (PC), which materials are appropriate,

how an industrialized manufacturing process looks like and what circumferential speeds can be achieved.

In [8], the development process (Technology Readiness Level 1–3) of a closed impeller in metal-FRP hybrid design (cf. Figure 1) is conducted by combining the engineering design process in accordance with VDI guideline 2221 [9] with the use of the fiber composite-compatible failure criterion of CUNTZE [10]. The design concept is such that the blades are bonded between the cover and carrier discs. The composite impeller shown in Figure 1, left is a structural-mechanical functional model, whereas aerodynamic aspects are not considered.

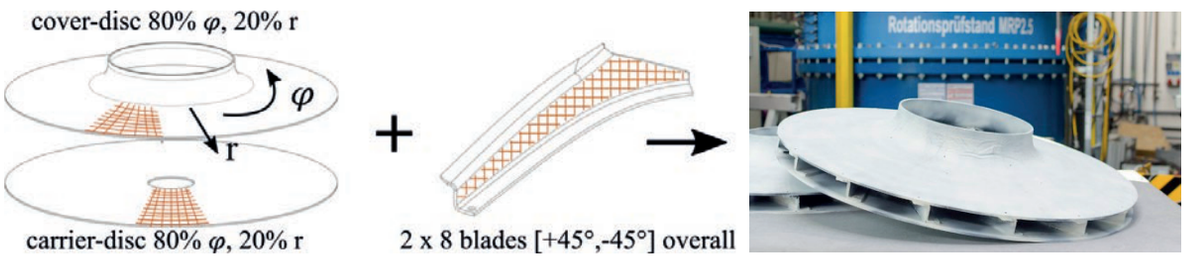


Figure 1: design concept of the modular composite-metal radial-impeller with material orientations (left, center) and assembled impeller (right) [8]

There is an edge at the transition from the blade to the disc. This impeller was manufactured using a simplified manufacturing process chain, whereby the composite components were produced by using prepreg in combination with autoclave (cf. Figure 2).

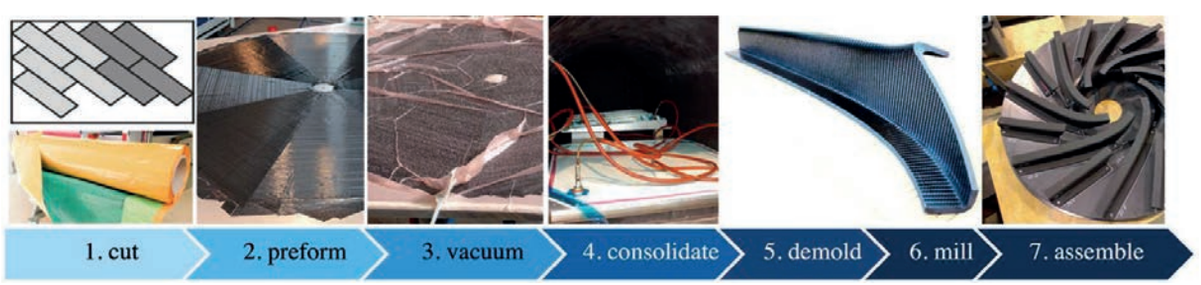


Figure 2: manufacturing process of the composite parts and assembling [8]

This concept was implemented as a functional model and successfully tested at circumferential speeds up to 538 m/s [11] on a rotor test rig. The relevant failure mode in this design is the detachment of the blades around the bond to the disc, whereby a fracture occurs not only in the joining zone between blades and discs. It is a mixed fracture that leads to splitting of the blades (cf. Figure 3, pic. 3 and 4).

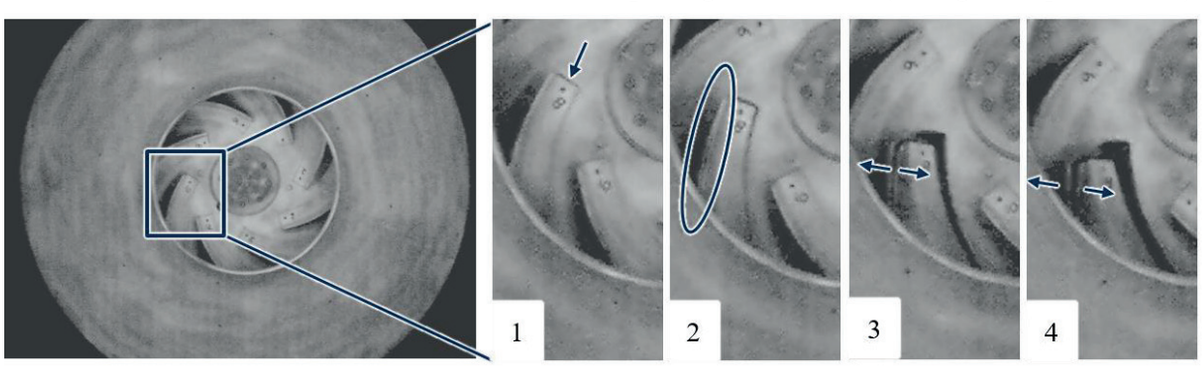


Figure 3: images from the high-speed test of the impeller, initial failure and the splitting of a blade (right) [2]

The design process, including analysis of vibrations, damping behavior [11] and failure, was demonstrated using simplified numerical models. Even though the technology of modular

FRP impellers shows great potential, the technology still needs to be further refined and adapted to different requirements for use in various application scenarios.

DESIGN, DIMENSIONING AND MANUFACTURING OF MODULAR RADIAL IMPELLER FOR DIFFERENT PERFORMANCE CLASSES (PC)

The basic modular design of [8] with continuous fiber reinforcement is further developed to meet different requirements. Three adapted designs are derived that meet the following scenarios:

- Scenario 1: a cost-effective solution at low to medium circumferential speeds up to 225 m/s at medium temperatures up to 100 °C and lower requirements for aerodynamic performance at component edges (PC1),
- Scenario 2: for high circumferential speeds up to 381 m/s at higher temperatures of up to 150 °C and medium requirements on the fluid mechanical performance at component edges (PC2)
- Scenario 3: for high circumferential speeds up to 440 m/s at higher temperatures of up to 200 °C and high requirements on the aerodynamic performance at component edges (PC3).

For scenario 1, a design is derived, which is based on a glass fiber reinforced plastic (GFRP) impeller combined with an epoxy resin with a maximum glass transition temperature of $T_g \approx 120$ °C (PC1). For scenario 2 and 3, CFRP impellers with high-temperature-resistant epoxy resin ($T_g \approx 200$ °C) are developed (PC2 and PC3). This matrix system only just fulfils the required design temperatures. However, due to the lack of availability of high-temperature resin systems, this material must be used. Possible blade-disc connections are shown in Figure 4, where the aerodynamic design of the flow channel between the blades is shown schematically. The blade and disc are glued together in all concepts (C1, C2, C3, C4 and C5).

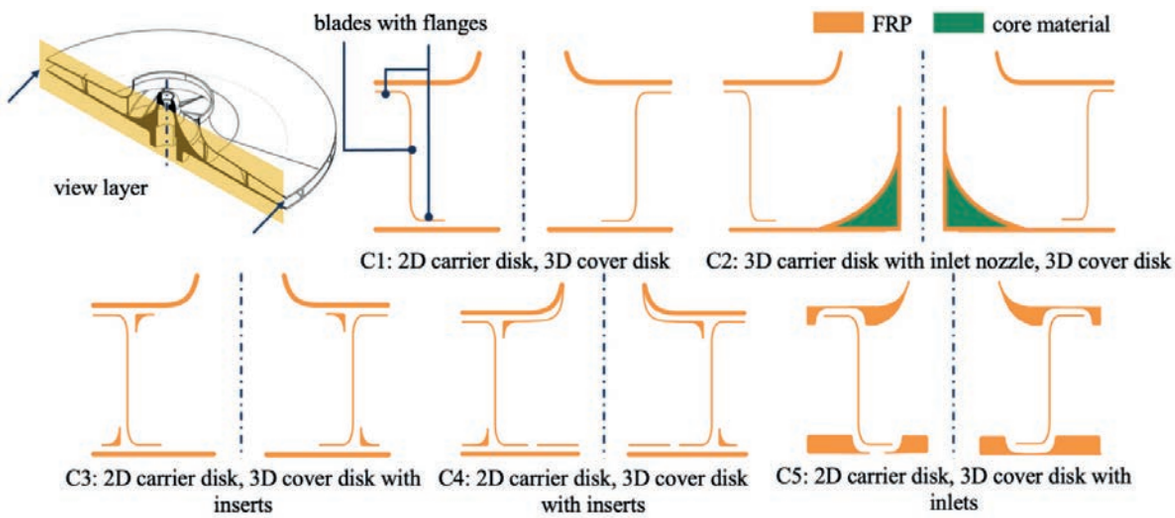
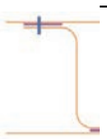
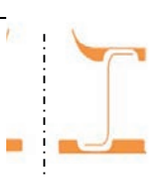


Figure 4: overview of different design cencepts (C1-5) for the carrier and cover disc using integral and differential elements to shape the flow channel between the blades and their flanges

Concept C1 is a variant in which the blades and discs are simply glued. C2 and C3 have increasing fairings for better aerodynamic performance. Table 1 shows the three impeller classes examined, the circumferential speed to be realized, the design temperature and the torque transmitted by the blades during compression of the fluid and the selected blade and disc design.

Table 1: design recommendations for blade designs according to the various requirements of the performance classes

class	rcumferential speed [m/s]	design temperature [°	blade de	disc design
PC1	225	100		
PC2	381	200		
PC3	440	300		

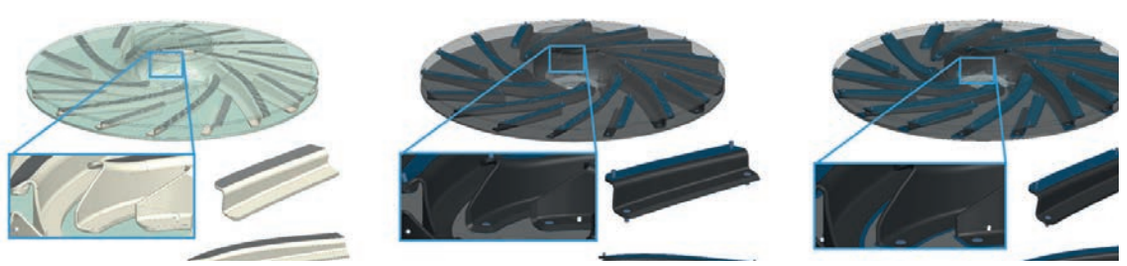


Figure 5: CAD design of performance class 1 (left), performance class 2 (center) and performance class 3 (right) whereby the flanges in the blades of PC3 are submerged in thicker discs (see also Figure 6)

To meet the high aerodynamic requirements of PC 3, the discs are thicker, and the blade flange is recessed to create a flat flow surface (cf. Figure 6). The metal connecting elements at the ends of the blade flanges are clearly visible.

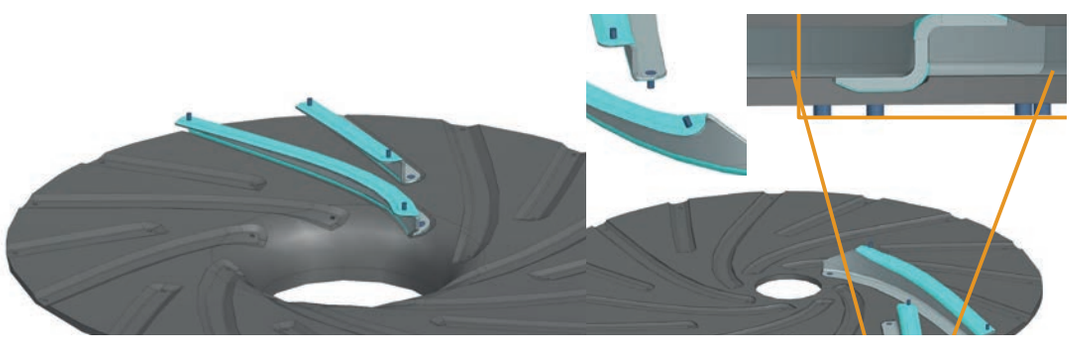


Figure 6: adapted design for performance class 3 with blades recessed into the discs

Based on these detailed CAD models of the impellers, numerical models are derived that depict the key design details, such as the blade flanges, the adhesive layer and the indentations in the discs (cf. Figure 7). The metallic joining elements and their mechanical preload force are considered, and orthotropic material properties and linear elasticity of the fiber-polymer composite are considered. The models are implemented as cyclically symmetrical segments with corresponding symmetry boundary conditions.

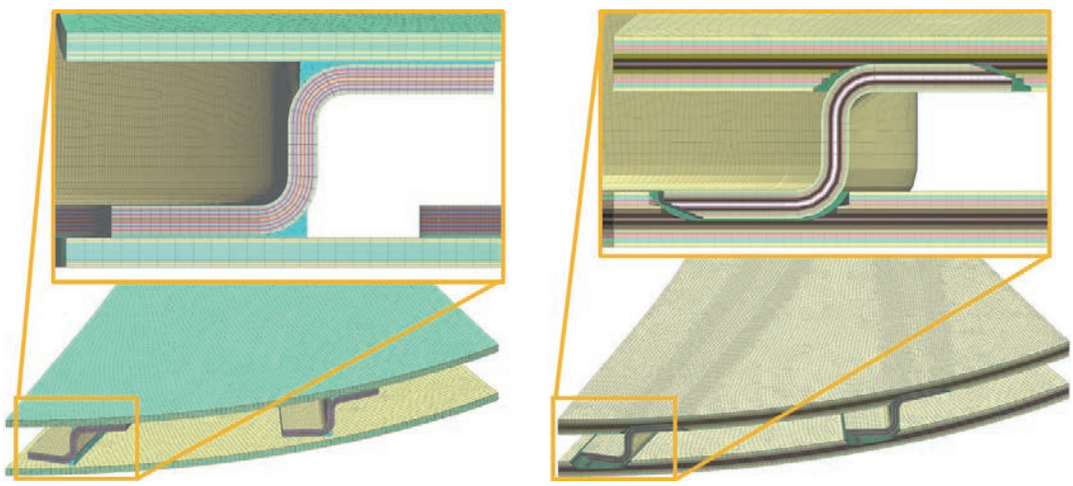


Figure 7: section models with individual layers of PC2 (left) and PC3 (right)

The impellers are manufactured using a process that differs from the preliminary work [8]. The aim is to improve quality and increase reproducibility. A single-sided metallic tool is still used to manufacture the discs. Instead of pre-impregnated prepreg material, a dry semi-finished product is used, which is infiltrated in a vacuum build-up using epoxy resin. The Vacuum Assisted Resin Infusion (VARI) process is used. The blades are produced in a two-sided mold using a Resin Transfer Molding (RTM) process. The dry fiber preform is placed into a closed mold, evacuated prior to infiltration and the resin is injected and cured under pressure. Figure 8 shows schematically the tools used in the preliminary work (left) and the tools used in this study (center and right). In the preliminary work process, prepreg is processed in an autoclave. Pre-impregnated semi-finished products are compacted under increased pressure and temperature. This results both in high fiber volume contents (FVC) and good component quality. Closed tools are only possible to a limited extent, which means that the surface is more undefined than the area towards the tool. In the VARI process for the discs in the current study, dry semi-finished fiber products are infiltrated with resin at room temperature and pressure by vacuum suction. This requires less process effort. Here, too, high-quality surfaces are only possible on one side, resulting in a lower FVC. The blades are manufactured using the RTM process. Here, resin is injected into dry semi-finished fiber products under pressure. This results in the highest component quality and FVC with high-quality surfaces on both sides. However, this is also associated with increased heat treatment costs.

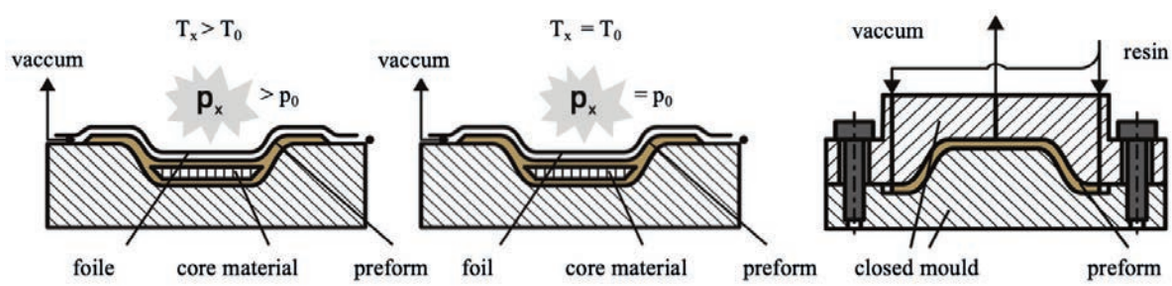


Figure 8: schematic representation of the tool technology used in the preliminary work [8] (left), the adapted technology for manufacturing the discs (center) and the blades (right)

Figure 9 shows the manufacturing and assembling steps of the individual parts - carrier disc, cover disc and blades - from preforming to CNC edge trimming and the subsequent joining of the individual parts to form an impeller as well as the balancing of the resulting test specimens. Great care was taken to ensure that the individual parts, their post-processing and the assembly processes were as reproducible as possible to achieve consistent impeller quality and thus failure speed.

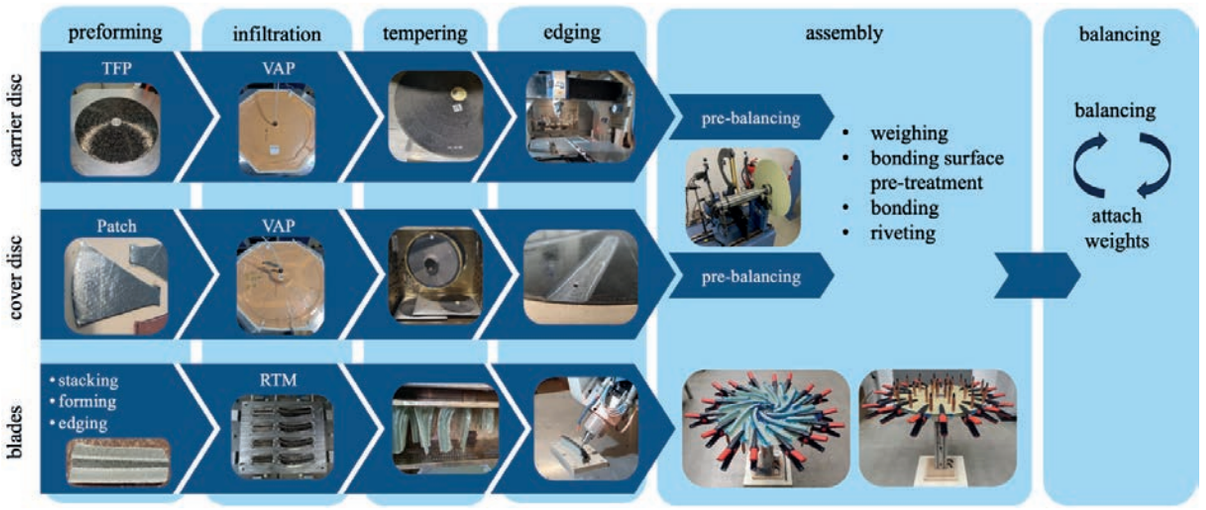


Figure 9: process for manufacturing the impellers from preforming to balancing (vertical arrangement) and the parallel processes for manufacturing the individual components (left, horizontal arrangement) and assembly and balancing (right)

Using this manufacturing method, four testable impellers were manufactured for each performance class, with four impellers each being tested for spin tests in a normal climate, while one impeller of each performance class being stored under media load beforehand. Climate conditioning took place for 45 days in the climate chamber at temperature 70 °C and 85 % relative humidity. The increase in mass was recorded.

RESULTS AND DISCUSSION

The numerical results show that all impellers achieve the required circumferential speeds (Figure 10). PC1 has an expected ratio of rated to bursting RPM of 1.1, PC2 of 1.8 and PC3 of 1.3. For all structures, the location of initial failure is located in the cover disc towards the nozzle at the front of the blade's flange. Furthermore, PC1 and PC2 have critical areas in the blades at the nozzle.

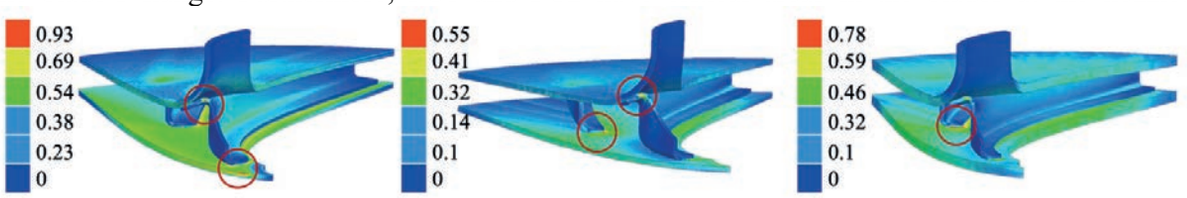


Figure 10: results of the FEA showing the effort according to CUNTZE for PC1 at 225 m/s with a maximum of 0.93 (left, red circle), PC2 at 381 m/s with a maximum of 0.55 (middle, red circle) and PC3 at 440 m/s with a maximum at 0.78 (right, red circle)

The impellers were spun until they burst during observation with high-speed cameras. For each performance class four impellers were tested. Figure 11 shows the image of the respective impeller at the moment of failure. The first failure mode observed is the detachment of the blades, which dissolve and are ejected (e.g. PC1 no. 1, no. 2, no. 3, PC2 no. 2 and no. 3).

FAN 2025
Antibes Juan-les-Pins (France), 9 – 11 April 2025

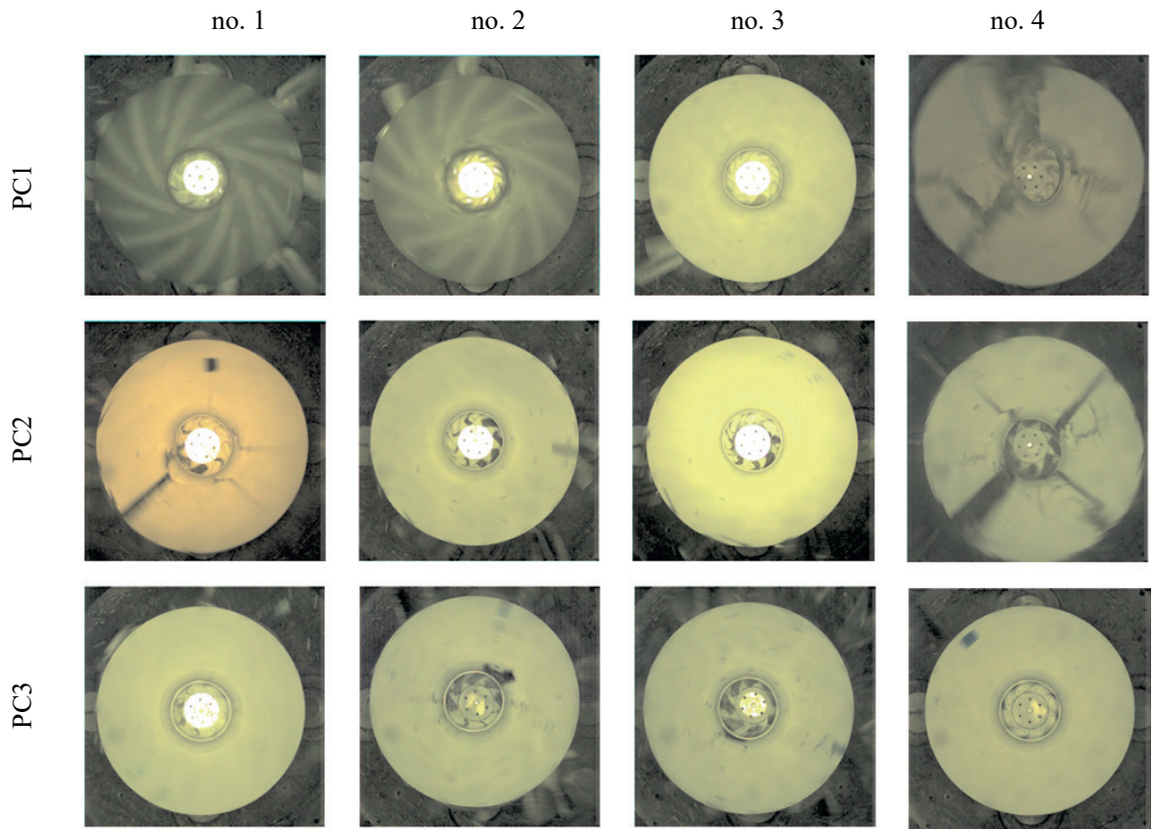


Figure 11: results of the experiments: overview of the primary failure modes of the impellers

In some impellers the shroud fails (e.g. PC1 no. 4, PC2 no. 1 and no. 4). PC3 fails mainly due to detachment of the intact blades from the vanes. Table 2 shows the values achieved during the test until burst. Column one lists the performance class (PC) and column two lists the impellers tested, whereby no. 1-3 were tested under normal conditions and no. 4 was stored in the climate chamber until moisture saturation. Column three lists the revolutions per minute (RPM) and column four the achieved revolutions per minute. This results in the ratio of rated to bursting RPM and the circumferential speed at bursting. Hereby, a further reduction by the lower strength at the higher design temperature is not taken into account.

Table 2: Overview and results of the performed spin tests

PC	no.	condition	rated RPM	bursting RPM at room temperature	ratio of rated to bursting RPM	circumferential speed [m/s]
1	1	dry impeller	7,674	12,500	1.6	367
	2	dry impeller		14,700	1.9	431
	3	dry impeller		13,930	1.8	408
	4	conditioned impeller		14,515	1.9	426
2	1	dry impeller	13,000	17,100	1.3	501
	2	dry impeller		15,130	1.2	444
	3	dry impeller		13,030	1.0	382
	4	conditioned impeller		18,364	1.4	538
3	1	dry impeller	15,000	15,300	1.0	449
	2	dry impeller		15,727	1.0	461
	3	dry impeller		15,570	1.0	456
	4	conditioned impeller		11,819	0.8	347

The PC1 dry impellers achieve at room temperature an average circumferential speed of 402 m/s and have a standard deviation of 32.7 m/s, giving a relative deviation of 8 %. The preconditioned impeller

achieved a speed 6 % higher than the average. A moist matrix seems to have a positive influence on the occurrence of failure. When switching from glass to carbon fiber and the high-T_g matrix system in PC2, the burst speed at room temperature increases to an average of 442.3 m/s, which is 9 % higher. This increase is surprisingly small considering that the carbon fibers have much better mechanical properties in fiber direction. Probably the intermediate fiber strength is an important factor here. However, the standard deviation of the three PC2 impellers tested is 59.7 m/s, i.e. 13 %. The burst speed of the conditioned impeller is 13 % higher than the average speed. For PC3 with the same carbon fiber and high-T_g resin as in PC2, the average burst speed at room temperature is 455.4 m/s, which is 13 % higher than for PC1. The standard deviation is 6.3 m/s or only 1%. Humidity, on the other hand, has a significant negative effect on bursting speed at -24 %. The surprisingly low performance of PC2 and PC3 impellers can be attributed to the mechanical performance of the high-T_g matrix system under the high interlaminar shear and out of plane tensile loading at spin test conditions. Single lap shear (SLS) tests, performed for the two fiber matrix combinations used, showed only 66 % tensile shear strength for the carbon fiber high-T_g matrix combination compared to the glass fiber matrix combination [12].

The modular designs incorporate glass and carbon fiber reinforcements. Advanced manufacturing techniques, including tailored fiber placement, were used to preform the continuous fibers. A research-scale manufacturing process chain was established using metal tooling to ensure reproducible fabrication of functional samples. Advanced numerical models were developed to predict structural behavior, and all samples were tested to failure in a centrifugal test rig, including pre-saturation in some cases. Failure modes were analysed and compared with the numerical predictions.

CONCLUSION

This study demonstrates the successful adaptation of a modular composite impeller design for three distinct performance classes. By integrating advanced materials like glass and carbon fiber composites, along with optimized manufacturing techniques such as Vacuum Assisted Resin Infusion and Resin Transfer Molding, the designs achieved improved reproducibility and performance tailored to specific operational requirements.

The results underline that the modular design concept can be effectively scaled to meet varying circumferential speeds, thermal loads, and aerodynamic demands. PC1 offers a cost-effective solution for moderate operating conditions, while PC2 and 3 meet higher mechanical and aerodynamical requirements with superior structural integrity. A major shortcoming is the unavailability of high-temperature resin systems as a matrix material, which severely restricts the temperature stability of the impellers. PC2 and 3 do not fulfil the requirements.

Centrifugal burst tests validated the numerical predictions and highlighted differences in failure modes across material systems and environmental conditions. Pre-saturation of samples revealed intriguing effects of humidity on matrix behavior, warranting further exploration to optimize designs for specific environmental challenges. Additionally, optimizing the manufacturing process further enhances the load-bearing capacity of critical components such as blades, enabling higher first-damage speeds. The numerical and experimental results still show certain deviations. The deviations of up to 13 % that occurred in the experiments must be reduced.

Future work will include advanced spin rig testing to assess the structures up to their ultimate failure limits, providing deeper insights into the maximum achievable speeds and long-term performance characteristics. This research lays a strong foundation for industrial-scale production and continued development of modular fiber-reinforced impellers for diverse applications.

ACKNOWLEDGEMENTS

The authors would like to thank the Forschungsvereinigung für Luft- und Trocknungstechnik (FLT) and the BMWK for financial support in the HoRa project (grant agreement no. 21813 BR/1). Special thanks go to Dr. Peter Hermerath for his commitment to the project as chairman of the project committee.

BIBLIOGRAPHY

[1] Frøjk, M. M. N., Bjergmark, N. F. H., Bjerg, R. L., Gomila, R., & Valero, P. (**2020**). *Metal to composite: Redesign of centrifugal pump impeller*. In Proc. The 8th Student Symposium on Mechanical and Manufacturing Engineering (pp. 1-8).

[2] Spitzer, S., Grothe, R., Gude, M., Pohl, M., & Hermerath, P. (**2022**). *Endless Fibre Reinforced Composite-Metal-Impeller: High Speed Burst Testing-Damage and Failure Analysis*. International Conference on Fan Noise, Aerodynamics, Applications and Systems, FAN 2022, Senlis, France. https://doi.org/10.26083/tuprints-00021698.

[3] Mihalache, R., Vintila, I. S., Deaconu, M., Sima, M., Malael, I., Tudorache, A., & Mihai, D. (**2021**). *Novel carbon fibre composite centrifugal impeller design, numerical analysis, manufacturing and experimental evaluations*. Polymers, 13(19), 3432.

[4] Lin, J., Jin, Y., Zhang, Z., & Cui, X. (**2014**). *Strength Analysis of the Carbon-Fiber Reinforced Polymer Impeller Based on Fluid Solid Coupling Method*. Mathematical Problems in Engineering, 2014(1), 803261.

[5] Patil, M., & Müller, N. (**2013**). *Structural analysis of continuous fiber wound composite impellers of a multistage high-speed counter rotating axial compressor for compressing water vapor (R-718) as refrigerant using Finite Element Analysis*. Materials & Design, 50, 683-693.

[6] Tian, Y. B., Qi, X. Y., & Hu, J. X. (**2011**). *Preferentialness design of a composite impeller with ultra-low unit speed centrifugal pump*. Advanced Materials Research, 308, 2353-2357.

[7] Wang, J., Patil, M., Olortegui-Yume, J., & Müller, N. (**2010**). *Mechanical design of wound composite impeller using FEM*. In ASME International Mechanical Engineering Congress and Exposition (Vol. 44465, pp. 195-201).

[8] Spitzer, S., Pohl, M., Grothe, R., Langkamp, A., Hermerath, P., & Gude, M. (**2018**). *Endless fibre-reinforced composite-metal-impeller: material related design and dimensioning process for hybrid radial-fans*. In Darmstadt: Paper presented at the International Conference on Fan Noise, Aerodynamics, Applications and Systems. International Conference on Fan Noise, Aerodynamics, Applications and Systems FAN 2018, Darmstadt, Deutschland.

[9] VDI-Gesellschaft Produktentwicklung und Projektmanagement: VDI-Richtlinie 2221 Blatt 1 Entwicklung technischer Produkte und Systeme - Modell der Produktentwicklung. Ausg. Nov. **2019**.

[10] Cuntze, R. G., & Freund, A. (**2004**). *The predictive capability of failure mode concept-based strength criteria for multidirectional laminates*. Composites Science and Technology, 64(3-4), 343-377.

[11] Pohl, M., Spitzer, S., Dannemann, M., Hermerath, P., König, R., Langkamp, A., & Gude, M. (**2022**). *Endless Fibre-reinforced Composite-Metal-Impeller: Investigation and Comparison of the Damping Behaviour*. International Conference on Fan Noise, Aerodynamics, Applications and Systems FAN 2022, Senlis, France. https://doi.org/10.26083/tuprints-00021706

[12] Dargel, A.; Kunze, E.; Barth, J.; Ebert, C. and Gude, M. (**2024**): *Prelimenary studies on fan impellers made of continuous fibre-reinforced polymer in modular design for improved performance in sustainable energy applications*. SAMPE Europe Conference & Exhibition 2024; Belfast, United Kingdom, 24 – 26 September 2024. ISBN/EAN: 978-90-833728-1-5

C1 Artificial Intelligence & Machine Learning

10 April - 9:30 - Auditorium
Chairman: Lorenzo Tieghi

List of papers

AI Based Prediction of Noise Emission of Protective Grilles in Axial Fan Assemblies

- Andreas LUCIUS – ebm-papst Mulfingen GmbH & Co. KG (Germany)
- Marc SCHNEIDER – ebm-papst Mulfingen GmbH & Co. KG (Germany)
- Lionel DSILVA – ebm-papst Mulfingen GmbH & Co. KG (Germany)
- Thomas GEYER – German Aerospace Center (Germany)

Broadband Noise Prediction of a Low-Pressure Fan Based on Machine Learning

- Soichi SASAKI – Nagasaki University (Japan)
- Takeru HOSOI – Nagasaki University (Japan)

Data-Driven Prediction of Fan Broadband Noise

- Z ZHOY – Universite de Sherbrooke (Canada)
- Andrea ARROYO RAMO – Universite de Sherbrooke (Canada)
- Ralph Kinte POUHE HIOL – École de technologie supérieure (Canada)
- Saurabh PARGAL – Michigan State University (USA)
- Stéphane MOREAU – Universite de Sherbrooke (Canada)
- Marlène SANJOSÉ – École de technologie supérieure (Canada)

AI BASED PREDICTION OF NOISE EMISSION OF PROTECTIVE GRILLES IN AXIAL FAN ASSEMBLIES

Andreas LUCIUS[1], Marc SCHNEIDER[1],
Lionel DSILVA[1], Thomas GEYER[2]

[1] *ebm-papst Mulfingen, Bachmühle 2, 74673 Mulfingen, Germany*

[2] *German Aerospace Center (DLR), Lieberoser Straße 13a, 03046 Cottbus, Germany, formerly: Brandenburg University of Technology Cottbus – Senftenberg, Siemens-Halske-Ring 14, 03046 Cottbus, Germany*

SUMMARY

The paper describes a method for prediction of sound power spectra of protective grilles installed on the pressure side of an axial fan. It is based on wind tunnel experiments for tandem cylinders in crossflow. These measurements are used to train a neural network for the prediction of sound spectra. In addition, these measurements show that commonly used ring distances in combination with low flow angles lead to increased noise due to ring interaction. The flow field around the rings is derived from a standard CFD of the fan without protective grille. The neural network is used to predict noise spectra for each ring. This workflow enables the prediction of sound power spectra with high accuracy for different protective grilles and can be utilized to optimize the ring arrangement according to specific design requirements.

INTRODUCTION

Protective grilles are an important component of axial fan assemblies. The grilles serve as contact protection and are intended to prevent injury from the rotating impeller. The workflow presented is applicable for pressure side installation. The grille is placed in the turbulent wake of the impeller and generates both: an additional pressure loss and an additional noise emission compared to the fan alone. Especially at high volume flow rates, some protective grilles show high impact on noise emission. Low noise designs represent an important development goal for the fan manufacturer. As the fan self-noise is reduced with advanced design, other components like the protective grille may dominate the overall noise emission of the fan assembly.

A protective grille consists of many closely spaced rings that are attached to a supporting structure. The supporting structure also serves as a connection between the upright housing and the fan with motor. In addition, thin retaining struts are provided to stiffen the construction. To ensure reliable contact protection, DIN EN ISO 13857 [1] specifies maximum distances between the rings, restricting the design options. Commonly the maximum allowed distances are chosen to achieve minimal number of rings and blockage of the flow. One finding of this investigation is, that this arrangement may not be optimal considering noise

emission. For a numerical optimization towards low noise design a prediction workflow is needed. CAA (Computational Aero-Acoustics) simulations on complete fan assemblies are possible but with very high numerical effort. The turbulent flow around each ring in the turbulent wake of the fan has to be resolved with high accuracy. Beside traditional Navier Stokes CFD the Lattice-Boltzman Method is a favorable method for such computations. Lörcher et al. [2] applied the Lattice-Boltzmann Method to compute the noise emission in a radial fan with complex housing.

The authors present a method, that is based on vortex shedding at the rings as the major mechanism of sound generation. The model is cheap and does not rely on heavy CAA computations and is therefore attractive as prediction method in an optimization process.

NOISE EMISSION OF TANDEM CYLINDERS IN CROSSFLOW

The main noise emission mechanism of protective grilles is the flow around the narrow-spaced rings and the support structure. Measurements of the fan with support structure but without rings show minor influence, in the following the focus is on the rings only. As the diameter of the rings is much larger in comparison to the wire diameter, the curvature of the ring is neglected. The problem is idealized to flow around straight cylinders. The noise emitted by cylinders in crossflow is well known and dominated by Aeolion tones due to vortex shedding [3]. In case of turbulent inflow conditions additional broadband noise is emitted. There are design approaches to reduce vortex shedding with modified cylinders. In Stadtmüllers patent [4] twisted sharpe-edged cross sections instead of circular rings are applied for noise reduction of protective grilles. Geyer and Sarradj [5] published a study on cylinders with porous coating for noise reduction. In the present paper the focus is not on modified ring geometry, the authors try to find guidelines for optimal positioning of conventional cylindrical rings.

The positioning of rings in a guard grill arrangement must follow design rules specified by norms. According to DIN EN ISO 13857 [1] typical inter ring distances close to the blade are in the range of 10 mm to avoid that fingers can touch the rotating blade. This leads to very narrow-spaced rings. A key figure is the ratio of center-to-center distance of 2 rings to the wire diameter (P*= d/D). The angle between cylinder alignment and flow direction is the second key figure. In case of small angles, the wake of the upstream cylinder interferes with the second cylinder leading to increase force fluctuations and noise. Figure 1 shows a protective grille assembly in the right-hand side. At maximal flow rate the flow direction downstream the fan is almost axial. For a specific pair of rings, the angle depends on flow direction and the ring arrangement in the grill assembly. The definition of angle and distance is displayed in the left-hand side of Figure 1. The plot shows the flow field from a quasi 2D Large Eddy Simulation (LES) with P*=3.2 and α=20° with disturbed inflow conditions.

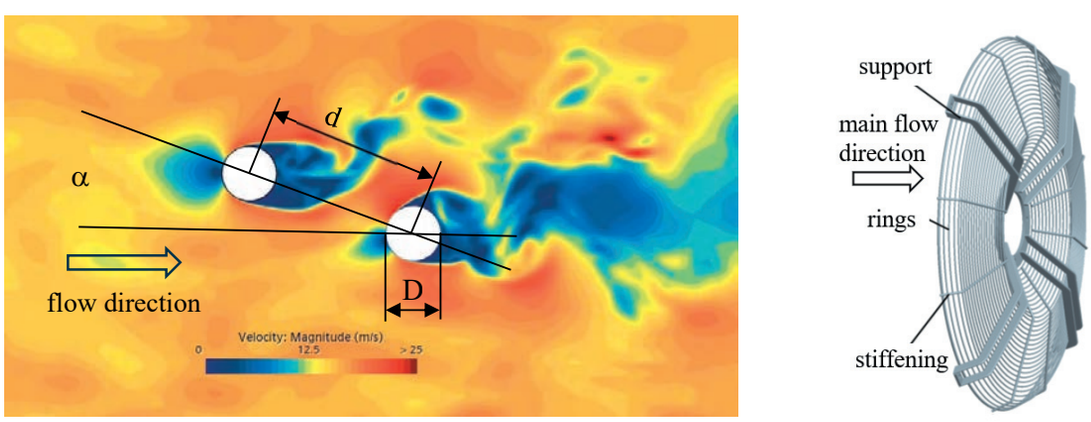


Figure 1: flow around tandem cylinders in crossflow from quasi 2D CAA (left) and fan grille (right)

The flow around tandem cylinders in crossflow has been the topic of various research papers. A comprehensive summery of the effects is given in the research paper by Zhou and Alam [6]. For small distances the wake of the first cylinder interacts with the second cylinder leading to increased fluctuating forces and noise. As there is a lack of measurement data especially for noise in the required range of Reynolds numbers the authors decided to measure the noise of tandem cylinders in crossflow in the acoustic wind tunnel of the BTU Cottbus.

The range of parameters is given in Table 1. Inflow turbulence was generated by two turbulence grids namely G1 and G2 with turbulence intensity of 5.5 and 7.5 %. Noise was measured with a microphone array mounted on a plate. With this setup can unfortunately not measure sound power which is the key figure in the protective grill model. This requires some corrections mentioned later. In a recent publication Geyer et al [7] measured noise emission for single cylinders in the same wind tunnel with the corresponding array. They investigated a larger range of Reynolds number with larger diameter of the cylinder. They found that the vortex shedding peak Strouhal number depends on Reynolds number and on the inflow turbulent length scale.

Table 1: parameters range in experimental investigation

Parameter	Range
P* = d/D	2.8, 3.2, 3.8, 4.4
Velocity	10, 15, 20, 25, 30
Angle	0° – 90°
Re	1700 – 5000
Tu	5.5%, 7.5%

The analysis of the noise measurements presented in this paper confirms the expected behavior as documented in the literature for fluctuating forces [6]. Figure 2 displays the spectra for the nondimensional distance P*=3.8 at 20 m/s inflow velocity. Spectra are averages of 5 microphones selected from the array, which are almost on a horizontal line in the mid of the cylinders height. The angle has strong influence on peak amplitude and frequency. For low angles there is one major peak at Strouhal number St=0.2 and a weak second harmonic. With increasing angle the peak level decreases, at angles higher than approx. 40° the peak splits into 2 separate peaks. The distance of the peaks in frequency slightly changes with increasing angle.

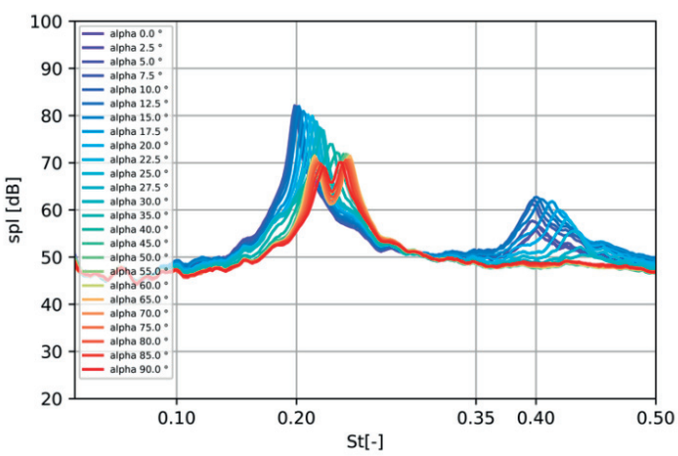


Figure 2: sound pressure spectrum depending on angle, P=3.8, u=20 m/s, G2*

The corresponding contour plot for all measured angles and distances is displayed on the left of Figure 4. It illustrates the overall sound pressure level (SPL) in the range of Strouhal number from 0.1 to 0.5. The shown conditions are constant velocity of 20 m/s and high turbulence intensity of 7.5%. It clearly demonstrates that angles smaller than 30° result in significantly increased noise emission. With respect to distance, maximal SPL appear at P* in the range of 3.2 to 3.8, with a very strong decrease toward small distances. Some more details on the acoustic measurements together with a simple analytical prediction approach were presented at the DAGA 2022 [8].

MODELLING THE SOUND SPECTRA WITH ANN

Due to the complex shape of the spectra (different number of peaks depending on angle, additional effect of turbulence on broadband noise) the authors decided to model the spectra with an ANN (Artificial Neural Network) of the classical MLP (Multi Layer Perceptron) approach. All computations were done using the python package TensorFlow [9]. The input parameters are distance, velocity, angle and turbulence intensity. The output is a spectrum in Strouhal number ranging from 0.1 to 0.5 discretized by 401 points. For training the ANN all single spectra are interpolated to these discrete Strouhal numbers (left diagram in Figure 3). The data was randomly split into 80% training and 20% test data. The authors used 2 hidden layers with increasing number of neurons in each layer. The hyperparameters of the model (number of epochs, learn rate, number of neurons, activation function) were varied to study their influence. The results presented in the following graphs are evaluations of the model with best results concerning mean absolute error of the overall sound pressure level. Figure 3 shows the comparison of model prediction and experimental result. The left diagram displays the spectra for 2 exemplary selected samples. The red curves indicate the first training sample, whereas the blue curve represents the first sample of the test data. There are slight differences in the peak levels in the range of 1 dB. The right diagram of Figure 3 shows the overall sound pressure level (OASPL) of all samples. Again, red points indicate training samples and blue points test data. The agreement of model prediction and experimental values is very good with a mean average error of 0.5 dB.

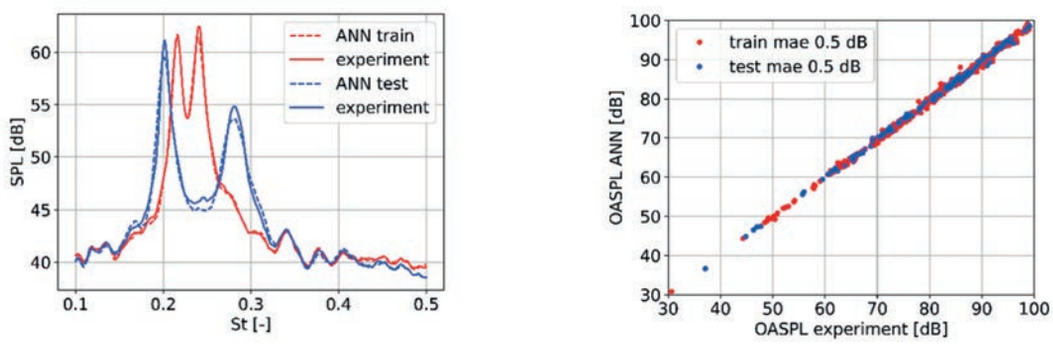


Figure 3: assessment of the ANN prediction quality in terms of sample spectra (left) and overall sound pressure level (right), data is split into train (red) and test (blue)

Another target was to avoid local under- or overshoot, which is commonly known as overfitting. The smooth model behaviour concerning overall SPL distribution is displayed in the right-hand side of Figure 4. The ANN is evaluated with a high resolution in terms of angle and distance. Measurements and ANN prediction show a good agreement. The model results show the final state with additional information from CAA simulations.

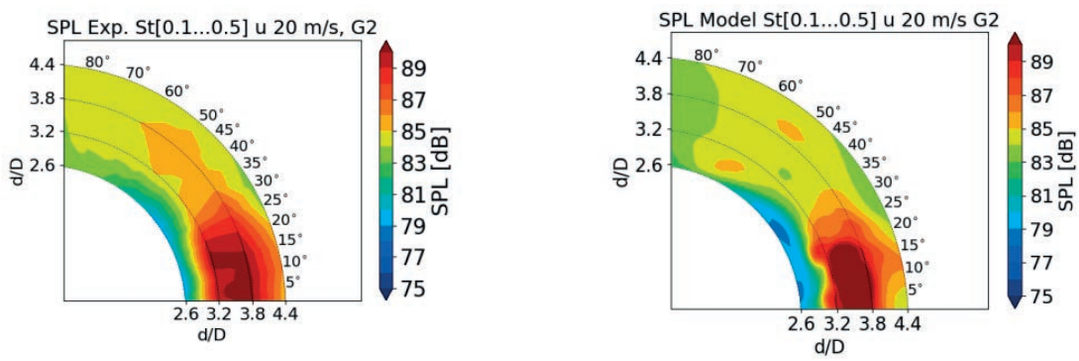


Figure 4: overall sound pressure level for20 m/s G2, measurement (left) and ANN prediction (right) CAA included

Using the initial training data from measurements, the ANN model behavior with respect to velocity and especially turbulence intensity was not satisfactory. Figure 5 displays ANN predictions at α=20°. The dots indicate measured values. Rising SPL towards low velocities is not a physical bevaviour. Depending on the operating point of the fan velocities lower than 10 m/s may be important. As additional reference, u^5 dependance is drawn in the diagram, which is a good approximation of the measurements. This is actually no limitation of the modeling approach, it is just an effect of extrapolation. This issue may also be handled via limiting the velocity or adding low velocity measurements. As the data was generated in a single closed measurement campaign we were not able to add lower velocity experiments.

Even more challenging is the limitation to only 2 different values for turbulence levels. The graph on the right-hand side of Figure 5 shows very strong increase towards high turbulence levels. At measured turbulence intensities the SPL prediction suddenly drops and increases again towards low turbulence levels.

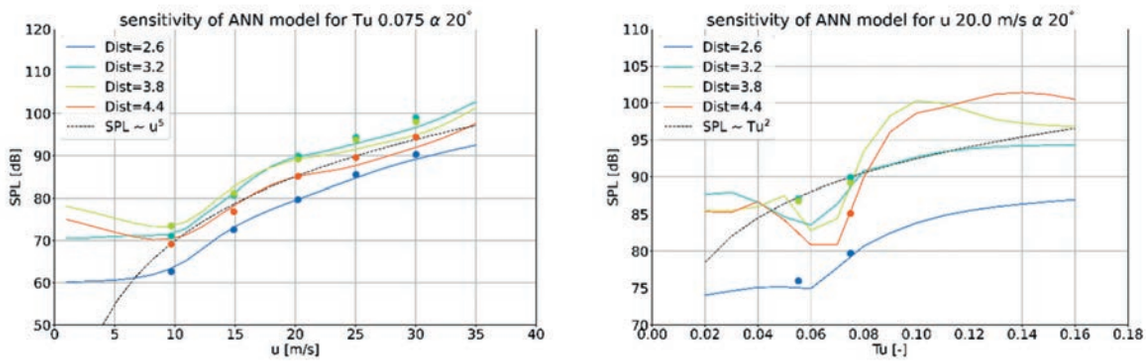


Figure 5: ANN prediction of the overall sound pressure level depending on velocity (left) and turbulence intensity (right), points indicate measured values

Amiets model [10] suggests an increase of SPL with an exponent of 2 with respect to turbulence intensity. A case-to-case comparison demonstrated that most data points follow the expected trend, but in the range of cylinder interference (low distance and angle) behaviour changes. For some data points even a decrease of SPL with increasing turbulence level is found. Again, we face the problem of extrapolation.

QUASI 2D CAA OF TANDEM CYLINDERS

As it was hard to realize substantially different turbulence levels with a grid, the idea was to introduce quasi 2D CAA simulations as shown in Figure 1 to extend the range of this parameter. These simulations were initially done as validation of the CAA method at ebm-papst. Compressible Large Eddy Simulations in StarCCM+ (WALE subgrid scale) are applied, the far field noise was calculated with the FW-H integral method for receiver positions corresponding to the experimental setup. In spanwise direction a periodic boundary condition was applied.

A variation of spanwise extension with a single cylinder showed 6 D is sufficient to provide independent results. The non-reflecting free stream boundary condition was used for all other far field boundaries. The inflow turbulent fluctuations were realized with a synthetic method. Anisotropic linear forcing [11] generates turbulent fluctuations in a simulation volume. User specified fields are used as reference turbulence conditions. The mesh size of each CAA simulation is in the range of 8 million polyhedral cells. The large computational effort allows only limited number of computations. The additional usage of computations is useful to improve the prediction process but is not an option to replace the measurements (approx. 800 data points) completely with CAA. Exemplary comparison of CAA results and measured spectra is shown in Figure 6. Left-hand side shows α=20° and the right-hand side α=40°, with distance P*=3.2 and 15 m/s inflow velocity.

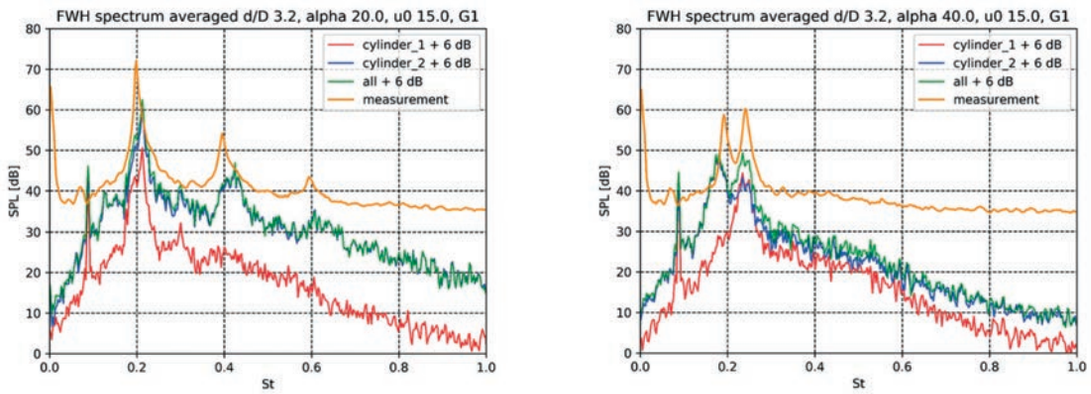


Figure 6: average sound pressure spectra of quasi 2D CAA results versus experiments

The most prominent difference is a level offset of roughly 10 dB. Neglecting this offset at least the trends of measurement and CAA are in good agreement. The CAA sound pressure levels are scaled to match the experimental cylinder length. In experiments the microphones are mounted on a rigid plate. This results in a SPL offset of +6 dB compared to free field CAA results. The remaining difference of 10 dB is attributed to installation effects in the wind tunnel (cylinders between two plates). The change of spectrum shape due to variation of angle and distance was well predicted by the CAA method. There is a spurious peak below St 0.1 which is attributed to the periodic boundary conditions in spanwise direction. It does not affect the downstream process. The CAA method also allows to split the effect into single cylinder contributions. For most cases the downstream cylinder dominates sound emission of the tandem configuration. Left graph in Figure 6 shows this effect at an angle of 20 degrees. The spectra on the right show an interesting detail: for 40 degrees at distance 3.2 the tandem cylinder measurement shows 2 peaks. The first peak slightly below St=0.2 is attributed to the downstream cylinder 2. At the second peak at St=0.25 both cylinders evaluated show the same peak amplitude. The resulting spectrum emitted by both cylinders is 6 dB above due to in phase vortex shedding at both cylinders.

This splitting into each cylinder's contribution is later used to transfer the tandem cylinder measurement to a single cylinder evaluation for the protective grill noise model. In the model each cylinder is treated as the downstream cylinder of the tandem arrangement. For each of the simulations the difference of overall SPL between second cylinder and the tandem cylinders is calculated. This leads to a correction field depending on angle and distance which was limited to values between -3.0 and 0.0 dB. If there is no interference (high distances and angles) the correction approaches -3.0 dB, which means that the downstream cylinder spectrum is equal upstream cylinder spectrum. The resulting tandem cylinder spectrum from the measurement is corrected by -3.0 dB to get the downstream spectrum. For low angles and distances, the correction field approaches zero, the downstream cylinder spectrum is almost equal to the noise measurement from two cylinders (as illustrated on the left graph of Figure 6). The correction field value for any specific combination of angle and distance is calculated via inverse distance interpolation from the existing points evaluated with a CAA simulation. This simple correction is good initial suggestion, but not able to account for special phenomena illustrated in the right graph of Figure 6.

Initially 23 simulations were performed for validation of existing measured test configurations (all with G1 turbulence and 15 m/s) and computation of the SPL correction described above. In the following additional 20 simulations were done with free variation of the 4 parameters (P*, u, α, Tu). The parameters were chosen with a latin hypercube sampling. All simulations results use the same inputs and yield the same outputs as the experiment. This allows the integration into the ANN workflow with an additional parameter describing the source of the sample (experiment or simulation). With additional information obtained from CAA, significant improvement of the ANN prediction for measurements was achieved as displayed in Figure 7. The increase of SPL toward low velocities is avoided, as low velocity information is provided from the CAA. At very high velocities outside the range of the database non-physical increase of SPL is observed due to extrapolation. For the fan used as validation testcase, velocities are always below 20 m/s. Handling this issue may be needed for other applications. For turbulence intensity very high sound pressure levels at high Tu are not observed any

more. The model with additional simulation data shows smooth increase of sound pressure level with increasing turbulence intensity.

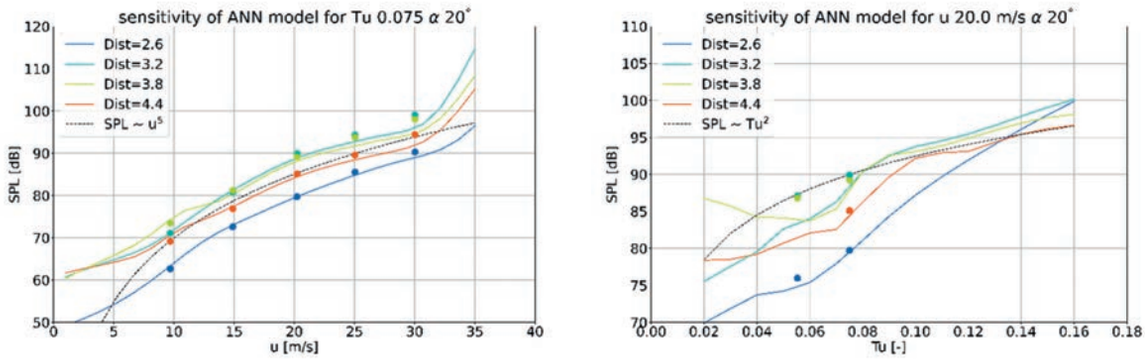


Figure 7: ANN prediction of the overall sound pressure level depending on velocity (left) and turbulence intensity (right), training data from measurement and quasi 2D CAA

High turbulence intensities could not be realized with the ALF method. The method was initially designed to provide synthetic turbulent fluctuations in a boundary layer [11]. For mean flows without gradient the method tends to produce smaller fluctuations compared to the specified reference value. For our application the realized turbulence intensity was measured via point probes. This value was then used as input for training the ANN model. The model prediction is improved with additional CAA input, but still shows strong increase of SPL towards high values of turbulence intensity. The reason is lack of high turbulence intensity samples. For practical application in the downstream process, the input turbulence level is limited to avoid unphysically high SPL

MODEL FOR SOUND POWER OF PROTECTIVE GRILLES

With the ANN model from the previous section a prediction of sound pressure spectra for any geometric and flow parameter is possible. ANN model performance was shown in the typical range of flow parameters and ring distances for a fan protective grille. The chosen testcase is an axial fan with 800 mm diameter rotating with 900 revolutions per minute. In the next step we integrate the ANN into a sound power prediction workflow for protective grilles.

The starting point is a CFD simulation of the fan. At ebm-papst these simulations are done in a standardized workflow using starCCM+ with the k-epsilon realizable turbulence model in a Multi Reference Frame (MRF) simulation. Figure 8 displays the comparison of measured to simulated performance curves. Integral results are in close agreement with measurements. The strong correlation of the integral results instills confidence in the reliability of the field data. The authors use a CFD of the fan without protective grille as reference. This approach has the advantage, that a single CFD is sufficient for any ring arrangement of a protective grille. On

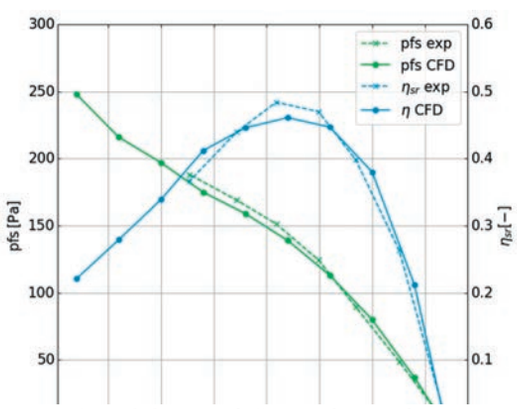


Figure 8: validation of CFD - fan performance curve

the other hand, the influence of the rings on the flow field is neglected. Especially for narrow-spaced rings the blockage will lead to a redistribution of the flow velocities.

In the next step the required flow parameters for all cells in the region of interest are stored in python readable binary files. For each of the rings, all cells close to the ring position are extracted. For every of these cells an ANN prediction of the SPL spectrum is done for the cells flow parameters. The turbulence levels are limited to a threshold, which can be optimized e.g. depending on turbulence model. For the final model turbulence level is limited to 12.5 %. CFD cell values higher than this threshold use the limit as input for the ANN model. The velocity field is evaluated in cylindrical coordinates. Only the radial and axial component of the flow velocity are used. The circumferential component is aligned with the ring and does not contribute to noise emission. The flow angle needs to be transferred to the ANN model definition, it is the angle between the center-to-center line of two adjacent rings and the flow velocity. The sound pressure spectrum for each ring is now calculated as the logarithmic sum over all cell values. Before summation, the SPL(St) spectrum from ANN prediction is transferred to frequency in One-third octave bands for a consistent summation. The data processing in the company test rig returns One-third octave band spectra only, narrow band spectra of sound power are not available. As described above, the main contribution comes from the downstream cylinder. We assume that each ring is a downstream cylinder in a tandem arrangement. To correct the tandem cylinder spectrum to the downstream cylinder a constant SPL correction is subtracted from the ANN spectrum depending on distance and angle of the tandem configuration. This process is repeated for every ring. The final spectrum is the logarithmic sum of all single ring spectra. The advantage of the ring wise approach is, that in addition to the integral result for all rings, we can evaluate single ring contributions and identify critical rings.

The sound power spectrum of the fan including protective grille is finally calculated as logarithmic sum of the One-third octave spectra from the fan measured without grille and the model prediction as shown in Figure 9. The result is compared to a measurement of the fan with protective grill in the same operating point. A constant offset of -11.0 dB is added to the predicted model spectrum to account for the conversion from sound pressure spectrum of the ANN model to sound power. Figure 9 shows exemplary comparisons for one of the selected protective grilles. For the free blowing condition on the right the peak levels at 1000 and 1250 Hz are overpredicted by the model, but the overall level is very close to measurement. For the operating point with minimal acoustic emission on the left, peak levels predicted at 1000 Hz are in close agreement to measurements. The model correctly shows the main effect of the protective grille around 1000 Hz. A comparison of the measurements with and without grill indicate a broadband increase of roughly 2 dB for most frequencies outside the main influence region. This offset is not predicted by the model. A reason is probably the limitation of all spectra to Strouhal number from 0.1 to 0.5.

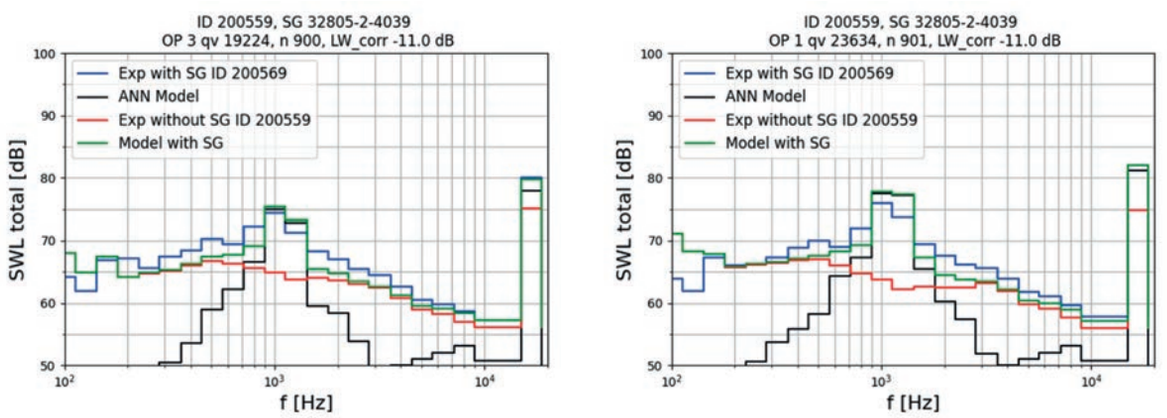


Figure 9: prediction of sound power spectra vs measurements, best acoustics (left) and free blowing condition (right)

The value of the constant offset is determined via fitting the sound power curves of 3 different protective grilles with different ring arrangement. Figure 10 shows that the model accuracy is very good for these three cases. The predicted overall sound power level deviates less than 1 dB from the measured sound spectra. Slightly higher deviations are found at very low flow rates. These operating points are of minor interest, as efficiency is low and noise emission of the fan itself is high.

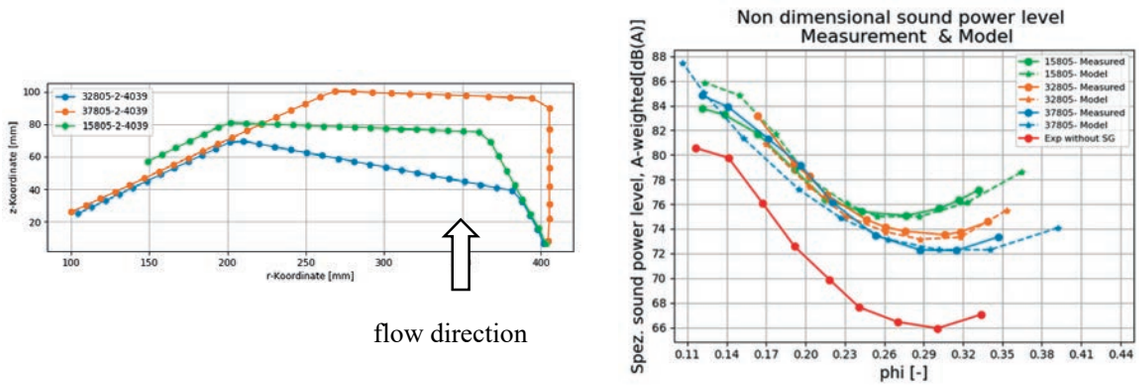


Figure 10: ring arrangement (left) and comparison of sound power measurements to model predictions for different protective grilles (right)

The reason for the strong increase of sound power at high flow rates is found as combination of high flow velocities and low angles in the range of 20 degrees. At free blowing conditions the flow direction is almost axial, such that the angle as shown in Figure 1 is equal to the angle of the ring arrangement. In addition, the velocity profile downstream the impeller is typically not uniform but increasing in radial direction toward the blade tip. Grille 15805 has several rings with critical angle in the high velocity region. For Grille 32805 the critical angles are not located at high velocity regions. Grille 37805 has no critical angles. In addition, the rings are located further downstream. Turbulence decays with increasing distance and high velocity spots e.g. in the tip leakage flow mix out further downstream.

SUMMARY

The authors present a workflow for the prediction of sound power emitted by a protective grille installed on the pressure side of an axial fan assembly. The process is applicable for any fan as it uses the flow field downstream the fan from a standard CFD. It is limited to cylindrical rings. For validation a testcase with 3 different grilles was chosen for one specific fan. Very good agreement in terms of One-third octave spectra as well as overall sound power level was found. The method is based on an ANN model for the noise emission of tandem cylinders in a wind tunnel experiment. Due to insufficient variation of turbulence levels in experiment, quasi 2D CAA computations were used as additional input. A synthetic turbulence generation approach enabled the realization of different turbulence levels. Even though the number of additional data points were small compared to the measurements significant improvement was achieved. Since both types of input data were classified with an additional parameter, the systematic deviation of CAA and measurements did not deteriorate the predictions. For further improvement of the prediction method the effect of the protective grille on the flow field is needed. The actual workflow relies on the flow field from a fan without grill. The wind tunnel measurements show that there is large potential for noise reduction with more narrow-spaced rings. In such a case the authors expect more influence of the presence of the rings on the flow field with less accurate predictions of the emitted sound power. Finally more testing for other fan and grill configurations is required to prove the general applicability of the approach.

BIBLIOGRAPHY

[1] DIN EN ISO 13857: *Sicherheit von Maschinen – Sicherheitsabstände gegen Erreichen von Gefährdungsbereichen mit den oberen und unteren Gliedmaßen*, **2019**

[2] F. Lörcher, S. Hub, M. Sanjosé, S. Moreau – *Investigations Concerning the Flow Stabilization of Backward Curved Centrifugal Impellers at Low Flow Rate.* Proceedings of fan 2022 Conference Senlis, **2022**

[3] Beyer, R.T.: *Sounds of our times: two hundred yours of acoustics*, Springer-Verlag, New York, p. 95, **1999**

[4] U. Stadtmüller – *Schutzvorrichtung*, DE 10 2012 020 245 B4, **2015**

[5] T. Geyer, E. Sarradj - *Circular cylinders with soft porous cover for flow noise reduction,* Experiments in Fluids 57(3), **2016**

[6] Y. Zhou, M.M. Alam - *Wake of two interacting circular cylinders: a review,* International Journal of Heat and Fluid Flow 62, p 510-537, **2004**

[7] T. Geyer, A. Lucius, M. Schneider, L Enghardt - *Aerodynamic noise from circular cylinders under turbulent inflow conditions,* Proceedings of the 30th AIAA/CEAS Aeroacoustis Conference, Rome, **2024**

[8] Shokri, M., Lucius, A., Schneider, M. and Geyer, T.: *Aeroacoustics of Tandem cylinders in crossflow – application to fan guard grills*, Proceedings of DAGA 2022 Stuttgart, **2022**

[9] M. Abadi, P- Barham, J. Chen, Z. Chen, A. Davis, J. Dean, M. Devin, S. Ghemawat, G. Irving, M. Isard, M. Kudlur, J. Levenberg, R. Monga, S. Moore, D. G. Murray, B. Steiner, P. Tucker, V. Vasudevan, P. Warden, M. Wicke, Y. Yu, X. Zheng - *TensorFlow: A system for large-scale machine learning,* Proceedings of the USENIX Symposium on Operating Systems Design and Implementation, **2016**

[10] A. R. Amiet - *Acoustic Radiation from an airfoil in a turbulent stream,* International Journal of Sound and Vibration 41(4), p 407-420, **1975**

[11] B. De Laage de Meux, B. Audebert, R. Manceau, R. Perrin - *Anisotropic linear forcing for synthetic turbulence generation in large eddy simulation and hybrid RANS/LES modeling*, Physics of Fluids 27 (3), **2015**

BROADBAND NOISE PREDICTION OF A LOW-PRESSURE FAN BASED ON MACHINE LEARNING

Soichi SASAKI and Takeru HOSOI

Nagasaku University, Graduate School of Integrated Science and Techanology,
1-14 Bunkyo-machi, Nagasaki, Japan

SUMMARY

A machine-learning-based methodology was introduced for the prediction of broadband noise generated from a low-pressure fan. The pressure power spectral density (PSD) at the blade trailing edge, a key parameter in prediction theory, was experimentally determined using the measured sound pressure PSD of a flat plate in a wind tunnel test. Machine learning-based prediction accurately predicted the overall noise level, including the discrete frequency noise generated by Karman vortex shedding. The predicted broadband noise indicated that the broadband noise of the fan consisted of low-frequency wake vortex noise and high-frequency trailing-edge noise, with the noise being more prominent near the blade tip owing to higher circumferential velocity.

INTRODUCTION

Low-pressure fans are widely used in our daily lives in air conditioners, ventilation systems, automobile engine cooling systems, etc. Thus, improved aerodynamic performance and reduced fan noise are important technical issues. Fukano et al. proposed a prediction theory for broadband noise generated by Karman vortex street based on an experiment on a rotating isolated blade [1]. However, the prediction theory was modeled on macroscopic wake characteristics, making it difficult to explain the spectral distribution of broadband noise, especially in the high-frequency domain. Amiet indicated that the aerodynamic sound source of a flat plate was formed in the vicinity of the trailing edge through the backscattering of turbulent flow and expressed the spectral distribution of broadband noise [2]. The main parameters in the prediction theory were the radiation integral and pressure power spectral density (PSD). In many studies of model analyses, Schwarzschild's analogy solution was used for the radiation integral [3-4]. The pressure PSD is also an unknown function. Many researchers have proposed original pressure PSD models in their investigation [5-7]. However, it is difficult to theoretically determine the pressure PSD through model analysis or numerical simulations with high accuracy [8-9]. On the other hand, in the last decade, many studies on machine learning have been conducted in the field of fluid engineering. Regression models in machine learning are useful for identifying the relationships between the factors hidden in a large amount of data. However, to the best of our knowledge, few practical studies have been conducted on the prediction of fan noise using machine learning. If the pressure PSD can be determined based on machine learning, it may be possible to deploy machine learning to predict the fan noise.

Therefore, in this study, we developed a regression model in machine learning for the pressure PSD, after which we predicted the broadband noise generated from a low-pressure fan. First, the features obtained from the wind tunnel test were fed into a machine-learning model to create a regression model of the pressure PSD. The pressure PSD of the rotating blade elements was obtained when feature values in the relative flow regime were applied to the regression model. The broadband noise of the low-pressure fan was predicted by superimposing the pressure PSD of the segmented blade elements and multiplying by the number of blades. We discussed the features of the actual measured broadband noise compared to the predicted noise based on machine learning.

EXPERIMENTAL SETUP

Figure 1 is the configuration of the overall view of the wind tunnel facility for measuring the noise of a flat plate. The facility consists of a centrifugal fan, plenum chamber, anechoic room, and a measurement section. The size of the anechoic room is 2.1m height, 3.6m width and 2.3m depth. The flow straightening in the plenum chamber was constricted by a 100 mm square nozzle and discharged to the measurement part. The turbulence ratio of the main flow at the center of the nozzle was less than 1.0%. The sidewall of the anechoic room was covered with a sound insulation wall with an air layer. The sound-absorbing material was pasted on the ceiling and walls.

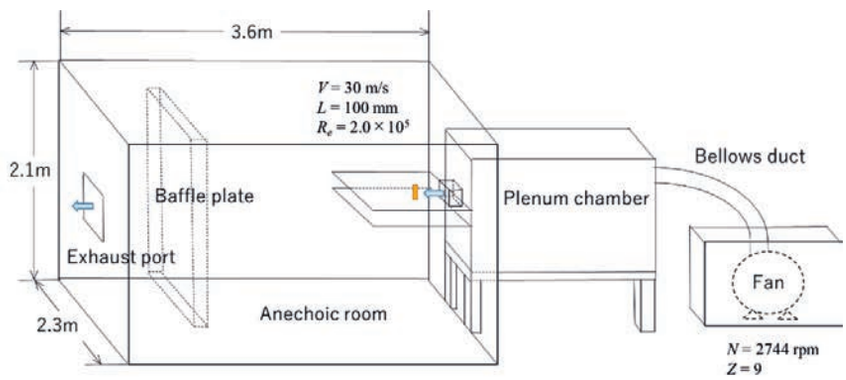


Figure 1: Overall view of the wind tunnel with anechoic room

Figure 2 is an enlarged view of the measurement section. The blade chord of the flat plate was 40 mm, span length was 100 mm, and thickness was 2 mm. The leading edge of the plate was placed 100 mm away from the nozzle exit. A sound level meter (Ono Sokki, LA-4350) with a 1/2 inch microphone was placed 500 mm from the trailing edge of the blade. The signal from the sound level meter was input to an FFT analyzer (Ono Sokki, CF5210), and the frequency response of the aerodynamic noise was analyzed.

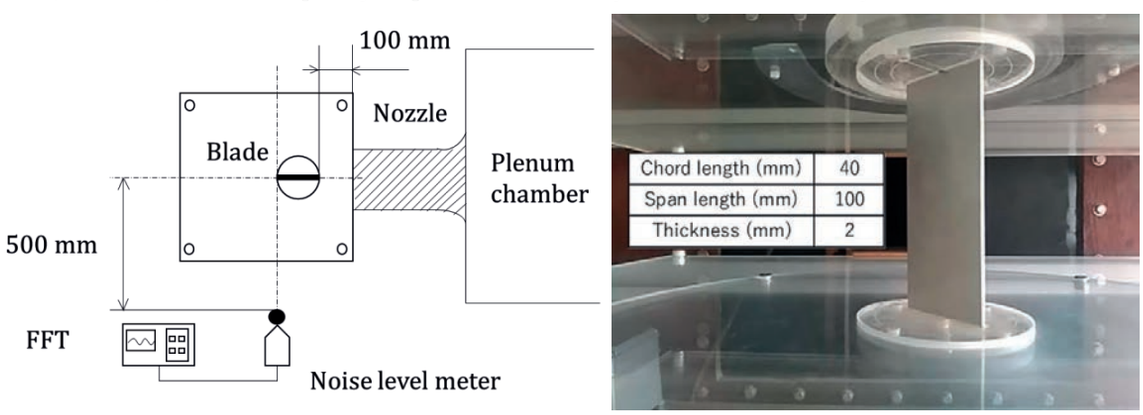


Figure 2: Enlarged view of the test section of the wind tunnel

In Figure 3, a schematic of the test bench used for the assessment of the fan performance is shown. The diameter of the impeller was 613 mm, hub ratio was 0.424, and the number of blades was 14. The height and width of the duct are 1.0 m each. The dynamic pressure was measured 600 mm upstream of the impeller using a pitot tube. The flow rate was deduced from the dynamic pressure and controlled by an adjustable throttle at

the duct exit. The static pressure of the fan was measured 400 mm upstream from the exit. The shaft torque of the motor was measured using a torque meter (Ono Sokki, SS-500), and the efficiency of the fan was estimated based on the ratio of shaft power to theoretical power. A 1/2-inch microphone (Ono Sokki, LA-4350) was set at distance of 1.0 m from the impeller inlet on the rotational axis of the impeller. The frequency signal of the measured fan noise was input into an FFT analyzer (Ono Sokki, CF5210).

The model used for the numerical simulation is shown in Figure 4 . The flow around the impeller was analyzed using numerical simulation. Cradle CFD was employed for the numerical simulation (CFD). A rectangular space (4.0 m) is placed on the exit side to ensure uniform flow on the duct outlet side. A second-order MUSCL scheme was employed to analyze the advection terms, and a modified SIMPLEC algorithm was used to analyze the pressure terms. The SST k–ω model was applied to the turbulence model. The flow rate was set at the inlet boundary, and atmospheric pressure was set at the outlet boundary.

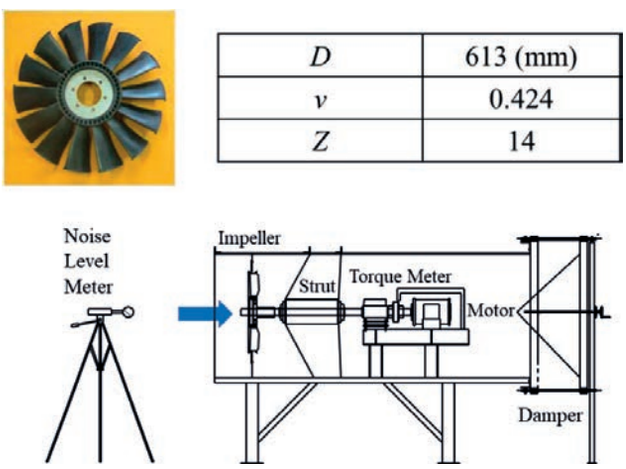


Figure 3: Impeller and test bench of the low pressure fan

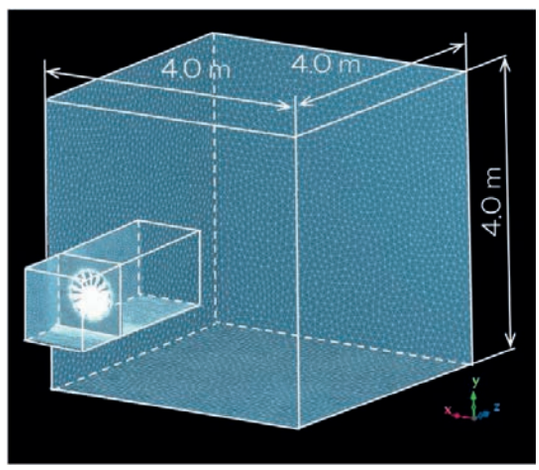


Figure 4: CFD model of the fan

BROADBAND NOISE PREDICTION

The turbulence passing through the trailing edge of the blade is illustrated in Figure 5. A boundary layer is formed between the mainstream of the uniform main velocity and the solid wall surface. The boundary layer thickness was sufficiently larger than the trailing edge thickness, which was also sufficiently smaller than the chord length. The turbulence inside the boundary layer passes through with convection velocity, and the turbulence is released into the wake. When the trailing edge of the blade is the criterion for the position, the pressure fluctuation propagates toward the leading edge on the blade surface from the trailing edge owing to the disturbance of the wake flow.

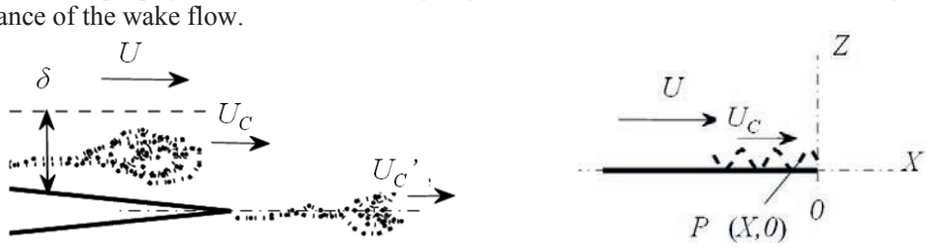


Figure 5 :Model of the turbulence passing through the trailing edge of the blade.

Equation 1 is the far-field sound pressure PSD proposed by Amiet.

$$S_{pp}(x,0,z,\omega) = \left(\frac{\omega b z}{2\pi c_0 \sigma^2}\right)^2 l_y(\omega) d |I|^2 S_{qq}(\omega,0) \tag{1}$$

where S_{pp} is the sound pressure PSD, l_y is the spanwise correlation length [10], d is the wetted span length, I is the radiation integral, and S_{qq} (ω,y) is the pressure PSD at the blade trailing edge. In this study, the pressure PSD was experimentally determined using the measured sound pressure PSD of

the flat plate in the wind tunnel test; the pressure PSD was used as the training data for machine learning.

A decision tree is employed in the regression model for the pressure PSD, as shown in Figure 6. A decision tree learns the given training data, selects highly relevant feature quantities among the parameters to be predicted, and forms a tree by repeating the case analysis. The region for distinguishing these is determined such that the residual sum of squares RSS is minimized.

$$RSS = \sum_{i \in R} (y_i - \bar{y}_R)^2 = \sum_{i \in R_1} \left(y_i - \bar{y}_{R_1}\right)^2 + \cdots + \sum_{i \in R_j} \left(y_i - \bar{y}_{R_j}\right)^2 \quad (2)$$

where $\bar{y}_R$ is the average value of sound pressure in each region, and each average values in these regions are the predicted value.

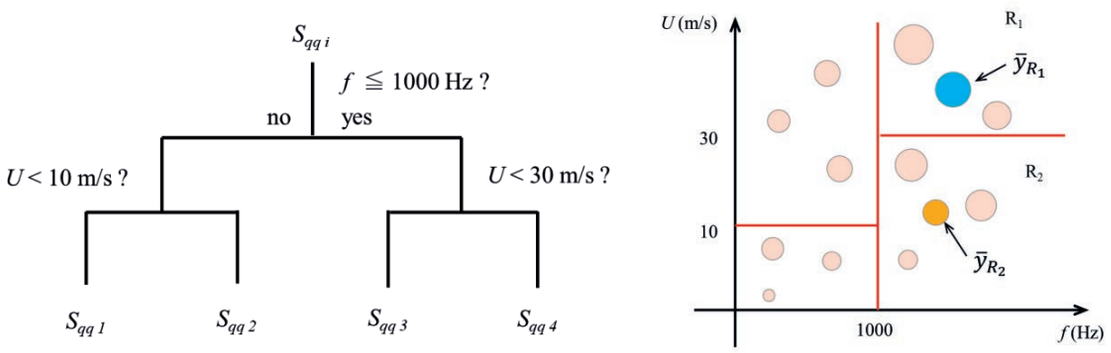


Figure 6: Schematic view of the decision tree

The feature values of the impeller wake were analyzed using CFD at five cross-sectional positions from the hub to the blade tip. The analytical position of the wake flow in each span was 5 mm behind the trailing edge of the blade elements. The relative velocity and deviation angle were calculated by circumferential averaging, and it was assumed that the relative flow field and absolute flow field of the wind tunnel test were similar, as shown in Figure 7. The regression model of machine learning uses the deviation angle, relative velocity, and frequency as feature values. The S_{pp} of the blade element in the relative flow field was obtained as the objective variable.

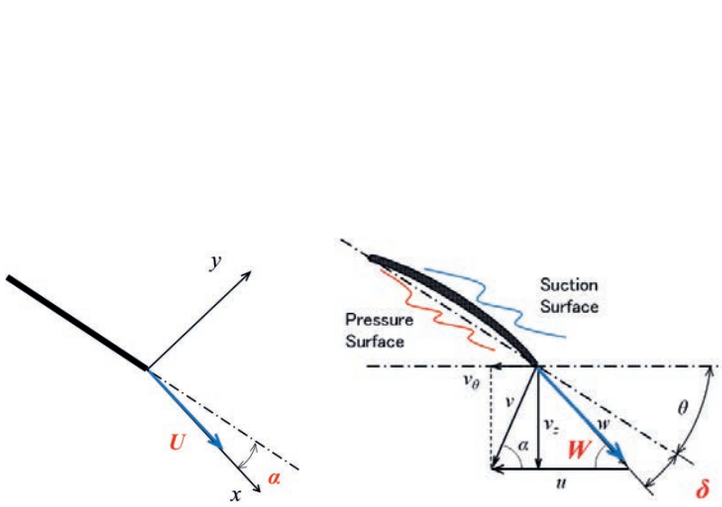


Figure 7 : Similarity of the relative flow field and absolute flow field

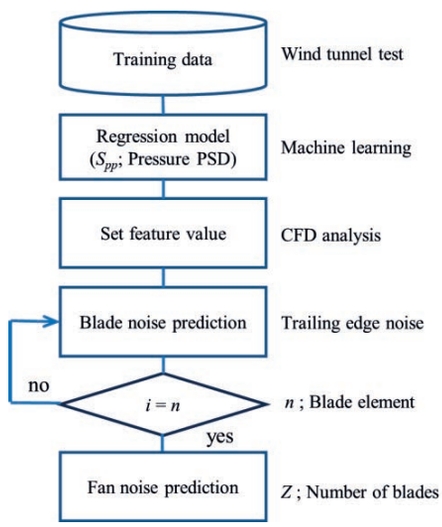


Figure 8 : flowchart of the fan noise prediction

Figure 8 shows a flowchart of the prediction of the fan noise based on machine learning. First, the feature values obtained from the wind tunnel test were placed in the decision tree to create a regression model for the pressure PSD. When the feature values were applied to this regression model, the spectral distribution of the

trailing-edge noise generated by the blade elements was obtained. The total pressure PSD of a single impeller was predicted by superimposing the pressure PSD of n-segmented blade elements from the hub to the blade tip. Fan noise was predicted by multiplying the number of blades.

RESULTS AND DISCUSSION

The measured broadband noise of the flat plate with the predicted values based on the three pressure PSD models is shown in Figure 9. Trailing-edge noise, which consists of a short wavelength, has the feature of being high-frequency noise. In the comparison of the three models, Glibe's model represents the tendency of actual measurements in the high-frequency domain. Muridge's model is similar to the measured value in the low-frequency domain of 200–1000 Hz, as in the original paper. However, the spectra of the predicted values of the Willmarth-Roos model were sufficiently smaller than those of the measured values in all frequency domains. However, no model can predict the spectral distribution of broadband noise on its own.

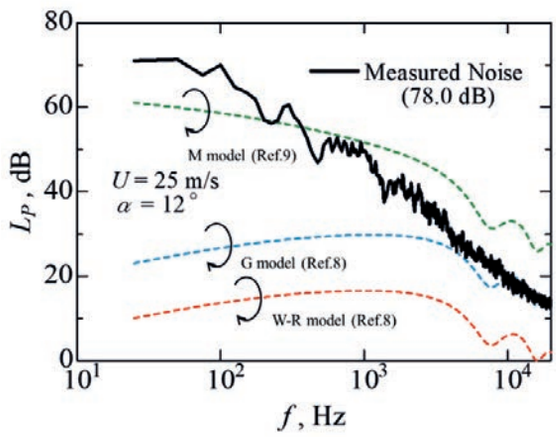
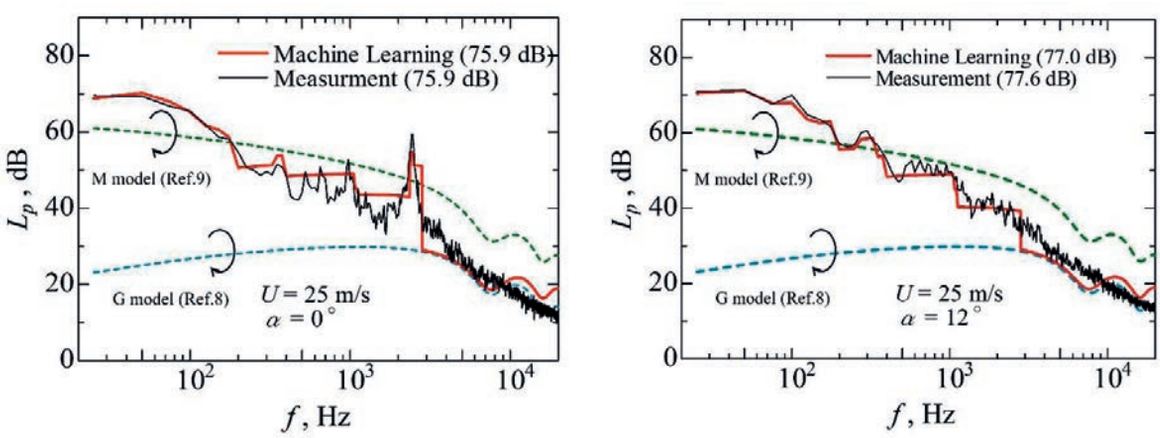


Figure 9 :Noise prediction by conventional analytical model

The predicted noise spectral distribution obtained using machine learning is shown in Figure 10. The main flow velocity was set to 25 m/s. Although the conventional pressure PSD model could not predict the broadband noise, machine learning could predict the overall noise level with high accuracy in both angles of attack. In the vicinity of 2500 Hz, as shown in Fig. (a), discrete frequency noise (DFN) was generated by Karman vortex shedding. Machine learning can predict not only the broadband noise but also the DFN generated from Karman vortex street.



(a) $\alpha = 0^\circ$ (b) $\alpha = 12^\circ$

Figure 10 :Noise prediction by machine learning model

The measured noise levels and predictions at each frequency are compared in Figure 11. The main flow velocity was 25 m/s. Table 1 summarizes the combinations of training data for the prediction model. The predicted value of Case 1, which has little training data, overestimated the measured value. Even though the

regression model of case.3 was not provided with the training data of the mainstream velocity of 25 m/s, the model could predict the measured sound pressure level within ± 5 dB error. Furthermore, this comparison indicates that the regression model, given a large amount of training data, can predict measured values with small errors.

Figure 12 shows a comparison of the measured static pressure characteristics with those of the numerical simulation. The flow coefficient ϕ and pressure coefficient ψ of the fan were defined using Equation 3.

$$\phi = \frac{4Q}{\pi(1-\nu^2)D^2U}, \psi = \frac{2P_s}{\rho U^2} \tag{3}$$

where Q is the flow rate, ν is the hub ratio, D is the impeller diameter, U is the circumferential velocity of the blade tip, P_s is the static pressure, and ρ is the density. The maximum efficiency of the fan is 48.7%, which is approximately ϕ =0.3. In this study, the flow rate at the design point was set to ϕ =0.3 near the maximum efficiency point.

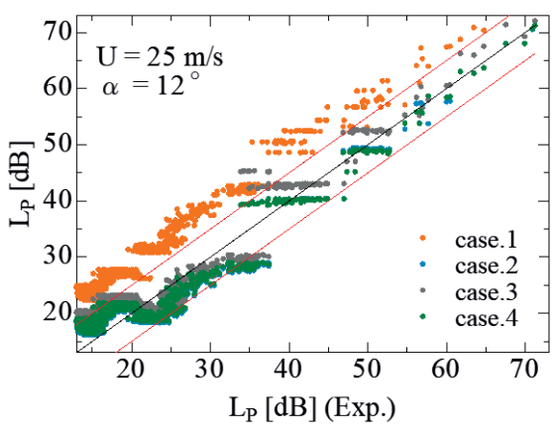


Figure 11: Comparison on the noise levels

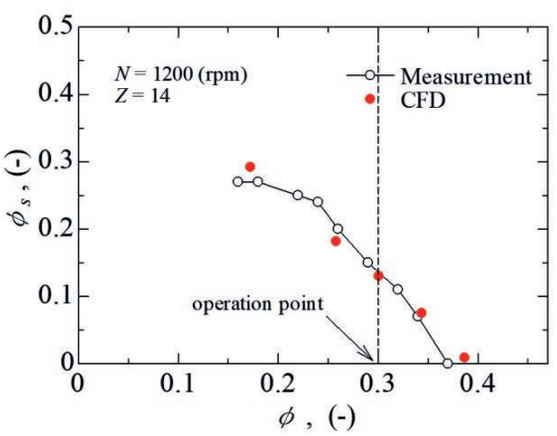


Figure 12: Performance curve of the low pressure fan

Table 1: Summary on the combinations of the training data for the regression model

	17.5 m/s	20 m/s	22.5 m/s	25m/s	27.5 m/s	30 m/s
case.1		○				○
case.2		○		○		○
case.3		○	○		○	○
case.4	○	○	○	○	○	○

The spectral distributions of the measured and predicted fan noises are compared in Figure 13. The overall noise level of the Glibe's model [5] was 19.8 dB less than the measured noise level, whereas the B. D. Mugridge model [6] was 1.0 dB more than the measured noise level. Although the noise level with the machine learning model overestimated the noise level in the low-frequency domain, it could represent the shape of the spectral distribution of the actual value. The rotation speed is1200 rpm, then the blade passing frequency (BPF) for this operating condition is 280 Hz. The discrete frequency noise at this frequency is generated by the gap between the partition and impeller caused by the slight eccentricity of the rotor blade attachment. That is, this gap becomes one pseudo-stator, and the rotor-stator interference noise is radiated with no attenuation owing to its interference [11]. Therefore, machine learning based on the training data measured in the wind tunnel test of the flat plate immersed in the uniform velocity cannot predict the interference noise and its harmonic discrete frequency noise.

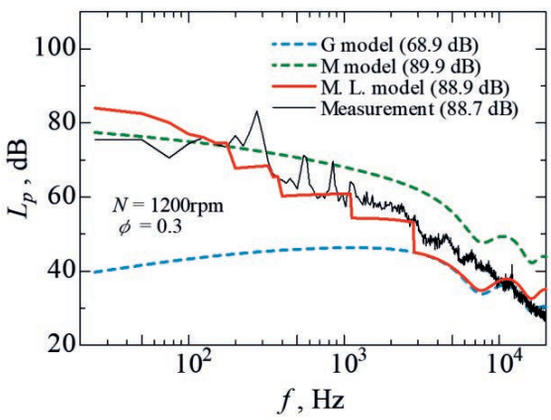


Figure 13: Comparison of the measured fan noise spectral distributions with the prediction

The predicted noise distribution in the impeller-span direction is shown in Figure 14. Figure (a) is the overall noise level generated in the blade elements at each span position of the single impeller. The aerodynamic noise generated by the impeller reached its maximum value at the tip of the blade where the peripheral velocity was higher. Figure (b) is the predicted noise spectra for each span position. At high frequencies, at least above 1000 Hz, the broadband noise increased uniformly near the wing tip owing to the effect of the relative velocity associated with the circumferential speed. Because the trailing-edge noise is not affected by the angle of attack, it is considered that high-frequency broadband noise is trailing-edge noise. On the other hand, in the band from 100 Hz to 300 Hz, the narrowband noise increases irregularly at the radial position r/R = 0.81. In the wind tunnel test of the flat plate, periodic narrowband noise generated by wake vortex shedding occurred in the frequency band. These results indicate that the broadband noise of the fan consists of low-frequency wake vortex noise [1] and high-frequency trailing-edge noise [2].

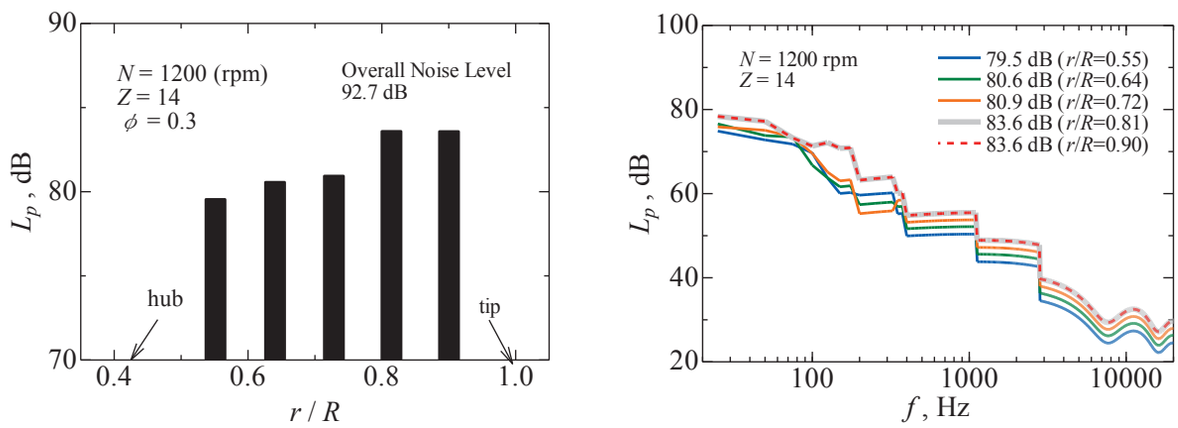


Figure 14: The predicted noise distribution in the impeller-span direction

SUMMARY

We experimentally extracted the training data of the pressure PSD from the wind tunnel experiment of a flat plate and proposed a prediction methodology for the broadband noise generated from a low-pressure fan based on the pressure PSD using the regression model. The prediction of machine learning could estimate not only the broadband noise of the flat plate, but also its discrete frequency noise to the same levels as the actual measurement. In the prediction of machine learning, the regression model trained on a large amount of training data could predict the actual noise with a small error. Furthermore, the relationship between broadband noise and the flow regime around the impeller was discussed based on the results of the relative velocity and deviation angle analyzed by CFD. The proposed methodology can predict the broadband noise of a low-pressure fan using machine learning. We indicated that broadband noise is not only generated at the blade tip, but there are also two types of broadband noise: wake vortex noise in the low-frequency domain and trailing edge noise in the high-frequency domain.

ACKNOWLEDGEMENT

This work was supported by JSPS KAKENHI Grant Number JP24K08325.

REFERENCE

[1] T. Fukano, H. Saruwatari, H. Hayashi, H. Isobe, M. Fukuhara – *Periodic velocity fluctuations in the near wake of a rotating flat-plate blade and their role in the generation of broadband noise*, Journal of Sound and Vibration, 181(1), **1995**

[2] R. K. Amiet – *Noise due to turbulent flow past a trailing edge*, Journal of Sound and Vibration, 47(3), **1976**

[3] M. Roger, S. Moreau – *Back-scattering correction and further extensions of Amiet's trailing-edge noise model. Part 1: Theory*, Journal of Sound and Vibration, 286(3), **2005**

[4] S. Moreau, M. Roger – *Back-scattering correction and further extensions of Amiet's trailing-edge noise model. Part II: Application*, Journal of Sound and Vibration, 323(1–2), **2009**

[5] W. W. Willmarth, F. W. Roos – *Resolution and structure of the wall pressure field beneath a turbulent boundary layer*, Journal of Fluid Mechanics, 22(1), **1965**

[6] B. D. Mugridge – *Acoustic radiation from aerofoils with turbulent boundary layers*, Journal of Sound and Vibration, 16(4), **1971**

[7] P. Glibe, et al. – *Aeroacoustic Prediction Codes, NASA Technical Repots Server*, NASA/CR-2000-210244: 110-111, **2000**

[8] Y. Rozenberg, G. Robert, S. Moreau – *Wall-pressure spectral model including the adverse pressure gradient effects*, AIAA Journal, 50(10), **2012**

[9] G. Grasso, J. Christophe, C. Schram – *Broadband trailing-edge noise prediction of a four-bladed axial fan using a semi-analytical method*, *FAN 2015* – International Conference on Fan Noise, **2015**

[10] G. M. Corcos – The structure of the turbulent pressure field in boundary-layer flows, Journal of Fluid Mechanics, 18(3), **1964**

[11] J.M. Tyler, T.G. Sofrin, – Axial flow compressor noise studies, SAE Technical paper, Vol.70, **1962**

APPENDIX

The two-dimensional pressure on the blade surface can be expressed by Equation (A1)

$$\frac{\partial^2 P}{\partial X^2}+\frac{\partial^2 P}{\partial Z^2}+\mu^2 P=0$$
$$P(X,0)=-e^{-\mathrm{i}\,\overline{K}\,X\left[\,\alpha+\left(\frac{M^2}{\beta^2}\right)\right]}\quad(X\geq 0) \tag{A1}$$
$$\frac{\partial P}{\partial Z}(X,0)=0\qquad(X<0)$$

where,

$$\mu=\frac{\overline{K}M}{\beta^2},\ \overline{K}=\frac{\omega}{U},\beta^2=1-M^2,\ \alpha=U/U_C$$

where, P is the pressure variable, μ is the frequency parameter, M is the Mach number, $\overline{K}$ is the convective wavenumber, ω is the angler frequency, β is the compressibility parameter, α is the mainstream to convection speed ratio, and U_c is the convention speed. In the case of a low-pressure fan, the Mach number is $M \ll 1$. The pressure, P, for $X < 0$ and $Z = 0$ is given by Equation (A2) from Schwarzschild's solution.

FAN 2025
Antibes Juan-les-Pins (France), 9 – 11 April 2025

$$P(X,0) = -\frac{e^{i\,\mu\,X}}{\pi}\int_0^{\infty}\sqrt{\frac{-X}{\xi}}\frac{e^{-\mathrm{i}\,[\alpha\,\overline{K}+(\,1+M)\mu\,]\,\xi}}{\xi - X}d\xi \tag{A2}$$

where ξ is a wavelength parameter. The integral on the right side was calculated using the mathematical procedure shown in Equation (A3).

$$\int_0^{\infty}\sqrt{\frac{-X}{\xi}}\frac{e^{-\mathrm{i}\,A\,\xi}}{\xi - X}d\xi = \pi\; e^{-\mathrm{i}AX}\left[1 - \frac{e^{i\,\pi/4}}{\sqrt{\pi}}\int_0^{-Ax}\frac{e^{-\mathrm{i}t}}{\sqrt{t}}dt\right] \tag{A3}$$

Subsequently, the complex functions in Equation (A4) are introduced.

$$E^*(x) = \int_0^{x}\frac{e^{-\,it}}{\sqrt{2\;\pi\;t}}dt = C_2(x) - i\;S_2(x) \tag{A4}$$

Here, C_2 and S_2 are Fresnel integrals. Therefore, when $X < 0$, the transfer function, which is the radiation integral of the pressure fluctuation on the blade surface, is given by (A5).

$$|I| = \frac{1}{\Theta}\left|(1+i)\left\{\sqrt{\frac{\left(1+M+{}^{\overline{K}}/_{\mu}\right)}{(1+{}^{x}/_{\sigma})}}E^*[2\mu(1+{}^{x}/_{\sigma})]e^{-i2\Theta} - E^*\left[2\left((1+M)\mu+\overline{K}\right)\right]\right\} + 1 - e^{-i2\Theta}\right| \tag{A5}$$

where I is the radiation integral. Equation (A5) is the radiation integral model of the pressure fluctuation due to backscattering at the trailing edge of a semi-infinite flat plate derived by Amiet [2].



DATA DRIVEN PREDICTION OF FAN BROADBAND NOISE

Ziyang ZHOU[1], Andrea ARROYO RAMO[1], Ralph Kinte POUHE HIOL[2], Saurabh PARGAL[3], Stephane MOREAU[1], Marlene SANJOSE[2]

[1] *Université de Sherbrooke, Sherbrooke, Quebéc, J1K2R1, Canada*
[2] *École de technologie supérieure, Montréal, QC, H3C1K3 Canada*
[3] *Michigan State University, East Lansing, MI 48824, USA*

SUMMARY

This work serves to benchmark several existing empirical models and recently developed models based on data-driven approaches to predict the wall pressure spectrum under a turbulent boundary layer. This is done with the purpose of evaluating the contribution of trailing edge noise to overall fan acoustic emissions. Initial benchmark tests on a Controlled Diffusion airfoil showed that even though the ANN showed sharper high frequency roll off than the other models, it displayed superior performance in the reattachment location of the laminar separation bubble near the leading edge. On the other hand, both the ANN and the GEP models showed weaker performance than the Lee and Pargal models at the tip region where mean flow is distorted by corner recirculation.

INTRODUCTION

The prediction of fan noise can be crucial to understanding its noise mechanisms and the development of measures to mitigate them. Among several noise sources, trailing edge noise is significant because it represents the minimum achievable noise level at design conditions. This is especially relevant in low speed fans such as the automotive ring fan [1] where trailing edge noise represents the main contributor at higher frequencies beyond 4 kHz [2]. Although large eddy simulations (LES) simulations [3, 4] are able to capture the broadband spectrum of farfield noise generated by these rotating machines, these are computationally expensive for rapid design studies of turbomachinery.

To tackle this, analytical approaches have been developed to predict noise with speed and accuracy. These models [5–7] use boundary layer parameters which can be obtained from RANS simulations to predict Wall Pressure Spectrum (WPS) on the airfoil. Amiet's solution [8, 9] can then be used to

FAN 2025
Antibes - Juan-les-Pins (France), 9 - 10 April 2025

obtain the trailing edge noise caused by the turbulent boundary layer for stationary airfoil in subsonic flows. Subsequently, by approximating rotating blades as a stack of airfoils in rectilinear motion [10], trailing edge noise from turbomachines may be computed. With such an approach that allows noise predictions for an isolated fan in a minute [1, 11], the accuracy of noise levels are highly dependent on the modeling of turbulent boundary layer. The correct functional form for the WPS was first found by Goody [12] for turbulent boundary layers under zero pressure gradient over a flat plate. To better account for the effect of Adverse Pressure Gradients (APG), Rozenberg [13] proposed a new model which accounted for pressure gradient effects through the Cole's wake parameter Π, Clauser's parameter $\beta_C = \frac{\theta}{\tau_w}\frac{dp}{dx}$ and the displacement thickness δ^*. Lee [5] improved upon this by tuning several constants in the Rozenberg model to capture the smoothing of the spectral roll-off with a decrease in APG. However, the model still loses its validity in separated flows due to its dependence on τ_w. This was addressed by Pargal [6] who proposed a semi-empirical model which was more robust for predicting the WPS under flows with high adverse pressure gradient and flow separation. This was done by replacing parameters that tended to have undefined values in areas of flow separation with alternatives. For instance, the pressure scaling chosen was $|uv^+|_{max}$ instead of u_τ. The use of R_T was substituted by the use of the sum of inner and logarithmic layer thicknesses, y_w, which served as indication of the overlap region size in the pressure spectrum. Finally, the use of Cole's parameter Π was included to model the reduction of the overlap range when APG is strengthened.

Recent work on modelling WPS have adopted a data-driven approach. Fritsch *et al.* [7] and Kurhade *et al.* [14] have used Genetic Expression Programming (GEP) which searches for the correct functional form for the WPS model using an evolutionary algorithm trained on airfoil data. On the other hand, Dominique [15] used an Artificial Neural Network (ANN) to approximate the functional relationship between boundary layer parameters and the WPS. His approach relies on the classical physical parameters and scaling of the turbulent boundary layer wall-pressure spectra. Arroyo [16] took this further by introducing an autoencoder to perform dimensional reduction of boundary layers. The latent space parameters which were learned were then used as input to the ANN to represent the local condition of the boundary layer profile. Lastly, Shubham *et al.* [17] and Sanjose [18] used the empirical and GEP models as input to Amiet's [10] rotor broadband noise model and compared analytical predictions to Large Eddy Simulation (LES) simulation results and far-field noise measurements. In their evaluations, good agreement was found for broadband noise predictions generated using Lee, Pargal and GEP models.

The present work presents the performance of the ANN model [16] in comparison to previous empirical and GEP models in their ability to model noise on a full fan configuration. Firstly, the analytical broadband noise model are described. This will be followed by a short description of each empirical WPS model used. Validation results for these models on an airfoil and a full fan configuration are then provided.

ANALYTICAL MODEL

Amiet's approach for fan self noise

The approach by Amiet [10] for modelling fan broadband noise takes advantage of the fact that flow features on a rotating segment are similar to what happens on an isolated airfoil [19] if the flow is assumed to remain attached and radial equilibrium over the blade is achieved. By modeling the response of rotating blades as the response of a stack of airfoils in rectilinear motion and neglecting blade-to-blade correlation, the farfield acoustic spectra of a fan consisting of B blades is given by:

$$S_{pp} = \sum_{k=0}^{N_s} \frac{B}{2\pi} \int_0^{2\pi} \left(\frac{\omega_e}{\omega}\right)^2 S_{pp}^k\left(x(\phi), \omega_e\right) d\phi, \tag{1}$$

where ω_e is the doppler shifted frequency, ω is the frequency in the far field, k is the index of the N_s airfoil sections and $S^k_{pp}(x(\phi),\omega_e)$ is the acoustic spectra of each airfoil section. Furthermore the doppler factor ω_e/ω is related to the tangential Mach number M_r and the axial Mach number M_x by

$$\frac{\omega_e}{\omega} = 1 + \frac{M_t \sin\Theta_0 \sin(\phi - \Phi_0)}{\sqrt{1-(M_x \sin\Theta_0)^2}} \tag{2}$$

where Φ_0 and Θ_0 are the azimuthal and polar angles of the blade respectively. The trailing edge response at each strip $S^k_{pp}(x(\phi),\omega_e)$ is given by:

$$S^{TE}_{pp}(x,\omega) = \left(\frac{\omega b x_3}{\pi c_0 S_0^2}\right) d \left|L^{TE}(K_x,K_y,W/c_0)\right|^2 \phi_{pp}(\omega) l_2(\omega) \tag{3}$$

where L^{TE} represents the aeroacoustic response function [9] and l_2 is the spanwise length scale that is approximated by the Corcos model [20]. ϕ_{pp} is the WPS and represents the noise sources contributing to trailing edge noise. The models for ϕ_{pp} tested in this work are listed in the next paragraph. A full review of existing empirical models may be found in [2].

Wall Pressure Spectrum Models

Lee's model

Lee's model [5] builds on preceding work by Rozenberg [13] by extending it for both low and high pressure gradient flows. The model was tested and validated on data within $1.4\times10^3 < Re_\theta < 2.34\times10^4$ for ZPG flows and within $0.5\times10^3 < Re_\theta < 1.65\times10^4$ for APG flows with a maximum Clauser parameter β_c of 28.57. Lee's model is given by the equation

$$\frac{\phi_{pp} U_e}{\tau_w^2 \delta^*} = \frac{\left[\max(a,(0.25\beta_C - 0.52)\,a)\right]\widetilde{\omega}^2}{\left[4.76\widetilde{\omega}^{0.75} + d^*\right]^e + \left[C_3\widetilde{\omega}\right]^{h^*}} \tag{4}$$

where $\tilde{\omega} = \frac{\omega\delta_*}{U_e}$ The definition of the constants in this model is given in [2, 5].

Pargal's model

Pargal [6] showed that existing empirical models which used τ_w as pressure scaling tended to unrealistic values in regions of high adverse pressure gradient as τ_w tends to zero. Pargal then proposed a model in which this was remedied by using Reynold's stress $\rho|uv^+|_{max}$ as the pressure scaling instead. Pargal further introduced y_w, which represents the upper limit of the logarithmic layer, and Cole's wake parameter Π into the model to represent history effects of the adverse pressure gradient on the WPS. The final form of the model is:

$$\frac{\phi_{pp}(\omega)\,U_e}{\delta\left|\rho\overline{u'v'}\right|^2_{\max}} = \frac{3\left(\frac{\omega\delta}{U_e}\right)^2}{\left[\left(\frac{\omega\delta}{U_e}\right)^{\left(0.8+3.34\times10^{-4}\Pi^{1.864}y_w^{0.7575}\right)} + 0.7\right]^{3.7} + \left[y_w^{-0.365}\left(\frac{\omega\delta}{U_e}\right)\right]^7}. \tag{5}$$

GEP 2023

The GEP 2023 model is based on previous work by Fritsch *et al.* [7] and consists of the selection of the most suitable function to fit input data built from a set of chosen variables and constants over a large experimental database informed from RANS boundary layer predictions. Shubham *et al.* [17]

extended this model by expanding its database using simulation data of a CD airfoil [21] to address performance issues at high pressure gradients. The final model is given by:

$$\frac{\phi_{pp}U_e}{Q^2\theta} = \frac{C_f\left(\bar{f}_1\right)^{1.29} + \Delta^{(-G-2.23)}\bar{f}_1^{-0.096}}{\left[3.02R_T^{0.178}\bar{f}_2\right]^{1.92H} + \left[7.96G - C_f - 3.78\bar{f}_1^{-0.96}\right]5.23\beta_c} \tag{6}$$

where $Q = \frac{1}{2}\rho U_e^2$, $\beta_c = (\delta/Q)(dp/dx)$, $H = \delta^*/\theta$, $C_f = \tau_w/Q$, $G = \sqrt{\left(2.0/C_f\right)}(1-1/H)$, $\overline{f_1} = \frac{\delta}{U_e}f$ and $\overline{f_2} = \frac{\theta}{U_e}f$.

ANN 2025

The ANN model predicts the WPS using an distributed architecture of basic computational units called neurons which are connected in layers [22]. As shown in [23], the ANN can be used to approximate any continuous function. This approach was applied to the prediction of WPS by Dominique *et al.* [15] and Arroyo *et al.* [24]. Dominique used an ANN to approximate the dimensionless $\frac{\phi_{pp}U_e}{\delta^*\tau_w^2}$ as a function of $\tilde{\omega}$ and 7 classical dimensionless parameters that describe turbulent boundary layer [15] following the approach used in former empirical model developments. Arroyo *et al.* [24] used another approach in which an autoencoder was first trained to perform a dimension reduction of the boundary layer mean velocity profiles from the dataset of a set of airfoils into 3 latent space parameters L_1, L_2 and L_3. To provide a more robust model over the fan database, the initial model by Arroyo *et al.* [24], has been trained again, removing the dependency on Mach and angle of attack from the airfoil database, and using a scaled ϕ_{pp} as target. The ANN 2025 model, used in the present work, approximates the following function g:

$$\frac{\phi_{pp}U_\infty}{Q_\infty^2 c} = g(L_1, L_2, L_3, Re, x/c), \tag{7}$$

where $Q_\infty = \frac{1}{2}\rho U_\infty^2$, c is the chord length, x/c is the location along the chord where the wall-pressure spectra has to be evaluated and Re is the airfoil Reynolds number based on the upstream velocity U_∞ and the chord length.

EVALUATION OF WALL PRESSURE SPECTRUM MODELS ON AN AIRFOIL

In this section, the aforementioned models will be used to evaluate wall-pressure spectra at different streamwise locations on the suction side of a CD (Controlled Diffusion) airfoil at $\alpha = 8°$. It is relevant to validate the models on the CD airfoil as the highly adverse pressure gradient is also seen on the blades of turbofans and particularly at the midspan of the low-speed H380EC1 fan which will be investigated in the next section. Note that the GEP and ANN models were trained on databases of flow around the CD airfoil at 8° obtained with HiPSTAR DNS solver [21, 25]. Similarly, Lee's and Pargal's models include this flow configuration knowledge [5, 6].

The WPS density (PSD) computed from a DNS simulation performed with a Lattice Bolzmann Method [26] will be used to benchmark the models. An instantaneous flow visualization of the boundary layer development is provided in Fig. 1. This simulation is not the flow information directly used in the training of the GEP and ANN models, but very similar to those considered. The locations of these wall PSD extractions correspond to the locations of remote microphone probes (RMP) in the experiment [27] which are shown by pink dots in the Fig.1. As shown in previous results [21, 26], the CD airfoil exhibits a laminar separation bubble (LSB) which starts at the leading edge (LE) and reattaches at probe 5 (see Fig. 1). The reattached flow then transitions to turbulence and convects downstream as an attached turbulent boundary layer. This boundary layer first encounters a favorable

Table 1: Input boundary layer parameters for evaluating empirical model.

RMP #	U_e [m/s]	δ [mm]	$\delta*$ [mm]	θ [mm]	β_C	R_T	$1000 \times C_f$	$1000 \times C_{uv}$
5	22.5	0.8	0.49	0.10	2.8	1.1	1.7	17.0
7	21.9	1.8	0.26	0.17	-0.0	6.2	4.9	3.0
9	21.6	2.1	0.33	0.21	0.2	6.9	0.5	3.1
21	18.4	3.5	0.94	0.53	1.9	6.0	2.9	4.6
24	17.6	4.0	1.20	0.65	2.7	5.6	2.5	5.7

pressure gradient (FPG), followed by a region of zero pressure gradient encompassing probes 7 and 9 before entering a region of adverse pressure gradient caused by airfoil camber at probes 21 and 24. The boundary layer parameters at the aforementioned RMP locations are used as inputs to the WPS models and are listed in Table 1. Similarly to the wall shear stress, the Reynolds stress is expressed in a coefficient form $C_{uv} = \rho|uv^+|_{max}/Q$. For the ANN model, the mean velocity profile is directly provided to the autoencoder that computes the 3 latent space values.

As seen in Fig. 2 the Lee, GEP and ANN models capture the levels of zero pressure gradient (probe 7 and probe 9) and adverse pressure gradient locations (probe 21 and probe 24) correctly. Meanwhile, Pargal's model underpredicts wall power spectral density (PSD) levels as the present CD airfoil simulation sees lower levels of $|uv^+|_{max}$ than the results of Wu [21] at probes 7, 9, 21 and 24 which were used to calibrate the model. The ANN is able to outperform all other models at probe 5 which coincides with the location of the laminar separation bubble (LSB). It is also the only model capable of capturing the low frequency plateau in wall PSD below 1000 Hz. On the other hand, the ANN model predicts a sharper decay at high frequencies than seen in the simulation. Both observations are consistent with results in [24].

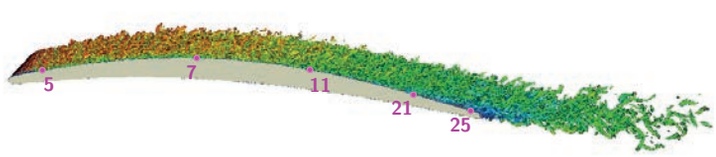
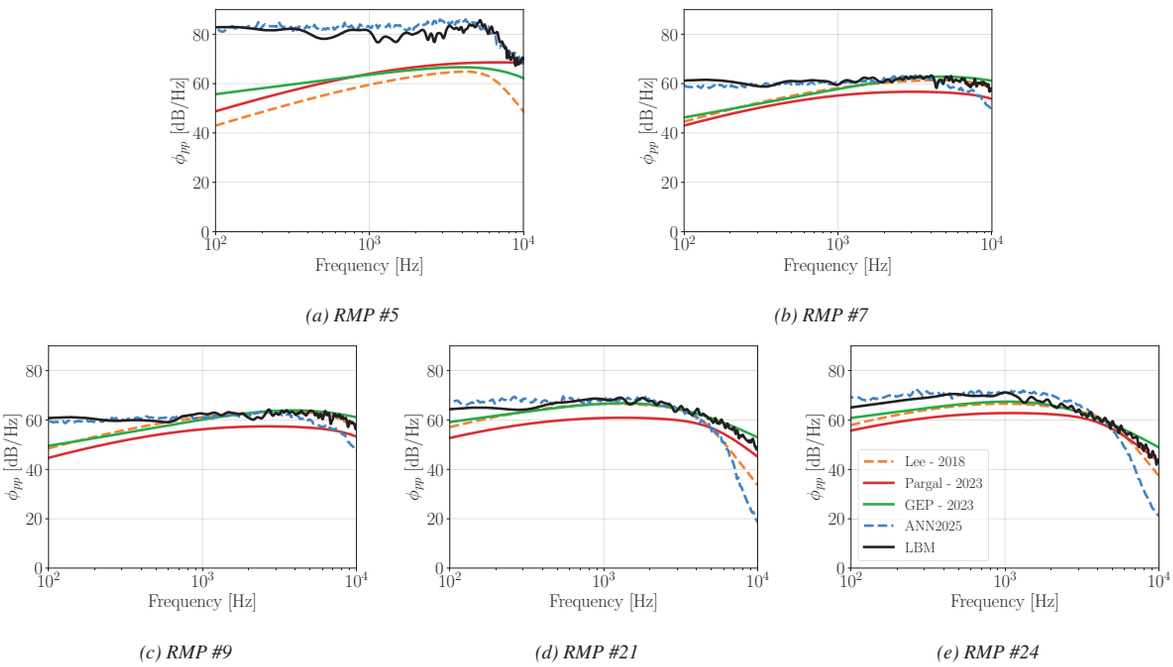


Figure 1: Isosurface of $\lambda_2 = -1 \times 10^{-7}$ s^{-2} near the surface of the airfoil (Colored by x velocity). The numbers indicate the remote microphone probe ID where wall pressure spectra are investigated.

EVALUATION OF WALL PRESSURE SPECTRUM MODELS ON FAN CONFIGURATIONS

In this section, the models for WPS are evaluated on rotating machines. Two configurations are considered. The first one, H380EC01, is a low-speed fan designed for automotive engine cooling system [3]. The previously investigated CD airfoil geometry at 8° correspond to the scale 2 of the mid-span blade section of this fan at its design operating condition. The second configuration, EDAT, is a ducted fan designed for a distributed anti-torque system of a helicopter [28, 29]. For both cases, RANS simulations are used to provide mean boundary layer profiles close to the trailing-edge at several locations along the blade span. This information is used to compute the boundary layer parameters for the WPS models. The spectra computed with the selected models are compared with extractions from large eddy simulations which serve as reference. Finally, far-field noise computed using Amiet's approach described above is compared with measured sound power levels and numerical far-field noise spectra.



(a) RMP #5 *(b) RMP #7*

(c) RMP #9 *(d) RMP #21* *(e) RMP #24*

Figure 2: Wall-pressure spectrum at selected RMP on the suction side of the CD airfoil.

H380EC01 database

The H380EC01 configuration is a low-speed axial fan in clean inflow. The fan has 9 uniformly distributed blades, a tip radius of 380 mm, and a tip to hub ratio of 0.4. Its bi-swept blades feature varying chord lengths and stagger angles, which correspond to a CD airfoil at mid-span. The blade tips are attached to an L-shaped ring. The rotating speed of the fan is 2500 rpm, and the tip Mach number is 0.15. This configuration has been largely investigated both experimentally and numerically [3, 30]. In particular, performance and wake measurements have been used to validate the progress in RANS and scale resolving simulations over the years [31, 32] and far-field noise measurements have been used to evaluate improvements in analytical approaches [1, 17, 30]. Two operating conditions are considered, the flow rate at best efficiency point at 2500 m^3/h, and a higher flow rate at 3500 m^3/h. In the former operating point, both leading-edge noise and trailing edge noise have been shown to be competitive broadband noise sources, while in the later the trailing-edge noise is the dominant one.

The mean boundary layer profiles from reference RANS simulations for the two operating conditions are extracted at several locations along the span of the fan blade close to the trailing-edge at $x/c = 0.85$ [1]. The input parameters to the WPS models at 2500 m^3/h and 3500 m^3/h are shown in Fig. 3. Note that at the lower flow rate of 2500 m^3/h, the parameters are outside the training range of GEP and ANN models.

The previously defined WPS models are used to generate predictions of wall-pressure spectrum along the trailing edge. The WPS at 3 radial positions for the design operating conditions are shown in Fig. 4 where they are compared to the resolved WPS extracted from the LES performed using the Lattice Bolzmann Method (LBM) as implemented in Powerflow [32]. Although the LBM results are used as reference for WPS model evaluation, it should also be noted that the LBM simulations are under-resolved causing the early cut-off frequency around 2000 Hz, except for the 90% span location where a finer mesh is used. Nevertheless, from the results it can be seen that Lee and Pargal models are very close in term of predictions. The GEP model provides similar spectral shape as Pargal's and Lee's models at 50% and 75% span, but with higher levels. The GEP model has a nonphysical behavior in

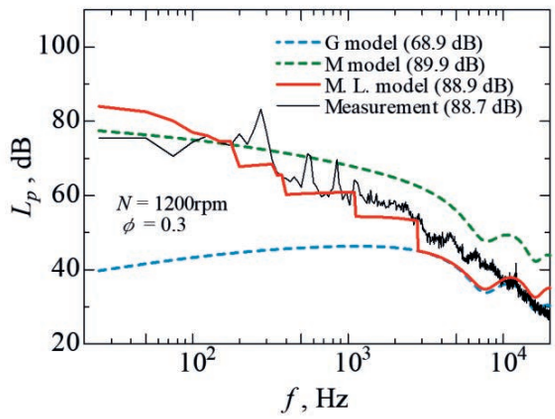


Figure 13: Comparison of the measured fan noise spectral distributions with the prediction

The predicted noise distribution in the impeller-span direction is shown in Figure 14. Figure (a) is the overall noise level generated in the blade elements at each span position of the single impeller. The aerodynamic noise generated by the impeller reached its maximum value at the tip of the blade where the peripheral velocity was higher. Figure (b) is the predicted noise spectra for each span position. At high frequencies, at least above 1000 Hz, the broadband noise increased uniformly near the wing tip owing to the effect of the relative velocity associated with the circumferential speed. Because the trailing-edge noise is not affected by the angle of attack, it is considered that high-frequency broadband noise is trailing-edge noise. On the other hand, in the band from 100 Hz to 300 Hz, the narrowband noise increases irregularly at the radial position r/R = 0.81. In the wind tunnel test of the flat plate, periodic narrowband noise generated by wake vortex shedding occurred in the frequency band. These results indicate that the broadband noise of the fan consists of low-frequency wake vortex noise [1] and high-frequency trailing-edge noise [2].

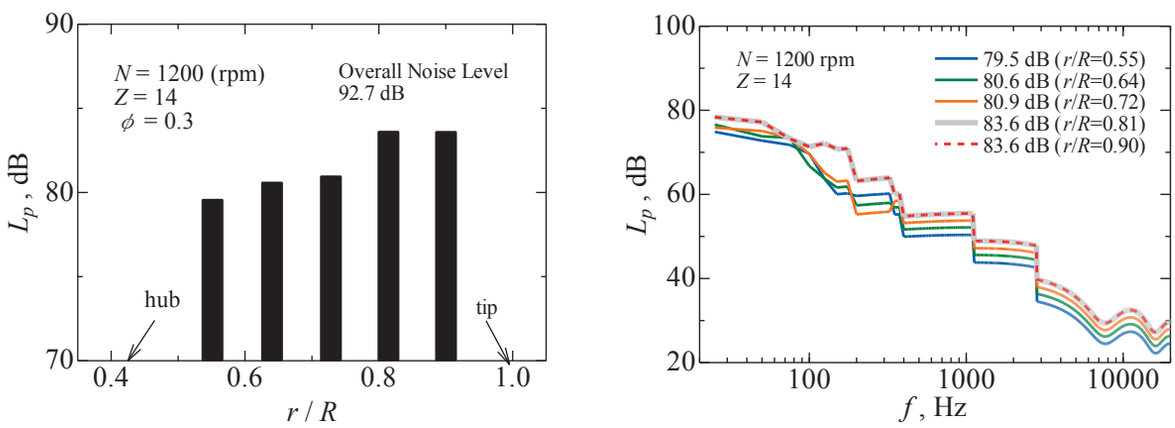


Figure 14: The predicted noise distribution in the impeller-span direction

SUMMARY

We experimentally extracted the training data of the pressure PSD from the wind tunnel experiment of a flat plate and proposed a prediction methodology for the broadband noise generated from a low-pressure fan based on the pressure PSD using the regression model. The prediction of machine learning could estimate not only the broadband noise of the flat plate, but also its discrete frequency noise to the same levels as the actual measurement. In the prediction of machine learning, the regression model trained on a large amount of training data could predict the actual noise with a small error. Furthermore, the relationship between broadband noise and the flow regime around the impeller was discussed based on the results of the relative velocity and deviation angle analyzed by CFD. The proposed methodology can predict the broadband noise of a low-pressure fan using machine learning. We indicated that broadband noise is not only generated at the blade tip, but there are also two types of broadband noise: wake vortex noise in the low-frequency domain and trailing edge noise in the high-frequency domain.

and Pargal's model demonstrate a very similar spectral shape.

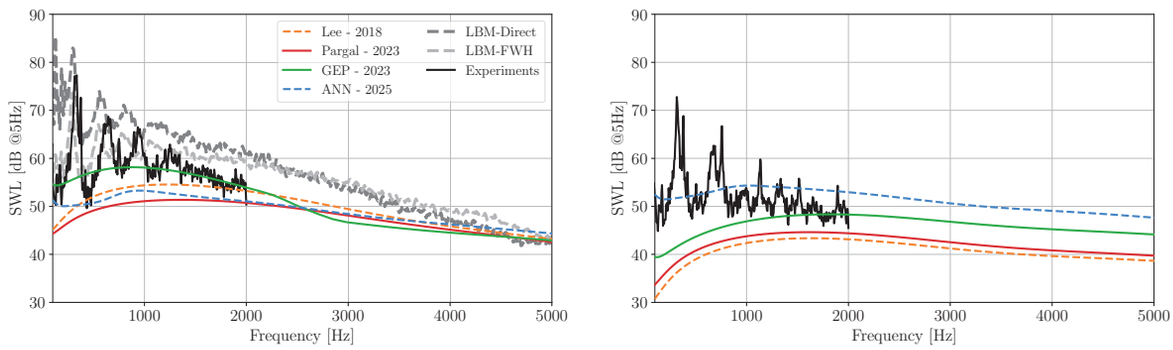


Figure 5: Sound power levels of the H380EC01 configuration at 2500 m^3/h (left) and 3500 m^3/h (right).

EDAT database

The EDAT configuration corresponds to a rotor-stator assembly installed in a short duct in clean inflow. The fan has 4 uniformly distributed blades, a tip to hub ratio of 0.3. Apart from its root, the blade has a quite constant chord, a varying pitch and profile shape from hub to tip as shown in Fig. 6. The tip Mach number is 0.42 and the tip Reynolds based on the chord is 455,000. The blade ends at a constant radius with a constant gap of about 10% of the chord length at tip. The noise levels have been measured in the anechoic room of Université de Sherbrooke (UdS) [28]. The design operating point has been investigated using RANS simulations and LES [29, 33, 34]. A noise mechanism decomposition analysis has shown that the rotor is the main contributor for broadband noise. In the present work, only the trailing-edge noise is considered which is dominant at high frequency.

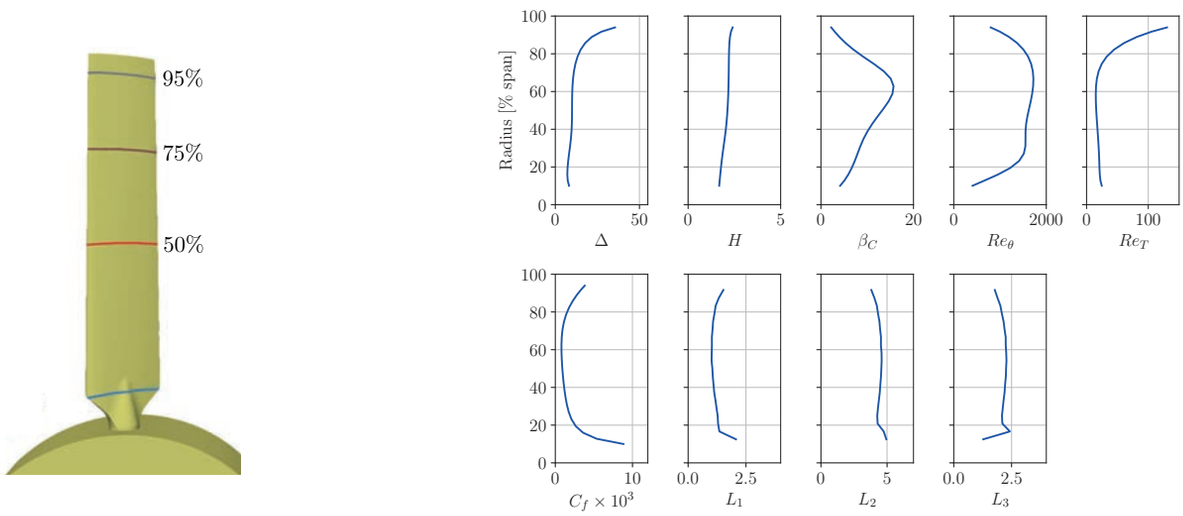


Figure 6: Input parameters for the EDAT configuration computed from the boundary layers extracted on the blade suction side along the trailing edge.

The mean boundary layer profiles from RANS simulations for the design operating conditions are extracted at several locations along the span of the fan blade close to the trailing-edge at $x/c = 0.85$. The input parameters to the WPS models are shown in Fig. 6. Compared with the previous low-speed fan discussed earlier, the main differences appear in much larger Re_θ and Re_T values. The variation along the radius of the different quantities are similar as the 3500 m^3/h case of the H380EC01 configuration, consistent with a low loading of the fan blade required to produce a maximum of thrust. The

WPS at selected radial positions are shown in Fig. 7 and compared with measured spectra in recent LES performed with the AVBP compressible Navier-Stokes solver [29]. The evaluated models show large differences in amplitude and spectral shape. The ANN model provides an accurate prediction of the fluctuation levels predicted by the LES, the GEP model captures the right location of the spectrum roll off but with slightly lower amplitude levels. Lee's model fail to predict the amplitude levels, but accurately captures the roll off location and the high frequency slope of the spectrum.

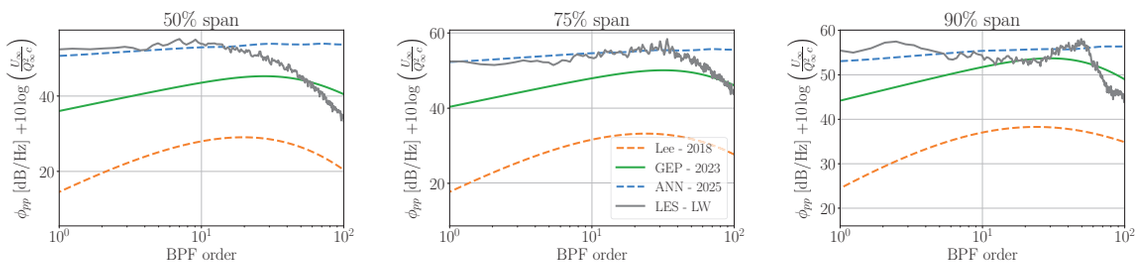


Figure 7: Dimensionless wall-pressure spectra at selected radial locations on the suction side of the EDAT fan blade.

The acoustic power obtained with the computed WPS in Amiet's approach is shown in Fig. 8 and compared with experiments and LES predictions obtained with the FWH analogy. The trough around 28 BPF in the experimental spectra is associated with installation effects [28]. Lee's model yields an underestimation of the sound power levels, consistently with what was found previously on the high-speed NASA Source Diagnostic Test turbofan [35]. The ANN and GEP models provide a relatively good estimate of the broadband noise levels, the ANN model providing higher levels, and the GEP one, a better high-frequency spectral shape. The quantification of the leading edge noise and the tip vortex noise should be included for a more refined analysis.

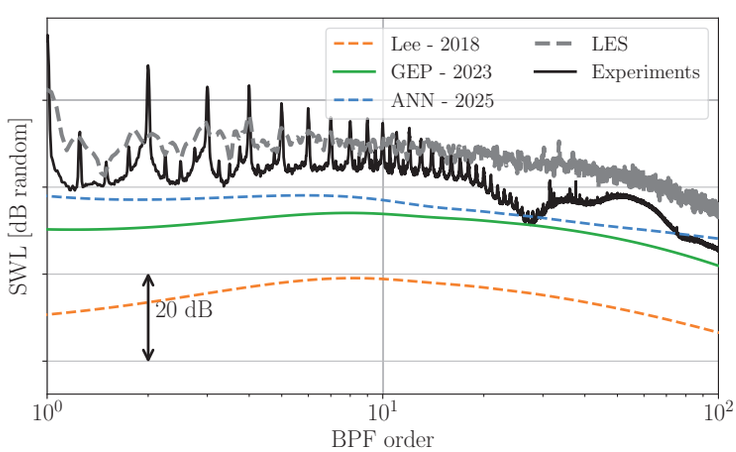


Figure 8: Sound power levels of the EDAT configuration.

CONCLUSION

Several recently developed Wall Pressure Spectrum (WPS) models have been evaluated for predicting the broadband noise of rotating machinery. The model evaluations are based on the use of boundary layer information provided by RANS simulation and the use of Amiet's approach for the prediction of trailing edge broadband noise for rotating machines. Four WPS models were selected for the present work. Lee's and Pargal's models, developed to capture WPS under boundary layer in different

pressure gradient, and two data-driven models, a Genetic Evolutionary Programming (GEP) and an Artificial Neural Network (ANN), recently developed on large airfoil boundary layer databases. The initial benchmark test on the CD airfoil showed that all models could capture the WPS at zero and adverse pressure gradient conditions. The ANN showed a significantly more accurate prediction in the LSB compared to the other 3 models because this case is close to its training database and the autoencoder could reproduce all velocity profiles along the airfoil accurately. The models are then tested on two fan databases. The H380EC01 configuration is a low speed fan with detached flow conditions at the upper radial locations of the blade. The EDAT configuration is a higher Mach and Reynolds configuration used in a helicopter anti-torque concept. In both cases, RANS simulations provide the WPS models with a parameterization of the boundary layer near the trailing edge. The model spectra are then compared with spectra measured in LES of the same configuration. The far-field noise obtained with the analytical approach is compared with experimental and numerical results. For the low-speed fan configuration, the data-driven models provide a limited improvement over the Lee and Pargal models. In the EDAT configuration, which is characterized by a higher Reynolds number, the GEP and ANN models provide a huge improvement in the spectral shape and noise level, respectively. Through this detailed study, it is clear that data-driven models provide an excellent opportunity, provided that new and accurate airfoil and fan databases become available.

ACKNOWLEDGMENTS

The simulations were carried out on the Niagara supercomputer administered by the Digital Research Alliance of Canada. The authors acknowledge the partners of the UHEQ Consortium II and III at Université de Sherbrooke, which develops and provides the acoustic software PyFanNoise for this research. This research is founded by NSERC Discovery Grants RGPIN-2020-05919 and RGPIN-2019-05844.

REFERENCES

[1] M. Sanjosé and S. Moreau. *Fast and accurate analytical modeling of broadband noise for a low-speed fan*. The Journal of the Acoustical Society of America 143(5).

[2] S. Lee, L. Ayton, F. Bertagnolio, S. Moreau, T. P. Chong, and P. Joseph. *Turbulent boundary layer trailing-edge noise: theory, computation, experiment, and application*. Progress in Aerospace Sciences 126.

[3] S. Moreau and M. Sanjose. *Sub-harmonic broadband humps and tip noise in low-speed ring fans*. The Journal of the Acoustical Society of America 139(1). DOI: 10.1121/1.4939493.

[4] T. Zhu, D. Lallier-Daniels, M. Sanjosé, S. Moreau, and T. Carolus. *Rotating coherent flow structures as a source for narrowband tip clearance noise from axial fans*. Journal of Sound and Vibration 417.

[5] S. Lee. *Empirical wall-pressure spectral modeling for zero and adverse pressure gradient flows*. AIAA Journal 56(5).

[6] S. Pargal. *Non-equilibrium wall-bounded turbulence and associated noise generation*. PhD dissertation, ProQuest Dissertations & Theses Global, **2023**.

[7] D. J. Fritsch, V. Vishwanathan, C. J. Roy, K. Todd Lowe, W. J. Devenport, P. Croaker, O. Tkachenko, D. Pook, G. Lane, S. Shubham, and R. D. Sandberg. *Modeling the Surface Pressure Spectrum Beneath Turbulent Boundary Layers in Pressure Gradients*. AIAA Journal 61(5). DOI: 10.2514/1.J062074.

[8] R Amiet. *Correction of open jet wind tunnel measurements for shear layer refraction*. In *2nd Aeroacoustics Conference*, page 532, **1975**.

[9] M. Roger and S. Moreau. *Back-scattering correction and further extensions of amiet's trailing-edge noise model. part 1: theory*. Journal of Sound and vibration 286(3).

[10] R. K. Amiet. *Noise produced by turbulent flow into a rotor: theory manual for noise calculation*. National Aeronautics and Space Administration, Langley Research Center, **1989**.

[11] P. Pépin and M. Sanjosé. *Aero-Acoustic Analysis of an Axial Fan*. In *FAN 2022 – International Conference on Fan Noise, Aerodynamics, Applications and Systems*, Senlis, France, **2022**. DOI: 10.26083/tuprints-00021694.

[12] M. Goody. *Empirical spectral model of surface pressure fluctuations*. AIAA journal 42(9).

[13] Y. Rozenberg, G. Robert, and S. Moreau. *Wall-pressure spectral model including the adverse pressure gradient effects*. AIAA journal 50(10).

[14] N. N. Kurhade, N. R. Vadlamani, and A. Haridas. *Artificial neural networks and guided gene expression programming to predict wall pressure spectra beneath turbulent boundary layers*. Physics of Fluids 35(8).

[15] J. Dominique, J Van den Berghe, C. Schram, and M. Mendez. *Artificial neural networks modeling of wall pressure spectra beneath turbulent boundary layers*. Physics of Fluids 34(3).

[16] A. Arroyo Ramo, S. Moreau, R. D. Sandberg, M. Bauerheim, and M. C. Jacob. *Direct Numerical Simulation of Controlled Diffusion airfoil self-noise*. In *28th AIAA/CEAS Aeroacoustics 2022 Conference*, page 2815, **2022**.

[17] S. Shubham, S. Pargal, S. Moreau, R. D. Sandberg, J. Yuan, A. Kushari, and M. Sanjose. *Data-driven empirical wall pressure spectrum models for fan noise prediction*. In *AIAA AVIATION 2023 Forum*, page 3508, **2023**.

[18] M. Sanjose. Evaluation of Wall Pressure Spectrum Models for Fan Noise Prediction. https://zenodo.org/records/14041275, Montreal, QC, Canada, **2023**.

[19] M. Roger, S. Moreau, and A. Guedel. *Broadband fan noise prediction using single-airfoil theory*. Noise control engineering journal 54(1).

[20] A Caiazzo, S Pargal, H Wu, M Sanjosé, J Yuan, and S Moreau. *On the effect of adverse pressure gradients on wall-pressure statistics in a controlled-diffusion aerofoil turbulent boundary layer*. Journal of Fluid Mechanics 960.

[21] H. Wu, S. Moreau, and R. D. Sandberg. *On the noise generated by a controlled-diffusion aerofoil at Rec=1.5×105*. Journal of Sound and Vibration 487. DOI: 10.1016/j.jsv.2020.115620.

[22] I. Goodfellow. Deep learning, **2016**.

[23] G. Cybenko. *Approximation by superpositions of a sigmoidal function*. Mathematics of control, signals and systems 2(4).

[24] A. Arroyo Ramo, A. Alguacil, M. Bauerheim, S. Moreau, and M. C. Jacob. *Artificial neural networks prediction of wall-pressure spectrum*. In *30th AIAA/CEAS Aeroacoustics Conference (2024)*, page 3140, **2024**.

[25] M. Deuse and R. D. Sandberg. *Different noise generation mechanisms of a controlled diffusion aerofoil and their dependence on mach number*. Journal of Sound and Vibration 476.

[26] Z. Ziyang, S. Moreau, and M. Sanjosé. *Direct numerical simulation of installation effects on control diffusion airfoil noise*. In *AIAA AVIATION 2023 Forum*, page 4512, **2023**.

[27] D. R. Neal. *The effects of rotation on the flow field over a controlled-diffusion airfoil*. Michigan State University, **2010**.

[28] P. Jaiswal, J. Rendon, Y. Pasco, M. Sanjose, and S. Moreau. *Aeroacoustic investigation of a ducted tail rotor*. In *AIAA AVIATION 2023 Forum*, San Diego, CA and Online. American Institute of Aeronautics and Astronautics, **2023**. DOI: 10.2514/6.2023-3512.

[29] R. K. Pouhe Hiol and M. Sanjose. *Aeroacoustic analysis in a tail rotor configuration using Large Eddy Simulations and Ffowcs Williams and Hawkings' analogy*. In *Annual Conference of the CFD Society of Canada*, Montreal, QC, CA, **2025**.

[30] S. Moreau and M. Roger. *Competing Broadband Noise Mechanisms in Low-Speed Axial Fans*. AIAA Journal 45(1). DOI: 10.2514/1.14583.

[31] J. Foss, D. Neal, M. Henner, and S. Moreau. *Evaluating CFD Models of Axial Fans by Comparisons with Phase-Averaged Experimental Data*. In *1995 Vehicle Thermal Management Systems Conference and Exhibition*, pages 2001–01–1701, **2001**. DOI: 10.4271/2001-01-1701.

[32] M. Sanjose, D. Lallier-Daniels, and S. Moreau. *Aeroacoustic Analysis of a Low-Subsonic Axial Fan*. In *ASME Turbo Expo 2015: Turbine Technical Conference and Exposition*, V001T09A015, Montréal, Canada. American Society of Mechanical Engineers, **2015**. DOI: 10.1115/GT2015-43737.

[33] J. M. Rendon Arredondo, P. Jaiswal, M. Sanjosé, Y. Pasco, and S. Moreau. *Aeroacoustic investigation of a ducted tail rotor using the Lattice-Boltzmann Method*. In *Progress in Canadian Mechanical Engineering. Volume 6*, Sherbrooke, Canada. Université de Sherbrooke. Faculté de génie, **2023**. DOI: 10.17118/11143/20856.

[34] M. Sanjosé. Interaction noise for a rotor-stator assembly in a short duct. https://doi.org/10.5281/zenodo.14041738, Montreal, QC, Canada, **2023**.

[35] M. Sanjosé, P. Kholodov, C. Pérez Arroyo, and S. Moreau. *CFD modeling of a realistic turbofan blade for noise prediction. Part 2: Analytical Acoustic Predictions*. In *Proceedings of Global Power and Propulsion Society*, Beijing, China, **2019**.

C2 Psychoacoustics & Sound Quality

10 April - 9:30 - Room 1 Fitzgerald

Chairmen: Nicolas Chouard, Michel Besombes

List of papers

Sound Quality Evaluation of Small Fan Noise by TTNR/TPR and Determination of Those Thresholds for Annoyance

- Takefumi NAKANO – Hosei University (Japan)
- Gaku MINORIKAWA – Hosei University (Japan)

Improving the Psychoacoustic Assessment of Automotive Fan- Systems

- Denis SCOUARNEC – Valeo Power Division (France)
- Saad BENNOUNA – Valeo Power Division (France)
- Thibault VICENTE – Le Mans Université (France)
- Adrien PELAT – Le Mans Université (France)
- Nicolas CHOUARD – Le Mans Université (France)
- Alban GODART – Le Mans Université (France)
- Armand COMPAIN – Le Mans Université (France)

Impact of Distorted Inlet Flow on Axial Fan Psychoacoustics

- Michail VOURAKIS – Chalmers University of Technology (Sweden)
- Elias ZEA – KTH Royal Insitute of Technology (Sweden)
- Sassan ETEMAD – Chalmers University of Technology (Sweden)
- Mikael KARLSSON – KTH Royal Insitute of Technology (Sweden)
- Niklas ANDERSSON – Chalmers University of Technology (Sweden)



SOUND QUALITY EVALUATION OF SMALL FAN NOISE BY TTNR/TPR AND DETERMINATION OF THOSE THRESHOLDS FOR ANNOYANCE

Takefumi NAKANO[1], Gaku MINORIKAWA[2],

[1] *Graduate school of Hosei University, 3-7-2, Kajinocho, Koganei-shi, Tokyo, 1840002, Japan*

[2] *Hosei University, 3-7-2, Kajinocho, Koganei-shi, Tokyo, 1840002, Japan*

SUMMARY

Tone-to-Noise Ratio and Prominence Ratio are defined as evaluation indices for evaluating the effects of tonal components on hearing in ECMA-418-1 and other standards. These evaluation indices evaluate individual tonal components in noise and cannot evaluate multiple tonal components in noise comprehensively. Therefore, we have proposed and studied Total Tone-to-Noise Ratio and Total Prominence Ratio as new evaluation indices to comprehensively evaluate noise with multiple tonal components. This study has attempted to determine the thresholds of these evaluation indices, using the sensory test. If the accuracy of these annoyance thresholds for information equipment can be improved, this evaluation method may be extended to evaluate the sound quality of other fields in the future.

INTRODUCTION

Information devices, such as personal computers and projectors, have become necessities in modern life, and their using frequency has increased since the onset of the Coronavirus Disease 2019 (Covid-19) pandemic. Many of these devices are equipped with small fans for cooling purposes. Although the A-weighted sound pressure level itself has been reduced to a low level due to advances in the noise reduction of small fans, the sound generated by such fans can still be perceived as harsh in a quiet living environment. This is primarily attributed to the tonal components in the noise, which are caused by the rotation of fans and motors.

The Tone-to-Noise Ratio and the Prominence Ratio are defined in ECMA-418-1[1] and other standards as evaluation indices for evaluating the effects of tonal components on hearing. These evaluation indices evaluate individual tonal components in noise, and cannot comprehensively evaluate multiple tonal components in noise. Therefore, we have proposed and studied the Total Tone-to-Noise Ratio and the Total Prominence Ratio as new evaluation indices to comprehensively evaluate noise with multiple tonal components. In our previous studies, these new evaluation indices were confirmed to be effective as evaluation indices for subjective harshness (annoyance) [2].

In this study, the thresholds of subjective harshness (annoyance) of these evaluation indices were estimated by a sensory test (rank order method) using the operating sound source of the projector as the test sound.

Furthermore, their validity is verified by comparing them with thresholds obtained in previous studies and by using the RT method, which is one of the solution methods of the Mahalanobis-Taguchi System. In addition, the Mahalanobis-Taguchi System is usually referred to as the MT system.

EVALUATION METHODS OF TONAL COMPONENTS

Tone-to-Noise Ratio and Prominence Ratio

The prominence of a tonal component is determined by the physical relationship between the level of the tonal component and the level of the surrounding band noise that masks the tonal component. The surrounding frequency band is called the critical band and is centered on the frequency of the tonal component. In the standards such as ECMA-418-1, the evaluation methods of the certain prominent discrete tone in information technology equipment are prescribed as the Tone-to-Noise Ratio (abbreviated as TNR, symbol ΔL_T) and the Prominence Ratio (abbreviated as PR, symbol ΔL_P), in the very similar manners. In this study, the methods of ECMA-418-1 are used to determine the TNR and the PR of each tonal component of interest.

The TNR is defined as the decibel value of the ratio of the power of the tonal component and the other noise component in the critical band. In ECMA-418-1 [1], if the TNR exceeds by 8 dB at 1 kHz or higher, the tonal component is classified as a prominent discrete tone. If there are multiple peaks exist in the same critical band or if the noise levels adjacent to the critical band are significant, the TNR values tend to be larger or smaller. The PR is defined as the decibel value of the ratio of the critical band power including the tonal component and the average of the adjacent critical band power on both sides. In ECMA-418-1 [1], if the PR exceeds by 9 dB at 1 kHz or higher, the tonal component is classified as prominent discrete tone. Figure 1 is a schematic view of calculating the TNR and the PR calculation [1].

$$\Delta L_T = 10 \log_{10} \left(\frac{W_t}{W_n} \right) \tag{1}$$

where ΔL_T (dB) is the TNR according to ECMA-418-1, W_t (Pa^2) is the power of tone, and W_n (Pa^2) is the power of other components in critical bands.

$$\Delta L_P = 10 \log_{10} \left[\frac{W_M}{(W_L + W_U)/2} \right] \tag{2}$$

where ΔL_P (dB) is the PR according to ECMA-418-1, W_M (Pa^2) is the power of middle critical band, W_L (Pa^2) is power of lower critical band, and W_U (Pa^2) is the power of upper critical band.

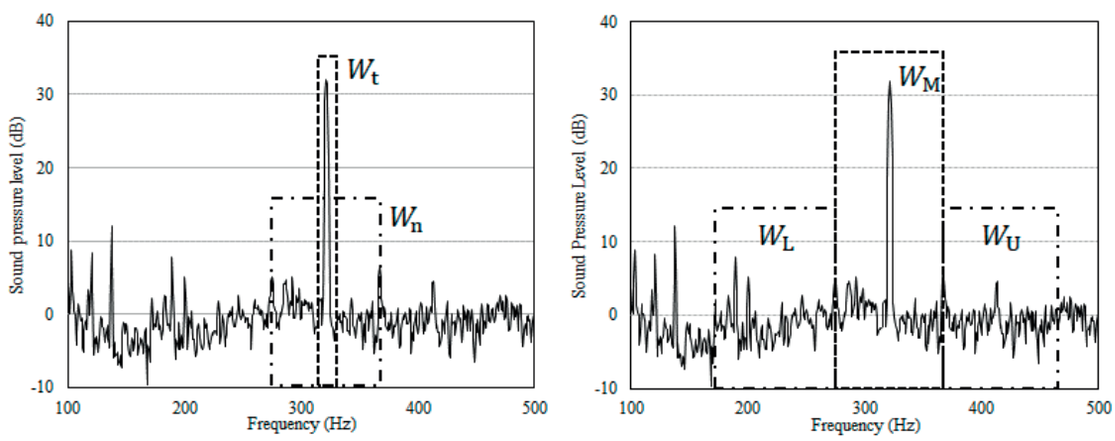


Figure 1: schematic view of TNR and PR calculation (Left: TNR, Right: PR)

Total Tone-to-Noise Ratio and Total Prominence Ratio

In evaluating fan noise, it is important to identify and quantify the tonal components for product quality control, noise source specification and noise reduction. In the Tonality, the calculation method is a bit complicated and it is difficult to identify which tonal components have high contribution. On the other hand, the TNR and the

PR can be the indicators of the prominent discrete tone of each tonal component. However, they do not yet consider the relationship between the multiple tonal components [2].

In this study, two new evaluation parameters, the Total Tone-to-Noise Ratio (abbreviated as T-TNR, symbol $\langle L_T \rangle$) and the Total Prominence Ratio (abbreviated as T-PR, symbol $\langle L_P \rangle$), are introduced. The individual levels are determined for each of several tonal components in the noise spectrum of interest by the TNR or the PR calculation methods, and their power sum is defined as the evaluation parameter as the T-TNR or the T-PR, respectively. A schematic view of the T-TNR and the T-PR calculations is shown in Figure 2, respectively. These calculation methods are published in ECMA TR/108 [3].

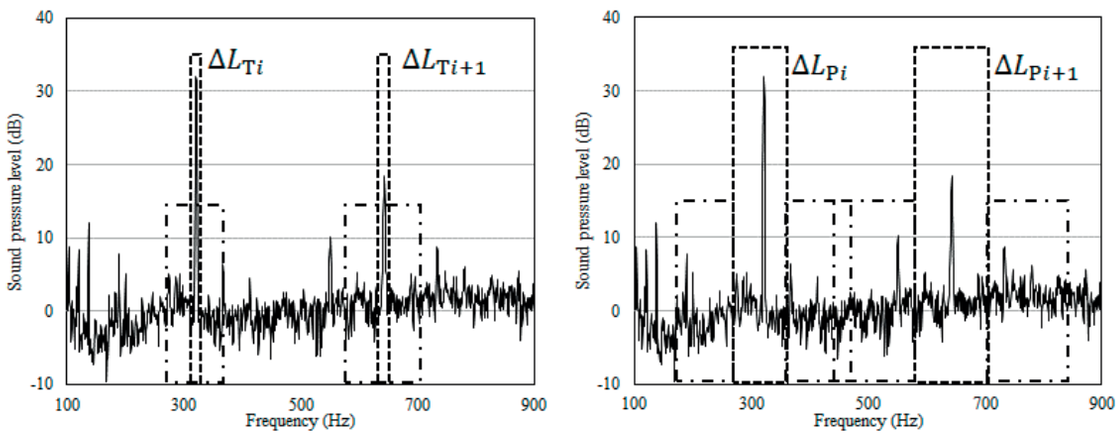


Figure 2: schematic view of T-TNR and T-PR calculation (Left: T-TNR, Right: T-PR)

$$\langle L_T \rangle = 10 \log_{10} \left(\sum_{i=1}^{N} 10^{\Delta L_{T_i}/10} \right) \tag{3}$$

$$\langle L_P \rangle = 10 \log_{10} \left(\sum_{i=1}^{N} 10^{\Delta L_{P_i}/10} \right) \tag{4}$$

where $\langle L_T \rangle$ (dB) is the T-TNR, ΔL_{T_i} (dB) is the TNR of i-th tonal component, $\langle L_P \rangle$ (dB) is the T-PR, and ΔL_{P_i} (dB) is the PR of i-th tonal component. N is the number of tonal components in the noise spectrum.

Threshold levels of Total Tone-to-Noise Ratio and Total Prominence Ratio

In order to judge whether the fan noise is good or bad, it is necessary to determine the boundary level of the T-TNR or the T-PR that is subjectively perceived as harsh or not harsh, the threshold level. In this study, the T-TNR or the T-PR thresholds are determined using a commercially available projector noise as a reference sound source. The subjective harshness (annoyance) thresholds of the T-TNR or the T-PR are treated in this study as symbol$\langle L_T \rangle_0$ or $\langle L_P \rangle_0$ respectively.

MAHALANOBIS-TAGUCHI SYSTEM (MT SYSTEM)

This chapter is simply a summary of the basic concept of the MT system. This system quantitatively judges the target sample according to its distance from the normal group by using only one normal group as the criterion, the judgement scale integrating many pieces of information. In other words, if the target sample to be judged is located close to the normal group, it is the sample that resembles the normal group, if it to be judged is located not close to the normal group, it is an abnormal sample that does not resemble the normal group. In the MT system, the normal group is called the "unit space," and the reference point for judgement is determined by it. The degree of separation from the reference point is quantified by the "Mahalanobis' distance", the judgement scale that integrates many pieces of information. Therefore, the degree of similarity to the normal group can be quantitatively represented by the Mahalanobis' distance [4].

Although there are many methods of data processing depending on the purpose for MT systems, we used the "RT method" which is one of these methods in this study.

SENSORY TEST

In our previous studies, the T-TNR and the T-PR were confirmed to be valid evaluation indices for the subjective harshness (annoyance) of noise with multiple tonal components [5].

TEST SOUND FOR SENSORY TEST

In this study, five commercially available projectors of different specifications and manufacturers were prepared as sound sources. These were all designed for tabletop use. These projectors were turned on and the sounds of their operation were recorded with a microphone placed 300 mm above the projectors while the video signal was input. The five projectors were designated as Type-1 to Type-5, respectively. Concurrently, the sound sources were employed as test sound sources and thus designated as Sound1-1 to Sound1-5, respectively. Table 1 shows the main noise characteristics of the projectors. Furthermore, the OASPL values presented in the following tables represent the A-weighted sound pressure level.

Next, the sound sources for which the loudness values were adjusted to be in close alignment with the loudness values of Type-5 (Sound1-5) in Table 1 were designated as "Test Sound Set 2" (abbreviated as Set 2). These test sound sources were designated as Sound2-1 to Sound2-5, in that order. Finally, the sound sources whose tonal components were modified Type-4 (Sound1-4) and Type-5 (Sound1-5) in Table 1 were designated as "Test Sound Set 3"(abbreviated as Set 3). These test sound sources were designated as Sound3-1 to Sound3-5, in that order. And the sound sources whose tonal components were modified Type-3 (Sound1-3) and Type-4 (Sound1-4) in Table 1 were designated as "Test Sound Set 4"(abbreviated as Set 4). These test sound sources were designated as Sound4-1 to Sound4-5, in that order.

The specific modification policies are as follows. The modification of the tonal components of Sound1-4 has resulted in a reduction in the T-TNR and the T-PR of Sound3-4. The modification of the tonal components of Sound1-5 has resulted in a reduction in the T-TNR and in an increase in the T-PR of Sound3-5. The modification of the tonal components of Sound1-3 has resulted in an increase in the T-TNR and T-PR of Sound4-3. The modification of the tonal components of Sound1-4 has resulted in a reduction in the T-TNR and T-PR of Sound4-4. Furthermore, the sound sources for Set 3 and Set 4 were adjusted to the Loudness value of Sound1-5 in a manner analogous to that employed for Set2. Tables 1 to 4 showed the noise characteristics of each test sound set.

Table 1: specific characteristic of test projectors (Set 1)

Projector [Sound Source]	$\langle L_T \rangle$ dB	$\langle L_P \rangle$ dB	Loudness sone	Sharpness acum	OASPL dB(A)
Type-1 [Sound1-1]	7.0	12.4	3.11	1.03	42.8
Type-2 [Sound1-2]	11.6	12.3	5.03	1.18	50.3
Type-3 [Sound1-3]	6.9	13.0	3.08	0.88	43.1
Type-4 [Sound1-4]	13.3	15.5	6.51	1.61	50.4
Type-5 [Sound1-5]	20.5	15.5	3.11	1.08	41.9

Table 2: specific characteristic of Set 2

Sound Source	$\langle L_T \rangle$ dB	$\langle L_P \rangle$ dB	Loudness sone	Sharpness acum	OASPL dB(A)
Sound2-1	11.5	10.6	3.17	1.04	44.5
Sound2-2	7.0	12.4	3.12	1.03	42.9
Sound2-3	6.9	13.0	3.11	0.88	43.2
Sound2-4	13.0	14.7	3.14	1.37	41.3
Sound2-5	20.5	15.5	3.11	1.08	41.9

Table 3: specific characteristic of Set 3

Sound Source	$\langle L_T \rangle$ dB	$\langle L_P \rangle$ dB	Loudness sone	Sharpness acum	OASPL dB(A)
Sound3-1	11.3	10.4	3.06	1.04	44.2
Sound3-2	7.0	12.3	3.00	1.02	42.4
Sound3-3	7.0	13.0	2.99	0.87	42.8
Sound3-4	12.6	14.8	2.95	1.17	42.3
Sound3-5	13.1	16.8	3.05	1.32	40.7

Table 4: specific characteristic of Set 4

Sound Source	$\langle L_T \rangle$ dB	$\langle L_P \rangle$ dB	Loudness sone	Sharpness acum	OASPL dB(A)
Sound4-1	7.0	12.3	3.00	1.02	42.4
Sound4-2	7.0	13.0	2.99	0.87	42.8
Sound4-3	17.5	14.1	3.01	0.95	44.0
Sound4-4	12.6	14.8	2.95	1.17	42.3
Sound4-5	12.8	15.0	3.04	1.36	41.0

MEATHOD OF SENSORY TEST

The sensory test was employed the ranking method. This method is employed for the purpose of ranking the strength of preference or sensation for a given sample. Although it is less accurate than the paired comparison method, it is considered a superior method in that it is less onerous for the jury [5]. In this study, the test sounds in the test sound set were played in an arbitrary manner, and the full ranking method was employed to rank all of them without overlap. The ranking was based on the test sound source that was not perceived as annoying, which was assigned the ranked first. Furthermore, the juries were requested to select the test sound source that they could tolerate without finding it annoying at the same time as ranking.

The juries for the sensory test were 20 university students (aged between 21 and 24 years old) with normal hearing ability, selected at random. The juries were presented with a set of five test sounds and asked to rank them in order of increasing perceived harshness (annoyance). This test was executed for all four test sound sets. The order in which the four test sound sets were presented was randomized, and the order in which the test sounds were listened to within the test sound set was left to the discretion of each jury. In addition, the Set 1 and Set 2 were included twice in one test, and a total of six sound sets were executed as the sensory test for one jury.

RESULT AND DISCUSSION

This chapter describes the evaluation of sensory test results, determination of thresholds and the evaluation of thresholds.

EVALUATION OF SENSORY TEST

The Kendall's coefficient of concordance was calculated to verify the significance of the tests by using the sensory test results. The availability of the evaluation indices was verified by rank correlation.

Table 5 shows the results of the calculation of the residual sum of squares and the Kendall's coefficient of concordance from the sensory test results. The 1% significance point for S is 641.2 and the 5% significance point for S is 468.5 when the number of samples n = 5 and the number of juries K = 20. Because all S in these experimental results were greater than these values, the agreement between the juries' evaluations is high and it can be confirmed that there is a statistically significant agreement [7][8].

Table 5: Kendall's coefficient of concordance

	Set 1 (1st)	Set 1 (2nd)	Set 2 (1st)	Set 2 (2nd)	Set 3	Set 4
S	2890	3100	2080	2090	2118	2026
W	0.72	0.78	0.52	0.52	0.53	0.51

The correlation coefficients between the evaluation indices and the average rankings for each sound of the four sound source sets were calculated.

In the first time and second time of Set 1, the Loudness, which is an index of loudness, and the Sharpness, which is an index of the sharpness and height of sound, showed higher correlations than the other evaluation indices. In Set 1, the Loudness of the test sound sources was not adjusted, so the results showed that the juries' judgments were based on loudness.

In Set 2, the Loudness of the test sound source was kept almost constant, so the T-TNR and the Sharpness showed a high correlation. For the T-PR, the correlation coefficient was around 0.7. Therefore, it is assumed that the T-TNR and the T-PR are effective for evaluating the noise of small fans when there is no difference or small difference of difference in loudness. The rank sum showed a similar trend in the two tests of Set 1 and Set 2. Therefore, the effect of the order effect in the sensory test is considered to be small.

Next, the results of Sets 3 and 4 will be discussed. These test sounds include sounds with deliberately adjusted tonal components. In Set 3, the T-TNR and the Sharpness showed a high correlation. This is the same trend as the second time for Set 2. On the other hand, in Set 4, the T-PR and the Sharpness showed a high correlation. This is the same trend as the first time for Set 2. As the TNR and the PR are complementary, if the correlation of either the T-TNR or the T-PR is low, the correlation of the other may be high.

For the Sharpness, there was a general trend towards a high correlation. In other words, it is thought that the judgments of subjective harshness (annoyance) made by juries were also influenced by sharpness and height of sound.

Based on the above results, it is thought that the proposed the T-TNR and the T-PR evaluation indices can be applied as subjective harshness (annoyance) evaluation indices for projector products with built-in small fans.

Table 6: correlation between ranking averages and evaluation indices

Sound Set	$\langle L_T \rangle$	$\langle L_P \rangle$	Loudness	Sharpness	OASPL
Set 1 (1st)	0.56	0.56	0.87	0.93	0.76
Set 1 (2nd)	0.69	0.69	0.77	0.90	0.63
Set 2 (1st)	0.91	0.75	-0.03	0.72	-0.70
Set 2 (2nd)	0.79	0.69	0.01	0.81	-0.73
Set 3	0.84	0.48	-0.11	0.85	-0.35
Set 4	0.51	0.77	-0.18	0.82	-0.45

DETERMINATION OF THRESHOLD

The thresholds of subjective harshness (annoyance) were determined on the basis of the results of the sensory test. The test sound sources that were selected as acceptable by each jury were extracted, and the median values of their T-TNR and T-PR were determined as the thresholds $\langle L_T \rangle_0$ and $\langle L_P \rangle_0$. The median values were adopted as the thresholds due to the non-normal distribution of the results for each set of test sounds and for all test sounds. The results were shown in Table 7. The thresholds were found to be $\langle L_T \rangle_0$ = 11.4 (dB) and $\langle L_P \rangle_0$ = 13.0 (dB). These were then compared with the single fan thresholds that had been determined in our previous study [5]. The thresholds determined in this study were found to be lower than those determined in previous study. The discrepancy was thought to be attributable to the divergence in the calculation methodologies employed for T-TNR and T-PR between the previous study and this study. In case of the consideration of the standard deviations for our previous study's thresholds [5], it was confirmed that this study's both thresholds determined were within their ranges.

Table 7: threshold levels for projectors (all sound).

	$\langle L_T \rangle_0$ - dB	$\langle L_P \rangle_0$ - dB
Threshold Level	11.5	13.0

EVALUATION OF THRESHOLD USING MT SYSTEM

In the case of utilizing the MT system for product inspection, it is desirable that the "unit space", which constitutes the normal group, is comprised of a substantial number of normal products. In this study, the decision was taken to utilize the test sound sources from Sets 2 to 4, in which the projector sound sources were adjusted, due to the difficulty in collecting a substantial number of normal product data. In the RT method, the number of normal product data for "unit space" is not constrained. However, the small number of normal product data may be unstable as a criterion for judgement.

First, when each data ($\langle L_T \rangle$ and $\langle L_P \rangle$) showed in Table 1 were blow each threshold $\langle L_T \rangle_0$ and $\langle L_P \rangle_0$ showed in Table 7, the sound source was considered as normal. Therefore, the projectors Type-1 and Type-3 were judged as normal (good). Next, the unit space was created with the data judged to be normal (good) among the test sound sources from Set 2 to Set 4 (Sound2-1, Sound2-2, Sound2-3, Sound3-1 Sound3-2, Sound3-3, Sound4-1, and Sound4-2). The RT method was employed to judge the projector sound source, Type-1 and Type-3 were judged to be the normal (good). The results were the same as the results of the threshold-based judgement.

The results showed that when the threshold values obtained in this study were applied for product evaluation, products that below each threshold $\langle L_T \rangle_0$ and $\langle L_P \rangle_0$ were considered as normal products, which was consistent with the judgement results using the RT method. While it is necessary to examine the unit space for the RT method in terms of the number of normal product data, we think that we have demonstrated the validity of the thresholds obtained in this study.

Table 8: threshold evaluation

Projector [Sound Set]	$\langle L_T \rangle$ dB	$\langle L_P \rangle$ dB	Judgement by Threshold	Judgement by RT Method
Type-1 [Sound1-1]	7.0	12.4	Good	Good
Type-2 [Sound1-1]	11.6	12.3	Bad	Bad
Type-3 [Sound1-3]	6.9	13.0	Good	Good
Type-4 [Sound1-4]	13.3	15.5	Bad	Bad
Type-5 [Sound1-5]	20.5	15.5	Bad	Bad

ADDITIONAL EXAMINATION OF THE JUDGEMENT THRESHOLDS

The rank sum of the sensory test for Set 1 is shown in Table 9. If these results are compared with the results in Table 7 and assume that the sum of the ranks of the normal products is around 50 or less, the results of the two are the same. Based on these results, the thresholds for T-TNR and T-PR are able to narrowed down to $\langle L_T \rangle_0$= 7.0 (dB) and $\langle L_P \rangle_0$= 13.0 (dB). Although there was no change in $\langle L_P \rangle_0$, the threshold for $\langle L_T \rangle_0$ showed a tendency to decrease further. The normal product data were limited to sound sources with $\langle L_T \rangle_0$= 7.0 (dB) or less and $\langle L_P \rangle_0$= 13.0 (dB) or less in the sound source from Set 2 to Set 4 (Sound2-2, Sound2-3, Sound3-2, Sound3-3, Sound4-1, and Sound4-2), the RT method was used for evaluation and obtained the same results as in Table 8. Next, the evaluation was conducted to ascertain which sound sources within each sound source set were deemed acceptable. The sound source that was judged to be acceptable by the majority of juries (in cases where the number of juries was the same, the sound source with the lowest rank sum) was shown in Table 10 as the representative value for each sound source set. Firstly, for the same sound source sets (Set 1 and Set 2), the results for the first and second evaluations were the same, so it was thought that the juries' evaluations were stable. Next, when the results of Sound Source Sets 1 and 2 were compared, it can be seen that the tolerance for T-TNR is more lenient and the tolerance for T-PR is stricter in Sound Source Set 2, which has been adjusted for loudness. Sets 3 and 4 were thought to show the same trend as Set 2, as they were sound source sets with the adjusted same loudness as Set 2. However, Set 3 showed the same trend as Set 2, and Set4

showed the same trend as Set 1. It is thought that these discrepancies can be attributed to the variations in T-TNR and T-PR included in the sound source set. Finally, for all sound sources sets, it can be found that the values are around or below estimated thresholds in advance. Therefore, it is thought that the thresholds for T-TNR and T-PR would be appropriate at $\langle L_T \rangle_0$= 11.5 (dB) and $\langle L_P \rangle_0$= 13.0 (dB), respectively.

Table 9: rank sum of Set 1

Projector [Sound Set]	Set 1 (1st) Rank sum	Set 1 (2nd) Rank sum
Type-1 [Sound1-1]	42	41
Type-2 [Sound1-1]	71	67
Type-3 [Sound1-3]	28	24
Type-4 [Sound1-4]	95	95
Type-5 [Sound1-5]	64	73

Table 10: each evaluation index that was judged to be an acceptable sound source

Sound Set	$\langle L_T \rangle$ dB	$\langle L_P \rangle$ dB	Loudness sone	Sharpness acum	OASPL dB(A)
Set 1 (1st) [Sound1-1]	7.0	12.4	3.11	1.03	42.8
Set 1 (2nd) [Sound1-1]	7.0	12.4	3.11	1.03	42.8
Set 2 (1st) [Sound2-1]	11.5	10.6	3.17	1.04	44.5
Set 2 (2nd) [Sound2-1]	11.5	10.6	3.17	1.04	44.5
Set 3 [Sound3-1]	11.3	10.4	3.06	1.04	44.2
Set 4 [Sound4-1]	7.0	12.3	3.00	1.02	42.4

APPLYING THE JUDGEMENT THRESHOLDS TO OTHER SOUND SOURCES

The thresholds obtained in this study were applied to the small fan (single fan) used in previous studies, and the effectiveness of their thresholds were evaluated. The seven types of small fan were subjected to evaluation. The values for each of their evaluation indices were shown in Table 11. Furthermore, the frequency range for selecting tone components was set to the full range specified in the standard [1], and the tone selection conditions were also the same as in this study. Consequently, so the T-TNR and the T-PR values differ from reported values in previous study [5].

Table 11: specific characteristic of small fans

Fan Name	$\langle L_T \rangle$ dB	$\langle L_P \rangle$ dB	Loudness sone	Sharpness acum	OASPL dB(A)
Fan A	5.7	6.9	1.16	1.81	30.8
Fan B	2.8	9.9	0.73	1.41	27.0
Fan C	3.6	7.4	0.32	1.90	22.5
Fan D	6.7	11.2	0.86	1.73	29.1
Fan E	11.0	15.1	2.82	1.91	38.8
Fan F	14.5	18.7	2.06	1.70	35.9
Fan G	5.7	13.7	1.19	1.76	30.9

The results of these were shown in Table 12. First, in the judgment for using the thresholds estimated in this study (in which small fans with both evaluation values below the threshold value are judged to be normal), Fan A to Fan D were judged to be normal. Next, in the judgment for using the RT method, all fans with the

exception of Fan E and Fan F were judged to be normal. The only case in which the judgments differed between the two methods was Fan G. In the case of Fan G, the T-TNR is below the estimated threshold, whereas the T-PR is above the estimated threshold, so it is judged to be abnormal. However, Fan the T-PR of Fan G is in a vicinity of the threshold value. As there were no setting for the T-PR between 13 (dB) and 14 (dB) in the sound source sets used in this study, it is possible that the T-PR threshold was not narrowed down sufficiently.

Table 12: threshold evaluation for small fan

Fan Name	$\langle L_T \rangle$ dB	$\langle L_P \rangle$ dB	Judgement by Threshold	Judgement by RT Method
Fan A	5.7	6.9	Good	Good
Fan B	2.8	9.9	Good	Good
Fan C	3.6	7.4	Good	Good
Fan D	6.7	11.2	Good	Good
Fan E	11.0	15.1	Bad	Bad
Fan F	14.5	18.7	Bad	Bad
Fan G	5.7	13.7	Bad	Good

CONCLUSION

The objective of this study was to determine the thresholds of the T-TNR and the T-PR, which are new evaluation indices for noise with multiple tonal components, using the sensory test. If the accuracy of these annoyance thresholds for information equipment can be improved, this evaluation method may be applied to evaluate the sound quality of other fields in the future. The $\langle L_T \rangle_0$ and the $\langle L_P \rangle_0$ thresholds for subjective harshness (annoyance) of the projector products were estimated and the validity of these thresholds was verified using the MT system. The validity of the thresholds was verified using sound sources that the juries judged to be tolerable for subjective harshness (annoyance). The T-TNR and the T-PR thresholds estimated in this study were applied to the noise of a small fan to verify their effectiveness. The issues to be considered are improving the accuracy of the thresholds and their practical application.

BIBLIOGRAPHY

[1] ECMA-418-1, *Psychoacoustic metrics for ITT equipment – Part1 (prominent discrete tones)*, 1st Edition, December **2020**

[2] T. Nakano, G. Minorikawa, Study on the evaluation index of pure tones that occurs from small fan. *PROCEEDINGS OF THE 2017 AUTUMN MEETING THE INSTITUTE OF NOISE CONTROL ENGINEERING OF JAPAN*, 47-50, **2017**

[3] ECMA TR/108 Proposal of new parameters, *T-TNR and T-PR for total evaluation of multiple tones*, 1st edition, June **2019**

[4] K. Tamura, *Easy to understand MT System* [Translated from Japanese.], Japanese Standards Association, **2009**

[5] T. Nakano, G. Minorikawa, Study on Evaluation Method of Tonal Components for Small Fans. *Turbomachinery Society of Japan, Turbomachinery Vol.48, No.3*, 166-175, **2020**

[6] S. Namba, S. Kuwano, *Psychological measuring method for sound evaluation* [Translated from Japanese.], CORONA PUBLISHING CO., LTD., **1998**

[7] S. Ichihara, T. Kajitani, R. Komatsubara, *Sensitivity and Sensory evaluation data analysis for product development* [Translated from Japanese.], Research Institute for Sensory Evaluation, **2015**

[8] G. Minorikawa, T. Nakano, Sound quality evaluation of small fan noise by tonal components. *Proceedings of INTER-NOISE 2024*, **2024**



IMPROVING THE PSYCHOACOUSTIC ASSESSMENT OF AUTOMOTIVE FAN-SYSTEMS

Denis SCOUARNEC[1], Saad BENNOUNA[1], Thibault VICENTE[2], Adrien PELAT[2]
Nicolas CHOUARD[2], Alban GODART[2], Armand COMPAIN[2]

[1] *Valeo Power Division, 8 rue L.Lormand, 78320 La Verrière, France*

[2] *LAUM, Le Mans Université, Avenue Olivier Messiaen. 72085 Le Mans, France*

SUMMARY

Beyond first order noise ranking using global indicators, e.g. overall Sound Pressure Level or Loudness, the second order factors to assess annoyance cannot be robustly described by a single criterion. This paper focuses on fan-system annoyance at a fixed global level based on pairwise comparison through jury test with a set of 8 fan-system noises. Then potential preference models, consisting of equations combining several psychoacoustics metrics, are assessed and correlated with jury evaluation. The resulting parametric equation to assess and rank fan-system noise annoyance at fixed global level combines a signal modulation metric, a frequency content balance in addition to a tonal criterion.

INTRODUCTION

The automotive NVH is progressively putting effort in studying embedded systems that were previously hidden by internal combustion engines. This is due to the worldwide automotive electrification which increases the perceived noises of those systems inside and outside the car cabin. Among embedded systems, thermal systems are major noise contributors especially because of the fan-system while being mandatory to provide thermal comfort, ensure battery thermal management and comply with applicable regulations. In case of pedestrians exposed to fan-system noise, the main acoustic indicators are global ones: overall Sound Pressure Level or Loudness. At first order, these two global indicators of noise ranking are correlated despite remaining gaps between them. Beyond first order factors, the second order ones which also contribute to annoyance are not robustly highlighted by a single criterion [1]. Indeed, one tonal criterion could not take into account all the various tonal annoyances from symmetric to highly asymmetric distribution of fans. The latter could especially involve roughness increase because of several high level tones above broadband noise and the subsequent fast modulation impacting the subjective evaluation for fan-system noise.

A study of a large range of fan-systems through various existing tonal criteria highlights that the subjective annoyance ranking is not robustly assessed between the various samples at their respective global level. In order to focus on the second order's acoustic criteria also impacting subjective annoyance, a jury evaluation - with about thirty listeners- at the same overall SPL is then useful. A set of 8 fan-system sounds assessed using pairwise comparisons allows to combine tonal criteria, with other psychoacoustic criteria such as level variation and frequency content indicators leading to a combination of several metrics.

FRONTEND MODULE DESCRIPTION AND PSYCHOACOUSTIC METRICS

Frontend cooling module description and related airflow noise

The frontend cooling module ensures thermal needs of the vehicle thanks to a Fan-System (FS) pulling airflow through thermal exchangers when necessary.

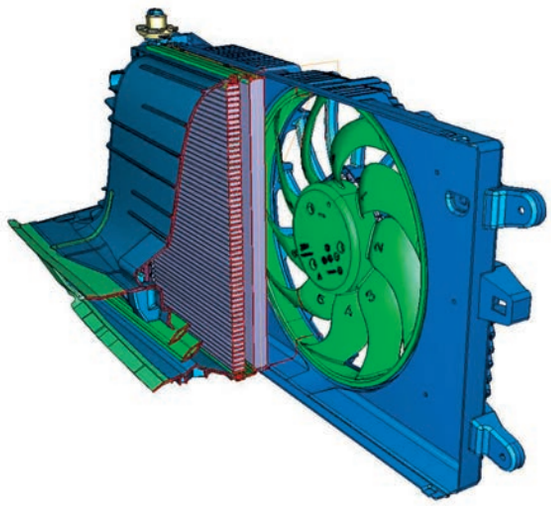


Figure 1: Example of frontend cooling module in cross-sectional view

Aerodynamic noise sources from axial fans of automotive cooling systems have already been extensively studied. These sources are resulting from the interaction mechanisms between airflow and blades or static obstacles of the module. The FS noise behavior is mainly dipolar and characterized by both broadband and tonal components. The broadband noise comes from interaction with turbulent airflow. It could rise from the fan blade itself, from the upstream exchangers or from the leakages as tip clearance. The tonal noise is due to the periodic fluctuation of forces applied on the blades or on close obstacles such as FS arms or stators. It is especially linked to non uniform inflow speeds on blades, blade wake impact on downstream obstacles and even back impact on blades coming from these obstacles.

Psychoacoustic metrics overview

There are several criteria to predict noise annoyance, and especially criteria that integrate the human hearing perception specifics: detection threshold, frequency masking, frequency bandwidth variability function of the frequency….

First comes the tonal content assessment using Tone-to-Noise Ratio (TNR) and Prominence Ratio (PR) that are standardized through ECMA-74 [2]. The PR is the ratio between the energy in the critical band centered on the tonal peak and the energy average in the two adjacent critical bands. The TNR measures the level of a tone compared to the level of the noise in the critical band centered around the peak. According to ECMA-74, “the tone-to-noise ratio method may prove to be more accurate for multiple tones in adjacent critical bands, for example when strong harmonics exist. The prominence ratio method can be more effective for multiple tones within the same critical band”.

Tonality Aurès/Therardt is another indicator highlighting the tonal components in a noise spectrum. Its calculation is based on a comparison between the amplitude of the tonal component and the amplitude of the noise at the neighboring frequencies. An extra frequency dependent weighting function such as the maximum tonality perception at 700 Hz is applied [3].

A new calculation method called psychoacoustic Tonality, or Tonality HMS (Hearing Model of Sottek) is promoted in the norm ECMA-418: “psycho-acoustic metrics for ITT Equipment” part 2: “model based on human perception” addressed in appendix G of ECMA-74 norm [4]. Human perception of tones is better taken into account by using the bark scale for critical frequency bands, by using the Loudness to compare the tone to the background noise for each critical band and considering the hearing thresholds and masking effect. The Loudness of each audible frequency component is compared to the background Loudness within each critical

band considering possible masking effects. Tonality calculation method was upgraded between first release in ECMA in 2018 and the updated version in 2021 [2]. However, this Tonality method needs to be modified to account for the influence of signals with multiple prominent tonal components, as it was not designed for this type of signal [5]. A solution to improve the Tonality HMS was proposed after the work of Becker & Al [6] for identification of multiple tone effects and the tonal perception of narrow-band noise. The tonality levels for each of the components are summed up to provide the global tonality value in t.u HMS.

Some other metrics were designed to account for our perception of signals modulated in amplitude over time. Fluctuation Strength is dedicated to low-frequency modulation signals with maximum value for 4Hz frequency. The Fluctuation strength perception persists up to 20 Hz when the Roughness perception takes over. Roughness quantifies the subjective perception of fast amplitude modulation of a sound from ~20 to ~300 Hz. For sounds with envelope variation rates above 300 Hz, the pure amplitude-modulated tones become audible as individual tones. The roughness depends on the center frequency of the sound, the modulation rate f_{mod} and the temporal masking depth ΔL in Zwicker's simplest approximated model shown in Equation 1 [7]. With increasing modulation depth, the roughness feeling increases, and the Roughness impression strongly decreases towards very low or high modulation rates.

$$R \sim f_{mod}\, \Delta L \tag{1}$$

The ECMA-418-2 standard, revised in 2022, describes in clause 7 a new Roughness implementation based on the same hearing model already used for Tonality. In this hearing model, the outer and middle ear filtering combined with the auditory filter bank gives a time-frequency representation of the signal as a superposition of band-pass signals. These signals are segmented in time before computing the specific Loudness values. The computation of the sound quality metrics starts by applying the hearing model on the input signal. The ECMA 418-2 standard first considers Zwicker and Fastl Roughness curves [7] as a reference. Then Roughness calculation process starts from the segmented band-pass signals obtained from the hearing model. Their low-frequency envelope spectra carry the information of modulation, that can be extracted with a specific peak analysis procedure, applied to each critical band within each time window. The specific Roughness values are calculated from the modulation rates and their amplitude with a non-linear transform that fits the Zwicker and Fastl curves. Some difficulties of computational implementation based on missing information or subjected to interpretation in ECMA-74 standard were highlighted by Wanty [8]. These issues were avoided owing to the original implementation in Artemis software by Head acoustics.

Last major metric for fan noise psychoacoustics assessment is the Sharpness. It is a frequency content indicator which describes high versus low frequency balance by calculating the center of gravity of Loudness spectral distribution. The ISO 532-1 norm for Loudness calculation is used to determine the Sharpness according to Aures calculation method, which takes into account the absolute Loudness influence on the Sharpness level. This method is thus preferable to assess the sharpness of the sound in case of significant loudness differences. Sharpness results from the ratio of critical band's Loudness divided by the total Loudness according to Equation 2 from [9], where Loudness N is the integral of specific Loudness (N') over critical-band rate:

$$S_A = 0.11\, \frac{\int_0^{24} N'(z).\ g_A(z).dz}{\int_0^{24} N'(z).\ dz} \tag{2}$$

with g_A weighting function for Aures method in equation 3 below, which increases with Loudness.

$$g_A(z) = 0.078\, \frac{e^{0.171.z}}{z} \cdot \frac{N}{\ln(0.05.N+1)} \tag{3}$$

This weighting function means that Sharpness increases exponentially towards high frequencies, and thus limiting the contribution of critical bands in low frequency [10]. Based on subjective evaluations from Fastl and Zwicker, the general case is that sensory pleasantness decreases with Sharpness increase.

JURY EVALUATION FOR NOISE RANKING THROUGH EQUATIONS

Previous studies or existing psychoacoustics equation

Single psychoacoustics criteria taken separately -each one focusing on specific content of the acoustic pressure signal- are not able to provide engine cooling module acoustic quality. For this reason several studies tried to highlight the link between human annoyance and objective criteria. However, these studies rarely involved low speed rotating machines as automotive cooling FS. For Valeo fan-systems, investigations were performed especially by Rinaudo [11] to search for an equation combining several psychoacoustic metrics based on jury evaluations. However, these conclusions were not applied following inconclusive results [12] potentially linked to high Loudness levels masking other sound quality trends [13]. Schneider [14] focused on the perceived sound quality of fan systems and highlighted that Loudness can be used as the main metric whereas secondary metrics are Sharpness and tonal indicators. The modified Psychoacoustic Annoyance PA* including Tonality is shown in Equation 4,

$$PA^{*} = PA\,(1+T) \tag{4}$$

where PA in Equation 4 is based on the initial work from Zwicker and Fastl [7] for synthetic and technical sounds, and trying to establish a single criteria using Loudness, Roughness, Sharpness and Fluctuation strength. Note that this work is based on results from psychoacoustic experiments with modulated versus unmodulated narrow-band and broadband sounds, thus not dedicated to rotating machines including major tonal components.

$$PA = N_5 \left(1 + \sqrt{(0.25.\log(N_5+10).(S-1.75))^2 + \left(\frac{2.18}{N_5^{0.4}} .(0.4.F+0.6.R) \right)^2} \right) \tag{5}$$

But PA* still includes an overall indicator: the percentile Loudness N_5 (e.g. the Loudness value reached or exceeded in 5% of the measurement time, which is often close to the maximum Loudness).

In this paper, taking into account first order importance of global level criteria on annoyance ranking, we choose to cancel Loudness impact, which means to consider a different combination of various psychoacoustic metrics. The single indicator from Schneider could thus be used later for analysis and comparison between FS noises at different levels.

New study

For this jury evaluation, pairwise comparison method is preferred to get feedback from non-expert public [14]. Each of the 8 FS sounds measured at its dedicated operating point is equalized at ~70 dBA to ensure an acceptable listening for the 30 minutes test duration. The pairwise comparison are presented only once to avoid participants' fatigue. Else reversing each pair results in 56 comparisons, and subsequent listener concentration loss risk increase. The consistency assessment is thus only performed through duplication of one of the 8 sounds. This additional sound results in 36 comparisons assessed by a jury of 30 people (24 years old on average).

From each listener's evaluation, SQala software from Artemis (Head Acoustics) calculate the preference order of all the sounds, with 0 to 8 score, from worst to best. This provides a distribution diagram for each sound score with minimum, maximum, mean value in addition to lower and upper quartiles as shown in Figure 2.

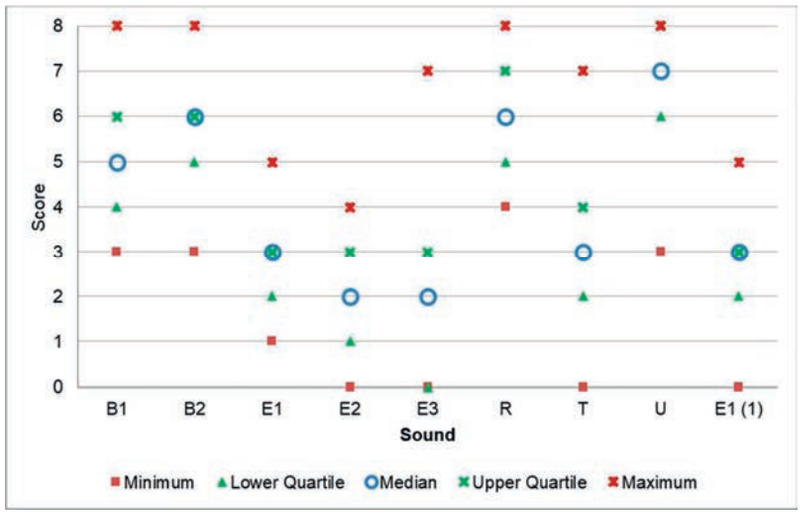


Figure 2: Score distribution (from 0 to 8) of each sound assessed by the 30 listeners.

Median and mean score displayed in Figure 3 are quite close, especially accounting the confidence interval around the mean value.

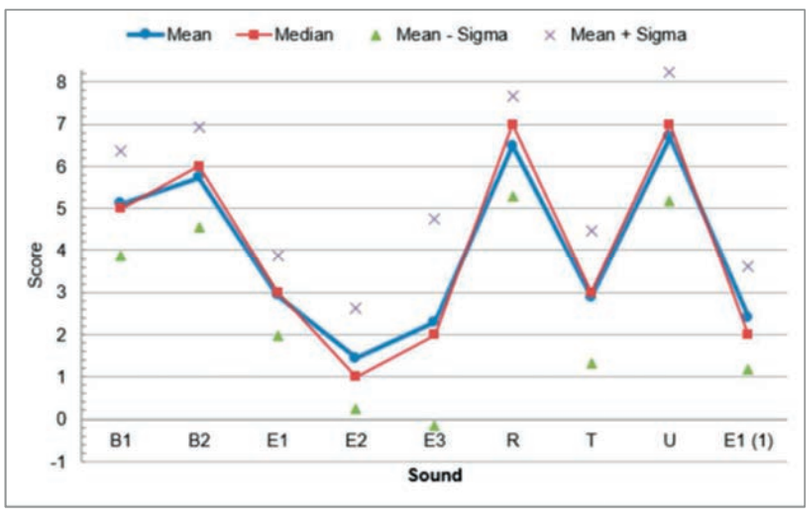


Figure 3: Confidence interval around the mean Score for each sound.

To ensure listeners reliability for results analysis, a method based on circulars triads study is used: if A>B and B>C, then A>C should be fulfilled. Only 27 of the 30 people were at a consistency coefficient over 0.6. Based on a reference study from Parizet [16], recommending at least a coefficient higher than 0.5, three listeners whose reliability scores are considered uncertain were not in the final analysis database. Consistency coefficient closer to 1 could only be possible using sounds with significantly different overall levels which contradicts our intended focus on second order parameters.

RESULTS ANALYSIS THROUGH NEW PARAMETRIC EQUATION

Several models combining various number of parameters

Selected results could be used to search for correlations between each FS score from the jury test and various psychoacoustics metrics using multi-linear regression calculation. This leads to expressing the FS ranking according to Equation 6:

$$C^n = b + \sum_{i=1}^{N} \alpha_i * a_i^n \quad (6)$$

with C^n the sound n ranking (or score), a_i^n the psychoacoustic criterion i applied to the sound n, α_i the weighting coefficient of psychoacoustic criterion i, and b a constant offset value. Several models could result following the selected combination of different parameters among PR, TNR, Tonality, Roughness, Fluctuation strength and Sharpness. The calculated models with various metrics number and choices are summarized Table 1 and listed with increasing quadratic correlation coefficient value. The linear combination without limiter is preferred. No need to limit with sigmoid function the scale for the score based on pair comparison contrary to range of values based on judgment with usual trend to avoid extrema.

The Roughness calculation results from combination of the two channels of the binaural signal, while the other criteria only come from the channel with maximum value. The maximum level over the 5s of single channel signal is selected for each of the following metric: Tonality, TNR and PR. The average value is preferred for Sharpness, Fluctuation Strength and Loudness. The Tonality value according to Sottek hearing model is determined using a temporal averaging of the signal along the time, after a 300ms start phase skipping.

Table 1: Sum-up of the various models calculated by multi linear regression

Model	b	Roughness ECMA-418-2	Sharpness ISO532-1 Aurès	Tonality max ECMA-418-2	TNR max	PR max	Fluctuation Strength	Loudness ISO532-1	R^2
2 metrics	38,47	-10,90	-9,09						0,72
	38,61		-9,05		-0,11				0,79
3 metrics	35,49	-13,42	-7,66	-2,64					0,94
4 metrics	10,88	-6,97	-7,74	-2,40				0,93	0,96
	35,47	6,84	-7,70	-1,97	-0,18				0,95
5 metrics	-7,98	95,34	-11,78	-0,91		-0,99		2,32	0,98

The best model with 2 parameters combines Sharpness & TNR but reaches an insufficient quadratic correlation coefficient with an R^2 of only 0.79. Adding metrics that cover the same subjective annoyance criteria should preferably not be used to avoid doubling the weight of tonal criterion in the same model. Considering similar metrics, Fluctuation Strength and Roughness are both dealing with level variation over time, but Roughness is significantly more dedicated to the studied spectra. Regarding the Loudness, it should be a low impact criteria taking into account the too small difference between equal SPL sounds studied. Many metrics could then be removed to avoid unnecessarily complex model without substantial improvement of correlation with the jury evaluation.

Selected model with 3 psychoacoustic metrics

The selected model has only one criterion for each type of annoyance. One single metric for "tonal", also one for "level variation or fluctuation", in addition to the spectral distribution metric. As a result, the following parametric Equation (7) is reached:

$$\text{Score} = 35.49 - 13.42 * R_{\text{ECMA-418-2}} - 7.66 * S_{\text{AURES}} - 2.64 * T_{\text{ECMA-418-2}} \quad (7)$$

A quadratic correlation coefficient R^2 of 0.94 is enough for reliability. It means that the combination of Roughness ($R_{\text{ECMA-418-2}}$), Sharpness (S_{AURES}) and Tonality HMS ($T_{\text{ECMA-418-2}}$) could be the simplest model to qualify acoustic annoyance from FSs at the same sound pressure level.

To confirm the relevance of this model with 3 parameters, the ranking found with only 2 parameters (Sharpness and TNR) then 4 parameters (Roughness/Sharpness/Tonality HMS- and Loudness) is also compared to the Jury test result (green curve) in figure 4.

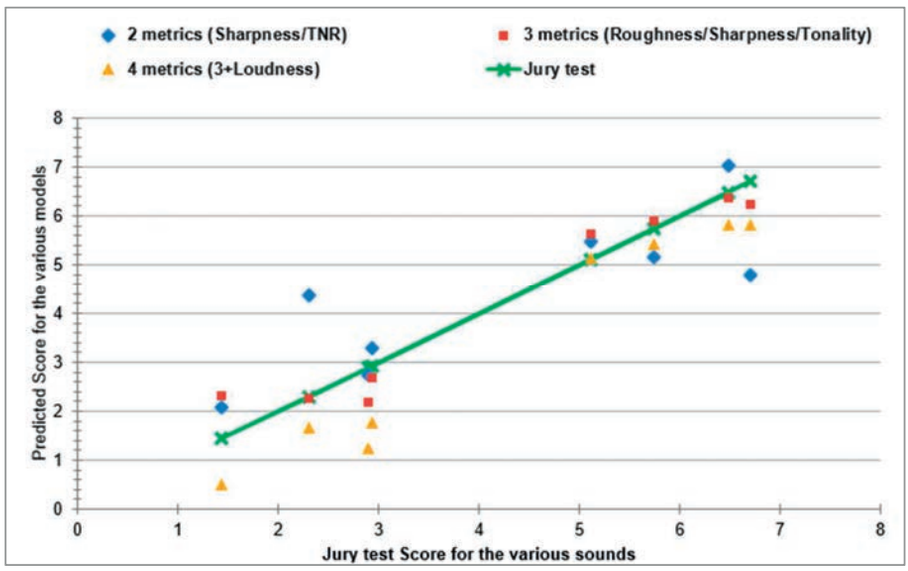


Figure 4: comparison of several models with the Jury test ranking.

CONCLUSION AND NEXT STEPS

At a similar global noise level, the subjective annoyance of FSs is very variable and a jury evaluation is relevant to correlate noise ranking with a combination of criteria. Beside regional and particular cultural preferences, this should help ranking of all remaining influent noise parameters at the same global level. Even if the consequent parametric equation including Roughness, Tonality HMS and Sharpness is based on a small set of FSs, it is a promising way to simultaneously combine tonal annoyance with level fluctuation and taking into account the spectral centroid.

In a potential next step, the Loudness could also be added to this parametric equation for a complete indicator. In addition, with similar ranking through jury evaluation, the "modified Psychoacoustic annoyance" proposal [14] could also be studied. A future PA* criterion calculation should then take into consideration recent improvement through psychoacoustic Tonality by Sottek [17] and also Roughness based on ECMA-418-2 calculation, and even Loudness. Then Equation 4 could be updated for future study:

$$PA_{HMS}{}^{*} = PA_{HMS}\,(1+T_{HMS}) \tag{8}$$

with PA_{HMS} resulting from equation 5 with N and R replacement by the modified metrics based on the Sottek hearing model published in ECMA-418-2 [4].

BIBLIOGRAPHY

[1] D. Scouarnec, S. Bennouna – *Psychoacoustic assessment of automotive fan-systems*. Proceedings of Internoise, Nantes, **2024**

[2] ECMA 74 – *Measurement of Airborne Noise emitted by ITT Equipment*, 19th Edition/December 2021, ECMA international,CH-1204 Geneva, Switzerland, **2021**

[3] W. Aures – Procedure for calculating the sensory pleasantness of various sounds, Acustica, 59 (vol. 59), pp. 130-141, **1985**

[4] ECMA 418-2 – *Psychoacoustic metrics for ITT equipment — Part 2 (models based on human perception)*, 2nd Edition/December 2022, ECMA international,CH-1204 Geneva, Switzerland, **2022**

[5] T. Lobato and R. Sottek – *Modeling the perceived tonal loudness of multiple tonal components.* DAGA 2023, Hamburg, **2023**

[6] J. Becker, R. Sottek, T. Lobato – *Progress in tonality calculation.* Proceedings of International Conference on Acoustics - ICA 2019, Aachen Germany, **2019**

[7] H. Fastl, E. Zwicker – *Psychoacoustics - Facts and Models*. Springer, Berlin, Germany, **2006**

[8] S. Wanty – *ECMA-418-2 roughness, a challenging implementation.* Proceedings of Internoise, Nantes, **2024**

[9] K. Genuit – *Status of Psychoacoustics in Noise Analysis*. JASA, **2015**

[10] E. Parizet – *Perception acoustique et qualité sonore.* Techniques de l'Ingénieur, R 6 140, **2009**

[11] S. Rinaudo, A. Sanon, P. Duputel – *The sound quality of cooling fan systems.* SAE technical paper, 980587, Detroit, USA, **1998**

[12] G. Jolivel – *Caractérisation psychoacoustique de groupes moto-ventilateurs*. ESTACA engineering school training report, **2004**

[13] A. Sanon, S. Naji – *Human perception and fan noises.* Proceedings of Fan 2015, Lyon, **2015**

[14] M. Schneider – *Psychoacoustic evaluation of fan noise.* Proceedings of Fan 2015, Lyon, **2015**

[15] A. Compain, A. Godart – *Caractérisation de la gêne acoustique de Groupes Moto-Ventilateurs*. ENSIM 5A project report, **2024**

[16] E. Parizet – *Paired comparison listening tests and circular error rates.* Acta Acustica united with Acustica, 88, pp.594-598. ffhal-00849430. **2002**

[17] R. Sottek – *Sound Quality Metrics using Psychoacoustic Standards*. Proceedings of Automotive NVH Comfort 2023, Le Mans, **2023**



IMPACT OF DISTORTED INLET FLOW ON AXIAL FAN PSYCHOACOUSTICS

Michail VOURAKIS[1], Elias ZEA[2],
Sassan ETEMAD[1], Mikael KARLSSON[2],
Niklas ANDERSSON[1]

[1] *Chalmers University of Technology, Department of Mechanics and Maritime Sciences, Division of Fluid Dynamics, Hörsalsvägen 7A SE-412 96 Gothenburg, Sweden*

[2] *KTH Royal Institute of Technology, Department of Engineering Mechanics, The Marcus Wallenberg Laboratory for Sound and Vibration Research, Teknikringen 8, 100 44 Stockholm, Sweden*

SUMMARY

Axial cooling fans operating downstream of obstructions are often exposed to distorted inlet flow conditions, consequently impacting acoustic performance. Herein, the impact of upstream obstructions with simple geometries on the psychoacoustics of an axial fan with a rotating ring is investigated. Different loading conditions and inlet shroud lengths are considered, while a reference non-obstructed installation is also recorded. Results show a significant increase in loudness for obstructed installations at intermediate and free discharge loading conditions, regardless of inlet shroud lengths tested. Sharpness, fluctuation strength and roughness demonstrate no sensitivity to loading conditions for obstructed installations, while tonality levels depend on inlet shroud length.

INTRODUCTION

Currently, low-pressure axial fans are widely used in the vicinity of humans due to their utilization in HVAC (Heating Ventilation Air Conditioning) units and cooling systems found in buildings and vehicles. To this end, studies focusing on the perceived quality of sound emissions from such axial fans have been motivated. Specifically, the identification of a single-number value psychoacoustic metric for fan noise, which combines relevant psychoacoustic metrics, was investigated by Schneider and Feldmann [1]. The perceptual dimensions of fan noise and derivation of relevant indexes

was researched by Töpken and Van de Par [2]. Rong et al. [3] established a sound quality prediction model for high-voltage fans which bypasses subjective sound quality evaluation. More recently, Scouarnec and Bennouna [4], studied the development of a preference model which utilizes several psychoacoustic metrics for evaluating fan-system noise annoyance.

In addition, several aspects of fan design and their effects on sound quality metrics have been explored. Zenger et al. [5] compared modified forward- and backward-skewed blades to an unskewed blade geometry, observing reduction of loudness for all modified geometries, and reduction of sharpness for backward skewed blade modifications. The improvement of sound quality for an axial fan with forward swept blades, compared to straight blades, was also reported by Muiyser et al. [6]. However a dependence on the operating point was observed concerning the level of improvement. The effect of uneven blade spacing on the psychoacoustics of axial fans was researched by Cattanei et al. [7]. It was reported that uneven spacing decreased tonality at the expense of increased values of roughness and fluctuation strength. Recently, Novakovic et al. [8] investigated the impact of geometric modifications on psychoacoustic metrics for small axial fans. The metrics of loudness, tonality and roughness were described as showing the greatest variability among tested fan geometries.

An aspect that may influence acoustic fan performance are the installation effects imposed by inherent components of cooling systems and HVAC units located upstream or downstream of the fan. This has been investigated over different installation setups. Peng et al. [9] established a theoretical model for prediction and control of discrete noise from an ACFM (Automotive Cooling Fan Module). Their method incorporated a non-uniform rotor blade design, based on a combined numerical and experimental analysis of the ACFM. An additional case of an ACFM was studied by Amoiridis et al. [10] via utilization of sound localization. It was reported that the radiator of the ACFM induced negligible effects on sound generation and propagation for the operating conditions tested. The effect of heat exchanger geometry on the sound emission of axial fans was researched by Czwielong et al. [11]. A strong dependence of the fan's discrete noise on the heat exchanger geometry was found. Park et al. [12] investigated the impact of system resistances, including condenser and radiator, on tonal noise of an axial fan. An increase of tonal noise levels under system resistances was reported for all operating points apart from stall conditions. However, the aforementioned studies did not evaluate installation effects with regard to sound quality. Aside from a recent investigation by Sen and Bilgin [13] on the impact of fan-evaporator distance on psychoacoustic metrics, studies that assess the sound quality of axial fans in combination with installation effects are scarce. The case study herein expands on the existing knowledge of installation effects on axial fan psychoacoustics by incorporating parameters of inlet shroud length, loading conditions, and system resistances in the form of obstructions with simple geometries.

The remainder of the paper is organized as follows: The first section showcases the experimental setup utilized, including instrumentation and data processing methods. The subsequent section includes the principal results, and the final section discusses the main conclusions.

EXPERIMENTAL SETUP

Installations and instrumentation

A fan test facility, described as closed-loop and plenum-to-plenum, is utilized for the acoustic and aerodynamic measurements. Further information about the fan test facility operation and performance characteristics, including the accuracy of principal parameters, is given by Gullberg [14]. Acoustic measurements are conducted upstream of the fan via a microphone grid comprising of 13 free-field microphones, as shown in Fig. 1. The microphone grid consisted of $1/2''$ type GRAS 46AE and Brüel & Kjær 4189-A-021. The fan's rotational speed is measured via a remote optical laser sensor

tachometer (ROLS-MONARCH INSTRUMENT) combined with reflective tape. The modular data acquisition system (DEWESOFT SIRIUS Modular) is utilized for microphone and optical sensor signals. It should be noted that room-acoustical effects at the upstream chamber affect sound spectra below 200 Hz, while the spectra above 200 Hz are considered unaffected and reliable.

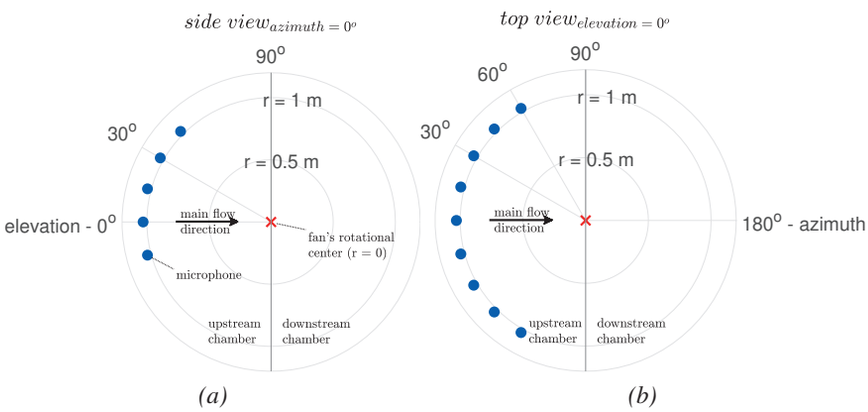


Figure 1: Measurement positions of utilized microphone grid at (a) 0° azimuth and (b) 0° elevation.

The tested fan is a commercially available plastic axial fan with a rotating ring and electric motor. Fig. 2 depicts a sketch of the fan along with installation configurations tested. More information about the tested fan and relevant results is given by Vourakis and Karlsson [15]. The shortest inlet shroud (80 mm, see Fig. 2), utilized for all installation configurations tested, is machined from medium-density fiberboard and is selected based on satisfying a compact installation while allowing access for future measurements of inlet velocity. The bell-mouth design is based on ISO 5801:2017 [16] featuring a quarter circle profile. The inlet shroud extensions (120 mm and 155 mm) and bell-mouth are 3D-printed via laser sintering with polyamide PA12. The tested obstructions are made from plexiglass and are chosen as generic representations of resistances in cooling systems.

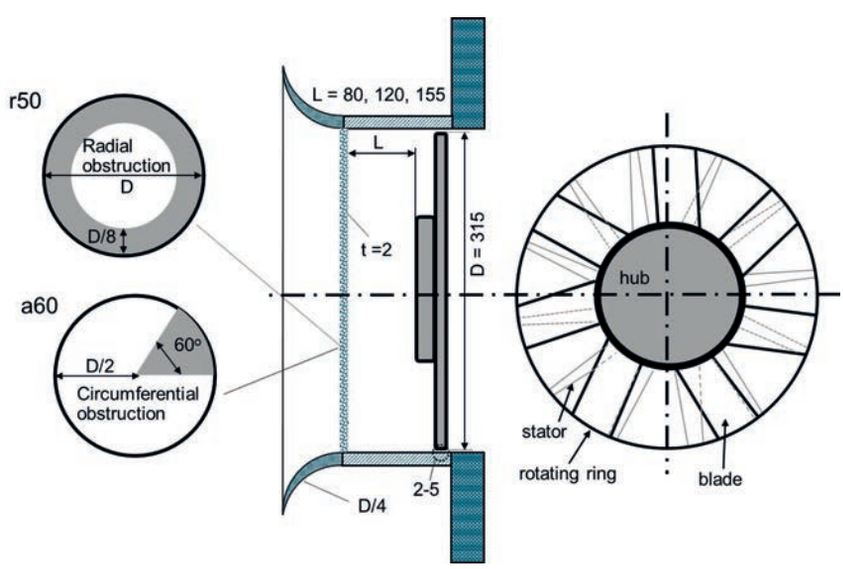


Figure 2: Sketch of tested fan and installation configurations (not to scale). Length values in mm.

Data processing and measurement cases

Data is processed in `MATLAB` (version R2019b). The system's pressure, density, and volume flow rate, utilized for estimating the non-dimensional pressure rise ψ and volume flow rate ϕ, are acquired

over 65 seconds segments once the system has stabilized. A linear average of the non-dimensional parameters is estimated in accordance with [17]:

$$\psi = \frac{\Delta p_{ts}}{\frac{\pi^2}{2}\rho D^2 n^2}, \tag{1}$$

$$\phi = \frac{\dot{V}}{\frac{\pi^2}{4} D^3 n}. \tag{2}$$

Here, Δp_{ts} (in Pa) denotes the total to static pressure difference, corresponding to the pressure differential between upstream and downstream chamber (see Fig. 1), D (in m) stands for the fan diameter, ρ (in kg/m^3) for the density, $\dot{V}$ (in m^3/s) for the volumetric flow rate, and n (s^{-1}) for the rotational speed, which is set to 75 s^{-1}. The sampling frequency for acoustic and tachometer signals is set to 50 kHz while data acquisition time is the same as aforementioned.

The power spectral densities are estimated with the `MATLAB` built-in function `pwelch`, using 50 % overlap, a Hanning window size of 2^{16}, and setting power as `'spectrumtype'`. The spectra of the microphones are subsequently spatially averaged over the microphone grid. Prior to the psychoacoustic analysis, a high-pass filter with a cut-on frequency of 60 Hz is applied to the microphone spectra. Filtering is implemented via the function `high-pass` with finite impulse response and steepness of 0.85. The usage of the high-pass filter is motivated by the presence of low-frequency background noise from neighboring test labs during the recordings.

The psychoacoustic analysis is performed via the open-source toolbox SQAT (Sound Quality Analysis Toolbox) [18], that is implemented in `MATLAB`. SQAT is utilized for estimating the mean value (for each microphone recording) of instantaneous: loudness, sharpness, roughness, fluctuation strength, tonality and PA (Psychoacoustic Annoyance). The specific (time-averaged) loudness is also estimated. Subsequently, a statistical distribution of the metrics over the microphone grid is calculated to evaluate spatial variability. The PA is calculated with the model of Di et al. [19] as implemented in SQAT. Further information about the implemented models and definitions of considered metrics can be found in [18].

The tested configurations, including inlet shroud length and obstruction type (see Fig. 2), along with operating points and corresponding acronyms, are listed in Table 1. The operating points are picked to represent loading conditions at high pressure and high efficiency (HP), intermediate pressure (MP), and free discharge (FD). The operating conditions at FD are realized as an overpressure of $\sim$ 10 Pa and not zero, in favor of system stability. It is also noted that the case of radial obstruction (r50) is only tested for operating points HP and FD as the imposed system losses limited the range of the system's characteristic curve (see Fig. 3).

Table 1: Tested configurations, operating points and their acronyms.

Inlet shroud length (acronym)	**Obstruction (acronym)**	**Operating point (acronym)**
80 mm (SL1)	no obstruction (def)	ϕ = 0.11 (HP)
120 mm (SL2)	circumferential (a60)	ϕ = 0.155 (MP)
155 mm (SL3)	radial (r50)	$\psi \sim 0$ (FD)

FAN 2025
Antibes - Juan-les-Pins (France), 9 - 10 April 2025

RESULTS

System performance

The system characteristics are depicted in Fig. 3. Here, it is noted that the case of SL2 is omitted for clarity and is within measurement error to the values obtained for case SL3. The system loss curves, i.e., the system without a fan, were obtained by removing the fan from the shroud while the compensation fan of the facility generated the flow. The losses of the radial obstruction are substantially higher than that of the circumferential obstruction since the former obstructs an area that is 2.5 times the obstructed area of the latter. One can also note that the level of losses is not altered for the different inlet shroud lengths considered. However, the system characteristics with fan indicate reduced volume flow rate and pressure rise as the fan-obstruction distance decreases. This cannot be attributed solely to a more efficient system due to the elongation of the inlet shroud since the case of no obstruction (def) exhibits minor gains. Consequently, it is suspected that the distorted inlet flow profiles introduced by the obstructions do not recover for the shortest inlet shroud (SL1).

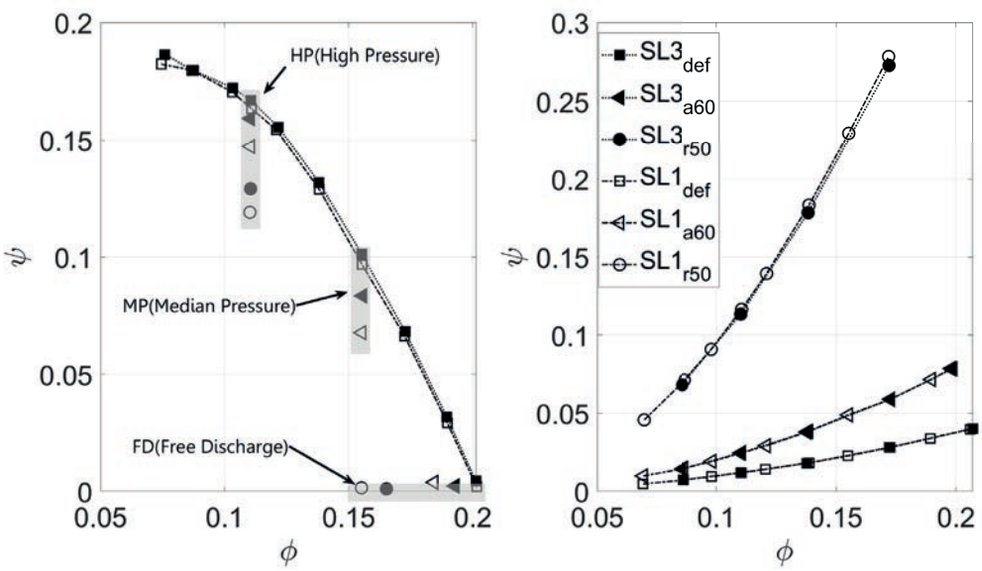


Figure 3: System characteristics for different installation configurations (left) with fan and (right) without fan.

The spatially averaged sound pressure levels for the shortest inlet at free discharge, with and without the fan, and different obstructions are depicted in Fig. 4. The combination of the operating point and inlet shroud length is selected to demonstrate any self-noise aspects induced by the obstructions. At free discharge conditions, the main flow speeds are of the highest magnitude, while the fan noise emissions are at the lowest levels. Thereby, this operating point is the most prone to self-noise effects. It is observed that the spectra of the systems with only obstructions are overall lower than the fan system without (def). The cases of low-frequency tones, corresponding to the system with radial obstruction (r50) and no fan, which are above the levels of the fan system without obstruction (def), can be attributed to the operation of the compensation fan at high rotational speeds to provide the targeted volume flow. These tones are absent when the system is coupled to the fan, while the acquired sound pressure levels are higher than those without a fan. Conclusively, it is presumed that self-noise effects have a negligible influence. Similar results were obtained for the longest inlet shroud considered (SL3) but are not included for brevity. A final remark about the fan systems with obstructions is the substantial increase of broadband and discrete sound pressure levels compared to the system without obstruction until ~ 2 kHz.

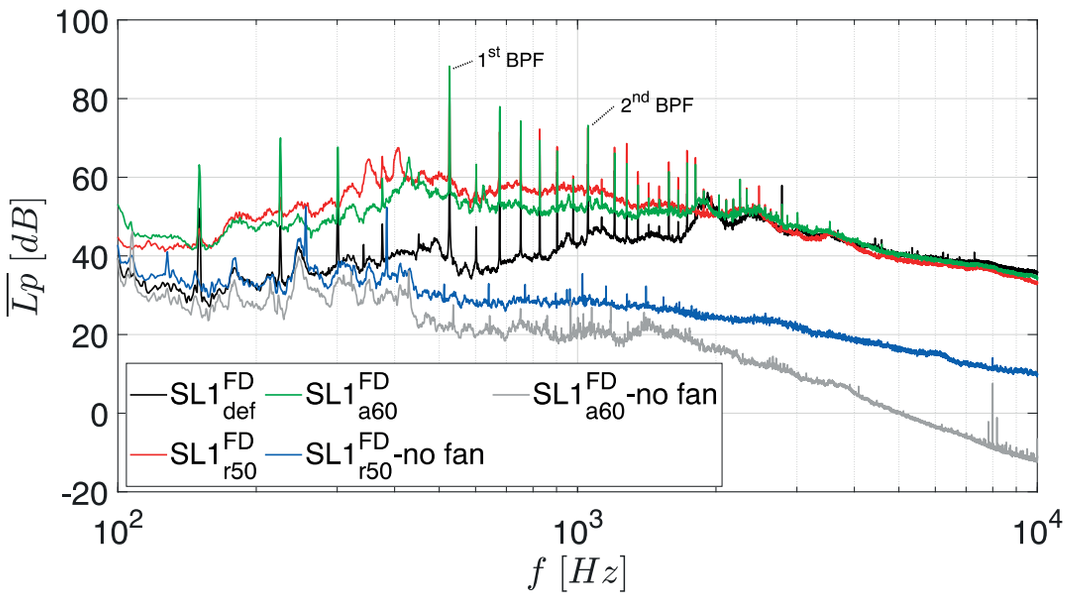


Figure 4: Spatial averaged sound pressure levels of the system with and without the fan.

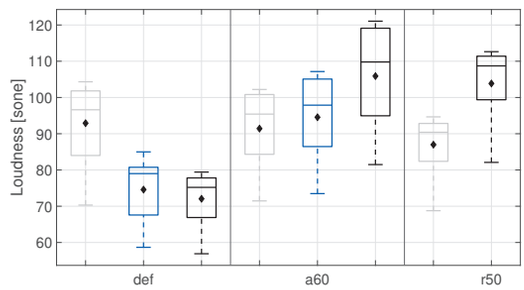
Psychoacoustics

The statistics of the instantaneous psychoacoustic metrics across the microphone grid for different operating points and obstructions are depicted in Fig. 5. Aside from tonality, the remaining metrics demonstrated weak dependence on inlet shroud length, and therefore only the case of SL1 is presented for brevity. Tonality values are presented for all three inlet shroud lengths tested.

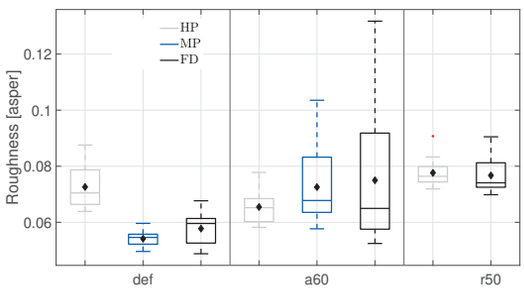
The mean (instantaneous) loudness values at high loading (HP) in Fig. 5a demonstrate minor sensitivity to blocking conditions. However, the presence of obstructions significantly increases loudness at intermediate loading (MP) and free discharge conditions (FD). The loudness metric is closely linked to the obtained sound pressure levels, generally decreasing towards higher volume flow rates [5], [6], [8]. These results indicate a significant increase in sound pressure levels due to obstructions in corresponding operating conditions.

The mean roughness values in Fig. 5b, fluctuation strength in Fig. 5c, and sharpness in Fig. 5d exhibit small dependence on loading conditions at the presence of obstructions (a60 and r50). On the contrary, the system without obstruction (def) showcases a clear increase of sharpness values towards free discharge conditions, typical of low-pressure axial fans [5]. Roughness values corresponding to def are also lower at intermediate and free discharge conditions compared to a60 and r50. The fluctuation strength demonstrates similar values for all systems at high and intermediate loading conditions (HP and MP). However, a highlighted spatial variation is observed at free discharge (FD) condition for the system without obstruction.

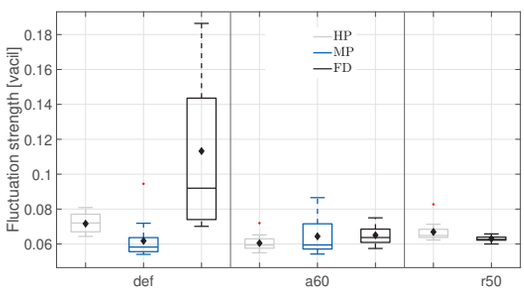
The mean tonality in Fig. 5e showcases a significant increase in the presence of obstructions at intermediate (MP) and free discharge conditions (FD) for the shortest inlet shroud tested (SL1). The elongation of the inlet shroud (see Figs. 5g and 5h) affects the tested configurations differently. Specifically, the configuration without obstruction (def) demonstrates a weak dependence on the inlet shroud length. The configuration with radial obstruction (r50) exhibits a decrease in tonality values at FD but marginal differences at HP for elongated inlet shrouds. The configuration with circumferential obstruction (a60) exhibits a decrease of tonality values at MP and FD for elongated inlet shrouds, while no apparent effect is exhibited at HP. The aforementioned variations of tonality can be interpreted as corresponding variations of unsteady blade forces experienced by the fan [20]. These variations are experienced due to a spatially non-uniform inlet flow imposed by the upstream obstructions. How-



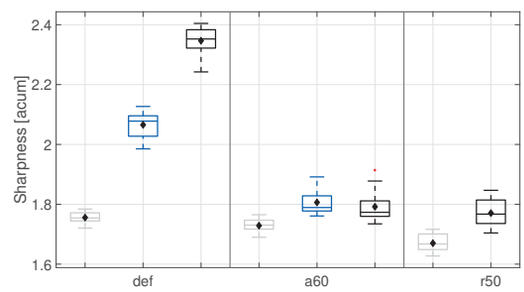
(a) Loudness - SL1.



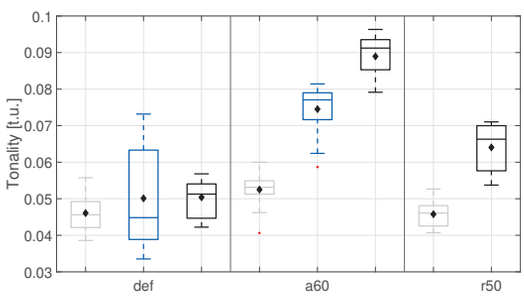
(b) Roughness - SL1.



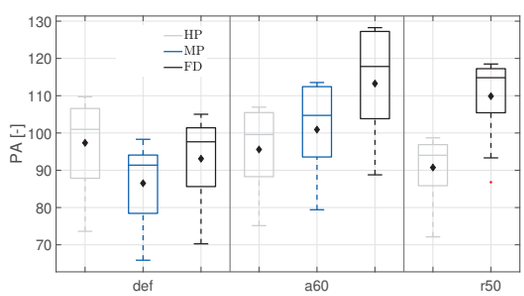
(c) Fluctuation strength - SL1.



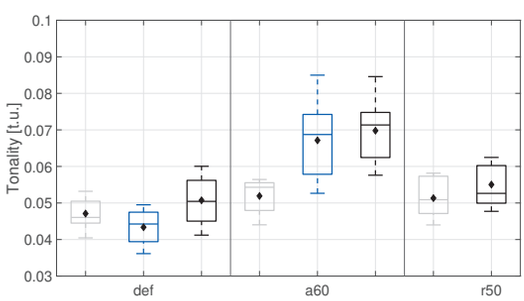
(d) Sharpness - SL1.



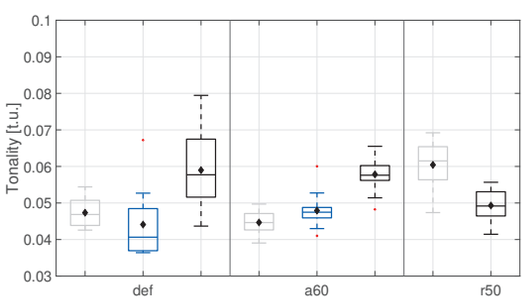
(e) Tonality - SL1.



(f) Psychoacoustic annoyance (PA) - SL1.



(g) Tonality - SL2.



(h) Tonality - SL3.

Figure 5: Statistics of the instantaneous psychoacoustic metrics across the microphone grid for different obstructions (def, a60, and r50) and operating points (HP, FD, and MP). The horizontal line in the boxes indicates the median, while the bottom and top edges of the boxes indicate the 25^{th} and 75^{th} percentiles, respectively. The whiskers extend to extreme data points, while + indicates outliers. Diamonds represent the mean values.

ever, the installation of the obstructions further upstream attenuate the non-uniformity of the ingested flow, thus tonality variations are less pronounced.

The combined effect of the aforementioned psychoacoustic metrics according to the model of Di et al. [19] are represented in Fig. 5f for SL1. The trends for the three configurations considered, def, a60, and r50, are mainly affected by loudness and sharpness. Thereby, for the configurations with obstructions (a60 and r50), the trend of combined psychoacoustic annoyance (PA) resembles that of corresponding loudness since sharpness demonstrates weak dependence on loading conditions. The configuration without obstruction depicts a PA trend that does not resemble corresponding loudness at FD since sharpness values are substantially higher.

The spatial mean of the specific loudness at different loading conditions and configurations for SL1 is presented in Fig. 6, given the significance of loudness on PA and the evident discrepancies observed over the mean instantaneous values at MP and FD (see Fig. 5a). The additional scale included (bark) is associated to the initial 24 critical bands of auditory perception. Despite values being similar at HP (see Fig. 5a), the absence of obstructions marginally reduces specific loudness for frequencies below 1 kHz. Beyond that point, the configuration without obstruction (def) demonstrates marginally higher values than obstructed configurations (a60 and r50).

At intermediate loading conditions (MP), the observed differences between configurations with and without obstruction are highlighted below 1 kHz. At frequencies below 1 kHz, the sound spectra are described by broadband and high amplitude tonal components associated with the blade passing frequencies. In turn, the amplitude of these components can be affected by perceived inlet flow conditions.

At free discharge conditions (FD), the loudness levels of def are substantially lower than a60 and r50 for frequencies up to 2 kHz. The observed differences between a60 and r50 can be partly attributed to the different levels of losses (see Fig. 3) along with the imposed inlet velocity profiles.

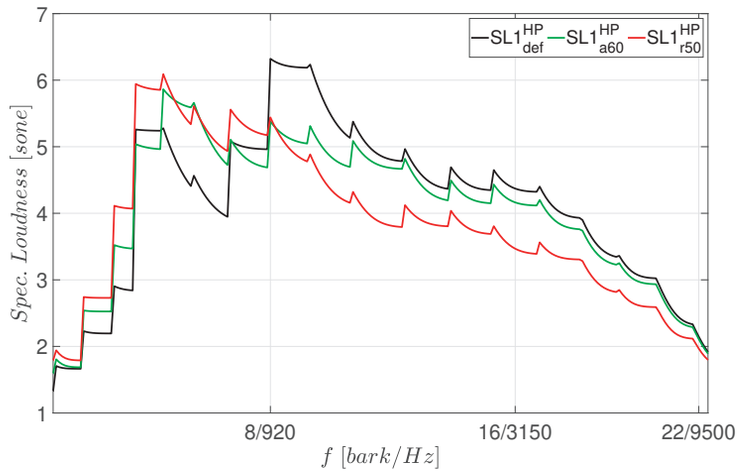
CONCLUSIONS

A study case of an axial fan with a rotating ring operating under the effect of upstream obstructions has been presented. The obstructions are realized via radial and circumferential geometries. The analysis is focused on the evaluation of psychoacoustic metrics. Principal results demonstrate a significant increase in loudness in the presence of obstructions for intermediate and free discharge loading conditions. The complementary examination of specific loudness demonstrates obstruction effects for frequencies below 1 kHz and 2 kHz at intermediate and free discharge loading conditions, respectively. Effects of inlet shroud length are mainly limited to tonality for configurations with obstructions. It is suggested that the persistence of a non-uniform inlet flow field, being intensified for a shorter inlet shroud length, leads to increased levels of tonality. Moreover, sharpness levels are decreased due to obstructions, an effect which is more apparent towards free discharge.

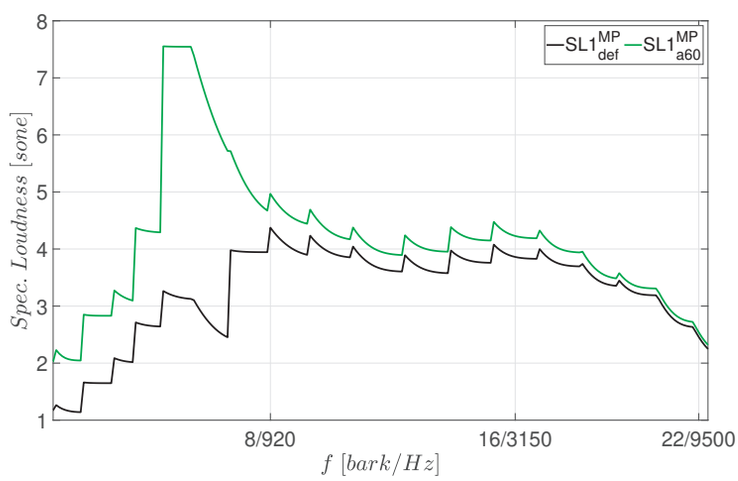
A complementary characterization of the perceived inlet velocity profiles at the fan's aerodynamic interface may provide valuable insights regarding alterations of sound pressure spectra observed but not analyzed here. Extending to different obstruction and fan geometries can also lay the basis for generalizing the observed effects.

ACKNOWLEDGMENTS

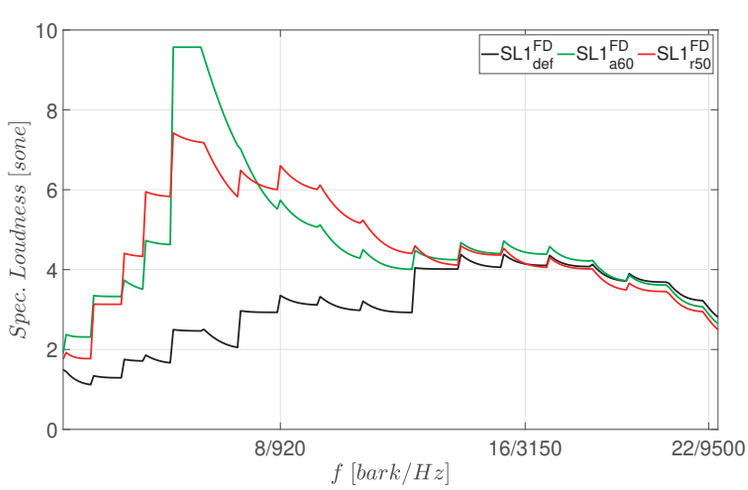
This work is part of the project: eFan, a key enabler for eMobility, part II and is funded by the Swedish Energy Agency, grant number 2020-016065. Volvo Group Trucks Technology is acknowledged for providing measurement facilities and equipment. The authors would like to acknowledge Antonio Ortiz for designing the fan shrouds and obstructions along with Karl Levenstam for designing and manufacturing of testing and measurement equipment.



(a)



(b)



(c)

Figure 6: Spatial mean of specific loudness for SL1 at different operating points and obstruction type.

REFERENCES

[1] M. Schneider and C. Feldmann, *Psychoacoustic evaluation of fan noise*, in *Proc. of Fan*, **2015**, pp. 1–12.

[2] S. Töpken and S. Van de Par, *Perceptual dimensions of fan noise and their relationship to indexes based on the specific loudness*, Acta Acustica united with Acustica vol. 105, no. 1, pp. 195–209, **2019**.

[3] G. Rong, T. Mi, S. Ye, Y. Jiang, J. Lv, and Z. Wang, *Modelling and intelligent prediction of sound quality for high-voltage fans on fuel cell vehicles*, Proceedings of the Institution of Mechanical Engineers, Part D: Journal of Automobile Engineering vol. 236, no. 6, pp. 1246–1258, **2022**.

[4] D. Scouarnec and S. Bennouna, *Psychoacoustic assessment of automotive fan-systems*, in *INTER-NOISE and NOISE-CON Congress and Conference Proceedings*, Institute of Noise Control Engineering, vol. 270, **2024**, pp. 105–114.

[5] F. Zenger, S. Münsterjohann, and S. Becker, *Efficient and noise reduced design of axial fans considering psychoacoustic evaluation criteria*, Applied Mechanics and Materials vol. 856, pp. 181–187, **2017**.

[6] J. Muiyser, J. van der Spuy, and A. Bekker, *Comparison of sound quality metrics for axial flow fans with straight and forward swept blades*, in *Proc. of Fan*, **2018**, pp. 1–11.

[7] A. Cattanei, F. M. Zecchin, A. Di Pasquali, and A. Lazari, *Effect of the uneven blade spacing on the noise annoyance of axial-flow fans and side channel blowers*, Applied Acoustics vol. 177, p. 107 924, **2021**.

[8] T. Novaković, L. Čurović, M. Hočevar, and J. Prezelj, *Impact of geometric modifications of small axial fans on psychoacoustic metrics*, Applied Acoustics vol. 218, p. 109 913, **2024**.

[9] Z. Peng, Y. Wu, J. Tian, and H. Ouyang, *Discrete noise control of cooling fan module: Stator and rotor interaction*, Applied Acoustics vol. 165, p. 107 308, **2020**.

[10] O. Amoiridis, A. Zarri, R. Zamponi, *et al.*, *Sound localization and quantification analysis of an automotive engine cooling module*, Journal of Sound and Vibration vol. 517, p. 116 534, **2022**.

[11] F. Czwielong, J. Soldat, and S. Becker, *On the interactions of the induced flow field of heat exchangers with axial fans*, Experimental Thermal and Fluid Science vol. 139, p. 110 697, **2022**.

[12] M. Park, D.-J. Lee, and H. Lee, *Inflow effects on tonal noise of axial fan under system resistances*, Applied Acoustics vol. 192, p. 108 737, **2022**.

[13] B. Sen and E. Bilgin, *Experimental insights on sound characteristics and psychoacoustic parameters on axial fan performance in heat pump systems*, in *INTER-NOISE and NOISE-CON Congress and Conference Proceedings*, Institute of Noise Control Engineering, vol. 270, **2024**, pp. 5564–5572.

[14] P. V. Gullberg, *Optimisation of the flow process in engine bays-3d modelling of cooling airflow*. Chalmers Tekniska Hogskola (Sweden), **2011**.

[15] M. Vourakis and M. Karlsson, *Aeroacoustic interaction effects between parallel low-pressure axial flow fans*, in *10th Convention of the European Acoustics Association, Forum Acusticum*, **2023**, pp. 10–15.

[16] *ISO 5801:2017 Fans - Performance testing using standardized airways*. International Organization for Standardization, **2017**.

FAN 2025
Antibes - Juan-les-Pins (France), 9 - 10 April 2025

[17] T. Carolus, *Fans: aerodynamic design-noise reduction-optimization*. Springer Nature, **2023**.

[18] G. F. Greco, R. Merino-Martínez, A. Osses, and S. C. Langer, *Sqat: A matlab-based toolbox for quantitative sound quality analysis*, in *INTER-NOISE and NOISE-CON Congress and Conference Proceedings*, Institute of Noise Control Engineering, vol. 268, **2023**, pp. 7172–7183.

[19] G.-Q. Di, X.-W. Chen, K. Song, B. Zhou, and C.-M. Pei, *Improvement of Zwicker's psychoacoustic annoyance model aiming at tonal noises*, Applied Acoustics vol. 105, pp. 164–170, **2016**.

[20] W. Neise and U. Michel, *Aerodynamic noise of turbomachines*, Deutsche Forschungsanstalt für Luft- und Raumfahrt e.V., DLR, Institut für Strömungsmechanik, Abt. Turbulenzforschung, Berlin vol. 5, **1994**.

D1 Numerical Methods For Design and Performance Analysis

10 April - 11:00 - Auditorium

Sybrand Johan van der Spuy, Piero Danieli

List of papers

The Role of Computational Fluid Dynamic (CFD) Analysis in Creating DOE Compliant Fan and Blower Product Range Performance Data

- Anthony Geoffrey SHEARD – AGS Consulting, LLC (USA)
- Alain DEMEULENAERE – The Rothalpy Project, LLC (USA)
- Sean EDWARDS – Minetek (Australia)

Mesh Sensitivities for the RANS Simulation of Low-Reynolds Number Propellers

- Jorge SANTAMARIA – Ecole de technologie supérieure (Canada)
- Andre BIERRENBACH-LIMA – Ecole de technologie supérieure (Canada)
- Marlène SANJOSÉ – Ecole de technologie supérieure (Canada)



THE ROLE OF COMPUTATIONAL FLUID DYNAMIC (CFD) ANALYSIS IN CREATING DOE COMPLIANT FAN AND BLOWER PRODUCT RANGE PERFORMANCE DATA

Anthony Geoffrey SHEARD[1], Alain DEMEULENAERE[2], Sean EDWARDS[3]

[1] *AGS Consulting, LLC, Hilton Head Island, South Carolina, USA*

[2] *Rothalpy Project, LLC, San Francisco, California, USA*

[3] *Minetek Pty Ltd, Sydney, Australia*

SUMMARY

The U.S. Department of Energy (DOE) established a standardized test procedure for fans and blowers to measure their electrical input power, flow, and pressure. The Final Rule for this procedure took effect on May 31, 2023, and all representations of fan and blower energy efficiency and usage in the U.S.A. must comply with it as of October 30, 2023. Recognizing the challenges faced by manufacturers, the DOE introduced an Alternative Efficiency Determination Method (AEDM) to streamline the creations of fan performance characteristics. This paper explores the challenges and complexities of developing and implementing the AEDM, uses it to predict performance characteristics of a new range of mixed flow fans and concludes with an estimate of the reduction in laboratory testing required.

INTRODUCTION

Regulation has entered the U.S. market for commercial and industrial fans and blowers through a test procedure published by the U.S. Department of Energy (DOE), effective October 30, 2023 [1]. Many fan manufacturers have yet to replace legacy performance data with information compliant with the new requirements.

The test procedure was published by the DOE in anticipation of an energy standard for fans and blowers, however on January 13, 2025, the Office of Management and Budget (OMB) officially withdrew the energy standard for fans and blowers and circulating fans, thus concluding all further work on the rulemaking by the U.S. Department of Energy for the foreseeable future.

The federal test procedure, along with any associated legal obligations triggered by it, has remained in effect since its effective date and is enforceable by law. Non-compliance penalties apply from the date the DOE deems a product non-compliant. Therefore, the withdrawal of the energy standard for fans and blowers does not exempt fan companies from complying with the federal test procedure, which remains a legal requirement.

The withdrawal of the energy standard for fans and blowers eliminates the federal requirement for a minimum FEI rating for commercial and industrial fans and blowers. However, minimum FEI ratings have been incorporated into building regulations:

- Model building energy standard: ASHRAE 90.1 – 2019
- Model building energy code: International Energy Conservation Code (IECC) – 2021
- Model high-performance building (green) building standard/code ASHRAE 189.1 / Intl. Green Construction Code (IGCC) -2020
- State building regulations: California Title 24; states that adopt ASHRAE 90.1

Therefore, it is necessary to test fans in accordance with federal test procedures, calculate FEI from the measured fan performance data, and, when compliance with applicable codes, standards, and regulations is required, ensure that only fans meeting or exceeding the mandated minimum FEI are placed on the market.

The regulation applies to manufacturers of complete fans produced or imported for sale in the United States. It indirectly affects system designers, as certain operating points for some fans may no longer be compliant. While replacement fan components are exempt, the regulation does apply to equipment manufacturers who purchase impellers and inlet cones to incorporate into their own fabricated fan housings and plenum assemblies. The regulation covers a power range of 1 hp (0.74 kW) to 150 hp (110 kW) at the fan shaft output.

The compliance metric is the Fan Energy Index (FEI) [2], a dimensionless value reflecting a fan's electrical power consumption at a specific operating point compared to that of a "reference fan" with defined minimum efficiency at the same operating point. To ensure broad applicability across fan types, FEI uses wall-to-air (W2A) electrical power measurements rather than shaft power. This shift impacts cataloged power values and fan selection software. FEI calculations are based on fundamental fan characteristics - flow, pressure, and power and apply to each combination of these parameters. Notably, FEI limits the operating point on the fan curve, not the fan itself, emphasizing how operating point selection directly impacts power consumption.

FEI has already been integrated into commercial construction codes and standards [3], [4], with general fans and blowers typically required to achieve an FEI of 1.00 or greater. Additionally, California introduced its own statewide regulation [5] mandating all fans sold after March 15, 2023 achieve an FEI of at least 1.00.

Despite the regulation, many manufacturers have not updated their performance data to comply with the new test procedure due to the scale of the task. The test procedure mandates compliance with AMCA 210 [6] or ISO 5801 [7] standards. Older products may have performance data derived from non-compliant methods, necessitating re-testing. Manufacturers must process new laboratory data into FEI-compliant results and integrate them into fan selection software to ensure products meet the FEI $\geq$ 1.00 threshold.

While a single fan test is not time-intensive, manufacturers often manage hundreds of products with thousands of variants. Decades of product development make re-testing every fan impractical due to two key challenges:

1. **Laboratory Constraints:** Manufacturers must perform contract testing for a significant percentage of orders, verifying performance aligns with contractual requirements. This process consumes most of the laboratory's capacity.
2. **Empirical Methods:** Historically, manufacturers used empirical methods to estimate performance changes due to configuration adjustments. While these methods provided reasonable estimates, they are no longer traceable to compliant laboratory tests.

These challenges compound, leaving manufacturers in a difficult position: federal law prohibits publishing non-compliant performance data, yet re-testing all legacy products is logistically and practically unfeasible.

COMPUTATIONAL METHODS

Over the past five decades, the aerospace fan community has systematically developed computational methods [8]. Although commercial computational codes have been available since the 1980s, their complexity and the challenges of practical application initially hindered widespread adoption by the air movement and control community. It was not until the early 2000s that these methods began to be effectively utilized. Although aerospace fans do incorporate features in the airstream, they are both minimized and aerodynamically optimized. In contrast, low-speed fans designed for air systems include electrical motors and their associated

conduit in the airstream, which cause flow separation, complicating computational modeling. These differences made the application of commercial codes particularly challenging.

From 2000 to 2010, efforts focused on developing techniques to achieve converged solutions that could predict fan performance with reasonable accuracy across the stable operating range while utilizing practical computational resources. By 2010, the air movement fan community had resolved the fundamental issues with applying commercial codes. This progress allowed designers to extend computational methods to broader aspects of the fan design process, including:

- **Research:** Investigating complex flow physics that are difficult to study in laboratory settings.
- **Development:** Reducing or eliminating the need for traditional laboratory testing of fans designed for air systems.
- **Application:** Formalizing the fan design process to enable routine use of computational codes by less experienced engineers.

Today, computational fluid dynamics (CFD) codes are routinely used as design tools within the air movement and control community [9]. Commercial CFD codes based on Reynolds-averaged Navier-Stokes (RANS) methodologies can reliably predict the performance characteristics of both axial and centrifugal fans. These predictions are sufficiently accurate over the stable portion of a fan's performance curve to be of practical value to designers. Additionally, RANS-based methodologies achieve these results with computational effort that is realistic for most fan industry professionals.

Although RANS-based methodologies cannot predict fan behavior in stall, they can reliably indicate when a fan is approaching stall. Since fan designers prioritize avoiding stall conditions, the ability to identify stall boundaries is sufficient. For this reason, RANS-based methodologies remain the preferred choice in the air movement community.

The successful integration of CFD tools into the design process has been a significant achievement for fan designers. The cost of the necessary hardware has become increasingly affordable, and the advent of fan regulations makes the case for using computational methods to reduce the laboratory testing burden stronger. The time is now ripe for fan companies to adopt these tools more broadly to optimize their design and testing processes.

PRODUCT RANGE

One of the most demanding applications for air movement fans is the ventilation of deep mines. Historically, variable pitch-in-motion axial fans have been utilized to draw air up vent shafts and out of mines [10]. However, in deep mines, it is necessary to install fans within the mine tunnel system to ensure proper ventilation throughout. Due to the underground installation requirements, axial fans are preferred, but the duty-point pressure in such applications often exceeds the capacity of a single-stage axial fan. While compact two-stage axial fans [11] can meet these pressure demands, they require double-ended motors that are typically subject to long lead times. This limitation makes them less desirable to mine operators, who prioritize the ability to strip, repair, and rebuild equipment on-site, especially in remote and difficult-to-access locations.

Mixed-flow fans [12] present a viable alternative, combining the axial flow feature of axial fans with the pressure-generating characteristics more commonly associated with centrifugal fans. Thanks to their conical hubs, mixed-flow fans can generate pressures equivalent to those of two-stage axial fans, but in a single stage. This makes them inherently more cost-effective and allows the use of standard off-the-shelf motors.

Mixed-flow fans have been used in underground mine ventilation, although their application is limited. The only two mines that are using this type of fan are the Freeport McMoRan's Grasberg complex in Indonesia [13] and Glencore's Ernest Henry mine in Australia [14]. Both mines are operating without mine ventilation fan issues, indicating that mixed-flow fans are a viable option, and their lower cost compared to two-stage axial fans plus compatibility with conventional motors make them an attractive option for such applications.

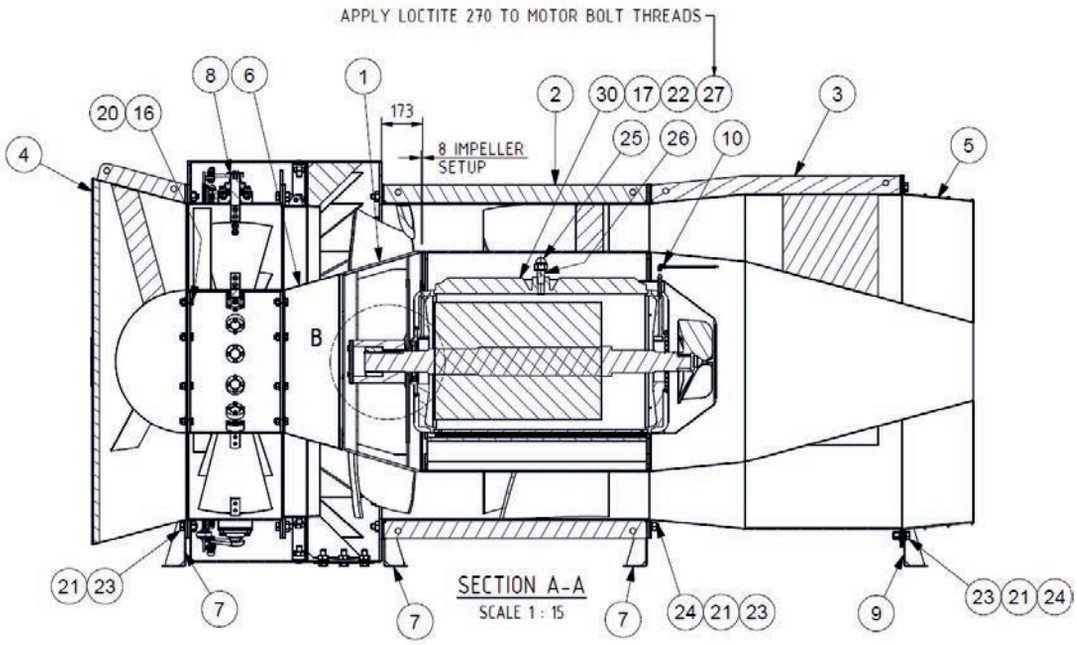


Figure 1: A pre-production 1,394 mm diameter mixed-flow fan developed using axial fan static part design processes, combined with a new mixed-flow impeller aerodynamic design.

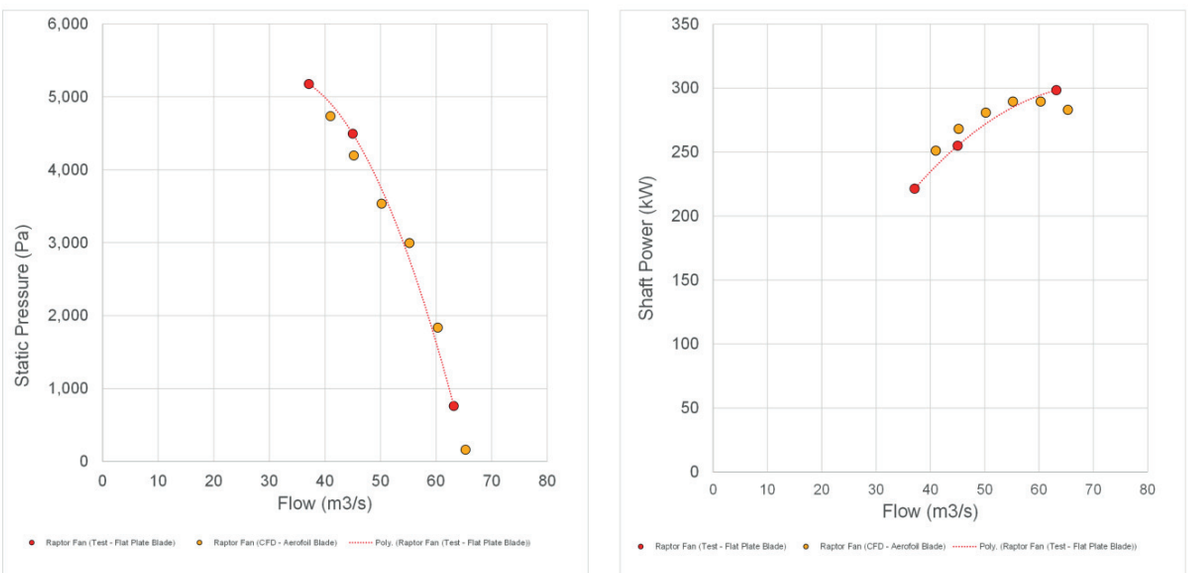


Figure 2: ISO 5801-compliant test system results for the pre-production mixed-flow fan, compared with CFD analysis conducted during the design process.

For fan manufacturers with experience in designing and manufacturing axial fans for mine ventilation, the development of a mixed-flow fan presented primarily an aerodynamic challenge rather than a mechanical design or manufacturing obstacle [15], [16], Figure 1.

The pre-production fan, with a diameter of 1,394 mm, was tested in an ISO 5801-compliant test system, and the results were compared to computational fluid dynamics (CFD) simulations conducted during the design process (Figure 2). The laboratory results deviation from the 3D CFD simulations falls within the measurement uncertainty of the laboratory tests [17]. Notably, the CFD simulations were based on 3D CAD models of the fan rather than a 3D scan of the as-built impeller. Although the manufactured impeller adhered to predefined tolerances, it differed slightly from the CAD model. Despite these variations and the inherent uncertainties in the laboratory measurements, the agreement between the two was considered excellent.

Table 1: The pre-production 1,394 mm diameter mixed-flow fan blade was adapted into a range of fans, with sizes ranging from 1,020 mm to 3,200 mm in diameter.

Outlet Hub Diameter	Inlet Hub Diameter	Fan Diameter										
		1,020	1,220	1,394	1,615	1,850	2,200	2,400	2,600	2,800	3,000	3,200
761	439	L6.07										
910	525		L6.06									
1,040	600			L6.01								
1,205	695				L6.05							
1,380	796					L6.04						
1,641	947						L6.03					
1,791	1,033							L6.08				
1,940	1,119								L6.09			
2,089	1,205									L6.10		
2,238	1,291										L6.11	
2,387	1,377											L6.02

The final fan range spanned diameters from 1,020 mm to 3,200 mm (Table 1). While the agreement between laboratory-tested and CFD-predicted performance for the 1,394 mm pre-production fan was good, it did not imply that the performance of the other fans in the range could only be predicted using CFD. In theory, each fan in the range could have been physically built and laboratory tested, as was the case with the 1,394 mm pre-production fan.

However, testing fans larger than 2,800 mm is both expensive and time intensive. With eleven fans in the range, conducting a laboratory test campaign for all was deemed impractical. In contrast, a CFD campaign to predict the performance of all eleven fans offered a significantly lower cost and shorter timeframe compared to full-scale laboratory testing.

ALTERNATIVE EFFICIENCY DETERMINATION METHOD

As DOE allows fan manufacturers to determine fan performance using an alternative method for determining a fan's performance characteristics (i.e., an alternative efficiency determination method, or AEDM). This method is outlined in the DOE Code of Federal Regulations (CFR) under 10 CFR 429.70 that defines the criteria an AEDM must satisfy:

I. The AEDM is derived from a mathematical model that predicts the performance characteristics of the fan as measured using the applicable DOE test procedure.
II. The AEDM is based on engineering or statistical analysis, computer simulation or modeling, or other analytic evaluation of actual performance data; and,
III. The manufacturer has validated the AEDM.

Validation is the action of proving the AEDM's accuracy, and therefore before using an AEDM, the fan manufacturer must compare the AEDM's predicted fan performance characteristics to the laboratory measured fan characteristics.

I. For each type of fan to which the AEDM is applied, the fan manufacturer must select at least two fans to which the AEDM is applied.
II. Using the AEDM, calculate the characteristics of the laboratory tested fans.
III. Test the two fans in accordance with the DOE's test procedure.
IV. The AEDM predicted fan characteristics for each fan must be less than or equal to 105 % of the efficiency determined through laboratory testing.
V. When making representations of values other than efficiency (i.e., flow, pressure, and power) all other representations are required to be based on the same AEDM.

Validation of the AEDM therefore comprises two elements. First, the AEDM is used to predict fan performance characteristics, the fan is then laboratory tested, and the measured performance characteristics are compared to those predicted using the AEDM. Second, the same fan, but a different example of the fan, is laboratory tested. The laboratory tested performance characteristics for both the first and second fan tested must be within 105 % of the AEDM predicted fan performance characteristics. This requirement to build and laboratory test two identical fans is included to verify that manufacturing tolerances from fan to fan do not result in fan performance changing from one fan to another by more than 5 % of the AEDM predicted fan performance.

After validating the AEDM, a fan manufacturer is required to periodically select a fan from the range that the AEDM has been applied, laboratory test and verify that the laboratory measured performance characteristics remain within 5 % of the AEDM predicted performance characteristics.

Finally, the fan manufacturer must have available for inspection by the DOE records showing:

(A) The method or methods used to develop the AEDM.
(B) The mathematical model, the engineering or statistical analysis, computer simulation or modeling, and other analytic evaluation of performance data on which the AEDM is based.
(C) Complete test data, equipment information, and related information that the fan manufacturer has generated.
(D) The calculations used to determine the performance characteristics of the fans to which the AEDM was applied.

If requested by the DOE, the fan manufacturer must:

(E) Conduct simulations to predict the performance of a fan specified by the DOE.
(F) Provide analyses of previous simulations, and/or;
(G) Conduct testing of a fan selected by the DOE.

THE CFD CAMPAIGN

In practice the DOE's requirements for use of an AEDM require a fan manufacturer to predict and laboratory measuring the performance characteristics of a pre-production fan (Figure 2) and then test the first production fan to verify its performance remains the same as the pre-production fan, within laboratory measurement uncertainties. In combination with good engineering practice, documenting the AEDM and the associated laboratory test results, this gives fan manufacturers the option to use CFD rather than build and test other fans from the range.

A key factor in deciding to undertake a computational fluid dynamics (CFD) campaign rather than a laboratory testing campaign was the availability of Amazon Web Services. This provides fan manufacturers with access to computational resources beyond what could be realistically achieved with in-house infrastructure. By leveraging Amazon's computational clusters, the CFD simulations could be completed overnight, regardless of the number of simulations launched. This capability was critical due to the following considerations:

- The fan range includes eleven models.
- Each fan blade can be set to any angle within a specified range.
- Fans are offered with both full and part blade counts.
- Defining a single fan curve requires seven data points.

In typical fan selection, blade angles are adjusted in one-degree increments. However, building and laboratory testing fans at every degree increment is impractical, as is conducting CFD simulations for such small intervals. The fan manufacturer, therefore, adopted a five-angle increment strategy: maximum, minimum, and three intermediate angles.

The size of the CFD campaign becomes evident when considering the above parameters:

Fans in the range	Blade angles	Blade counts	Simulations per curve	**Total simulations**
11	5	2	7	**770**

This campaign ran for approximately six weeks, operating seven days a week, with an average of twenty simulations completed daily. While computational power was not a constraint, time was required to set up and launch each simulation.

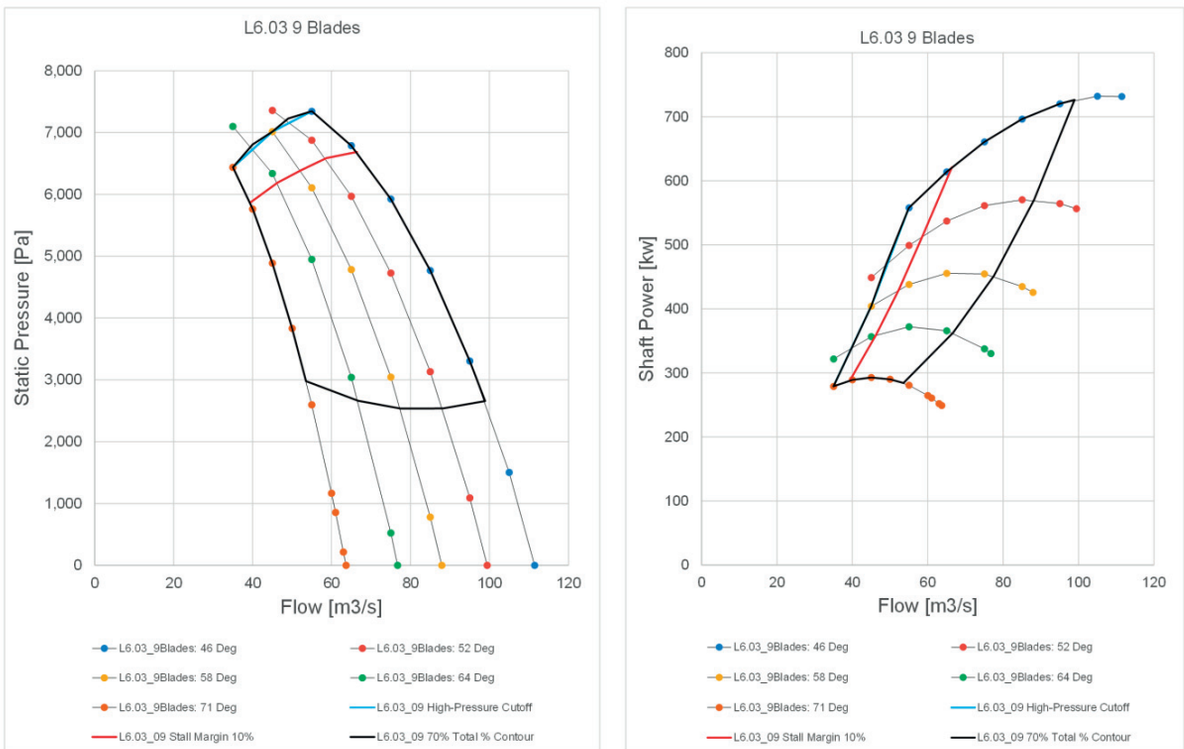


Figure 3: Example results from the CFD campaign for a single fan at five blade angles with one of the two available blade counts. Some simulations left-of-peak were excluded, as they indicated fan stall.

The CFD campaign produced datasets defining fan performance characteristics for each fan at five blade angles and for each blade count (Figure 3). Not all simulations are shown, as those indicating fan stall (left-of-peak) were excluded. Additionally, the flow-pressure curves include points clustered at low static pressures, representing additional simulations aimed at predicting fan performance near zero static pressure. Accurate low-pressure data minimizes interpolation errors during post-processing, where each characteristic must be extrapolated to zero static pressure.

All simulations began with assumed flow values, scaled from the performance of the 1,394 mm pre-production fan to the size and speed of other fans in the range. While these starting points enabled convergence, they were not precise enough for accurate predictions near zero static pressure, necessitating additional low-pressure simulations. Similarly, these initial flows could not reliably predict the peak pressure point at which the fan stalls, requiring multiple iterative simulations to identify peak pressure points.

Importance of Peak Pressure Identification

Determining the peak pressure point is crucial, as selecting a fan to operate above this point leads to stall and risks in-service failure. In the example data (Figure 3), the red line represents a peak pressure reduced by 10 %, establishing a safety margin for fan selection. While this margin limits the fan's selectable range, accurate CFD predictions ensure the margin is not overly conservative, preserving more of the fan's operating range.

Efficiency Contours

The CFD campaign also plotted a 70 % total efficiency contour. The black contour represents the 70% contour (Figure 3). While no universal threshold defines commercially viable efficiency, 70 % was deemed a reasonable benchmark for this campaign, with the understanding that specific applications might require higher or lower limits.

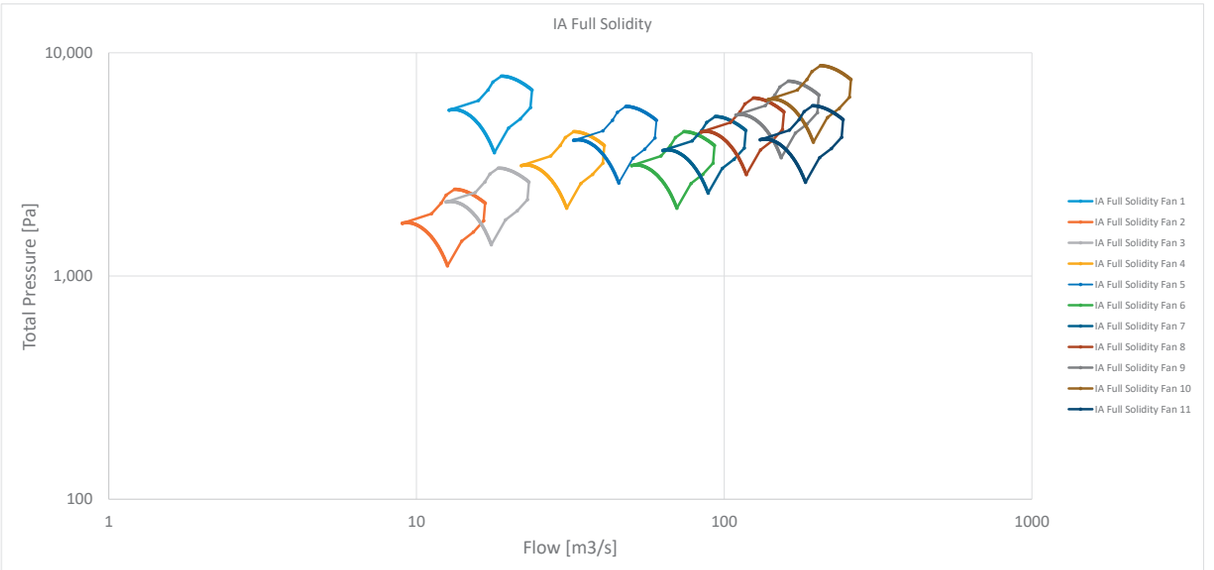


Figure 4: The 70% total efficiency contours for all eleven fans in the range, plotted on log-log scales, illustrate the extent of range coverage.

INTERPOLATION

The need for additional fan diameters in the range was evaluated by plotting the 70 % total efficiency contours on log-log flow-pressure axes (Figure 4). Ideally, these contours would overlap to provide continuous coverage from the range's minimum to maximum flow. However, in practice, some gaps appeared between the 70 % total efficiency contours, indicating that achieving a fan selection at certain flows with efficiencies above 70 % would not always be possible. After consideration, the decision was made to accept these limitations for three reasons:

- **Preliminary Quotations:** Larger or smaller fan diameters could be scaled to the required diameter-speed combination, enabling the fan manufacturer to issue quotations.
- **Follow-Up CFD Campaigns:** With the initial CFD campaign completed, existing fan designs could be scaled and adapted to intermediate diameters and characterized in additional CFD campaigns, which could be completed within a week.
- **Historical Inquiries:** A review of historical inquiries indicated that the gaps in range coverage did not coincide with customer demand, making them less significant in practical terms.

Having determined that the range coverage was satisfactory, the final step in the CFD campaign involved smoothing and interpolating the predicted performance data to make it suitable for input into a fan selector tool. Minimal smoothing was required because the CFD data points for each fan characteristic aligned closely with polynomial curves. Before fitting the polynomials, each characteristic curve was manually extended down to zero static pressure, and a cutoff point was determined to prevent selections too close to peak pressure.

Once the polynomial curves were fitted for each of the five predicted blade angles, interpolation was performed in one-degree increments of blade angle using the interpolation method defined in AMCA 214, Annex E [2]. To ensure consistency between interpolated flow, pressure, and power, total efficiency was calculated for each point. However, the resulting total efficiency curves initially appeared inconsistent due to small interpolation errors in power. These errors were particularly impactful because the power curves were relatively flat, meaning even minor inaccuracies caused noticeable deviations in the calculated total efficiency.

To address this, flow-static pressure and flow-total efficiency curves were interpolated directly, with power values back-calculated. The resulting power curves (Figure 5) were visually indistinguishable from the originally interpolated curves, highlighting the sensitivity of efficiency calculations to minor power interpolation errors.

With the interpolation process complete, the product range was fully characterized. Across the range, eleven fans with two blade counts each resulted in twenty-two distinct datasets, providing a comprehensive dataset for the fan selector tool.

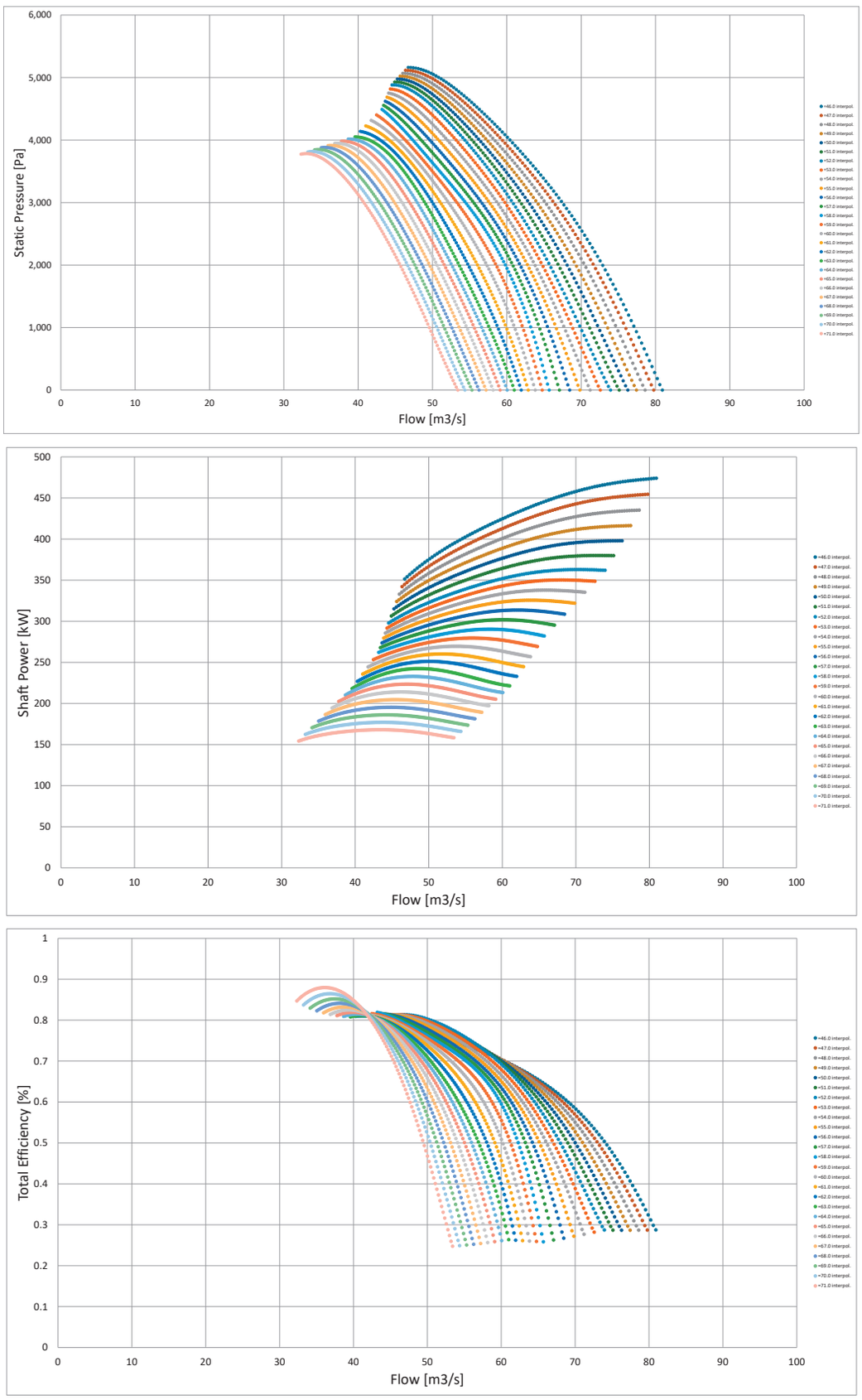


Figure 5: Example smoothed and interpolated data for one fan from the range. Fan performance data is interpolated in one-degree increments of blade angle, with one hundred points equally spaced from zero static pressure to peak pressure.

DISCUSSION

The total time taken for the CFD campaign to predict fan performance across the product range was approximately three months. The first month involved preparing the 3D CAD models, identifying issues with the CFD mesh generator, and resolving them. The core six weeks were dedicated to running CFD simulations and exporting key performance parameters. During the final weeks, additional simulations were conducted, and the interpolation effort increased.

Typically, it takes about three months to manufacture and deliver one pre-production fan to the laboratory for testing. While this duration could be shorter, customer requirements for contract-specific laboratory requirements often extend the timeline.

While this three-month timescale is typical for fans with diameters up to 1,600 mm, for larger fans, particularly those over 2,800 mm, the time and effort required for building and testing increases significantly, with testing only occurring in exceptional cases. Thus, while building and testing each fan within three months was theoretically possible, it was impractical.

Moreover, the three-month timeline from launching the CFD campaign to loading performance data into the fan selector was shorter than the time between issuing a preliminary and final quotation. Therefore, the day the CFD campaign started, the fan manufacturer began issuing quotations for fans within the new product range. Initially, performance data was scaled from the 1,394 mm pre-production prototype, and fans were launched for CFD simulation in the same order they were being quoted (Figure 3) to ensure final quotations were based on CFD predictions rather than scaled data.

The first orders for fans in the new product range were placed a few weeks after the performance data was integrated into the fan selector. These fans were installed, commissioned, and operational by early 2023. After approximately two years in service, they are performing at their selected duty points with power consumption in line with the specifications.

This method contrasts with traditional fan development, where CFD simulations are used during development, but the data entered into fan selectors comes from laboratory tests. CFD campaigns offer an alternative approach for developing new products and generating fan performance data for legacy products that do not meet the DOE’s test procedure requirements.

CONCLUSIONS

- Regulation for commercial and industrial fans and blowers has arrived in the U.S. market through a test procedure published by the U.S. Department of Energy (DOE), effective October 30, 2023.
- Many fan manufacturers have yet to replace historic performance data with data compliant with the new test procedure.
- A range of eleven mixed-flow fans for mine ventilation systems was characterized using one pre-production prototype test plus one production fan test to validate CFD simulation results.
- The remaining ten fans in the range were characterized through a CFD campaign that involved approximately 770 individual simulations.
- The CFD campaign lasted about three months, including time to interpolate CFD-predicted fan performance data.
- The campaign also included a stress-test to ensure the resulting product range coverage met requirements.
- The product range has been deployed, with the fans operating at their selected duty points and meeting contract specifications.
- The speed of CFD simulations was reliant on the availability of a cluster.
- The methodology developed could be effectively applied to historic fan ranges without performance data compliant with the U.S. DOE test procedure.

BIBLIOGRAPHY

[1] *Energy Conservation Program: Test Procedure for Fans and Blowers, Federal Register*, Vol. 88, No. 83, Monday, May 1, 2023 / Rules and Regulations, **2023**

[2] *Test Procedure for Calculating Fan Energy Index (FEI) for Commercial and Industrial Fans and Blowers*, ANSI/AMCA Standard 214-21, The Air Movement and Control Association, Arlington Heights, Illinois, USA, **2021**

[3] *Energy Standard for Buildings Except Low-Rise Residential Buildings*, ANSI/ASHRAE/IES 90.1-2022, American Society of Heating, Refrigerating and Air-Conditioning Engineers, Inc., Atlanta, Georgia, USA, **2022**

[4] *2021 International Energy Conservation Code*, American National Standards Institute, Washington, DC, USA, **2021**

[5] *California Code of Regulations Title 20. Public Utilities and Energy Division 2. State Energy Resources Conservation and Development Commission Chapter 4. Energy Conservation Article 4. Appliance Efficiency Regulations Sections 1601 – 1609 As related to Commercial and Industrial Fans and Blowers*, State of California Office of Administrative Law, January 17, **2023**

[6] *Laboratory Methods of Testing Fans for Certified Aerodynamic Performance Rating*, ANSI/AMCA Standard 210-16, The Air Movement and Control Association, Arlington Heights, Illinois, USA, **2016**

[7] *Fans - Performance testing using standardized airways*, ISO standard 5801, The International Organization for Standardization Geneva, Switzerland, **2017**

[8] Corsini, A., Delibra, G. and Sheard, A.G. - *A Critical Review of Computational Methods and Their Application in Industrial Fan Design* - International Scholarly Research Network, Mechanical Engineering, vol. 2013, article ID 625175, pp. 1–20, **2013**

[9] Sheard, A.G. - *The Application of Computational methods in Industrial Fan Design* – Sigel Press, Cambridge, Cambridgeshire, United Kingdom, **2016**

[10] Sheard, A.G. - *The Effect of Inlet Box Aerodynamics on the Mechanical Performance of a Variable Pitch in Motion Fan* - Advances in Acoustics and Vibration, vol. 2012, article ID 278082, pp. 1–10, **2012**

[11] Sheard, A.G. and Daneshkhah, K. - *The Conceptual Design of High Pressure Reversible Axial Tunnel Ventilation Fans - Advances in Acoustics and Vibration*, vol. 2012, article ID 562309, pp. 1–11, **2012**

[12] Eck, B. - Fans: Design and Operation of Centrifugal, Axial-Flow and Cross-Flow Fans - 4th Edition, Pergamon Press Oxford, UK, 1972

[13] Duckworth, I. Loomis, K. Karmawan, C. Chmura & K. Lownie, - *Selection of mixed-flow fans for PT Freeport's DOZ Mine, West Papua, Indonesia* – Proceedings of the 11th U.S./North American Mine Ventilation Symposium, The Pennsylvania State University, University Park, Pennsylvania, USA, June 5 – 7, **2006**

[14] Van Baalen, O. and Stewart, C. - *Starting-up the Ernest Henry underground mine – thermal and occupational hygiene challenges* - Proceedings of 11th Underground Operators' conference, Canberra, Australian Capital Territory, Australia, pp. 151-158, **2011**

[15] Bourcier, R.M. - *Improvements in Fans* - Patent No. AU 2018223216, 23 February, **2017**

[16] Bourcier, R.M. - *Systems and Methods for Ducted Ventilation* - Patent No. AU 2018223217, 28 July **2017**

[17] Stevens. M. - *Lab to Lab Variation in Testing Fans* - Proceedings of the Fan 2015 Conference, Lyon, France, 15–17 April, **2015**



MESH SENSITIVITIES FOR THE RANS SIMULATION OF LOW-REYNOLDS NUMBER PROPELLERS

Jorge SANTAMARIA[1], Andre BIERRENBACH-LIMA[1,2], Marlene SANJOSE [1]

[1] *Ecole de Technologie Superieure, Mechanical Engineering*
1100 rue Notre Dame Ouest Montreal, H3C 1K3, Quebec, Canada

[2] *Institut Superieur de l'Aeronautique et de l'Espace*
10 Av. Edouard Belin, 31400 Tolouse, France

SUMMARY

A mesh sensitivity study for the RANS simulation of a representative Unmanned Aerial Vehicle (UAV) propeller is presented. The chord-based Reynolds number falls within the transitional regime and the effects of this operating condition are investigated. First, a two-dimensional study defines the prismatic layer parameters to capture the boundary layer accurately. Then, a single-blade passage simulation using a frozen rotor interface is used to study the sensitivities to mesh refinements in critical regions of the computational domain. The thrust coefficient and Figure of Merit are in good agreement with experimental values. Lastly, a semi-empirical model is used to predict broadband noise due to turbulent boundary layer scattering finding reasonable agreement with the acoustic measurements.

INTRODUCTION

During the past decade, Unmanned Aerial Vehicles (UAVs) have found a wide range of applications from agriculture, industrial inspection, and art, to the transport of critical medical supplies. Compared to conventional helicopters, UAVs have smaller propellers and, thus, different flight parameters. Their chord-based Reynolds number (10^4 to 10^5) evolves in the transitional regime, which can affect their aerodynamic performance similarly to low-speed fans used in HVAC applications. Accurate propeller performance prediction is critical at the design stage as it will strongly impact the UAV's autonomy. With the continuous computational power growth, high-fidelity simulations are becoming commonplace, but their use during the propeller design phase is significantly limited, especially if a whole

range of operating conditions is desired. Moreover, it has been shown that hovering performance, in particular, is challenging to predict with discrepancies up to about 12% with experimental data [1, 2]. Equally important to aerodynamic performance is the noise signature of UAVs. It has been demonstrated that the broadband component of UAV propeller noise is of greater annoyance given the human ear's frequency response [3].

To avoid the computational cost of high-fidelity simulations where a single operating point may take days to converge, low-order methods are necessary in the design phase. Classical Blade Element Momentum Theory tools or advanced Vortex Element Techniques [4] can be used to provide blade loading for optimization purposes. Reynolds Averaged Navier-Stokes (RANS) simulations can be used to provide a more accurate estimation of viscous and realistic installation effects. While RANS simulations cannot resolve any turbulence scales to predict broadband noise, the boundary layer data can be used to model trailing edge noise [5–8], which accounts for most of the broadband noise while hovering.

Among the large number of turbulent closure models for RANS, few have become references for specific applications. For example, the k-ε is well adapted for jet flows with intense mixing, the Spalart- Almaras is largely employed in external aerodynamic applications, or the v2f for turbulent flow involving heat transfer [9]. The $k-\omega$ SST turbulence model has become the standard for turbomachinery and internal flow modeling, but its use for low-Reynolds numbers applications may result in inaccurate predictions. The performance degradation at low-Reynolds number is often related to the formation of laminar separation bubbles (LSB) [10] caused by adverse pressure gradient, which drives the transition to turbulence. Different approaches to handle low-Reynolds number can be found in the literature [11] but in the context of RANS simulations the Langrtry-Menter, $\gamma - Re_\theta$ model has become widely used and has been validated for several engineering applications [12].

The present study investigates mesh sensitivities of a representative drone propeller in RANS simulations using fully turbulent and transitional models. It aims to provide general guidelines to design a mesh to predict low-Reynolds number propeller performance. In addition, the RANS results are coupled with a semi-analytical method based on Amiet's theory to predict trailing edge noise.

METHODOLOGY

A representative 2-bladed drone propeller of diameter $D = 12.5$ cm with constant pitch (10°) and chord (25 mm) with a NACA0012 blade section that has been extensively studied experimentally [13, 14] and numerically [15–17] was chosen for the present study. The RPM range is between 4000 and 8000, yielding a chord-based Reynolds number range between 88000 and 176000 using the blade tip speed. The corresponding tip Mach numbers are 0.15 and 0.3 respectively. It is expected, then, that transitional effects play an essential role in aerodynamic performance, whereas compressibility effects can be disregarded.

This study investigates two configurations: the first corresponds to a NACA0012 airfoil section, and the second to a blade passage configuration of a propeller made out of the same airfoil. In both cases, the objective is to obtain performance sensitivities to mesh parameters. Additionally, the low-computational-cost 2D simulations allow defining the surface mesh to be used on the propeller.

The airfoil domain extends 10 chord lengths downstream from the trailing edge and 5 chords upstream from the leading edge. The boundary conditions are: inlet velocity, outlet pressure and periodic in the spanwise direction. The propeller computational domain is divided into two regions: a large stationary domain and a rotating domain, as shown in terms of the propeller radius R in Fig. 1. The RANS equations are solved in a moving reference frame (MRF) in the rotating domain, introducing the Coriolis and centripetal components of the acceleration in the momentum equations. In both

cases the air is modeled as an incompressible medium with constant temperature, using the CFX default physical and transport properties for air at $25°C$.

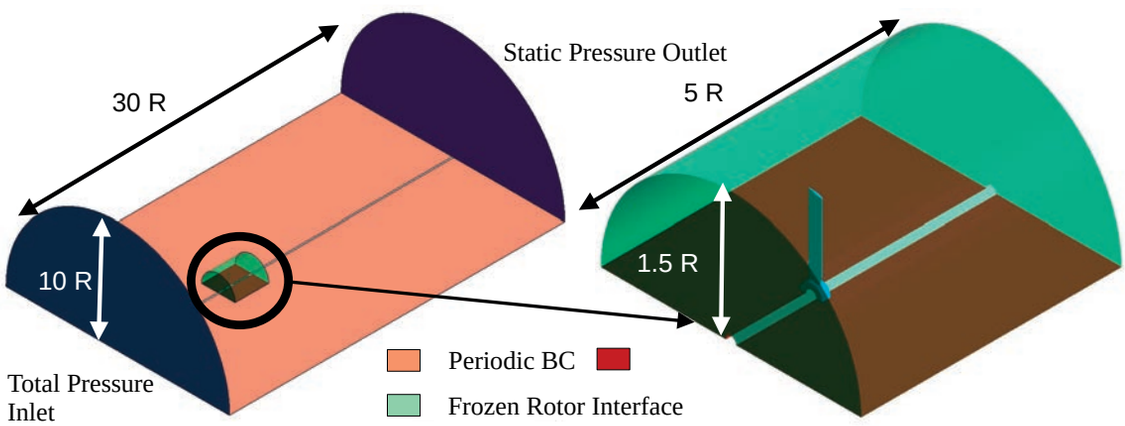


Figure 1: Stationary and rotational domains for the propeller simulations.

The simulations are performed with the *High Resolution* advection scheme. For closure of the RANS equations, the $k-\omega$ SST model is used. For all configurations considered, the simulations are performed twice, first using the fully developed turbulence, then the transitional modeling by activating the $\gamma - Re_\theta$ model based on the Langtry-Menter model. The $\gamma - Re_\theta$ [11] is a two-equations local correlation-based transition model (LCTM). The first equation is for the intermittency γ, and the second one is for the transition onset momentum thickness Reynold number Re_θ. The intermittency is zero for laminar boundary layers where the production of turbulence kinetic energy is inhibited, and it is one for turbulent boundary layers where k evolves according to its transport equation. The transport equation for Re_θ connects empirical correlations to the onset criteria in the γ equation. It accounts for non-local effects due to changes in the freestream turbulence and in the pressure gradient at the edge of the boundary layer. A standard diffusion term in the Re_θ equation propagates this information towards the wall. Due to its empirical nature, the $\gamma - Re_\theta$ model does not aim to reproduce the complex physics of transition but rather to model the consequences of the transition in the flow. The transition physics are thus entirely contained in the empirical correlations.

AIRFOIL MESH SENSITIVITY

The airfoil grid, created using the CentaurSoft grid generator, consists of a hybrid mesh with quadrilaterals close to the wall and triangles everywhere else. The airfoil simulations objective is to define the first layer thickness, number of layers and aspect and stretching ratios for the quadrilaterals. These parameters play a key role in accurately capturing the boundary layer and, thus, are critical for trailing edge noise prediction. The stretching ratio and the number of prismatic layers are fixed to 1.15 and 25, respectively, based on the ANSYS CFX transition modeling guide recommendations. Thus, the variable parameters are the first layer thickness and the cell aspect ratio, as shown in Table 1 for a total of fifteen meshes. The velocity components on the inlet conditions of the airfoil domain are extracted at 50% of the blade span from a prior simulation of the propeller spinning at 6000 rpm [7] yielding a Reynolds number of 66000. The simulations are then run for fully turbulent ($k-\omega$ SST) and transitional ($\gamma - Re_\theta$) models.

In terms of convergence, all the fully turbulent cases except for the case with the smallest first layer thickness reached RMS values below 10^{-6}, while for the transitional model, only the cases with the largest aspect ratio and thicker first layer reached the threshold. The skin friction coefficient distribu-

Table 1: Mesh prismatic layer test matrix

Aspect ratio	First layer thickness(%c)	Number of prismatic layers	Stretching ratio
10	0.01,0.015,0.02,0.03,0.04	25	1.15
20	0.01,0.015,0.02,0.03,0.04	25	1.15
40	0.01,0.015,0.02,0.03,0.04	25	1.15

tion is shown in Figs. 3 and 2 for the transitional and turbulent cases, respectively. The fully turbulent results tend to collapse except for the smallest first layer thickness. In contrast, the transitional results show greater variation. The transition location can be inferred from the change in curvature in the c_f curves. The laminar-turbulent transition takes place around $x/c = 50\%$ for the cases with a smooth c_f distribution. The effect of the aspect ratio is marginal for the turbulent results, while it can significantly impact the skin friction distribution for the transitional cases. Similar sensitivity of the $\gamma - Re_\theta$ model to grid parameters has been reported in the case of a helicopter rotor in hover [18].

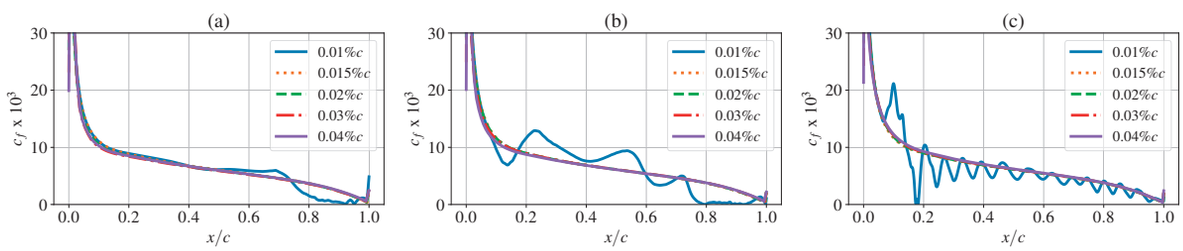


Figure 2: Suction side skin friction coefficient distribution as a function of first layer thickness for an aspect ratio of (a) 40, (b) 20, (c) 10 using the k-ω SST model

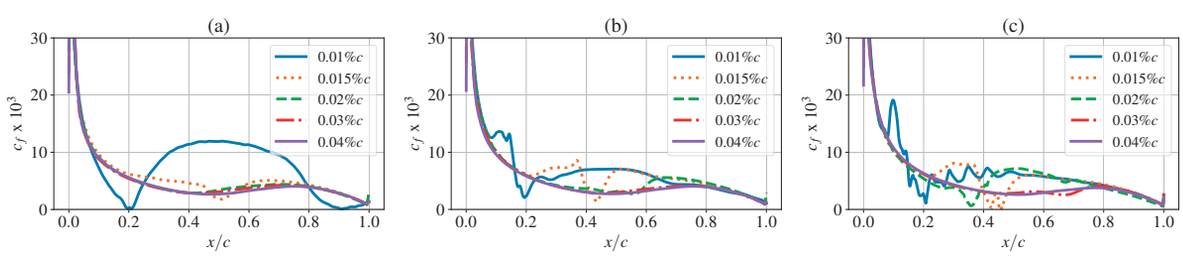


Figure 3: Suction side skin friction coefficient distribution as a function of first layer thickness for an aspect ratio of (a) 40, (b) 20, (c) 10 using the $\gamma - Re_\theta$ model

Overall, larger aspect ratios produce smoother skin friction coefficient distributions and improve convergence. It is important to note that for transitional simulations, it is recommended to have a finer discretization in the streamwise direction to capture laminar separation bubbles. Therefore, for this particular configuration, a trade-off between solution smoothness and accurate modelling must be made.

The averaged y^+ values measured in the different simulations are reported in Table 2 for the suction side and at $x/c = 10\%$. The effects of the first layer thickness and the aspect ratio on the airfoil drag coefficient C_D are shown in Fig. 4. The transitional results (right in Fig. 4) show a lower drag coefficients compared to the turbulent solution as a result of the laminar region. The results highlight the marginal impact of the grid on the turbulent drag predictions and the high sensitivities for the transitional ones. The latter can be associated to the shifting location of the transition on the different

grids as highlighted in the c_f distribution in Fig. 3. As the y^+ value increases, the transition is delayed downstream, resulting in lower c_f on a larger portion of the airfoil surface, yielding a lower drag coefficient. The aspect ratio influence is unclear for transitional simulations. On the contrary, C_D increases as the aspect ratio increases and the first layer thickness for fully turbulent simulations (left in Fig. 4). The unstable c_f distribution seen for the first layer thickness of $0.01\%c$ in Figs. 2 and 3 are associated to the too low y^+ value of 0.5.

Table 2: Suction side y^+ values at 10% of the chord for the different first layer thickness tested.

First layer thickness	$0.01\%c$	$0.015\%c$	$0.02\%c$	$0.03\%c$	$0.04\%c$
$\mathbf{y}^+$ at $x/c = 10\%$	0.5	0.7	1.0	1.5	2.0

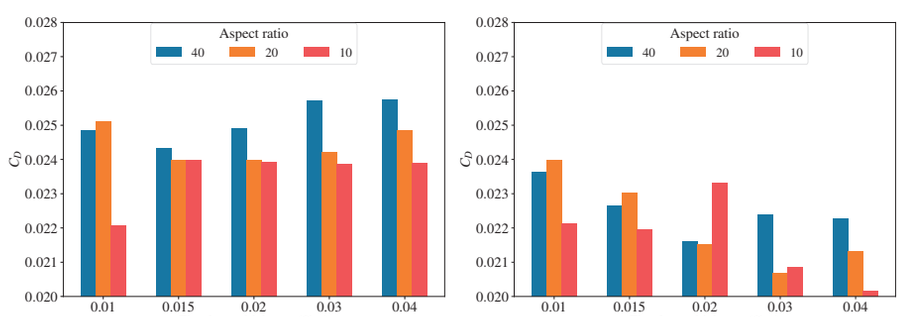


Figure 4: Drag coefficient sensitivity to first layer thickness and aspect ratio for fully turbulent (left) and transitional (right) simulations.

In order to design a mesh that is suitable for both fully turbulent and transitional simulations at the lowest computational cost, a balance must be struck between the two parameters. To reduce the possibilities of oscillatory solutions, the first layer thickness will be set to 0.03% of the chord and the aspect ratio to 20 for the propeller surface mesh. With these parameters, 324 points around the airfoil are obtained, and ensure a y^+ below 1 for $x/c > 15\%$.

PROPELLER MESH SENSITIVITY

Having defined the surface mesh for the blade, this section presents the mesh requirements for the propeller near and far fields. The single passage grid consists of a hybrid mesh with triangles discretizing the blade surface and a prismatic layer close to the wall where the boundary layer is expected to evolve. Tetrahedrons are used to fill the rest of the domain. The tetrahedral mesh regions of interest are the propeller tip vortex, the propeller wake, and the far-field, as shown in the meshing strategy in Fig. 5. Several meshes are generated, where individual size parameters are tested. A fully turbulent and transitional RANS simulation is performed for each mesh. The thrust, torque coefficients and Figure of Merit, defined in Eq.(1), Eq.2 Eq. (3) respectively, are used to evaluate the grid impact on the solution.

$$c_T = \frac{T}{\rho(\Omega R)^2 \pi R^2} \quad (1) \qquad c_Q = \frac{Q}{\rho(\Omega R)^2 \pi R^3} \quad (2) \qquad \mathrm{FM} = \frac{c_T^{3/2}}{\sqrt{2} c_Q} \quad (3)$$

where T is the thrust, Q is the torque, ρ is the ambient density, R is the propeller radius, and Ω is the rotational speed (in rad/s).

Firstly, keeping the blade mesh resolution (based on the airfoil study) identical and the stationary domain mesh resolution fixed, the cell size in the hollow cylinder region (in red in Fig. 5) is varied. This region is necessary to capture the propeller wake and the tip vortex system. The calculated

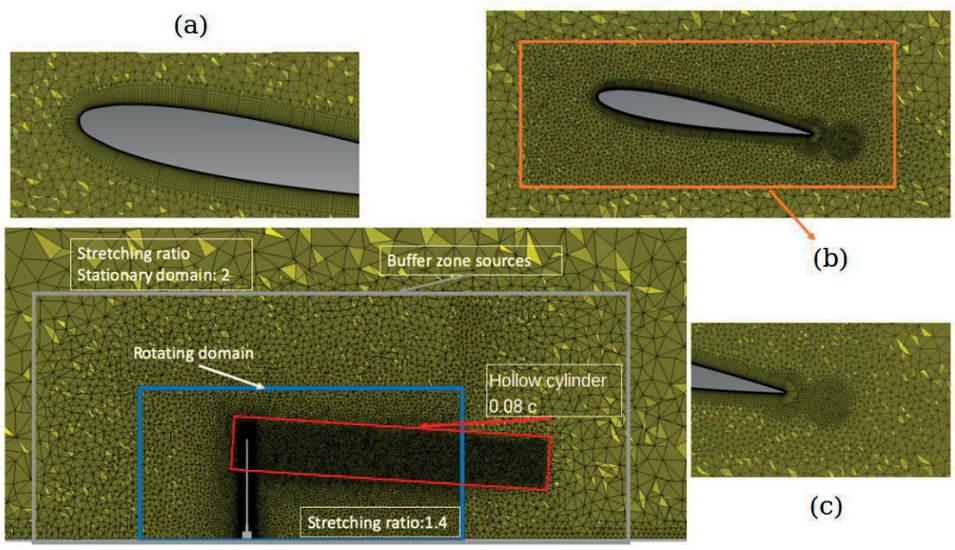


Figure 5: Meshing strategy: (a) leading edge, (b) blade near field, and (c) blade wake

performances are shown in Fig. 6 as a function of the element size. A low resolution of the propeller wake and tip vortex yields significant under-prediction of the aerodynamic performance.

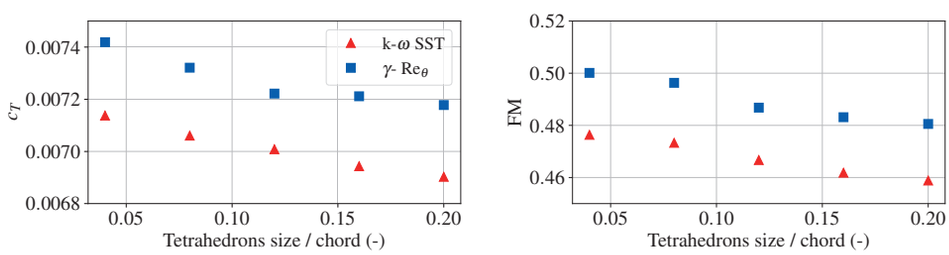


Figure 6: Thrust coefficient (c_T) and Figure of Merit (FM) sensitivity to tetrahedral element size in the hollow cylinder region.

The dramatic difference that the refinement in this region can have on the overall flow is highlighted in Fig. 7. The propeller wake refinement allows improving the resolution of the downstream propagation of the tip vortex, which modifies the resulting performance of the simulated propeller.

Secondly, the maximum tetrahedral size in the stationary domain are modified, keeping a smooth coarsening from the rotor domain to the external boundary conditions. The performance evaluations for the tested grids are shown in Fig. 8. A limit of the maximum tetrahedral size of about twice the chord yields the same results as finer tested meshes. It can be concluded that the mesh requirements in the stationary domain have a limited impact on the performance predictions.

Having set the mesh maximum size in the stationary domain and the mesh refinement zones in the rotational domain, a grid convergence study is performed by scaling down the tetrahedron size in the rotational domain (blue rectangle in Fig. 5) in a global manner. This results in an exponential increase in the tetrahedron number. Note that this does not affect the surface and the prismatic regions close to the blade. As seen in Fig. 9 the thrust coefficient and Figure of Merit tend to an asymptotic value with an increasing number of elements. A rational polynomial fit is shown to highlight the trend and the shaded regions represent a region within 1% of the asymptotic value.

An experimental data set from ISAE[6] is used to validate the simulation results. In the experimental campaign, two 3D-printed rotors were designed in clean and tripped configurations. The clean version is identical to the one in the simulations whereas the tripped one has cylinders at 10% from the

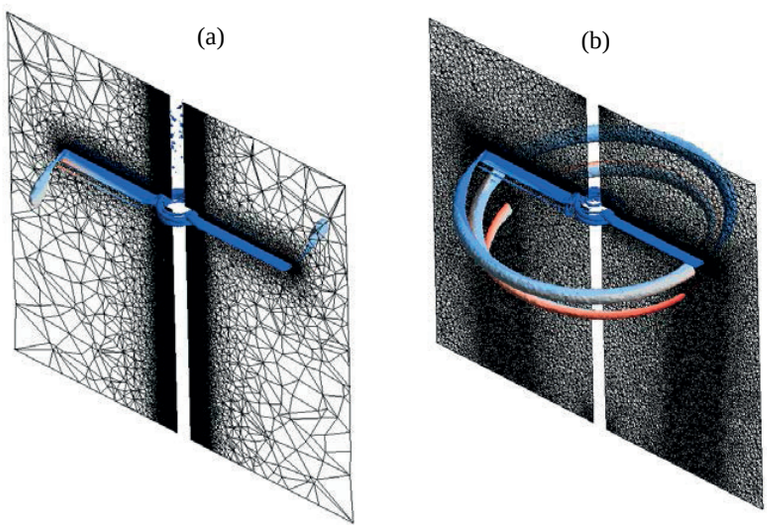


Figure 7: Isosurfaces of the Q-criterion colored by the eddy viscosity ratio for meshes (a) without and (b) with propeller wake refinement at 6000 RPM

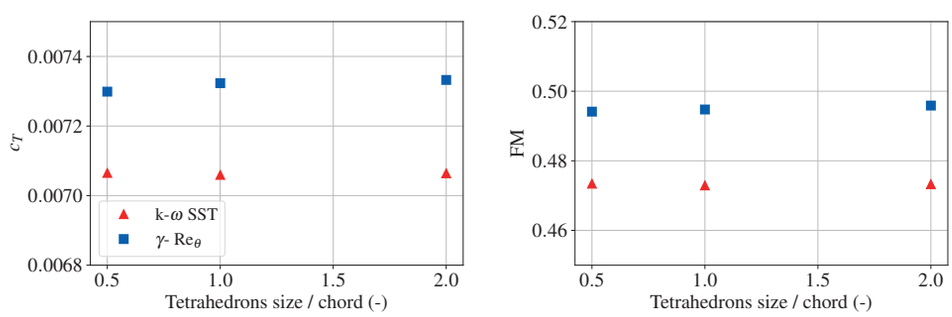


Figure 8: Thrust coefficient (c_T) and Figure of Merit (FM) sensitivity to tetrahedral element size in the stationary domain

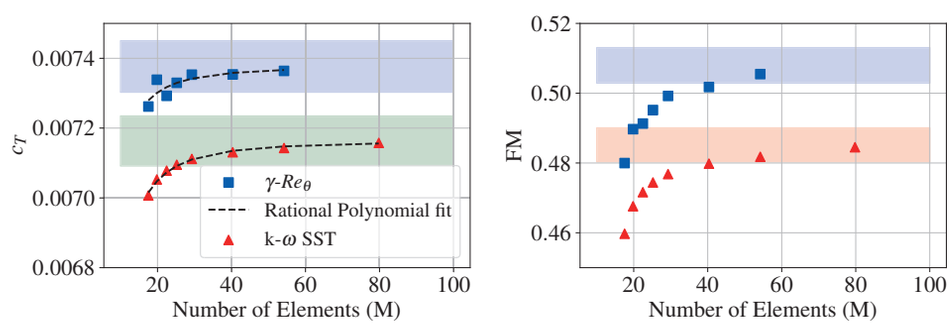


Figure 9: Grid convergence

leading edge to force transition to turbulence. The former is used for reference for the transitional simulations, while the latter serves as a reference for the fully turbulent ones. Details of the trip sizing and distribution can be found in [19]. The comparison of the numerical results with experimental data is shown in Fig. 10 the error bars represent the experimental uncertainty as reported in [16].

Both the fully turbulent and transitional simulations are in reasonable agreement with their experimental counterparts. The thrust coefficient for both cases is within the experimental uncertainty for all RPMs (except the 5000 RPM fully turbulent case) whereas the Figure of merit is in very good

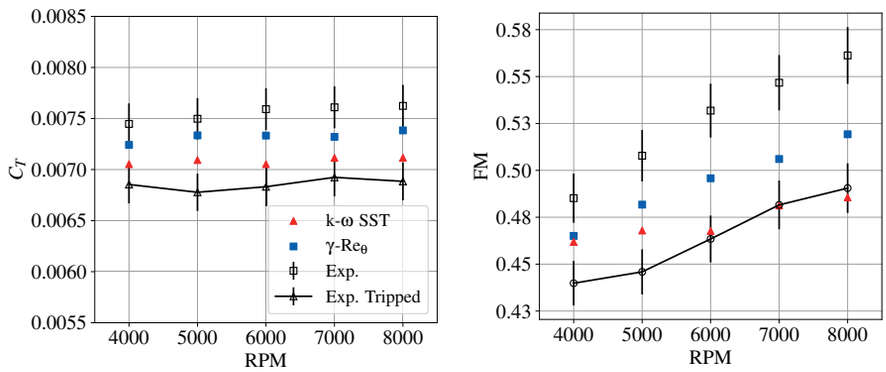


Figure 10: Comparison of thrust coefficient (c_T) and Figure of merit (FM) with experimental data

agreement for the fully turbulent case for RPM greater than 5000 and with a good trend prediction for the transitional case. It is worth pointing out that even with high-fidelity simulations the aerodynamic performance prediction of low-Re number propellers is still challenging and discrepancies of up to 12% with experimental data have been reported [1, 20, 21].

To better understand the flow topology over the blade, the streaklines are presented in Fig. 11. The blade is colored by intermittency contours that identify the regions where the flow is laminar (red) or turbulent (blue). The contours range is selected based on recommendations in [22]. In the tip region of the blade ($r/R > 0.75$), the boundary layer is in a transitional state and the transition position moves closer to the leading edge along the span. This is consistent with the increasing Reynolds number as the entrainment velocity increases with radius. Similarly, the percentage of blade span in the transitional regime increases with increasing RPM. The transition line (white) obtained experimentally from Infrared Thermography (IRT) [23] in a similar, albeit 3-bladed, propeller at 6500 RPM is shown for a qualitative comparison.

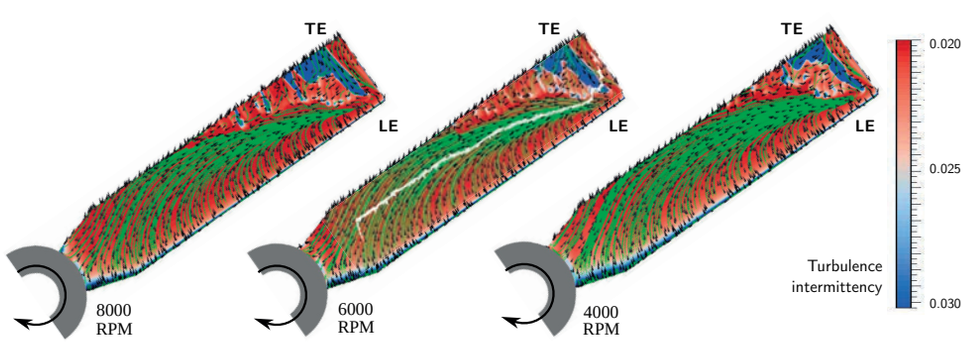


Figure 11: Wall-shear streaklines over contours of intermittency for the transitional solution.

TRAILING EDGE NOISE PREDICTION

Given the good agreement of clean and tripped configurations with the experimental data, the simulation results were used for trailing edge noise prediction. The complete methodology is described in [5]. It consists in the extraction of boundary layer parameters at different positions along the span at $x/c = 85\%$ to model the pressure fluctuations wall-pressure spectrum using semi-empirical models. Lee's empirical model[] is used in this study as input in Amiet's model [24].The computation for the propeller far-field noise follows a strip-approach where noise sources are assumed to be uncorrelated for each strip and an azimuthal average over one revolution is done to account for the Doppler Effect. The computation is done with the in-house code PyFanNoise. Given the propeller small chord, the leading edge back-scattering [25]was included.

In the experimental campaign [6] an array of 13 microphones was used at a distance of 1.62 m from the propeller axis and spanning an arc from 60° to -60° (with 90 ° being the upstream direction) to record the far-field acoustics. Further details of the experimental campaign and the anechoic facility can be found in [13]. The sound power level (SWL) was obtained by computing the acoustic intensity and then by integrating this result along the spherical area spanned by the microphone array. Fig. 12 shows the SWL for the clean and tripped configurations. The broadband signals are obtained by smoothing the original signal with a Savitzky-Golay filter. The modeled results match the experimental data for frequencies between 1-10 kHz regardless of the turbulence model employed. It is worth noting that the hump centered around 12 kHz is related to instabilities in the pressure side laminar boundary layer and cannot be captured with this approach.

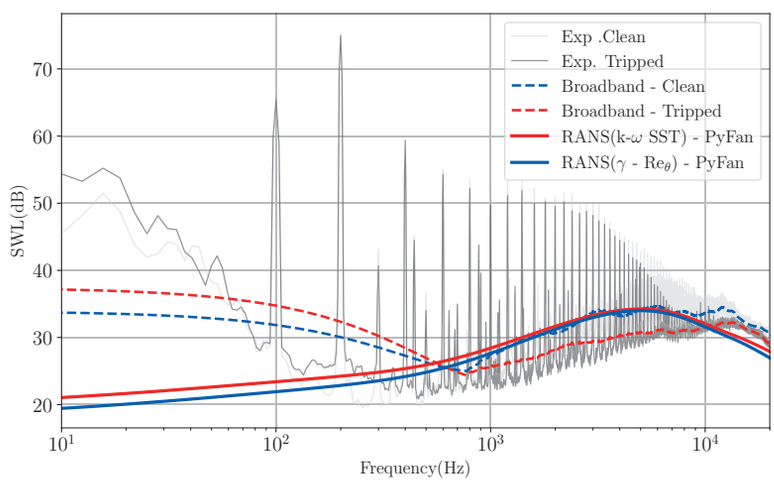


Figure 12: Sound Power Level from experimental results compared with trailing edge noise modelling based on RANS simulations

CONCLUSIONS

A mesh sensitivity study was conducted to predict the performance of a representative drone propeller using RANS simulations. The predictions using the fully turbulent $k-\omega$ SST model and the transitional γ-Re_θ model were compared with their experimental counterparts with the thrust coefficient falling within experimental uncertainty (95 % confidence interval). The prismatic layer was defined based on an airfoil analysis, finding high sensitivity of the transitional model to the first layer thickness and aspect ratio.

The propeller analysis demonstrated the importance of sufficient resolution of the propeller wake and the tip vortices for accurate thrust and Figure of Merit predictions. It was shown that the γ-Re_θ model is able to capture the transition location along the span. Lastly, a semi-empirical method based on Amiet's theory was used to predict the broadband noise due to the scattering of the boundary layer yielding good agreement with the experimental results.

ACKNOWLEDGMENTS

The simulations were carried out on the Narval supercomputer administered by the Digital Research Alliance of Canada. J. Santamaria is thankful for the support from the FRQNT PR-300387 and NSERC RGPIN-2020-05919. The authors acknowledge the partners of the UHEQ Consortium II and III at Université de Sherbrooke, which develops and provides the acoustic software PyFanNoise for this research. Additionally, the authors acknowledge Dr. Romain Gojon for experimental data on the NACA0012 propeller.

FAN 2025
Antibes - Juan-les-Pins (France), 9 - 10 April 2025

REFERENCES

[1] Christopher Thurman, D. Douglas Boyd Jr, Pieter Buning, Gabriel Reboul, and Christophe Benoit. *NASA/ONERA Collaboration on Small Hovering Rotor Broadband Noise Prediction Using Lattice-Boltzmann Method and Structured Navier-Stokes Solvers*. In *30th AIAA/CEAS Aeroacoustics Conference (2024)*. American Institute of Aeronautics and Astronautics, **2024**. DOI: 10.2514/6.2024-3106.

[2] Damiano Casalino, Gianluca Romani, Raoyang Zhang, and Hudong Chen. *Lattice-Boltzmann calculations of rotor aeroacoustics in transitional boundary layer regime*. Aerospace Science and Technology 130. DOI: 10.1016/j.ast.2022.107953.

[3] Nikolas S. Zawodny, D. Douglas Boyd, and Casey L. Burley. *Acoustic Characterization and Prediction of Representative, Small-Scale Rotary-Wing Unmanned Aircraft System Components*. In *VFS International Powered Lift Conference*, West Palm Beach, FL, **2016**.

[4] Yeongmin Jo, Thierry Jardin, Romain Gojon, Marc C. Jacob, and Jean-Marc Moschetta. *Prediction of Noise from Low Reynolds Number Rotors with Different Number of Blades using a Non-Linear Vortex Lattice Method*. In *25th AIAA/CEAS Aeroacoustics Conference*, Delft, The Netherlands. American Institute of Aeronautics and Astronautics, **2019**. DOI: 10.2514/6.2019-2615.

[5] Marlène Sanjosé and Stéphane Moreau. *Fast and accurate analytical modeling of broadband noise for a low-speed fan*. The Journal of the Acoustical Society of America 143(5). DOI: 10.1121/1.5038265.

[6] Jorge Santamaria, Marlene Sanjose, Romain Gojon, Sylvain Belliot, and Stephane Moreau. *Installation and Manufacturing Effects of Propeller Trailing Edge Serrations*. In *30th AIAA/CEAS Aeroacoustics Conference (2024)*, Aeroacoustics Conferences. American Institute of Aeronautics and Astronautics, **2024**. DOI: 10.2514/6.2024-3322.

[7] Jorge Santamaria, André Bierrenbach-Lima, Marlène Sanjosé, and Stéphane Moreau. *Shape considerations for the design of propellers with trailing edge serrations*. Journal of Sound and Vibration 595. DOI: 10.1016/j.jsv.2024.118771.

[8] Seongkyu Lee, Lorna Ayton, Franck Bertagnolio, Stephane Moreau, Tze Pei Chong, and Phillip Joseph. *Turbulent boundary layer trailing-edge noise: Theory, computation, experiment, and application*. Progress in Aerospace Sciences 126. DOI: 10.1016/j.paerosci.2021.100737.

[9] Bruno Chaouat. *The State of the Art of Hybrid RANS/LES Modeling for the Simulation of Turbulent Flows*. Flow, Turbulence and Combustion 99(2). DOI: 10.1007/s10494-017-9828-8.

[10] M. Carreño Ruiz, M. Scanavino, D. D'Ambrosio, G. Guglieri, and A. Vilardi. *Experimental and numerical analysis of hovering multicopter performance in low-Reynolds number conditions*. Aerospace Science and Technology 128. DOI: 10.1016/j.ast.2022.107777.

[11] Robin B. Langtry and Florian R. Menter. *Correlation-Based Transition Modeling for Unstructured Parallelized Computational Fluid Dynamics Codes*. AIAA Journal 47(12). DOI: 10.2514/1.42362.

[12] Manuel Carreño Ruiz and Domenic D'Ambrosio. *Validation of the $\gamma - Re_\theta$ Transition Model for Airfoils Operating in the Very Low Reynolds Number Regime*. Flow, Turbulence and Combustion 109(2). DOI: 10.1007/s10494-022-00331-z.

[13] Romain Gojon, Thierry Jardin, and Hélène Parisot-Dupuis. *Experimental investigation of low Reynolds number rotor noise*. The Journal of the Acoustical Society of America 149(6). DOI: 10.1121/10.0005068.

[14] Romain Gojon, Hélène Parisot-Dupuis, Bertrand Mellot, and Thierry Jardin. *Aeroacoustic radiation of low Reynolds number rotors in interaction with beams*. The Journal of the Acoustical Society of America 154(2). DOI: 10.1121/10.0020672.

[15] Jose Rendon, Stephane Moreau, Romain Gojon, and Michaël Bauerheim. *LBM and iLES Comparison for the Aaerodynamic and Acoustic Characteristics of a Low-speed Rotor*. In *30th AIAA/CEAS Aeroacoustics Conference (2024)*, Aeroacoustics Conferences. American Institute of Aeronautics and Astronautics, **2024**. DOI: 10.2514/6.2024-3046.

[16] Pietro Li Volsi, Gianluigi Brogna, Romain Gojon, Thierry Jardin, Hélène Parisot-Dupuis, and Jean-Marc Moschetta. *Analysis of MAV Rotors Optimized for Low Noise and Aerodynamic Efficiency with Operational Constraints*. Fluids 9(4). DOI: 10.3390/fluids9040096.

[17] D. V. Shenoy, R. Gojon, T. Jardin, and M. C. Jacob. *Aerodynamic and acoustic study of a small scale lightly loaded hovering rotor using large eddy simulation*. Aerospace Science and Technology 150. DOI: 10.1016/j.ast.2024.109219.

[18] François Richez. *Numerical Investigation of Turbulence Transition Models for the Prediction of Helicopter Rotor Performance in Hover*. In *Vertical Flight Society 80th Forum*, Montréal, Canada, **2024**.

[19] E.R. Gowree, T. Jaroslawski, B. Mellot, and R. Gojon. *Noise reduction on low Reynolds number rotors by boundary layer transition*. Applied Acoustics 210. DOI: 10.1016/j.apacoust.2023.109446.

[20] Damiano Casalino, Gianluca Romani, Lorenzo Maria Pii, and Riccardo Colombo. *Flow confinement effects on sUAS rotor noise*. Aerospace Science and Technology 143. DOI: 10.1016/j.ast.2023.108756.

[21] Edoardo Grande, Gianluca Romani, Daniele Ragni, Francesco Avallone, and Damiano Casalino. *Aeroacoustic Investigation of a Propeller Operating at Low Reynolds Numbers*. AIAA Journal 60(2). DOI: 10.2514/1.J060611.

[22] ANSYS. Visualizing Laminar and Turbulent Regimes | Ansys Courses, **2024**.

[23] Tomek Jaroslawski, Maxime Forte, Jean-Marc Moschetta, and Erwin R. Gowree. *Boundary layer forcing on a rotating wing at low Reynolds numbers*. Experiments in Fluids 64(3). DOI: 10.1007/s00348-023-03597-9.

[24] R. K. Amiet. *Noise due to turbulent flow past a trailing edge*. Journal of Sound and Vibration 47(3). DOI: 10.1016/0022-460X(76)90948-2.

[25] Michel Roger and Stéphane Moreau. *Back-scattering correction and further extensions of Amiet's trailing-edge noise model. Part 1: theory*. Journal of Sound and Vibration 286(3). DOI: 10.1016/j.jsv.2004.10.054.

D2 Optimization of Fan Installation To Reduce Noise

10 April - 11:00 - Room 1 Fitzgerald

Chairman: Stéphane Moreau

List of papers

Numerical and Experimental Investigations of the Sound Generation and Possible Optimization Techniques of Wires for Fan Guard Grills

- Sandra HUB – ZIEHL-ABEGG SE (Germany)
- Frieder LÖRCHER – ZIEHL-ABEGG SE (Germany)

ADVentAGe: Scalable Hybrid Noise Control Systems for Fans

- Valentin MEES – Fraunhofer LBF (Germany)
- David GOECKE – Fraunhofer IBP (Germany)

Experimental and Numerical Study of Aerodynamic Noise of Small- Size High-Speed Centrifugal Impeller

- Zerong Yu -Shanghai Jiao Tong University (China)
- Yixin HUANG – Shanghai Jiao Tong University (China)
- Weigang YANG – Ningbo Fanta Kitchen Ware Co Ltd (China)
- Bin LI – Shanghai Jiao Tong University (China)
- Peixang YU - Shanghai Jiao Tong University (China)
- Hua OUYANG – Shanghai Jiao Tong University (China)
- Yadong WU – Shanghai Jiao Tong University (China)

NUMERICAL AND EXPERIMENTAL INVESTIGATIONS OF THE SOUND GENERATION AND POSSIBLE OPTIMIZATION TECHNIQUES OF WIRES FOR FAN GUARD GRILLES

Sandra HUB, Frieder LÖRCHER

ZIEHL-ABEGG SE, Pre-Development Aerodynamics & Acoustics, Heinz-Ziehl-Straße, 74653 Künzelsau, Germany

SUMMARY

For recent self-noise optimized axial fans, the additional noise emission by guard grilles mounted downstream of the fan can be one of the dominant noise sources. In the present case, the sound power level is increased by up to 2 dB. Based on narrow band acoustic measurements and numerical Lattice-Boltzmann simulations of wind tunnel arrangements of round wires, it can be observed that periodic flow separations downstream of the round wires (von Kármán vortex street) cause a significant hump in the noise spectra at a frequency range that corresponds to the noise emission increase by the guard grille of an axial fan under comparable flow conditions. By investigating different wire geometries, it was found out that interrupting the von Kármán vortex street in longitudinal direction of the wire and making the flow separation less homogeneous in that respect, the sound generation can be reduced significantly.

INTRODUCTION

In various fan applications, a protection of rotating parts with a guard grille which is mounted on the pressure and / or the suction side of the fan must be foreseen. It is a common observation, that such guard grilles may cause a significant increase of noise emission. For fans with low self-noise, the additional noise sources caused by the guard grilles are often dominant with respect to the overall fan noise.

Figure 1 (left) shows an axial fan with diameter $D = 450\ mm$, which can be used e.g. in heat pumps. *Figure 1 (right)* shows the same fan with a guard grille mounted downstream of the impeller, which is essentially constituted of round wires which are arranged in circles of increasing radius. The round wires are consolidated by a supporting structure crossing the wires, with which the guard grille is attached to the outer housing of the fan. In the present case, the guard grille has additionally the function of supporting the motor with the impeller and fixing it to the housing.

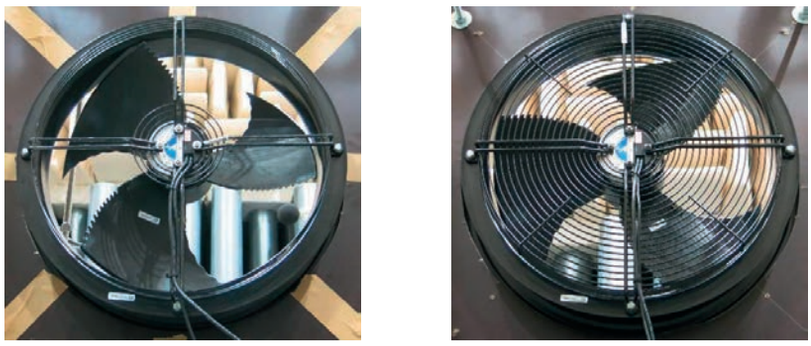


Figure 1: Experimental setup for sound measurements of an axial fan without (left) and with (right) a downstream guard grille

The noise emission of the two fan installations is measured experimentally in the ZIEHL-ABEGG anechoic facility. This consists of two large anechoic rooms separated by a partition wall where the fan and the nozzle are mounted. The sound power of the fan is recorded independently both on the suction and the pressure side using an enveloping measurement surface. *Figure 2 (left)* shows the dimensionless static pressure rise ψ_{stat} and the sum of the specific pressure side sound power level $L_W 6_{spec}$ as function of the specific diameter δ as measured for the presented axial fan at rotation speed $n = 990\ rpm$ (for definition of specific fan parameters ψ_{stat} and δ, see [1]). The noise emission of the fan with guard grille (blue) is significantly increased compared to the measurement without guard grille (red). Especially for low δ, corresponding to high volume flow rates, $L_W 6_{spec}$ is increased by about 2 dB due to the guard grille. For deeper insight, the spectral content of $L_W 6_{spec}$ at $\delta = 1.5$ is presented in *Figure 2 (right)*. The integral of this spectra is the sum shown in *Figure 2 (left)* at $\delta = 1.5$. The sound power level spectrum of the fan with guard grille is dominated by a hump with its maximum around a frequency of $f = 600\ Hz$. This hump can be seen for different duty points along the whole performance curve. The frequency increases with the volume flow. Schneider et al. [2] described a similar behaviour for axial fans with guard grilles.

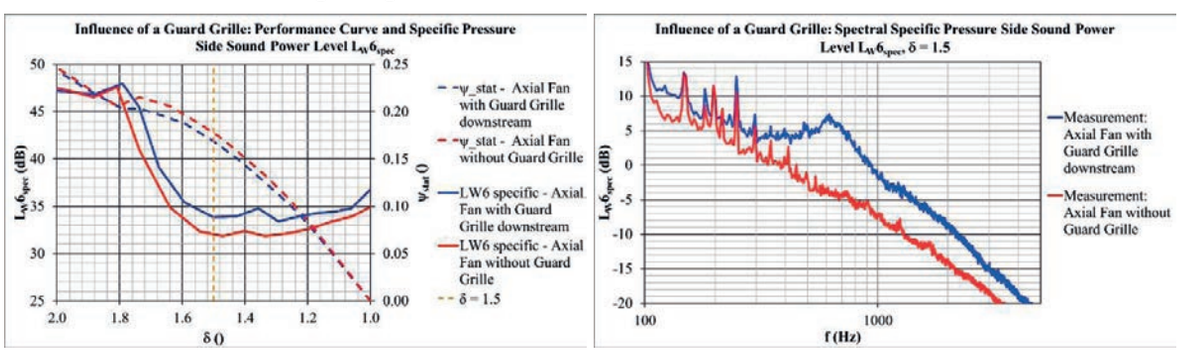


Figure 2: Experimental results of an axial fan without (red) and with (blue) a downstream guard grille at $n = 990\ rpm$: specific pressure side sound power level $L_W 6_{spec}$ (left) and spectral content thereof at $\delta = 1.5$ (right)

For a cylinder in a crossflow, model for the wires of a guard grille, periodic flow separations (Kármán vortex street, [3]) can be observed, and a tonal or narrow banded noise is generated. The frequency f of the vortex shedding thereby corresponds to the frequency f of the emitted noise and depends on the far field flow velocity v_∞, estimated by the volume flow rate and the outlet area of the nozzle, and the diameter D_{wire} of the wire and can be described with help of the Strouhal number (see [4, 5, 6]) by the relation $f = Sr \cdot v_\infty / D_{wire}$. The Strouhal number depends on the Reynolds number Re. For the performance curve shown in *Figure 2 (left)* the maximum flow velocity is $v_\infty = 7\ m/s$ (without blockage of the guard grille) and $v_\infty = 10\ m/s$ (with blockage of the guard grille). Locally behind the fan, for bigger fan sizes or for higher fan speeds the flow velocity is even higher. This means the, for the investigation and optimization of the sound generation of wires for fan guard grilles, relevant velocity range is $v_\infty = [4, \dots, 20]\ m/s$ and $Re = [650, \dots, 3250]$. According to [6] the Strouhal number can be chosen with $Sr = [0.2, \dots, 0.21]$.

For the duty point shown in *Figure 2 (right)* at $\delta = 1.5$, the upstream velocity v_∞ can be estimated to $v_\infty = 4.5\ m/s$ (without blockage by the guard grille) and $v_\infty = 6\ m/s$ (with blockage) and $D_{wire} = 2.5\ mm$. This

result is a vortex shedding frequency f of about $400 - 500\ Hz$, with $Sr = 0.21$, which fits roughly to the hump in the narrow band spectra in *Figure 2 (right)*.

For a basic investigation of the noise generation of an arrangement of differently shaped wires, a wind tunnel is conceived and constructed to carry out experimental sound measurements, and unsteady Lattice-Boltzmann simulations of this wire arrangement in the wind tunnel are performed.

EXPERIMENTAL INVESTIGATION

Wind Tunnel Configuration

To investigate the noise generation of the flow around a wire arrangement, the wind tunnel depicted in *Figure 3 (left)*, has been conceived and manufactured with help of a 3D-Printer. The wind tunnel consists of a smooth inlet cone with circular cross section and a similar outlet cone. In the central throughflow region with square cross section, up to nine wires can be positioned with equal distance to each other (*Figure 3 (right)*). The distance between the wire axes is $10\ mm$ as for the guard grille in *Figure 1 (right)*. The transition of the cross sections is designed very smooth with a long calming section to ensure a homogeneous flow where the wires are positioned. Due to boundary layer formation, the flow profile may not be completely homogeneous but well reproducible for the relative comparison of different wires in an industrial context. The wires can be manufactured of metal, coated material or they can be printed with the resin printer Elegoo Jupiter 6K. For the acoustic measurement, the wind tunnel is positioned in the centre of the partition wall in the ZIEHL-ABEGG anechoic facility. With the auxiliary fan of the test rig different flow velocities v_∞ are generated. Sound absorbers between the auxiliary fan and the anechoic rooms guarantee that there are no disturbing noise signals at the recording microphones. The acoustic measurement is done up- and downstream outside of the wind tunnel with twelve microphones on an enveloping measurement surface with radius $1.5\ m$.

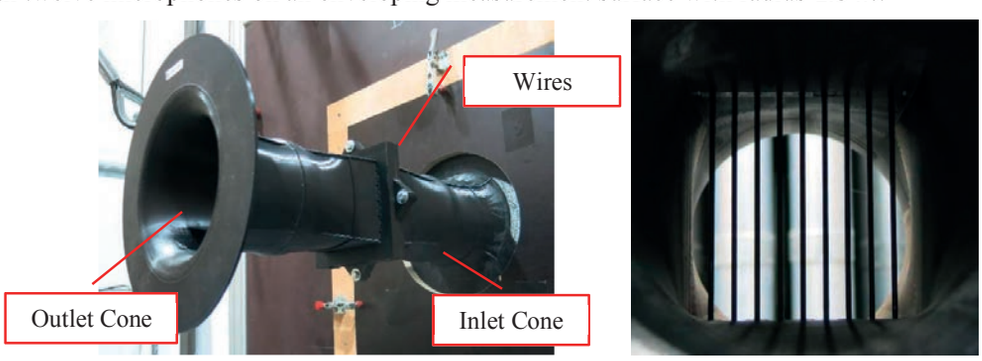


Figure 3: Wind tunnel for experimental investigations of wires (left) and array of nine wires in the wind tunnel (right)

Experimental Results

Figure 4 shows the experimental results for the noise generated by nine round wires with $D_{wire} = 2.5\ mm$ positioned equally spaced in the wind tunnel (see *Figure 3 (right)*). The pressure side sound power level $L_W 6$ increases significantly with the flow velocity (*Figure 4 (left)*, red line). The self-noise of the wind tunnel, measured without wires, is for flow velocities $v_\infty \geq 12\ m/s$ neglectable (*Figure 4 (left)*, blue line). In *Figure 4 (right)* the narrow band spectra of the wire array is compared for different upstream flow velocities v_∞, determined by the quadratic cross section area at the wire position (without blockage) and the volume flow rate measured in the test rig. For all v_∞, a major hump can be observed. The frequency f and the height of the major humps increase with increasing v_∞. This behaviour corresponds to the theory of the von Kármán vortex street [3]. Anyhow, as summed up in *Table* 1, the experimentally observed frequency of the emitted tone is higher than the theoretical vortex shedding frequency f_{theo}, calculated without blockage and $Sr = 0.21$, as described in this section. Is the blockage not neglected, the experimentally observed frequency fits better to the theoretical vortex shedding frequency $f_{theo,9wires}$. A possible reason for the remaining discrepancies are uncertainties due to inhomogeneous flow velocities in the wind tunnel because of boundary layers and the change of the cross section contour of the wind tunnel from round to quadratic.

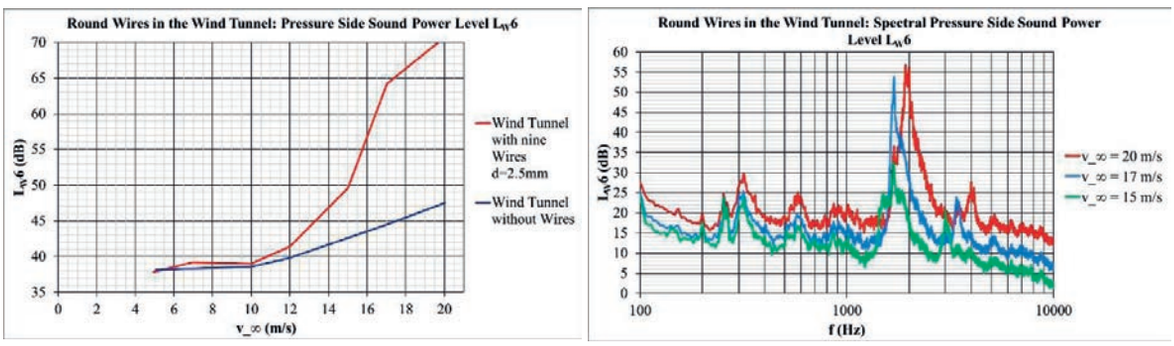


Figure 4: Experimental results of the sound power emitted by nine equally spaced round wires with $D_{wire} = 2.5\ mm$: Pressure side sound power level L_W6 as a function of v_∞ (left) and comparison of the narrow band spectra L_W6 for different values of v_∞ (right)

In further experiments with $D_{wire} = [1.5, \dots, 3.5]\ mm$ the relative change of the frequency f of the emitted noise confirms the theoretical relation of D_{wire} and the frequency f. Therefore, the conceived wind tunnel seems suitable for subsequent investigations under reproducible flow conditions concerning possible optimization approaches considering the wire design.

NUMERICAL INVESTIGATION

Numerical Setup

For deeper insight, numerical simulations using the PowerFLOWsolver 5.5a based on the Lattice-Boltzmann Method (LBM) are performed.

The Lattice-Boltzmann Method is naturally transient and compressible providing a direct insight into hydrodynamic mechanisms responsible for the acoustic sources but also into acoustic propagation. The LBM tracks the time and space evolution of a truncated particle distribution function on a lattice grid. The particle distribution evolution is driven to the equilibrium by the so-called collision operator. The discrete Lattice-Boltzmann equations are solved with 19 discrete velocities for the third order truncation of the particle distribution function, which has been shown sufficient to recover the compressible Navier-Stokes equations for a perfect gas at low Mach number in isothermal conditions [7]. In PowerFLOW, a single relaxation time is used, which is related to the dimensionless laminar kinematic viscosity [8]. This relaxation time is replaced by an effective turbulent relaxation time that is derived from a systematic Renormalization Group procedure detailed in [9]. It captures the large structures in the anechoic room but also the small turbulent scales that develop along the wall surfaces in a Large Eddy Simulation manner.

To reduce the simulation effort, only a simplified wind tunnel is modelled (*Figure 5*). The two anechoic rooms are neglected. The wind tunnel consists of an inlet channel of length $1\ m$ and an outlet channel of length $1.5\ m$. The whole model has a constant square cross section of width $15\ cm$. As for the experiments, a model of a single wire or an array of several wires can be placed between the inlet and the outlet channel. On the inlet, the left red surface, the atmospheric pressure $p = 101325\ Pa$ is imposed, while the volume flow rate Q_V defining for the given cross section area the upstream velocity v_∞ is imposed on the outlet, the right red surface. The walls of the wind tunnel are modelled as solid walls without acoustic damping conditions. Therefore channel modes and reflections on the wall are possible and may pollute the acoustic signal. But the relative change of the results are assumed to be comparable. The mesh resolution in the modelled wind tunnel is defined through successive embedded volumes. The mesh size is decreased by a factor of 2 between them. In the section of the wind tunnel where the main flow phenomena and noise sources are expected, $25\ mm$ upstream and $115\ mm$ downstream of the wires, the mesh size is $0.4\ mm$. The finest mesh size of $0.1\ mm$ is defined in an $1\ mm$ thick offset area around the wires. For the acoustical analysis inside the wind tunnel, nine microphones are placed uniformly distributed on several cross sections up- and downstream of the wires. For the results shown in the following diagrams, the nine microphones are summed up using the whole cross section area of the wind tunnel as enveloping surface. Using, as in the experiment, microphone positions outside the wind tunnel for the far field acoustics would require a much higher simulation effort. In the region of the microphones, the mesh size is $0.8\ mm$. The total numerical domain for the simulation of a single wire counts $141\ million$ fluid cells and $8\ million$ surface elements and $168\ million$ fluid cells and $11\ million$ surface elements for the simulation of 15 wires. The simulations are performed for different upstream

velocities v_∞ prescribed in terms of the flow rates Q_V at the outlet. For the initialization of the computations, a simulation with a coarse mesh (minimum cell size $0.4\ mm$), without applying the two finest mesh refinements, is performed. The simulations on the fine mesh are running about $0.066\ s$ physical time and the numerical data are acquired for the last $0.04\ s$.

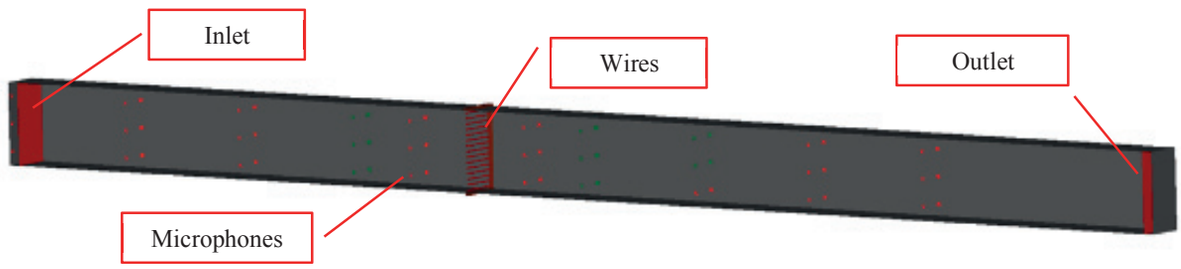


Figure 5: Computational domain of the wind tunnel

Numerical Results

To validate the numerical model, the results are compared to the experimental measurements obtained in the ZIEHL-ABEGG facilities as described in *Wind Tunnel Configuration* and *Experimental Results*.

Figure 6 shows the third-octave band spectra of L_W6 of one round wire with $D_{wire} = 2.5\ mm$ in the virtual wind tunnel for different values of v_∞. The microphones are positioned $125\ mm$ downstream of the wires. For each value of v_∞ the hump in the sound power level spectra can be observed. As in the experimental data (*Figure 4, right*), the height and the centre frequency of the humps increase with the v_∞. This behaviour fits to the theory of the von Kármán vortex street. *Table 1* shows the comparison of the theoretical expected vortex shedding frequency f_{theo} calculated without blockage and with $Sr = 0.21$, the experimentally measured frequency f_{exp} with nine wires in the wind tunnel in the ZIEHL-ABEGG facilities as well as the simulated centre frequency f_{sim} with one wire in the virtual wind tunnel (LBM) for different velocities v_∞ without blockage. It is obvious that the numerical results match well with the theory. As the acoustic humps can be observed in equivalent manner to the physical experiment and in a good agreement to the theoretical vortex shedding frequency, it is concluded that the simulation model can be used for a deeper analysis of the flow field, the noise generation mechanisms and for the investigation of acoustic optimization approaches concerning the wire geometry.

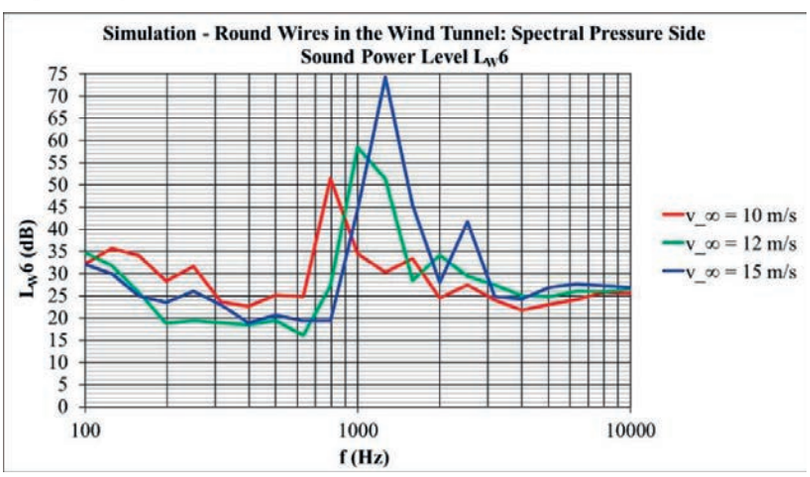


Figure 6: Simulation results of one round wire with $D_{wire} = 2.5\ mm$ in the wind tunnel: comparison of the third-octave band spectra L_W6 for different upstream velocities v_∞

Table 1: Comparison of the theoretical vortex shedding frequency f_{theo} without blockage and $f_{theo,9wires}$ with blockage by nine wires, the hump frequency f_{exp} obtained in the experiment (nine wires) and f_{sim} obtained in the simulation (one wire)

$v_\infty\ (m/s)$	$f_{theo}\ (Hz)$ $(Sr = 0.21)$	$f_{theo,9wires}\ (Hz)$ $(Sr = 0.21)$	$f_{exp}\ (Hz)$	$f_{sim}\ (Hz)$
10	840	1120		790
12	1008	1344		1000
15	1260	1680	1675	1260
17	1428	1904	1690	
20	1680	2240	1925	

Figure 7 gives an impression of the flow structures developing downstream the wire. Visualizing the vorticity magnitude on a plane perpendicular to the wire axis shows, as expected, the von Kármán vortex street (*Figure 7, left*). On a horizontal plane through the wire axis, a rather coherent vortex shedding behaviour in longitudinal direction of the wire can be observed (*Figure 7, right*).

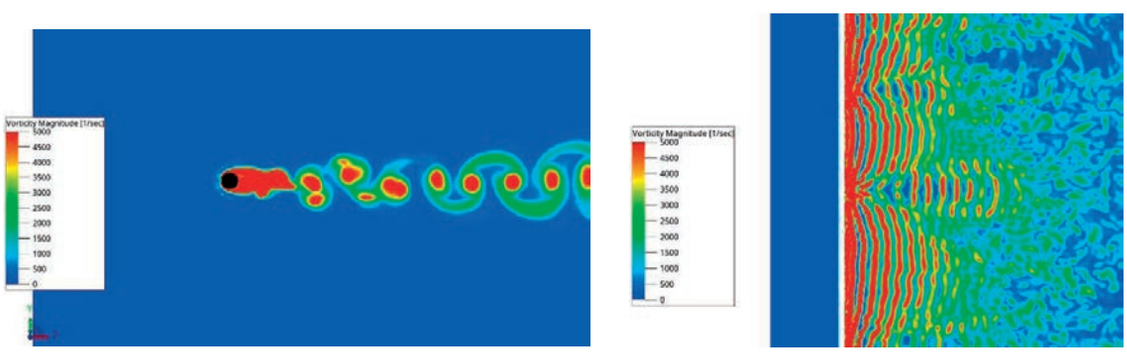


Figure 7: Simulation results of one wire with $D_{wire} = 2.5\ mm$ at velocity $v_\infty = 10\ m/s$: vorticity magnitude at a plane perpendicular to the wire axis (left) and on a plane parallel through the wire axis (right)

WIRE OPTIMIZATION

Following the hypothesis that coherent vortex shedding in longitudinal direction of the wire is causal to the strength of the hump in the acoustic spectra, it is the aim of the optimization approaches to modify the wire in a way that the vortex shedding gets more inhomogeneous in this view.

In [10] and [11], a Scruton-helix along a cylinder axis to reduce the vortex shedding of a cylindrical building is described. This idea was transferred to the guard grille wires. They were designed using 3D-CAD and, for the experimental measurements, printed with the resin printer. The numerical simulations show a slight reduction of the noise emission at the vortex shedding frequency. In addition, it can be observed that the vortex shedding downstream of the wire becomes more inhomogeneous. But the industrial usability of this geometry, especially for guard grilles made of metal wires, may be difficult and not suited for mass production.

For that reason, the aim is it to achieve a similar effect with disruptive bodies on the surface of the wire, as it is sketched for two examples in *Figure 8*. For the investigation, the number ($4 - 8\ bodies\ per\ cm^2\ surface$) and size ($0.6\ x\ 0.3\ x\ 0.3\ mm$ up to $1\ x\ 0.5\ x\ 0.5\ mm$) of the disruptive bodies applied on the wire surface is varied whereas the diameter D_{wire} is unchanged. *Figure 9 (left)* shows the simulated third-octave band spectra of the sound power level L_W6 of wires with disruptive bodies on the surface compared to a reference wire without disruptive bodies at $v_\infty = 10\ m/s$ (red line). It can be observed that the disruptive bodies reduce the noise emission at the vortex shedding frequency by $10\ dB$ up to $30\ dB$. In the simulation, the best results can be achieved for the wire with the most and biggest disruptive bodies on the surface (version 1, green line). The experimental investigation shows at $v_\infty = 15\ m/s$ similar effects (*Figure 9 (right)*). A comparison at the same velocity v_∞ is not possible as in the experiment at $v_\infty = 10\ m/s$ the self-noise of the wind tunnel is too high and as the simulations have not yet been done for higher velocities. For the measurement, the wires are printed with a resin printer and arranged in an array of nine equally spaced wires. *Figure 9 (right)* shows the measured narrow band spectra of L_W6 of the modified wires compared to reference wires without disruptive bodies (red

line). In agreement to the numerical results, the noise emission at the vortex shedding frequency (tone at $f \sim 1600\ Hz$) is reduced by $10 - 20\ dB$ due to the disruptive bodies on the surface. Additionally the second harmonic (tone at $f \sim 3000\ Hz$) is reduced by $10\ dB$. The tones at lower frequencies ($f = 250 - 300\ Hz$) belong to the self-noise of the wind tunnel and can be neglected in this investigation. In the experiments, the differences between the three optimized geometries are smaller compared to the simulations, and the wire with the less and biggest disruptive bodies on the surface gives the best results (version 2, pink line). One possible reason for these deviations is that in the simulation, the mesh resolution is not fine enough to resolve all effects of the disruptive bodies. Because of the high computational effort, a mesh refinement has not been considered.

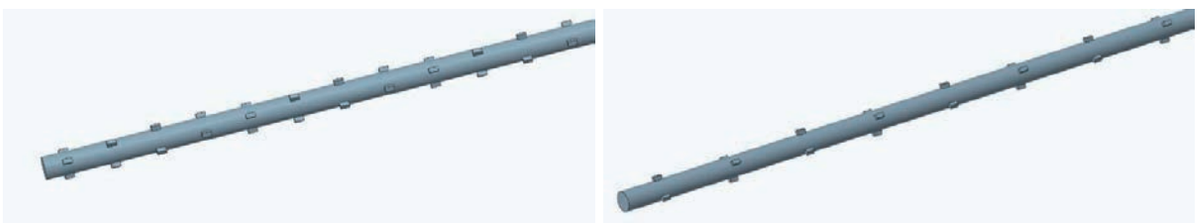


Figure 8: Two versions of the optimized wires with disruptive bodies on the surface (left: version 1 and right: version 2)

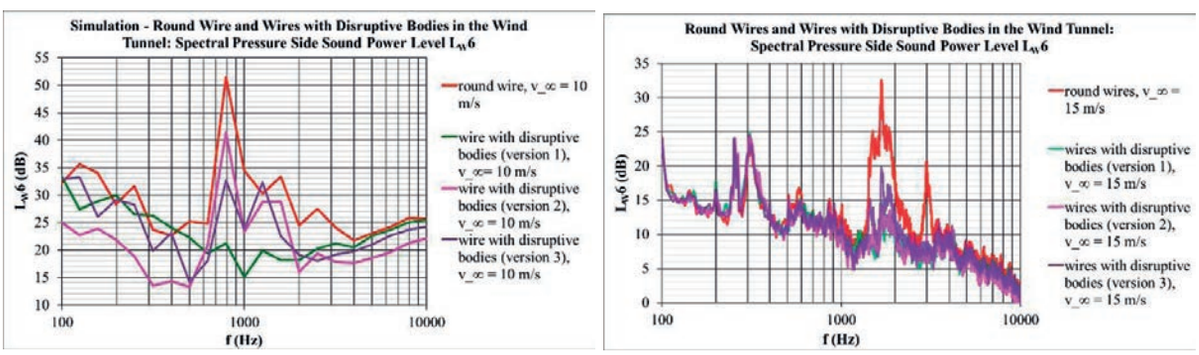


Figure 9: Numerical and experimental results of round wires with disruptive bodies in the wind tunnel: comparison of the simulated third-octave band spectra of L_W6 at $v_\infty = 10\ m/s$ (left) and comparison of the experimentally measured narrow band spectra L_W6 at $v_\infty = 15\ m/s$ (right)

For the wires with disruptive bodies, a vortex shedding, the von Kármán vortex street is visualized in *Figure 10, left*. Comparatively to the reference wire, the vortex shedding is still clearly present in less homogeneous and less symmetrical form. Visualizing the vorticity magnitude on a horizontal plane through the wire axis as depicted in *Figure 10 (right)* shows that the vortex shedding, compared to a round wire (*Figure 7, right)*, is, due to the disruptive bodies on the surface of the wire, less homogeneous and less coherent in longitudinal direction of the wire. This is assumed to be the reason for the reduced noise emission.

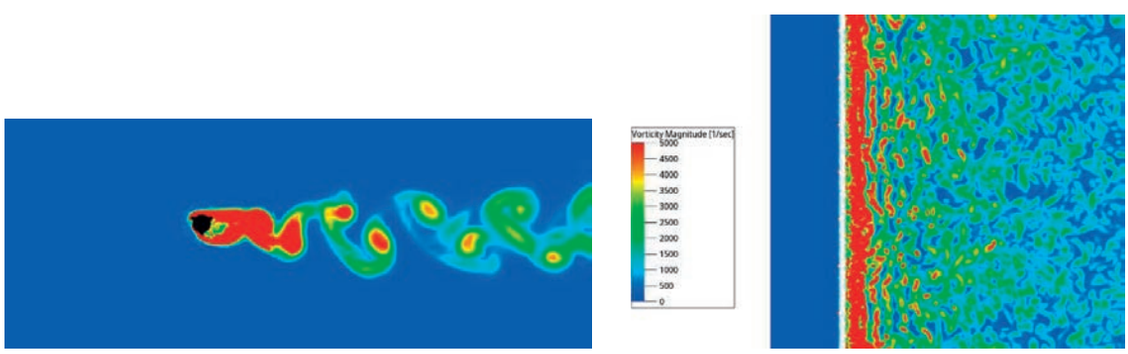


Figure 10: Simulation results of one wire with $D_{wire} = 2.5\ mm$ and disruptive bodies (version 1) at velocity $v_\infty = 10\ m/s$: vorticity magnitude on a plane perpendicular to the wire axis (left) and on a plane parallel through the wire axis (right)

Complementing, the shaping of the wire cross-section as an ellipse with $y = \pm 0.57\sqrt{4 - x^2}$ or like an aerofoil with chord length $4\ mm$ and maximum thickness $1.5\ mm$ has been investigated. Anyhow, this design increases the sound emission at the vortex shedding frequency by up to $20\ dB$ (*Figure 11, left*) and the vortex shedding downstream of the wire becomes more homogeneous and coherent in the longitudinal direction

(*Figure 11, right*). This confirms the assumption that a homogeneous and coherent vortex shedding in longitudinal direction of the wire is a condition for a high tonal noise emission at the vortex shedding frequency.

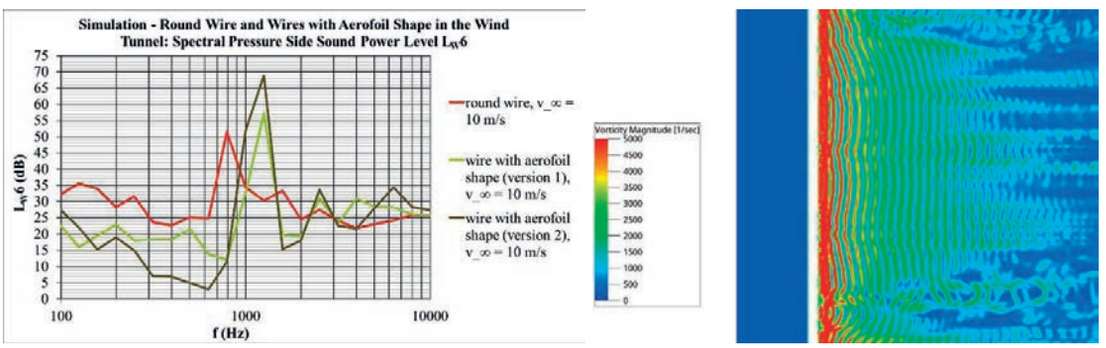


Figure 11: Numerical results of wires with aerofoil shape for $v_\infty = 10\ m/s$: comparison of the simulated third-octave band spectra L_w6 (left) and vorticity magnitude on a plane parallel through the wire axis (right)

Experimental Results of an Implementation

For the industrial usage it seems difficult and costly to manufacture wires with disruptive bodies on the surface. An approach to overcome this disadvantage is it to integrate or to attach small particles like sand in the coating of the wires to generate a rough and disrupting surface on the wires. To investigate that, some wire probes are coated, and sand was applied randomly on the wet coating. The grain size and the amount of sand is varied. *Figure 12* shows enhanced photographs of wire samples manufactured in that way. The experimental sound measurements of these prototype wires confirm the effect of the disruptive bodies on their surface (*Figure 13*). Compared to the round steel wire with smooth surface (*Figure 13, left,* red line), L_W6 is reduced in the whole upstream velocity range by the sand on the surface (blue lines). For high velocities ($v_\infty \geq 15\ m/s$), the noise reduction of the best prototypes printed in resin could not be achieved. Anyhow, the comparison of the narrow band spectra of L_W6 at $v_\infty = 15\ m/s$ shows a significant reduction of the acoustic hump at the vortex shedding frequency and the second harmonic due to the sand on the surface of the steel wires (*Figure 13, right*). The noise emission at other frequencies is not severely influenced.

In further investigations, the influence of grain size, density and arrangement of the disruptive bodies on the surface of the round steel wires has to be investigated and optimized. Additionally, this method is still to be transferred to an entire guard grille, and the acoustic and aerodynamic performance has to be proofed in fan measurements.

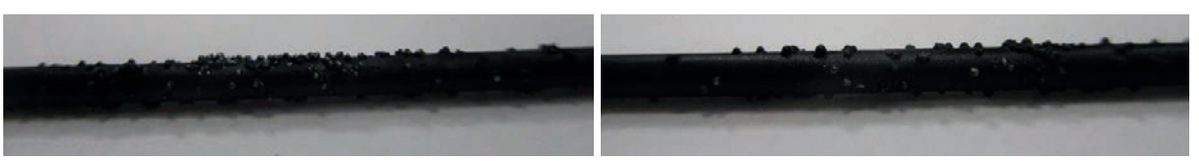


Figure 12: Round steel wires with sand on their surface

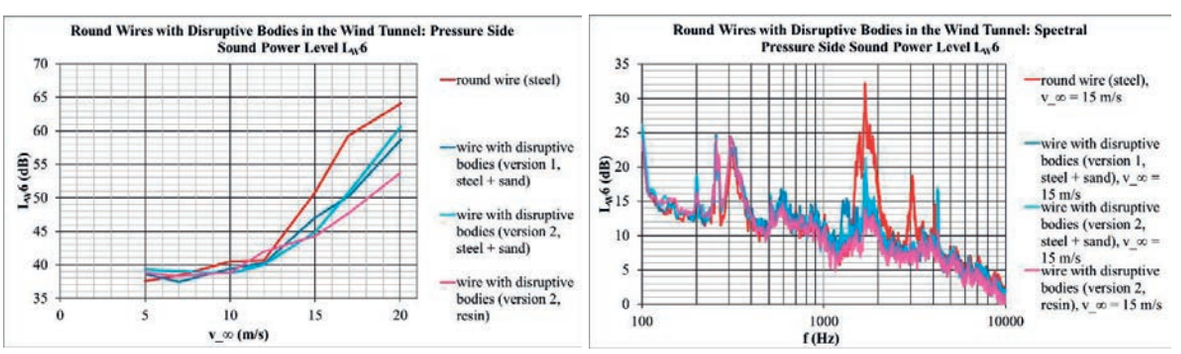


Figure 13: Experimental results for round steel wires with $D_{wire} = 2.5\ mm$ and disruptive bodies on the surface (sand): pressure side sound power level L_W6 as a function of v_∞ (left) and comparison of the narrow band spectra of L_W6 at $v_\infty = 15\ m/s$ (right)

CONCLUSION

In axial fan applications, the rotating parts often must be protected with a guard grille. Such guard grilles are commonly built up by wires of circular cross-section. Especially for modern fans generating low self-noise, the additional noise emission caused by the guard grilles can become an important or dominant noise source. In the investigated axial fan case, the pressure side sound power level is increased by up to $2\ dB$.

For basic experimental investigations of the sound generation induced by a flow around wires, a wind tunnel as well as a numerical model using a Lattice-Boltzmann solver of it have been built up. The frequency range of the generated sound, found both in the experiment and in the simulation, corresponds to the increase of the noise emission due to the guard grille of the investigated axial fan under comparable flow conditions. The unsteady simulations show that periodic flow separations (von Kármán vortex street) cause a significant increase in the emitted sound power in a frequency region that depends on the wire diameter and the flow velocity. Further, it can be observed in the simulation results that downstream the round wires, the von Kármán vortex street is very homogeneous and coherent in longitudinal direction.

In further CFD simulations and experiments it was found out that interrupting the von Kármán vortex street in longitudinal direction of the wire and making the flow separation more inhomogeneous and incoherent, the noise emission at the vortex shedding frequency can be reduced significantly. Known structures to achieve this are protruding helix spirals on the wire surface. The industrial usability, however, is challenging, as it is complex to implement helix spirals on the wires. In this work, the approach to make the flow separation more inhomogeneous by putting small disruptive bodies on the surface of the wires shows a high potential. The possibility to include small particles in or on the coating of the wires to generate a rough and disrupting surface on the wires was investigated. The results are very promising and a substantial sound power reduction could be proven experimentally for wires with randomly integrated sand grains on their surface.

As next steps, the disruptive bodies will be applied to a whole guard grille and their beneficial effect has to be assessed in fan measurements. For industrialization, the process of the surface modification is still to be developed. Additionally, further properties of the new guard grilles with modified surfaces like the pressure drop and the resistance to corrosion must be examined.

ACKNOWLEDGEMENTS

This work was supported within the project “WarmHome” Förderkennzeichen 03EN4065E funded by the Bundesministerium für Wirtschaft und Klimaschutz - BMWK.

BIBLIOGRAPHY

[1] Eck, B.: *Ventilatoren.* 6. Edition, Springer Verlag, **1991**

[2] M. Schneider, A. Lucius, R. Pazhanisamy – *Einfluss von Schutzgittern auf die Akustik von Axialventilatoren*. DAGA - Jahrestagung für Akustik, Wien, **2021**

[3] Th. V. Kármán – *Über den Mechanismus des Widerstandes, den ein bewegter Körper in einer Flüssigkeit erzeugt, Nachr. Ges. Wiss., Math. Phys. Klasse*, *509-517 http://eudml.org/doc/58812 Göttingen*, **1911**

[4] V. Strouhal – *Über eine besondere Art der Tonerregung, Ann. Phys. Und Chemie, Neue Folge 5*, *216-251*, https://doi.org/10.1002/andp.18782411005, **1878**

[5] H. Henn, Gh. R. Sinambari, M. Fallen – *Ingenieurakustik* 4., überarbeitete und erweiterte Auflage, Vieweg+Teubner, ISBN 978-3-8348-0255-2, **2008**

[6] T. Wahl – *Simulation und experimentelle Untersuchung von Fluid-Struktur-Interaktionen am Beispiel der Umströmung eines Zylinders sowie einer Zylinder-Quader-Konfiguration.* Master-Thesis Fachhochschule Düsseldorf, **2012**

[7] S. Chen, G.D. Doolen – *Annual Review of Fluid mechanics 30:329-364 ISSN 00664189, 1545-4479,* **1998**

[8] S. Marié – *Etude de la méthode Boltzmann sur Réseau pour les simulations en aéroacoustique., Ph.D. thesis Université Pierre et Marie Curie – Paris VI,* **2008**

[9] H. Chen, O. Filippova, J. Hoch, K. Molvig, R. Shock, C. Teixeira and R. Zhang – *Physica A: Statistical Mechanics and its Applications 362:158-167 ISSN 03784371,* **2006**

[10] DBZ Deutsche Bauzeitschrift - *thyssenkrupp Testturm, Rottweil*, https://www.dbz.de/artikel/thyssenkrupp-testturm-rottweil-3156533.html

[11] SKI Consult - *Wirbelerregte Querschwingung,* https://ski-consult.de/taetigkeitsbreiche/strukturanalysen/wirbelerregte-querschwingung/

ANNEXES / APPENDIXES

Variable Symbols, Units and Definitions

D	(m)	outer diameter of the fan
D_{wire}	(m)	diameter of the wire
f	(Hz)	frequency
f_{theo}	(Hz)	theoretical vortex shedding frequency
$f_{theo,9wires}$	(Hz)	theoretical vortex shedding frequency with blockage of nine wires
f_{exp}	(Hz)	experimentally measured frequency
f_{sim}	(Hz)	simulated frequency
$L_W 6$	(dB)	pressure side sound power level
$L_W 6_{spec}$	(dB)	specific pressure side sound power level
n	(rpm)	rotation speed of the impeller
p	(Pa)	pressure
Q_V	(m^3/h)	volume flow rate
Re	$(-)$	Reynolds number
$Sr = f \cdot D_{wire}/v_\infty$	$(-)$	Strouhal number
v_∞	(m/s)	far field flow velocity
δ	$(-)$	specific diameter
ψ_{stat}	$(-)$	dimensionless static pressure rise

ADVENTAGE: SCALABLE HYBRID NOISE CONTROL SYSTEMS FOR FANS

Valentin MEES[1], David GOECKE[2]

[1] *Fraunhofer LBF, Bartningstr. 47, 64289 Darmstadt, Germany*

[2] *Fraunhofer IBP, Nobelstr. 12, 70569 Stuttgart, Germany*

SUMMARY

The project ADVentAGe focuses on developing technologies for integrating hybrid reactive and active noise control systems into fan components, aiming to reduce noise emissions and enhance sound quality. Traditional passive noise control often struggles with installation constraints and high demands for noise reduction. Active systems provide a compact, adaptable alternative but can be costly, posing challenges for small and medium-sized enterprises (SMEs). The project seeks scalable, cost-effective solutions, showing potential for up to 15 dB tonal noise reduction in initial tests. This hybrid approach not only opens new market opportunities for fan manufacturers but also establishes a new business area, particularly beneficial for SMEs in meeting stringent noise regulations.

INTRODUCTION

Fans are used in different sizes and installation conditions depending on the application and requirements. The most common types are axial and centrifugal fans. During operation, unwanted noise is generated by moving air and fan blades, which propagates from both the inlet and exhaust sides and radiates into the acoustic free field. The ADVentAGe research project aims to develop and validate technologies that modify fan housings or typical fan components, such as inlet nozzles, protective grilles, and diffusers, with integrated hybrid active noise control systems to reduce acoustic emission and optimise sound quality. While components such as guard grilles or guide vanes generally introduce additional noise, diffusers or pre-guidance grilles often provide passive noise reduction in addition to improving the aerodynamic efficiency of fans. However, many applications require additional silencers to meet regulatory or customer requirements, which can be much larger than the fan itself and can represent a significant portion of the total fan system cost. Active noise control (ANC) systems can be a valuable addition due to their compact design, adaptability to variable operating and installation conditions, and higher noise reduction in certain circumstances.

Until now, it has been possible to meet existing noise control requirements with conventional passive noise control measures, so there was no significant market pressure to implement active noise control

measures. In the past, fan manufacturers also had only limited expertise in the areas of active control technology, signal processing, microelectronics, and acoustic transducer systems, which has been a significant barrier to entry for the product integration of ANC systems.

An increasing number of variants, as well as rising noise control requirements with the same or tighter installation space requirements, are pushing conventional passive noise control measures to their limits, so that fan manufacturers are increasingly considering more space-efficient systems like ANC as a future addition, leading to hybrid active noise control systems. This is also because modern fans often already have powerful electronics integrated for control and regulation technology. Larger fan manufacturers have therefore increasingly built in-house expertise in control technology and electronics in recent years. This has significantly reduced the barrier to market-driven product integration of hybrid active noise control systems. For SMEs with no electronics development of their own, the entry hurdle still remains high. Technology transfer measures for SMEs are therefore an integral part of the 'ADVentAGe' project.

In summary, five requirements can be formulated that must be met from the perspective of fan manufacturers and their customers for the commercially successful implementation of hybrid active noise control systems in fans:

1. Compactness: In most fan applications, the installation space is very limited. Noise control measures must therefore be very compact. This applies in particular to active noise control systems to compensate for the increased technological complexity compared to purely passive measures.

2. Simplicity: A major challenge in the implementation of noise control systems is to ensure that installation, commissioning, and maintenance are simple. The hybrid active noise control system must be highly automated and robust, and kept as simple as possible for operators; for example, the system should not require complex on-site adjustment by the end customer.

3. Flexibility and compatibility: The hybrid active noise control system must have a high degree of self-adaptability and function for different installation situations and derivatives so that the overall system of fan and noise control system can be delivered by the fan manufacturer to the device manufacturer in such a way that the device manufacturer can integrate and use the overall system directly in his device or equipment (plug & play).

4. Reliability and service life: The hybrid active noise control system should also be able to achieve the high service life of 25,000 to 40,000 operating hours required for fans, even under the influence of weather conditions.

5. Costs: The active noise control system must be cost-effective and, if possible, use standard components. However, this requirement cannot be easily quantified in a monetary amount. The additional costs accepted by the market depend on the explicit added value of the system regarding the criteria listed under points 1 to 4 and on the base price of the fan system. Even though active noise control systems are already being mass-produced in the automotive sector, the absolute costs for an application-specific hybrid active noise control system can only be quantified after extensive preliminary investigations. The focus of the ADVentAGe research project is therefore not only on acoustic optimisation but also on developing scalable solutions that, on the one hand, remain very compact in terms of installation space and, on the other hand, cause the lowest possible additional costs in production, operation, and maintenance.

Two exemplary fan applications are used as case studies to demonstrate the design and implementation of hybrid systems of any combination of passive absorbers, activated resonators and adaptive ANC systems. Each of these measures has its own set of challenges, limitations, and potential. Passive absorbers, for example, are particularly effective at reducing higher frequencies, although a significant amount of material is required to achieve a notable effect at low frequencies. The objective of the project is to combine these potential benefits in an optimal way, while simultaneously addressing the challenges associated with future implementations.

ACOUSTIC EMISSION IN FAN SYSTEMS

In collaboration with research institutions and the project-supporting group, we will analyse the boundary conditions based on the fans' technical specifications and installation conditions. The selected scenarios will represent typical applications, and benchmark studies will be conducted on the experimental setups. We will assess the potential for hybrid active noise control systems based on the benchmark tests and fan characteristics. Industry partners provided the necessary technical data and specifications for the fans and any existing add-on components.

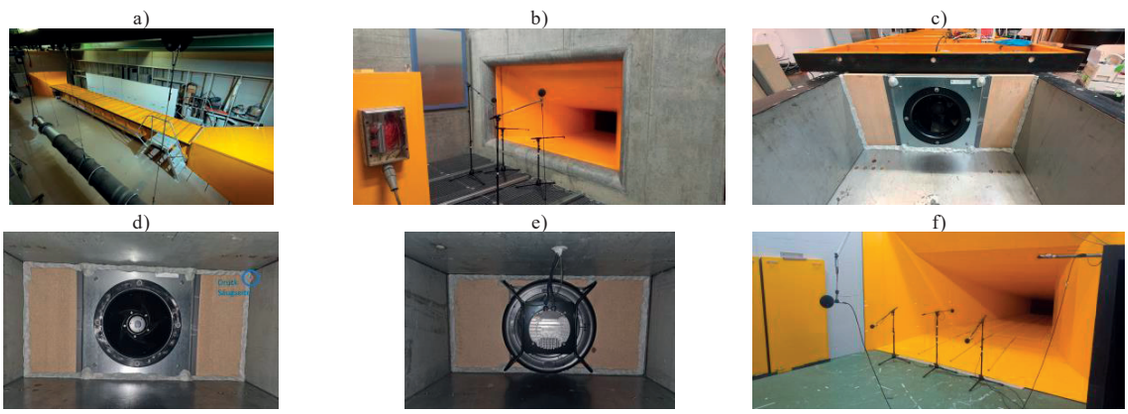


Figure 1: Experimental setup of the radial fan. © Fraunhofer IBP
a) Wind tunnel at Fraunhofer IBP, b) Sending room with microphone, c) Radial fan in the open wind tunnel, d) Radial fan in the closed wind tunnel, inlet side, e) Radial fan in the closed wind tunnel, f) Receiving room with microphone

To discuss sound reduction, it is first necessary to define the characteristics of the fan noise in question. For the present project, two types of fans are examined: an axial fan and a radial fan. The axial fan is configured like an air heat pump, drawing in air through a heat exchanger and blowing it out freely. The radial fan is mounted inside a ventilation duct. Both configurations have significant differences, but also similarities in the fundamental noise characteristics.

Figure 1 shows the experimental setup in the wind tunnel at Fraunhofer IBP. The radial fan is centred inside the duct using a rigid adapter plate. The pressure difference between inlet and exhaust is measured using a circular manifold around the inlet and a test tube on the exhaust side. The pressure difference can be adjusted by setting the air flow in the wind tunnel. Figure 2 shows the experimental setup of the axial fan in a box covered by a perforated plate to emulate the flow resistance of a heat exchanger.

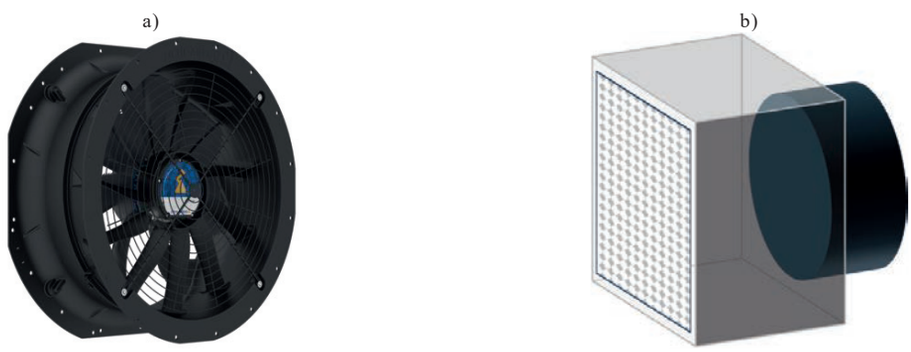


Figure 2: a) Axial fan Ziehl-Abegg FE2owlet © Ziehl-Abegg; b) Experimental setup in covered box.

INITIAL MEASUREMENTS

The setup for the wind tunnel tests, as depicted in Figure 1, examines the acoustic behaviour within and downstream of a ventilation system relative to the wind tunnel. The fan is affixed to a wooden

plate and positioned centrally within the wind tunnel tube that is 100 cm wide and 50 cm high. Initial benchmark measurements in acoustic diffuse fields in both the sending room (see Figure 1b) and the receiving room (see Figure 1f) have already been conducted. Presented are the results where only the fan, and not the wind turbine of the wind tunnel, was activated.

The experimental setup at Fraunhofer LBF consists of a 6 m long section of straight ventilation duct with the same inner dimensions as the previously mentioned wind tunnel, i.e. 100 cm wide and 50 cm high. This is chosen for comparability with the wind tunnel tests. The fan is mounted to a rigid plate, centred in the duct. Microphones are placed along the centre of the duct at 75 cm and 225 cm upstream and downstream from the fan. On the exhaust side, additional microphones are placed at 1/3rd and 2/3rd of the duct height, 15 cm from the walls at 75 cm from the fan and 5 cm from the walls at 225 cm from the fan. The exhaust outlet is enclosed by a quarter sphere according to [40].

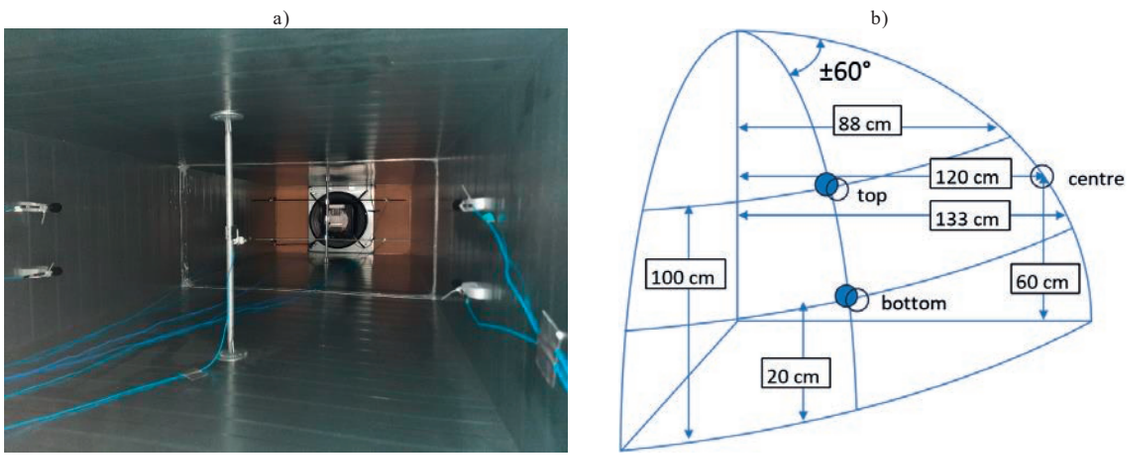


Figure 3: a) Radial fan in the ventilation duct, exhaust side with microphones, b) Quarter sphere arrangement

The measurements in both setups yield comparable results in terms of amplitude and frequency content. While the wind tunnel measurements show slightly more prominent 2nd, 4th and 6th blade passing harmonics, the duct measurements show additional peaks at the 3rd and 5th blade passing harmonics with an elevated noise floor at the bottom microphones. This is likely due to turbulences at the outlet combined with the low clearance of 20 cm between the microphones and the floor.

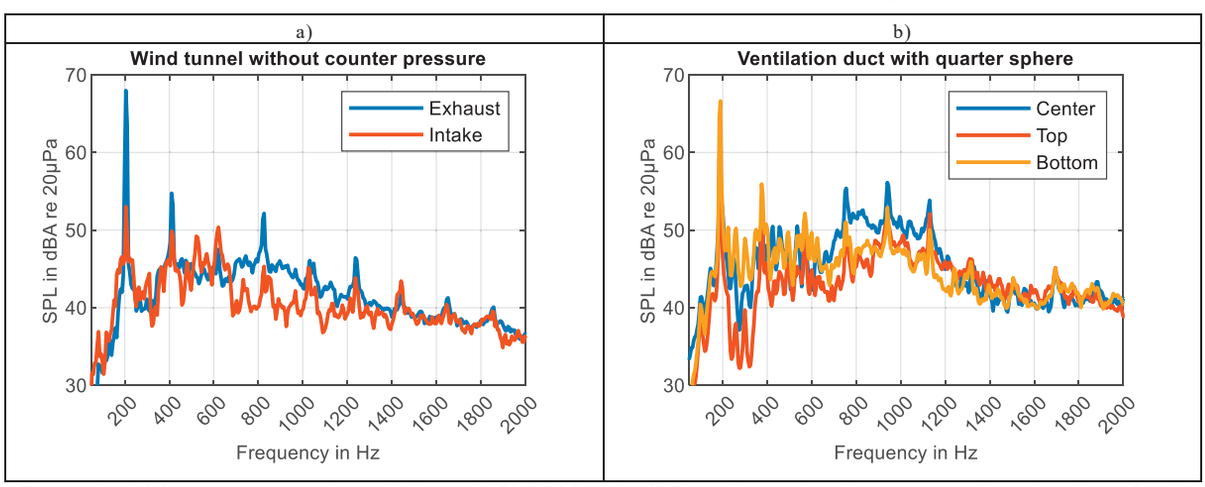


Figure 4: a) Measurement results with fan at 2473 RPM in the IBP wind tunnel without activated wind turbine. Intake side measured in the sending room (see Figure 1b), exhaust side measured in receiving room (see Figure 1f). b) Measurement results with fan at 2460 RPM in the ventilation duct setup (see Figure 3). Exhaust side measured on quarter sphere above reflective surface.

Both setups show the most prominent noise component at the primary blade passing frequency of 205-206 Hz. This peak can be reduced by 10-15 dB until the 2nd and 4th harmonic become more prominent.

With these initial results, the characterisation and development of (re)active measures against the identified (tonal) sound components will show the potential to reduce the noise of these fans. An overview of possible approaches to fan noise reduction is given below, focussing on the challenge of being effective at the low frequency of 200 Hz.

CURRENT STATE OF RESEARCH AND DEVELOPMENT

Passive Absorbers

Passive noise control measures for fans are usually based on acoustically absorbent materials such as rock wool or specially designed acoustic resonators (Helmholtz resonators). Porous absorbers remove kinetic energy from sound waves through internal friction and are effective across a broad spectrum. Resonators, on the other hand, are tuned to a specific frequency and only absorb sound waves in a limited frequency band. The effectiveness of both principles is limited at low frequencies because the required installation space increases with decreasing frequency and therefore increasing acoustic wavelength.

Active noise control systems are not subject to the same limitations as passive noise control measures. Especially at low frequencies, noise reductions can be achieved in a compact space that cannot be realised with passive measures. Active noise control systems can generally be categorised into approaches with feedback and feed-forward control concepts. Examples of implementation in the field of ventilation technology can be found, for example, in the field of active noise control with activated resonators or ANC systems (see Figure 6).

Activated Resonators

An instance of an active feedback control system is the active resonator silencer created at Fraunhofer IBP [1]. Recently, the emphasis in advancing active resonators has been on shrinking the size of the units to broaden their applications [2–4]. Moreover, the examination of the control circuit and partial automation of system fine-tuning were approached from a signal processing perspective [5]. In the finished internal Fraunhofer research initiative "ReinluftAkustik" [6], aimed at the "Optimization of Compact Ventilation Systems and Air Purification Devices", soundproofing concepts for air purifiers with activated resonators were devised and their efficacy assessed [7,8].

An example of a successful application is active resonator silencer cassettes (ASCs), which have been under development at Fraunhofer IBP for over twenty years [9]. The housing of the active resonator includes a microphone, a loudspeaker, and an electronic module. The loudspeaker and the air volume behind it create a spring-mass system that maximizes insertion loss at its resonance frequency. The microphone located close to the loudspeaker membrane, and the electronic module form a control loop where the microphone voltage, proportional to the sound pressure, gets inverted and sent back to the loudspeaker. This loop actively aids membrane movement, considerably boosting insertion loss compared to the non-amplified scenario. A continuous shift of this attenuation peak can be achieved by placing a second microphone behind the loudspeaker, in the rear volume [10]. A challenge in developing feedback control systems is carefully designing this feedback loop to ensure efficient and robust performance under practical conditions [2].

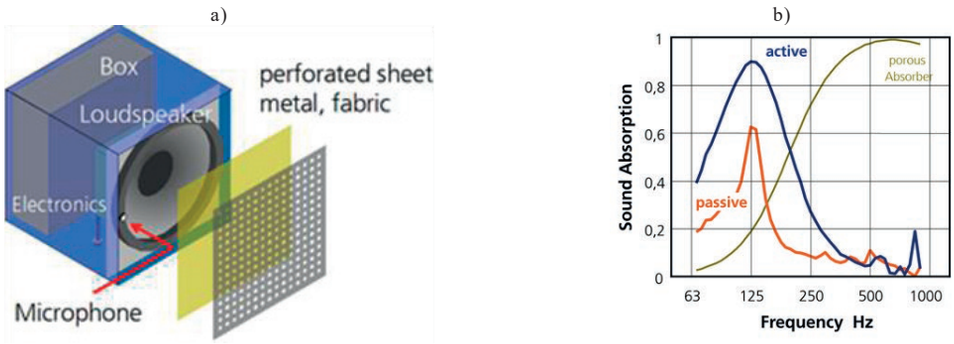


Figure 5 a) 3D drawing of an ASC; b) sound absorption coefficient (normal incidence angle) of a porous absorber and an ASC with open and closed control loop. © Fraunhofer IBP

An ASC consists of a loudspeaker housed in an airtight casing, a microphone placed near the loudspeaker membrane, and an analogue electronic control circuit with adjustable gain. The fundamental components of a "classical" ASC are depicted in Figure 5a). Essentially, a passive ASC functions as a mass-spring-damper system. The loudspeaker membrane acts as the mass, while the membrane suspension and the enclosed air volume within the casing form the spring. Viscoelasticity in the membrane suspension and other effects introduce some damping to the resonant system. Figure 5 b) shows that the absorption coefficient of the passive ASC (control off) has a relatively sharp peak at approximately 125 Hz, which corresponds to the resonance frequency of the mass-spring-damper system. Closing the feedback loop around the microphone-loudspeaker pair (control on) enhances the natural membrane movement around the ASC resonance frequency. Figure 5b) illustrates that for the absorption coefficient of the activated ASC, the peak around 125 Hz is broader in frequency and has a higher amplitude. For comparison, Figure 5b) also presents the absorption characteristics of a porous absorber, which is inefficient at low frequencies.

Previously, ASCs have been effectively used as low-frequency absorbers in various technical noise control scenarios [11–13]. Figure 6 presents three designs for ASC silencer systems. The first design, depicted in Figure 6a), features an ASC flush-mounted in the wall of a duct, with porous absorption material on the opposite duct wall. This setup is ideal for air ventilation ducts with relatively low airflow speeds and standard climate conditions. The second design, shown in Figure 6b), is similar to the first but tailored for use in the exhausts of heating systems, where burners generate low-frequency noise. In this setup, the ASC is situated in a duct branch to remove it from the flow and lessen the effects of high exhaust gas temperatures, which affects the ASC's effective resonance frequency. A protective foil shields the electro-mechanical components from heat and condensate. The third design, illustrated in Figure 6c), includes an ASC installed in a labyrinth wall opening. Such openings in building walls and enclosures are often necessary for pressure equalization, natural ventilation, fresh air intake, and exhaust gas expulsion.

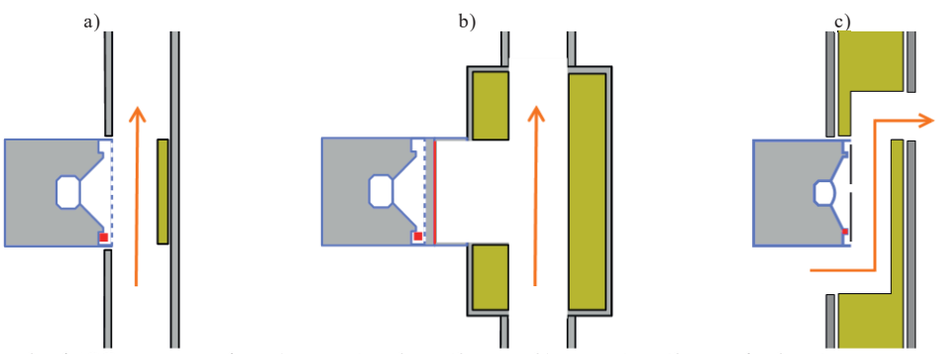


Figure 6: Sketch of ASCs concepts for: a) an active duct silencer; b) an active silencer for heating systems; c) an active labyrinth wall opening. © Fraunhofer IBP

Adaptive Active Noise Control Systems

ANC systems with feedforward control concepts are an efficient way of actively controlling noise [14], e.g. noise propagation in ventilation ducts [15–17]. In typical broadband feedforward ANC systems, a microphone placed upstream in the duct measures sound waves propagating as a reference signal. This signal is filtered by a controller so that a control loudspeaker placed downstream generates a sound wave with the same amplitude and inverted phase. When these two sound waves overlap, they cancel each other out. The concept of feedforward ANC systems was first developed and patented in the 1930's [18]. Adaptive digital filters are often used as controllers which automatically adapt to the sound wave propagating in the duct in real time. This ensures that the control loudspeaker is optimally driven to cancel out the propagating sound wave, even when the operating conditions of the ventilation system vary. Common algorithms for the automated adaptation of the controller are the LMS algorithm and variants that enable faster (e.g. FxNLMS) or more robust adaptation (e.g. RLS), albeit with a higher computational load [19,20]. A functional demonstrator of a ventilation duct with a feedforward ANC system has already been implemented at the Fraunhofer LBF [21] and presented at the Hannover Messe (HMI) in 2015. As part of a further development, the control was implemented on low-cost hardware [22] and methods for automated controller adjustment to a time-variant excitation and controlled system behaviour were investigated [23].

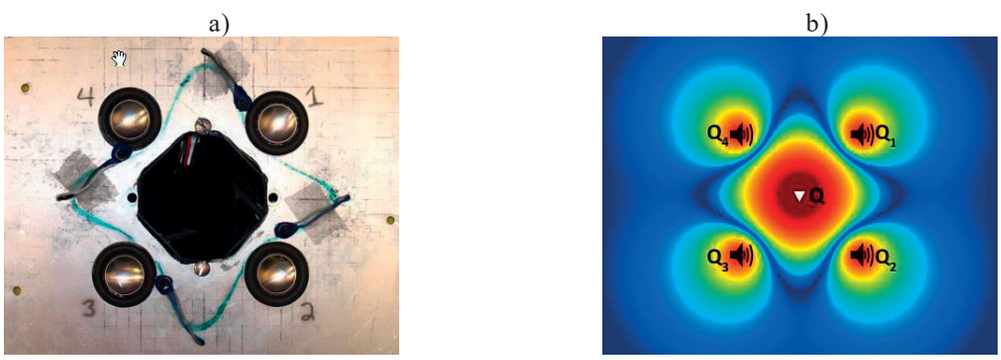


Figure 7: Symmetrically placed speakers outside the fan. a) experimental setup; b) ideal ANC with simplified fan model.[24].

In the case of fan noise, it is often the tonal components of the noise spectrum correlated to the fan speed that dominate the overall level and, from a psychoacoustic point of view, are particularly noticeable. In this case, narrowband feedforward ANC systems can be used in which the reference microphones are omitted, and a fan speed measurement input is added to the controller. These systems are computationally very efficient, robust, and allow for a more compact system configuration since the reference and control signals do not necessarily have to be time-causal [25]. If a fan is installed in a wall opening or in ducts with a large cross-section, it may be necessary to use a multi-channel control system (MIMO) with several sensors and actuators to adequately detect and effectively influence the acoustic field due to the geometrically complex sound radiation. Figure 7 shows the implementation of a MIMO feedforward ANC system for a fan installed in the wall opening [24]. Despite their greater complexity, multichannel narrowband feedforward ANC systems can be implemented very efficiently in terms of computing time for speed-correlated disturbances [25]. MIMO ANC systems have already been investigated and implemented at Fraunhofer LBF to reduce broadband road-induced vehicle interior or fan noise [17,26].

Further challenges in the development of feedforward ANC systems are discretisation errors and delays caused by the hardware, which must be considered in a system design [27,28]. The strategies for application can be categorised according to the type of fan or the location of the active noise control system. It is advantageous to place the secondary sources close to the primary source in terms of wavelength. Thus, primary and secondary sources can be considered as a coupled system and the radiated sound power of the system can be effectively reduced [29]. For centrifugal fans with a

housing, approaches exist that use ANC actuators in the transition to the pipe flange [30]. Centrifugal fans with slightly longer pipes in the exhaust direction also allow for ANC based on the modal propagation in the pipe [24]. For axial fans, there are both coaxial approaches that either mount additional loudspeakers on or in front of the axis [31] or excite the fan itself [32,33], as well as sound field-based approaches in which several loudspeakers are placed outside the rotating system [34,35]. The latter can also be considered as an "Electronically Controlled Acoustic Shadow" (ECAS) [36,37]. In the recently completed internal Fraunhofer research project “ReinluftAkustik”, a broadband feedforward ANC system for reducing the sound radiated into the free field was implemented as a prototype for an air purification device by Fraunhofer LBF (Figure 8) The noise is captured by five microphones close to the source, just above the filter outlet. A noise-cancelling signal is calculated by the adaptive digital controller and emitted by a loudspeaker array at the air outlet. The sound radiation in the low frequency range up to about 700 Hz can be clearly observed in the plane about 40 cm above the air outlet. This corresponds to the preferred frequency range for ANC systems. A subsequent determination of the sound power in accordance with ISO 3744 showed relevant level reductions for all operating conditions.

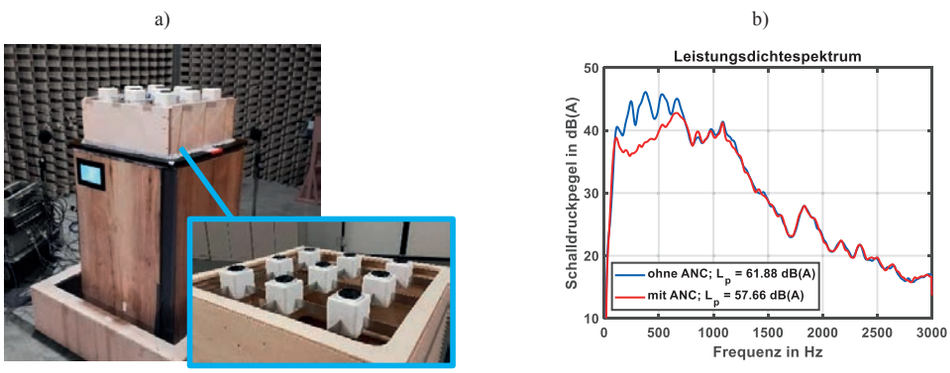


Figure 8: Characterization of a feedforward ANC system for an air purification device at Fraunhofer IBP. a) experimental setup; b) average sound pressure level 40 cm above the air outlet © Fraunhofer LBF

SCIENTIFIC AND TECHNICAL APPROACH

Beyond the state of the art, the ‘ADVentAGe’ project is working on integrating hybrid active noise control measures into compact fan attachments. The necessity for combining the noise control measures arises from the application-specific requirements for the simultaneous reduction of tonal noise peaks, low-frequency hum, and broadband random noise. Beyond the state of the art, the hybrid active noise control measures are specifically designed to reduce the sound radiation of fans into the acoustic free field: In this context, current research includes approaches for considering the primary and secondary source as a coupled system [38] and approaches for optimising the far-field radiation behaviour of ANC systems using beam forming [39]. Transferring these methods is a useful extension of the state of the art.

The aim of the project is to develop compact fan attachments with hybrid active noise control measures for broadband reduction of noise radiation, especially into the acoustic free field. The developed hybrid active noise control measures will be integrable into typical fan attachments and combinable with them. They will be scalable to any size and applicable to different fan types and typical application scenarios. The desired high degree of autonomy of the active noise control systems will meet the requirements for easy implementation. For testing and validation purposes, a functional demonstrator is being constructed that will be tested within the project on the inlet and exhaust side of an axial fan and a radial fan. The requirements for the reduction of tonal or broadband components as well as the installation situation result in application-specific requirements for active noise control systems. Depending on the application, the focus is on tonal and/or broadband noise components.

FAN 2025
Antibes Juan-les-Pins (France), 9 – 11 April 2025

The full noise reduction potential will only be achieved by combining active and passive concepts in a hybrid active noise control system.

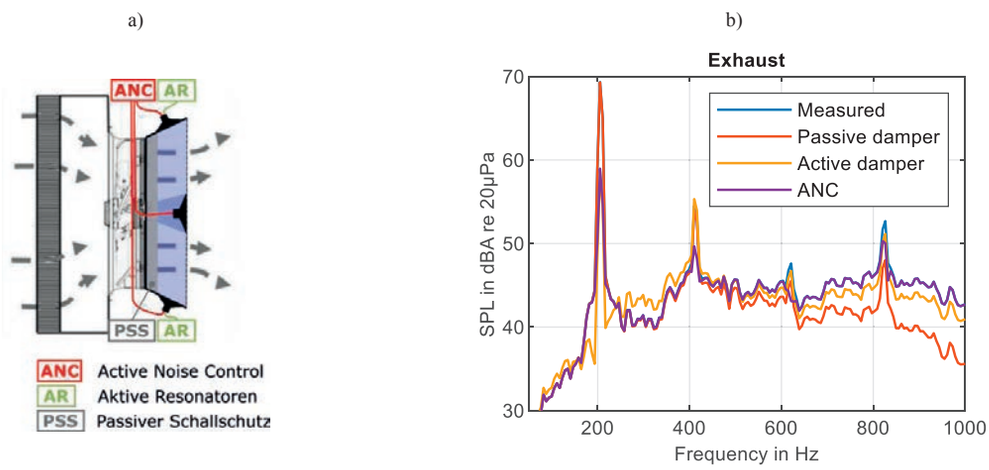


Figure 9: a) Concept for a hybrid active noise control system in 'ADVentAGe'. b) Schematic representation of the effective ranges of the individual sound insulation measures; blue: initial spectrum, red: effect of passive damping, *yellow: level reduction through active resonators, purple: effect of an active narrowband feedforward ANC system*

CONCLUSION & OUTLOOK

As described in ACOUSTIC EMISSION IN FAN SYSTEMS, noise emission depends on the type of fan used and the installation conditions. Typically, the highest setting will produce the loudest noise. However, depending on the ventilation requirements, a lower setting may be used for most of the operating time, generally with a lower equivalent continuous sound level than the maximum setting. On the other hand, there may be mechanical resonance frequencies excited by an intermediate speed setting. Therefore, the intended operating conditions must be evaluated as first step in the design of a noise control system. If the setup already exists, the sound emission can ideally be measured under realistic conditions. Additionally, a model-based approach combining measurements under laboratory conditions with numerical models can be used.

The development approach for hybrid active noise control systems consists of five steps:

1. Estimation or measurement of operating noise and spectral analysis.
2. Identification of target sound components and required reduction.
3. Selection and design of appropriate partial measures.
4. Iterative optimization of joint performance of hybrid system.
5. Implementation of designed components

The ADVentAGe project systematically explores the integration of hybrid noise control systems in fans, focusing on both reactive and active components to reduce noise emissions and improve sound quality. Traditional passive noise control faces challenges due to installation constraints and demand for high noise reduction. Active systems, while providing a compact and adaptable solution, often present cost barriers, particularly for SMEs. The project explores scalable and cost-effective solutions, with initial tests indicating potential reductions of up to 15 dB in tonal noise. This approach could foster new market opportunities and establish a novel business area, aiding SMEs in navigating stringent noise regulations.

Future research will focus on the optimization of hybrid systems for different fan types and installation scenarios, ensuring adaptability and effectiveness. The project also highlights the importance of technology transfer, helping SMEs overcome entry barriers and promoting the adoption of advanced noise control solutions in the ventilation industry. This will facilitate the development of quieter, more efficient ventilation systems that align with environmental and regulatory standards.

ACKNOWLEDGEMENTS

The project ADVentAGe (01IF23285N) is funded by the Federal Ministry for Economic Affairs and Climate Action as part of the 'Industrial Collective Research' programme on the basis of a decision by the German Bundestag.

BIBLIOGRAPHY

1. Leistner, P.; Leistner, M.; St. Zimmermann. Schallabsorber und Schalldämpfer - Innovation für Maßnahmen zur Lärmbekämpfung und Raumakustik, Teil 4: Absorber mit aktiven Komponenten. *Bauphysik* **2002**, *24*, 361–367, doi:10.1002/bapi.200201540.
2. Rohlfing, J.; Bay, K.; Brandstätt, P. *Design and applications of lean active resonator silencer cassettes*, 2019.
3. Busse, T.A. Anwendung Aktiver Schalldämpfer in einer Fensterlüftung. Bachelorarbeit; Universität Stuttgart, Stuttgart, 2016.
4. Hanft, T. Anwendung aktiver Schalldämpfer in einem runden Kanal. Masterarbeit; Universität Stuttgart, Stuttgart, 2018.
5. Song, Z. Signalverarbeitungstechnische Analyse von Aktiv-Schalldämpfer-Systemen. Masterarbeit; Universität Stuttgart, Stuttgart, 2020.
6. Projektseite »ReinluftAkustik« – Akustische Optimierung kompakter Lüftungssysteme und Luftreinigungsgeräte. Available online: https://www.ibp.fraunhofer.de/de/projekte-referenzen/reinluft-akustik.html (accessed on 21 November 2024).
7. Bay, K.; Rohlfing, J. Zur Akustik von Luftreinigungsgeräten. In *DAGA 2022 - 48. Jahrestagung für Akustik*, 21.-24. März 2022, Stuttgart und Online; Leistner, P., Ed.; Deutsche Gesellschaft für Akustik e.V: Berlin, 2022, ISBN 9783939296201.
8. Beer, D.; Fritzsche, P.; Fiedler, B.; Rohlfing, J.; Bay, K.; Troge, J.; Millitzer, J.; Tamm, C. Luftreinigungsgeräte - akustische Anforderungen und Optimierungsmöglichkeiten. In *DAGA 2022 - 48. Jahrestagung für Akustik*, 21.-24. März 2022, Stuttgart und Online; Leistner, P., Ed.; Deutsche Gesellschaft für Akustik e.V: Berlin, 2022, ISBN 9783939296201.
9. Leistner, P.; Krüger, J.; Leistner, M. Hybride Schalldämpfer - Hohe Dämpfung bei tiefen Frequenzen. *Heizung Lüftung/Klima Haustechnik HLH 47* **1996**, 85–90.
10. Brandstätt, P.; Bay, K.; Kristen, R. Aktiv-Schalldämpfer mit einstellbarem Dämpfungsspektrum. Available online: https://www.ibp.fraunhofer.de/content/dam/ibp/ibp-neu/de/dokumente/ibpmitteilungen/451-500/458.pdf (accessed on 21 November 2024).
11. Bay, K.; Brandstätt, P.; Krämer, M. Modellierung aktiver Kompaktschalldämpfer. *DAGA 2006*.
12. Bay, K.; Leistner, P. Active sound insulation of wall and enclosure openings. *EURONOISE 2006 - The 6th European Conference on Noise Control: Advanced Solutions for Noise Control*, 2006.
13. Bay, K.; Leistner, P.; Brandstätt, P. Applications of Active Resonators at Cooling Units of Rail Vehicles. In *INTER-NOISE 2008.* 37th International Congress and Exposition on Noise Control Engineering 2008, Shanghai, China, 2008.
14. Nelson, P.A.; Elliott, S.J. *Active Control of Sound;* Academic: London, 1992.
15. Gardonio, P.; Rohlfing, J. Modular feed-forward active noise control units for ventilation ducts. *J. Acoust. Soc. Am.* **2014**, *136*, 3051, doi:10.1121/1.4900571.
16. Rohlfing, J.; Gardonio, P. Ventilation duct with concurrent acoustic feed-forward and decentralised structural feedback active control. *Journal of Sound and Vibration* **2014**, *333*, 630–645, doi:10.1016/j.jsv.2013.09.022.
17. Millitzer, J.; Kim, J.-K.; Mees, V.; Lee, J.; Oh, C.; Ranisch, C.; Ih, K.-D. Development, System Integration and Experimental Investigation of an Active HVAC Noise Control System for a Passenger Car. In *SAE Technical Paper Series.* 11th International Styrian Noise, Vibration & Harshness Congress: The European Automotive Noise Conference, NOV. 03, 2020; SAE International400 Commonwealth Drive, Warrendale, PA, United States, 2020.

18. *P. Lueg, "Process of silencing sound oscillations," U.S. patent 2,043,416 (1936)*, 1936.
19. Elliott, S.J. *Signal Processing for Active Control;* Elsevier, 2001, ISBN 9780122370854.
20. Kuo, S.M.; Morgan, D.R. *Active noise control systems*: *Algorithms and DSP implementations;* Wiley: New York, Chichester, 1996, ISBN 0-471-13424-4.
21. Berben, P. Aktives Schallschutzmodul für Lüftungsanlagen. Bachelorarbeit; Hochschule Darmstadt, Darmstadt, 2015.
22. Griesing, J.; Klaus, T.B.; Rohlfing, J. Implementierung eines ANC-Reglers auf einer Low-Cost Hardware-Plattform; Technische Universität Darmstadt Fachgebiet rtm, Deutschland, 2016.
23. Gimpl, J. Systemidentifikation und Kompensation breitbandiger Störungen mit adaptiven digitalen Filtern bei zeitvariantem Systemverhalten. Masterthesis; TU Darmstadt, Darmstadt, 2016.
24. Esplin, J.J.; Boyle, J.K.; Sommerfeldt, S.D.; Gee, K.L. Active control of centrifugal fan noise: Modeling design guidelines. *Proceedings of Meetings on Acoustics* **2015**, *12*, 40009, doi:10.1121/2.0000016.
25. Kauba, M.; Millitzer, J.; Mayer, D.; Hanselka, H. Multi-channel narrowband Filtered-x-Least-Mean-Square algorithm with reduced calculation complexity. In *5th ECCOMAS Thematic Conference on Smart Structures and Materials SMART'11.* 5th ECCOMAS Thematic Conference on Smart Structures and Materials SMART'11, Saarbrücken, 2011; pp 49–61.
26. Gäbel, G.; Millitzer, J.; Atzrodt, H.; Herold, S.; Mohr, A. Development and Implementation of a Multi-Channel Active Control System for the Reduction of Road Induced Vehicle Interior Noise. *Actuators* **2018**, *7*, 52, doi:10.3390/act7030052.
27. Potrafke, T. Modellbildung dynamischer Systeme für die Anwendung in Signal-level-Hardware-in-the-Loop-Versuchseinrichtungen: Modeling of dynamic systems for signal level hardware-in-the-loop applications. Master-Thesis; Technische Universität Darmstadt, Darmstadt, 2017.
28. Millitzer, J.; Rohlfing, J.; Mees, V.; Döring, A. Simulation of active control systems considering different levels of detail in the signal processing chain. In *Proceedings of ISMA2018 and USD2018.* International Conference on Noise and Vibration engineering, Leuven, Belgium, 17.-19.09.2018, 2018.
29. Shafer, B.M.; Gee, K.L.; Sommerfeldt, S.D. Verification of a near-field error sensor placement method in active control of compact noise sources. *J. Acoust. Soc. Am.* **2010**, *127*, EL66-72, doi:10.1121/1.3272632.
30. Koopmann, G.H.; Neise, W.; Chen, W. Active Noise Control to Reduce the Blade Tone Noise of Centrifugal Fans. *Journal of Vibration and Acoustics* **1988**, *110*, 377–383, doi:10.1115/1.3269529.
31. Gérard, A.; Berry, A.; Masson, P. Control of tonal noise from subsonic axial fan. Part 2: active control simulations and experiments in free field. *Journal of Sound and Vibration* **2005**, *288*, 1077–1104, doi:10.1016/j.jsv.2005.01.022.
32. Strömbäck, L.; Oretorp, M. RotoSub – The self silencing fan technology. In *Proceedings of inter.noise 2012.* inter.noise 2012, New York, US, 2012.
33. Lauchle, G.C.; MacGillivray, J.R.; Swanson, D.C. Active control of axial-flow fan noise. *J. Acoust. Soc. Am.* **1997**, *101*, 341–349, doi:10.1121/1.417979.
34. Sommerfeldt, S.D.; Gee, K.L. Active control of axial and centrifugal fan noise. In *Proceedings of Meetings on Acoustics.* ICA 2013 Montreal, Montreal, Canada, 2 - 7 June 2013; ASA, 2013; p 30009.
35. Quinlan, D.A. Application of Active Control to Axial Flow Fans. *Noise Control Eng. J.* **1992**, *39*, 95, doi:10.3397/1.2827822.
36. Wright, S.E.; Vuksanovic, B. Outdoor active noise control. In *IEE Colloquium on Active Sound and Vibration Control.* IEE Colloquium on Active Sound and Vibration Control, London, UK, 24 Nov. 1997; IEE, 1997; p 4.

37. Wright, S.E.; Atmoko, H.; Vuksanovic, B. Convergence conditions for multi-channel free-field sound cancelling systems. In *Proceedings of the 2002 IEEE International Conference on Control Applications*, September 18-20, 2002, Glasgow, Scotland, U.K. 2002 IEEE International Conference on Control Applications, Glasgow, UK, 18-20 Sept. 2002; Institute of Electrical and Electronics Engineers, Ed.; IEEE: Piscataway, NJ, 2002; pp 459–464, ISBN 0-7803-7386-3.
38. Budnik, M.; Mees, V. *Simulation-Based Design Strategy and Experimental Validation of an Active Noise Control Setup*, 2023.
39. Miller, L.P. An Analysis of Acoustic Beam-forming with Sparse Transducer Arrays for Active Control. Masterthesis; The Pennsylvania State University, 2018.
40. *DIN EN ISO 3744:2011-02 Akustik - Bestimmung der Schallleistungs- und Schallenergiepegel von Geräuschquellen aus Schalldruckmessungen*: *Hüllflächenverfahren der Genauigkeitsklasse 2 für ein im Wesentlichen freies Schallfeld über einer reflektierenden Ebene;* Beuth Verlag GmbH: Berlin.

EXPERIMENTAL AND NUMERICAL STUDY OF AERODYNAMIC NOISE OF SMALL-SIZE HIGH-SPEED CENTRIFUGAL IMPELLER

Zerong YU [1], Yixin HUANG [1], Weigang YANG [2], Bin LI [2], Peixiang YU [1], Hua OUYANG [1], Yadong WU [1]

1. School of Mechanical Engineering, Shanghai Jiao Tong University, Shanghai, 200240,China

2. Ningbo Fanta Kitchen Ware Co Ltd, Ningbo, 315136,China

SUMMARY

To reduce the aerodynamic noise of a high-speed centrifugal fan used in a cleaning product, this study integrates experimental testing, numerical simulation, and theoretical analysis to investigate the issue comprehensively. Experimental tests identified significant discrete tonal noise in the centrifugal fan, with a total sound pressure level of 79.4 dB(A) and a tonal noise level of 77.2 dB(A), constituting 60.6% of the total noise. Numerical simulations revealed that the circumferential force fluctuations in the rotor blades were notably more pronounced than the radial and axial forces. The spectrum of the circumferential force displayed a distinct peak at four times the rotor frequency, which was attributed to the number of guide vanes swept by a single rotor blade within one cycle. Modal analysis, based on the Lowson model, demonstrated that the dominant mode at the blade passing frequency (BPF) noise was closely linked to the interference frequency, which is determined by the number of guide vanes. By reducing the number of guide vanes, the dominant mode at BPF noise was enhanced, leading to a reduction in discrete tonal noise and a significant decrease in the total sound pressure level. Applying this methodology, a high-performance centrifugal fan was redesigned. The results indicated that decreasing the number of guide vanes from 13 to 10 resulted in a 1.9 dB reduction in BPF noise, a 1.9 dB decrease in the total sound pressure level, and a reduction in the tonal noise contribution from 54.1 % to 40.9 %. This innovative approach not only addresses the specific noise issues in the studied fan but also offers a promising strategy for noise reduction in various high-speed centrifugal fan applications, potentially improving the acoustic performance of similar systems in the future.

INTRODUCTION

Small high-speed centrifugal impellers are composed of impellers, diffusers and cylindrical housings, etc. They are widely used in household appliances because of large flow coefficients and compact structures. As the size of centrifugal impellers becomes smaller, the rotational speed of the impeller is increasing. During operation, turbulence on a larger scale is generated in the flow channel, which increases the non-constant aerodynamic forces on the impeller blades, resulting in a high level of

noise. In order to improve product competitiveness, reducing noise while maintaining performance is becoming an issue that needs to be studied in depth[1-5] .

Studies have shown that the noise in high-speed centrifugal impellers for cleaning products has both discrete and broadband characteristics, in which the discrete noise mainly comes from the periodic pressure pulsations on the rotating impeller and the guide vane blades[6] , which play a dominant role in the total sound pressure level. Numerous investigations have studied the control of discrete noise and proposed various solutions. Neise[7] summarised the early work to reduce the noise at the blade passing frequency (BPF) by changing the shapes of the impeller and the tongue, such as increasing the gap between the blade and the volute, increasing the radius of curvature of the tongue and inclining the tongue /blade, etc. Boltežar *et al*.[8] studied the noise of cooling fans in AC motors by considering the blades as dipole point sources, evaluating the fan's discrete noise at the blade passing frequency by the fluctuation amplitude of the blade force, and comparing the noise level of fans with different blade spacing with the experimental results, and found that non-uniformly distributed blades cause the noise at the original BPF to be dispersed to the harmonics of all orders, thus reducing the peak noise at the discrete frequency, but there is no significant effect on the unweighted total sound pressure level . In addition to changing the moving vanes, there have been many studies on changing the geometry of the guide vanes. In order to change the phase of the outflow gas at the trailing edge of the blade when it interacts with the guide vane, and to reduce the interaction between the impeller and the leading edge of the guide vane to achieve the effect of reducing the pressure pulsation at the leading edge of the guide vane, Jeon *et al*.[9] designed an impeller blade with a inclined trailing edge, which resulted in a reduction of the total sound pressure level of the fan by about 4 dB; Paramasivam *et al*.[10] trimmed the leading edge of the guide vanes based on the original guide vanes, and comparisons revealed that the circumferential velocity distribution at the outlet of the impeller after blade cutting became smoother, and the amplitude of pressure pulsation was greatly reduced, resulting in a reduction of noise at all orders of BPF, with a reduction of up to 6.8 dB of discrete noise at the BPF.

According to the duct model developed by Tyler and Sofrin[11] , it is known that by matching the appropriate number of dynamic and static blades, the noise and its harmonics at the BPF can be made to be generated in an up-to-modal manner, and its acoustic modes decay exponentially after leaving the source location, thus achieving the reduction of the discrete noise. Modal identification is essential to understand the mechanism of fan aerodynamic noise and to improve the design of fan dynamic and static blade counts, however, most of the research on modal identification has been applied in the field of compressors. Some scholars[12] have extended it to models such as axial cooling fans, while it has been less studied in centrifugal fans. Chen Binbin[13] carried out numerical simulation of centrifugal fan with different combinations of dynamic and static blades through Actran, and found that the noise at the BPF is related to the number of blades, and with the increase of the number of blades, the reduction of the fundamental frequency noise is more significant. However, there is no in-depth analysis of the causes of noise reduction in the literature.

This paper measures and analyses the noise characteristics of a small high-speed centrifugal fan within a cleaning product. Firstly, the noise of the impeller is tested and analysed through acoustic tests, and then combined with numerical simulation and the Lowson model[14-16] , the circumferential propagation characteristics of the BPF noise are investigated, and finally, the noise reduction method of matching the number of guide vanes is proposed, and the noise characteristics of the impeller with different numbers of guide vanes are explored through the experiments.

RESEARCH OBJECT AND NUMERICAL SIMULATION

Subject of the study

The research object of this paper is a small high-speed centrifugal impeller for cleaning products, the structure of which is shown in Fig 1, mainly containing the casing, impeller containing 9 moving

blades, tandem impeller grille consisting of two rows of 13 guide vanes and motor frame and other components. During operation, the motor drives the impeller to rotate at a high speed (impeller speed between 78,000 rpm and 82,000 rpm), which creates a negative pressure at the inlet and inhales the gas. The gas flows out radially after the centrifugal impeller does its work, and then the gas flow direction turns to axial after the casing is forced to be folded, and finally it is discharged after the tandem impeller grille expands the pressure.

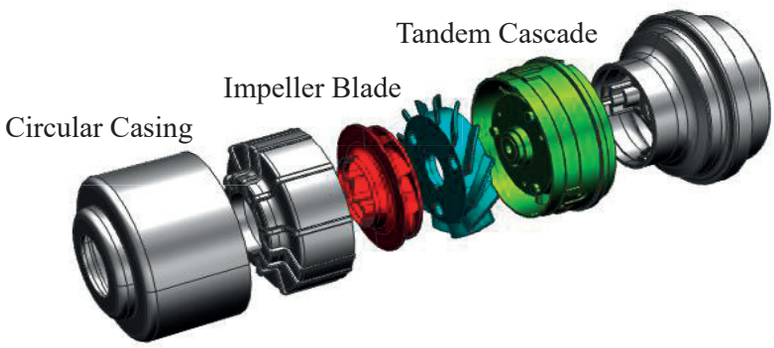


Fig 1: geometric model of a centrifugal impeller

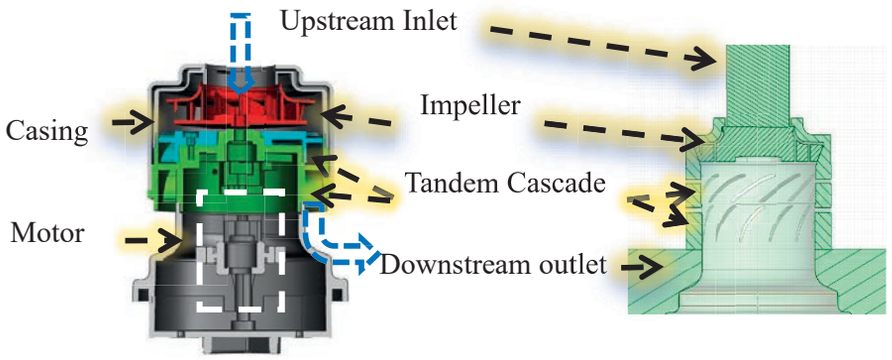
Numerical modelling

The computational domain of the numerical simulation consists of four fluid domains, which are inlet domain, impeller domain, guide vane domain and outlet domain. In order to improve the mesh quality as well as to reduce the computational time, some geometrical structures are simplified in the fluid domain. In addition, in order to better simulate the actual measurement conditions so that the airflow is fully developed in the inlet and outlet segments, the inlet and outlet segments are set to be extended in the form of cylinders, as shown in Fig 2.

In this paper, ICEM and TURBO GRID software are used to mesh the centrifugal impeller, and the meshes are in the form of structural meshes. Flow field calculation uses commercial computational fluid dynamics (CFD) software Ansys CFX. Due to the high-speed centrifugal impeller internal air flow turbulence, there are a large number of secondary flow phenomenon, in order to the turbulent flow inside the impeller to accurately model, and then more accurately predict the distribution of the flow field inside the impeller, so the turbulence model using SST model. Due to the high rotational speed of the centrifugal impeller (around 80,000 rpm), the rotational Mach number at the maximum radius of the impeller is about 0.45, at this time, the air compressibility needs to be taken into account, so the compressible Navier-Stokes equations are used, and the complete gas model is used. Opening boundary conditions are used for both inlet and outlet, and the inlet static pressure varies with the working conditions; since the outlet gas is discharged to the environment, the outlet static pressure is set to atmospheric pressure.

The wall surfaces are all non-slip wall surfaces. The impeller fluid domain is defined as rotating domain, and the rest is stationary domain, and the data are transferred by Frozen Rotor method at the dynamic-static interface. For the convergence criterion, the residuals of the control equations are set to 10^{-5} and the inlet flow rate is used as a parameter to judge the convergence.

Five sets of grids were divided for the centrifugal impeller model with grid numbers of 1.26 million, 2.28 million, 3.82 million, 4.5 million and 5.5 million. By comparing the inlet flow rate obtained with different number of grids, it is found that the flow rate is basically stable when the number of grids is 3.82 million, 4.5 million and 5.5 million. Therefore, the subsequent study is analyzed using 3.82 million grids.



(a) Actual Model *(b) Cross Section Of Fluid Domain*

Fig.2 Schematic diagram of fluid domain

The reliability of the CFD simulation results is verified through the test. The test airflow stage is built according to GB/T 38043-2019 , shown in Fig 3. The centrifugal impeller performance test reset mainly consists of a 500 x 500 x 500 mm box, an aerodynamic snap-in indexing dial consisting of a 2 mm ± 0.1 mm thick stainless steel orifice plate with 10 different flow rate adjusting holes,

and an AC/DC power meter, among other components. In the measurement, the inlet conditions are controlled by different sizes of orifice plates (50 mm, 40 mm, 30 mm, 23 mm, 19 mm, 16 mm, 13 mm, 10 mm and 6.5 mm), the centrifugal impeller rotational speed is controlled by the method of pulse-width modulation, and after the impeller is stabilized, the corresponding static pressure difference, flow rate and other data are measured.

Fig 4 shows a comparison of the CFD and experimental test results, indicating that the numerically calculated flow-vacuum curves match the trend of the experimental results well, with only small deviations. Overall, the above CFD simulation can accurately predict the performance of the centrifugal impeller and meet the reliability requirements.



(a) Exterior view *(b) Aerodynamic chuck type indexing dials*

Fig.3 Aerodynamic performance experimental apparatus

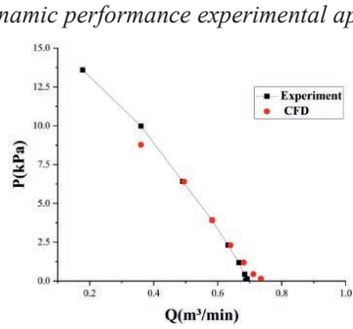


Fig.4 Comparison of impeller performance between the simulation and experiment

FAN 2025
Antibes Juan-les-Pins (France), 9 – 11 April 2025

EXPERIMENTAL TESTS

The aerodynamic noise test of the fan was carried out in a semi-anechoic chamber with background noise below 20 dBA and a cut-off frequency of 100 Hz. The test rig is shown in Fig 5, with fan placed vertically and fixed on the top of the box of size 0.7 m × 0.7 m × 0.7 m. The side wall of the box was open to adjust the flow rate. According to GB/T 4214.1-2017, three microphones Sig 1 to 3 are arranged uniformly in the circumferential plane, and Sig 4 is arranged on the rotating axis of the fan. The distance of each microphone from the center of the fan is 1 m. The acoustic signals are sampled by the microphone, then converted into voltage signals by the preamplifier and finally sent to the data acquisition system. Pulse width modulation is used to control the rotational speed of the fan, and data acquisition is carried out after stable operation.

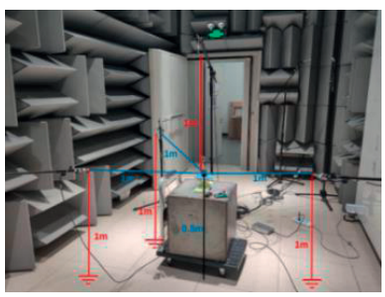
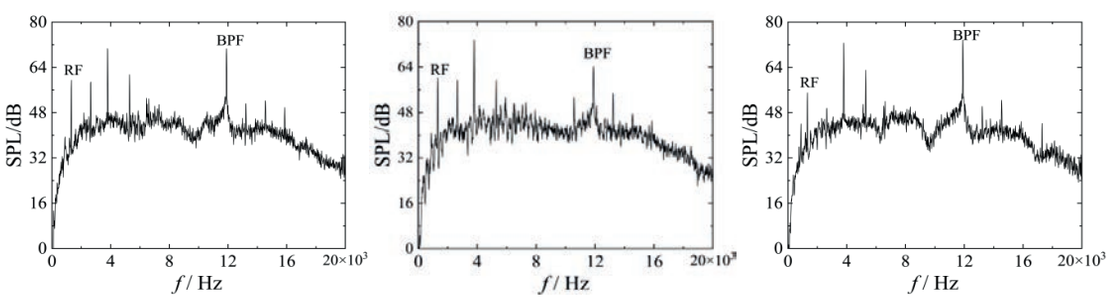


Fig.5 Location of microphones

The A-weighted noise spectra of the fan at the design operating point are shown in Fig 6. The noise of the impeller consists of a broadband spectrum superimposed with significant discrete noise at RF and BPF. The discrete noise at RF and its harmonics is often caused by the eccentricity of the impeller due to manufacturing errors in impeller processing. Since the number of rotor blades 9 and the number of guide vane blades 12 are non-mutual in the studied impeller, it may cause internal resonance in the impeller, which also generates additional discrete noise; the noise at BPF is mainly due to the mutual interference between the rotor blades and the guide vane blades, which generates unsteady aerodynamic forces with periodic variations on the blades.



(a)Sig 1 *(b) Sig 2* *(c) Sig 3*

Fig. 6 Noise spectrum of the high-speed centrifugal impeller

The average total sound pressure level L_p was calculated from four measurement points as the evaluation index of the overall noise level, and its calculation formula is as follows:

$$L_p = 10 \times \lg\left(\frac{1}{4} \times \left(\sum_{i=1}^{4} 10^{L_{pi}/10}\right)\right) \quad (1)$$

L_{pi} is the A-weighted sound pressure level at each measurement point. The average total sound pressure level L_p , discrete total sound pressure level $L_{p\text{dis}}$ and broadband total sound pressure level $L_{p\text{bnd}}$ at the four measurement points were calculated to be 79.4 dB(A), 77.2 dB(A) and 75.4 dB(A), respectively. The noise energy share can be calculated by the following formula, the discrete monotone noise and wide frequency noise energy share are 60.6 % and 39.4 % respectively, in which the monotone noise is prominent and is the key point to be considered for noise reduction.

$$\eta_{\mathrm{dis/bnd}} = \frac{10^{SPL_{p\mathrm{dis}}/10}}{10^{SPL_{p\mathrm{bnd}}/10}} \tag{2}$$

NUMERICAL NOISE SIMULATION

Aerodynamic noise simulation method

This section uses the Lowson point force source model for analysis. The model is based on the Lighthill acoustic analogy theory developed for a fan or compressor radiation monotone noise prediction model, which can reflect the different noise impacts of different force sources on the blades, and is suitable for predicting the rule of change of noise.

Rotor blade force analysis

For the design condition (Φ13 orifice plate), the unsteady calculations are carried out based on the steady results. Time step is set as the time when the impeller rotates through 7.2°, i.e., 7.50×10^{-6} s. The residuals of the calculation iteration are 1×10^{-5}. The data of 20 revolutions of the impeller are intercepted from the 6th revolution for analysis.

The impeller, the main noise source, is extracted and analyzed for its surface force, and the impeller force *F* in the Cartesian coordinate system is decomposed into axial force *T*, circumferential force *D*, and radial force *E*. The values of the blade force pulsating with time step are shown in Fig 8. The blade force on the impeller blades varies periodically, with the circumferential force being the most pronounced. Since the impeller mainly push the fluid in the radial direction, resulting in the largest amplitude of radial force *E*, while axial *T* and circumferential force *D* are smaller.

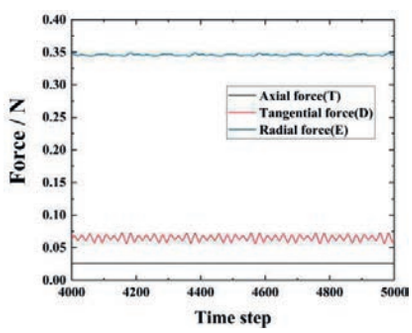
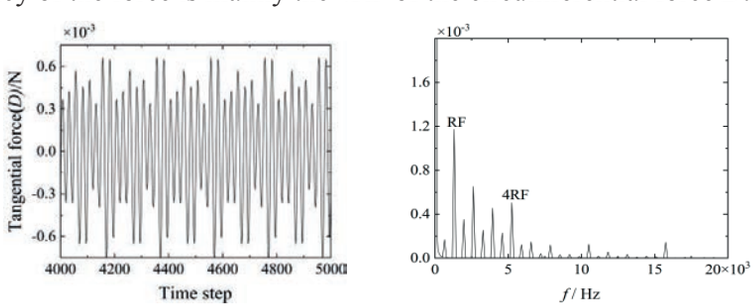
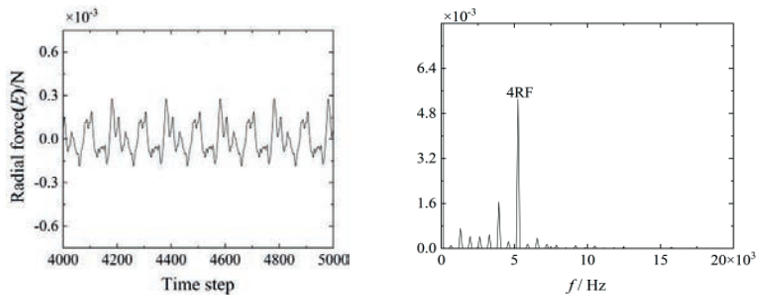


Fig.8 Spectra of blade force in time/frequency domain

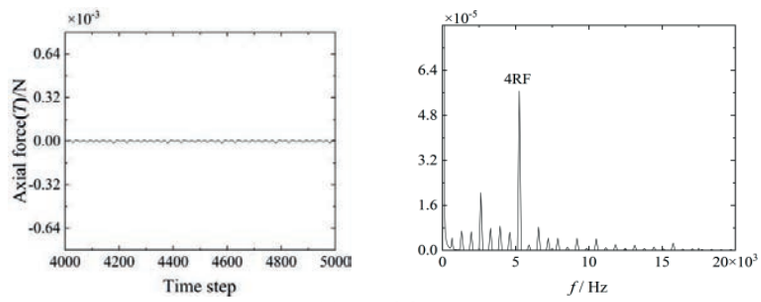
For subsonic wind turbines, the noise generated by the interference effect is dominant. As shown in Fig 9, the interference between the rotor blade rotating in the circumferential direction and the downstream guide vane mainly affects the change of the circumferential force due to the fact that the blade surface is almost parallel to the shaft, resulting in the circumferential force being significantly larger than the forces in the other two directions. Through the Fourier transform, it is found that the fluctuation frequency of the force is mainly the 4RF of the circumferential force *D*.



(a)Tangential force



(b) Radial force



(c) Axial force

Fig.9 Spectra of blade pulsation force in time and frequency domain

For the 4RF peak of the circumferential force D, it is considered to be related to the interference of the impeller blades with guide vanes. As shown in Fig 10, the blade span β_1 is 72° due to the large rotor blade span in the circumferential direction. When the number of guide vanes is 12, the guide vane spacing β_2 is 30°. The rotor blade interferes with three primary guide vanes at the same time.

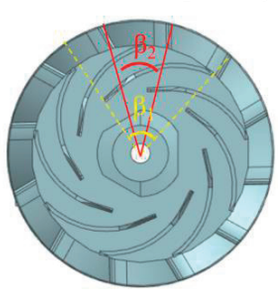


Fig.10 Schematic diagram of rotor-stator interaction of 12 guide vanes

By dividing the guide vanes into groups of 3, the 12 guide vanes can be divided into 4 groups, resulting in an interference frequency at 4RF on the rotor blade force. The calculation formula for the above interference frequency λ = 4RF is expressed as:

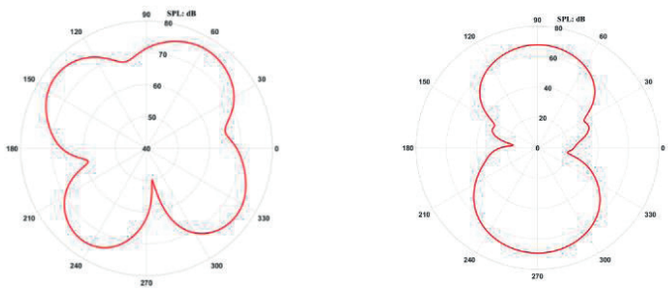
$$\lambda = \left(\mathrm{V} / \left\lceil \frac{\beta_1}{\beta_2} \right\rceil \right) \times \mathrm{RF} \tag{3}$$

λ is the interference frequency, V is the number of guide vanes, β_1 is the impeller blade span angle, β_2 is the guide vane spacing angle, $\lceil\ \rceil$ is the upward rounding symbol, and $\lceil \beta_1 / \beta_2 \rceil$ indicates the number of guide vanes corresponding to one impeller blade.

Lowson model based circumferential acoustic calculations

Fig 11 shows the distribution of BPF sound pressure level according to the Lowson model by taking the circumferential plane and axial plane of Sig 1~3 in the test and averaging 360 measurement points at 1° intervals. Due to the complex superposition of multimodal states, the sound pressure level is not consistent at different angular positions on the same circumferential direction, and the maximum BPF

sound pressure level of 360 points on the circumferential direction is 76.6 dB, and the minimum value is 50.1 dB. The SPL at BPF of Sig 1~3 in the test are 70.6 dB, 64.1 dB, and 73.6 dB, which are all within the range. The axial plane is also within the range of values, which proves that the Lowson point-force model can be applied to the prediction of the discrete noise of high-speed centrifugal impeller.



(a) circumferential direction *(b) axial direction*

Fig.11 The sound pressure level on the Sig1~3 circumferential ring at BPF

The BPF noise on the circumferential direction where Sig 1~3 are located is modally decomposed, and the corresponding amplitude of each mode is shown in Fig 12. Multiple modes exist simultaneously due to the complexity of the interference force source, and the modal spectrum is more continuous. The Fig 12 shows that the number of primary modes on the circumferential direction is 5 and the number of secondary modes is 9.

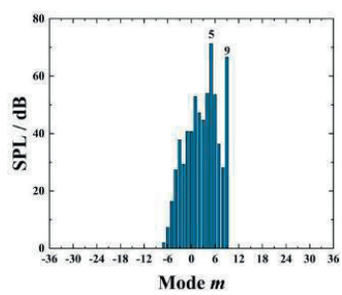


Fig.12 Mode amplitude of noise on Sig1~3 circumferential ring at BPF

According to the dynamic-static interference model, the pressure modes different from the blade rotor speed rotation are due to the non-constant aerodynamic forces generated on the rotor of the high-speed centrifugal impeller. The circumferential acoustic modes under the BPF and its harmonics on the noise spectrum can be expressed as[18]:

$$m = nB - \lambda \tag{4}$$

m is the number of interference modes, n refers to the number of orders, B is the number of moving blades, and λ is the interference frequency. For the first order BPF, the interference force on 4RF will produce an interference mode of m = 9 – 4 = 5, corresponding to the dynamic interference noise; the force on zero frequency produces a mode of m = 9 – 0 = 9, which corresponds to the constant force noise due to blade loading. Due to the control of the Bessel function, the lower order modes are easier to propagate, so the 5 mode may dominate.

Impeller noise reduction based on duct modes

As described in Section 2, the fan is ducted for airflow operation, and monotone noise is the main source of aerodynamic noise. Based on the theory of duct acoustics, the higher the circumferential modal order, the faster the noise decays, so the noise at BPF can be attenuated by increasing the modal number, thus reducing the total sound pressure level of the impeller.

Considering the special non-coprime nature of the fan, which has 9 blades on the impeller and

12 guide vanes. Another high-speed centrifugal fan containing 9 impeller blades and 13 guide vanes is analyzed in this section, as shown in Fig 13(a). The impeller blade circumferential span β_1 is 73°. When the number of guide vanes blades is 13, the spacing β_2 is 27.7°. From the conclusion of section 3.2,the interference frequency λ = 4.33RF, which is close to 4RF.Thus the main modal number of the BPF noise corresponds to m = 9 - 4 = 5.And when the number of guide vane blades is reduced to 10, the guide vane spacing β_2 is 36°, and its interference frequency λ = 3.33RF, which is close to 3RF, and it is presumed that the number of main modes of the BPF noise will be elevated to m = 9 - 3 = 6, at which time the BPF noise is more easy to attenuate in the propagation process.



Fig.13 Schematic diagram of rotor-stator interaction of 13 guide vanes

Through the test rig and analysis method in section 2, the noise of the impeller with 10 and 13 guide vanes number was tested respectively, and the test results are shown in the table below. When the number of guide vanes is reduced from 13 to 10, the BPF noise is reduced by 1.9 dB, the discrete noise is reduced by 3.2 dB, and the total sound pressure level is reduced by 1.9 dB, and the results are consistent with the above inference. At this time, the proportion of discrete noise is reduced to 40.9 %, which is no longer the main source of noise; and the broadband noise is reduced by 0.9 dB, which may be related to the flow optimization.

Table.1 Summary of centrifugal impeller noise with 10 and 13 guide vanes

	10 guide vanes	**13 guide vanes**
L_{BPF} **/ dB**	55.7	57.6
L_{pi} **/ dB**	72.4	74.3
L_{dis} **/dB**	68.5	71.7
L_{bnd} **/dB**	70.1	71.0
Proportion	40.9 %	54.1 %

CONCLUSIONS

In this paper, the aerodynamic noise characteristics of a certain model of high-speed centrifugal impeller for cleaning household products are investigated, the directivity and components of the noise are analyzed, and according to the pipeline modal theory, the discrete noise and the total sound pressure level of the high-speed centrifugal impeller are significantly reduced by adjusting the number of guide vanes, and the main conclusions of this paper are as follows:

(1) The interference at the RF frequency of the impeller blade is caused by dynamic and static interference. Due to the large span of the rotor blades, when rotating for one circle, the rotor blades will form interference with multiple guide vanes, thus generating an interaction frequency.

(2) Reasonable matching of the number of rotor blades and guide vanes can effectively reduce the noise. When the number of rotor blades and guide vanes is non-mutual, due to the high speed of the impeller (80,000rpm), the noise will be obvious in the noise spectrum at RF and its octave. When the number of blades is non-mutual, the monotone noise can be effectively reduced by increasing the number of BPF noise circumferential modes.

BIBLIOGRAPHY

[1] HUSTLE, J.X. WU, S.W. HU, *et al*. *Hood MultiStudy on main noise sources and partition contribution of a multi-blade centrifugal fan in a range hood*. Fluid Machinery, **2023**, 51(12): 64-70.

[2] LEI Jian, QIN Guoliang, WU Yandong, *et al*. *Cause analysis and suppression method of outlet vortex ofmulti-blade centrifugal fan*. Fluid Machinery, **2022**, 50(12): 65-71.

[3] LI M, HOU G L, SHU L, *et al*. *Detection and optimization of vibration noise of centrifugal fan for automobile air conditioning*. Fluid Machinery, **2021**, 49(12): 80-94.

[4] ZHU Z H, CHEN X J, LI S. *Study on aerodynamic noise of centrifugal fan in radar antenna system*. Fluid Machinery, **2021**, 49(03): 52-59.

[5] HU S B, WANG B, CHEN Q M, *et al*. *Experimental study on small high speed and low noise centrifugal fan*. Fluid Machinery, **2020**, 48(04): 1-5.

[6] CAI J, QI D T, ZHANG Y. *A numerical study of the blade passing frequency noise of a centrifugal fan*//201 2 International Mechanical Engineering Congress and Exposition. USA: ASME, **2012**: 335-343.

[7] NEISE W. *Review of noise reduction methods for centrifugal fans*. Journal of Engineering for Industry, **1982**, 104(2): 151-61.

[8] BOLTEZAR M, MESARIC M, KUHELJ A. *The influence of uneven blade spacing on the SPL and noise spectra radiated from radial fans*. Journal of Sound and Vibration, **1998**, 216(4): 697-711.

[9] JEON W H, REW H S, KIM C J. *Aeroacoustic characteristics and noise reduction of a centrifugal fan for a vacuum cleaner*. KSME International Journal, **2004**, 18(2): 185-192.

[10] PARAMASIVAM K, RAJOO S, ROMAGNOLI *A. Suppression of tonal noise in a centrifugal fan using guide vanes.* Journal of Sound and Vibration, **2015**, 357(21): 95-106.

[11] TYLER J M, SOFRIN T G. *Axial flow Compressor noise studies*. Transaction of the Society of Automotive Engineers, **1962**, 70: 309-332.

[12] SUN Z H, TIAN J, ZHANG X B, et al. *Aerodynamic noise control technology of electronic device cooling fan based on duct acoustic mode cutoff.* Journal of Applied Acoustics*, **2020**, 39(2): 189-198.*

[13] CHEN B B. *Study on the aerodynamic performance and noise of the centrifugal fan for vacuum cleaners*. Nanjing: Nanjing University of Aeronautics and Astronautics, **2018**.

[14] LOWSON M V. *Theoretical analysis of Compressor noise*. Journal of the Acoustical of America, **1970**, 42(5):371-385.

[15] XU K B, QIAO W Y, HUO S Y, et al. *Research of mode identification and error transfer property on fan tonal noise.* Journal of Propulsion Technology, **2018**, 39(1): 185-195.

[16] CHOI H L, LEE D J. *Development of the numerical method for calculating sound radiation from a rotating dipole source in an opened thin duct*. Journal of Sound and Vibration, **2006**, 295: 739-752.

[17] QIAO Weiyang. *Aeroacoustics of aircraft engines*. Beijing University of Aeronautics and Astronautics Press, **2010**.

E1 Artificial Intelligence and Optimization Techniques

10 April - 13:30 - Auditorium

Chairmen: Lorenzo Tieghi, Massimo Masi

List of papers

Redesign and Optimisation of a Large Axial Fan Using 3D Inverse Design Method

- Walter ANGELIS – Wolong Electric Group Co., Ltd (China)
- Peng WANG – Advanced Design Technology (Shanghai) Ltd (China)
- Mingding ZHANG – Advanced Design Technology (Shanghai) Ltd (China)
- Liyi LIU – Wolong Electric Group Co., Ltd (China)
- Qian ZHAO – Wolong Electric Group Co., Ltd (China)
- Mehrdad ZANGENEH – University College London (United Kingdom)



REDESIGN AND OPTIMISATION OF A LARGE AXIAL FAN USING 3D INVERSE DESIGN METHOD

Waler ANGELIS [1], Peng WANG[2], Mingding ZHANG[2],
Liyi LIU[1], Qian ZHAO[1], Walter ANGELIS[1],
Mehrdad ZANGENEH[3]

[1] *Wolong Electric, 1801 West Renming Road, Shangyu District, Shaoxing, Zhejiang, China, 312300*

[2] *Advanced Design Technology (Shanghai) Ltd, 628 Huaxu Highway, Qingpu, Shanghai, China, 20702*

[3] *Department of Mechanical Engineering, University College London, Torrington Place, London, WC1E 7JE, United Kingdom*

SUMMARY

Axial fans play a critical role in various applications, such as ventilation systems, air-conditioning units, electronic cooling, and energy storage, where stringent performance requirements are essential. These include high pressure rise, robust flow capacity, superior efficiency, optimized power density for space-constrained environments, and low noise. In this paper, we present the redesign and optimisation of a legacy axial fan by the 3D inverse design methodology using a smaller sized fan blade. Contrary to the conventional design steps which usually begins with CAD modelling, the new design was achieved through an internal flow focused inverse design method which prescribes the pressure jump between the upper and lower surfaces of the blades. A commercial code TURBOdesign1 was utilised to generate the blade geometry that adheres to the prescribed pressure distribution along the meridional contour at various spanwise positions. Additionally, a nonlinear distribution of Euler work was applied at the blade exit, further optimizing performance.The final redesigned fan demonstrates performance improvements in terms of the pressure rise, operating range, efficiency, and noise generation over the legacy model, which are confirmed through aerodynamic and aeroacoustic measurements.

FAN 2025
Antibes - Juan-les-Pins (France), 9 - 10 April 2025

INTRODUCTION

Wolong Electric as Chinese company is still new in the field of EC fans. The product portfolio is constantly being expanded and improved. In this case, for example, an aerodynamic and geometric optimisation of the existing product (installation space) was carried out and significant improvements have already been achieved.

The previous product in size 450 mm was equipped with an EC (electric cooling) internal rotor motor, but it had the disadvantage of requiring too much axial installation space for battery cooling in renewable energy applications. At the same time, the fan to be developed should also be applicable for other usual applications, such as ventilation systems, air conditioning systems, electronics cooling, etc. The aerodynamic performance of the fan and the noise emission should significantly exceed or improve the existing product in terms of static pressure increase, maximum volume flow and achievable efficiency. At best, the performance data of the next size up, 500 mm, can be achieved and thus the requirements for increased power density can be met. Thanks to these improvements, it can also be used in previously unattainable applications.

Further on, it was detected during the development phase that the diameter of the impeller versus the inlet radius of the fan wall plate could be increased for a better performance behavior. The impeller diameter was increased by reducing the radius of the fan wall plate without changing the connecting points by screw points (interface to the customer) in the fan wall plate considering the smallest possible tip clearance between the impeller diameter and the air duct and considering the competitors' performance target. So, an impeller with a diameter of 464 mm instead of 450 mm was detected as the best choice and a new impeller for this size was developed.

DESIGN METHOD

For this study, the 3D inverse design code TURBOdesign1 (TD1) was employed to design a new fan to replace its predecessor. This method has already been extensively documented in literature in terms of the theoretical background by Hawthorne et al[1], [2], Borges[3], [4], and Zangeneh[5], and wide applications, including sub- and transonic compressors (Zangeneh [6], [7], Wang [8]), centrifugal pumps (Goto[9]), radial and axial turbines (Zhang [10]), centrifugal fans (Zhang [11] and Bleiziffer et al[12]), etc. Rather than starting from creating the blade geometries like the traditional method, this inverse design method generates blade profiles subject to the prescribed blade loading distributions. Usually, the tangentially averaged swirl velocity rV_t^* is prescribed at the leading and trailing edges from the hub to shroud sections. This term is normalised by the product of blade exit mean radius and rotational speed, i.e., $rV_t^* = r_2 V_{2,t}/r_2^2\omega$. In the left side of Fig. 1 is shown a typical spanwise work coefficient distribution for axial fans. We are assuming there is no preswirl at the inlet since no inlet guide vane is used in this case. At the blade trailing edge, a forced vortex style distribution is used. The hub section is clearly less loaded than the shroud in order to avoid the over-turning of the blade causing strong flow separations near the trailing edge.

For incompressible flows, the swirl velocity rV_t^* is related to the pressure jump or blade loading between the upper and lower surface of the blade via

$$p^+ - p^- = \frac{2\pi}{NB}\rho W_{mbl}\frac{\partial rV_t^*}{\partial m}, \tag{1}$$

in which W_{mbl} is the flow meridional velocity on the blade surface and the subscript m means the meridional component. Assuming the boundary layer effect is very minor, the flow behavior is largely driven by the pressure field, and thus the prescription of the pressure distribution can control the flow physics very well. The solver will be iteratively run until a blade geometry satisfying the given blade loading is found. As time taken for this process to complete is within a few seconds, it allows

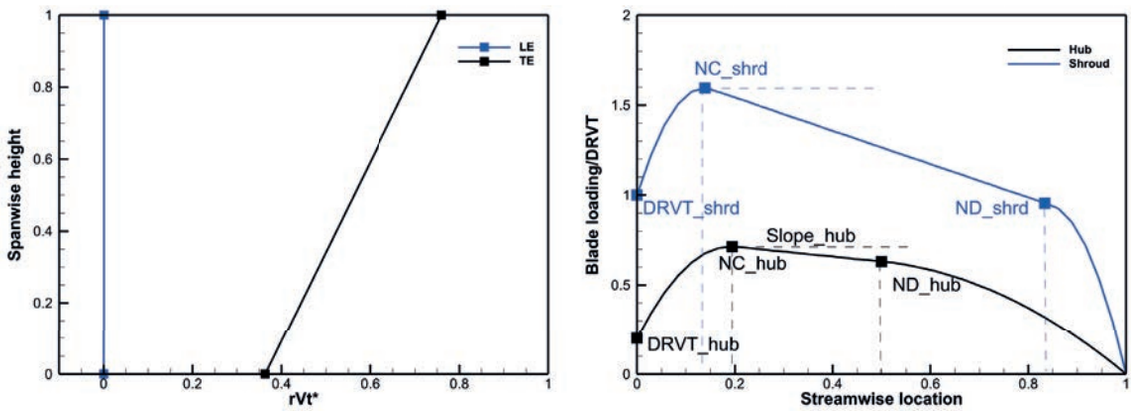


Figure 1: Blade loading distributions in TD1. Left: Spanwise rV_t^* distributions; Right: Streamwise loading $\frac{\partial rV_t^*}{\partial m}$

designers to update the designs very fast. On the right side of Fig. 1 is shown the streamwise blade loading distribution, $\frac{\partial rV_t^*}{\partial m}$. It can be specified at different spanwise positions. At a particular spanwise position, 4 parameters (NC, ND, Slope and DRVT) are used to define a loading distribution curve. The curve is made of 3 segments. A straight line is used in the middle between NC and ND. Two parabolas are used to connect each end of the straight line with the leading and trailing edges. It should be noted that the blade loading value at the trailing edge is always zero in order to satisfy the Kutta-condition. At the leading edge, DRVT is used to control inlet flow incidence. The distribution shown on Fig. 1 is a both for-loaded hub and shroud prescription, which has proven to be very effective for axial flow machines.

Apart from the key aerodynamic parameters explained above, the geometric inputs are also needed for the inverse design solver. Figure 2 shows the meridional contour and the stacking angle distribution at the blade trailing edge. By gradually increasing the radius of the hub contour from inlet to outlet, we obtained a converging flow channel, which is useful to mitigate flow separations near the blade root. A nonlinear distribution of stacking angle is specified at the blade trailing edge to achieve better exit flow behaviors.

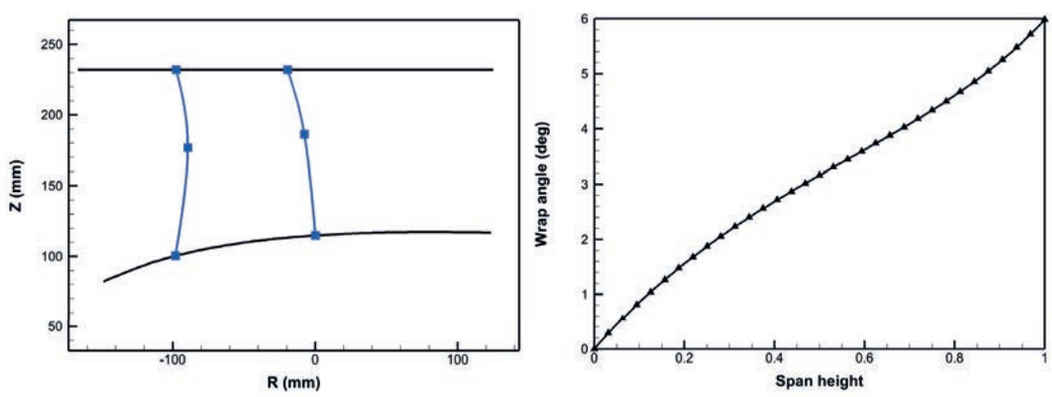


Figure 2: Meridional contour and the stacking distribution at the exit

In Fig. 3 is shown the final blade loading used in the study and the resultant product prototype also shown. It can be seen that a strong fore-loading is applied at the leading edge for both hub and shroud sections.

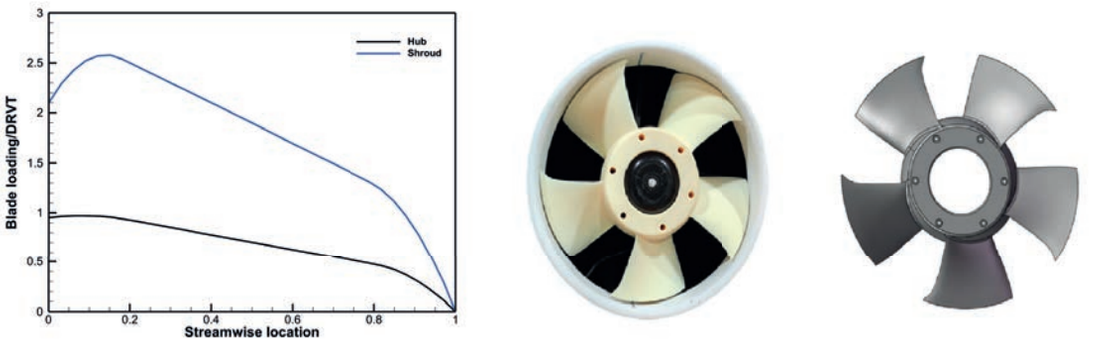


Figure 3: Left: Final blade loading. Middle: Prototyped fan. Right: CAD modelling

RESULTS

CFD setups

The newly designed fan was simulated using ANSYS CFX to predict its aerodynamic performance. The CFD model consists of two big blocks at the front and back of the fan blade and they are meshed unstructurally, as is shown in Fig. 4. The fan blade was meshed in TurboGrid to obtain the structural grid with a size about 1 million elements. A first layer thickness of 0.005 mm was used, as is shown in Fig. 5. It finally leads to a YPlus value no greater than 3 on the blade surface, which is suitable for SST turbulence model.

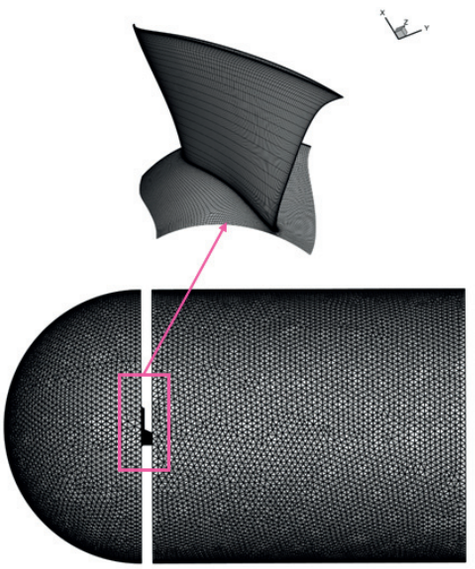


Figure 4: CFD domain

Test verifications

In Fig. 6 are shown comparisons between CFD data and measurements at two different speeds. Overall, CFD calculations provide a good estimation of the performance curve in terms of the trend. At the higher flows, CFD's prediction have good agreement with the measurements. However, as the mass flow reduces, discrepancy becomes more prevailing. CFD calculations clearly underestimate the pressure rise, which could be due to the unsteadiness nature of the flows.

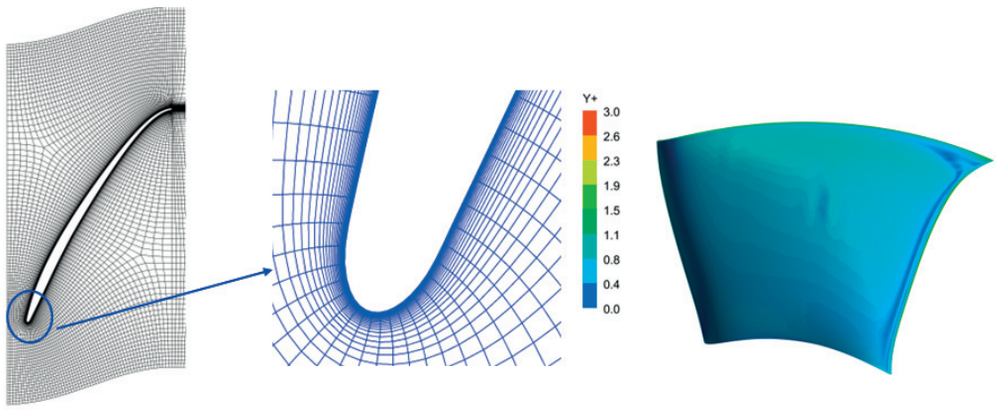


Figure 5: Fan blade mesh and Y plus value

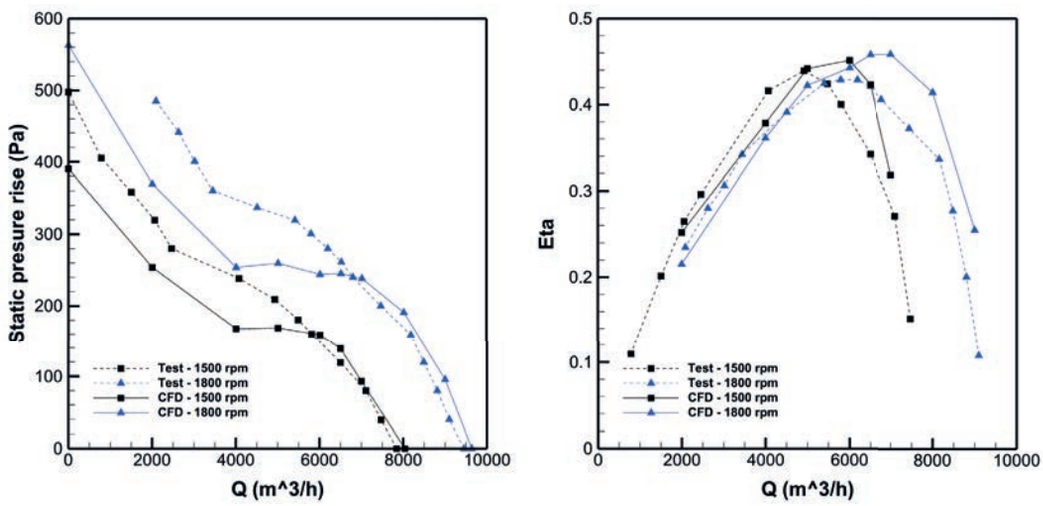


Figure 6: Comparisons between CFD and test results at 1500 and 1800 rpm

Comparison with existing designs

Figure 7 shows the three different fans' performance measurements. It is quite clear to see that this newly developed fan with 464 mm exit diameter demonstrates better operating ranges, higher pressure rise, and greater efficiency. Acoustic tests were also performed for the 450 mm and 464 mm fans. In order to establish a fair comparison, the rotating speed of the 464 mm fan was carefully adjusted in the test so it can achieve the same flow rate and static pressure rise, as is shown in the left side of Fig. 8. On the right hand side, the noise level measurements are presented when two fans' operating flow and pressure rise are the same. We can see that this new design generates significantly less noise almost over the entire operating range.

CONCLUSION

As has been shown in the previous sections, the performance parameters such as increasing the static pressure, the maximum volume flow and the achievable efficiency were implemented very effectively. In addition, a significant reduction in noise emission in the application range was achieved. With these performance parameters, new areas of application can be found, e.g. in the renewable energy sector and its requirements for installation space. Further product parameters and fans of other sizes are now being further developed.

FAN 2025
Antibes - Juan-les-Pins (France), 9 - 10 April 2025

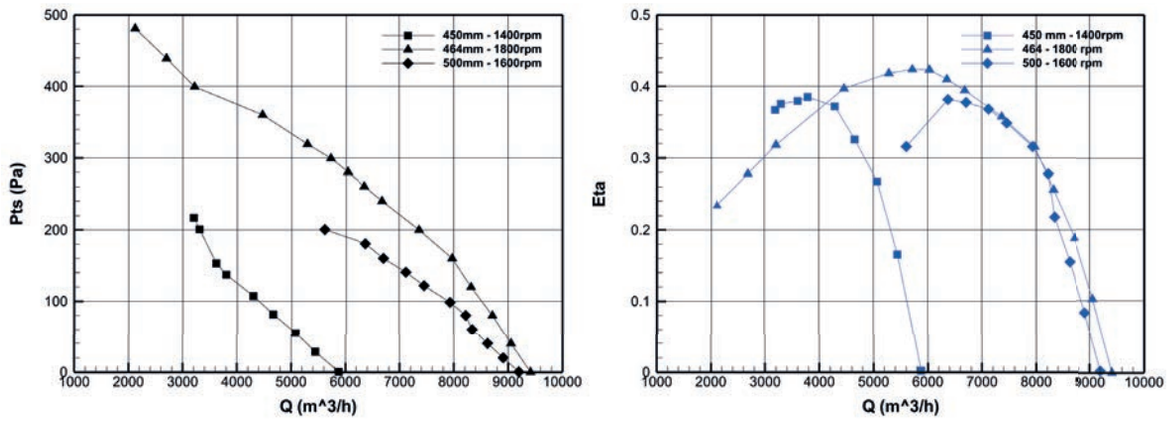


Figure 7: Aerodynamic performance of the two existing (450 and 500 mm) and new designs (464 mm)

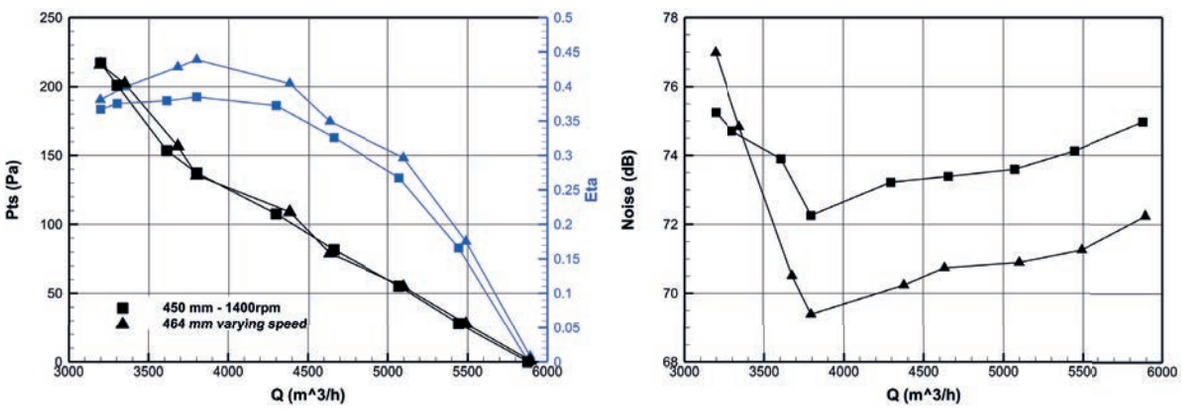


Figure 8: Aerodynamic and aeroacoustic performance comparisons between the existing 450 mm and newly developed 464 mm fan

REFERENCES

[1] W.R.Hawthorne, C. Wang, C. Tan, and J. McCune, *Theory of blade design for large deflections: Part i - two-dimensional cascade*, Journal of Engineering for Gas Turbines and Power vol. 106, pp. 346–353, **1984**.

[2] C. Tan, W. Hawthorne, J. McCune, and C. Wang, *Theory of blade design for large deflections: Part ii - annular cascade*, Journal of Engineering for Gas Turbines and Power vol. 106, pp. 354–365, **1984**.

[3] J. Borges, *A three-dimensional inverse method for turbomachinery: Part i - theory*, Journal of Turbomachinery vol. 112, pp. 346–354, **1990**.

[4] J. Borges, *A three-dimensional inverse method for turbomachinery: Part ii - experimental verification*, Journal of Turbomachinery vol. 112, pp. 355–361, **1990**.

[5] M. Zangeneh, *A compressible three-dimensional design method for radial and mixed flow turbomachinery blades*, Internal Journal of Numerical Methods in Fluids vol. 13, no. 1151, pp. 599–624, **1991**.

[6] M. Zangeneh, A. Goto, and H. Harada, *On the design criteria for supression of secondary flows in centrifugal and mixed flow impellers*, Journal of Turbomachinery vol. 120, pp. 723–735, **1998**.

[7] M. Zangeneh, N. Amarel, K. Daneshkhah, and H. Krain, *Optimization of 6.2:1 pressure ratio centrifugal compressor impeller by 3d inverse design*, Proceedings of ASME Turbo Expo 2011: Power for Land, Sea and Air, **2011**.

[8] P. Wang, M. Zangeneh, B. Richards, K. Gray, J. Tran, and A. Andah, *Redesign of a compressor stage for a high-performance electric supercharger in a heavlily downsized engine*, Journal of Engineering for Gas Turbines and Power vol. 140, pp. 042602-1–042602-12, **2018**.

[9] A. Goto, T. Takemura, and M. Zangeneh, *Redesign of a compressor stage for a high-performance electric supercharger in a heavlily downsized engine*, Journal of Turbomachinery vol. 118, pp. 544–551, **1996**.

[10] J. Zhang and M. Zangeneh, *Increasing pulse energy recovery of radial turbocharger turbines by 3d inverse design method*, ASME Turbo Expo 2015: Turbine Technical Conference and Exposition, **2015**.

[11] J. Zhang and M. Zangeneh, *Multi-point, multi-objective optimisation of centrifugal fans by 3d inverse design method*, Int. J. Turbomach. Propuls. Power vol. 8, **2023**.

[12] M. Bleiziffer, A. Sivaramakrishnan, R. Schoele, M. Zangeneh, and J. Zhang, *Modern design of automotive axial cooling fans using inverse methods*, Fan2022, **2022**.

E2 Experimental Methods For Characterizing Noise Sources

10 April - 13:30 - Room 1 Fitzgerald
Chairman: Peter Pelz

List of papers

Slit Tube Probe and Multi-Port Method for the Acoustical Characterisation of Ducted Axial Fans

- Jörg RIEDEL – LSTM Erlangen (Germany)
- Stefan BECKER – LSTM Erlangen (Germany)
- Stefan JACOB – PTB (Germany)



SLIT TUBE PROBE AND MULTI-PORT METHOD FOR THE ACOUSTICAL CHARATERISATION OF DUCTED AXIAL FANS

Jörg RIEDEL[1], Stefan BECKER[1],
Stefan JACOB[2]

[1] *Universität Erlangen-Nürnberg, Lehrstuhl für Strömungsmechanik, Cauerstraße 4, Haus 2, 91058 Erlangen, Germany*

[2] *Physikalisch-Technische Bundesanstalt, Bundesallee 100, 38116 Braunschweig, Germany*

SUMMARY

Characterizing the acoustics of ducted fans is challenging in practice, due to the presence of multiple superimposed modes and the complex flow conditions. In this paper we compare two methods that are based on different principles, namely the slit tube probe measurement technique proposed in the international standard and the multi-port method. On a modular test rig, a 12-bladed axial fan is characterised using both measurement techniques. The comparison of the measurement results at two operating points shows that both measurement techniques can be suitable for the acoustic characterisation of ducted fans. The advantages and disadvantages of the two methods are discussed in detail to enable engineers to select the best method for their application.

INTRODUCTION

In industrial applications, axial fans are often integrated into complex duct systems. The systems often also contain other elements, such as dampers, orifice plates and auxiliary fans. Sound in ducts propagates in the form of acoustic modes. The number and the shapes of the modes depends on the frequency of the noise and the characteristic cut-on frequencies of the modes. The modes are reflected and superimposed which, creates modulated acoustic fields that can complicate the acoustic characterisation of turbomachinery in ducts. The exact value of the cut-on frequencies depends on the duct diameter and the flow velocity in the duct cross-section. Figure 1 shows the mode structures for the first six occurring duct modes for a duct diameter of 250 mm and no flow. The modes are

shown decomposed in the representation of sound pressure distributions in the duct cross-section. The frequencies given in the red box indicate the frequency from which the respective mode shape can propagate in the duct.

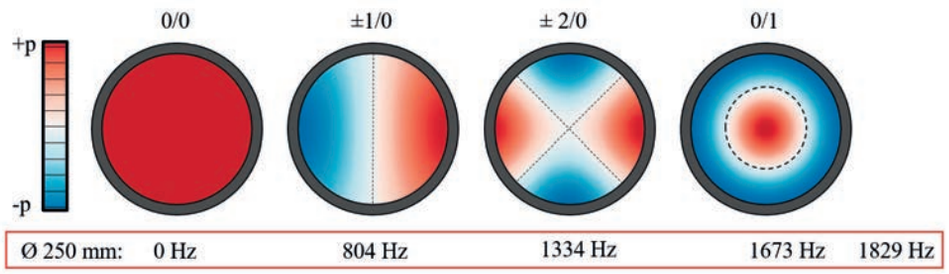


Figure 1: Representation of the decomposed mode structure of the first six duct modes by ascending cut-on frequency [1].

In DIN EN ISO 5136:2009 [2], using slit tube probes is recommended as the standard method for sound power measurements in ducts with moderate flow velocity. However, currently, there are no standardised slit tube probes available on the market, which requires the use of self-made devices to apply this measurement method. This means that although the standard specifies which properties the porous covering materials should have and in which ranges the correction factors of the method may lie, it can be difficult to compare measurements taken with different probes. Another disadvantage of the method is the requirement of subsequent measurements for at least three different locations around the duct, which complicates the test rig design.

Another approach to measuring sound power in ducts involves separating the sound field into duct modes, which can be generated and scattered by the fan. This method is commonly referred to as the multi-port method [3], [4]. Multi-port methods require the implementation of a mode decomposition scheme using data sampled from multiple microphones, with excitation provided by external sound sources. Typically, at least four microphones and two loudspeaker sources are needed for each propagating mode. This limits the method to the low- to mid-frequency range, where only a moderate number of modes can propagate. The multi-port method provides data on the reflection and transmission coefficients of the fan, as well as the emitted modal sound power under anechoic conditions, i.e., as radiated into a pipe with non-reflective boundaries. These results are independent of the test rig, which is advantageous when comparing data obtained at different facilities. Therefore, multi-port methods have been extensively used in the past, for example for propulsion noise [5]–[7] , in HVAC systems [8]–[11] , for impedance measurements [12]–[14] , and for the characterisation of noise absorption materials [15], [16] for aero engines and mufflers. Furthermore, multi-port data can be used to predict combinations of duct components using linear network theory [17], [18].

THEORETICAL PRINCIPLES OF THE MEASUREMENT METHODS

The slit tube probe

The slit tube probe is the measuring instrument of choice according to DIN EN ISO 5136 for determining the sound power radiated by fans and other turbomachinery in ducts. The slit tube probe is an approximately 50 cm long metal tube that is slit lengthwise. A 1/2 inch microphone is attached to the metal tube at the rear end of the probe. The slit is covered with a porous material, which can be for example felt-wool [19], cloth [20] or Kevlar [21]. In this study a thin metal wire mesh covered the slit. The design of the slit tube probe ensured that pressure fluctuations caused by the flow were damped and that the acoustic signal at the end of the probe could be detected by the microphone. The slit tube probe was inserted into the duct using a probe holder through a hole milled into the duct wall. We

ensured that the hole and holder was air-tight after inserting the probe using a precisely fitted cover piece. According to the standard, measurements must be taken with the slit tube probe at at least three different locations along the duct circumference for each fan operating point in order to take into account the mode structure of higher-order modes. The averaged sound pressure level $\overline{L_p}$ from the single measurements around the duct circumference is determined according to equation 1. In this equation, $n = 3$ is the number of single measurements, and L_{pi} corresponds to the sound pressure level of each single measurement. C accounts for a correction constant

$$\overline{L_p} = 10 \log \left[\frac{1}{n} \sum_{i=1}^{n} 10^{0,1 L_{pi}} \right] dB + C, \tag{1}$$

and

$$C = C_1 + C_2 + C_{3,4}. \tag{2}$$

According to equation 2 the constant C is obtained from the the free-field correction of the microphone C_1, the frequency response correction of the microphone windscreen C_2 and the correction for the mean flow velocity and mode distribution of the microphone windscreen $C_{3,4}$. C_1 can be found in the microphone manufacturer's data sheet. C_2 is determined by measurements according to a procedure described in the DIN-standard and $C_{3,4}$ is to be taken from the corresponding table of the DIN-standard as a function of the duct diameter and the present flow velocity.

Finally, the sound power level L_W of the sound radiated into the measuring duct is calculated according to equation 3. To the averaged sound pressure level from equation 1, the logarithmic ratio of the cross-sectional area of the measuring channel S_1, and the reference area with a value of 1m² S_0, is added. Another correction term relates to the logarithmic quotient of air density and speed of sound at measurement conditions ρc and the air density and the speed of sound at standard conditions $(\rho c)_0$. The latter component is assumed to be constant with the value 400 $N\frac{s}{m^3}$

$$L_W = \overline{L_p} + \left(10 \log \frac{S_1}{S_0} - 10 \log \frac{\rho c}{(\rho c)_0} \right) dB. \tag{3}$$

The multi-port-method

To support the theoretical deduction of the multi-port-method, Figure 2 was inserted. The upstream (A) and downstream (B) sections of a ducted fan can be modeled as waveguides containing aeroacoustic modes. For noise problems with sound pressure levels below 140 dB and frequencies where

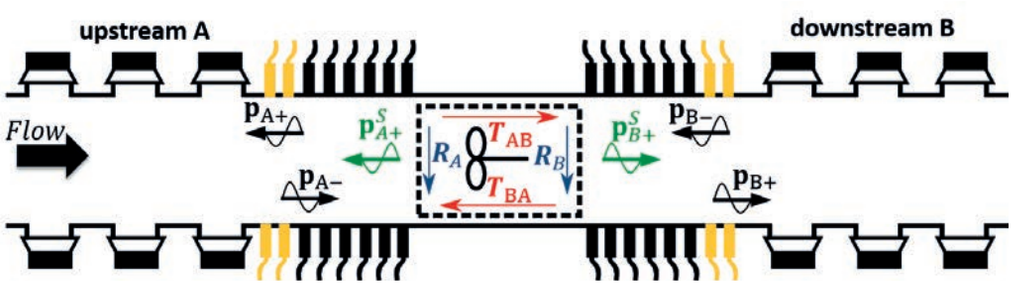


Figure 2: Technical sketch for explaining the multi-port-method theory.

only a small number of acoustic modes can propagate, the fan can be conveniently described as a linear, harmonic acoustic multi-port

$$p_+ = S p_- + p_+^S. \tag{4}$$

Here, $\begin{bmatrix} p_{A\pm} \\ p_{B\pm} \end{bmatrix}$ are vectors containing the complex-valued amplitudes of the modes at both sides of the fan, the index ± indicates positive and negative direction away from the fan, respectively. S is the scattering matrix which contains reflection and transmission coefficients, and $p^S_+ = \begin{bmatrix} p^S_{A+} \\ p^S_{B+} \end{bmatrix}$ is the source vector containing modes that are emitted by the fan under reflection free conditions. The model simplifies the aeroacoustics problem by treating the fan as a black box, enabling the deduction of fan-specific noise characteristics without requiring explicit knowledge of the aeroacoustic source mechanisms. The scattering matrix and the source vector can be determined from both experimental [17] and numerical data [10], typically using a two-step procedure.

In the first step, the scattering matrix is determined by using a set of external, flush-mounted sound sources to acoustically excite the fan. These sound sources must be uncorrelated with the fan noise and powerful enough to generate fields at least 6 dB louder than the fan noise. Under such conditions, p^S_+ can be neglected in equation 4, allowing S to be calculated by inverting p_-. Note that a well-conditioned inverse problem requires at least as many sound sources on each side of the fan as there are cut-on modes. The modal amplitudes are determined using a modal decomposition technique, which involves sampling the acoustic field with flush-mounted microphone arrays placed upstream and downstream of the fan. This requires at least one microphone per upstream and downstream propagation mode on each side of the fan. For a detailed description of the mathematical framework and practical guidelines for implementing the modal decomposition technique, the reader is referred to reference [3]. In a second step, p^S_+ is determined from direct noise measurements of the fan without external sources, using the previously obtained scattering matrix. To suppress flow noise, it is preferable to measure the modal sound power $p^S_+\ p^S_+*$ rather than directly measuring p^S_+, as explained in the references [3], [4]. The modal sound power provides an anechoic representation of the fan noise, describing the noise radiated upstream and downstream into a reflection-free duct.

DESCRIPTION OF THE TEST RIG

For this study, a new test rig was specially designed and built. The test rig comprised of a number of modular duct sections that could be exchanged individually. This allowed us to effortlessly switch between the slit tube probe and multi-port measurement. The total system resistance of the duct system was not changed when the test rig was modified. Also, the components for flow conditioning remained unaltered, which allowed us to better compare the two measuring techniques. Figure 3 shows

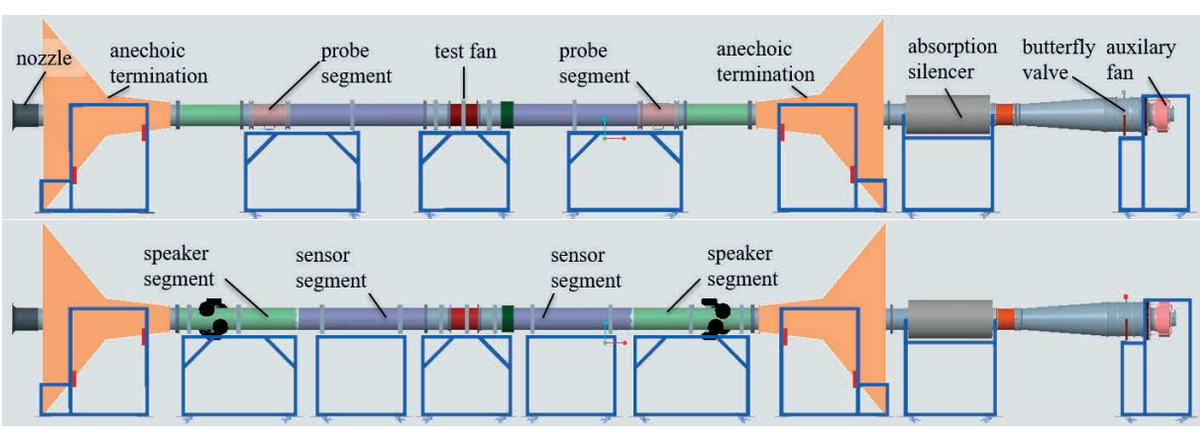


Figure 3: CAD-representation of the test rig, in the configurations slit tube probe (top) and multi-port method (bottom).

the test rig in its two configurations: in the upper part for the slit tube probe measurement technique and in the lower part for the multi-port method. The air entered the test rig via a standardized air-nozzle. The nozzle was also used to determine the volume flow. Subsequently, a symmetrically built measuring section was mounted, whereas the fan under test was located in the centre of the measuring section (shown in red). A photo of the installed fan is shown in Figure 4. The fan was a medium pressure axial fan with 12 impeller blades. Behind the impeller, there was a stationary guide vane. The rotational speed of the test fan was controllable continuously between 0 and 3600 rpm using a frequency converter.

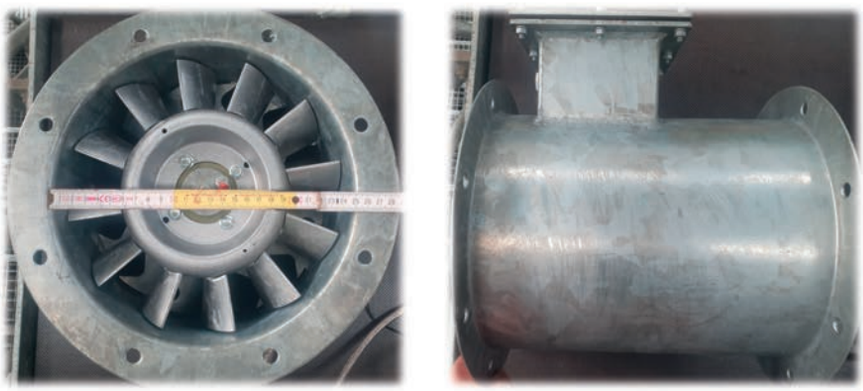


Figure 4: Photo of the axial test fan from the front view (left) and the side view (right).

The fan was embedded in two empty duct segments in line with the instructions in DIN EN ISO 5136. At the inlet and outlet of the measurement section, two probe segments were installed through which the slit tube probes were inserted. These segments were mounted with fixed/loose flange combinations that allowed us alter the probe's location. Figure 5 shows the slit tube probe used in the measurements with the associated aluminium holder and the 3D-printed cover. The measurement sections were



Figure 5: Photo of the slit tube probe used, including holder and cover segment.

terminated with anechoic terminations at the upstream and downstream side. The flow rate and back pressure was controlled through an butterfly valve and an auxiliary fan at the test rig's outlet. Some of the sections in the test rig could be replaced with loudspeaker and microphone arrays for performing the multi port measurement, as shown in Figure 3 (bottom). Figure 6 shows the microphone array and its attachment (left) and the loudspeaker array (right).

MEASUREMENT RESULTS

In this study, two operating points of the test fan were examined. In both cases, the fan rotated at 1800 rpm, which is half of is maximum allowed rotation speed. At the first operating point, the butterfly valve at the end of the test rig was completely closed, resulting to zero volume flow. At the second operating point, the butterfly valve was fully open and the auxiliary fan provided additional support at maximum speed. This resulted in an average volume flow of 0.6 m³/s, which corresponded to an average flow velocity of 12 m/s. For the sake of brevity, only the results downstream of the test

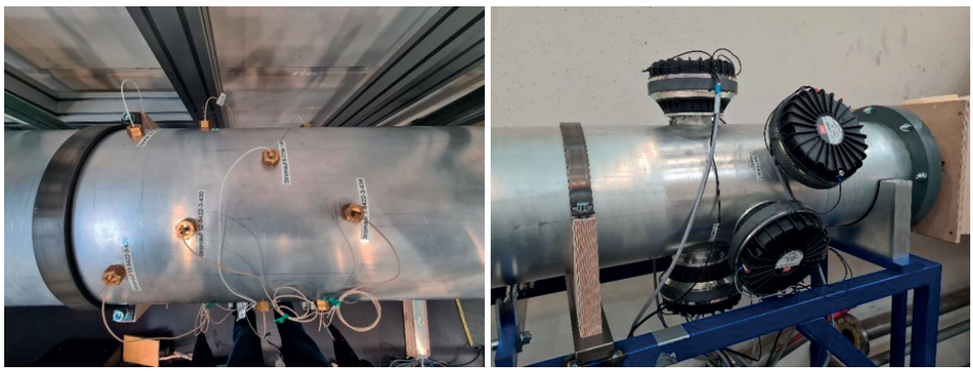


Figure 6: Photograph of the sensor segment (left) and the speaker segment (right).

fan are shown below. The presentation of the measurement results is limited to the range between 200 and 1805 Hz, whereas the upper limit was dictated by the number of modes that could be resolved with the microphone array in the multi-port method. The lower limit of 200 Hz was due to the characteristics of the loudspeakers used.

Slit tube probe

The measurement results for the two operating points examined using the slit tube probe can be seen in Figure 7. The analytically calculated frequencies of the blade passing frequency (BPF) and its higher harmonics, as well as the cut-on frequencies of the higher-order modes, are indicated by the vertical lines in both diagrams. Shown in blue, green and violet are the three individual measurements at angles of rotation of the slit tube probe of 120° respectively. Shown in red is the result averaged logarithmically according to equation 1. We found that the third, fourth and fifth blade passing frequency of the fan is only detected at the operating point with the higher volume flow. At the first cut-on frequency (804 Hz), a hump-like increase was seen in the spectrum for both measurements. For the other cut-on frequencies, no anomalies were observed in the measurement with the slit tube probe. The observation of the third blade passing frequency for the operating point at 0.6 m³/s showed that in particular the tonal components differed greatly depending on the positioning of the slit tube probe. While the 3rd blade passing frequency cannot be detected at all for the rotation angle of -120° (purple), it clearly stands out from the broadband ambient noise by approximately 8 dB for the rotation angle of 0° (blue) with a value of 58.2 dB. This highlights the necessity of carrying out several individual measurements along the duct circumference.

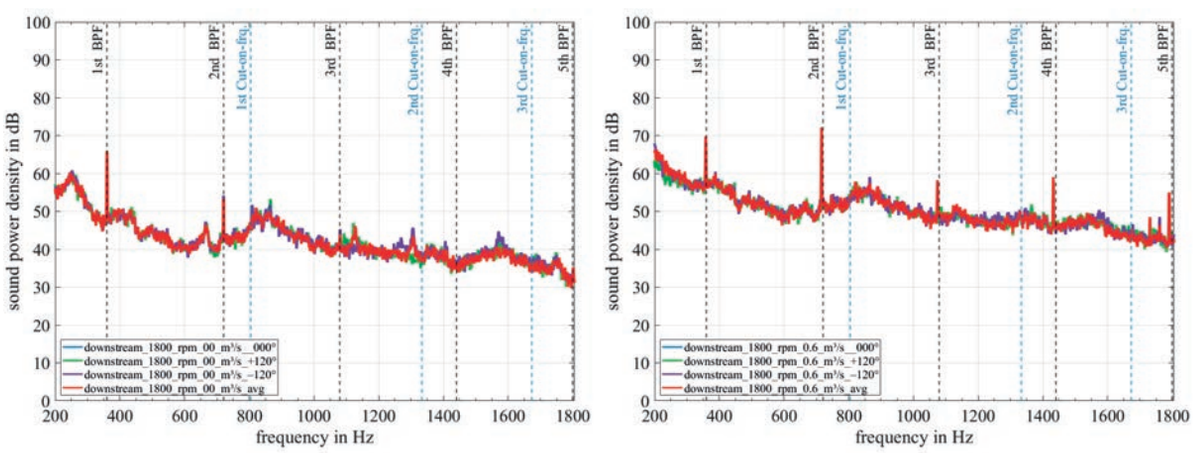


Figure 7: Results for the measurement with the slit tube probe downstream of the test fan with zero volume flow (left) and 0.6 m³/s (right).

FAN 2025
Antibes - Juan-les-Pins (France), 9 - 11 April 2025

Multi-port-method

The passive properties of the test fan determined in the first step of the procedure are shown for each mode in Figure 8. The transmission coefficients for the duct sections upstream (tauA) and downstream (tauB) of the fan are shown in blue and green, respectively. The reflection coefficients upstream (rhoA) and downstream (rhoB) of the test object are shown in red and black, respectively. Transmission coefficients with a value of 1 indicate perfect transmission, whereas Reflection coefficients with a value of 1 indicate perfect reflection. Hence, we found that the fan was transmissive for most frequencies for all modes, although there were narrow frequency bands for which the fan became reflective for all modes.

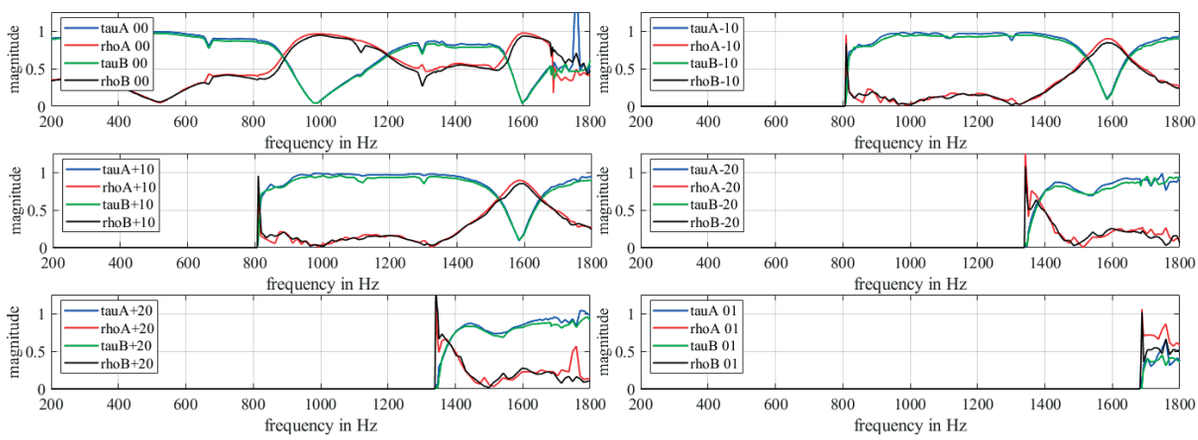


Figure 8: Passive properties of the tested axial fan for the first six duct modes.

Figure 9 shows the results for the active properties of the test fan calculated with the multi-port-method. On the left side, the results are shown for an operating point zero volume flow and on the right side for an operating point with a volume flow of 0.6 m³/s. It should be noted, that the passive properties that were used throughout the multi-port procedure were only measured at an quiescent fan, similar to the study in Reference [22]. The coloured lines correspond to the sound power that was

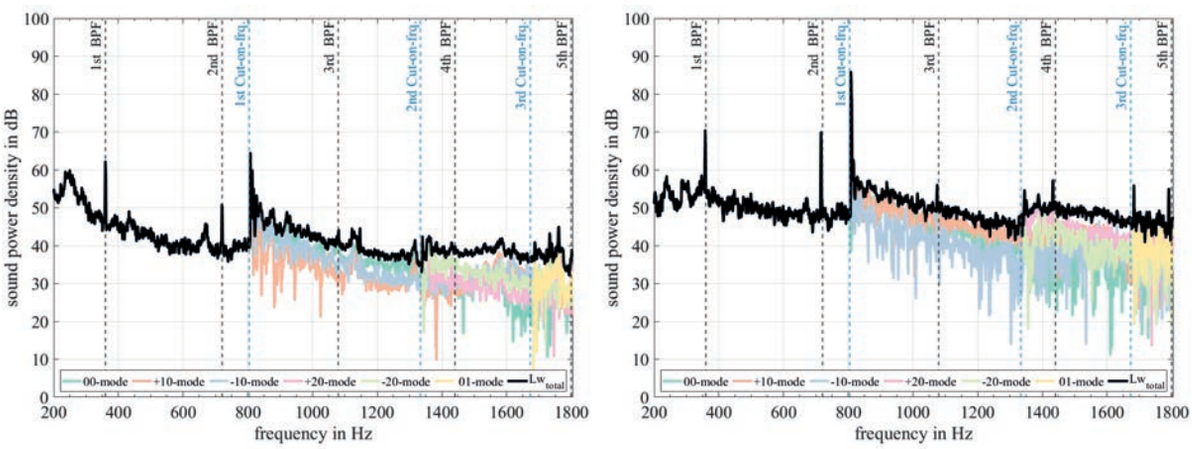


Figure 9: Active Properties as result of the multi-port-analysis downstream of the test fan for the operating points with zero volume flow (left) and 0.6 m³/s (right). The spectra of the individual duct modes are shown in colour. The calculated total sound power level Lw_{total} is shown in black.

emitted by the fan in the six individual duct modes. In order to be able to compare the measurement results with those of the slit tube probe, the sound power levels of the individual duct modes were logorathmically added in the corresponding range. This curve, declared as the total sound power level

Lw_{total}, is shown in black in both plots. We found similar characteristics of the spectrum regarding the blade passing tones. In addition, we found sharp increases of the sound power level at the cut-on frequencies, especially for the first one. Here, the mode decomposition method was ill-conditioned, and the frequency range around the cut-on frequencies should be excluded when the sound power is measured with the multi-port method.

DISCUSSION

Figure 10 shows the results obtained with the two measurement methods in direct comparison. For the zero volume flow variant, both curves are congruent over almost the entire frequency range, whereas for 0.6 m³/s, we saw an increase in sound power levels measured with the slit tube probe at low frequencies. The slit-tube probe is prone to hydrodynamic pressure fluctuations that can mask the acoustic signals for low-frequencies. Those fluctuations are removed with the multi-port method.

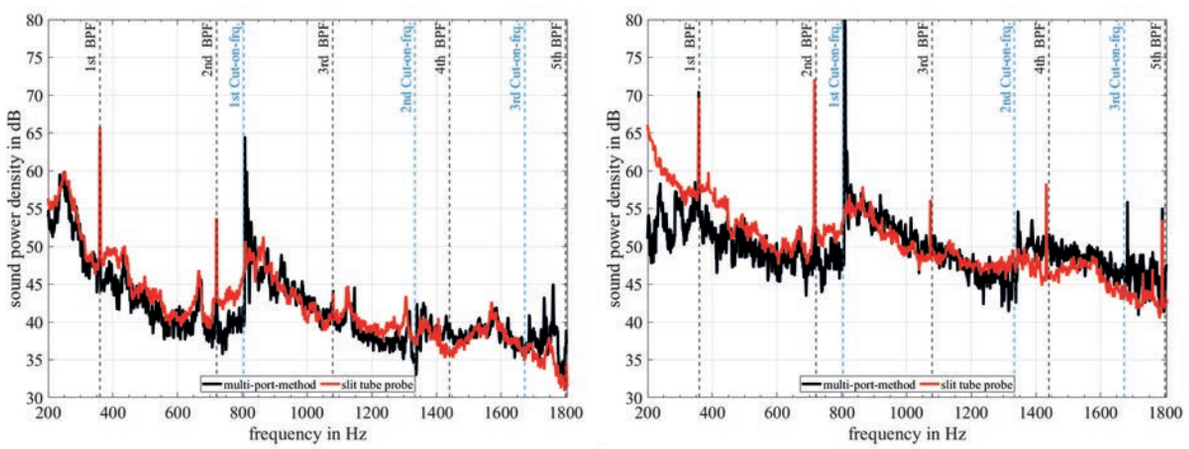


Figure 10: Comparison of the downstream measurement results with the slit tube probe (red) and the multi-port method (black) for operating points of the tested fan with zero volume flow (left) and 0.6 m³/s (right).

The sound spectrum of turbomachinery is often largely determined by the tonal components of the blade passing frequency and its higher harmonics. In the present case of the ducted axial fan, the tonal peaks also emerge significantly from the broadband noise. In order to be able to compare the two methods quantitatively at the characteristic frequency points, the values of the sound power density at the blade passing frequency and the higher harmonics are shown as single values in Table 1. The left half of the table describes the operating point at zero air volume flow and the right half of the table describes the operating point at 0.6 m³/s volume flow.

Table 1: Comparison of the sound power density values in db at the characteristic tonal components of the axial fan for the two methods, slit tube probe and multi-port method.

	0 m³/s					**0.6 m³/s**				
	1.BPF	**2.BPF**	**3.BPF**	**4.BPF**	**5.BPF**	**1.BPF**	**2.BPF**	**3.BPF**	**4.BPF**	**5BPF**
slit tube	65.8	53.7	43.9	36.1	34.7	69.6	72.1	56.1	58.3	53.5
multi-port	62.1	50.8	44.1	39.8	38.9	70.4	69.9	56.0	57.2	55.0

The similarities in both measurement results suggest that either method can be effectively used in practice to measure the sound power spectrum of ducted components. However, the methods differ significantly in terms of required hardware and measurement protocols. The slit tube probe requires less hardware, as a single probe is sufficient to perform the entire measurement. In contrast, the multi-port method demands multiple probes and additional loudspeaker sources for each propagating

duct mode. Therefore, in cases with many modes, the slit tube probe is the preferred option. For scenarios with a moderate number of modes, the multi-port method becomes a feasible alternative to slit tube probes. It can effectively eliminate internal reflections and hydrodynamic fluctuations, making it especially suitable for low frequencies and the plane wave range.

The initial test rig design is more challenging for the multi-port method compared to the slit tube probe, as the microphone and loudspeaker arrays must be carefully designed. However, once implemented, the multi-port method can be easily automated, whereas slit tube probe measurements require multiple sequential manual measurements or specialized auto-rotatable probe sections. A measurement setup in which three slit tube probes are used simultaneously is made complicated by the low availability of the probes as mentioned at the beginning and would furthermore increase the probability of artificially manipulating the flow field in the duct. Consequently, for repetitive testing or large test campaigns with the same duct diameter, the multi-port method might be preferable. On the other hand, if frequent modifications to the test rig (e.g., changes to the diameter of the test section) are required, the slit tube probe is more practical.

It should also be noted that data processing for slit tube probe measurements involves only averaging of multiple measurements. In contrast, the multi-port method requires more advanced post-processing, which can be error-prone due to the complexity of matrix operations and multi-dimensional data handling. The initial setup of post-processing tools for the multi-port method is more time-consuming and requires several validation steps. However, the multi-port method provides valuable information about both the emitted noise and the scattering properties of the component for all considered noise. This insight can be useful in research and development processes, such as the design of after-treatment systems like mufflers and filters.

CONCLUSION

In the present work, the two measurement techniques, slit tube probe and multi-port method, were compared with each other using measurements on an industrial ducted axial fan. The aim of the measurements was, on the one hand, to compare the obtained measurement results with each other and, on the other hand, to work out the advantages and disadvantages of the two measurement techniques in direct comparison. In summary, it can be said that the measurement technique with the slit tube probe is a proven and easy-to-implement method for characterising axial fans in duct flows. The comparison with the multi-port method showed almost identical results over the entire frequency range. The advantages of the multi-port method are particularly noticeable when examining small duct diameters and high flow velocities. In this case, the required measurement hardware remains manageable. In addition, the microphone correlation technique effectively suppresses flow noise.

REFERENCES

[1] B. Berchtenbreiter and S. Becker, *Charakterisierung der akustischen Eigenschaften von Axiallüftern in Rohrleitungen*, in *Fortschritte der Akustik - DAGA 2018*, **2018**.

[2] *DIN EN ISO 5136:2009-11: Akustik - Bestimmung der von Ventilatoren und anderen Strömungsmaschinen in Kanäle abgestrahlten Schallleistung - Kanalverfahren*, DIN-Norm, **2009**.

[3] S. Sack, M. Åbom, *et al.*, *On acoustic multi-port characterisation including higher order modes*, Acta Acustica united with Acustica vol. 102, no. 5, pp. 834–850, **2016**.

[4] J. Lavrentjev and M. Åbom, *Characterization of fluid machines as acoustic multi-port sources*, Journal of Sound and Vibration vol. 197, no. 1, pp. 1–16, **1996**.

[5] S. Jacob, E. Trigell, M. Mihaescu, and M. Åbom, *Acoustic scattering in a small centrifugal compressor based on the use of linearized equations in a rotating frame*, Journal of Sound and Vibration vol. 544, p. 117 315, **2023**.

[6] R. Veloso and Y. Elnemr, *Linear acoustic multi-port modeling of automotive charge air coolers*, Noise Control Engineering Journal vol. 65, no. 1, pp. 42–51, **2017**.

[7] R. Kabral and M. Åbom, *Investigation of turbocharger compressor surge inception by means of an acoustic two-port model*, Journal of Sound and Vibration vol. 412, pp. 270–286, **2018**.

[8] M. W. Nashed, T. Elnady, and M. Åbom, *Modeling of duct acoustics in the high frequency range using two-ports*, Applied Acoustics vol. 135, pp. 37–47, **2018**.

[9] C. Calmettes, E. Perrey-Debain, E. Lefrançois, and J. Caillet, *A multi-port scattering matrix formalism for the acoustic prediction in duct networks*, Acta Acustica vol. 7, p. 13, **2023**.

[10] S. Sack, M. Shur, M. Åbom, M. Strelets, and A. Travin, *Numerical eduction of active multi-port data for in-duct obstructions*, Journal of Sound and Vibration vol. 411, pp. 328–345, **2017**.

[11] O. Van Dessel, H. Denayer, and W. De Roeck, *Aeroacoustic two-port characterisation technique for ventilation valves*, Journal of Sound and Vibration vol. 575, p. 118 257, **2024**.

[12] A. M. Spillere, A. A. Medeiros, and J. A. Cordioli, *An improved impedance eduction technique based on impedance models and the mode matching method*, Applied Acoustics vol. 129, pp. 322–334, **2018**.

[13] Y. Aurégan, M. Leroux, and V. Pagneux, *Measurement of liner impedance with flow by an inverse method*, in *10th AIAA/CEAS aeroacoustics conference*, **2004**, p. 2838.

[14] T. Elnady, H. Bodén, and B. Elhadidi, *Validation of an inverse semi-analytical technique to educe liner impedance*, AIAA journal vol. 47, no. 12, pp. 2836–2844, **2009**.

[15] H. Denayer, W. Desmet, and W. De Roeck, *Indirect measurement of liner impedance under grazing flow using the two-port eduction method*, in *INTER-NOISE and NOISE-CON Congress and Conference Proceedings*, Institute of Noise Control Engineering, vol. 259, **2019**, pp. 304–314.

[16] L. de Santana, W. De Roeck, W. Desmet, and P. Ferrante, *Two-port indirect acoustic impedance eduction in presence of grazing flows*, in *17th AIAA/CEAS Aeroacoustics Conference (32nd AIAA Aeroacoustics Conference)*, **2011**, p. 2868.

[17] S. Sack and M. Åbom, *Investigation of orifice aeroacoustics by means of multi-port methods*, Journal of sound and vibration vol. 407, pp. 32–45, **2017**.

[18] A. Snakowska and J. Jurkiewicz, *A new approach to the theory of acoustic multi-port networks with multimode wave and its application to muffler analysis*, Journal of Sound and Vibration vol. 490, p. 115 722, **2021**.

[19] I. C. Shepherd and R. La Fontaine, *Microphone screens for acoustic measurement in turbulent flows*, Journal of Sound Vibration vol. 111, no. 1, pp. 153–165, **1986**.

[20] W. Neise and B. Stahl, *The flow noise level at microphones in flow ducts*, Journal of sound and vibration vol. 63, no. 4, pp. 561–579, **1979**.

[21] J. Riedel, F. Czwielong, and S. Becker, *Investigation of a new shielding material for slotted tubes regarding sound power measurements of ducted fans*, in *FAN 2022: International Conference on Fan Noise, Aerodynamics, Applications and Systems.*, **2022**.

[22] S. Sack, *Comparison of the scattering of an operating and a quiescent fan*, in *FAN 2015: International Conference on Fan Noise, Technology and Numerical Methods. 15 April 2015-17 April 2015, Lyon, France*, **2015**.

ACKNOWLEDGEMENT

The authors would like to thank the German Federal Ministry for Economic Affairs and Climate Protection (BMWK), which provided financial support for the research work as part of a project in the programme *Industrielle Gemeinschaftsforschung (IGF)* with the funding number IGF 20997. The authors would also like to thank the Forschungsvereinigung für Luft- und Trocknungstechnik (FLT e.V.) for their technical support of the project.

F1 Noise Prediction By Analytical / Numerical Models

10 April - 16:30 - Auditorium

Chairmen: Frieder Lörcher, Ossian Kaghad

List of papers

Validation of the Hybrid Fan Noise Simulation Techniques on EAA Axial Benchmark Fan

- Korcan KUCUKCOSKUN – Siemens Digital Industries Software (Belgium)
- Lars ERBIG – Siemens Digital Industries Software (Germany)

Assessing Sound Propagation Models for a Low-Speed Axial Fan

- Vinay RAVI – Siemens Digital industries Software (Belgium)
- Sophie LE BRAS – Siemens Digital industries Software (France)
- Lars ERBIG – Siemens Digital industries Software (Germany)
- Korcan KUCUKCOSKUN – Siemens Digital industries Software (Belgium)

On the Effect of Tip Flow on the Noise of a Ducted Rotor

- Jose RENDÓN-ARREDONDO – Université de Sherbrooke (Canada)
- Stéphane MOREAU – Université de Sherbrooke (Canada)



VALIDATION OF THE HYBRID FAN NOISE SIMULATION TECHNIQUES ON EAA AXIAL BENCHMARK FAN

Korcan KUCUKCOSKUN[1], Lars ERBIG[2],

[1] *Siemens Digital Industries Software, Interleuvenlaan 72, B-3001 Leuven, BELGIUM*

[2] *Siemens Digital Industries Software, Hanauer Landstraße 114, 60314 Frankfurt, GERMANY*

SUMMARY

Two hybrid aeroacoustics simulation methods based on constant density CFD simulation are applied to the EAA axial fan benchmark problem. The broadband noise generated by the axial fan is both studied with time domain volume source-based analogy and frequency domain surface source-based analogy. The results are validated with the experiments available in the literature. Very good agreement is observed between both methodologies and the experiment. The high frequency behavior of the selected methodologies is also discussed.

INTRODUCTION

Considering customer comfort, cooling fan noise is a concern for various applications including automotive, industrial machinery and home appliances. Engineers working in both integrators, OEMs and suppliers are looking for reducing the noise emitted by their fan designs. Simulation is a good alternative before creating physical prototypes.

There are various simulation techniques to tackle fan noise varying from simplified semi-analytical models [1,2] to highly resolved numerical solutions [3,4]. Engineers are looking for the best compromise to get the accurate results within an acceptable time.

For low-speed fan noise applications, the aeroacoustics problem can be split into two steps as first capturing the source field from flow simulation and later use acoustic propagation techniques. This lets the flow solution to be defined without acoustic propagation concerns hence might accelerate the end-to-end simulation time. Since the acoustic mesh constraints are not applied to the flow mesh, this can provide acoustic results for higher frequencies of concern too.

The well-studied 9-blade European Acoustics Association (EAA) Benchmark axial fan [5-10] presented in TU-Wien is used to validate the proposed hybrid methodology. Both measurement and previous simulations of EAA Benchmark fan is available in the literature. This fan is known to generate a rather broadband noise spectrum at the far-field microphones.

The flow problem is solved with a transient Large Eddy Simulation (LES). Since this is a low-speed fan noise application, the loading noise is considered to be the dominant contributor. Therefore, the transient surface pressure on the fan blades is exported to be used in the source modeling of the second propagation step.

The fan loading noise source is then used in a frequency domain Helmholtz solution for the propagation. An adaptive order Finite Element Method (FEMAO) is used to optimize the acoustic mesh and solution time. The installation effects including the surrounding duct and wall geometry are also accounted in the propagation part of the solution.

The acoustic pressure results show a good agreement with the measurements up to 6 kHz. Compared to alternative time-domain solutions where the flow and acoustics equations are solved with a similar mesh resolution, the accuracy at the higher frequencies is also improved with the proposed technique as the sound propagation to the far field microphones is not affected by potential temporal under-resolution.

LOW SPEED AXIAL BENCHMARK FAN

In this paper, the axial fan set-up presented in the benchmark database of EAA [5] is considered, based on the measurements by Krömer at FAU Erlangen-Nürnberg [6], and discussed in detail by Schoder et al. [7].

The fan has 9 blades and is mounted in a short duct with a diameter of 0.5 m. The duct is separating two rooms, where the measurements are taken in the upstream anechoic room. The rotation speed of the fan is fixed at 1486 RPM and operated at a volumetric flow rate of 1.4 m^3s^{-1}, which results in a 125.6 Pa pressure rise. Figure 1 shows a representation of the benchmark fan.

The flow field was measured with 15 flush mounted sensors located on the duct wall. The acoustic far-field is measured with 7 microphones located upstream of the fan as an arc with 1m radius.

This paper focuses on the acoustics propagation methodologies. A validation of the flow field with the proposed approach can be found in the related reference [11].

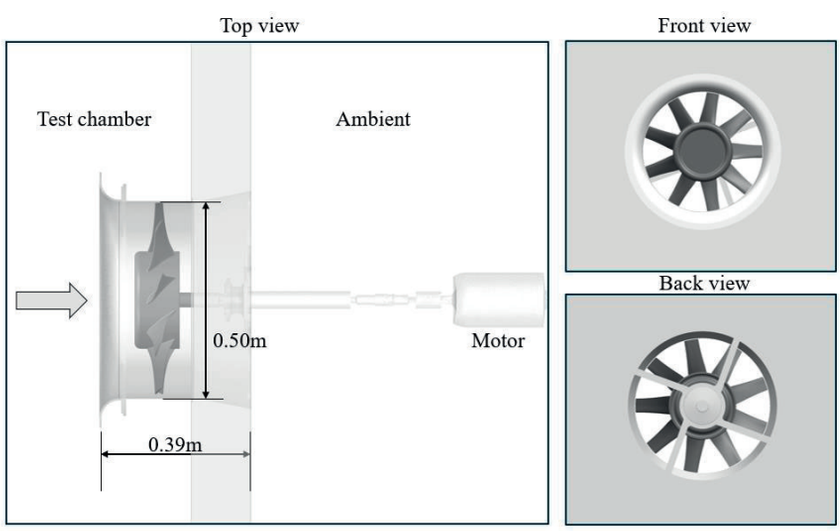


Figure 1: Axial fan benchmark geometry, retrieved from [5]

FAN 2025
Antibes Juan-les-Pins (France), 9 – 11 April 2025

NUMERICAL METHODOLOGY

With the given configuration and operating condition, the tip Mach number is less than 0.15. Since tip Mach number is well below 0.3, and since there have been no reports on acoustic feedback on this fan, one can separate the flow and acoustics fields in simulations [12]. This enables to use hybrid methods on this application.

The noise generated by the low-speed axial fan is simulated with two different hybrid methodologies. First, a time-domain Perturbed Convective Wave Equation (PCWE) [11,13] is solved on top of a constant density LES. In this method the acoustic propagation is calculated on the same mesh as the flow fields, using the flow quantities seamlessly. All noise source contributes, and reflective effects of the components modeled in the flow-field are considered.

The other hybrid methodology is based on the loading source of the axial fan [14]. From the constant density LES solution, the transient surface pressure of the fan is exported. The blade is split into compact segments for the highest frequency of interest. The pressure field of each compact segment is integrated and the center of gravity of each segment is assigned with a dipole field with the equivalent force strength. The propagation is performed in a FEMAO [15] solution in frequency domain. The FEMAO methodology relies on a single mesh solved for all frequencies of interest. It enables the degree of freedoms (dof)s of the mesh refined hierarchically without remeshing the problem. This allows a coarse mesh to be used for all frequencies, instead of a fine mesh which was designed for the highest frequency of interest. Needless to say, this methodology provides a faster run time compared to the solution of a such fine FEM mesh for all of the frequencies considered. The rotating dipole is projected to the high order dofs of the FEMAO mesh. The projected components apply as the source for the FEMAO solution and the acoustic pressure at the microphones are computed. It is worth to note that the microphones can be located outside of the FEMAO mesh thanks to the Automatically Matched Layer (AML) boundary located on the envelope of the finite element mesh [16]. This AML boundary on one hand does not reflect the acoustic waves generated from inside of the mesh, and also lets them propagate freely to the exterior microphones accounting for an infinite plane representative of the large wall where the fan is attached

APPLICATION TO THE BENCHMARK FAN

The numerical setup of the underlying CFD simulation closely follows the reference [11]. A second order accurate implicit temporal discretization with 2,000 time-steps per revolution of the fan is utilized. Space is discretized using a trimmed mesh with a target mesh size of 6.8 mm between the fan and the microphones, corresponding to approximately 12.5 cells per wavelength at a frequency of 4 kHz. The fan motion is modelled using a sliding mesh approach, in which a disk around the fan blades physically moves at each time-step. In contrast to the reference [11], the radius of the rotating disk is extended to include the duct walls. Hence, the boundary faces on these walls move, but are still treated as stationary walls, compensating the grid motion. This avoids potential discretization errors due to the mesh intersection in the sensitive tip gap area. On the hub and on the fan blades, a mesh size of 0.425 mm is used combined with 8 prism layer cells with a total thickness of 0.5 mm (see Figure 2). With these mesh settings $x^+ < 100$ and $y^+ < 3$ are achieved almost everywhere on the fan, which is in line with traditional requirements for wall-resolved LES and other simulations reported recently in the literature [8-10]. These mesh settings lead to more than 10 cells in the tip gap, and hence the tip gap vortices are well captured.

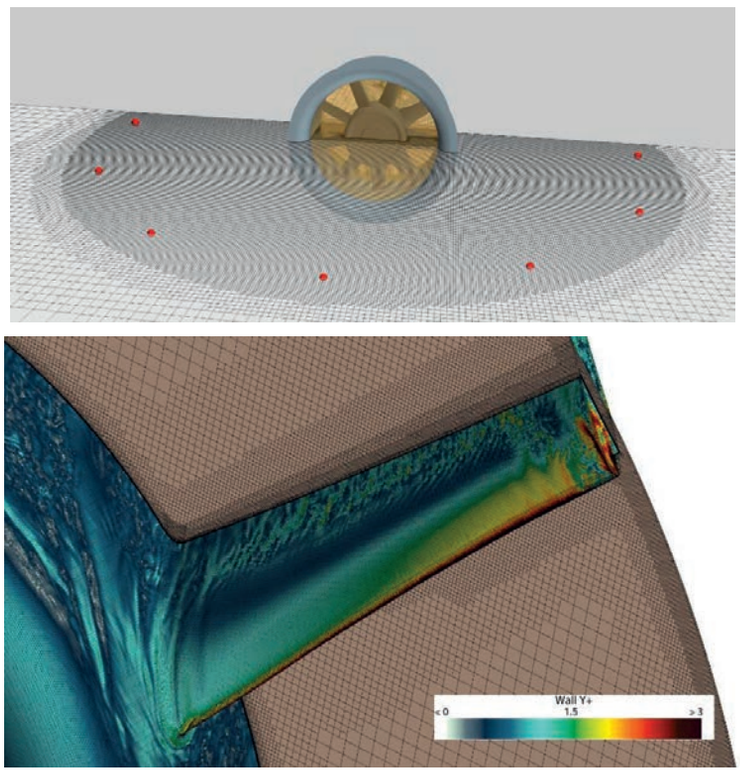


Figure 2: Mesh sections of the underlying CFD simulation. The rotating area is marked in yellow.

The methods defined above are applied to the axial benchmark fan. The flow field is resolved over 10 rotations of the fan, excluding the initialization phase. To obtain converged acoustic pressure spectra, the acoustic field is computed over 4 rotations with 50 % overlap. The resulting 4 blocks are then root-mean-square (RMS) averaged.

One of the items addressed in this paper is the high frequency broadband noise generated by the axial fan. The far-field microphone pressure results are targeted to be predicted till 8kHz using the same flow simulation. For the second method with FEMAO, the fan blades are split into segments which are equivalent to the half of the wavelength at 8 kHz [17]. Figure 3 shows some of the compact segments created on the blades. The hub is discarded from the source components, and the 9 blades are split into ~300 spanwise and chordwise compact segments. Please note that this high number of segments are needed only for high frequency problems. For general industrial applications, depending on the highest frequency and blade size, generally speaking, few 10s of segments are already good enough to capture the source terms.

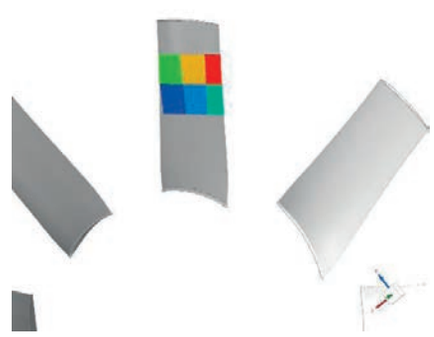


Figure 3: Fan blade segmentation representation

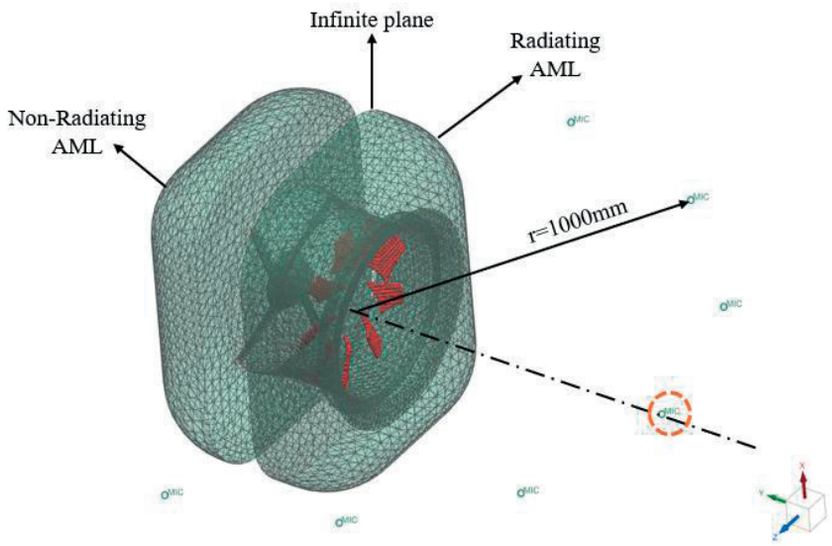


Figure 4: Finite Element model of the fan-duct simulation and microphone positions

The computed fan blade segments and the finite element model used in the FEMAO mesh are shown in Figure 4. The two rooms are represented as the two convex domains. The near-field surfaces such as the duct supports are also considered as rigid, so called reflective, surfaces. The fan blades and the hub are not modeled as reflective surfaces. The convex envelope facing the microphones is modeled as a radiating AML to get the microphone pressure field. The other convex faces are modeled as non-radiating AML since the microphones will not receive any contribution from those faces. Additionally, the wall outside of the duct. separating two rooms is modeled as Infinite Plane to make sure, the acoustic waves are reflected by the wall, even not physically modeled out of AML.

The far-field measurements are available over 7 microphones located ~1 m away from the rotation center as seen in Figure 4. The results are presented over the highlighted microphone on the rotation axis, and over the RMS average of the 7 microphones.

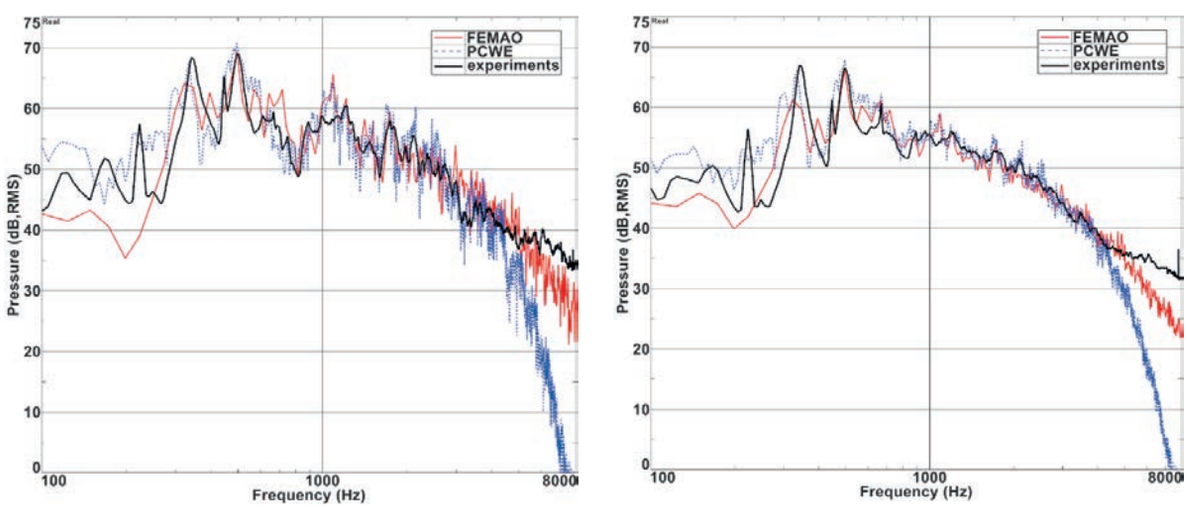


Figure 5: Acoustic pressure at the microphone on the rotation axis (left) and RMS averaged over 7 microphones (right)

Figure 5 (left) shows the acoustic pressure at the highlighted microphone located on the rotation axis as shown in Figure 4. Red, dashed blue and thick black lines represent the FEMAO methodology, PCWE solution and experiments, respectively. A very good agreement is observed with the simulated solutions and experiments in the frequency band of 500 Hz to 4 kHz where the difference is few dBs. For lower frequencies, some deviations are observed, yet still a fair agreement is visible. It is notable that for high frequencies the PCWE solution decays faster than FEMAO one since the resolution of acoustic waves are not possible with the used CFD mesh. For those frequencies, a finer mesh till the observers and corresponding time-step selection would be needed in the PCWE solution. A similar pattern is visible for the sound field averaged over 7 microphones too, as seen in Figure 5 (right). Both methods agree very well with the measurements for the frequency range till 4 kHz. The FEMAO one still catches up with the measurements for higher frequencies up to 6 kHz. The resulting difference at the highest frequencies can be due resolution of the flow field, or other noise sources that are not accounted in the loading noise contribution used in the FEMAO formulation. Nevertheless, the agreement shows that both methods are applicable for the axial benchmark for the frequency range of interest. This also cross-validates the time domain volume source based PCWE, and frequency domain surface source based FEMAO solutions implementations.

The PCWE solution is attractive since the far-field acoustic results can be obtained together with the CFD solution with limited overhead. The FEMAO one can be helpful to accelerate the CFD part since the acoustics requirements are not needed for the CFD meshing steps, even though it will use a second solve phase in FEMAO domain. In this paper, the same CFD solution is used, and this benefit is not demonstrated. On top of that, the FEMAO application is also capable to account for other reflective surfaces, without re-running the CFD simulation [14].

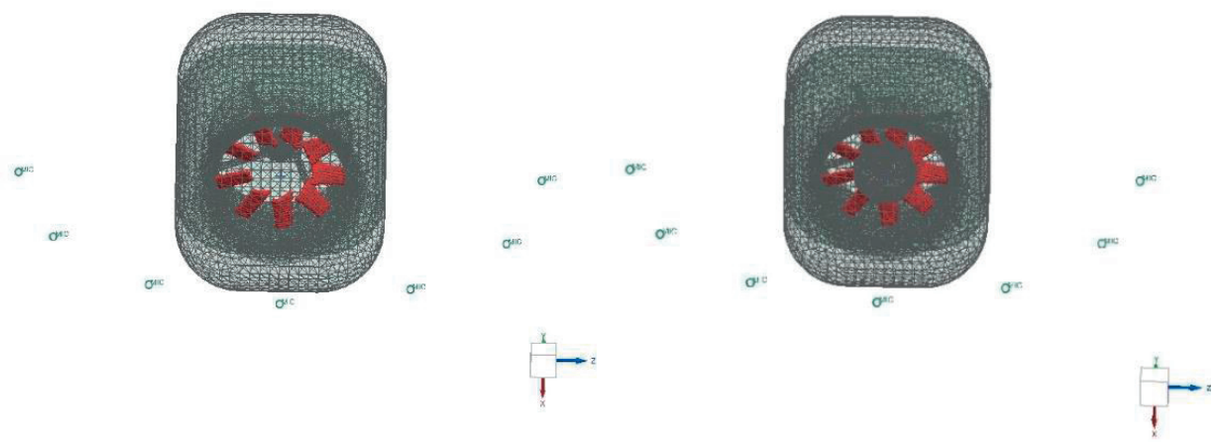


Figure 6: Finite element representation without (left) and with (right) hub as scattering surface

In the comparison presented in Figure 5, only the fan blades are used in the FEMAO modeling. The hub is discarded as a noise source or as a reflective surface. One can add the hub as reflective surface and recompute the acoustic far-field without re-running the CFD solution. Figure 6 shows the FEMAO setup without (left) and with the hub (right) as reflective surface. The same source force field is used in the simulation to compare the effect of the hub as scattering surface.

Figure 7 shows the acoustic response on the highlighted microphone (left) and the RMS-averaged microphone (right) results. The thick black line represents the experiments whereas the red line and blue dash line represent the simulations without and with the hub as reflective surface, respectively. The effect of the hub as reflective surface seems to be more visible at lower frequencies. Adding the hub as a reflective surface, the simulation results are further improved in the 400 Hz-600 Hz frequency band for both for the individual microphone and averaged over 7 microphones.

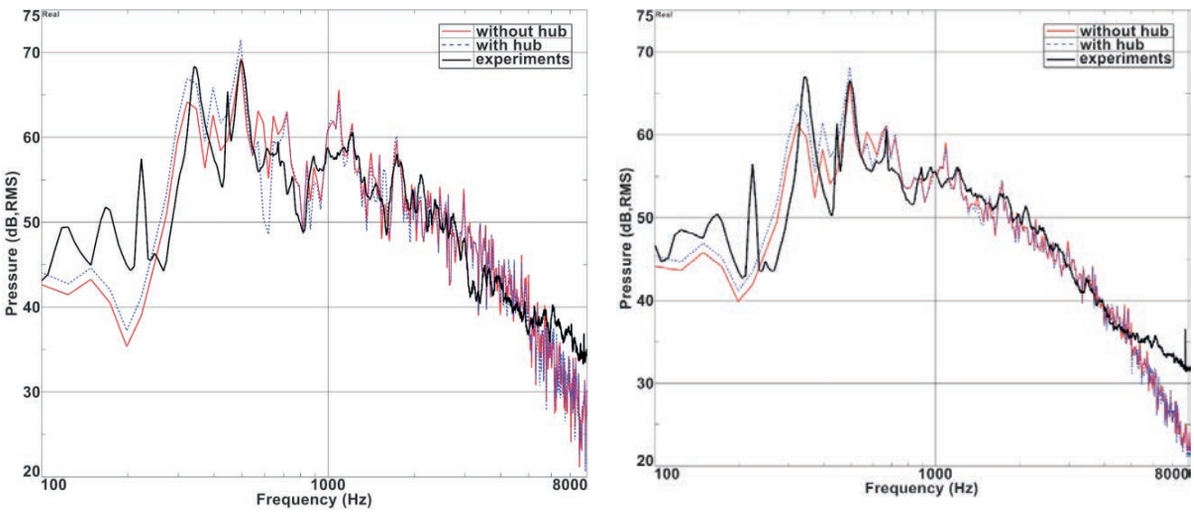


Figure 7: Acoustic pressure without (red solid) and with (blue dashed) the hub at microphone on the rotation axis (left) and RMS averaged over all 7 microphones (right).

CONCLUSION

Two hybrid aeroacoustics simulation techniques, using the same LES flow simulation as input, one focusing on PCWE in time domain, another on loading noise with FEMAO in frequency domain, are applied to the EAA axial-fan benchmark. Very good agreement is observed with both simulations compared to measurements available in the literature. Using the same constant density CFD solution, it is shown that the frequency domain FEMAO based solution does not suffer from the flow mesh resolution for the highest frequencies of interest. Since it is based on finite-element, it can also be coupled with arbitrary reflective and absorbing surfaces in the propagation domain without re-running the CFD simulation

BIBLIOGRAPHY

[1] A. Guédel, Y. Rozenberg, M. Roger, G. Perrin – *Prediction of fan trailing-edge noise* Proceedings of Fan Noise 2007 Symposium, Lyon, **2007**

[2] J. Christophe, et al. – *Experimental Validation of Ducted Low-Speed Cooling Fan Noise Prediction Methods Including Broadband Scattering,* AIAA Aeroacoustics Conference, Lyon, **2016**

[3] T. Carolus, M. Schneider, H. Reese – *Axial flow broad-band noise and prediction*, Journal of Sound and Vibration, 300, **2007**

[4] D. von Werne, et al. – *Fan Noise Prediction for Off-Highway Vehicle*, SAE Technical Paper 2017-01-1834, **2017**

[5] EAA benchmark database, URL: https://eaa-bench.mec.tuwien.ac.at/

[6] F. Krömer, – *Sound emission of low-pressure axial fans under distorted inflow conditions*, PhD Thesis, Erlangen, **2017**

[7] S. Schoder, et al. – *Computational aeroacoustics of the EAA benchmark case of an axial fan*, Acta Acustica, 4, (2020), 22, **2020**

[8] E. Antoniou, et al. – *Numerical flow noise simulation of an axial fan with a Lattice-Boltzmann solver*, Acta Acustica, 7 (2023), 65, **2023**

[9] D. Ghodake et al. – *Investigation of forward and backward sweep axial fan noise sources using Lattice Boltzmann Method*, Proceedings of Fan Noise 2022 Symposium, Senlis, **2022**

[10] S. Becker et al. – *On the fluid mechanical and acoustic mechanisms of serrated leading edges*, Proceedings of Fan Noise 2022 Symposium, Senlis, **2022**

[11] L. Erbig, S. Lardeau – Hybrid Aeroacoustic Simulation of EAA's Axial Fan Benchmark, DAGA, Stuttgart, **2022**

[12] R. Ewert, W. Schröder – *Acoustic perturbation equations based on flow decomposition via source filtering*, Journal of Computational Physics, 188, 2, **2003**

[13] Simcenter STAR-CCM+ User Guide (version 2021.3)

[14] K. Kucukcoskun, A. Kierkegaard – *Accuracy and advantages of hybrid solutions compared to direct noise calculations for low-speed fan noise*, Proceedings of Fan Noise 2022 Symposium, Senlis, **2022**

[15] H. Beriot, A. Prinn, G. Gabard – *Efficient implementation of high-order finite elements for Helmholtz problems*, International Journal for Numerical Methods in Engineering, 106, **2016**

[16] H. Beriot, A. Modave – *An automatic perfectly matched layer for acoustic finite element simulations in convex domains of general shape,* International Journal for Numerical Methods in Engineering, 122, **2021**

[17] Simcenter Nastran Acoustics User's Guide (version 2406)



ASSESSING SOUND PROPAGATION MODELS FOR A LOW-SPEED AXIAL FAN

Vinay RAVI[1], Sophie LE BRAS[2],
Lars ERBIG[3], Korcan KUCUKCOSKUN[1]

[1] *Siemens Digital Industries Software, Leuven, Belgium*

[2] *Siemens Digital Industries Software, Châtillon, France*

[3] *Siemens Digital Industries Software, Frankfurt, Germany*

SUMMARY

Fan noise simulations are performed using four hybrid numerical methods based on a one-way fluid-to-acoustic coupling. Four different sound propagation models fed with sound sources computed from an incompressible Large Eddy Simulation are considered, namely a Perturbed Convective Wave (PCW) model, a loading noise approach, a Ffowcs Williams and Hawkings (FW-H) approach and a Kirchhoff analogy. The relative performance of the four propagation models is studied for a two-bladed fan. While the PCW model and the loading noise model provide robust acoustic predictions, the FW-H and Kirchhoff results are found to be sensitive to the definition of the permeable surface. The hydrodynamic-acoustic decomposition provided by the PCW model is not sufficient to reduce this sensitivity.

INTRODUCTION

Fan noise is one of the dominant sound sources in a range of applications such as aircraft, cooling system of automotive and electronic devices or agricultural machinery. To minimize its impact on the environment, it is crucial to accurately predict the complex phenomena [1] associated with the sound generation and its propagation. Computational aeroacoustics [2] offer an attractive way to simulate such phenomena at the early stages of the design process. However, it is essential to appropriately select the numerical approach to maximize accuracy while keeping the computational cost reasonable. In this context, it is common to use aeroacoustic hybrid methods [3] which are based on a decomposition of the aeroacoustic problem into sub-problems solved with different methods. For low-Mach number flow applications, assuming a one-way fluid-to-acoustic coupling, the flow field can be calculated separately from the acoustic field using an incompressible CFD simulation. The flow data are then used to define sound sources for the acoustic simulation which can be done in the time or frequency domain, using either an analytical propagation model or a numerical discretization of the propagation equation(s).

Sound propagation approaches based on a discretization of the propagation equation(s) are particularly attractive when simulating problems including installation effects by arbitrary geometries, and/or convection and refraction effects by arbitrary flows. In many situations, the propagation is linear. Various linear acoustic operators exist in the literature depending on the properties of the propagation medium (e.g. wave equation, linear potential equation or linearized Euler equations). However, for industrial applications, such discretized approaches can remain computationally expensive for far-field noise predictions, due to the large computational domain and fine meshes often required to propagate sound noise up to the far-field microphones. To overcome these difficulties, analytical propagation models, such as those based on Kirchhoff or Ffowcs Williams and Hawkings (FW-H) extrapolation techniques, have been commonly used for several decades to obtain far-field noise predictions at relatively low turn-around times [4].

In this work, the performance of four hybrid approaches based on four acoustic propagation models is examined for a two-bladed axial fan operating at a rotational speed of 2950 rpm [5]. The flow simulation is carried out with an incompressible Large Eddy Simulation (LES). The four acoustic propagation models are listed below:

- Time-domain Perturbed Convective Wave approach (PCW)
- Frequency-domain loading noise approach based on rotating dipoles (LN)
- Time-domain FW-H approach with permeable surface (FW-H)
- Frequency-domain Kirchhoff approach with permeable surface (Kirchhoff)

The first two models rely on a discretization of the propagation equation(s) and have been successfully applied to various rotor configurations in previous studies by the authors [6, 7, 8, 9]. The time-domain PCW approach [10], based on an expansion around an incompressible flow [11], allows to solve the acoustic propagation problem accounting for unsteady flow and installation effects [12]. The frequency-domain loading noise approach [7], based on the resolution of a Helmholtz problem with dipole sources in a high-order finite-element framework, offers an alternative to PCW for loading noise applications.

The last two models rely on analytical propagation analogies. They are based on the definition of equivalent sound sources at a permeable radiating surface whose definition (size, position) is crucial to get accurate acoustic results. In particular, the radiating surfaces need to encompass the sound sources [13] and should not be crossed by turbulent eddies [14]. When these conditions are not met, acoustic predictions can be affected by substantial errors. To overcome this issue, various techniques have been proposed in the literature such as introducing additional terms in the extrapolation model [14], discarding surface portions crossed by vortical flow features, or vortical wave filtering techniques [15].

In this work, the relative performance of the FW-H and Kirchhoff techniques is examined for radiating surfaces located at various distances from the fan. The equivalent sources at the surfaces are defined from the LES and/or PCW simulations. The possibility of benefiting from the PCW variable decomposition into aerodynamic/acoustic components as a filtering technique to improve the robustness of Kirchhoff's and FW-H's models is studied. Numerical results are compared against available data from the literature, and the relative performance of the four hybrid approaches listed above is discussed.

This paper is organized as follows. The methodology adopted in this study is first presented. Secondly, the fan benchmark is described. The numerical set-up and results of the fan simulations are then discussed. Finally, the conclusions of this study are provided.

FAN 2025
Antibes Juan-les-Pins (France), 9 – 11 April 2025

METHODOLOGY

The present aeroacoustic simulations rely on a two-step hybrid approach dedicated to low-Mach number flow applications. In the first step, an incompressible wall-modeled LES is carried out using the software Simcenter STAR-CCM+ [16]. The simulations are based on an implicit second-order accurate backward differencing scheme together with the SIMPLEC algorithm [17]. The LES is based on the Wall-Adapting Local Eddy-viscosity (WALE) subgrid-scale model [18] and a constant-density equation of state. The fan rotation is modelled with rigid body motion and a sliding interface. In the second step, acoustic simulations are carried out using four different acoustic models, all fed with data from the LES performed in the first step. These four models, dedicated to both broadband and tonal noise predictions, are described in the following.

Time-domain Perturbed Convective Wave approach

The Perturbed Convective Wave (PCW) equation is a scalar wave equation for the velocity potential originating from the Linearized Perturbed Compressible Equations (LPCE) [10]. The LPCE and PCW models belong to the acoustic analogies derived as an expansion about an incompressible flow [11, 12]. In these analogies, the Navier-Stokes equations are studied under low-Mach number flow assumption. The flow variables are decomposed into incompressible components which represent the unsteady viscous flow and compressible components which describe the differences between the compressible and incompressible flow fields. The sound sources are directly computed from an incompressible unsteady base flow calculation. As for the acoustic variables, they are modelled as compressible perturbations around the base flow. The PCW model accounts for base flow convection and refraction effects as well as for sound scattering by arbitrary geometries.

The PCW equation for the acoustic potential ϕ^a is defined as:

$$\frac{\mathrm{D}^2\phi^a}{\mathrm{D}t^2} - c_0^2\nabla^2\phi^a - \frac{1}{\rho_0}\nabla\phi^a \cdot \nabla p_{\mathrm{inc}}^f = -\frac{1}{\rho_0}\frac{\mathrm{D}p_{\mathrm{inc}}^f}{\mathrm{D}t} \tag{1}$$

where $D/Dt = \partial/\partial t + \boldsymbol{v} \cdot \nabla$ is the material derivative with respect to the unsteady base flow, ρ_0 and c_0 are the constant density and constant speed of sound, and p_{inc}^f is the incompressible pressure fluctuation. From the potential ϕ^a, the acoustic pressure p^a and the acoustic velocity $\boldsymbol{v}^a$ can be computed from the following relations:

$$p^a = \rho_0 \frac{\mathrm{D}\phi^a}{\mathrm{D}t} \text{ and } \quad \boldsymbol{v}^a = -\nabla\phi^a \tag{2}$$

The pressure perturbation can then be obtained from the sum of acoustic pressure and the incompressible pressure fluctuations given by

$$p' = p^a + p_{\mathrm{inc}}^f \tag{3}$$

Thanks to this decomposition, the PCW approach offers a possibility to quantify the relative contributions of the aerodynamic and acoustic pressures at a given microphone.

The PCW model is implemented in the Simcenter STAR-CCM+ finite-volume framework. The scalar equation is discretized using a Newmark-alpha approach based on a second-order Hilber-Hughes-Taylor scheme to compute the time derivatives of the acoustic potential and solved on the same computational grid as the flow problem. This approach has been successfully applied in the past years to predict fan and propeller noise emissions [6, 8].

Frequency-domain Loading Noise approach

For low-Mach number flows where loading noise is the predominant noise contributor, acoustic predictions can be obtained by decomposing the fan blades into compact segments modelled as

rotating dipoles [7, 9]. The dipoles are positioned at the center of gravity of the segments and their strengths are obtained by integrating the LES incompressible pressure over the segments. These dipoles act as source terms in a Helmholtz problem efficiently solved using the high-order frequency-domain Finite Element Method Adaptive Order (FEMAO) [19] implemented in Simcenter 3D Acoustics [20]. This numerical approach can account for installation effects in the propagation field.

In FEMAO simulations, the interpolation order can vary from 1 to 10. The optimal order is automatically adjusted based on the frequency, the local grid size and the local mean flow properties to achieve a prescribed accuracy [19]. To represent sound radiation to the far field, Automatically Matched Layers (AML) are implemented around the computational domain to absorb any outgoing waves and remove spurious reflections [21].

Time-domain Ffowcs Williams and Hawkings approach (FW-H)

The Ffowcs Williams and Hawkings (FW-H) approach [4], derived from an exact rearrangement of the Navier–Stokes equations, is an inhomogeneous wave equation with two surface source terms and a volume source term, describing thickness, loading and quadrupolar noise sources, respectively. An integral solution can then be obtained by convoluting the wave equation with a free-space Green's function. It can be used for sound wave extrapolation. The derivation of the FW-H formulation can be written in the time domain [22] or in the frequency domain [23].

In this study, an on-the-fly implementation of the time-domain Farassat 1A FW-H model is used [22]. The sound region is surrounded by a permeable (fictitious) FW-H surface. The source terms within that region are replaced by a distribution of equivalent sources on the surface. This distribution is computed from pressure and velocity data. In this work, this data is computed either from the PCW simulation ($p^a, \boldsymbol{v}^a$) or from the LES + PCW simulations ($p^a + p^f_{\text{inc}}, \boldsymbol{v}^a + \boldsymbol{v}^f_{\text{inc}}$). The two approaches are investigated here and their sensitivity to noise pollution is discussed.

Frequency-domain Kirchhoff approach (Kirchhoff)

An alternative to the FW-H model commonly used in aeroacoustics is Kirchhoff's approach [24, 25]. Kirchhoff's equation can be retrieved from the FW-H formulation by linearizing the FW-H surface source terms and discarding the volumetric source terms. Because Kirchhoff's approach is based on linearized source terms, it is important for the permeable surface to be located in the linear flow region so that it includes all the non-linear flow effects and noise sources [26, 27, 28].

The present Kirchhoff approach is derived in the frequency domain, in the absence of background flow. Acoustic pressure and its normal derivative from the PCW simulation are recorded on the same permeable surface as for FW-H.

The performance of FW-H and Kirchhoff approaches have already been investigated in many studies [13, 27]. For a permeable surface placed in the linear region, the FW-H approach is found to be equivalent to Kirchhoff's method plus the volume integral associated with the quadrupole sound sources. However, when non linearities are encountered at the permeable surface, Kirchhoff's method has been reported to be less accurate than FW-H's method, with substantial errors found in the acoustic predictions.

DESCRIPTION OF THE FAN CASE

The configuration reproduces the two-bladed fan case under free field condition, as previously studied by Sorgüven et al. [5]. The radius of the rotor is of $r_p = 0.154$ m. The blades correspond to flat plates of dimensions of $0.1 \times 0.04 \times 0.004$ [m, m, m] inclined with an angle of 45° (figure 1). The fan operates at a rotational speed of 2950 rpm without flow stream, corresponding to a blade-tip Mach number of 0.14 and a chord-based Reynolds number of 1.3×10^4. The fan is installed on a cylindrical hub characterized by a radius of 0.058 m and a length of about 1 m. Acoustic predictions are computed

at a microphone located 1.8 m away from the hub (figure 2), corresponding to $11.8\ r_p$, at an angle of $82°$ from the propeller axis.

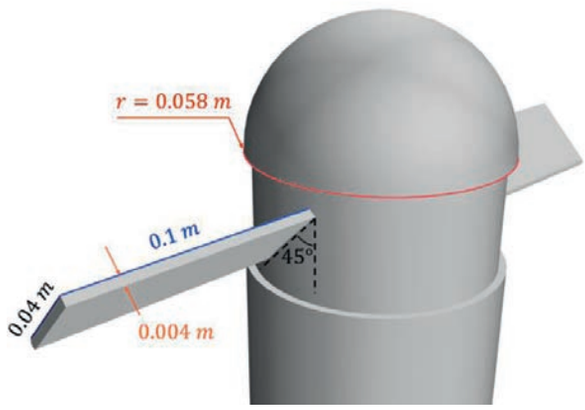


Figure 1: Fan dimensions

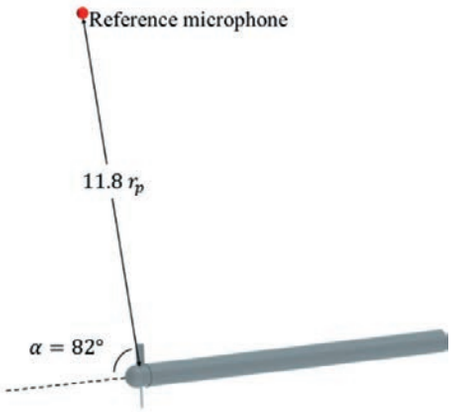


Figure 2: Microphone position

COMPUTATIONAL SETUP

Flow & PCW acoustic simulations

The CFD and PCW calculations are performed in a single simulation on a cylindrical domain with a radius of 2.5 m ($16.2\ r_p$). The domain is discretized using a trimmed cell mesh of 13.7 M cells, in which an octree based hexahedral template mesh with hanging nodes is cut with the geometry surface. As the focus of this study is put on the relative performance of various propagation models for a given flow dataset, the mesh has not been designed for optimal accuracy of the flow simulation. Instead, it has been built to match the standard requirements for the PCW acoustic simulation, and constitutes a good compromise between accuracy and reasonable restitution time for the flow simulation. It can also be seen as representative of industrial applications including some uncertainties on the fan geometry and testing conditions.

During the simulation, the propeller rotates following a sliding mesh approach. The rotor is embedded in a cylindrical rotating mesh region of radius and height $1.1r_p$. The rotating and stationary mesh regions are separated by a sliding interface. In the rotating region, the mesh cell size does not exceed 3.13 mm. At the blade surfaces, the mesh is quite coarse with $y^+ \simeq 150$ and wall modeling is thus applied.

To accurately propagate sound waves from the propeller region up to the microphone with the PCW model, the mesh size is below 25 mm, which still ensures at least 13 cells per wavelength at 1 kHz. Note that for a pure flow simulation, an even coarser mesh could be used in this region.

As we also need to extract flow data on radiating surfaces for the FW-H and Kirchhoff models, four additional cylindrical interfaces are introduced in the computational setup, see figure 3. Following the trimmed cell meshing strategy, these surfaces are introduced by cutting the octree mesh. As this procedure affects the local mesh quality, the simulations for the four different radiating surfaces are carried out independently. In total, four CFD meshes are thus performed leading to four LES and PCW simulations.

To obtain accurate mesh motion and acoustic predictions, time is discretized using 400 time-steps per revolution of the propeller, as this time-step size enables an accurate acoustic propagation of sound waves up to about 2 kHz and ensures the rotor is moved by less than 1° per time-step.

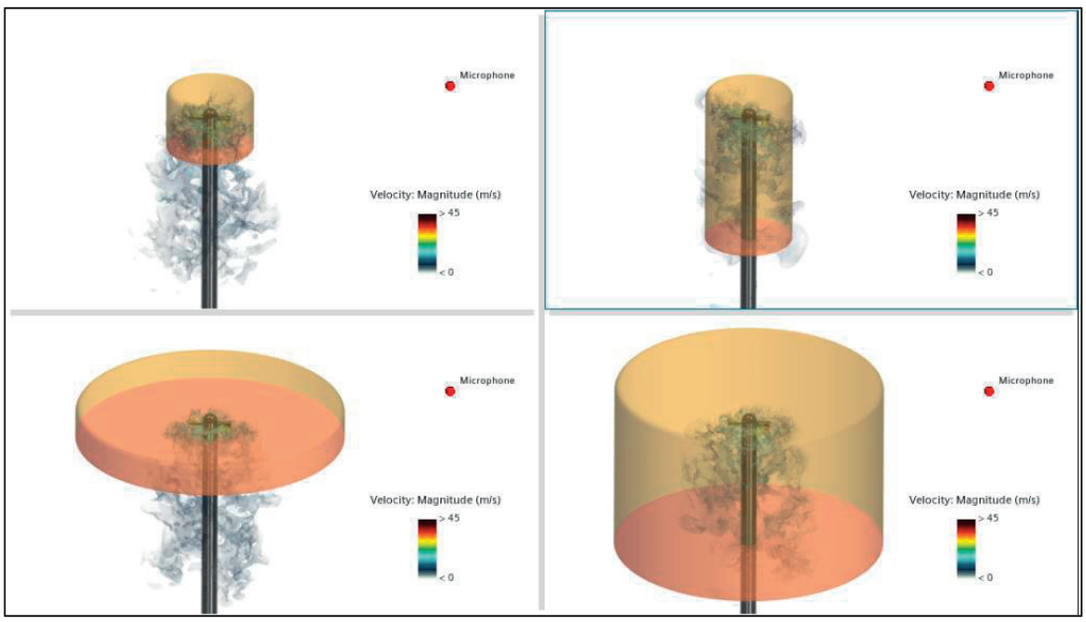


Figure 3: Permeable surface configurations. Top left: $r = 2.17r_p$ and $l = 3\ r_p$, Top right: $r = 2.17r_p$ and $l = 8\ r_p$, Bottom left: $r = 6.67r_p$ and $l = 3\ r_p$, Bottom right: $r = 6.67r_p$ and $l = 8\ r_p$.

To get a sufficiently fine spectral resolution for the acoustic spectra, the flow simulation is performed for 25 revolutions. The PCW equation is solved after the first revolution of the propeller, when the flow is already somewhat stabilized. The time domain signals are converted to frequency domain using FFT by considering the time signal as a single segment. This results in a spectral resolution of approximately 2.05 Hz. The maximum frequency range of interest is limited to 800Hz, and the dominant harmonics and broadband noise signature are expected within this frequency range [5]. To compare the results against the experimental data, the narrow band spectral data was converted to $1/12^{th}$ octave band spectra as in [5]. Furthermore, it should be noted that the band averaging reduces the stochastic noise of the narrowband spectrum.

FW-H's sound extrapolation

The on-the-fly FW-H calculations are performed in Simcenter STAR-CCM+ using the four permeable cylindrical surfaces characterized by different radii and axial lengths, as illustrated in figure 3. Two radii $r = 2.17r_p$ and $r = 6.67r_p$ are studied. Two axial lengths $l = 3\ r_p$ and $l = 8\ r_p$, referred to as short and long in the following, are considered. The front cap of the surfaces is positioned at a distance of $2\ r_p$ from the center of the rotor.

LN acoustic simulation

For the LN simulations, the Helmholtz problem with dipolar sources is solved using FEMAO as described in the methodology section. A cylindrical domain of radius $8\ r_p$ is considered for the simulations. A relatively coarse FE acoustic mesh made of linear tetrahedral elements with a maximum element size of $2.8\ r_p$ is designed to accurately compute sound predictions with FEMAO [19] up to 2 kHz. At the external boundaries of the FE domain, an AML consisting of 5 layers is defined to avoid spurious reflections.

The fan is located at the center of the domain. To define the dipole sound sources, the fan blades are split into compact segments of size $L_s = c_0/(N_s f_{max})$, where $N_s = 4$ is the number of segments per acoustic wavelength and $f_{\max} = 5$ kHz (chosen higher than the maximum frequency of interest (2 kHz) for the acoustic results to be on the safe side). For the present rotor, it leads to $L_s = 0.11r_p$ corresponding to 18 segments per blade.

Kirchhoff's sound extrapolation

The Kirchhoff calculations are carried out in Simcenter 3D Acoustics [20]. The same radiating surfaces as for the FW-H approach are considered here (see figure 3). For computational efficiency, a surface mesh four times coarser than the CFD one is used for the Kirchhoff extrapolation. Its resolution has been determined from a grid sensitivity study, not presented here for the sake of conciseness. A conservative mapping technique is used to interpolate the CFD data onto the Simcenter 3D grid [29].

RESULTS

In this section, the results obtained using the four different approaches introduced under the methodology section are presented. Results from the PCW and LN models are discussed first to highlight their validity and robustness. Furthermore, the results from the surface integral methods, FW-H and Kirchhoff, are presented. Their ability to reproduce the results of the PCW and LN approaches which are based on the same inputs is discussed.

When comparing our results with the experimental data, a few different factors need to be considered. First, there are a few unknowns about the testing conditions reported in the literature, such as the condition of the anechoic or semi-anechoic termination, the installation effects, the signal processing parameters, or the setup of the rotor's drive system. Second, as indicated in the previous section, our simulation setup follows a comparably pragmatic approach, using wall-modeled LES and targeting only low-frequency acoustic predictions. Consequently, achieving a good agreement between the simulation and experimental results was not the primary objective of this investigation, but rather to understand the consistency of the different acoustic simulation approaches.

However, figure 4 shows that the Sound Pressure Levels (SPL) from both the PCW and LN approaches show a decent agreement with the experimental data. The results from the four different CFD meshes closely follow the experimental predictions, capturing both the tonal and broadband content up to 800 Hz. The variation in the results between the different configurations are only due to the differences in the discretization of the radiating surfaces. They are less pronounced in the LN results, as the LN approach relies on incompressible pressure data at the blade surfaces which are similarly discretized in the four CFD meshes.

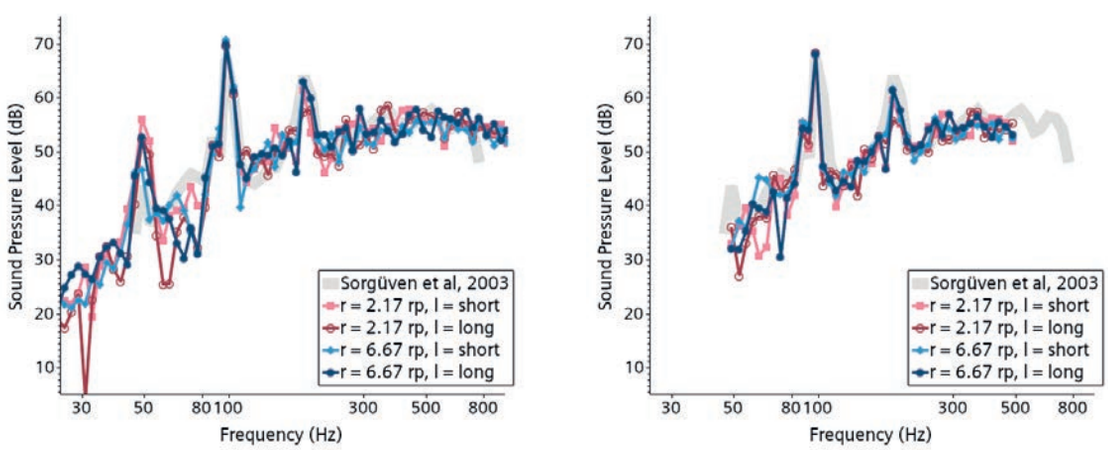


Figure 4: Left – SPL from PCW approach for all configurations, Right – SPL from loading noise approach for all configurations

Even though the PCW and LN approaches rely on fundamentally different physical assumptions, they lead to very similar SPL values at the first (98.3 Hz) and second (196.7 Hz) blade passing frequencies (BPF) as well as in the broadband range. This indicates that the loading noise is the dominant acoustic source mechanism in this case, which is in good agreement with past investigations of low-speed

axial fans [7, 9]. Through the decomposition of the pressure perturbation into acoustic and incompressible components (see methodology section), the PCW model can provide further insight into the flow behaviour in the far-field, as illustrated in figure 5. Below 60 Hz, the pressure perturbation shows significantly higher values than the acoustic pressure. This is attributed to large incompressible pressure fluctuations observed far away from the rotor. These fluctuations do not necessarily generate noise, but affect the pressure at the microphone.

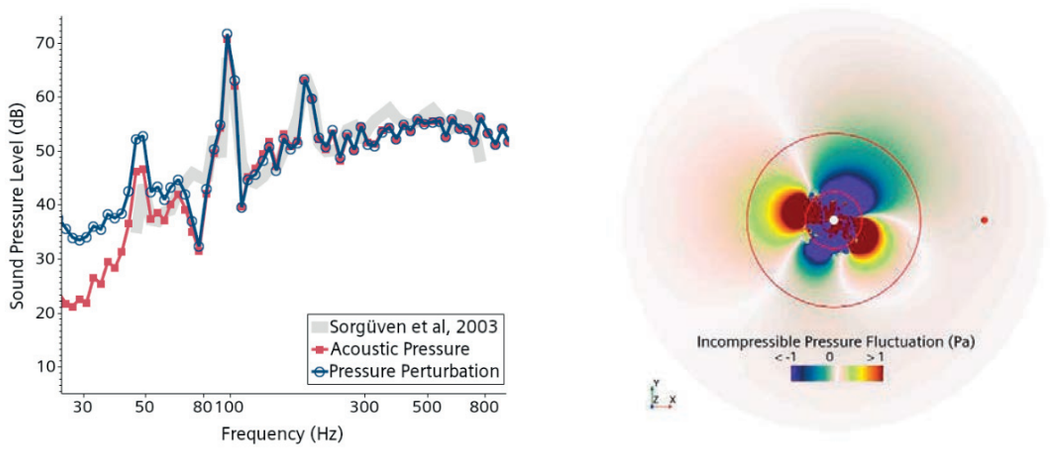


Figure 5: Left – Spectra of acoustic pressure and pressure perturbation from PCW approach at far-field microphone,
Right – Incompressible pressure fluctuation across the domain, with radiating surface positions indicated in red

As the PCW and LN discretization-based approaches provide robust results and a fair agreement with the experimental data of the literature, these results are used as reference to assess the performance of the extrapolation-based FW-H and Kirchhoff approaches. In figure 6, one can find the SPL from the FW-H approach (left) and from the Kirchhoff approach (right) compared against the PCW and LN results, respectively.

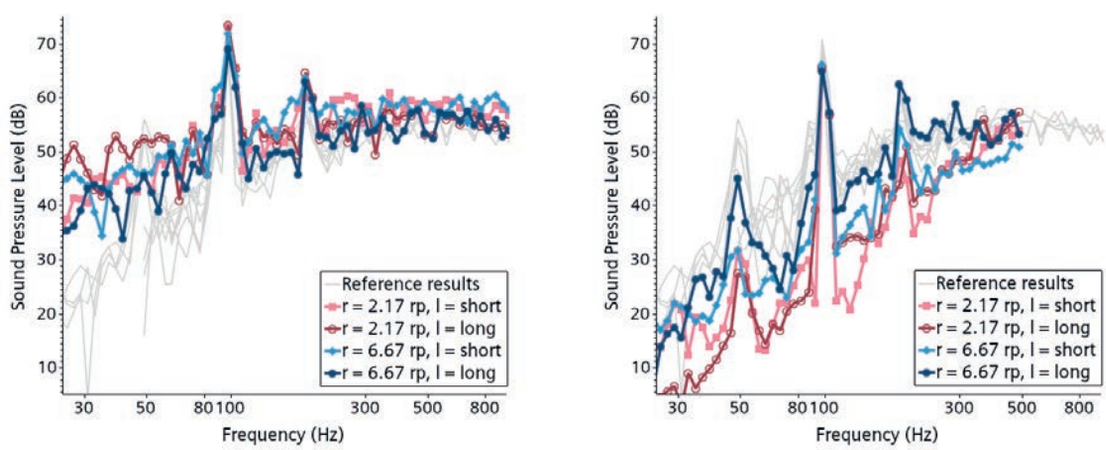


Figure 6: Left – SPL from FW-H's model from all surfaces, Right – SPL from Kirchhoff's model for all surfaces

In comparison, the Kirchhoff results, based on pure acoustic input quantities stemming from the PCW model, tend to underpredict the sound levels. The best agreement with the reference data is obtained for the largest radiating surface, suggesting that this configuration sufficiently encloses the non-linear flow effects and the noise sources within the computational domain. In contrast, all the other configurations strongly underpredict the reference results, indicating that not all relevant noise source mechanisms at play are encapsulated within the permeable surfaces. Even though we can provide these filtered acoustic variables as inputs, and even though the LN approach delivers meaningful results, the size of the permeable surface must be sufficiently large to avoid strong sensitivities of the

solution to the surface. This finding is clearly in contrast to the results obtained by the authors [30] for an HVAC duct, which reported similar acoustic predictions between a Kirchhoff approach based on a permeable surface very close to the fan and a PCW approach. It is likely that flow conditions in an HVAC duct, with a Mach number typically below 0.05, make a success of these approaches significantly more likely, and the filtering provided by the PCW approach helps there to eliminate the spurious noise that would be caused by the turbulent jet crossing the permeable surface.

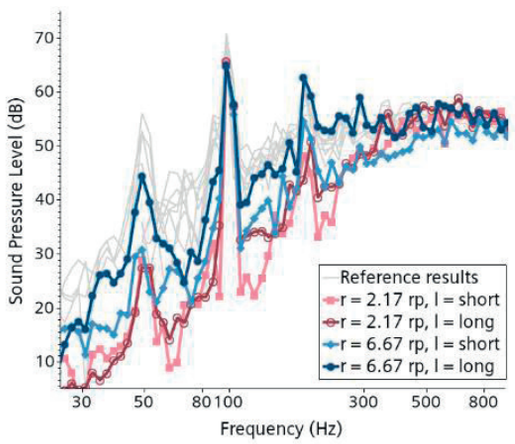


Figure 7: Left – SPL from FW-H's model using pure acoustic input quantities

In an attempt to better understand the above findings, we deviate from the standard practices of fetching the intended source quantities for the surface integral methods. For the FW-H model, this was done by replacing the typical flow-based input quantities with pure acoustic quantities. For Kirchhoff's formulation, flow-based quantities were fetched instead of pure acoustic quantities.

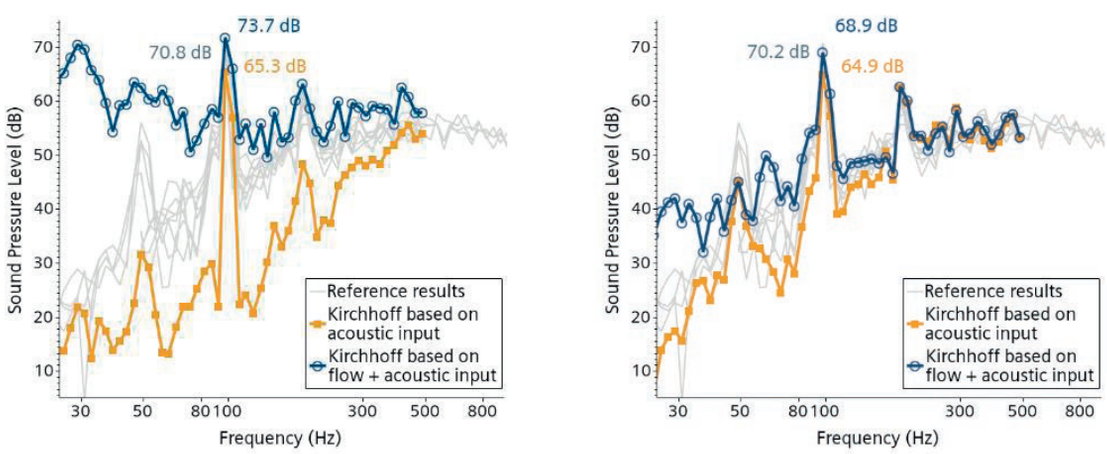


Figure 8: Left – SPL from Kirchhoff's model using different inputs for $r = 2.17\ r_p$ and $l = 8r_p$, Right – SPL from Kirchhoff's model using different inputs for $r = 6.67\ r_p$ and $l = 8r_p$

In figure 7, one can see that the results obtained from the FW-H approach based on acoustic inputs are in strong agreement with the classical Kirchhoff results presented in figure 6. Particularly, it is worth to note that the tendency of the FW-H approach to overpredict the reference levels in figure 6 is replaced by a tendency to underpredict levels in figure 7, just as it was seen in the Kirchhoff approach. Hence, the underpredicted sound levels from Kirchhoff's approach are likely due to a filtering effect of the sources provided by the PCW approach.

The left and the right panels of figure 8 show the SPL generated with Kirchhoff's approach with acoustic and flow+acoustic quantities for the configurations with length $l = 8r_p$. It is clearly visible in both configurations that the Kirchhoff model tendency to underpredict SPL is replaced by a

tendency to overpredict levels. Especially at low frequencies with a permeable surface that is close to the rotor, the overprediction is significantly more pronounced than in the classical FW-H approach. This clearly highlights the sensitivity of Kirchhoff's approach to the position of the permeable surface and to the input data used to define the equivalent sources at the surface. For the furthest surface from the sources, Kirchhoff's results become more acceptable and similar to those from the FW-H approach (with overpredicted levels at low frequencies compared to the reference data).

SUMMARY AND CONCLUSION

In this paper, four different hybrid numerical approaches were applied to predict the noise emitted by a low-speed axial fan. These approaches are based on four acoustic models, namely a PCW model, a LN approach, and FW-H's/Kirchhoff's models with permeable surfaces. These four acoustic approaches are all fed with sound sources computed from a single incompressible Large Eddy Simulation. While the PCW simulation is carried out during the CFD run in the same software environment, the LN approach uses a separate adaptive order FE solver in the frequency domain which is computationally efficient if sound waves are propagated over a long distance or if installation effects play a big role [30]. In contrast, the FW-H and Kirchhoff wave extrapolation approaches are of interest if the distance between the sources and the observer becomes even bigger. For the present fan case, it was proven that blade loading noise is the dominant noise source mechanism. Both the LN and the PCW approaches delivered meaningful and consistent predictions, while the FW-H and Kirchhoff results were found to be sensitive to the definition of the permeable surface. We further investigated whether the hydrodynamic-acoustic splitting provided by the PCW approach could serve to reduce this sensitivity. It was shown that this type of filtering indeed improves the consistency between the FW-H and Kirchhoff results and removes spurious noise. Unfortunately, for the present application, it led to significantly underpredicted noise levels when the radiating surface is not positioned in the linear acoustic region.

BIBLIOGRAPHY

[1] S. Glegg, W. Devenport — *Aeroacoustics of low Mach number flows: fundamentals, analysis, and measurement*, Academic Press, **2017**

[2] C. K. Tam — *Computational aeroacoustics-Issues and methods*, AIAA Journal, vol. 33, no. 10, pp. 1788-1796, **1995**

[3] S. Schoder, M. Kaltenbacher — *Hybrid aeroacoustic computations: State of art and new achievements*, Journal of Theoretical and Computational Acoustics, vol. 27, no. 04, p. 1950020, **2019**

[4] J. Ffowcs Williams, D. L. Hawkings — *Sound generation by turbulence and surfaces in arbitrary motion*, Philosophical Transactions for the Royal Society of London. Series A, Mathematical and Physical Sciences, vol. 264, no. 1151, p. 321–342, **1969**

[5] E. Sorgüven, F. Magagnato, M. Gabi — *Prediction of the far field noise of a simplified propeller with large eddy simulation*, DGLR Paper, 68, **2003**

[6] L. Erbig, S. Lardeau — *Hybrid aeroacoustic simulation of EAA's axial fan benchmark*, DAGA 2022 Stuttgart, Germany, **2022**

[7] K. Kucukcoskun, A. Kierkegaard — *Accuracy and advantages of hybrid solutions compared to direct noise calculations for low-speed fan noise*, FAN2022 Conference, Universitäts-und Landesbibliothek Darmstadt, **2022**

[8] K. Kucukcoskun, L. Erbig — *Validation of the hybrid fan noise simulation techniques on EAA axial benchmark fan*, Proceedings of Fan Noise 2025 Symposium, Antibes, **2025**

[9] S. Le Bras, K. Kucukcoskun, D. Acevedo-Giraldo, M. Roger — *Aeroacoustic Simulations of a Pylon-Mounted Propeller Configuration at Low Reynolds Number*, In 30th AIAA/CEAS Aeroacoustics Conference, AIAA paper 2024-3101, **2024**

[10] J. H. Seo, Y. J. Moon — *Linearized perturbed compressible equations for low Mach number aeroacoustics*, Journal of Computational Physics, vol. 218, no. 2, pp. 702-719, **2006**

[11] J. C. Hardin, D. S. Pope — *An acoustic/viscous splitting technique for computational aeroacoustics*, Theoretical and Computational Fluid Dynamics, vol. 6, pp. 323-340, **1994**

[12] J. Piepiórka, O. Von Estorff — *Numerical investigation of hydrodynamic / acoustic splitting methods in finite volumes including rotating domains*, Universitätsbibliothek der RWTH Aachen, **2019**

[13] K. S. Brentner, F. Farassat — *Analytical comparison of the acoustic analogy and Kirchhoff formulation for moving surfaces*, AIAA Journal, vol. 36, no. 8, pp. 1379-1386, **1988**

[14] G. Rahier, M. Huet, J. Prieur — *Additional terms for the use of Ffowcs Williams and Hawkings surface integrals in turbulent flows*, Computers & Fluids, vol. 120, pp. 158-172, **2015**

[15] S. Zhong, X. Zhang — *A sound extrapolation method for aeroacoustics far-field prediction in presence of vortical waves*, Journal of Fluid Mechanics, vol. 820, pp. 424-450, **2017**

[16] Siemens Digital Industries Software — *Simcenter STAR-CCM+ (version 19.06.008-R8)*, **2024**

[17] J. H. Ferziger, M. Perić, R. L. Street — *Computational Methods for Fluid Dynamics*, Berlin, Springer-Verla, **2019**

[18] F. Nicoud, F. Ducros — *Subgrid-scale stress modelling based on the square of the velocity gradient tensor*, Flow, Turbulence and Combustion, vol. 62, no. 3, pp. 183-200, **1999**

[19] H. Bériot, A. Prinn , G. Gabard — *Efficient implementation of high-order finite elements for Helmholtz problems.*, International Journal for Numerical Methods in Engineering, vol. 106, no. 3, pp. 213-240, **2016**

[20] Siemens Digital Industries Software — *Simcenter Nastran Acoustics User's Guide (version 2412)*, **2024**

[21] H. Beriot, A. Modave — *An automatic PML for acoustic finite element simulations with generally-shaped convex domains*, Int J Numer Methods Eng, vol. 122, pp. 1239-1261, **2020**

[22] F. Farassat — *Derivation of Formulations 1 and 1A of Farassat*, report NASA/TM-2007-214853, **2001**

[23] X. Gloerfelt, C. Bailly, D. Juvé — *Direct computation of the noise radiated by a subsonic cavity flow and application of integral methods*, Journal of Sound and Vibration, vol. 266, no. 1, pp. 119-146, **2003**

[24] F. Farassat, M. K. Myers — *Extension of Kirchhoff's formula to radiation from moving surfaces*, Journal of Sound and Vibration, vol. 123, no. 3, pp. 451-460, **1988**

[25] G. Kirchhoff — *Zur theorie der lichtstrahlen*, Annalen der Physik, vol. 254, no. 4, pp. 663-695, **1883**

[26] D. P. Lockard — *An efficient, two-dimensional implementation of the Ffowcs Williams and Hawkings equation*, Journal of Sound and Vibration, vol. 229, no. 4, pp. 897-911, **2000**

[27] A. S. Lyrintzis — *Surface integral methods in computational aeroacoustics—From the (CFD) near-field to the (Acoustic) far-field.*, International Journal of Aeroacoustics, vol. 2, no. 2, pp. 95-128, **2003**

[28] A. S. Lyrintzis — *Review: The use of kirchhoff's method in computational aeroacoustics*, Journal of Fluids Engineering, Transactions of the ASME, vol. 116, no. 4, **1994**

[29] G. Guilloud, P. Martinez, J. Golliard , C. Schram — *Toward Industry-Standard Flow-Induced Noise Prediction*, DAGA, Rotterdam, **2009**

[30] K. Kucukcoskun, L. Erbig — *A weakly-coupled simulation for HVAC duct aeroacoustics including propagation into the cabin*, AIAA AVIATION 2023 Forum, **2023**



ON THE EFFECT OF TIP FLOW ON THE NOISE OF A DUCTED ROTOR

Jose RENDÓN-ARREDONDO, Stéphane MOREAU,
Université de Sherbrooke, Sherbrooke, QC, J1K 2R1, Canada.

SUMMARY

This study focuses on the aeroacoustic aspects of ducted rotors that could possibly be used in future helicopter electrically driven tail rotor systems. It provides a comprehensive understanding of the tip flow evolution, and of the interaction with the stator stage. High-fidelity compressible numerical simulations are performed and compared with experimental results. A periodic variation is seen in the aerodynamic performance of the rotor blades, which is associated to a potential-interaction phenomenon. Additionally, the convection of the tip vortices and further impingement in the stator vanes generate torque fluctuations on these elements. Dilatation fields and P_{rms} contours confirm a noise source generated by the tip-vortex-stator interaction. Finally, excellent far-field noise comparisons between the numerical and experimental results are obtained for both, tonal and broadband noise.

INTRODUCTION

Urban Air Mobility (UAM) is currently undergoing incredible growth. However, social acceptance and recent regulations require these aircraft to minimize their noise levels. To do so, new designs rely on replacing combustion engines by fully electric or hybrid-electric propulsion systems. Additionally, the rotors, such as the ones used for tail rotors applications are also using two main approaches. The first one is a conventional open tail rotor, while the second is a shrouded tail rotor. The latter is mostly composed by a ducted axial fan with a single or multiple rotor architecture. These systems offer several advantages in terms of safety and aerodynamic and acoustic performance [1]. Additionally, they reduce the operational cost, improve safety for on-ground and in-flight conditions and mitigate the noise, leading to quieter operation [2].

Moreover, Jaiswal et al. [3] showed that at certain operational conditions, the tip vortex system is plunged downstream and therefore interacts with the stator. The same situation was seen by Rendon et al. [4] for a similar configuration where two different blade incidences were tested to evaluate the

evolution of the tip vortex system. Despite the aforementioned studies, most of the focus has been put on understanding the wake-interaction noise, while the tip-vortex-stator interaction has not been fully analyzed nor understood.

To better understand the effects of the tip-vortex/stator interaction in an electrical tail rotor, a combination of experimental and numerical simulations is used. The next section presents the duct fan system and its experimental setup. The numerical method and parameters are then described. After some verification and validation, the aero-acoustic performances of the system are shown. Finally, some conclusions are drawn.

ROTOR GEOMETRY AND REFERENCE EXPERIMENTAL SETUP

The ducted rotor used in this study is a possible design for future electrically driven helicopter tail rotor systems. The system consists of a four-blade rotor and a duct held by six stator vanes. The casing has a diameter of D, a diameter of the hub of 0 25 D, and a tip gap of approximately 0 05 D. The casing extends up to 0 25 D downstream of the center of rotation. The experiment was carried out inside the open-jet anechoic wind tunnel at the Université de Sherbrooke (UdS), which has a cut-off frequency below 100 Hz and wedge-tip to wedge-tip dimensions of 7 m long, 5.5 m width, and 4 m height. The ducted rotor is tested in hover in the middle of the anechoic chamber, as shown in Fig 1. Table 1 summarizes the main physical and geometric parameters.

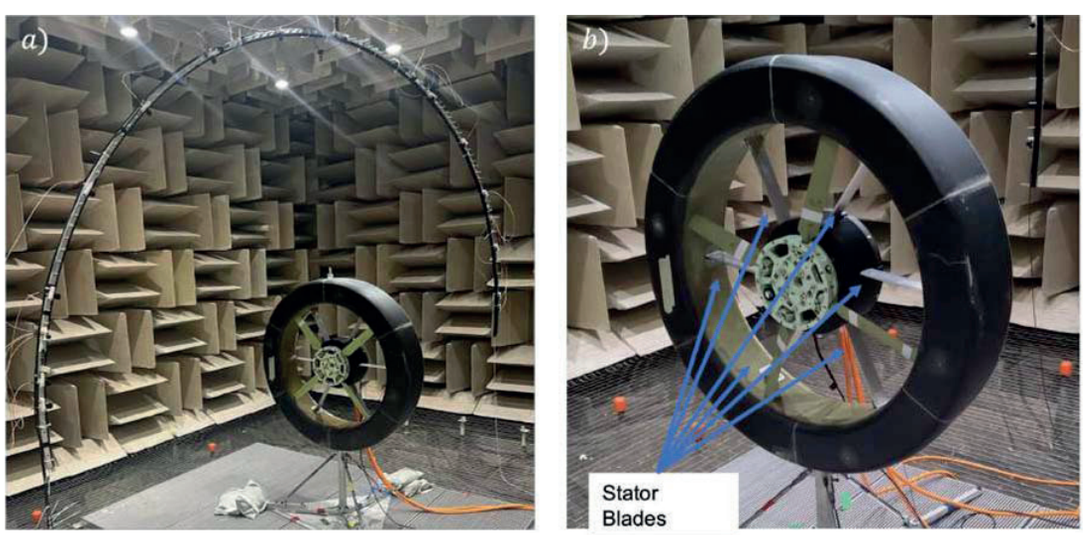


Figure 1: UdS experimental set-up: (a) overview with microphone array; (b) zoom on the ducted fan system.

Table 1: Main geometrical and flow parameters of the ducted fan system.

B	V	Ma_{tip}	Re_{tip}
4	6	0 417	$4\,2 \times 10^5$

Acoustic directivity measurements are performed using an arc of 2.3 D radius with its center aligned with the center of the rotor. The directivity antenna is instrumented with a total of 12 evenly distributed B&K 1/4" microphones type 4957 from 0 ° to 180 °, with 90 ° corresponding to the rotor disk plane. Windscreens are used in the microphones to reduce flow noise. The arc is rotated clockwise to different positions to account for the noise directivity. The acoustic signals are acquired at a sampling frequency of 65.5 kHz for 30 s. Acoustic narrow band spectra are computed from the time signals using Welch's periodogram method with a Hanning window, a number of segments defined

on the length of the signal, and a 50 % overlap. An accelerometer was placed on top of the casing to identify the vibrations of the system that contaminated the far-field acoustic measurements.

Additional tests are performed on an outdoor stand on which a load cell measures aerodynamic loads, mainly thrust (T) and torque (Q). Due to confidentiality concerns, the following sections will define the time-averaged thrust and torque under their dimensionless form as $C_T = T\ (\rho f^2 D^4)$ and $C_Q = Q\ (\rho f^2 D^5)$ respectively. ρ is the fluid density, f is the rotational frequency of the rotor, D is the diameter of the rotor and $T - Q$ are the time-averaged signals after the transient has decayed. The experimental mass-flow rate is also estimated from the inviscid conservation of mass-momentum. Even though load and acoustic measurements were not performed simultaneously, synchronous analysis is achieved in the simulations, the setup of which is described in the next section.

NUMERICAL METHOD AND SETUP

The complete experimental setup, including the anechoic environment, is reproduced in the simulation implemented using the Lattice-Boltzmann method (LBM) solver, PowerFLOW. The computational fluid domain, illustrated in Fig. 2, is a cubic volume of 14 D with all outer boundaries having free-flow conditions and therefore mimicking the hover state used in the experimental campaign. High artificial viscosity values are also imposed on the outer layers of the domain to prevent the reflection of acoustic waves. Subsequently, these boundary conditions were validated by checking the absence of any reflected noise coming from the outer layers of the domain in several instantaneous dilatation fields in the meridional plane of the rotor. Solid walls are used in the inner layer just after the last damping zone to delimit the anechoic environment. The ducted rotor presented in Fig. 1 is then used without any simplification and is placed at the same location as in the experimental campaign, using the solid walls mentioned before as a reference.

A total of 13 Variable Resolution (VR) regions are used to discretize the fluid domain with an octree mesh, where the grid is composed of cubic elements called voxels, with the finest VR placed around the rotor blade. A methodology similar to that implemented by [4] is used for the present work with an additional mesh refinement region placed in the interstage between the rotor and the stator, as shown in Fig. 2 b), to capture the correct tip flow and wake contraction. The smallest voxel size is $1\,6 \times 10^{-4}\ D$, resulting in an average $y^+ \approx 50$ and $y^+ \approx 30$ for the blade and casing surfaces, respectively. The intermediate VR zones have a voxel size based on the grid sizes reported by [5] and [6] for automotive ring fans with similar tip Reynolds numbers. The resulting number of fine equivalent voxels for the current setup is about 275 million.

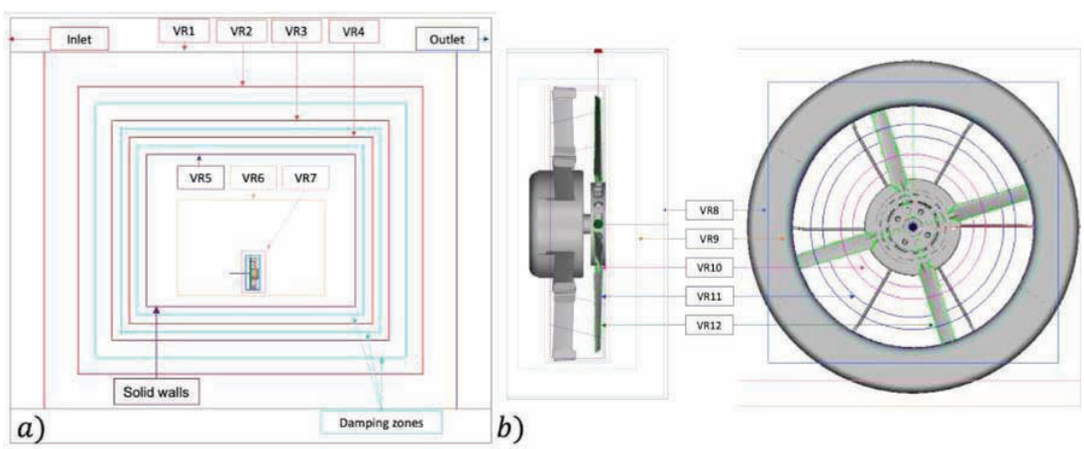


Figure 2: Computational domain and voxel refinement regions: (a) full domain; (b) zoom on the fan.

Surface probes are created on the casing and stator vanes. For the former, they are located in the azimuthal and axial directions with a 5° and 5% spacing, respectively. For the latter, the probes are located in both the spanwise and chordwise directions, both with a 5% spacing. Velocity and pressure are saved at each point to further evaluate the tip vortex trajectory and its interaction with the stator vanes. Probes mimicking the microphones used in the experimental campaign are also created with an averaging volume of characteristic size corresponding to the diameter of the B&K 1/4" microphones. Acoustic waves propagate directly towards these probes to evaluate the correlation with the data obtained from the casing and stator, as well as to assess the convergence of the simulation. Surface pressure, velocity and forces are recorded on the different components of the system to evaluate P_{rms}, wall pressure fluctuations, torque, and thrust. The first is also used to perform a hybrid approach by applying the solid formulation of the Ffowcs Williams and Hawkings (FW-H) acoustic analogy. This is done to assess the contribution of each component to the far-field noise and to compare these results with those obtained using the direct approach. Finally, two virtual half-spheres at the inlet and outlet of the module are used to determine the mass flow rate through the ducted tail rotor system.

An initialization run, with a simulated time of 3 s, is performed using a coarser mesh to establish the flow in the anechoic environment. The instantaneous flow field is then used to seed the fine mesh simulation, which, so far, has a simulation time of 0.26 s corresponding to 15 rotor rotations. After 8 transient rotations, results are obtained for the subsequent rotations, using a sampling frequency consistent with the experimental campaign.

SIMULATION VERIFICATION AND VALIDATION PROCESS

The convergence of the aero-acoustic simulation is monitored by the stabilization of the mass flow rate in the two mentioned surfaces and the pressure signal on the far-field probes mimicking the experimental microphones. Figure 3 shows that convergence is achieved for both variables after 0.05 s, corresponding to three rotations. This value is lower than the number of revolutions at which data storage begins, indicating that the transient behavior of the system has been properly removed. Furthermore, the difference between the mass flow rates recorded at the inlet and outlet surfaces is less than 2%, suggesting consistency in the simulation.

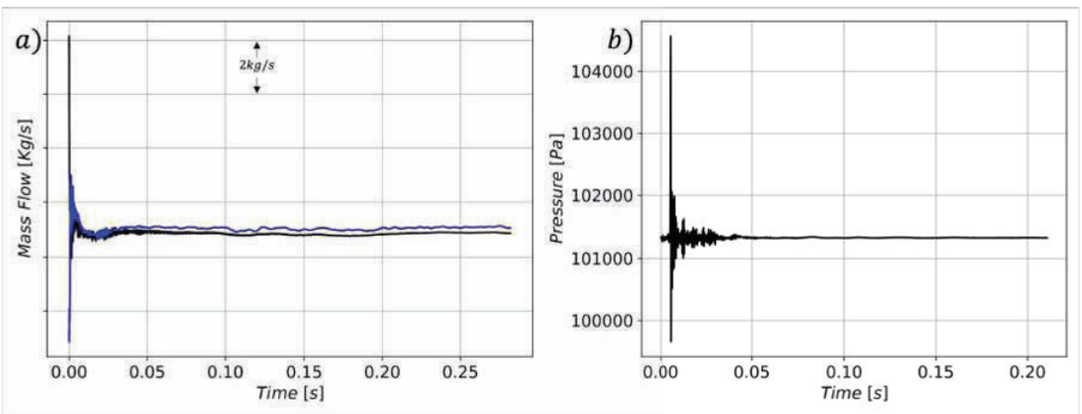


Figure 3: Convergence of (a) the mass-flow rate and (b) far-field acoustic pressure.

The aerodynamic performance and mass flow rate obtained from the LBM simulation are validated with respect to the experimental data acquired using the methodology described above and the results obtained previously by Jaiswal et al. [3], [7] and Rendon et al. [8]. Additional wall-resolved RANS and LES simulations using the Lax-Wendroff numerical scheme were conducted for the purpose of comparison. Table 2 summarizes the results, where the mass flow rates are normalized by the experimental value obtained, along with the relative error with respect to the experimental values.

FAN 2025
Antibes - Juan-les-Pins (France), 9 - 10 April 2025

Table 2: Comparison of the aerodynamic performance of the calculated cases with experiments.

	$\dot{m}[-]$	$\varepsilon_{\dot{m}}[\%]$	$C_T[-]$	$\varepsilon_{C_T}[\%]$	$C_Q[-]$	$\varepsilon_{C_Q}[\%]$
Experiment [7]	1	-	0.254	-	0.0134	-
RANS	0.783	21	0.214	15.7	0.0187	39.5
LES	0.993	0.7	0.219	13.7	0.0172	28.3
LBM Coarse [8]	0.888	11.2	0.229	9.8	0.0174	29.8
LBM Fine [3]	0.881	11.9	0.223	12.2	0.0170	26.8
LBM Current	0.913	8.7	0.237	6.7	0.0111	17.1

Although the discrepancies are up to 20%, all simulated performances lie within the same range, which stresses that the current experimental mock-up is realistic. The estimated experimental mass flow rate is systematically underpredicted by all methods, except for the LES, where this variable is imposed as a boundary condition of the simulation. Moreover, for this method, the thrust coefficient (C_T) is underestimated due to the lack of data in the stator region, as was also the case for the LBM Fine configuration. Between all the methods, the results obtained with RANS present the major discrepancies for all variables compared to the experimental results. These differences, as stated by Santamaria et al. [9], are attributed to the grid and the fully turbulent flow assumption, and to the lack of resolution in the wake region, which prevents calculating the correct trajectory and dissipation of the tip vortices under hover conditions. Therefore, for the present simulation, as stated in the numerical setup, an additional refinement region is added in the inter-stage between the rotor and the stator. This increases the resolution in the wake, which allows capturing the proper wake contraction and tip vortex trajectory, thereby improving the prediction of the aerodynamic performance and mass flow rate of the system compared to previous LBM simulations.

PERFORMANCE AND FLOW FIELD ANALYSIS

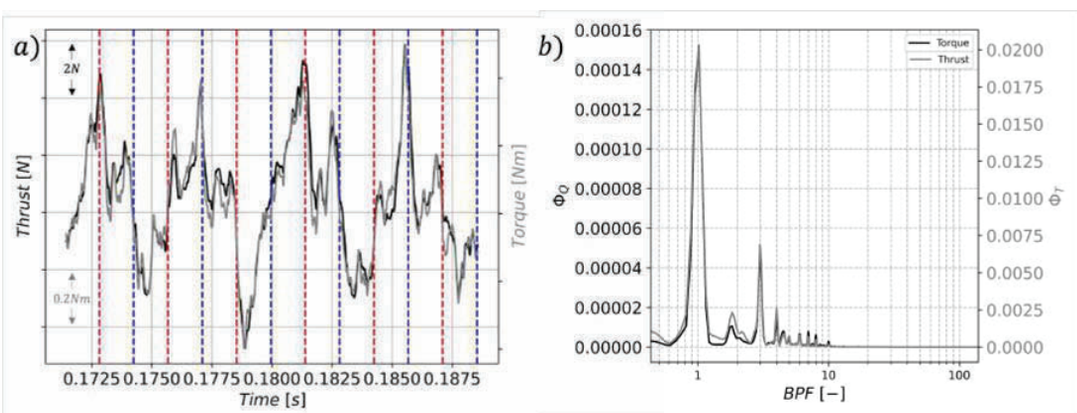


Figure 4: Integrated torque and thrust on the rotor blades. (a) Evolution over one rotation; (b) Power Spectral density.

Figure 4 shows the integrated torque and thrust on the rotor blades over one complete revolution and its associated FFT. A total of twelve peaks are visible in the time trace. The first of those happens at approximately 0.173 s, corresponding to the moment when a blade passes over a stator vane. This situation is marked in Fig. 4a) by the first red dotted line. At this instant, the two blades located at 0° and 180° are interacting with a stator vane, while those located at 90° and 270° are not. The latter, therefore, interacts with a stator vane after an angular displacement of 30°, corresponding to the first blue dotted line in Fig. 4a). Furthermore, the following vertical lines are separated by the

time it takes for each pair of blades to cover the angular displacement between two stator vanes (60°). A perfect match is observed between the guide lines and the four main peaks, while a shift is seen for the others. This shift is most likely due to the skewed design of the stator vanes, which either advances or delays the interaction with the rotor blades. Therefore, this situation implies that the thrust and torque variations presented in Fig. 4a) are mainly due to the potential interaction seen by the rotor blades as a consequence of the presence of the stator vanes. Future studies will be conducted to analyze the amplitude variations between the peaks. Figure 4b) shows the Welch periodogram method applied to the time signals of the rotor aerodynamic performance. Two main peaks located at the first and third BPF harmonics are depicted. The former is expected because it is located in the blade passing frequency related to the rotational speed and number of blades. The latter is present because of the potential interaction with the stator that causes a total of twelve peaks that provides the aforementioned frequency when divided by the total number of rotor blades.

A similar methodology is applied to the integrated torque on the stator vanes in Fig. 5. The same convention for the vertical lines is followed. As with the rotor, the displacement between lines is related to an angular displacement of 60°. Figure 5b) shows again the appearance of the 3rd harmonic of the BPF as the main contributor based on the number of peaks and blades in the system. In contrast to the rotor, the first harmonic of the BPF is not present as the data are now recorded in a stationary frame. Additionally, when Fig. 5a) is analyzed, a time shift is observed relative to the time trace in Fig. 4. This shift corresponds to an angular displacement of 23°, which is less than the distance between the two interactions with the stator vanes (30°). Therefore, the torque fluctuations are not related to the potential interaction phenomena but rather to some fluid-solid interaction. Rendon et al. [4] already showed in a similar configuration that the main interaction is between the plunging tip vortex and the stator vanes.

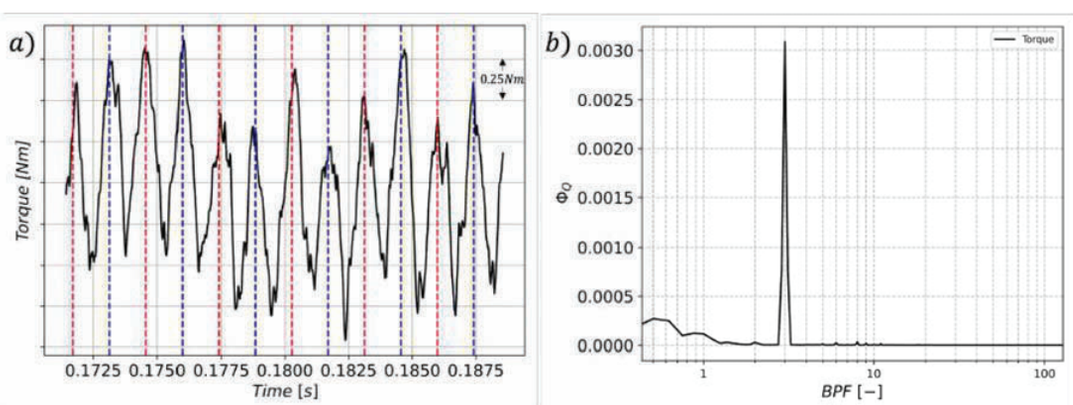


Figure 5: Integrated torque on the stator vanes. (a) Evolution over one rotation; (b) Power Spectral density.

Figure 6 shows the instantaneous vorticity magnitude projected onto several radial cuts at two different time frames. Figure 6a) corresponds to the first red dotted line in Fig. 6a), where one of the blades passes through the stator vane. On the other hand, Fig. 6b) is associated with the previously mentioned angular shift of 23°. As shown in Fig. 6a), a high-vorticity region, caused by the emission of the tip vortex, is present at the tip of the two blades. Additionally, a broader high-vorticity region lies downstream of this structure, which is associated with the tip vortex produced by the preceding blade. Moreover, Fig. 6b) shows this structure being convected downstream and interacting with the stator vane, generating a high-vorticity region. Thus, the fluid-solid interaction is linked to the interaction between the tip flow and the stator. Furthermore, in both figures, a high radial vorticity line related to the vortex sheet shed from the blade trailing edge is seen. These two main features, tip vortex and vortex sheet, therefore interact and generate a vortex-vortex interaction that may radiate to the far-field as an additional noise source.

FAN 2025
Antibes - Juan-les-Pins (France), 9 - 10 April 2025

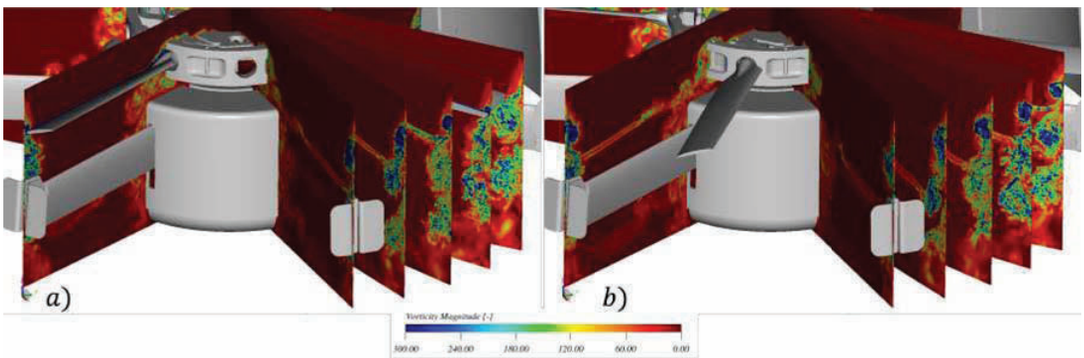


Figure 6: Iso-contours of instantaneous vorticity magnitude at two different instants in several meridional planes.

In Fig. 7, the instantaneous dilatation field computed as $-\partial\rho\ \ \partial t$ at 95% and 90% span provides a qualitative insight on the acoustic sources involved in the system. The focus is put in the stator region to get a better view of the vortex-vortex and fluid-solid interaction. Figure 7a) shows the merging point of the tip vortex and vortex sheet surrounded by the white circle. In addition to the hydrodynamic structures, acoustic waves are produced as a consequence of this interaction. Therefore, quadrupolar noise can be present in the far-field noise signature of the present ducted rotor. On the other hand, surrounded by the white circle in Fig. 7b), the interaction of the convected tip vortex with one of the stator vanes is seen. Due to this impingement, acoustic waves are emitted from the stator vane. The wave fronts are mostly masked by the presence of the trailing-edge noise source. However, there is a clear difference in the frequency of emission, with the stator source radiating at a lower value. Even though two potential noise sources are identified, future studies will be performed to evaluate if they contribute to the far-field noise or not. To do so, filtered dilatation fields will be used together with acoustic analogies to separate the contribution of each element in the noise generation. Now that the tip vortex-stator interaction is confirmed with a possible noise source related to it, the pressure fluctuations on the surface are analyzed.

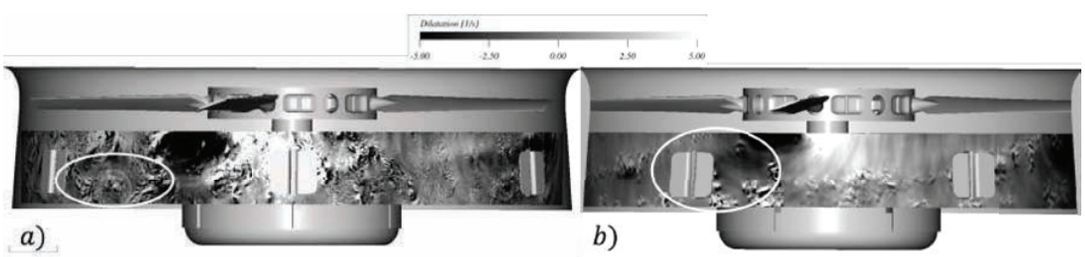


Figure 7: Iso-contours of instantaneous dilatation fields at two different instants at a) 95% and b) 90% span.

Figure 8 shows the P_{rms} on the surface of one stator vane along with the wall-pressure fluctuations (WPF) at the points depicted on the vane. A low homogeneous value of P_{rms} is seen along most of the radial extent of the vane (probe (1)), stressing a weak rotor-wake interaction. However, a high value, related to higher pressure fluctuations is visible in the tip region at 90 % span (probes (3) and (4)), which is related to the impingement of the tip vortex. It is confirmed as the high P_{rms} zone in the tip region follows a diagonal path similar to the slope of the convected tip vortices. As mentioned, the WPF are calculated at four locations including the zones with minimum and maximum P_{rms} variations. The spectra present a dominant tonal component aligned with the blade passing frequency of the rotor. For the probes located before mid-chord, the tones dominate up to the 10^{th} BPF harmonic. Contrarily, for the probes located near the tip region, even if the amplitude of the tones is higher by about 5 dB, they tend to disappear after the 5^{th} harmonic. For this region, the broadband component also increases, suggesting the presence of more turbulent structures over a wide range of length scales. Overall, the

impingement point appears to be associated with the highest levels for both the first BPF and the broadband component.

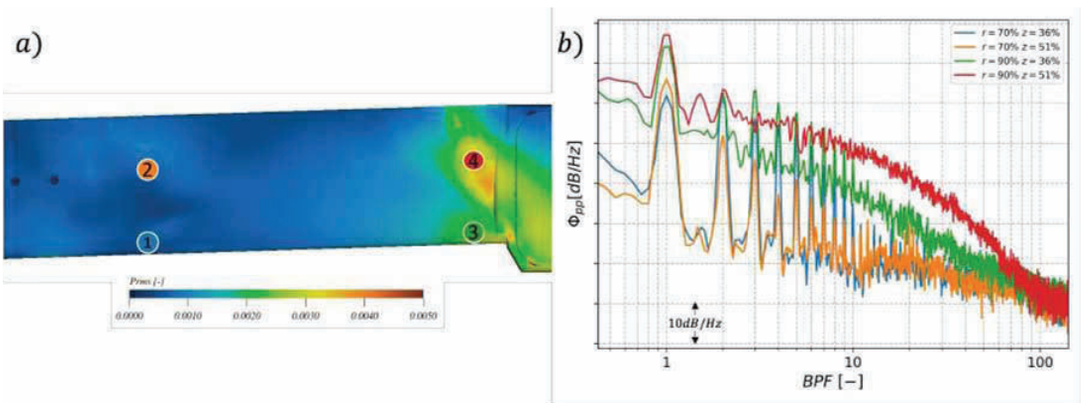


Figure 8: P_{rms} on a stator vane: (a) iso-contours with probe locations; (b) PSD of wall pressure at probes (1) to (4).

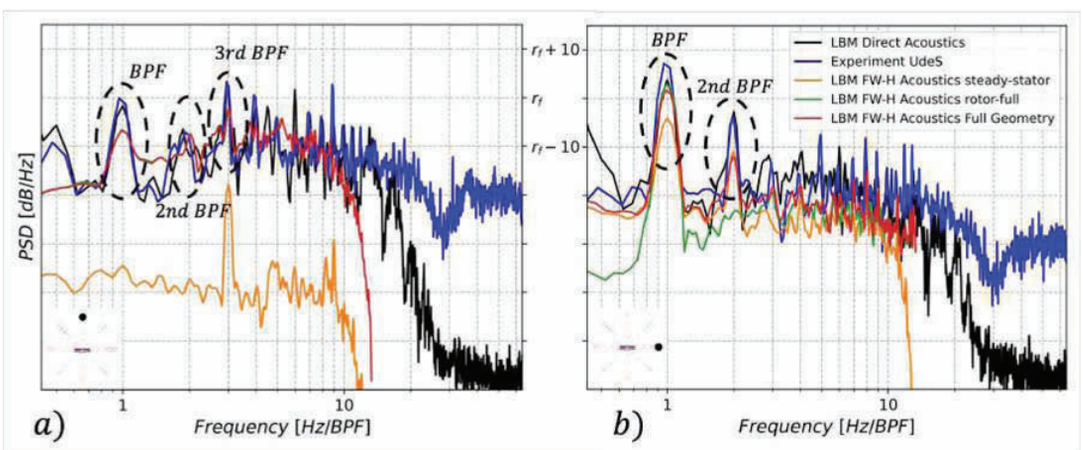


Figure 9: Far-field noise comparison between experiments and simulations for microphones located (a) upstream and (b) above the casing.

The pressure signals recorded at the far-field probes are used to provide direct noise acoustic levels, which are compared with the experimental and FW-H results. The experimental signal is resampled to achieve the same time length and sampling frequency to have the same parameters when performing Welch's periodogram. Comparisons are made for the microphone located upstream of the system (Fig. 9a)) and above the casing (Fig. 9b)). The spectra have strong tonal (BPF and harmonics) and broadband noise. The numerical results obtained from the direct propagation and the FW-H analogy show a general good agreement with experiments for the levels of the BPF and first harmonics at the evaluated locations. There is an improved prediction of the tonal and broadband noise when comparing the direct propagation with the results obtained by Rendon et al. [4]. The former is attributed to the better resolution of the periodic unsteady interstage flow and improved aerodynamic performance of the rotor system. The latter, on the other hand, is related to a better resolution of the turbulent interaction noise sources, such as the tip vortex, which are known to radiate in the upstream direction (Fig. 9a)). The acoustic analogy is then used to evaluate the contribution of both the rotor and the stator separately. Figure 9a) shows a spectra dominated by the rotor noise with a low level coming from the stator. This low level is related to a minimum noise radiation that happens aligned with the stator vanes as shown by Vella et al. [10] for the noise emitted by a beam in a rotor-strut configuration. Additionally, a peak is seen at the third BPF which is related to the main frequency of

fluctuation present in the stator vanes, as shown by the PSD of Fig. 5b). Figure 9b) shows a reduction in the tonal component after the third BPF harmonic. This reduction is associated with the masking effect generated by the presence of the casing as the length of the duct begins to be comparable with the wavelength associated to the frequency of emission. There is an increase in the stator noise level, with a dominant contribution especially at the second harmonic of the BPF. This frequency is related to the major tonal contribution regardless of the location, as seen in Fig. 8. The roll-off after the 10^{th} BPF harmonic is related to the cut-off frequency associated with the specific voxel size where the probes are located and the sampling frequency of the surface data.

CONCLUSIONS

High-fidelity compressible simulations have been performed for a ducted rotor used as a concept design for future electrically driven tail rotor systems. The complete experimental setup, including the anechoic chamber has been simulated with the LBM solver PowerFLOW. Special attention was paid to the meshing in the rotor-stator interstage to properly resolve the wake contraction and tip vortex trajectories and improve previous aerodynamic predictions of mean thrust and torque.

The time trace of the unsteady torque and thrust integrated over the rotor blades shows twelve main peaks during a rotational period, which can be traced to the potential interaction with the stator vanes. Similar twelve peaks are seen in the unsteady torque integrated over the stator vanes, but shifted by a time delay corresponding to an angular displacement of 23°. By using instantaneous vorticity magnitude fields, this time shift is related to the interaction of a blade tip vortex with a stator vane, and corresponds to its trajectory from its point of generation to its impact on the stator vane. This strong fluid-solid interaction between the blade tip vortices and the stator vanes also yields a main source of noise evidenced by the dilatation field at different blade-to-blade cuts. This interaction is also seen to occur near the tip region of the stator vane between 80% and 90% of the span, as shown by the local high pressure fluctuations together with an increase in the spectra levels for both tonal and broadband components. Moreover, a vortex-vortex interaction is evidenced in the tip region yielding an additional quadrupolar source.

Noise spectra obtained from a direct and hybrid approach are compared with those obtained from the experiments for the upstream and rotor plane locations. A good match between the experimental and numerical results is observed until the cut-off frequency at the 10^{th} BPF harmonic. An improvement in the tonal and broadband levels is accomplished when compared to previous simulations. The first one is related to the better prediction of the periodic unsteady loading also yielding improved aerodynamic performance while the latter is associated with the better resolution of the random turbulence interaction noise sources. Finally, the use of the FW-H acoustic analogy allows separating the noise from each element of the system. The rotor is shown to be the major noise contributor except for the second harmonic of the BPF where the stator dominates. This dominance is then related to the wall pressure fluctuations seen in the vanes as a result of the tip-vortex/stator interaction.

Future studies will do a deeper analysis in the evolution of the tip flow and its contribution to the far-field noise. Filtered dilatation fields will be used to have a qualitative insight in the presence of the new found noise sources in the microphone regions. Finally, the feasibility to create simple rules to detect if the rotor stator noise is dominated by either wake or tip vortex interaction will be evaluated.

REFERENCES

[1] A. Vuillet, *New aerodynamic design of the fenestron for improved performance*, in *Proc. 12th European Rotorcraft Forum, 1986*, **1986**.

[2] K. Stickels, M. Brunetti, M. Barber, *et al.*, *Advances in helicopter electric tail rotor drive*, in *Proceedings of the European Rotorcraft Forum*, **2017**, p. 662.

[3] P. Jaiswal, J. Rendon, Y. Pasco, M. Sanjosé, and S. Moreau, *Aeroacoustic investigation of a ducted tail rotor*, in *AIAA AVIATION 2023 Forum*, **2023**, p. 3512.

[4] J. Rendon, S. Moreau, and M. Sanjosé, *Influence of the rotor blade pitch angle on the far-field noise emissions of a ducted tail rotor*, in *30th AIAA/CEAS Aeroacoustics Conference (2024)*, **2024**, p. 3150.

[5] S. Moreau and M. Sanjose, *Sub-harmonic broadband humps and tip noise in low-speed ring fans*, The Journal of the Acoustical Society of America vol. 139, no. 1, pp. 118–127, **2016**.

[6] M. Piellard, B. B. Coutty, V. Le Goff, V. Vidal, and F. Pérot, *Direct aeroacoustics simulation of automotive engine cooling fan system: Effect of upstream geometry on broadband noise*, in *20th AIAA/CEAS Aeroacoustics Conference*, **2014**, p. 2455.

[7] P. Jaiswal, S. Moreau, and M. Sanjose, *Aeroacoustic investigation of a helicopter tail rotor.* Bulletin of the American Physical Society, **2022**.

[8] J. Rendon, P. Jaiswal, M. Sanjosé, Y. Pasco, and S. Moreau, *Aeroacoustic investigation of a ducted tail rotor using the lattice-boltzmann method*,

[9] J. Santamaria, A. Bierrenbach-Lima, M. Sanjosé, and S. Moreau, *Shape considerations for the design of propellers with trailing edge serrations*, Journal of Sound and Vibration vol. 595, p. 118 771, **2025**.

[10] E. Vella, R. Gojon, H. Parisot-Dupuis, N. Doué, T. Jardin, and M. Roger, *Mutual interaction noise in rotor-beam configuration*, in *30th AIAA/CEAS Aeroacoustics Conference (2024)*, **2024**, p. 3318.

F2 Case Studies

10 April - 16:30 - Room 1 Fitzgerald

Chairmen: Nazme Mohsina, Henrik Witt

List of papers

Assessing the Influence of Cooling Fans on Fire Risk Mitigation in Domestic Tumble Dryers

- Piero DANIELI – University of Padova (Italy)
- Edoardo BREGOLIN – University of Padova (Italy)
- Massimo MASI – University of Padova (Italy)

Experimental Validation of a CFD procedure for the Analysis of an Industrial Cyclone Separator

- Edoardo BREGOLIN – University of Padova (Italy)
- Piero DANIELI – University of Padova (Italy)
- Massimo MASI – University of Padova (Italy)



ASSESSING THE INFLUENCE OF COOLING FANS ON FIRE RISK MITIGATION IN DOMESTIC TUMBLE DRYERS

Piero DANIELI[1], Edoardo BREGOLIN[2], Massimo MASI[1]

[1] *University of Padova, Department of Management and Engineering, Stradella San Nicola 3, 36100 Vicenza, Italy*

[2] *University of Padova, Department of Industrial Engineering, Via Venezia 1, 35131 Padova, Italy*

SUMMARY

Over the lifetime of domestic tumble dryers, significant amounts of lint accumulate inside the casing, presenting potential fire hazards. The movement and accumulation of lint are affected by three key components: the rotating drum and the two small fans used to cool the electric motor and heat pump compressor. This study investigates by CFD the long-term lint accumulation process inside a domestic tumble dryer through a model that incorporates essential components such as the electronics, rotating drum, motor, and fans. The lint deposition process is analyzed by unsteady RANS that accounts for lint particles. An original strategy was developed to simulate the entire operation lifetime within a single run. The results demonstrate the potential of the model to aid a dryer design aimed at fire risk mitigation.

INTRODUCTION

In recent years, domestic tumble dryers have become essential appliances in modern households, particularly in urban areas where space for traditional drying methods is limited. Advances in technologies such as heat pump systems have significantly improved their energy efficiency, making these devices more sustainable and accessible. However, the widespread adoption of tumble dryers has introduced new challenges, particularly in meeting stricter environmental and safety regulations that aim to ensure safe and eco-friendly operation. One of the most critical safety concerns is the risk of fire caused by lint accumulation within the dryer housing. According to the U.S. Fire Administration, an average of 2,900 home dryer fires occurs annually, resulting in five fatalities, 100 injuries, and $35 million in property damage [1]. Lint, generated from fabric wear during drying, tends to accumulate in critical areas, where it can contact hot surfaces or electrical components, creating hazardous conditions. This issue has been explored in prior studies, such as [2], which investigates fire containment strategies specific to electric dryers, and [3], which examines the theoretical risks of spontaneous lint combustion. Consequently, predicting and controlling lint accumulation is vital for mitigating these risks. From a technical perspective, lint deposition is driven by the fluid dynamics within the dryer housing, which are influenced by the interaction of key components: the drum, the cooling fan for the heat pump compressor,

and the cooling fan for the drum motor. Note that the fan employed to move the warm air from the ambient, towards the heater and finally to the dryer basket is included into an air circuit which is independent from the housing so that it has no influence in the lint deposition. The fans, operating in between 2000-4000 rpm, have a much greater impact on airflow patterns compared to the drum, which rotates at approximately 30 rpm [4]. This is due to the significantly higher rotational speed of the fans and the fact that the drum is not designed as an air-moving device. In particular, it is not equipped with blades or any other aerodynamic elements. The airflow induced by the drum is solely the result of shear-driven motion along its surface, which is composed of chrome-plated aluminum characterized by low friction. This difference underscores the critical role of fans in understanding and modeling lint transport and deposition processes. In this context, the development of a Computational Fluid Dynamics (CFD) model capable of accurately predicting lint accumulation over the entire lifecycle of a dryer is of significant importance. Such a model could identify areas within the housing prone to high accumulation, enabling strategic design modifications. For example, fan repositioning could guide lint deposition to easily accessible areas for periodic cleaning, thereby reducing the risk of fire and improving overall safety. To date, no systematic studies have addressed the specific influence of fans on lint deposition in domestic dryer housings. This study introduces a novel CFD model that considers the complete internal fluid volume of a real dryer, incorporating key operational parameters throughout the appliance's lifecycle. The model was developed to analyze airflow patterns and lint particle behavior, providing a basis for optimizing fan placement or redesigning dryer components. The numerical results were validated against experimental data, and the model was subsequently used to evaluate the role of fans in influencing lint accumulation, highlighting their potential to either exacerbate or mitigate the risk of fire.

CFD MODEL

The first of the following sub-sections outlines the geometry of the reference dryer and the model constructed for numerical simulations. The second sub-section details the simulation setup used for the numerical validation of the model and provides an in-depth explanation of the validation process.

Geometrical model

Currently, various types of dryers are available on the market, but this study focuses exclusively on electrically powered heat pump models, as they are the most prevalent globally, with some regional exceptions favoring gas dryers. A typical domestic tumble dryer consists of: an external sheet metal casing; a drum (or tambour), which holds the clothes to be dried and occupies most of the internal volume; an electric motor (with its cooling fan); a fan that directs hot airflow into the drum; an air filter located downstream of the drum to capture textile fibers; and the heat pump system, which includes the compressor, heat exchanger, and compressor cooling fan. The compressor cooling fan is absent in gas-powered or resistance-heated models. Manufacturers may modify the positioning and arrangement of these components according to design and industrial requirements, as illustrated in [5, 6]. For this study, a detailed physical analysis was conducted on a specific tumble dryer model available at the Department of Industrial Engineering at the University of Padua, which served as the reference for numerical simulations. On-site disassembly was performed to identify and measure the internal components within the casing. Figure 1 shows the disassembled machine, revealing key components: (1) tubes for water transport from the condenser to the overhead reservoir; (2) heat exchanger (evaporator + condenser) for conditioning and recirculating air into the drum; (3) refrigerant tank connected to the heat exchanger; (4) electronics for the motor and refrigeration circuit; (5) electric motor; (6) condensate tank; (7) drive belt for drum rotation; (8) interference filter; and (9) additional electronic components. These measurements and observations formed the basis for developing the CFD model used in this study.



Figure 1: overview of the tumble dryer analyzed in this study.

The following Tab. 1 summarizes the overall dimensions of the various components of the dryer.

Table 1: Dryer dimensions

Components	**[cm]**
External casing (LxHxD)	59.5 x 85 x 63.8
Maximum drum diameter	56.5
Minimum drum diameter	53
Electronics casing (LxHxD)	6 x 14 x 36
Interference filter diameter	3.9
Refrigerant tank (Diameter x Height)	10.5 x 22
Condensate tank (LxH)*	13 x 19
Distance between drum and condensate tank	1.4
Motor (Diameter x Depth)	12 x 13
Heat exchanger + duct base area (LxD)	34 x 29
Motor cable box (LxHxD)	5.5 x 12.5 x 6.5
Belt section	1.2 x 0.3

The virtual model of the dryer was developed based on the measurements obtained during the physical analysis. Using the CAD functionality within Simcenter STAR-CCM+ software, the internal fluid volume of the dryer was accurately reconstructed. This volume represents the free space inside the casing, with structural and operational components subtracted from a base solid model. The left frame in Fig. 2 shows a transparent visualization of the fluid domain to highlight the internal empty spaces created by the presence of components such as the heat pump compressor, heat pump cooling fan, electric motor, motor cooling fan, and air duct.

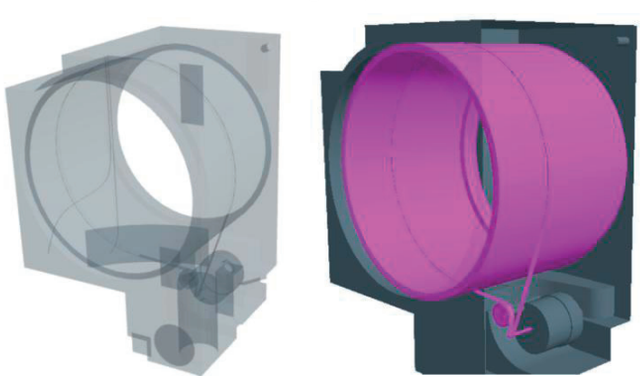


Figure 2: transparent view of the fluid volume within the dryer (left) and purple-highlighted rotating surfaces (right).

CFD model setup and numerical validation

The CFD simulation setup incorporates the following boundary conditions applied to the fluid volume described previously: i) a pressure outlet condition is applied to the wall region corresponding to the electronic board area, replicating the realistic opening in the casing designed to cool the electronic components; ii) the multi-reference frame (MRF) technique is employed to simulate the motion of the rotating drum in a steady-state analysis, as illustrated in the right frame of Fig. 2; iii) the fan momentum model available in STAR-CCM+ is utilized as a computationally efficient alternative to explicitly modeling the fan blades in full geometric detail. Instead of resolving the full blade geometry, the fan momentum model simulates the fan's effects as a localized force field applied to the fluid. This method significantly reduces computational complexity while effectively capturing the fan's influence on the airflow. The model computes the momentum imparted to the fluid in the tangential, axial, and radial velocity components based on the fan's operating characteristics, including its performance curve (pressure vs. flow coefficients) and rotational speed. Each fan is represented by two parallel surfaces: an inlet and an outlet, which define the boundaries of the fan's interaction with the fluid. The left-side frame of Fig.3 shows these inlet and outlet surfaces within the computational domain, where "Fan 1" corresponds to the compressor cooling fan and "Fan 2" to the motor cooling fan. The right-side frame of Fig. 3 reports in dimensionless form the pressure curve of the two fans. Fan 1 curve was derived from the available datasheet of the fan [7], whereas Fan 2 curve was reconstructed based on the available data for the rotor diameter (D) and rotational speed (ω) – equal to 0.06 m and 4000 rpm, respectively – and the estimate of the heat transfer required for motor cooling. The latter was quantified as follows.

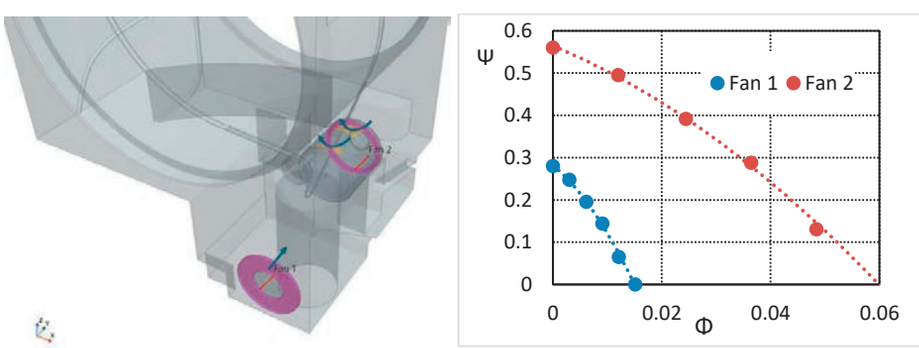


Figure 3: cooling fan geometrical models with flow direction (left) and fans' aeraulic performance (right).

Assuming 90% motor efficiency, the thermal power (Q) to be dissipated resulted equal to 30 W based on a motor's power rating of 300 W. Assuming ΔT=30 K as temperature difference between the motor surface and the cooling air, and given A=0.0415 m² as motor surface area (measured directly on the component), it was possible to calculate the value of the heat transfer coefficient (h) needed for motor cooling using eq. (1).

$$Q = h * A * \Delta T \ [W] \tag{1}$$

By applying the similarity low for turbulent natural convection in the form reported in eq.(2), where k [W/m·K], μ [Pa s], and cp [KJ/kgK] are the known thermal conductivity of mild steel, dynamic viscosity and specific heat of air, L [m] is the characteristic length of the motor surface (all needed to univocally define the Prandtl (Pr) and Reynolds (Re) numbers values), it was therefore possible to determine the air velocity (v).

$$h = \frac{0.037 * k}{L} * Pr^{0.33} * Re^{0.5} = f(k, L, \rho, v, \mu, cp) \tag{2}$$

The fan 2 volumetric flow rate (q_v, [m³/s]) was determined, considering the fan's surface area purple-highlighted in Fig. 4. Thus, it was possible to calculate the flow rate coefficient, as defined by eq. (3).

$$\phi = \frac{q_v}{\omega D^3} \tag{3}$$

The fan pressure (pf) and its dimensionless counterpart, that is the pressure coefficient defined by eq. (4), were obtained through iterative adjustments in the fan momentum setup to ensure consistency with the system's resistance curve, and the complete performance curve was finally constructed considering the same performance curve trend as Fan 1.

$$\Psi = \frac{p_f}{\rho \omega^2 D^2} \quad (4)$$

The physics setup used for the numerical validation of the model is detailed in Table 4. Notably, the numerical validation was performed based on the flow field solution alone, without considering particle injection.

Table 2: computational setup for numerical validation

Physics	Models
Turbulence modeling framework	Reynolds-Averaged Navier-Stokes (RANS)
Wall treatment model	Two-Layer All y+ Wall Treatment
Turbulence model	Realizable K-Epsilon Two-Layer
Air properties	Ideal gas, constant density

Given the absence of evidence suggesting the importance of detailed, localized fluid dynamic phenomena, the use of spatially uniform discretization across the fluid domain was deemed appropriate. Uniform computational grids were generated using the automated grid generation tools available in Simcenter STAR-CCM+. By setting proportional grid control parameters and limiting aspect ratio variations, distortions in cell geometry were minimized. Based on comparative studies, such as [8], which emphasizes the superior accuracy of polyhedral grids over tetrahedral ones, the former grid type was selected for all simulations in this study. Grid density at the near-wall regions was increased by inclusion of only two prismatic layers (to limit the computational at a level compatible with the available computational resources). For numerical validation, grid independence was assessed by comparing simulation results obtained from progressively refined grids, characterized by an eightfold increase in the cell numbers, achieved through successive doubling of the grid resolution along each spatial dimension. To ensure consistent comparisons, all grids were tested under identical physical modeling conditions. The key parameters fixed for all grids considered are collected in Tab. 3, while Tab. 4 details the grid parameters peculiar of each grid setup.

Table 3: grid parameters kept unchanged across grid refinements

Parameter	Value	Description
Base Size	0.805 m	Reference size for grid scaling
Surface Grow Rate	1.3	Surface ratio between adjacent cell sizes
Prism Layer Stretching	1.5	Factor of increase between adjacent prism layers
Volume Grow Rate	1.2	Transition factor between near-wall and bulk cells

Table 4: grid parameters changed with grid refinements and achieved degree of convergence.

Parameter	MESH 1	MESH 2	MESH 3
Number of cells	20,209	163,511	1,278,481
Target Surface Size (% of base size)	7.1	1.74	0.554
Minimum Surface Size (% of base size)	3.55	0.87	0.277
Near-wall Prism Layers	2	3	4
Residuals	1.00e-05	3.69e-04	9.87e-04

The last line in Tab.4 reports the residual reduction achieved at the end of each computation. Reductions in the range of 10^{-4} to 10^{-5} were deemed as acceptable in view of the low values of absolute velocities and temperature differences within the domain, and the large physical size of the domain, which inherently increase the uncertainty. The validation process involved evaluating velocity fields and mass flow rates in corresponding

domain regions/areas as obtained from calculations performed on different meshes. Velocity fields were analyzed in two configurations: one incorporating the effects of moving components within the fluid domain, such as the rotating drum and cooling fans, and a second, simplified scenario where these components were assumed at rest and only convective flows driven by thermal gradients on surfaces were allowed to develop. The surfaces temperature fixed for the thermal-convection-only simulation scenario are listed in Tab. 5.

Table 5: surfaces temperature for the grid sensitivity analysis of the thermal-convection-only scenario

Surfaces	Temperature [°C]s
Drum	250
Heat exchanger, air duct, motor	300
Other walls	25

The analysis was performed for multiple cross-sections of the fluid domain, strategically selected to capture the primary flow patterns and regions of interest. Additionally, mass flow rates were assessed across specific sections of the fluid domain. Figure 4 provides a comparison of velocity magnitude plots for MESH 2 (top frames) and MESH 3 (bottom frames) on the purple-highlighted cross-section in the bottom region of the dryer (central frame). The comparison includes both the convective-only scenario (right side frames) and the configuration with all rotating components active (left side frames), illustrating the impact of moving parts on flow dynamics.

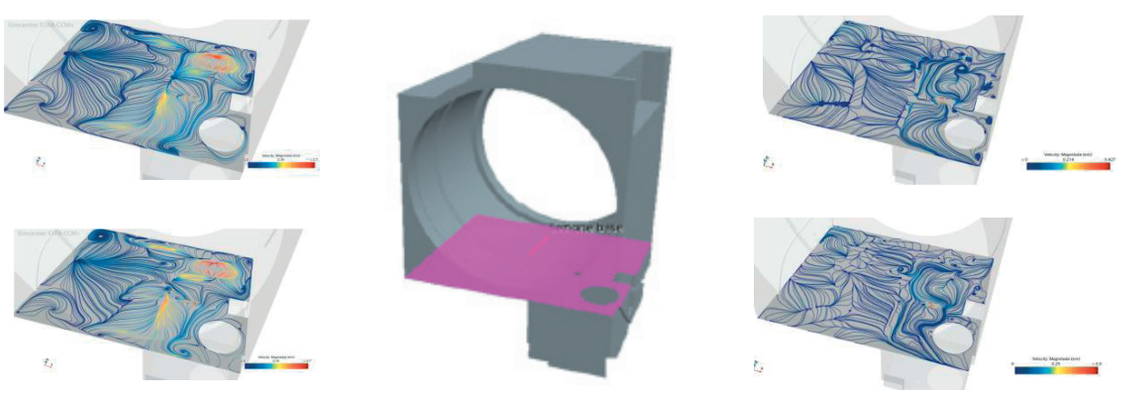


Figure 4: MESH 2 (upper) and MESH 3 (lower) velocity magnitude contour plots with all rotating components (left side frames) and convection only scenario (right side). Detail of the reference cross sectional surface (middle frame).

The comparison shows that MESH 2 and MESH 3 produce nearly identical results for both scenarios, with very good agreement in high-gradient regions. In contrast, MESH 1 (not shown in Fig. 4) exhibited noticeable deviations due to its coarser resolution, highlighting the importance of grid refinement for accurate predictions.

To further validate the grid resolution, mass flow rates across a selected section of the domain were calculated and compared for the different mesh configurations. The results indicate that MESH 2 and MESH 3 exhibit mass flow variations of less than 2% between them, while MESH 1 deviates by approximately 7% compared to MESH 2. This grid dependency analysis confirms that MESH 2 provides the optimal balance between computational efficiency and numerical accuracy.

SIMULATION STRATEGY

This section details the CFD-based methodology for simulating lint accumulation. The particle injection modeling setup is first presented, followed by a description of the simulation strategy employed to simulate the long-term lint deposition.

Particle injection modelling

The solid phase, representing lint particles, was modeled assuming a material with constant density equal to 50 kg/m³, as derived from literature dealing with cotton fibers [9-10]. This assumption ensured consistency and simplicity in representing lint, which typically does not exhibit variability in density due to the homogeneous nature of its composition. The particles are therefore not modelled as mass-free, because mass is crucial to accurately model particle inertia and deposition behavior. In addition, particles were assumed to have a sphericity equal to 0.22, derived from the analysis of available pictures of lint accumulation in real dryiers. These images were not included in this paper because of confidentiality reasons. The particle diameter was distributed statistically following a Rosin-Rammler distribution as suggested by [11]. The size distribution of the simulated particles is reported in the left-side frame of Fig. 5.

The particle motion was modeled using a Lagrangian Multiphase framework, where the trajectories and velocities of the particles were calculated by iteratively solving equations derived from Newton's second law. To minimize computational requirements, particles were grouped into parcels, which represent clusters of particles with identical size and velocity characteristics. A one-way coupling strategy was employed to enhance computational efficiency and align with the simplified modeling approach. In this method, the motion of the parcels was influenced by the surrounding gaseous phase, while the effect of the parcels on the gas flow was neglected. Particle-wall interactions were included in the model, whereas particle-particle interactions were not accounted. The lint's particles were assigned a sphericity of 0.22, obtained from the analysis of pictures reported by Kannan et al. [11] using the software ImageJ. The Haider & Lavenspiel model was chosen to determine the drag coefficient of the particles, which accounts for the influence of particle shape (see eq. 5).

$$C_D = \frac{24}{Re_p}\left(1 + AR{e_p}^B\right) + \frac{C}{1+\frac{D}{Re_p}} \quad (5)$$

Where Re_p is the particle Reynolds number, while A, B, C, D are parameters that depend on particle sphericity.. Particles were introduced into the simulation domain through the annular surface highlighted in the right-side frame of Fig.5, which represents the sole physical passage from which the lint could pass from the drum and the casing. Thirty-six equally spaced injection points were defined along the annular surface, with each injector configured to deliver the same mass flow rate. The injection time was defined to obtain the total mass entering the casing of the dryer as estimated for its entire lifetime. The simulation time-step of 0.003 s was chosen as a trade-off between the computational time and the particle Courant number, which allows for a correct and stable tracking of the particles for values below 1. The number of parcels and the tangential velocity (to account for the rotational motion of the drum) were both specified for each injector. The amount of lint accumulated inside the casing of the tumble dryer was calculated based on the average particle loss during the drying process of cotton sheets and the accumulation observed in the machine's lint filter [12]. It is hypothesized that one-tenth of the reported quantity (0.2g/cycle) in the literature penetrates into the casing. Estimating the usage of the appliance at 160 cycles per year, as specified by EU regulations [13], the introduced mass during 10 years of lifetime is approximately equal to 360g.

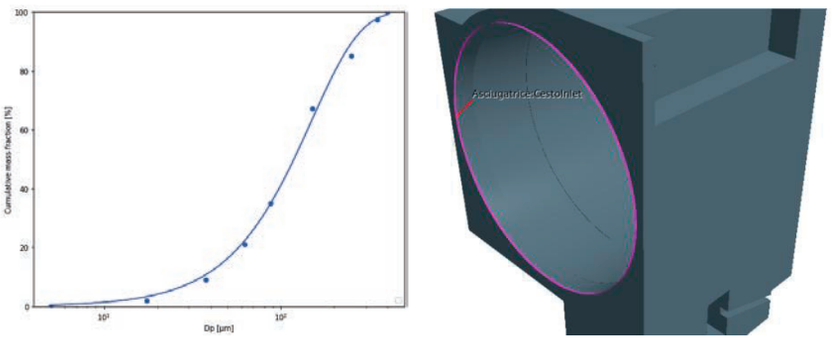


Figure 5: size distribution of lint particles (left) and annular particle injection surface (right).

Simulation steps

It is practically unfeasible to simulate the full 10-year operation of the dryer in real-time; therefore, a simulation strategy must be adopted to achieve reliable and representative results within reasonable computational timescales. The lifetime accumulation of lint was modeled through a single time-dependent simulation divided into two distinct steps. In the first step, all particles were injected into the domain simultaneously, with the dryer operating under nominal conditions. Here, fans are active, the drum is in motion, and internal surfaces are heated as for the real dryer operation. This phase continues until particle deposition on the internal surfaces reaches an asymptotic value, indicating that any further deposition is practically negligible. The simulation demonstrated that this condition is achieved after approximately 30 seconds, as shown in the deposition trend graph reported in Fig. 6.

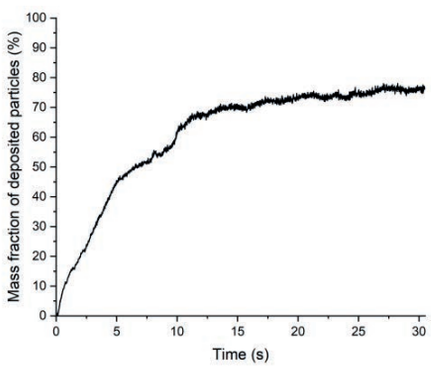


Figure 6: Deposition trend of lint particles.

In the second step the completion of the lint deposition process is simulated starting from the shutdown of the dryer. Fans are turned off, the drum is at rest, and the internal surfaces are allowed to cool. During this phase, particles that are still suspended due to aerodynamic effects at the end of the previous simulation step are allowed to settle. The simulation continues until at least 90% of the total particles were deposited on the surfaces, ensuring comprehensive coverage of the accumulation process.

Assessment of the fans' effect

To assess the fans' effect on the lint deposition inside the tumble dryer, another two-step unsteady simulation needs to be performed with the two fans turned-off. The conditions of the simulation without the fans are the same as before. After completion of the first step, characterized by the sole movement of the drum, the particles are allowed to settle as for the second step of the previously described simulation.

The availability of the two-simulation results makes it possible to analyse and compare the deposition pattern for the most representative surfaces of the tumble dryer.

RESULTS AND DISCUSSION

To validate the model, predicted lint accumulation patterns were compared with experimental measurements obtained from a real dryer of the same model used for the CFD simulations, after 10-years operation. Validation involved calculating the volume fraction of material accumulated in wall-adjacent cells as predicted by the CFD model and comparing them with measured data. In the simulations, the volume of deposited material in each cell was re-shaped as a conical volume with obliquity consistent with the observed lint accumulation gradients. The total material volume in each cell was calculated, and a three-dimensional plot of the accumulation surface was generated. To enable direct comparison and preserving data confidentiality, both the simulated and the experimentally measured accumulations on the dryer surfaces were normalised using the corresponding maximum calculated/measured height. The normalized plots shown in Fig. 7, provide both 3D and 2D representations of the accumulation patterns for the experimental results (left-side frame) and CFD predictions (right-side frame) on two walls of the dryer casing (one reported in the top and one reported in the bottom frames of the Figure). Experimental data for the other casing walls are unavailable. The upper charts in Fig. 7 reveal strong qualitative agreement between the experimental and simulated results. Both datasets exhibit higher lint accumulation near the upper-left region of the surface, with prominent peaks in deposit height. The spatial distribution trends are consistent, showing lower accumulation in central areas. Peaks in the experimental data align closely in both position and intensity with those predicted by the CFD model, particularly in the upper and lower sections of the surface. Similarly, the lower charts in Fig. 8 demonstrate strong agreement. Both plots show significant accumulation in the central regions, with the experimental peaks aligning well in position and magnitude with those predicted by the CFD model. Minor discrepancies are observed in some scattered regions, where experimental data display slightly broader peaks. However, these differences are minimal and do not detract from the overall strong correlation, validating the CFD model's ability to accurately replicate real-world lint accumulation patterns.

Influence of cooling fans on lint accumulation

As highlighted in the Introduction, the cooling fans play a crucial role in shaping the internal fluid dynamics of the dryer, significantly impacting the particle deposition process. With the validated CFD model, it was explored how the lint accumulation morphology changes when the cooling fans are deactivated. This comparative analysis provides valuable insights on how fan operation influences particle deposition patterns and how much the sensitivity of lint accumulation to changes in operational conditions is. Figure 8 presents a comparison of accumulation patterns predicted by the CFD model on four dryer casing surfaces when cooling fans are turned off (left frames) and turned on (right frames). In the former case, the deposit patterns are more localized, with reduced variability in magnitude. Lint accumulation is concentrated in smaller, isolated regions, with smoother transitions between high and low deposit areas. This behavior suggests a more static flow environment, where airflow is insufficient to redistribute particles effectively, and deposition is driven primarily by gravitational settling and the limited airflow generated by drum rotation. In contrast, in the latter case, the patterns show increased magnitude of the peaks and greater spatial variability. The accumulation becomes more widespread, with sharper peaks and more defined regions of high deposit height. This indicates that the fans generate a more organised airflow, redistributing particles across the surfaces more effectively. Overall, the comparison highlights that cooling fans significantly influence deposition dynamics by enhancing convective motions and promoting broader particle redistribution, leading to more varied and intense accumulation patterns.

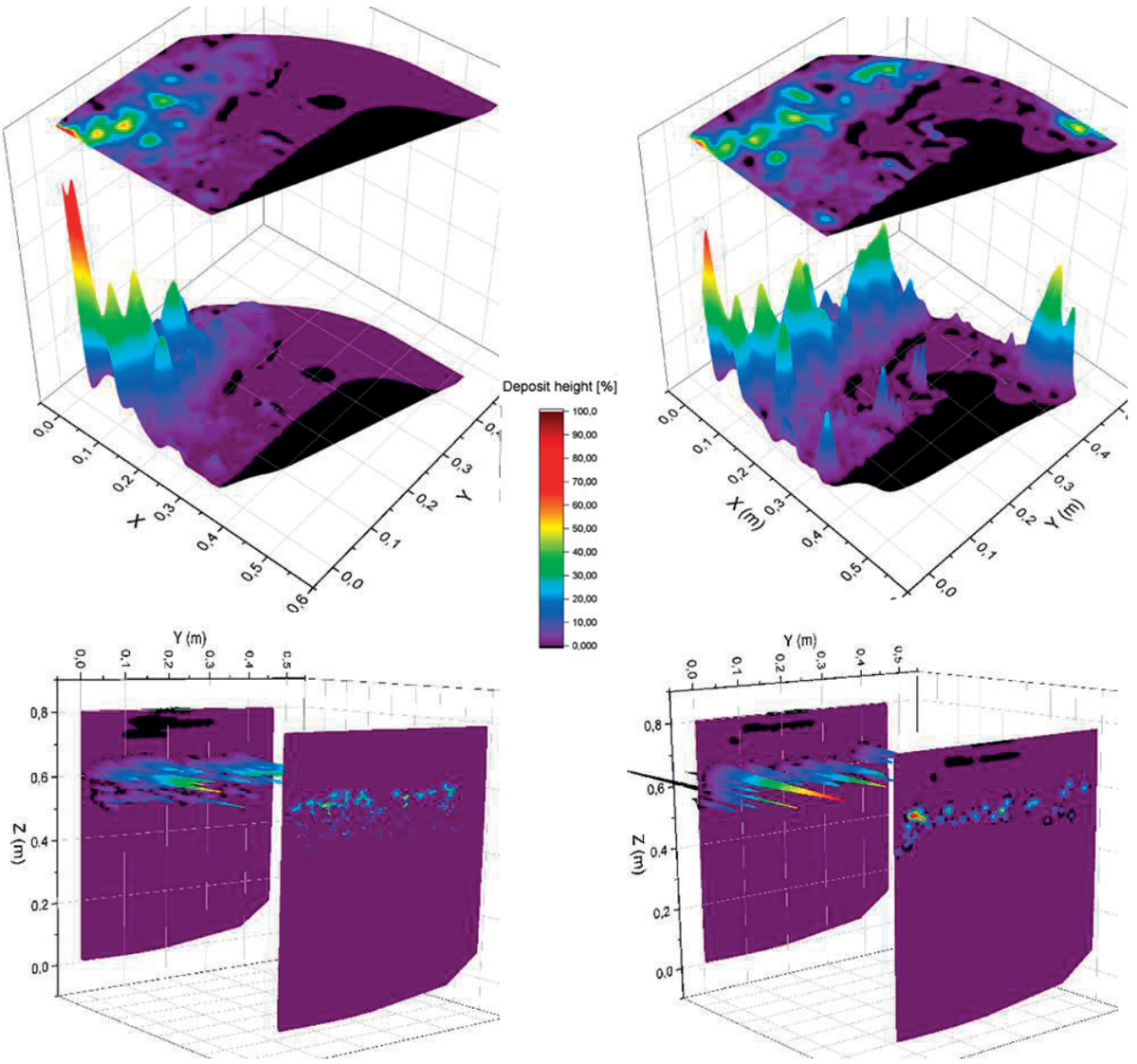


Figure 7: 3D and 2D lint accumulation patterns on two walls of the dryer as measured (left) and calculated by CFD model (right).

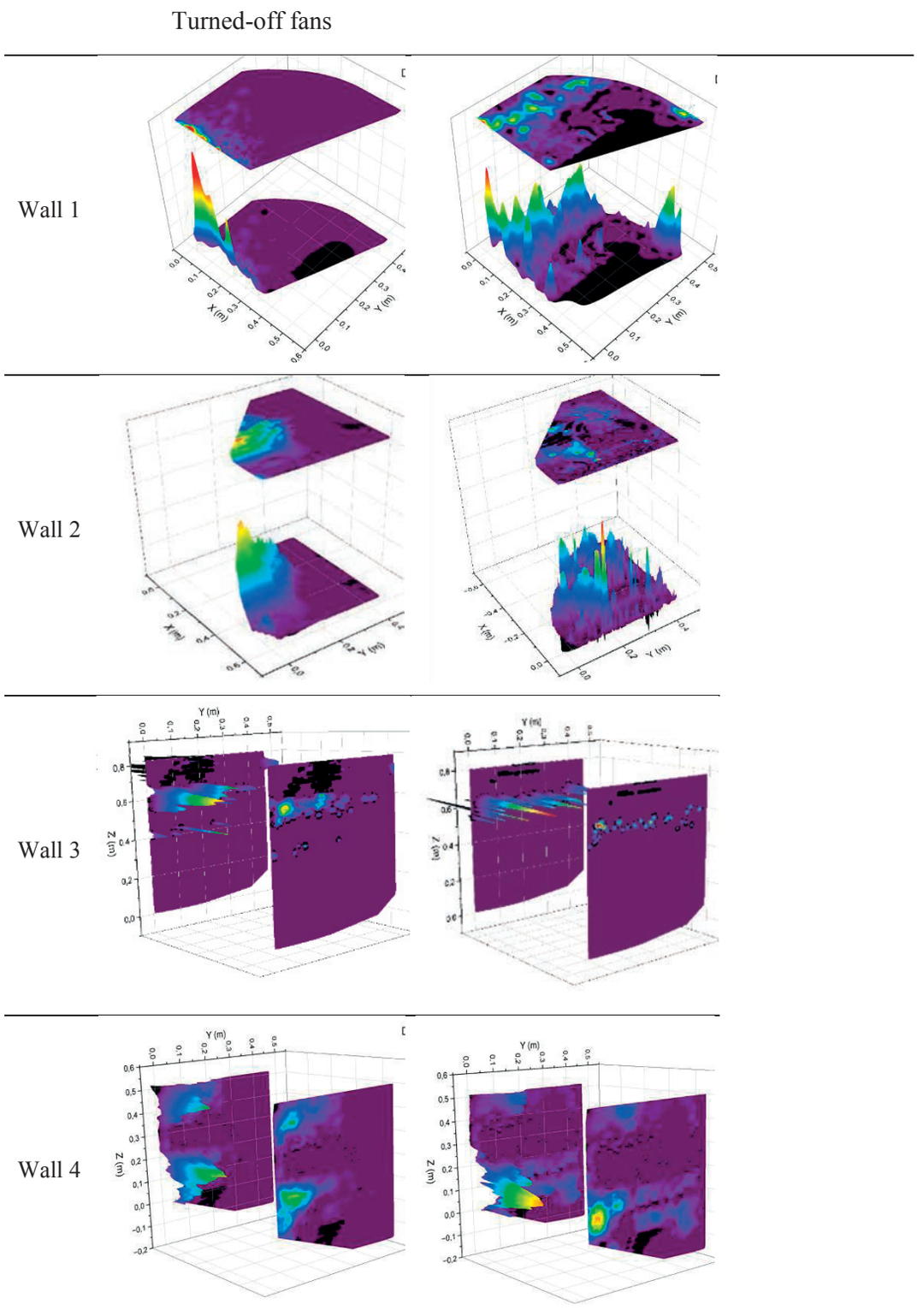


Figure 8: 3D and 2D lint accumulation patterns on four walls of the dryer as calculated by CFD model considering turned off (left) and turned on (right) cooling fans.

CONCLUSIONS

This study successfully developed and validated a novel CFD model to simulate the accumulation of lint within domestic tumble dryers over their operational lifecycle. The model demonstrated strong accuracy in replicating real-world lint deposition patterns, making it a valuable tool for analyzing and mitigating fire risks associated with lint accumulation. Key findings include:

- Cooling fans significantly influence the airflow dynamics inside the dryer, redistributing lint across internal surfaces. When fans are operational, lint deposition patterns are more widespread and exhibit greater variability in intensity. Conversely, without active fans, deposition is primarily localized and governed by gravitational settling.
- Validation of Results: The CFD model accurately predicted the spatial distribution of lint accumulation when compared to experimental data, demonstrating its capability to replicate real-world conditions.
- Design Implications: The insights from this study highlight the potential for optimizing fan placement and other design parameters to guide lint accumulation toward areas that are accessible for cleaning. This can significantly reduce fire risks by minimizing lint buildup near high-temperature components.
- Future Directions: Further research will focus on refining fan designs and exploring additional strategies to enhance lint management and improve safety standards for domestic tumble dryers.

The developed CFD tool provides a practical framework for manufacturers to design safer, more efficient tumble dryers while complying with stringent safety regulations.

BIBLIOGRAPHY

The reference section is placed at the end of the document, except if there are also appendices.

The references should be numbered and typed in consistent formalism, including at least, name of authors, title (italics), the source, and the year (bold) at the end.

[1] U.S. Fire Administration – *Help prevent clothes dryer fires*, Safety+Health **2022**

[2] Underwriters Laboratories– *Reducing injuries and damages electric clothes dryer fires*, Fire containment tests for the second edition of UL 2158, **2011**

[3] J. C. Jones – *A Theoretical Examination of the Possibility of Spontaneous Combustion of Laundry in Tumble Dryers.* Journal of Fire Science, 19, pp. 181-189, **2001**

[4] U.K. Whitegoods – *Tumble Dryer Fire Risks & Problems Explained*, **2011** (ukwhitegoods.co.uk)

[5] G. T. Sampson – *Clothes-Drier.* United States of America patent 476416, **1982???**

[6] A. Lee – *Final report on electric clothes dryer and lint ignition characteristics – May 2003.* U. S. Consumer Product Safety Commission - Directorate for Engineering Sciences, **2003**

[7] XinRuiLian Science & Technology Co. Ltd – *XFan AC Fan Model RAH1238B1.* Technical datasheet, **2013**

[8] W. Wang, Y. Cao, T. Okaze – *Comparison of hexahedral, tetrahedral and polyhedral cells for reproducing the wind field around an isolated building by LES.* Building and Environment, 195, 107717, **2023.**

[9] H. Metz, A. Ho, A. Clark e K. Nathe, «*Not from your belly button...*,» University of Oregon, Eugene, 2007.

[10] G. L. Barker, J. W. Laird, M. G. Pelletier e G. A. Holt, *Relative Velocity, Density, and Temperature Effects on Cotton Moisture Transfer Rates*. Journal of Cotton Science, n. 5, pp. 243-251, 2001.

[11] P. Kannan, F. Banat – *Investigating the residual characteristics of dryer lint for developing resource recovery strategies.* Applied Sciences, 2:1929, **2020**

[12] C. B. J. Hassenboehler, N. E. Wyatt – *Lint-Loss and Appearance-Change Tests for Blankets.* Textile Research Journal, pp. 583-587, **1979**

[13] Commission Delegated Regulation (EU) No 392/2012 of 1 March 2012 supplementing Directive 2010/30/EU of the European Parliament and of the Council with regard to energy labelling of household tumble driers Text with EEA relevance



EXPERIMENTAL VALIDATION OF A CFD PROCEDURE FOR THE ANALYSIS OF AN INDUSTRIAL CYCLONE SEPARATOR

Edoardo BREGOLIN[1], Piero DANIELI[2], Massimo MASI[2]

[1] *University of Padova, Department of Industrial Engineering - DII, Via Venezia 1 35131 Padova, Italy*

[2] *University of Padova, Department of Management and Engineering - DTG, Stradella S. Nicola 3, 36100 Vicenza, Italy*

SUMMARY

Cyclone separators play major role of extracting the dust produced from the shredding of metal scrap in fan assisted aeraulic systems for steel recycling. The accurate prediction of cyclone separation efficiency in real steel-recycling plants is therefore essential but very challenging because of the many factors that influence the separation process, most of all the wide size distribution and chemical composition of the dusts. To address this issue, the paper proposes a multiphase flow CFD model that uses the Eulerian-Lagrangian approach to simulate a cyclone separator installed in a real steel recycling plant in accordance with a three-steps simulation strategy. The model, validated against data measured on a cyclone in operation within the plant, demonstrates that the suggested procedure is effective for the simulation of industrial cyclones for steel recycling processes.

INTRODUCTION

In recent years, the use of scrap in steel production has increased as part of efforts to reduce greenhouse gases emissions and energy consumption of the metal industry [1-2]. The quality of the recycled iron, that is used in electric-arc furnaces to produce new steel, is heavily influenced by the recycling process' capacity to remove contaminants from the scrap [3]. One significant contaminant is dust composed of non-metallic materials, which is released in large amounts inside the shredder chamber during the comminution process. To prevent the dust from remaining with the scrap throughout the recycling procedure, it is suctioned from the shredder chamber and transported to a dedusting system. In steel recycling plants, the latter comprises aeraulic machines (e.g. cyclones, wet scrubber, bag filters etc.) that operate with an air flow driven by an industrial fan located downstream of the process. In particular, the first stage of the dedusting system consists in a tangential-inlet cyclone separator, which removes most of the dust mass. The subsequent separation stages, performed by wet scrubbers or bag filters, capture the finer particles. The primary performance indicator of an industrial cyclone separator is the particle collection efficiency, which is usually represented by the collection efficiency curve, defined as the mass fraction of collected dust against each particles' dimensions treated by the machine. The

accurate prediction of the collection efficiency curve is crucial for the design and optimization of cyclones [4-6], resulting as a difficult task due to complexities in managing the heterogeneous chemical composition of the dust.

Currently, computational fluid dynamics (CFD) is regarded as one of the most effective techniques for the analysis of cyclone separators. Early contributions (Griffiths & Boysan [7], Gimbun et al. [8]) used coarse-grid CFD simulations to evaluate the collection efficiency of small-scale cyclone separators. With advancements in CFD software capabilities and computational resources, many researchers have implemented accurate fine-grid models of laboratory-scale cyclones, with body diameter that ranges between 150 and 400 mm [9–11]. Bogodage et al. [12] investigated the impact of the bottom-outlet duct diameter on the collection efficiency of a laboratory cyclone. The CFD model they developed provided reasonable predictions of collection efficiency, with 13.34% maximum deviation from experimental data. El-Emam et al. [13] evaluated the collection efficiency of different small-cyclone geometries for the abatement of bio-particulate matter. Their CFD model showed that the cyclone configuration with the larger inlet dimensions and vortex-finder diameter gives the best separation performance for that case study. Wang et al. [14] studied the effect of the inlet angle on the collection efficiency of a 205 mm diameter cyclone with a CFD-DEM model. The results showed that the collection efficiency reaches the highest value when the inlet duct is 15° inclined with respect to the horizontal. Other works dealt with CFD models of industrial-scale cyclones, with body diameter that ranges between 700 and 6000 mm. Chu et al. [15] employed a CFD-DEM model to examine the impact of particle density distribution on the separation efficiency of an industrial cyclone used in coal mining. The simulation results show good agreement with experimental data, indicating that a higher average particle density enhances the cyclone collection efficiency. Kepa et al. [16] simulated a cyclone separator used in heat-generating plants for treating mono-density coal powders, analysing the effect of counter-cone positioning. The work demonstrates that a lower position of the counter-cone relative to the separation bin significantly increased the collection efficiency. Parno et al. [17] used a CFD-DEM model to optimize the geometry of a cyclone that treats cement powders with uniform material density. The study showed that increasing the vortex-finder length and reducing the body diameter produce a 6% increase in the total collection efficiency with a 4% reduction in the pressure drop. Winfield et al. [18] developed a CFD model of an industrial cyclone for blast furnace top-gas cleaning to examine the effect of different inlet configurations. The particles' densities used in the model were based on the average density of the flue dust. It was found that the triple-inlet configuration allowed for improvements of collection efficiency.

Despite the extensive literature on CFD models of cyclone separators, most studies consider the sole modelling case of laboratory-scale cyclones. The latter differ significantly from cyclones for industrial applications in terms of scale and operating conditions. Particularly, laboratory-scale cyclones work under controlled conditions of dust chemical composition and particle size distribution, making it unfeasible to apply the developed CFD models to industrial setups. On the other hand, the CFD models of industrial cyclones available in literature usually simulate systems where the particles density is often approximated as homogeneous (coal, cement, etc.). In steel recycling plants, dust exhibits significant chemical heterogeneity, which strongly impacts collection efficiency. Consequently, assuming a constant mass density of particles introduce substantial errors in efficiency predictions. To the best of the authors' knowledge, no CFD models of industrial cyclones specific for steel recycling plants are currently available in the literature. The novelty of the present study lies in two key contributions: (i) the development and validation of a CFD model for an industrial cyclone operating in steel recycling plants, and (ii) the demonstration that the average-density approximation fails to provide reliable predictions in such applications. To address these objectives, a CFD model incorporating particle properties with mass densities that reflect the diverse material composition of the dust, as derived from detailed chemical analysis, is proposed. The model has been validated against experimental measurements of collection efficiency curves from an industrial cyclone used in a steel recycling plant in northern Italy. Furthermore, the model's predictions were compared to analogous predictions for the simplified scenario generally considered in the literature, in which particles were represented using a single average density. The CFD model was developed using the commercial software Siemens Star CCM+ (version 19.1).

EXPERIMENTAL METHODS AND TOOLS

Dedusting system

The dedusting system of the present case study is employed for the dust abatement in an existing metal scrap recycling plant in the north of Italy. The left side of Fig. 1 shows a scheme of the plant that embeds pictures of each major component. The metal scrap enters the shredder's chamber and is crushed by the hammer mill.

The dust that is liberated during this procedure are suctioned by the air flow and transported to the cyclone separator. The 1.65 m diameter cyclone separates the large to fine particles while the wet scrubber separates the remaining smaller particles and discharge clean air into the atmosphere. The particles separated in the wet scrubber are mixed with water composing a slurry.



Figure 1: scheme of the dedusting system (left) and cyclone geometrical parameters (right)

The parameters defining the geometry of a cyclone for the dedusting system are reported in the right-side of Fig. 1.

Experimental measurements

The cyclone collection efficiency for a specific particle dimension $\eta(D_p)$ is defined as in eq. (1), which is used to build the collection efficiency curve of the cyclone.

$$\eta(D_p) = 1 - \frac{C_{out} \cdot f_{pout}(D_p)}{C_{in} \cdot f_{pin}(D_p)} \quad (1)$$

Where C_{in}, C_{out} are the dust concentrations in the air stream at the cyclone inlet and top air outlet, respectively, while $f_{pin}(D_p)$, $f_{pout}(D_p)$ are the mass fractions of particles with dimension D_p at the corresponding sampling points. The measurements on the industrial cyclone include air volumetric flow rate, air mass density, pressure, temperature, dust concentration and particle size distribution. The experimental measurements were conducted at three sampling points: cyclone inlet (IN), top air outlet (OUT) and at the bottom dust outlet (SEP).
The dust concentrations (C_{in}, C_{out}) were measured using sampling probes. The sampling probes are made up by a nozzle that was positioned coaxially to the air flow and collects a representative sample of the dust transported by the gas. The geometry and position of the access points have been chosen in accordance with the reference standard for sampling of industrial emissions [19]. The dust concentrations were derived from the ratio between the weight of the collected dusts (m_{dust}) and the volume of air collected by the sampling probe during the measurement (V_{air}), as described in eq. (2).

$$C = \frac{m_{dusts}}{V_{air}} \quad \left[\frac{kg}{Nm^3}\right] \quad (2)$$

The dust collected in the sampling probes was analysed to extract the particle size distribution (needed for the definition of cyclone efficiency, see eq.(1)) using a Laser Diffraction Particle Size Analyzer (LDPSA). The dust that is collected from the cyclone at the bottom outlet and discharged onto a moving conveyor, was instead experimentally characterised in terms of its mass flow rate ($\dot{m}_{sep}$) by using a dynamic balance. The particle size distribution within $\dot{m}_{sep}$ was measured using both LDPSA and vibrating sieves with mesh sizes ranging from 1000 μm to 40 μm. The experimental campaign consisted of three rounds of measurements, characterised by different air flow rates and types of metal scrap. In particular, air volumetric flow rates delivered by the fan equal to 26160 Nm^3/h were measured in the first and third round and equal to 21680 Nm^3/h in the second. As regard the processed metal scrap, mixed scrap was treated in the first and second round while sandwich panels' scrap in the third.

Metal scrap types

As mentioned in the previous section, two types of metal scrap have been considered in this work: mixed scrap and sandwich panels' scrap. The mixed scrap is originated both from municipal and industrial sources and is mainly composed of end-of-life products such as household objects, end-of-life vehicles and industrial by-products (see Fig. 2a). The sandwich panels' scrap consisted of disposed sandwich panels, which are composite

materials that consist of a low-density polymeric core, usually polyurethane, inserted between two metal-sheets, usually made up of aluminium or steel (see Fig. 2b).



Figure 2: scrap treated by the shredder and the corresponding dust separated from the cyclone for a) mixed metal scrap; b) sandwich panels' scrap.

To provide a fair modelling of the dust at the inlet of the cyclone (needed for CFD simulation) the chemical composition of the dust separated at the cyclone bottom outlet have been analysed using Inductively Coupled Plasma Optical Emission Spectroscopy (ICP-OES), Thermogravimetric analysis (TGA), XRD and XRF, following the standard procedure for waste characterization [20]. Although this is not a direct measurement at the cyclone inlet, it can still be considered a good approximation, as the vast majority of particles are effectively separated by the cyclone and therefore found at its bottom outlet. The content of alumina (Al_2O_3), magnetite (Fe_3O_4), magnesia (MgO), lime (CaO), zinc oxide (ZnO), silica (SiO_2), titania (TiO_2) and plastics inside the dust was characterized through the combination of the mentioned techniques.
Another key particle property to be properly defined is sphericity [21], since it strongly influences the cyclone performance. In particular, a low sphericity leads to a large particle drag coefficient, resulting in a high drag force acting on the particle and therefore, in a low collection efficiency. The perimeter sphericity S_P (see eq. (3)), which is the most reliable parameter to characterize particle sphericity from 2D images [22], was calculated by analysing multiple images taken with optical microscope.

$$S_P = \frac{P_C}{P_S} \tag{3}$$

Where P_C is the perimeter of a circumference having the same projected area as the particle, P_S is the perimeter of the particle. The analysis of dust pictures was conducted using the software ImageJ.

CYCLONE CFD MODELLING APPROACH

The industrial cyclone separator of the present work was simulated through a CFD mode developed using the commercial software Siemens Star CCM+ (version 19.1). The air flow was simulated using the Reynolds-averaged Navier-Stokes (RANS) model for incompressible flow. Although cyclone separators have a simple geometry, the gas flow field that develops within the machine is quite complex. Particularly, it is composed of two vortices: an outer vortex, where the gas at positive pressure is directed downstream to the bottom of the cone, and an inner vortex, where a negative-pressure air flow is sucked upstream by the air outlet duct. Therefore, the selection of an appropriate turbulence closure is essential to capture the anisotropic rotating flow within the machine. As demonstrated by Gronald et al. [23], the K-ε turbulence model is unsuitable for the prediction of complex rotating flows within cyclones. On the other hand, the Reynolds Stress model (RSM) showed to well-capture the swirling nature of the gas flow inside cyclone separators [24]. However, literature studies [25] have demonstrated that RSM hardly achieve a satisfactory residual level if utilized alone. Hence, in the present work the gas flow field within the cyclone is obtained through two simulation stages: first, the K-ε turbulence model was used to give an initial solution of the flow pattern then, starting from that solution, the RSM was used to obtain the final gas flow field.
The flow dynamics were solved using the coupled flow solver. The second-order upwind discretization scheme was selected for solving the convection and diffusion terms. The gas boundary layer near the wall regions was

treated using the high-y+ standard wall function. The roughness height of the internal walls' surface was set to 1.75 mm, in accordance with the values for steel tubes with deposits [26]. This was also confirmed by the inspection of the industrial cyclone internal surface condition at the recycling plant. Air was considered to have constant density of 1.184 kg/m^3 and dynamic viscosity of 1.855E-5 Pa/s, at ambient temperature of 25°C. Velocity inlet condition was chosen for the inlet boundary, with turbulence intensity of 4% and turbulent viscosity ratio of 10. Pressure outlet condition was set for the outlet boundary with a pressure of 101325 Pa. The residuals decrease chosen as solution convergence criterion was set to 10^{-4}.
The solid phase was simulated using the Lagrangian Multiphase Model [27], where particles are modelled as parcels. Each parcel comprises a group of particles sharing identical size and kinematics, enabling efficient resolution of the solid phase while significantly reducing computational time. The position and velocity of the parcels are tracked through the iterative resolution of Lagrangian equations, which are based on the Newton's second law. In this study, the one-way coupling model was employed, meaning that only the continuous phase (air) influences the motion of the solid phase (dust), accounting for particle-wall interactions while neglecting particle-particle collisions. This approach is suitable for multiphase flows where the mass ratio of the solid phase to the continuous phase is below 10% [28], which is verified for the present industrial cyclone. The spherical particle model was chosen together with the Haider & Lavenspiel model [29], which permits the definition of the drag coefficient for non-spherical particles (see eq. 4).

$$C_D = \frac{24}{Re_p}\left(1 + A Re_p^B\right) + \frac{C}{1+\frac{D}{Re_p}} \tag{4}$$

Where Re_p is the particle Reynolds number, while A, B, C, D are parameters that depends on particle sphericity S_p. This was chosen on the basis of the experimental value derived from the analysis of optical microscope's pictures. A fully-elastic behaviour was considered for particle-wall collisions, with normal and tangential restitution coefficient equal to 1. To simulate the randomness of particle motion inside the cyclone body, the turbulent dispersion model was employed. A second-order tracking integration method was used for the Lagrangian phase, which gives better tracking of particle trajectory in rotating flows.
The mesh grid was created using STAR-CCM+ integrated meshing tool. A directed fully-structured mesh of hexahedral elements was applied for the cyclone body, as hexahedrons better capture the swirling flow within the cyclone compared to, for example, polyhedrons. The collection bin with the rotary valve for discharging of dust was included in the model as well. The motion of the rotary valve was modelled using the rigid body model with an angular velocity of 3.35 rad/s. Given the complexity of the rotary valve geometry, a mesh composed of trimmed cells was generated to discretize the collection bin. The final mesh configuration for the cyclone is shown in Fig. 3.



Figure 3: grid mesh of the industrial cyclone.

A mesh sensitivity analysis was conducted to evaluate the best trade-off between solution accuracy and computational time of the CFD model. The results from coarse, medium and fine mesh with 89684, 587000 and 1120150 elements, respectively, have been compared.
As previously stated, the preliminary solution of the gas flow pattern was obtained with the steady-state K-ε turbulence model till convergence was reached. After this, the RSM was set in unsteady-state and solved with a time-step of 0.001 s for 1000 iterations, then it was decreased to 0.0003 s for the rest of the simulation. This

smaller time-step value was chosen as a trade-off between computational time and the resulting particle Courant number C_p (see Eq. 5), which assures a stable tracking of the particles when its value remains below 1.

$$C_p = \frac{v_p \cdot \Delta t}{\Delta x} \tag{5}$$

Where v_p is the particle velocity, Δt is the simulation time step, Δx is the characteristic cell size. After the achievement of a stable regime condition for the flow field, the solid phase was injected by a surface-type injector placed on the inlet surface, with particles homogeneously distributed and characterized by the same velocity as the gas flow. The mass flow rate of the injected particles was calculated as:

$$\dot{m}_p = \frac{C_{in}}{Q_g} \tag{6}$$

Where C_{in}, Q_g are the dust concentration of particles at the cyclone inlet section and the volumetric flow rate, respectively. For each simulation the number of parcels injected is 10000, since above this value the predicted collection efficiency changes by less than 0.1%. The different materials that compose the mixed scrap dust have been considered in the particles' composition by simulating the number of particles of each material respecting the mass fraction for each of them. A parcel is considered to be collected once it impacts with the walls of the collection bin. The particles' collection efficiency for each dimension D_p was evaluated from the number of particles that escape through the outlet section.

RESULTS

Experimental measurements

Table 2 shows the measured values (dimensionless due to company confidential data) of dust concentration at the cyclone inlet (C^*_{in}) and top air outlet (C^*_{out}), and mass flow rate of dust separated at the cyclone bottom ($\dot{m}^*_{sep}$) for the two different metal scrap types. The experimental results show that the sandwich panels' scrap produced a higher quantity of dust in comparison to the mixed scrap type, where the dust concentration at cyclone inlet for the sandwich panels' scrap is approximately 6 times greater than the measured valued of the mixed scrap. The reason for this is the foam core present in the sandwich panels, which produces a large quantity of light particles during the shredding process.

Table 2: Results of experimental measurements

Measurement ID	Metal scrap type	Q_g [Nm³/h]	C_{in} [/]	C_{out} [/]	$\dot{m}_{sep}$ [/]
1	Mixed scrap	26160	4.23	0.0125	0.0268
2	Mixed scrap	21680	2	0.0273	0.0126
3	Sandwich panels	26160	23.56	0.551	0.151

Figure 4 reports the experimental collection efficiency curves of the cyclone. The effect of the reduction in the air flow rate on the collection efficiency curve of the cyclone can be observed by comparing the curves (1) and (2) in Fig. 4. It is found that a 18% reduction of the air flow rate caused a 40% increase in the cut-off diameter D_{50} (diameter of the particle separated with an efficiency of 50%), owing to a decrease in the collection efficiency of the cyclone. The separation efficiency of the cyclone for the mixed scrap dust is higher compared to that for the sandwich panels' dust, with an approximately 4-times increase of the cut-off diameter D_{50} for the latter.

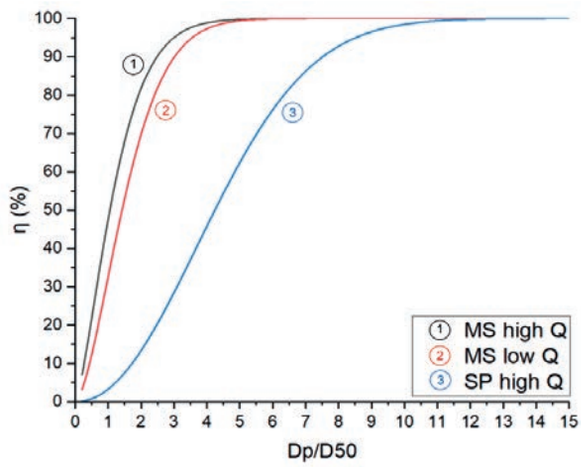


Figure 4: cyclone's collection efficiency curves for dust from (1) mixed scrap at high air flow rate, (2) mixed scrap at low air flow rate, (3) sandwich panels at high air flow rate.

Chemical analysis of dust

The resulted chemical composition of the dust from mixed scrap is reported in Tab. 3. The obtained chemical composition of the mixed scrap dust is comparable to the composition of mixed scrap shredder residues founded by Ferella et al. [30]. The chemical analysis of the dust from sandwich panels reported that they are mainly composed of plastics, in particular polyurethane.
In the CFD model, the simulated particles of mixed scrap have been discretized with different mass densities ρ_p on the base of the chemical composition of Tab. 2. On the other hand, the particles of sandwich panels' scrap were modelled with a constant density of 80 kg/m^3, corresponding to polyurethane foam (PU).

Table 3: chemical composition of dust produced from shredding of mixed scrap

Material	**Al_2O_3**	**Fe_3O_4**	**MgO**	**CaO**	**ZnO**	**SiO_2**	**TiO_2**	**Plastics**
Content [%]	3±0.1	12±1.2	1.6±0.4	10±2.1	5.8±0.02	7.3	2.5	49.3±3
Density [kg/m^3]	4000	4800	3580	3340	5610	2300	4230	800÷1000

Sphericity of dust's particles

The sphericity of the dust's particles was measured through the analysis of pictures taken at the optical microscope. Figure 5 shows an example of image analysing, where the particles are isolated and their shape properties are analysed. The results from particles' shape analyses reported a value of perimeter sphericity S_p equal to 0.6±0.05. This value was used in the CFD model for calculating the particle drag coefficient.

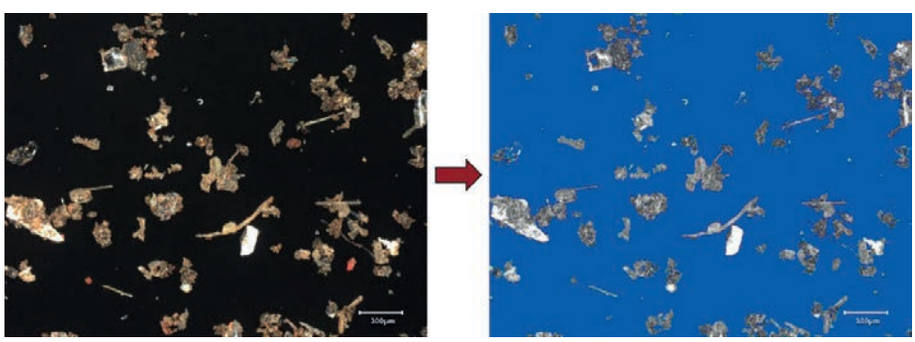


Figure 5: Example of particle shape analysis.

Numerical validation of the CFD model

The numerical validation of the CFD model was performed in terms of comparison between the profiles of tangential and axial gas velocity (see Fig. 6) and cyclone pressure drop (see Tab. 4) predicted by calculations performed on the three different-mesh-size grids.

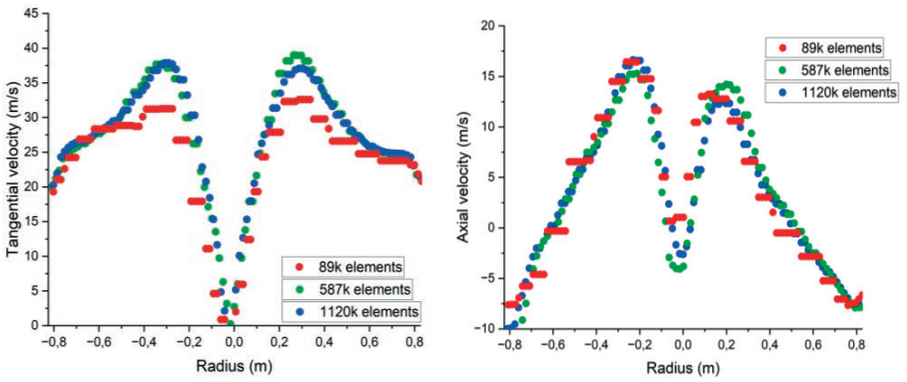


Figure 6: tangential and axial gas velocity profiles at height Z/D = 0.75.

The RSM effectively predicts the tangential component of the gas flow within the cyclone, composed of a forced-vortex up to a radius of 0.3 m and an outer free-vortex extending to the cyclone wall. The predicted axial velocity profile displays the characteristic W shape, showing negligible variation across the three evaluated mesh sizes. On the other hand, the tangential velocity profile obtained using the coarse grid significantly differs from those obtained with the medium and fine grids, which are comparable to each other. Considering the predicted pressure loss in the case of the three grids, reference can be made to the data presented in Tab. 4, which indicates that the predictions for the medium and fine grids differ by less than 1%. Based on these observations, it can be concluded that the medium grid provides sufficiently grid-independent results.

Table 4: comparison of different mesh grid sizes in predicting pressure drop and computational time to derive the gas flow pattern

Mesh ID	Mesh size	Pressure drop [Pa]	Computational time [h]
Coarse	89k	1491	5
Medium	587k	1750	24
Fine	1120k	1741	47

Experimental validation and evaluation of particle's modelling approach

The experimental validation of the model results was performed by comparing the predicted collection efficiency curves with the three experimental datasets, using the actual particle mass distribution calculated from the detailed chemical analysis. The experimental datasets pertain to mixed scrap at high flow rate (MS high Q), mixed scrap at low flow rate (MS low Q), and sandwich panel scrap (SP). Figure 7 compares the collection efficiency curves predicted by the CFD model with the experimental curves. The root mean squared error (RMSE) for the predictions under the conditions of MS high Q, MS low Q, and SP high Q were 4.7%,

3.2% and 5.9%, respectively. This confirms the validation of the proposed model.

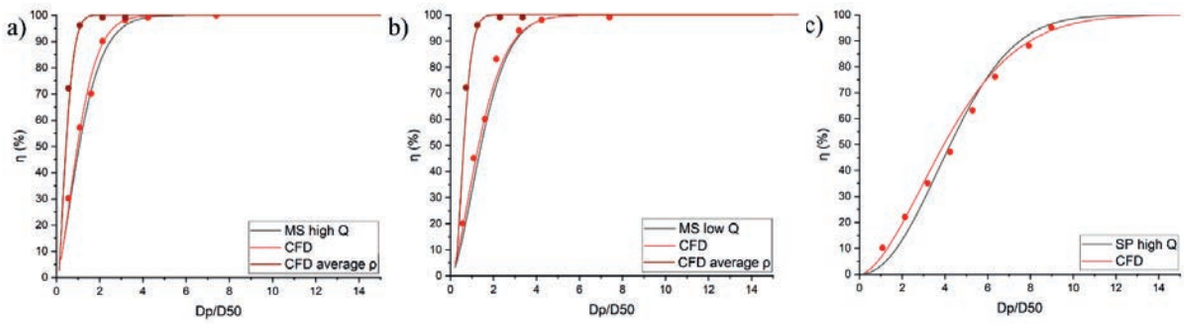


Figure 7: Experimental and predicted collection efficiency curves of the industrial cyclones for a) mixed scrap with high air flow rate, b) mixed scrap with low air flow rate, c) sandwich panels' scrap with high air flow rate.

To evaluate the inadequacy of the assumption of homogeneous particle density, Figs. 7a and 7b include the CFD model predictions obtained using an average density value. This comparison is not included for the case of sandwich panels, as the particle density distribution is very narrow, making the assumption of an average density a reasonable approach. This is corroborated by the comparison of the collection efficiency curves shown in Fig. 7c. It can be observed that the CFD model using particles modelled with unique density (brown curve) exhibited poor predictions of the experimental cases, with RMSE equal to 22.1% and 23.2% for MS high Q and MS low q conditions, respectively. The significant prediction errors in the latter case are caused by the great heterogeneity of materials that compose the mixed scrap dust.

CONCLUSIONS

This study presents a CFD model of an industrial cyclone separator used in the dedusting system of a steel recycling plant. The investigation focused on two types of metal scrap dust: mixed scrap dust and sandwich panel scrap dust. The suggested modelling approach provided a comprehensive analysis of the cyclone's collection efficiency when processing different input materials, that was validated in terms of predicted collection efficiency curves against experimental data collected from an existing dedusting plant.
The CFD model demonstrated excellent predictive accuracy, showing high sensitivity to variations in air flow rates delivered by the fan and to the type of metal scrap dust being processed. For mixed scrap dust, the model's performance was also evaluated under the assumption that all particles shared a uniform average density. In this scenario, the model significantly overestimated the collection efficiency curve, highlighting its reduced predictive capability. This discrepancy arises from the heterogeneous chemical composition of the mixed scrap dust, where the average mass density fails to represent the wide distribution of material densities accurately. These findings underscore the importance of accurately accounting for the precise chemical composition and density distribution of the dust for predicting the collection efficiency of industrial cyclones involved in steel recycling plant. The validated CFD model serves as a powerful tool for the design and optimization of industrial cyclones used in steel recycling plants, enabling the consideration of complex chemical compositions of treated materials.

AKNOLEDGEMENTS

The work was funded by Danieli & C. Officine Meccaniche S.p.A.

BIBLIOGRAPHY

[1] L. Holappa, "A general vision for reduction of energy consumption and CO2 emissions from the steel industry," *Metals (Basel).*, vol. 10, no. 9, pp. 1–20, **2020**

[2] B. Gajdzik, W. Sroka, and J. Vveinhardt, "Energy intensity of steel manufactured utilising eaf technology as a function of investments made: The case of the steel industry in poland," *Energies*, vol. 14, no. 16, **2021**

[3] J. Duan, D. Farrugia, C. Davis, and Z. Li, "Effect of impurities on the microstructure and mechanical

properties of a low carbon steel," *Ironmak. Steelmak.*, vol. 49, no. 2, pp. 140–146, **2022**

[4] M. Guo *et al.*, "An overview of novel geometrical modifications and optimizations of gas-particle cyclone separators," *Sep. Purif. Technol.*, vol. 329, no. September 2023, p. 125136, **2024**

[5] P. Khalili Ata Abadi, J. Vaziri Naeen Nejad, S. Kheradmand, and D. Khalili Ata Abadi, "A Dimensional optimization study on cyclone performance under the oscillating boundary condition," *Chem. Eng. Process. - Process Intensif.*, vol. 183, no. September 2022, p. 109217, **2023**

[6] G. Ravi, S. K. Gupta, and M. B. Ray, "Multiobjective Optimization of Cyclone Separators Using Genetic Algorithm," pp. 4272–4286, **2000.**

[7] W. D. Griffiths and F. Boysan, "Computational fluid dynamics (CFD) and empirical modelling of the performance of a number of cyclone samplers," *J. Aerosol Sci.*, vol. 27, no. 2, pp. 281–304, **1996**

[8] J. Gimbun, T. G. Chuah, T. S. Y. Choong, and A. Fakhru'l-Razi, "A cfd study on the prediction of cyclone collection efficiency," *Int. J. Comput. Methods Eng. Sci. Mech.*, vol. 6, no. 3, pp. 161–168, **2005**

[9] M. Morin, L. Raynal, S. B. R. Karri, and R. Cocco, "Effect of solid loading and inlet aspect ratio on cyclone efficiency and pressure drop: Experimental study and CFD simulations," *Powder Technol.*, vol. 377, pp. 174–185, **2021**

[10] M. Nakhaei, B. Lu, Y. Tian, W. Wang, K. Dam-Johansen, and H. Wu, "CFD modeling of gas-solid cyclone separators at ambient and elevated temperatures," *Processes*, vol. 8, no. 2, pp. 1–26, **2020**

[11] J. Song, Y. Wei, G. Sun, and J. Chen, "Experimental and CFD study of particle deposition on the outer surface of vortex finder of a cyclone separator," *Chem. Eng. J.*, vol. 309, pp. 249–262, **2017**

[12] S. Ganegama Bogodage and A. Y. T. Leung, "CFD simulation of cyclone separators to reduce air pollution," *Powder Technol.*, vol. 286, pp. 488–506, **2015**

[13] M. A. El-Emam, L. Zhou, W. Shi, and C. Han, "Performance evaluation of standard cyclone separators by using CFD–DEM simulation with realistic bio-particulate matter," *Powder Technol.*, vol. 385, pp. 357–374, **2021**

[14] S. Wang, H. Li, R. Wang, X. Wang, R. Tian, and Q. Sun, "Effect of the inlet angle on the performance of a cyclone separator using CFD-DEM," *Adv. Powder Technol.*, vol. 30, no. 2, pp. 227–239, **2019**

[15] K. W. Chu, B. Wang, A. B. Yu, A. Vince, G. D. Barnett, and P. J. Barnett, "CFD-DEM study of the effect of particle density distribution on the multiphase flow and performance of dense medium cyclone," *Miner. Eng.*, vol. 22, no. 11, pp. 893–909, **2009**

[16] A. Kępa, "The efficiency improvement of a large-diameter cyclone - The CFD calculations," *Sep. Purif. Technol.*, vol. 118, pp. 105–111, **2013**

[17] H. H. Parno, L. M. Rosa, J. Utzig, V. R. Wiggers, R. K. Decker, and H. F. Meier, "CFD-based redesign of large industrial-scale cyclones," *Powder Technol.*, vol. 448, no. July, p. 120306, **2024**

[18] D. Winfield, M. Cross, N. Croft, D. Paddison, and I. Craig, "Performance comparison of a single and triple tangential inlet gas separation cyclone: A CFD Study," *Powder Technol.*, vol. 235, pp. 520–531, **2013**

[19] "UNI EN 15259:2008." https://store.uni.com/uni-en-15259-2008

[20] "UNI EN 13657:2004." https://store.uni.com/uni-en-13657-2004

[21] Y. El Ashry, A. M. Abdelrazek, and K. A. Elshorbagy, "Numerical and experimental study on the effect of solid particle sphericity on cyclone pressure drop," *Sep. Sci. Technol.*, vol. 53, no. 15, pp. 2500–2516, **2018**

[22] R. Rorato, M. Arroyo, E. Andò, and A. Gens, "Sphericity measures of sand grains," *Eng. Geol.*, vol. 254, no. October 2018, pp. 43–53, **2019**

[23] G. Gronald and J. J. Derksen, "Simulating turbulent swirling flow in a gas cyclone: A comparison of various modeling approaches," *Powder Technol.*, vol. 205, no. 1–3, pp. 160–171, **2011**

[24] S. K. Shukla, P. Shukla, and P. Ghosh, "Evaluation of numerical schemes using different simulation methods for the continuous phase modeling of cyclone separators," *Adv. Powder Technol.*, vol. 22, no. 2, pp. 209–219, **2011**

[25] J. J. H. Houben, "Experimental investigation and CFD simulation on particle depositions in gas cyclone separators," vol. 10, no. 2, pp. 7–7, **2011**.

[26] I. E. Idelchik, *Handbook Of Hydraulic Resistance*. **2007**.

[27] T. C. Crowe, J. Schwarzkopf, M. Sommerfeld, and Y. Tsuji, *Multiphase flows with droplets and particles*. **2012.**

[28] K. Elsayed Khairy and C. Lacor, "Optimization of the cyclone separator geometry for minimum pressure drop using mathematical models and CFD simulations," *Chem. Eng. Sci.*, vol. 65, no. 22, pp. 6048–6058, **2010**

[29] O. . Levenspiel and A. Haider, "Drag Coefficient and Terminal Velocity of Spherical and Nonspherical Particles," *Powder Technol.*, vol. 58, pp. 63–70, **1989.**

[30] F. Ferella, I. De Michelis, A. Scocchera, M. Pelino, and F. Vegliò, "Extraction of metals from automotive shredder residue: Preliminary results of different leaching systems," *Chinese J. Chem. Eng.*, vol. 23, no. 2, pp. 417–424, **2015**

[31] A.J. Hoekstra, "Gas Flow Field and Collection Efficiency of Cyclone Separators." pp. 1–165, 2000.

[32] S. Pandey *et al.*, "CFD Investigations of Cyclone Separators with Different Cone Heights and Shapes," *Appl. Sci.*, vol. 12, no. 10, **2022**

G1A Prediction and Optimization of Cooling Fan Noise

11 April - 9:30 - Auditorium

Chairman: Mats Åbom

List of papers

Noise Prediction in Automotive Cooling Fans: A Lattice Boltzmann Based Simulation Approach and Experimental Validation

- Anand Sivaram SIVARAMKRISHNAN – Hanon Systems EFP Deutschland GmbH (Germany)
- Mihai BLEIZIFFER – Hanon Systems EFP Deutschland GmbH (Germany)
- Mehrdad ZANGENEH – Department of Mechanical Engineering, University College London (United Kingdom)
- Arturo RODOSTI – Hanon Systems Italia Campiglione srl (Italy)

Characterization of the Installation Effects on the Aeroacoustics Sources of the Automotive Cooling Module Using Lattice-Boltzmann Method.

- Tayyab AKHTAR – University of Sherbrooke (Canada)
- Safouane TEBIB – University of Sherbrooke (Canada)
- Stéphane MOREAU – University of Sherbrooke (Canada)
- Bruno DEMORY – Valeo Thermal Systems / BG (France)
- Manuel HENNER – Valeo Thermal Systems / BG (France)

NOISE PREDICTION IN AUTOMOTIVE COOLING FANS: A LATTICE BOLTZMANN BASED SIMULATION APPROACH AND EXPERIMENTAL VALIDATION

Anand Sivaram SIVARAMAKRISHNAN[1], Mihai BLEIZIFFER[1], Mehrdad ZANGENEH[2], Arturo RODOSTI[3]

[1] *Hanon Systems EFP Deutschland GmbH, Bad Homburg, Germany*

[2] *Department of Mechanical Engineering, University College London, Torrington Place, London, UK*

[3] *Hanon Systems Italia Campiglione srl, Campiglione, Italy*

SUMMARY

Reducing noise emissions from automotive cooling fans is crucial due to stricter regulations and consumer expectations. This study uses Lattice Boltzmann Method (LBM)-based Computational Aeroacoustic (CAA) simulation to predict noise in forward and backward-swept electric cooling fan (eCF) designs. Fans were developed using a 3D inverse design methodology for high aerodynamic efficiency without performance compromise. Noise characteristics, including Overall Sound Pressure Levels (OASPL) and Blade Passing Frequencies (BPF), were accurately predicted and validated experimentally. Results show forward-swept fans offer superior noise reduction while maintaining effective cooling, highlighting CAA's potential for optimizing aeroacoustic performance.

INTRODUCTION

The automotive cooling fan [Fig. 1], crucial for both internal combustion engine (ICE) and battery electric vehicles (BEVs), circulates air across the radiator to dissipate heat, improving engine longevity, fuel efficiency, and performance. In BEVs, it also regulates the temperature of the battery pack, motor, and power electronics, ensuring efficiency and durability. BEVs are quieter than ICE vehicles, making secondary noise sources like fan aerodynamic noise, vibrations, and motor humming more noticeable. Studies highlight the cooling fan as a significant noise source, especially during stationary operations like charging. Reducing fan noise is essential for maintaining cabin quietness and enhancing the BEV experience.

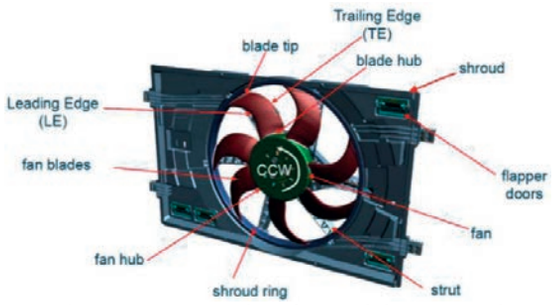


Fig. 1: Automotive cooling fan module: Nomenclature

AXIAL FAN NOISE

Axial fans are commonly used in a variety of applications, from HVAC systems to automotive cooling and even in industrial processes. These fans are often placed in environments where noise reduction is critical, particularly in proximity to humans. As the demand for sustainability grows, efficient and quieter axial fans have become a significant focus for designers and engineers. However, the design of axial fans is complex, as it involves multiple parameters, including aerodynamic optimization, flow dynamics, and acoustics.

AERODYNAMIC NOISE

Aerodynamic noise in axial fans arises from blade-airflow interactions, with key sources being blade passing frequency (BPF) noise and broadband noise. BPF noise is a tonal sound from periodic pressure fluctuations as blades pass stationary components. Broadband noise results from turbulent flow around blades, producing a hissing or whistling sound. Additional effects like tip vortex shedding and wake interaction amplify noise. Studies by Zhu *et al.* [4] and Liu et al. [5] show that optimized blade designs, such as serrated trailing edges and forward-swept blades, help reduce turbulence and suppress noise.

MECHANICAL NOISE

Mechanical noise in axial fans comes from the motor, bearings, and drive system. Bearing noise, often tonal, results from misalignment, wear, or lubrication issues. Motor noise stems from electromagnetic forces or imbalances, while drive system noise arises from belts, couplings, or misaligned gears. Shao *et al.* [6] and Yuan *et al.* [7] highlight that precise alignment of these components reduces mechanical noise.

MITIGATING FAN NOISE

Aerodynamic optimization in axial fans doesn't always ensure noise reduction, as some changes can increase vortex shedding or tonal noise (Becker et al. [1]). Engineers use CFD and CAA simulations to balance aerodynamics and acoustics, refining blade geometry with forward sweeps, tapered edges, and serrated trailing edges to reduce broadband noise. Mechanical improvements like precision manufacturing, quality bearings, noise-damping materials, and maintenance also help. Niu *et al.* [8] stress integrating aerodynamic and mechanical strategies, including vibration isolation and housing materials, for effective noise control.

AXIAL FAN SWEEP: OVERVIEW

This paper examines the influence of forward and backward sweep axial fan designs on aerodynamic and acoustic performance, building on prior research. Swept blades are effective in reducing noise and improving performance. Studies by Smith & Yeh [9] and Lewis & Hill [10] used swept cascades and actuator disk theory to analyze sweep effects. Vad *et al.* [11, 12] and Bamberger and *Carolus et al.* [13] demonstrated improvements in efficiency, stall-free operation, and tonal noise reduction.

FAN 2025
Antibes Juan-les-Pins (France), 9 – 11 April 2025

Forward-swept blades mitigate rotor-stator interaction noise and enhance acoustic performance [14–17]. Experimental work by Raj *et al.* [18] showed forward-swept blades reduce stall and improve tip flow under low airflow. Other studies highlighted their effectiveness in reducing radial velocity and turbulence ingestion noise compared to backward-swept blades [19, 20]. These findings underscore the advantages of swept designs in enhancing fan performance and noise reduction.

FAN DEVELOPMENT USING INVERSE DESIGN METHOD

The 3D inverse design method for axial fans, integrated with TURBOdesign Suite from Advanced Design Technology, uses spanwise work distribution to link pressure across the fan stage via Euler equations. The software specifies radial and meridional load distributions, which generate radial airfoil sections. This approach, based on a 3D inviscid code, computes the blade geometry under specified loading conditions, with loading determined by circumferentially averaged bound circulation, impacting aerodynamic performance. This is defined as

$$r\overline{V_\theta} = \frac{N}{2\pi}\int_0^{2\pi/N} r \cdot V_\theta d\theta \quad (1)$$

The Euler head (work coefficient) is defined by the spanwise $r\overline{V_\theta}$ (average angular momentum) distribution at the blade's leading and trailing edges, which can follow a constant free vortex design or vary along the blade. Research shows that a parabolic spanwise loading distribution improves efficiency and reduces noise in axial fans [24]. The inverse design method in axial fans requires inputs like the design point (flow rate, density, static pressure, rpm), load distributions, meridional geometry, thickness, and radial sweep distribution. Using TURBOdesign Suite, 3D blade shapes are computed from prescribed loading, unlike traditional methods specifying incidence angles (e.g., NACA profiles). Detailed methodologies in Sivaramakrishnan *et al.* [22] and Zanganeh *et al.* [23] highlight how inputs like load and geometry optimize aerodynamic performance. Forward and backward sweep fans were designed for balanced aerodynamic and acoustic performance, with a working point at a flow rate of 0.13 and a maximum of 0.24, ensuring robust off-design performance.

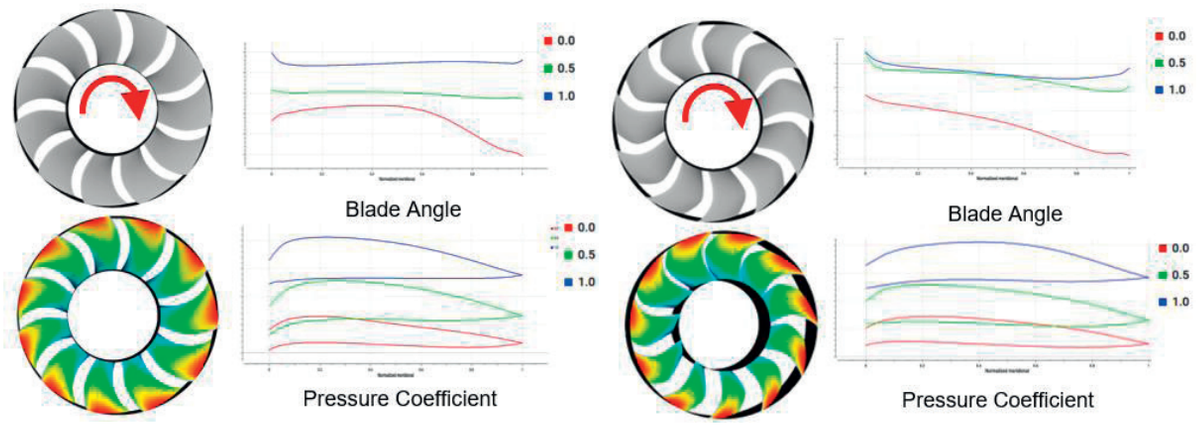
For more details on the axial fan design methodology, refer to Sivaramakrishnan *et al.* [22] and Zanganeh *et al.* [23]. Their work demonstrates how the software, using inputs like load distribution and meridional geometry, optimized aerodynamic performance. It also explains how forward and backward swept fans with similar aerodynamic characteristics were designed through optimization, balancing aerodynamic and acoustic performance. To meet design requirements, the fan's working point was set at a non-dimensional flow rate of 0.13, while ensuring it could achieve a maximum flow rate of 0.24. This off-design placement ensured balanced performance across the operating range. The following parameters were selected to ensure a valid comparison between the two fan configurations:

- **Design Point**: Identical for both configurations, ensuring consistency in flow rate, density, static pressure, and rotational speed.
- **Radial and Streamwise Load Distribution**: Derived to achieve comparable aerodynamic profiles.
- **Meridional Geometry**: Adapted according to the fan sweep design.
- **Thickness Distribution**: Uniformly applied at the hub and tip.

This consistent design framework ensures a robust comparison of the performance characteristics of the fan configurations.

Based on the specified design parameters such as: Hub-tip ratio of 0.49, Number of blades as 11, Speed of 3000 rpm at a design point flow rate of 0.22, the finally developed backward- and forward-swept cooling fans [Fig. 2] are analyzed. The results showcase the blade geometries with distinct sweep configurations and the pressure coefficient distributions across the blade surfaces, highlighting

aerodynamic performance. Blade angles and spanwise pressure coefficient distributions are provided for three key locations: hub, mid-span, and tip.



(a) *(b)*

Fig.2: Backward (a) & Forward (b) swept axial fan design outputs [22]

The automotive cooling fans, as previously shown, include a shroud to enhance performance and rigidity in the system [Fig. 3]. The shroud design remains identical for both the forward- and backward-swept fans, adhering to established design guidelines. Special attention is given to maintaining consistent gaps between the blades and the shroud for both configurations, ensuring a fair comparison of aerodynamic and acoustic performance while minimizing external influences on the results. This uniformity supports accurate evaluation of the impact of the blade sweep direction.

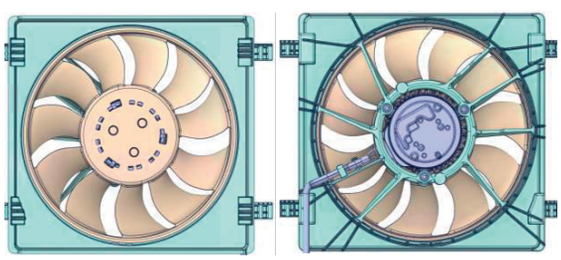


Fig.3: eCF assembly with backward sweep fan and shroud [22]

EXPERIMENTAL SETUP

During the development of our eCFs, each intermediate milestone achieved is rigorously tested to evaluate aerodynamic performance and acoustic characteristics. These tests ensure that the design meets performance requirements and validate the accuracy of numerical methodologies using prototype parts. All measurements are conducted in compliance with established standard norms, ensuring reliability and consistency throughout the validation process. This iterative approach allows for systematic refinement of both aerodynamic and acoustic features, leading to an optimized final design.

FAN PERFORMANCE TEST

Hanon Systems employs a certified ISO 5801 test rig for measuring fan performance [Fig. 4]. The ISO 5801 Fan Performance Test Rig is a standardized setup designed to measure the aerodynamic performance of fans. It ensures that tests comply with international standards for accuracy and reliability. The rig evaluates parameters such as flow rate, pressure rise, efficiency, and power consumption under controlled conditions. Equipped with advanced sensors and data acquisition systems, it accommodates various fan types and sizes. Tests can include setups with fans powered by

their own BLDC or external drives, with torque and efficiency metrics validated to maintain performance consistency. The measurements presented in this study were conducted using a BLDC drive with a known efficiency, providing reliable and consistent performance data for analysis.

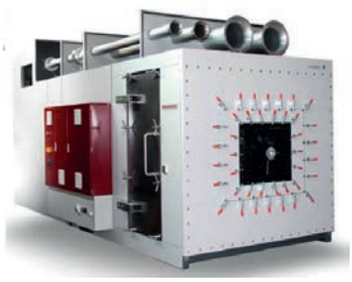


Fig.4: Fan Performance Test Rig (ISO 5801)

NVH PERFORMANCE TEST

The NVH measurements were conducted in a semi-anechoic chamber with controlled acoustic conditions, featuring a background noise level of 15 dB(A) and a lower cutoff frequency of 40 Hz. The fan was suspended using an aluminum frame and elastic bands to reduce vibration transmission. A microphone was placed 1 meter upstream from the fan hub and 1 meter above the ground, as per automotive testing standards. A sample setup is shown in [Fig. 5], with the eCF module suspended in free blow condition. Full-speed ramp (0 to max speed) and constant-speed tests were performed to capture the acoustic emission spectra, which were essential for validating the predicted NVH characteristics from CAA simulations.

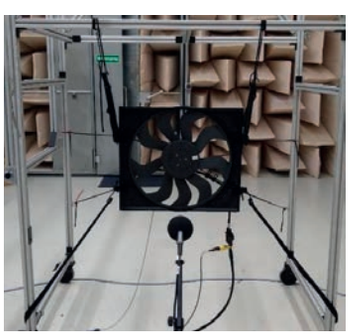


Fig.5: Semi Anechoic Chamber (NVH Setup)

COMPUTATIONAL AEROACOUSTICS

Since this paper focuses on aeroacoustic methodologies for predicting the acoustic characteristics of automotive cooling fans. Details on the RANS-based CFD simulations used for evaluating the aerodynamic performance of fans can be found in the work of Sivaramakrishnan *et al.* [22]

The Lattice Boltzmann Method (LBM) is a versatile tool in computational aeroacoustics (CAA), known for its ability to directly model fluid flows and associated acoustic phenomena with high precision. Unlike traditional Naiver-Stokes solvers, LBM operates on a mesoscopic scale by discretizing the Boltzmann equation over a lattice grid. For predicting acoustic phenomena, LBM is frequently coupled with Lighthill's acoustic analogy. This coupling allows LBM to provide detailed insights into the interaction between flow turbulence and acoustic wave propagation.

Ghodake *et al.* [25] used the Lattice Boltzmann Method (LBM) to study blade sweep impacts, showing backward-swept blades reduce broadband noise by smoothing pressure gradients, while forward-swept blades enhance efficiency but may increase tonal noise. Casalino *et al*. [26] optimized cooling fans with a hybrid LBM-VLES approach, revealing noise source distributions and sweep angle effects. Romani *et al.* [27] validated LBM's accuracy in modeling turbulent flow and acoustic

wave propagation in axial fans. Moreau *et al.* [28] coupled LBM with advanced turbulence models to predict noise in complex geometries. These studies highlight LBM's role in enhancing axial fan aerodynamic and acoustic performance.

NUMERICAL SETUP

Simulations were conducted using UltraFluidX, a GPU-accelerated Lattice Boltzmann Method (LBM) solver developed by Altair for high-performance transient aerodynamic and aeroacoustic analysis. The D3Q19 discretization scheme was chosen for its superior dissipation and dispersion properties, enabling accurate modeling of near-field acoustic sources and far-field propagation. The computational domain included an eCF module positioned 1m above a reflective floor in a semi-anechoic chamber, with damping zones to prevent reflections. Simplifications were applied to the module, and the octree-based grid refinement featured 10 levels, with voxel sizes ranging from 553 mm (RL0) to 0.54mm (RL10), resulting in a total of 400 million fluid voxels. Boundary conditions mirrored experimental setups, with a static pressure recorded at microphone positions and high-frequency sampling (5000 Hz). The simulation, run under free-blow conditions at defined fan speeds, modeled 1 second of rotations (excluding a 0.4-second initialization phase) and was completed on 2 GPUs in approximately 48 hours. Results aligned closely with experimental measurements, validating the model.

RESULTS & DISCUSSION

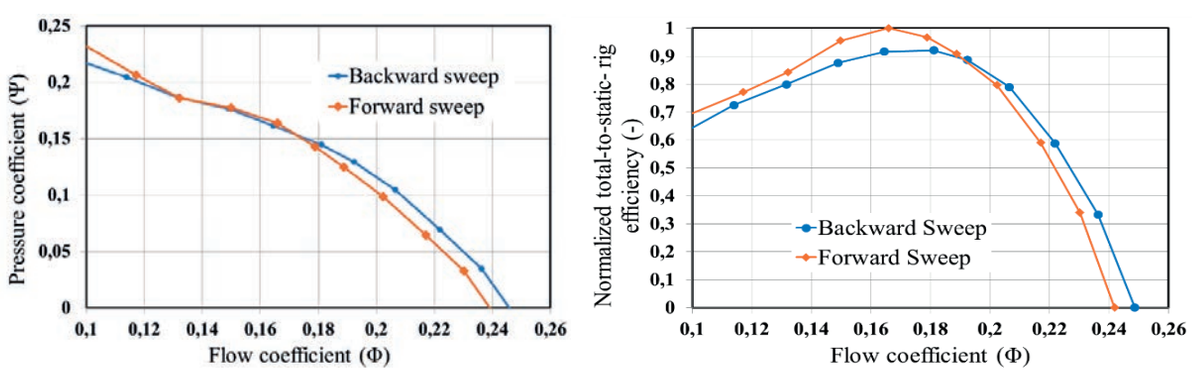
Aerodynamic Performance

One of the most crucial data points provided by fan manufacturers is the fan performance curve, which shows the relationship between airflow (Q) and pressure rise (Ps). Static pressure represents the system's resistance at different airflow rates. Both parameters can also be expressed as non-dimensional values to facilitate comparison and analysis across various fan systems, helping to assess their efficiency and performance under varying operating conditions. The non- dimensional pressure coefficient and flow coefficient is formulated as below

$$Pressure\ Coefficient\ , \Psi = \frac{2 \cdot \Delta p_{t-s}}{\pi^2 \cdot D^2 \cdot N^2} \tag{2}$$

$$Flow\ Coefficient, \Phi = \frac{4 \cdot \dot{V}}{\pi^2 \cdot D^3 \cdot N} \tag{3}$$

The performance measurement results for the prototypes are presented below. The tests were conducted using a BLDC drive, mounted within a shroud, and operated at a constant speed of 3000 rpm. The measured pressure performance curves of both fans were found to be almost identical, particularly within the operational range (ϕ = 0.12-0.18). See Fig.6(a).



(a) *(b)*

Fig.6: Performance Comparison between Backward & Forward Sweep Fans: Pressure coefficient & Efficiency

The efficiency in this range was also comparable, indicating that both fans required similar torque for operation, allowing them to be driven by the same drive. See Fig.6(b). The forward-swept fan achieved the highest peak efficiency, which is consistent with other literatures. On the other hand, at the operating point they both have the same flow and also the maximum flow is similar for both the fans. Currently the NVH is measured at the maximum flow point in this case and in the real system with the cooling pack they are measured at the flow coefficient of 0.18, which is the operating point.

Acoustic Performance

Systematic acoustic measurements were conducted on both forward-swept and backward-swept fans, offering an in-depth analysis of their sound pressure levels across the entire speed range. The acoustic measurement results revealed a significant difference in performance, with the forward-swept fan quieter than the backward-swept fan for the entire speed range. The observed difference in sound pressure levels ranged from approximately 2 dB(A) to 5 dB(A), highlighting the forward sweep's better acoustic performance for the full operating speed range. See Fig [7]

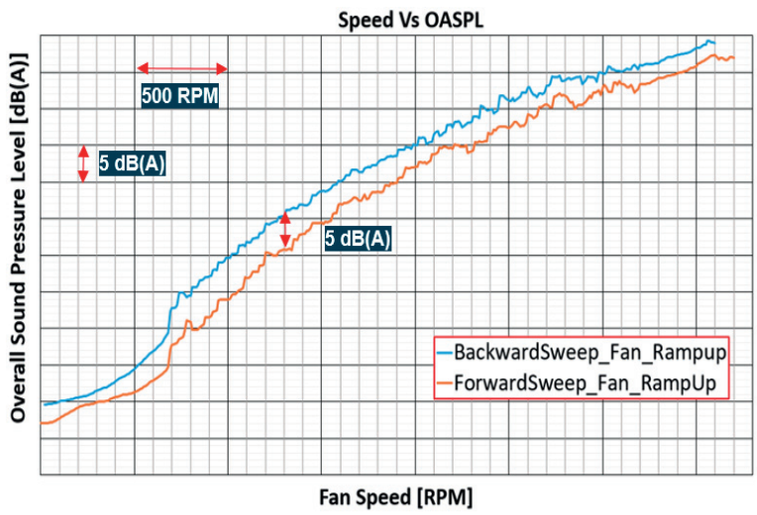


Fig.7: NVH Measurement for full speed range: Forward and Backward swept fan

Detailed comparison for the forward and backward swept fans based on the computational aeroacoustics and the stationary NVH measurements will be shown below. The comparison between simulation & measurement at 2500 rpm & 3000 rpm is shown in Fig [8] & Fig [9] for the two fans.

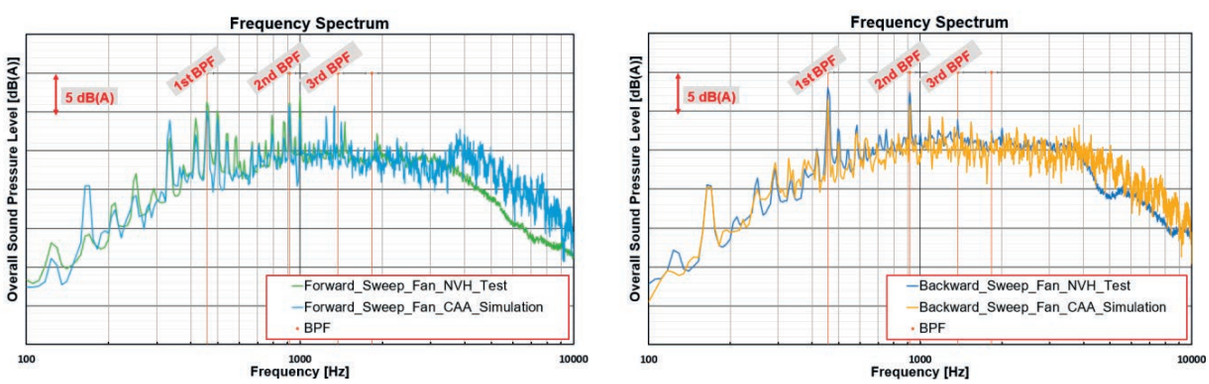


Fig.8: NVH Comparison Forward & Backward Sweep Fans: Measurement vs Simulation at 2500 Rpm

From the spectrums it is clear that the forward swept fan is more tonal than the backward swept fan. Most of the tonal peaks are predicted well by the CAA simulation, also the broadband behavior is comparable between the simulation and test up. The Overall sound pressure level of the spectrum

shows that the backward swept fan is approx. 2 - 2.5 dB(A) louder at the chosen fan speeds. This matches well with the full speed measurement shown in [Fig. 7].

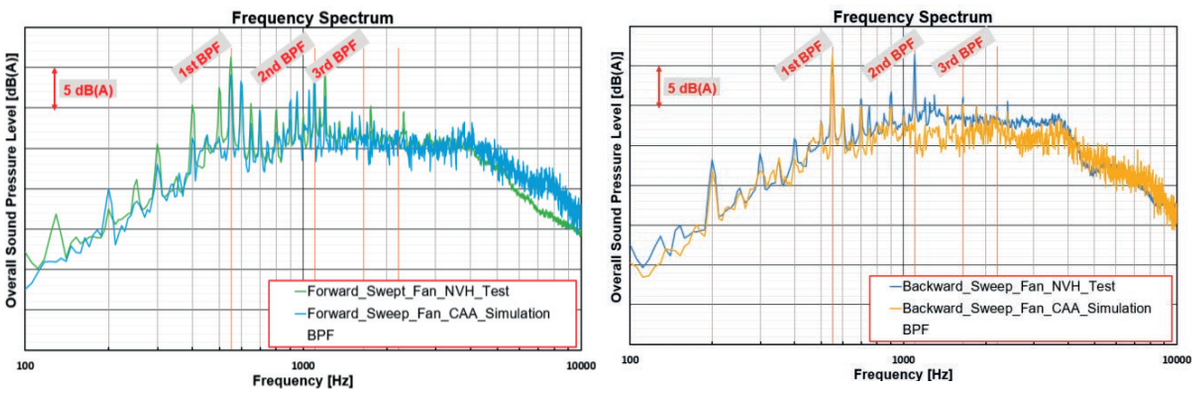
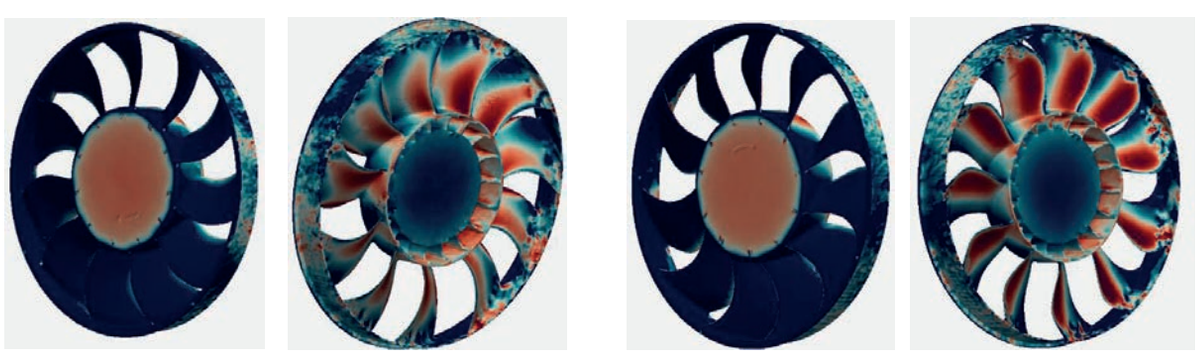


Fig.9: NVH Comparison Forward & Backward Sweep Fans: Measurement vs Simulation at 3000 Rpm

Based on these comparisons between CAA simulation and acoustic measurements, the overall sound pressure level for both the fans are predicted by simulation with a difference of approx. -1.5 dB(A) (under-predicted) to +1.3 dB(A) (over-predicted). This difference between the simulation and test could mainly come from the measurement setup, which is very dynamic as the fan rotates although the setup is same for both the fans and some geometrical simplifications considered in the simulation setup. Also, the cut off frequency that is resolved is lower compared to the measurement, which we can see on the results, a difference in the spectrum starting 5 kHz. Also, there is some geometrical tolerances, as the parts are 3D printed prototypes.

To understand more about the difference between those fans, surface data are evaluated to get more insight about the noise characteristics. The surface stagnation pressure, see [Fig 10] and the sound pressure level, see [Fig 11] at the around 475 Hz (1st BPF at 2500 Rpm) is compared below between the two fans and they clearly define the pressure fluctuations and we could see that, the leading edge of the backward swept fan has higher noise level and also at the fan ring in the suction side.

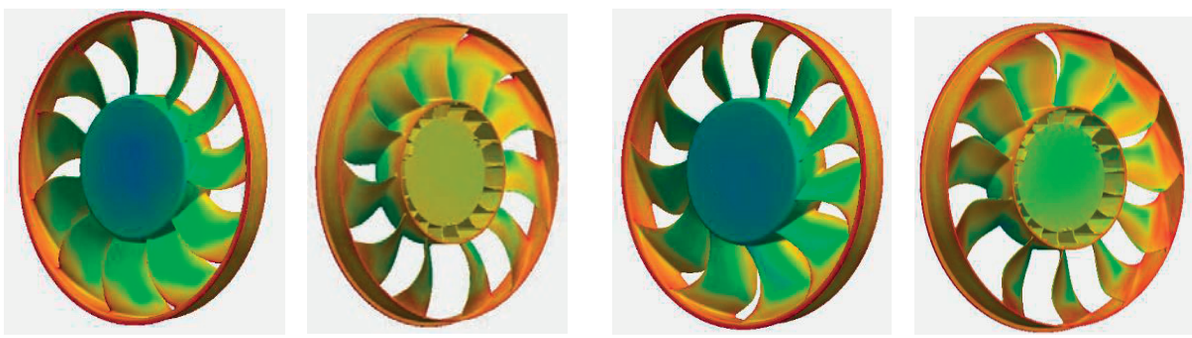


(a) *(b)*

Fig.10: Surface stagnation pressure: (a) Backward Sweep, (b) Forward Sweep

The comparison of surface stagnation pressure and surface sound pressure levels at the first blade passing frequency (BPF) reveals critical differences in noise characteristics between forward- and backward-swept axial fans. The surface stagnation pressure data highlights the regions of pressure fluctuations on the fan blades and surrounding components, directly correlating with noise generation. The backward-swept fan exhibits higher pressure fluctuations, particularly at the leading edge and on the pressure side near the fan ring or fan tip, which contribute to elevated noise levels in these regions. These fluctuations are linked to the interaction of the blade geometry with the airflow, causing turbulence and unsteady aerodynamic forces that amplify noise. In contrast, the forward-swept fan

demonstrates smoother pressure profiles, leading to reduced turbulence and lower SPL at the first BPF, reflecting its low noise performance. This analysis underscores the role of blade geometry in shaping aerodynamic behavior and its implications for noise reduction.



(a) *(b)*

Fig.11: Surface sound pressure level at 425-475Hz: (a) Backward Sweep, (b) Forward Sweep

CONCLUSION

This study successfully demonstrated the feasibility of predicting axial fan noise for automotive applications using a Lattice Boltzmann solver. Both forward and backward sweep fan designs were analyzed for their aerodynamic performance and noise characteristics, with comprehensive experimental investigations conducted to measure fan performance and NVH properties. These experimental results were then compared against Computational Aeroacoustic (CAA) simulation data. The aerodynamic behavior of the two fan designs, developed using ADT for the same design points, was assessed and contrasted. NVH tests were performed for stationary fan speeds and for full range of fan speed. As established in literature and corroborated by the current study, forward-sweep fans exhibit better NVH performance compared to backward-sweep designs. The CAA simulations accurately captured the Overall Sound Pressure Level (OASPL) and tonal noise components of the fans, aligning closely with experimental findings.

The results highlight the effectiveness of the CAA methodology in providing reliable predictions of fan noise and tonal characteristics. The demonstrated agreement between simulation and experimental results reinforces the solver's utility for early-stage noise prediction and optimization in industrial applications. This predictive capability enables developers to simultaneously address aerodynamic and acoustic challenges during the design process, facilitating more efficient and informed optimization of fan systems for improved NVH performance. The findings emphasize the forward sweep fan's advantage in NVH, making it a strong candidate for automotive applications where low noise is a critical design parameter.

REFERENCES

1. Ocker C, Czwielong F, Chaitanya P, Pannert W, Becker S. "*Aerodynamic and aeroacoustic properties of axial fan blades with slitted leading edges*." Acta acoustic, **2022**
2. Blake, W. "*The Mechanisms of Flow-Induced Noise on a Stationary Airfoil*." *Journal of Sound and Vibration*, 61[2], 291-303, **1978**
3. Wright, C. "*Noise Sources in Ducted Axial Fans: A Comprehensive Study."* Journal of Acoustical Engineering, **2008**

4. Zhu, W., Wang, Z., & Liu, H. "*Aerodynamic Noise Analysis and Reduction in Axial Fans.*" Journal of Sound and Vibration, 414, 14-24.**2018**
5. Liu, H., Zhang, S., & Li, X "*Broadband Noise Reduction Techniques for Axial Fans*." Applied Acoustics, 153, 96-104.**2019**
6. Shao, Y., Li, J., & Zhang, M. "*Mechanical Noise in Axial Fans: Bearing and Motor Contributions*." Tribology Transactions, 60[5], 866-873. **2017**
7. Yuan, X., Guo, Z., & Zhao, J. "*Impact of Mechanical Design on Noise Reduction in Axial Fans*." Journal of Mechanical Design, 142[4], 401-412. **2020**
8. Niu, F., Xu, Y., & Zhang, S. "*Integrated Design Approaches for Noise Reduction in Axial Fans*." International Journal of Vehicle Design, 76[3], 305-315. **2018**
9. Smith LH, Yeh H. "*Sweep and dihedral effects in axial-flow turbomachinery."* J. Basic Eng.; 85: 401–414. **1963**
10. Lewis R, Hill J. "*The influence of sweep and dihedral in turbomachinery blade rows"*. J. Mech. Eng. Sci.13: 266–285. **1971**
11. Vad J. "*Aerodynamic effects of blade sweep and skew in low-speed axial flow rotors at the design flow rate: an overview"*. Proc. Inst. Mech. Eng. A. J Power Energy; 222: 69–85. **2008**
12. Vad J. "*Forward blade sweep applied to low-speed axial fan rotors of controlled vortex design*: *An overview*". J. Eng. Gas Turbines Power **2013**
13. Bamberger K, Carolus K. "*Optimization of axial fans with highly swept blades with respect to losses and noise reduction"*. Noise Control Eng. J **2012**
14. Schulten, J. B. H. M. "*Sound generated by rotor wakes interacting with a leaned vane stator"*. AIAA J **1982**
15. Schulten, J. B. H. M. "*Vane sweep effects on rotor/stator interaction noise"* AIAA J **1997**
16. Hanson DB. "*Influence of propeller design parameters on far-field harmonic noise in forward flight"*. AIAA J **1980**
17. Wright T, Simmons WE. "*Blade sweep for low-speed axial fans"*. J Turbomach **1990**
18. Mohammed K, Prithvi Raj D. "*Investigations on axial flow fan impellers with forward-swept blades"*. J. Fluids Eng. **1977**
19. Hurault J, Kouidri S, Bakir F, Rey R. "*Experimental and numerical study of the sweep effect on three-dimensional flow downstream of axial flow fans"*. Flow Meas. Instrum. **2010**
20. Zenger FJ, Renz A, Becher M, Becker S. "*Experimental investigation of the noise emission of axial fans under distorted inflow conditions"*. J. Sound Vib. **2016**
21. Minjun Park, Duck-Joo Lee, Hakjin Lee, "*Experimental and computational investigation of the effect of blade sweep on acoustic characteristics of axial fan"*, Applied Acoustics,Volume 189, **2022**.
22. Sivaramakrishnan, A, Bleiziffer, M, & Girmscheid, F. *"Acoustic Evaluation of Forward and Backward Swept Axial Fan Design for Automotive Applications with Identical Aerodynamic Performance"* Proceedings of the ASME Turbo Expo **2024**
23. Zangeneh M., "*A compressible three-dimensional design method for radial and mixed flow turbomachinery blades",* International Journal for Numerical Methods in Fluids, 13 (5), **1991**

24. Okamoto H., Zangeneh M., Watanabe H., GotoA. "*Design of a box fan rotor using 3-D inverse design method",* IMechE International Conference on fans, London, **2004**
25. Dipali Ghodake , Marlène Sanjosé , Stéphane Moreau and Manuel Henner, "*Effect of Sweep on Axial Fan Noise Sources Using the Lattice Boltzmann Method"*, MDPI **2022**
26. Lorenzo M. Pii, Damiano Casalino, Gianluca Romani and Kartik Singal, "*Aeroacoustic Optimization of an Axial Cooling Fan with Fundamental Observations"*, AIAA **2024**
27. Evangelos Antoniou, Gianluca Romani, Andreas Jantzen, Felix Czwielong, and Stefan Schoder, "*Numerical flow noise simulation of an axial fan with a Lattice-Boltzmann solver"*, Acta Acustica **2023**
28. Stéphane MOREAU, "*Turbomachinery-related aeroacoustic modelling and simulation"*, Conference on Modelling Fluid Flow **2018**



CHARACTERIZATION OF THE INSTALLATION EFFECTS ON THE AEROACOUSTICS SOURCES OF THE AUTOMOTIVE COOLING MODULE USING THE LATTICE-BOLTZMANN METHOD

Tayyab AKHTAR[1], Safouane TEBIB[1], Stephane MOREAU[1]
Bruno DEMORY[2], Manuel HENNER[2]

[1] *Department of Mechanical Engineering,Université de Sherbrooke,*
2500 Boulevard de l'Université, Sherbrooke, QC J1K 2R1, Canada

[2] *Simulation and Reliability Discipline, Valeo Power,*
78320 La Verrière, France

SUMMARY

This study investigates the aeroacoustic behavior of automotive cooling modules in both conventional internal combustion engine (ICE) vehicles and electric vehicles (EVs), focusing on the impact of installation effects. Numerical simulations using the Lattice Boltzmann Method (LBM) are performed to evaluate the noise generation mechanisms and flow characteristics in four configurations. The study highlights the challenges of adapting classical cooling module components to EV setups, emphasizing the role of the heat exchanger (HE) and duct geometry in influencing noise levels and flow dynamics. The results indicate that while the HE smooths the upstream flow and improves rotor loading distribution, it marginally increases noise levels at blade-passing frequencies (BPF) for the classical modules. The addition of ducts in EV modules introduces significant flow disturbances and localized pressure fluctuations, resulting in areas of high flow rate and loading. Across all configurations, leading and trailing edge fluctuations are observed, originating from the blade tip and extending down to approximately midspan, with greater magnitudes observed in the EV module, making it the dominant source of pressure fluctuations. The direct far-field noise computations align well with the experimental data acquired at the anechoic chamber of the University of the Sherbrooke. The relative trend is well predicted at lower frequencies with a smaller over-prediction and a good match at mid-frequencies. Additionally, surface pressure fluctuations on the duct and shroud are investigated and their resemblance with duct modes is analysed.

INTRODUCTION

The thermal management system of an automobile heavily relies on the cooling module, typically located at the front of the vehicle. This module consists of at least one HE and a fan assembly, both designed to maximise heat transfer [1]. A critical component of this system is the low-speed axial fan, which ensures the thermal stability of the thermal or electric power train and thus plays a role in vehicle performance. It is designed to force the flow through the fins and louvers of the HE core with

a higher flow rate. While numerous studies have explored the flow dynamics and noise characteristics of axial fans using numerical [1-6] and experimental methods [7-11], detailed analyses of the integrated cooling module remain limited [12-14]. Performance curves derived from open-air conditions often diverge from actual on-system behaviour, as airflow and noise characteristics are influenced by the interaction of the module components. This discrepancy is particularly pronounced when various fan configurations are mounted downstream of the same radiator [15]. Research has established that the HE disrupts large vortical structures and induces non-uniform turbulence upstream of the fan [16-18]. Wang [19] experimentally demonstrated that the presence of the HE increases flow resistance (pressure drop) as fan speed rises. Furthermore, the spacing between the HE and the fan is critical, as it influences radiated noise levels [20]. Similarly, the geometry of the HE tubes and the casing may contribute to both broadband and tonal noise components [21]. These interactions become even more complex when the cooling module is placed in realistic vehicle compartments, where high drag further alters flow dynamics. The challenge is compounded in EVs, where cooling modules play an increasingly vital role, particularly during battery charging, which requires a high airflow. Since this process occurs while the vehicle is stationary, there is no dynamic air pressure, unlike in combustion-powered vehicles, leading to higher power consumption and increased noise generation.

This study addresses these challenges by investigating the flow and acoustic field of an electrical module designed to replicate the spatial constraints of a vehicle compartment and comparing them with the conventional cooling module. To understand the noise generation mechanisms and their propagation, interaction and coupling within such a complex system, a detailed three-dimensional flow field is essential. This objective is achieved by employing the commercial software, Powerflow which has already demonstrated its capability for predicting accurate aeroacoustics results of automotive cooling fan and complete module [22-25]. The work builds upon Tebib's findings [26, 27], who analyzed similar configurations at constant rotational speeds with different mass flow rates, by adapting those numerical modelling strategies to investigate flow and noise behaviour under identical mass flow rate conditions. The configurations investigated in this work are outlined in the next section, followed by a comprehensive description of the experimental setup. The following section details the numerical methodology and provides an analysis of the velocity and pressure fields. The final section focuses on the aeroacoustic characteristics and concludes with a summary of the main findings and their implications.

TEST ORGANIZATION

The studied cooling module is designed and supplied by Valeo Thermal Systems, a tier-one supplier specializing in automotive thermal management solutions. This module comprises several key components: a fan, shroud, motor, heat exchanger, inlet duct, and outlet duct, as illustrated in Fig. 1. To thoroughly investigate the primary noise sources and quantify their contributions, four distinct configurations were analyzed, as detailed in Table 1. Each configuration employs the same fan and motor setup to ensure consistency and comparability across simulations. The first configuration, *cm_nHE* (classical module without heat exchanger), includes only the fan, motor, and shroud, serving as a baseline setup due to its simplicity, with fewer components to consider. This initial configuration helps establish the fundamental flow field and noise mechanisms of the fan, motor, and shroud assembly. For the second configuration, *cm_wHE* (classical module with heat exchanger), a HE with dimensions of 549 mm × 389 mm × 17.8 mm was added 25 mm upstream of the fan hub. This addition facilitates a detailed analysis of the HE acoustic contribution at a specific distance and its impact on the flow field.

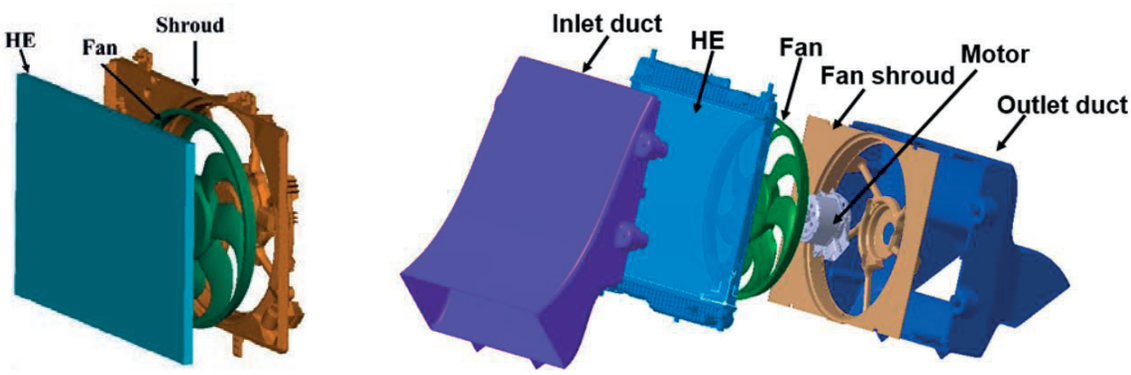
Once the acoustic signatures of the complete classical cooling unit are characterized under ideal conditions (without compartment drag), the same procedure is applied to an EV module. In the EV setup, the cooling module is not directly positioned at the front of the vehicle; instead, it encounters additional drag from the inlet and outlet ducts, tailored to the available space in the engine

compartment. The third configuration, *em_nHE* (electrical module without heat exchanger), incorporates this duct to evaluate its effect on system performance without the HE. Finally, the fourth configuration, *em_wHE* (electrical module with heat exchanger), combines both the duct and HE to assess their combined influence on noise levels and system efficiency.

This systematic approach provides a comprehensive understanding of the individual and combined contributions of the HE and duct to the overall noise characteristics of the cooling module. The tested fan features seven unevenly spaced blades with a diameter of 380 mm and a hub-to-tip ratio of 0.4. The radial distance of the ring gap is 6 mm. Additionally, five downstream struts support the motor and fan, connecting directly to the stationary shroud.

Table 1: Test configurations

Acronym	Parts	Speed	Mass Flow Rate
cm_nHE	Fan, Shroud, Motor	2550rpm	0.77kg/sec
cm_wHE	Fan, Shroud, Motor, Heat Exchanger	2550rpm	0.63kg/sec
em_nHE	Fan, Shroud, Motor, Inlet-Outlet Duct	3400rpm	0.77kg/sec
em_wHE	Fan, Shroud, Motor, Heat Exchanger, Inlet-Outlet Duct	3400rpm	0.63kg/sec



a) Classical module (cm) b) Electrical module (em) [27]

Figure 1: Complete cooling module.

EXPERIMENTAL SETUP

The experimental campaign is conducted in the anechoic chamber at the University of Sherbrooke, using the setup depicted in Fig. 2. Only the configurations with HE (both classical and electrical modules) are measured experimentally as these are the designed setups. To capture the far-field acoustic pressure radiated by the cooling module, an arc-shaped array with a radius of 1.8 meters is employed, consisting of thirteen microphones spaced at 15-degree intervals, covering a total of 180 degrees. Microphone 1 is positioned axially upstream, while microphone 13 is located axially downstream, perpendicular to the plane of rotation. The centre of the arc is aligned with the centre of the fan hub. The complete cooling module is mounted on a fixed frame rather than an ISO-5801 standard test plenum, meaning only the design point condition is evaluated. Sound pressure data is collected using pre-polarized Brüel & Kjær (B&K) 1/4-inch condenser microphones, and the signals are simultaneously processed using a B&K front-end spectrum analyzer. The acoustic signals are sampled at a frequency of 65.536 kHz, with a frequency resolution of 3.125 Hz. Given the anechoic chamber's cut-off frequency of 80 Hz, only spectral data above this threshold is analyzed.

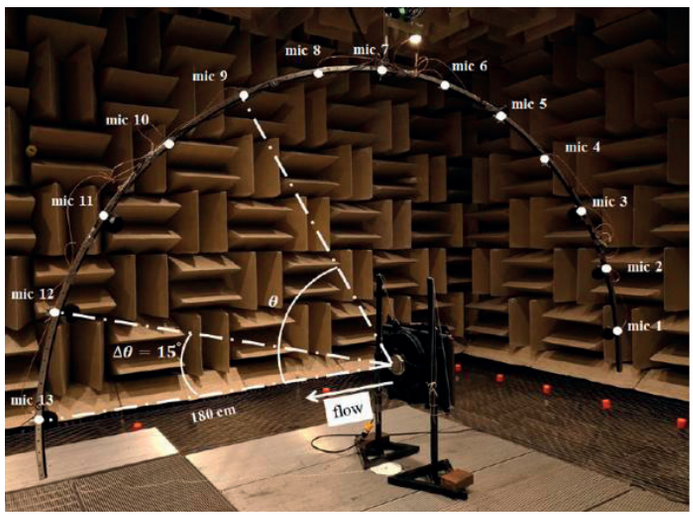


Figure 2: Experimental setup [26].

NUMERICAL SETUP

The numerical simulations are performed using the hybrid LBM/Very Large Eddy Simulations implemented in the commercial software PowerFlow 6-2024-R4 version. The whole domain is divided into ten variable resolution (VR) regions with three damping zones (DZ) i.e. like the wedges in the anechoic chamber. To reproduce the experimental setup, these zones, employ increasingly high isotropic viscosity (starting from the physical viscosity of VR4) to effectively absorb the reflected waves and ensure the free field condition. The smallest donut VR having a voxel size of 0.5mm covers the fan tip and blade area where the highest velocity gradients are expected. The heat exchanger and shroud are placed in the VR9 region. The resolution of remaining VR regions decreases by a factor of 2. The ceiling, floor and all walls are modelled as solid with no-slip and inlet, outlet with uniform pressure (static pressure with free flow direction) and reflection damping boundary conditions as shown in Fig.3 (a). The HE is modelled as an equivalent porous media, a technique previously validated against experimental data by Tebib [27]. The same porous media is used for this simulation. In equivalent porous media pressure loss depends on the inflow velocity, resulting in higher pressure loss for higher-velocity regions as demonstrated by Wang [19], see the resistance curve implemented for this simulation in Fig.3 (b).

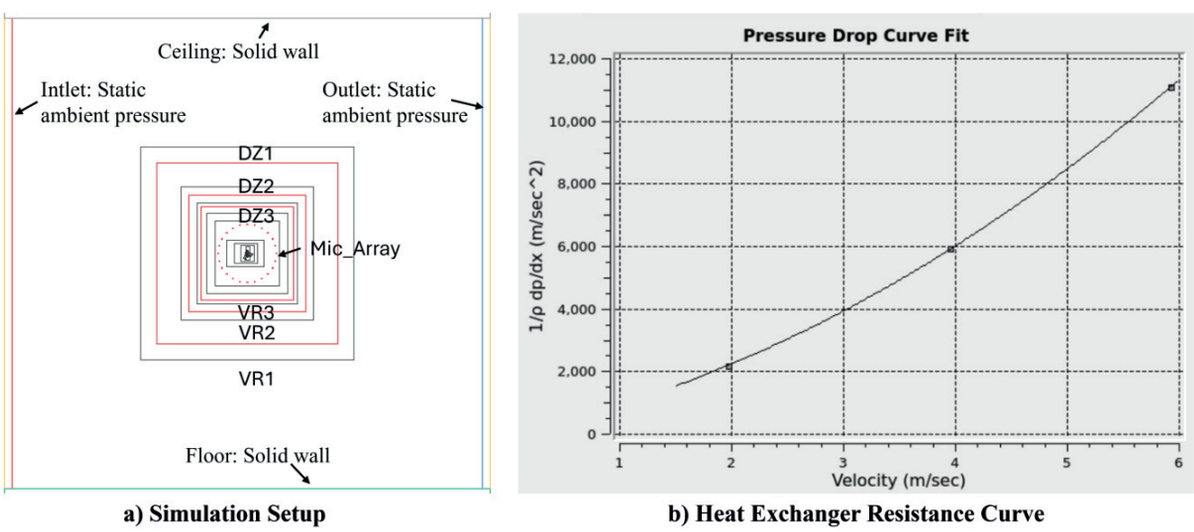


Figure 3: Numerical setup (a) Representation of variable resolution regions and damping zones, (b) The resistance curve imposed for heat exchanger pressure loss.

The simulation runs for a physical time of 0.53 seconds, covering a total of thirty fan revolutions. This setup results in a sampling frequency of 37.155 kHz, with a data recording period of ten timesteps. The physical timestep is set to 8.411×10^{-7} seconds, corresponding to approximately 3,000 timesteps per blade passage and around 21,000 timesteps per full revolution.

Twenty-four direct microphone probes of diameter 6.35 mm, spaced every 15-degree are positioned around the module in the VR5 region, where the voxel (cubic element) size is 16 mm and the maximum achievable frequency is 9.66 kHz. These probes are used to capture the radiated noise directly. Additionally, direct fluid probes, each with a diameter of 2 mm, are radially inserted upstream and downstream of the fan, covering the entire fan diameter (196 mm to -196 mm) except for the hub section. Upstream of the fan, 124 probes are positioned 5 mm—less than one axial chord length—away from the fan hub, with a uniform spacing of 2 mm between them. Downstream, the probes are placed 50 mm from the fan hub, maintaining the same 2 mm spacing. All probes are located within the VR9 region, where the voxel size is 1 mm, and the sampling frequency of 148.623 kHz with a recording period of eight timesteps. These probes directly measure all three instantaneous velocity components and static pressure from the flow field. Both sets of probes operate within a stationary frame of reference, ensuring accurate data capture for flow analysis.

AERODYNAMIC RESULTS

Velocity Field

The time-mean velocity field is analyzed in a meridional plane passing through the hub centre. A comparison of the flow establishment is presented in Fig. 4 in terms of the mean velocity magnitude to understand the effect of the upstream obstructions on the mean flow field. Both electrical and classical HE configurations exhibit smoother flow compared to cases without HE, with this effect being more pronounced for the electrical module. The placement of the duct adds drag, disturbing the flow field and creating an imbalance: the lower rotor section experiences higher flow rates, while the upper section faces increased loading. This disturbance is mitigated by the presence of the HE, which smoothens the flow. Additionally, classical module comparisons show that the upstream HE introduces flow resistance, increasing fan blade loading. This results in more separated downstream flow in the HE configuration, unlike the case without HE, where the flow remains nearly axial. A consistent feature across configurations is gap leakage flow, driven by the pressure difference between upstream and downstream regions.

To provide a clearer visualization compared to the velocity magnitude contours, time-averaged velocity vectors are plotted in Fig. 5. These vectors, representing the resultant of radial and axial velocity components, are scaled with the corresponding tip velocity to ensure consistent comparison. The locations of the measurement probes are also indicated in Fig. 5. The analysis of gap leakage flow shows that the HE configuration experiences less leakage compared to the case without HE. For the classical module, this behavior is clarified through the combined insights from Figs. 4 and 5, which indicate that in the HE configuration, leakage flow immediately moves downward due to the strong convergent flow through the gap. Conversely, in the configuration without HE, the leakage flow returns at a specific radius, as depicted in the streamlines for both cases. However, in the ducted configuration, both cases exhibit nearly identical leakage flow magnitudes in the lower section of the rotor. In the upper section, the difference arises due to the disturbed flow, which results in higher loading in the absence of the HE. The overall flow field validates the observations discussed in the previous section, confirming that HE configurations distribute the flow more evenly along most of the blade span.

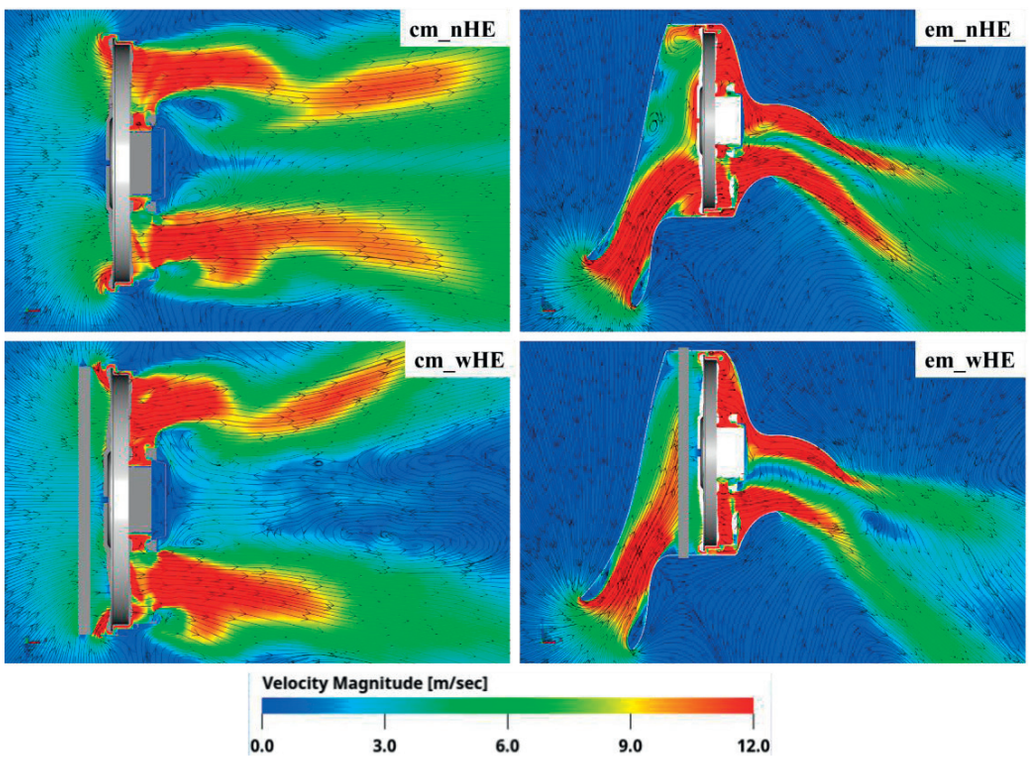


Figure 4: Time-averaged velocity magnitude contours in the meridional plane.

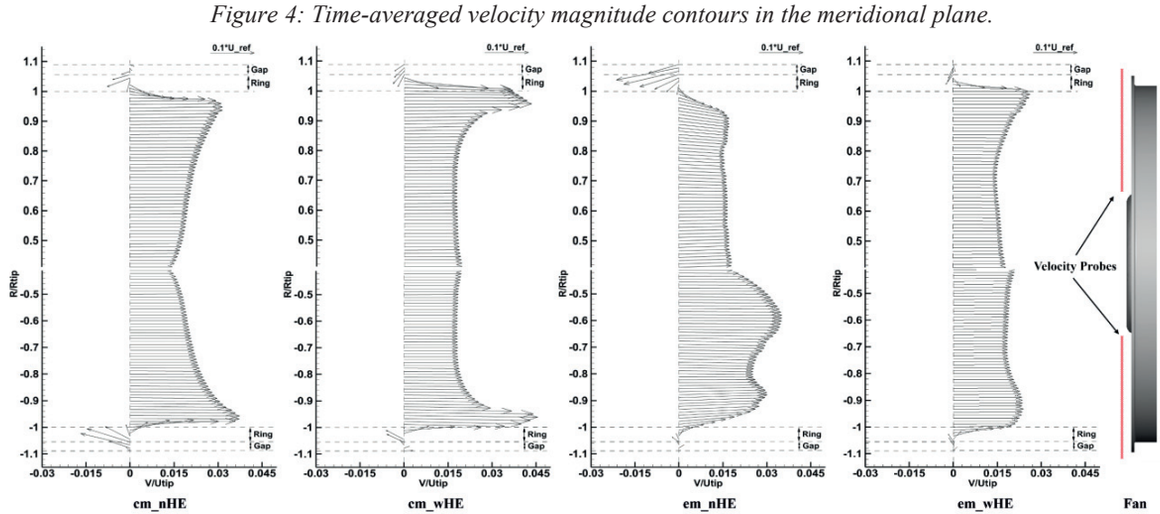


Figure 5: Resultant vectors of mean radial and axial velocity components and the location of velocity probes.

Pressure Field

After analyzing the velocity field behavior, the impact of installation on the pressure field is examined. The time mean pressure rise across each rotor, computed using the direct fluid probes, is shown in Fig. 6. Overall, all rotors experience reduced loading near the hub and increased loading toward the tip, with maximum levels in the tip region. This is caused by the distribution of tangential velocity along the blade span. The placement of the HE improves this distribution, corroborating the earlier velocity field observations. A clear installation effect is evident in the classical module, where the presence of the HE increases loading due to a reduced flow rate. However, in the electrical module, the nHE case experiences higher loading than the wHE case in regions of low flow rate and lower loading in regions of high flow rate, which aligns with the observed flow field behavior. Following the analysis of loading distribution, pressure fluctuations on the rotor surface are evaluated

FAN 2025
Antibes Juan-les-Pins (France), 9 – 11 April 2025

to identify sound sources. According to acoustic analogy, these fluctuations are the primary contributors to noise. To understand the expected noise generation mechanisms, the RMS of pressure fluctuations is presented in Fig. 7. The results indicate that, across all configurations, a consistent feature is the dominant pressure fluctuations on the leading and trailing edges of the suction surface, primarily due to flow separation. In the classical module, these fluctuations increase with the presence of the HE, extending up to the mid-span of the blade and introducing additional trailing-edge fluctuations near the hub. In contrast, the electrical module experiences fewer fluctuations when the HE is present, as it helps mitigate flow disturbances. However, the installation of the duct further amplifies these fluctuations, with contributions even from the forward curvature section of the blade surface. At lower blade radii, flow separation caused by strong radial components from the hub shape is evident but becomes less pronounced with the HE installed—and even more so with the duct—due to variations in incidence angles.

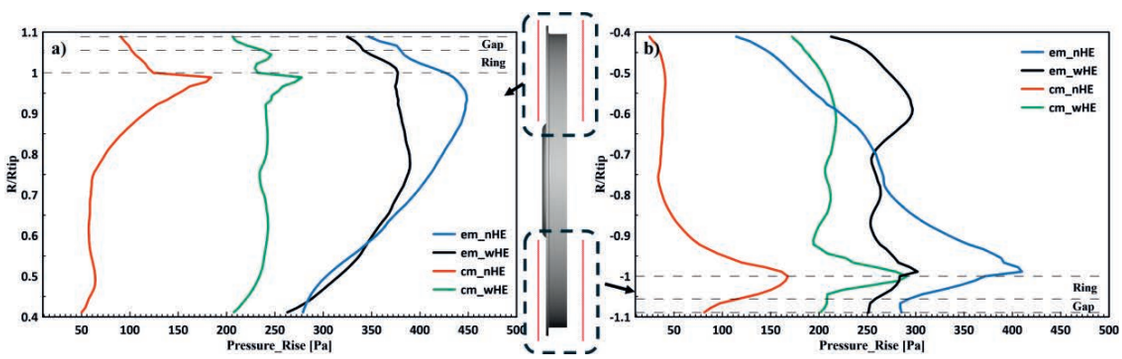


Figure 6: Mean pressure rise curves across the rotors: a) Upper section of the rotor, b) Lower section of the rotor.

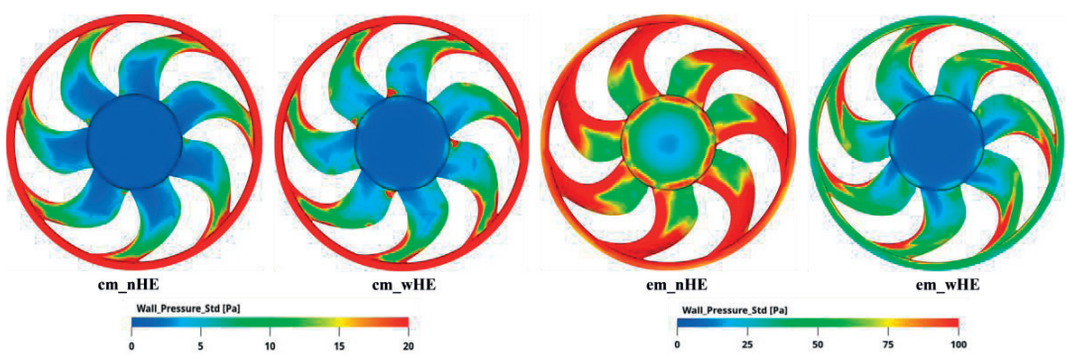


Figure 7: Rotor surface suction side pressure fluctuations_RMS.

AEROACOUSTICS RESULTS

The far-field pressure spectrum, obtained via direct probes as detailed in the numerical setup, is compared in Fig. 8(a) for HE configurations (classical and electrical modules) against experimental data. Good agreement is found at mid-frequencies (1-3 kHz). At high frequencies, the experimental spectrum shows troughs that could be alleviated by removing acoustic diffraction effects as shown by Pasco [28]. At low frequencies, the LBM result overpredicts the noise levels most likely because of the fan deflection that closes the tip gap and significantly reduces the noise levels below 1 kHz as already shown on the classical module by Tebib [27]. Furthermore, a comparison of the four configurations in Fig. 8(b) highlights the installation effects on radiated noise. For the classical module, the HE has minimal impact on the noise spectrum, apart from a slightly higher BPF peak compared to the nHE case. However, for the electrical module, the HE configuration exhibits lower noise levels in the low-frequency range compared to the nHE case, ascribed to the previously mentioned flow field. Additionally, the duct is introducing the troughs and humps which are not

present in the classical module, probably due to duct modes. For all configurations, frequencies above 1.5 kHz remain unaffected by the installation effects of HE and duct, with all setups exhibiting almost similar broadband noise levels.

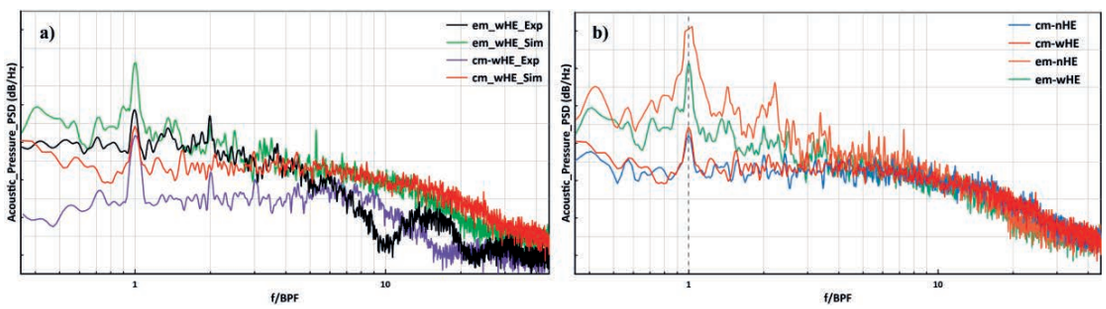


Figure 8: The Far-Field Radiated Noise Spectrum parallel to the rotation plane (1.85m up the hub centre), a) Validation of numerical results with the experimental data, b) Analysis of installation effects on the radiated noise.

To analyze the peaks in the spectrum, pressure fluctuations on the duct and shroud surfaces are extracted at these frequencies, with the fan fluctuating pressure regions discussed previously. Fig. 9 (a) shows power spectra centered on the BPF and its first harmonic, spanning ±50 Hz. The pressure fluctuations are scaled in decibels (dB) for consistent comparison with radiated noise. For brevity, only shrouds of the classical module are presented here as both configurations show a similar trend. Surface pressure contours indicate that, around the BPF, leakage flow and supporting struts are the primary contributors to observed fluctuations. However, at the first harmonic of the BPF, the influence of leakage flow diminishes, with the struts becoming the dominant source of fluctuation zones.

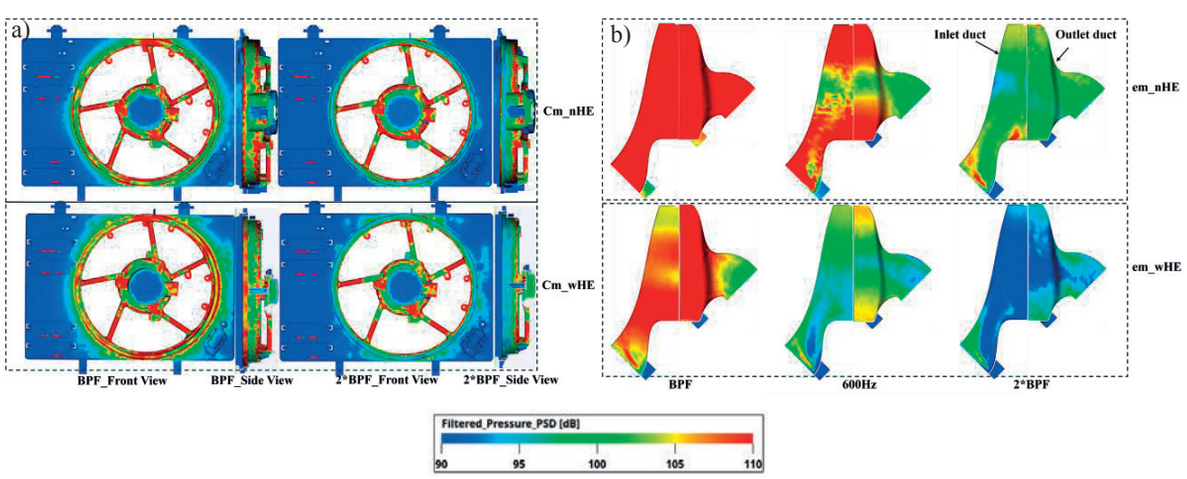


Figure 9: Power Spectrums of the shroud surface pressure fluctuations filtered around BPF and 1st Harmonic, a) Classical module, b) Electrical module.

However, the filtered pressure fluctuations on the duct are shown in Fig. 9 (b), for 600 Hz, along with the BPF and its first harmonic, as this frequency range exhibits two peaks in the ducted configurations. At the BPF, both HE and nHE configurations display high fluctuations, with the nHE case showing more elevated levels due to a more disturbed flow field and higher mass flow rate compared with the HE configuration. At 600 Hz and the first harmonic, the HE configuration shows fluctuations only at the outlet duct sharp corners, whereas the nHE configuration exhibits fluctuations on both sides. These fluctuations are likely due to the duct response to the fan acoustic field, as observed by Tebib [26] for duct modes. Interestingly, despite the variation in the fan rotational speed between the classical and electrical modules, the similarity in power spectra suggests that these duct surface pressure fluctuations probably play a dampening role, mitigating the acoustic field levels generated

by the fan. The acoustic field is being restructured into duct modes as seen by the troughs and humps of spectra in Fig.8.

Finally, the installation effects on the directivity of radiated noise are analyzed in Figs 10 and 11. Discrepancies in the lower frequency range are likely due to the differences observed in the spectra. Both configurations tend to overpredict radiated noise, primarily due to the leakage noise differences discussed earlier. However, a comparison between the electrical and classical modules above 1 kHz reveals that both configurations produce similar noise levels, except along the rotational axis, where the duct inlet and outlet play a significant role in the electrical module. The classical module exhibits strong axial dipole characteristics across both frequency ranges, whereas the electrical module shows a slightly deflected axial dipole across the entire frequency range, with a dipole shift toward the ground at higher frequencies.

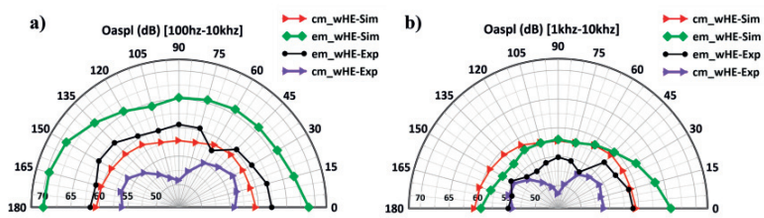


Figure 10: Directivity comparison with the experimental data for HE configurations.

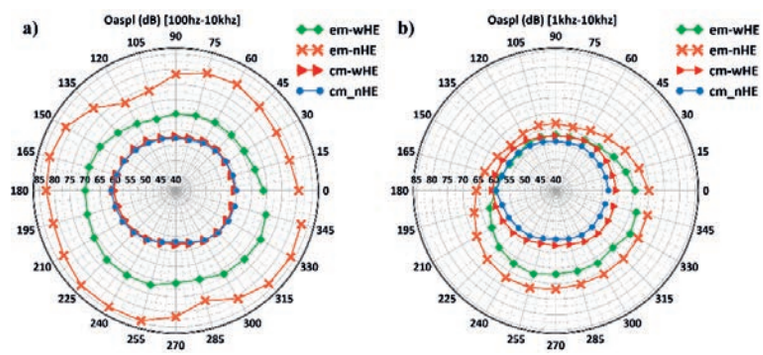


Figure 11: Directivity comparison for installation effects in two different frequency ranges.

CONCLUSION

The aeroacoustic behavior of an automotive cooling module is analyzed using the hybrid LBM/VLES, focusing on the installation effects of upstream obstructions. This study evaluates the challenges of adapting a conventional cooling module fan and HE, designed for classical vehicles, to EVs by testing four configurations, starting from the simplest classical module setup. Results show that the placement of an upstream HE smooths the flow field upstream of the fan and improves rotor loading along the radius. However, it causes slightly higher noise levels at the BPF in the classical module. The introduction of a duct, on the other hand, creates significant flow disturbances due to its geometry. This leads to non-uniform upstream flow, localized regions of high flow rates, and increased loading zones, all of which amplify pressure fluctuations. Furthermore, the duct adds resistance, requiring the fan to operate at higher rotational speeds to maintain the designed mass flow rate. Despite this, the far-field spectra reveal minimal impact from these installations on broadband noise levels at higher frequencies (above 1.5 kHz). The numerical results have been validated with the experimental data. A good agreement is observed at mid-frequencies, while lower frequencies are overestimated but still capture the overall trend effectively for the electrical module. These findings suggest that adapting conventional cooling fans to EVs not only introduces additional noise sources, primarily driven by the response of inlet and outlet ducts tailored to fit the compartment spatial constraints but also changes the directivity of the radiated sound.

BIBLIOGRAPHY

[1] M. Henner, B. Demory, M. Alaoui, M. Laurent and B. Behey, *Effect of blade curvature on fan integration in engine cooling module,* Acoustics, vol. 2, no. 4, pp. 776-790, **2020**.

[2] M. Henner, F. Franquelin, B. Demory, Y. Beddadi, C. Roland and A. Serran, *Hump-shaped broadband noise on a fan at off-design conditions,* in *Proceedings of the Fan 2015 Conference,* **2015**.

[3] D. Ghodake, M. Sanjosé, S. Moreau and M. Henner, *Effect of sweep on axial fan noise sources using the lattice Boltzmann method*, International Journal of Turbomachinery, Propulsion and Power, **7**(4), p. 34, **2022**.

[4] F. J. Krömer, S. Moreau and S. Becker, *Experimental investigation of the interplay between the sound field and the flow field in skewed low-pressure axial fans*, Journal of Sound and Vibration, 442, pp. 220-236, **2019**.

[5] S. Moreau and M. Roger, *Competing broadband noise mechanisms in low-speed axial fans,* AIAA Journal, vol. 45, no. 1, pp. 48-57, **2007**.

[6] S. Moreau and M. Sanjose, *Sub-harmonic broadband humps and tip noise in low-speed ring fans,* The Journal of the Acoustical Society of America, vol. 139, no. 1, pp. 118-127, **2016**.

[7] F. Krömer, A. Renz and S. Becker, *Experimental investigation of the sound reduction by leading-edge serrations in axial fans,* AIAA Journal, vol. 56, no. 5, pp. 2086-2090, **2018**.

[8] R. Longhouse, *Control of tip-vortex noise of axial flow fans by rotating shrouds,* Journal of Sound and Vibration, vol. 58, no. 2, pp. 201-214, **1978**.

[9] C. Sarraf, H. Nouri, F. Ravelet and F. Bakir, *Experimental study of blade thickness effects on the overall and local performances of a controlled vortex designed axial-flow fan,* Experimental Thermal and Fluid Science, vol. 35, no. 4, pp. 684-693, **2011**.

[10] E. Tannoury, B. Demory, M. Henner, P.-A. Bonnet, P. Caule and Y. Creteur, *A design of experiment for evaluating installation effects and the influence of blade loading on the aeroacoustics of an automotive engine cooling fan,* in *Proceedings of FAN 2012 Conference,* France, **2012**.

[11] T. Zhu, D. Lallier-Daniels, M. Sanjosé, S. Moreau and T. Carolus, *Rotating coherent flow structures as a source for narrowband tip clearance noise from axial fans*, Journal of Sound and Vibration, 417, pp. 198-215, **2018**.

[12] A. Karim, M. Mehravaran, B. Lizotte, K. Miazgowicz and Y. Zhang, *Computational aero-acoustics simulation of automotive radiator fan noise,* SAE International Journal of Engines, vol. 8, no. 4, pp. 1743-1749, **2015**.

[13] M.-J. Park and D.-J. Lee, *Sources of broadband noise of an automotive cooling fan,* Applied Acoustics, vol. 118, pp. 66-75, **2017**.

[14] M. Zhu, K. Wang, P. Zhang and Z. Li, *Numerical and experimental investigation of aerodynamic noise from automotive cooling fan module,* Journal of Vibroengineering, vol. 17, no. 2, pp. 967-977, **2015**.

[15] M. Sortor, *On-system engine cooling fan measurement as a tool for optimizing cooling system airflow performance and noise,* SAE International Journal of Materials and Manufacturing, vol. 4, no. 1, pp. 1221-1230, **2011**.

[16] A. Suzuki and A. Soya, *Study on the fan noise reduction for automotive radiator cooling fans,* SAE Technical Paper, 0148-7191, **2005**.

[17] A. Zarri, M. B. Botana, J. Christophe and C. Schram, *Aerodynamic investigation of the turbulent flow past a louvered-fin-and-tube automotive heat exchanger,* Experimental Thermal and Fluid Science, vol. 155, p. 111182, **2024**.

[18] F. J. Zenger, A. Renz, M. Becher and S. Becker, *Experimental investigation of the noise emission of axial fans under distorted inflow conditions,* Journal of Sound and Vibration, vol. 383, pp. 124-145, **2016**.

[19] Z. Wang et al., *Numerical and experimental investigation on the integrate performance of axial flow cooling fan and heat exchanger,* Applied Thermal Engineering, vol. 245, p. 122814, **2024**.

[20] S. Wagner and J. Rohlfing, *Effects of the fan-heat exchanger interaction on the noise emissions of heat pumps: Experimental and Numerical Studies,* Journal of Thermal Engineering Studies, **2019**.

[21] F. Czwielong, J. Soldat and S. Becker, *On the interactions of the induced flow field of heat exchangers with axial fans,* Experimental Thermal and Fluid Science, vol. 139, p. 110697, **2022**.

[22] D. Lallier-Daniels, M. Piellard, B. Coutty and S. Moreau, *Aeroacoustic study of an axial engine cooling module using Lattice-Boltzmann simulations and the Ffowcs Williams and Hawkings' Analogy,* European Journal of Mechanics-B/Fluids, vol. 61, pp. 244-254, **2017**.

[23] J.-o. Mo and J.-h. Choi, *Numerical investigation of unsteady flow and aerodynamic noise characteristics of an automotive axial cooling fan,* Applied Sciences, vol. 10, no. 16, p. 5432, **2020**.

[24] M. Piellard, B. B. Coutty, V. Le Goff, V. Vidal and F. Pérot, *Direct aeroacoustics simulation of automotive engine cooling fan system: effect of upstream geometry on broadband noise,* in *20th AIAA/CEAS Aeroacoustics Conference,* **2014**.

[25] M. Sanjose and S. Moreau, *Direct noise prediction and control of an installed large low-speed radial fan,* European Journal of Mechanics-B/Fluids, vol. 61, pp. 235-243, **2017**.

[26] S. Tebib et al., *Aeroacoustic investigation of automotive engine cooling modules using the Lattice-Boltzmann method,* in *28th AIAA/CEAS Aeroacoustics 2022 Conference,* p. 2859, **2022**.

[27] S. Tebib et al., *Detailed noise analysis of automotive engine cooling modules using the Lattice-Boltzmann method,* in *AIAA AVIATION 2023 Forum,* p. 3205, **2023**.

[28] Y. Pasco and S. Moreau, *Sound radiation of a smoke-removal fan system,* Acta Acustica united with Acustica, vol. 105, no. 1, pp. 86-94, **2019**.

G1B Fluid-Structure-Acoustic Interactions

11 April - 10:10 - Auditorium
Chairmen: Sassan Etemad, Zhiping Wang

List of papers

An Enclosed Centrifugal Fan as a Benchmark Case for Fluid-Structure- Acoustic-Interaction: An Overview

- Felix CZWIELONG – LSTM (Germany)
- Patrick HEIDEGGER – IGTE (Austria)
- Manuel LAUBER – LSTM (Germany)
- Christoph HEIGL – LSTM (Germany)
- Andreas WURZINGER – IGTE (Austria)
- Marco Fritzsche – Polytec GmbH (Germany)
- Stefan SCHODER – IGTE (Austria)
- Manfred KALTENBACHER – IGTE (Austria)
- Stefan BECKER – LSTM (Germany)

1-way FSI Simulation Approach to Assess Low-pressure Axial FanAerodynamic and Aeroacoustics Performance Variation

- Juan David LAGUNA – Dassault Systemes Deutschland GmbH (Germany)
- Evangelos ANTONIOU – Dassault Systemes Deutschland GmbH (Germany)
- Fabian QUINTERO – Dassault Systemes Deutschland GmbH (Germany)
- Mario PESCE – Dassault Systemes Deutschland GmbH (Germany)
- Felix CZWIELONG – Institute of Fluid Mechanics, FAU (Germany)
- Stefan SCHODER – Institute of Fundamentals and Theory in Electrical Engineering, TU Graz (Austria)



AN ENCLOSED CENTRIFUGAL FAN AS A BENCHMARK CASE FOR FLUID-STRUCTURE-ACOUSTIC-INTERACTION: AN OVERVIEW

Felix CZWIELONG[1], Patrick HEIDEGGER[2], Manuel LAUBER[1], Christoph HEIGL[1], Andreas WURZINGER[2], Marco FRITZSCHE[3], Stefan SCHODER[2], Manfred KALTENBACHER[2], Stefan BECKER[1]

[1] *LSTM, Institute of Fluid Mechanics, Friedrich-Alexander-University Erlangen-Nuremberg, 91058 Erlangen, Cauerstraße 4, Germany*
Contact: felix.czwielong@fau.de

[2] *IGTE, Institute of Fundamentals and Theory in Electrical Engineering, TU Graz, Inffeldgasse 18, 8010 Graz, Austria*

[3] *Polytec GmbH, Polytecpl. 1-7, 76337 Waldbronn, Germany*

SUMMARY

In the course of a joint research project between the Institute of Fluid Mechanics (LSTM) and the Institute of Fundamentals and Theory of Electrical Engineering (IGTE), an international benchmark case for fluid-structure-acoustic interaction was created. An enclosed centrifugal fan was chosen as the research object and its aerodynamic, aeroacoustic and structure-acoustic properties were characterised by experimental measurements. The paper gives an overview of the fan used and it's enclosure, the centrifugal fan test rig and the experimental investigations carried out. The focus is not on the interpretation of the results, but rather on the general presentation of the benchmark case and an overview of the available data.

INTRODUCTION

Fans are used in a wide range of products, which means that there are a large number of these machines worldwide. The sheer number of fans therefore has a significant impact on humanity's energy consumption. However, it is not only energy consumption that is important, but also the noise emitted by fans. Their use in ventilation, air conditioning, heating and refrigeration puts them in close proximity to people and can therefore affect the quality of life if noise levels are too high. For this

reason, it is essential for future developments to understand and optimise the noise generation mechanisms in fans on a physical basis. In the case of centrifugal fans, which are usually equipped with a spiral casing, a complex fluid-structure-acoustic (FSA) interaction occurs in addition to the purely aeroacoustic noise generation, which causes the casing of the centrifugal fan to vibrate. Due to the complexity of the rotating turbomachine, the sound generation and the interaction with the structure, an enclosed centrifugal fan represents a system in which the exact FSA interaction mechanisms are not clearly known. This interaction reaches the limits of the available software tools. In recent years, the approach of making public reference cases available to the general public has proved particularly effective for such difficult scientific challenges. The benchmark cases were usually simplified case studies and provided a comprehensive database for the validation and comparison of simulations and experiments. In the field of fans, for example, the benchmark case for low-pressure axial fans from Zenger et al. [1] should be mentioned here [2], [3]. In order to better understand the complex FSA interaction of enclosed centrifugal fans and to further develop corresponding software tools, a benchmark case for a centrifugal fan from the Institute of Fluid Mechanics (LSTM) was developed. A simplified housing was designed for the fan in order to better reproduce the FSA interaction numerically. The benchmark case of the enclosed centrifugal fan is the result of a collaboration between the Institute of Fluid Mechanics (LSTM) and the Institute for Fundamentals and Theory of Electrical Engineering (IGTE). This article serves as an overview of the extensive database of this benchmark case. For this reason, the focus is on the presentation of the measurement data and the interested reader is made aware of which data is available for the benchmark case.

CENTRIFUGAL FAN AND CASING

The test fan is a centrifugal fan with 12 blades and an outer diameter of 400 mm. The fan has a design operating point of $0.28\,\mathrm{m}^3/\mathrm{s}$ and a pressure rise of 700 Pa at a design rotational speed of 1800 rpm. Consequently, the fan's fundamental frequency is 30 Hz and the first blade passing frequency is 360 Hz. Aerodynamic and aeroacoustic properties of the benchmark fan, without casing, can be found in the literature [4]–[6]. The fan is equipped with miniature surface pressure sensors, which enable the telemetry system to determine the pressure fluctuations on the blade surface during the rotation of the fan. A special spiral housing based on a logarithmic spiral [7], [8] was designed for this test fan (see Figure 1). The spiral housing consists of four individual parts made of aluminium (AlSi1MgMn – 3.2315), each with a wall thickness of 8 mm. The parts are bolted together. This construction has the most homogeneous structural properties possible and at the same time avoids the need for reinforcement struts or undefined welded connections. On the one hand, there is a geometry version of this spiral housing that has no modifications, and on the other hand, there is a version that allows fluid mechanical investigations through customisation for optical and pressure sensor measurement technology. For example, a optical window has been incorporated in the tongue area of the housing, which enables the flow field to be measured using optical measuring methods. In addition, 54 measuring positions are provided for wall pressure sensors, which allow the recording of pressure fluctuations. After the spiral housing, there is a duct system that starts with a transition from a rectangular to a square duct. This funnel is followed by a canvas connection piece, which serves to decouple the housing from the rest of the duct system in terms of structural mechanics. The funnel-type transition has a thinner wall thickness of 2 mm and is also made of aluminium (AlMg3). There are 4 measuring positions for static pressure on this funnel component. The complete geometry will be provided as a open-source CAD data on request or at the LSTM-Homepage.

FAN 2025
Antibes - Juan-les-Pins (France), 9 - 10 April 2025

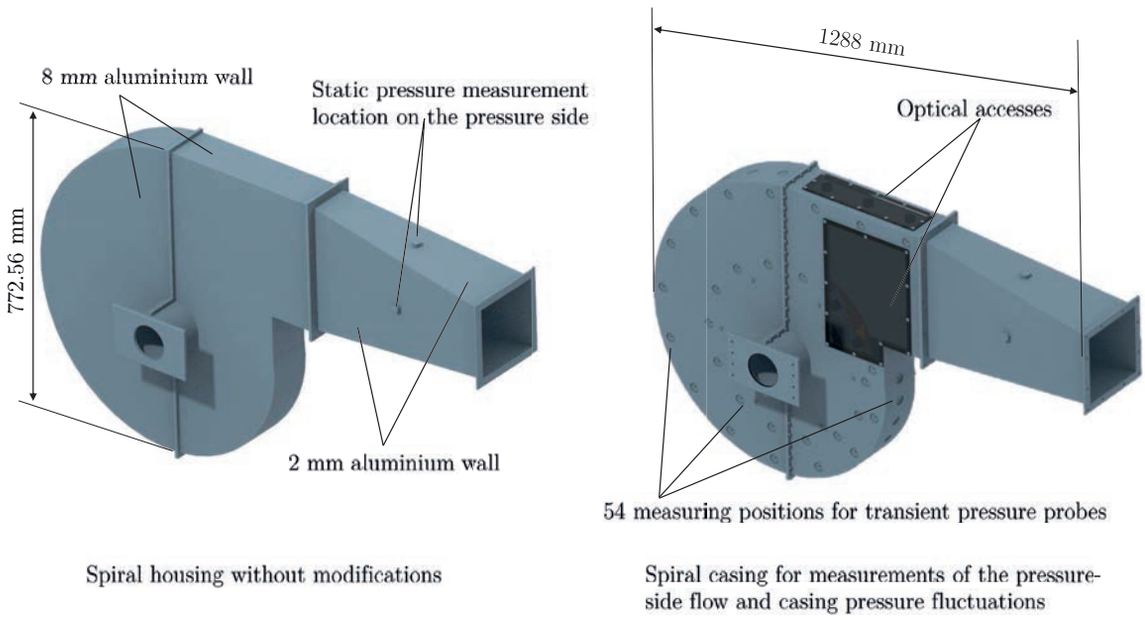


Figure 1: Representation of the two housing versions of the logarithmic spiral housing of the centrifugal fan.

TEST ENVIRONMENT AND TEST RIG

The centrifugal fan test rig of LSTM is specially designed for the aerodynamic and aeroacoustic testing of centrifugal fans and provides a quiet and homogeneous inflow in front of the fan. Figure 2 shows a schematic representation of the test rig with the most relevant components. In order to analyse the free-field sound radiation of the centrifugal fan and the housing, the part of the test rig that follows the duct silencers is integrated into the anechoic room of the LSTM. This means that the room's properties can be used to analyse the sound radiation of the fan without any disturbing influences from outside. In addition, noise sources such as the auxiliary fan and the throttle element, which are necessary for the aerodynamic properties of the test rig, are located outside the anechoic room. The inflow to the impeller is made as quiet as possible by suitable silencers, and flow straighteners and screens reduce the turbulence level in the inflow. To avoid standing waves in the pressure-side duct system of the test rig, there is an anechoic termination [9], [10] at the end of the duct system.

EXPERIMENTAL DATA SETS

The following sections provide an overview of the measurements carried out on the radial fan and its housing. The results of the measurements serve as the basis for the public benchmark case and can be used by the fan community and software developers to validate their simulation codes or to test new evaluation methods based on the measurement data. The following chapters are therefore intended to give the reader a general overview of the available data and not to discuss in detail the physical mechanisms behind the generation of noise by the centrifugal fan.

Measurement of inflow conditions

The flow field downstream of the flow conditioning screens of the radial fan test rig was measured using 3D hot-wire anemometry (Dantec Dynamics). The measurement plane is located 8 cm downstream of the screens. There are 180 points in the measurement plane at which the instantaneous values of the three velocity components were recorded with the hot-wire system for a period of 10 s

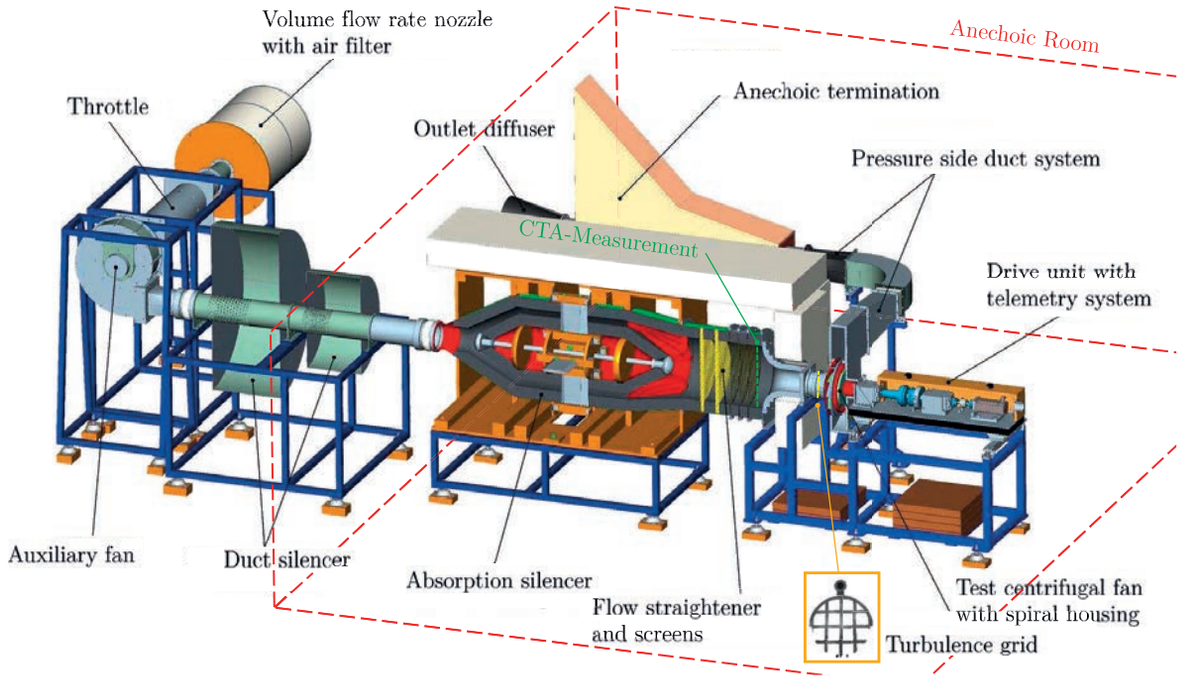
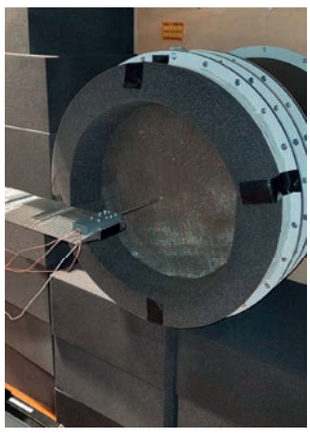


Figure 2: Design of the centrifugal fan test rig at LSTM in Erlangen. The anechoic room is indicated by a red dotted line. The measuring plane for the CTA measurements for the inflow profile is marked with a green dashed line. The location at which turbulence grids can be installed in front of the fan is marked with a yellow dashed line.

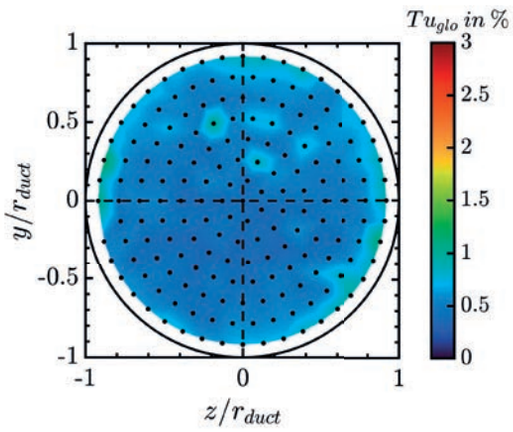
at a sampling rate of 48 kHz. After each measurement point, a new measurement point is approached using a traversing system. In order to eliminate the influence of the traverse movement and possible vibrations, a waiting period of 5 s is applied after each movement before the measurements are started [11]. The measurement data obtained are available for five different volume flows (0.1 m^3/s, 0.16 m^3/s, 0.22 m^3/s, 0.28 m^3/s, 0.35 m^3/s) and include data on mean velocities as well as the velocity fluctuations. From the velocity fluctuations it is possible to determine the integral length scale and the turbulence intensity. The measurement plane with the corresponding measurement data can be used as an inlet condition for flow simulations of the test case, thus offering the possibility of adjusting the numerical calculations with the correct inlet conditions. Figure 3 shows a photo of the measurement with the 3D hot-wire probe downstream of the flow screens of the test rig and, as an example, the resulting turbulence intensity in the measurement plane for a volume flow of 0.1 m^3/s. Due to the flow control devices of the test rig, turbulence levels of less than 1% are present downstream of the flow screens. Both velocity and turbulence distribution show a homogeneous profile.

Generation of disturbed inflows and flow field characterisation

Downstream of the flow screens of the test rig is an inlet nozzle which reduces the cross-section area to the inlet duct ($D = 158$ mm) of the centrifugal fan. Within this inlet duct it is possible to install various turbulence grids 130 mm upstream of the fan inlet to create perturbed inflow conditions for the centrifugal fan and study their influence on the sound radiation. In real-world applications, disturbed inflow conditions on the suction side of fans are created by pipe bends, throttle valves, heat exchangers or protective grids [12]. In order to simulate these different effects on the flow, a total of four turbulence grids and three velocity gradient grids were analysed and studied. All of the grids have a similar blockage rate of approximately 36% (+/- 1%). The flow fields downstream of the grids were measured using the 3D hot-wire technique with the same settings as for the measurements of the incoming flow profiles downstream of the flow screens of the test rig. The flow analyses for the seven grids and the free, undisturbed inflow were carried out for three volume flow rates (0.1 m^3/s,



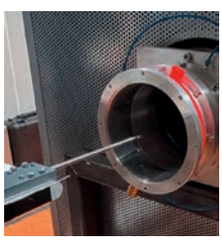
(a) Photograph of the measurement of the inlet profile.



(b) Global turbulence intensity downstream of the flow screen.

Figure 3: Representation of the measurement of the flow field downstream of the turbulence screens of the radial fan test rig using 3D hot-wire anemometry and turbulence distribution in the measuring plane for a volume flow rate of $0.1\,\mathrm{m}^3/\mathrm{s}$.

$0.28\,\mathrm{m}^3/\mathrm{s}$, $0.35\,\mathrm{m}^3/\mathrm{s}$) each. Examples of photographs of three grids and the turbulence intensities measured downstream are shown in Figure 4.



(a) Free Inflow.



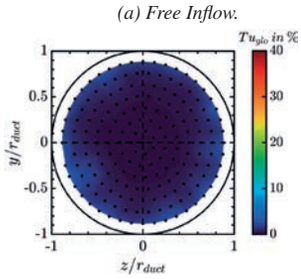
(b) Turbulence grid TG4.



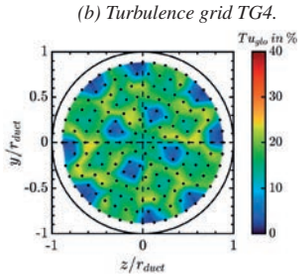
(c) Velocity gradient VG1.



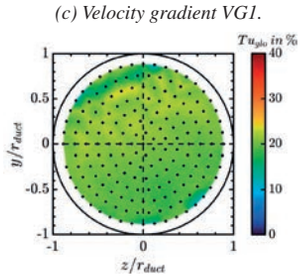
(d) Velocity gradient VG1.



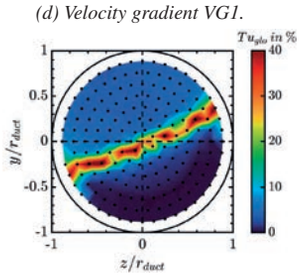
(e) Tu free inflow.



(f) TU TG4.



(g) TU VG1.



(h) TU VG3.

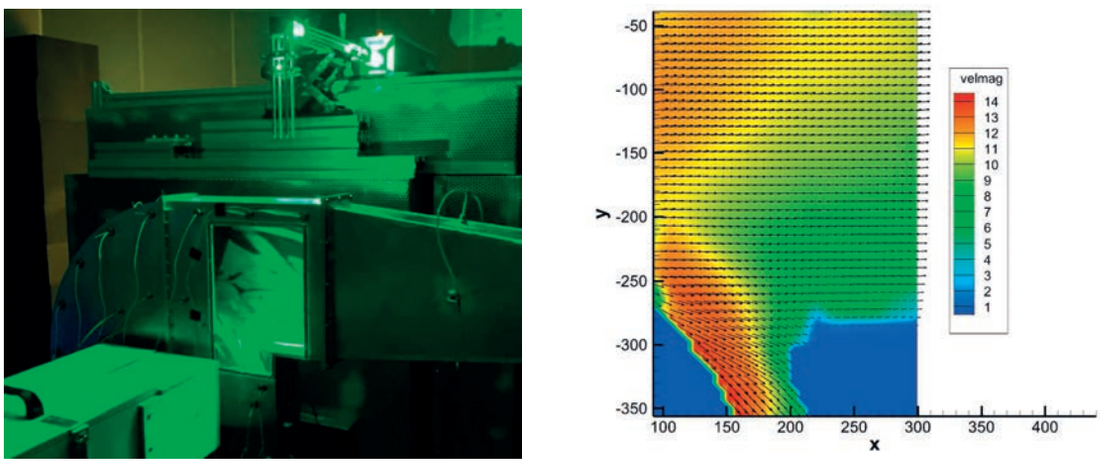
Figure 4: Examples of integrated turbulence and velocity gradient grids with corresponding turbulence intensity distributions downstream of the grids at a volume flow rate of $0.28\,\mathrm{m}^3/\mathrm{s}$.

The turbulence plot downstream of the flow grids shows that the flow field changes significantly compared to the free inflow (without disturbing installations in the duct). This increases the turbulence intensity and changes its spatial inhomogeneity, which in turn causes a change in the sound radiation of the fan [6], [13]. The measured data can be used as input conditions for flow simulations, which has the advantage that no flow grids need to be meshed and thus computing time can be saved.

PIV investigations of the outflow area

On the pressure side of the centrifugal fan, there are viewing windows inside the casing in the area of the casing tongue, which can be used for flow measurements. Tracer particles in the flow field were illuminated with a laser light sheet and the scattered light was recorded with a high speed camera. Figure 5 shows a photo of the PIV measurements [14] and the calculated flow vectors on the pressure

side of the fan. The PIV measurements were evaluated for the free inflow of the fan at a rotational speed of 1800 rpm for fourteen different volume flow rates on the characteristic curve. The measured data can be used to validate flow fields from simulations and provide information on the flow in the tongue area of the casing, which is an important source of noise in enclosed centrifugal fans [15].



(a) Photograph of the PIV-measurements.

(b) Velocity vector field from PIV data.

Figure 5: Photograph and measurement result of the PIV measurements in the area of the housing tongue of the centrifugal fan at a volume flow rate of $0.28\,\mathrm{m^3/s}$.

Static pressure measurements

The static pressure is determined by means of wall pressure taps at various measuring points on the test rig. At the volume flow nozzle at the inlet of the test rig, the volume flow rate is determined from the static pressure difference to the ambient pressure by means of a standardised nozzle according to DIN EN ISO 5801 [16]. In addition, the static pressure is measured in the duct in front of the centrifugal fan and directly in front of the fan blades on the suction side. The pressure loss of the turbulence grid that has been installed can be measured from the difference between these two pressure values. On the pressure side, there is a measuring location just downstream of the spiral housing. In addition, the static pressure inside the anechoic chamber is measured. All static pressures are measured in relation to the ambient pressure outside of the anechoic chamber. The pressure increase of the impeller can be determined from the difference between the static pressure directly at the impeller suction side and the pressure on the pressure side in the spiral casing. In order to take into account the influence of temperature fluctuations and density changes, the temperature is determined over time, both in the environment and inside the anechoic chamber. The measurements are carried out for a measurement time of 30 s each with a sampling rate of 1 kHz. The pressure measurements form the basis for the characteristic aerodynamic curve of the fan and were carried out for all the different inflow conditions, as well as for the free inflow at four different rotational speeds (1200 rpm, 1500 rpm, 1800 rpm, 2000 rpm).

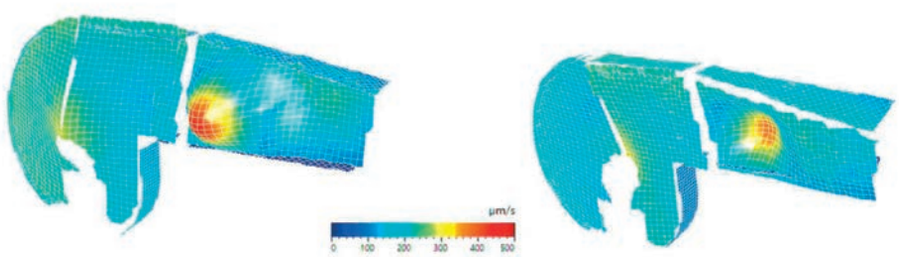
Recording of temporal pressure fluctuations

Inside the impeller, there are 15 miniature pressure sensors (Kulite) that can be used to analyse the time-varying pressure fluctuations directly on the blade surface. The sensors are positioned on both the pressure and suction sides of a fan blade and are distributed spatially so that there are sensors along the length of the blade from the leading edge to the trailing edge. The measurement data are available for a rotational speed of 1800 rpm under all eight different inflow conditions and for three volume flows ($0.1\,\mathrm{m^3/s}$, $0.28\,\mathrm{m^3/s}$, $0.35\,\mathrm{m^3/s}$). In addition to the 15 sensors inside the radial fan, 54 miniature sensors (Kulite) were mounted flush with the wall on the inside of the spiral housing at

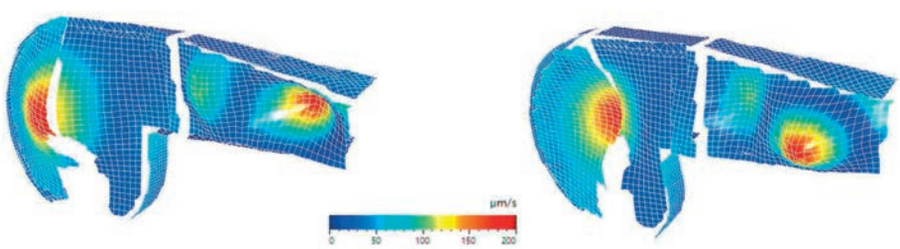
various positions. The measurement data were taken simultaneously with the microphone measurements on the outside of the housing at a sampling rate of 48 kHz for a duration of 30 s. Data for the pressure fluctuations on the inner wall of the housing are available for all operating points and inflow conditions examined. Pressure spectra can be derived from the transient pressure data, which are suited for validating flow simulations, but also provide insights into the localisation of sound sources.

Modal and operational mode analysis of the housing

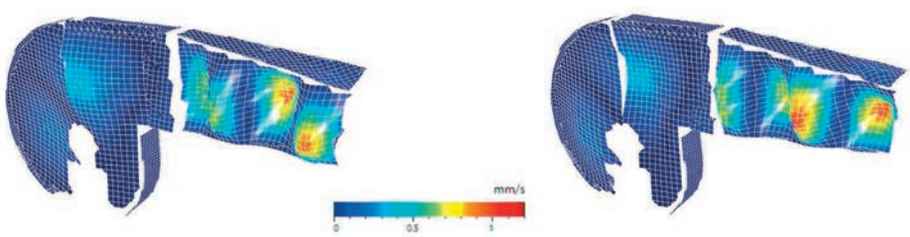
The rotation of the fan creates pressure fluctuations and acoustic sources within the flow field. The casing, which contains the acoustic and flow field generated by the fan, is excited to vibrate by these forces. This results in a fluid-structure-acoustic interaction. The vibration of the excited enclosure structure in turn induces sound waves in the external environment of the enclosure, resulting in sound radiation. This sound radiation is perceived by people in the vicinity. The sound emission of the structure depends on the excitation, but also on the properties of the structure itself (geometry, material, etc.). In order to help one better understand the structural mechanics of the enclosure under investigation, 3D laser scanning vibrometry (Polytec) measurements were carried out. On the one hand, a modal analysis of the enclosure was performed, where the eigenmodes of the system were determined while the excitation was performed with a modal hammer. Figure 6 shows selected mode images of the fan housing.



(a) Structure vibration at 103 Hz.



(b) Structure vibration at 200 Hz.



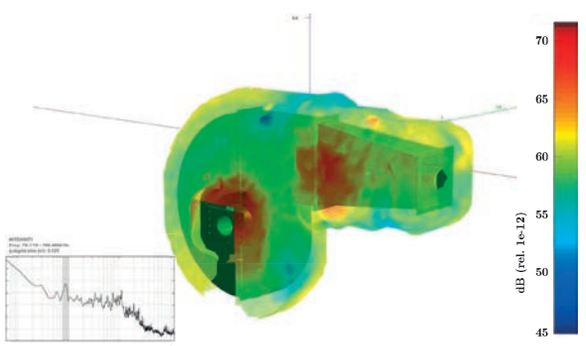
(c) Structure vibration at 334 Hz.

Figure 6: Exemplary mode formation of the radial fan housing at three different frequencies.

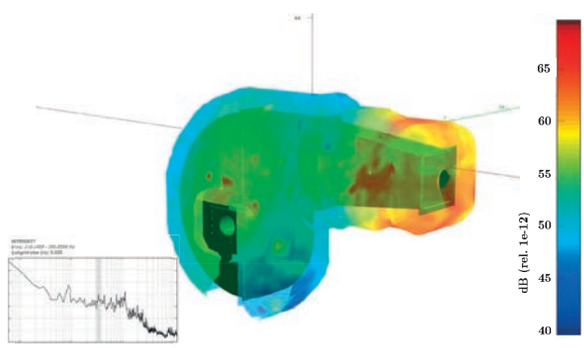
The analysis of the structural modes of the enclosure provides information about which parts of the sound pressure level spectrum can be directly attributed to the enclosure because its eigenmodes were excited. This data can also be used to validate numerical modal analyses. In addition to the pure modal analysis, an operating mode analysis was also carried out. For this purpose, the excitation was realised by the rotation of the fan. The analysis was performed at the design rotational speed of 1800 rpm and at undisturbed inflow for three volume flows rates ($0.1\,\mathrm{m}^3/\mathrm{s}$, $0.28\,\mathrm{m}^3/\mathrm{s}$, $0.35\,\mathrm{m}^3/\mathrm{s}$). As a result, velocities of the structure are given, which were phase-triggered to a specific rotational position of the fan. The results can be used as input parameters for numerical sound radiation simulations, such as the boundary element method [17], [18], but also to validate simulations of the fluid-structure-acoustic coupling from the flow field and the spiral-housing.

Sound intensity measurements

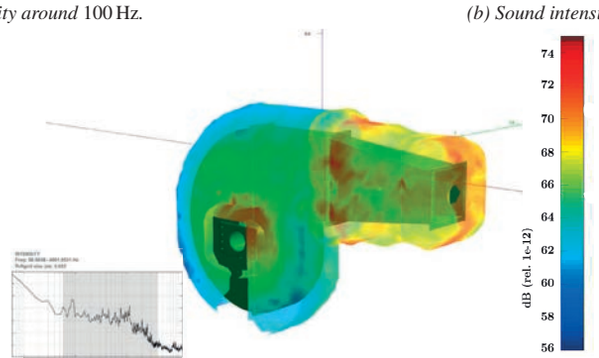
Using a sound intensity probe (Microflown), it is possible to determine not only the sound pressure but also the sound particle velocity vector. This measurement method thus offers the possibility to measure the sound intensity in the direct near-field of the centrifugal fan geometry. Figure 7 shows the sound intensity as an enveloping surface around the centrifugal fan housing for different frequency ranges. In combination with the modal analyses carried out, the strength and also the cause of the sound radiation can be better understood. For example, it clearly shows that at 100 Hz, sound radiation mainly occurs where the highest surface velocity of the structure is present. The sound intensity measurements also provide a good opportunity to validate the simulated sound radiation of the structure over an enveloping surface.



(a) Sound intensity around 100 Hz.



(b) Sound intensity around 350 Hz.



(c) Sound intensity over the entire frequency range from 55 Hz *to* 4 kHz.

Figure 7: Sound intensity around the radial fan housing for various frequency ranges. Operating point at $0.28\,\mathrm{m}^3/\mathrm{s}$ *at a rotational speed of* 1800 rpm *with free, undisturbed inflow. The small spectrum on the left of the images shows in grey the range that was taken into account for the sound intensity.*

The measurements were carried out at free inflow and design rotational speed for three volume flow rates ($0.1\,\mathrm{m}^3/\mathrm{s}$, $0.28\,\mathrm{m}^3/\mathrm{s}$, $0.35\,\mathrm{m}^3/\mathrm{s}$). In addition, measurements were carried out at the volume flow rate of $0.28\,\mathrm{m}^3/\mathrm{s}$ for the disturbed inflow with TG4 and VG3.

Free-field sound radiation

A total of 8 free-field microphones were positioned at various points within the anechoic room. The distance of each microphone to the housing surface was 500 mm. Figure 8 shows a photo of the microphone positions. For each operating point and each inflow condition, the sound radiation of the enclosed centrifugal fan was measured for 30 s at a sampling rate of 48 kHz. This means that narrowband spectra of the sound pressure are available at the respective microphone positions, although an overall sound pressure level can also be determined for each operating point. If the overall sound pressure levels are plotted over the respective volume flow rate of the operating point, the acoustic characteristic curve of the enclosed centrifugal fan can be specified in the same way as the aerodynamic characteristic curve. The narrowband spectra and the overall sound pressure level can be used to validate structural-acoustic simulations.

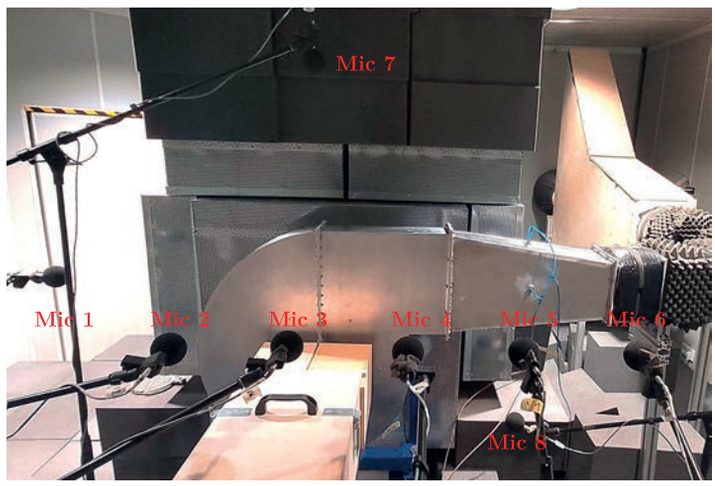


Figure 8: Photograph of the microphone setup for measuring the free-field sound radiation.

SUMMARY AND OUTLOOK

The paper presented an overview of the experimental investigations carried out on an enclosed benchmark centrifugal fan. The complete measurement data and geometry files are made available to the public and should serve to better understand the physical mechanisms in the fluid-structure-acoustic interaction of enclosed centrifugal fans. In addition, the data can be used to validate CFD, CAA and structural acoustic simulations. Besides the experimental data, high-resolution flow simulations are also carried out for the benchmark fan, which serve as the basis for the hybrid acoustic approach to calculate the source terms within the flow field. The acoustic data, as well as the fluid mechanical data, are used as excitation for a structural acoustic simulation, which allows a specific insight into the FSA interaction of the radial fan. Experimental data and CAD-files can be requested from the author F. Czwielong (felix.czwielong@fau.de) and will be published at the LSTM-homepage in 2025.

ACKNOWLEDGEMENT AND FUNDING

This research was funded in whole, or in part, by the Deutsche Forschungsgemeinschaft (DFG, German Research Foundation) under No. 468338100. The authors gratefully acknowledge the scientific support and HPC resources provided by the Erlangen National High Performance Computing Center (NHR@FAU) of the Friedrich-Alexander-Universität Erlangen-Nürnberg (FAU) under the NHR project b142dc. NHR funding is provided by federal and Bavarian state authorities. NHR@FAU hardware is partially funded by the German Research Foundation (DFG) – 440719683. This research was funded in whole, or in part, by the Austrian Science Fund (FWF) [I 5515-N].

BIBLIOGRAPHY

[1] F. Zenger, C. Junger, M. Kaltenbacher, and S. Becker, "A benchmark case for aerodynamics and aeroacoustics of a low pressure axial fan," SAE Technical Paper, Tech. Rep., **2016**.

[2] S. Schoder and F. Czwielong, *Dataset fan-01: Revisiting the eaa benchmark for a low-pressure axial fan*, arXiv preprint arXiv:2211.12014, **2022**.

[3] S. Schoder, C. Junger, and M. Kaltenbacher, *Computational aeroacoustics of the eaa benchmark case of an axial fan*, Acta Acustica vol. 4, no. 5, p. 22, **2020**.

[4] F. Czwielong, T. Uffinger, and S. Becker, *Controlled inflow conditions for radial fans-an aeroacoustic radial fan test rig*, in *15 th European Conference on Turbomachinery Fluid dynamics & Thermodynamics*, EUROPEAN TURBOMACHINERY SOCIETY, **2023**.

[5] T. Uffinger, F. Czwielong, A. Renz, *et al.*, *Development of a test rig for the investigation of flow-induced mechanisms of sound generation at radial fans*, Applied Acoustics vol. 211, p. 109 553, **2023**.

[6] T. Uffinger, *Strömungsakustik von Radialventilatoren unter kontrollierten Versuchsbedingungen*. Shaker Verlag, **2019**.

[7] T. Carolus, *Fans: aerodynamic design-noise reduction-optimization*. Springer Nature, **2023**.

[8] L. Bommes, *Ventilatoren*. Vulkan-Verlag GmbH, **2003**.

[9] W. Neise, *Messungen in strömungen*, Messtechnik der Akustik, pp. 643–712, **2010**.

[10] A. Guedel, *Design of terminating ducts for fan noise testing*, in *29th International congress and exhibition on noise control engineering*, **2000**, pp. 27–30.

[11] T. F. Geyer and E. Sarradj, *Trailing edge noise of partially porous airfoils*, in *20th AIAA/CEAS aeroacoustics conference*, **2014**, p. 3039.

[12] F. Czwielong, J. Soldat, and S. Becker, *On the interactions of the induced flow field of heat exchangers with axial fans*, Experimental Thermal and Fluid Science vol. 139, p. 110 697, **2022**.

[13] F. J. Krömer, "Sound emission of low-pressure axial fans under distorted inflow conditions," Ph.D. dissertation, Dissertation, Erlangen, Friedrich-Alexander-Universität Erlangen-Nürnberg . . ., **2018**.

[14] M. Raffel, C. E. Willert, F. Scarano, C. J. Kähler, S. T. Wereley, and J. Kompenhans, *Particle image velocimetry: a practical guide*. springer, **2018**.

[15] Y. Wei, L. Zhu, W. Zhang, and Z. Wang, *Numerical and experimental investigations on the flow and noise characteristics in a centrifugal fan with step tongue volutes*, Proceedings of the Institution of Mechanical Engineers, Part C: Journal of Mechanical Engineering Science vol. 234, no. 15, pp. 2979–2993, **2020**.

[16] Deutsche Norm DIN EN ISO 5801, International Organization for Standardization, *Industrial fans-performance testing using standardized airways*, **2007**.

[17] S. Kirkup, *The boundary element method in acoustics: A survey*, Applied Sciences vol. 9, no. 8, p. 1642, **2019**.

[18] A. Wurzinger, F. Kraxberger, P. Maurerlehner, *et al.*, *Experimental prediction method of free-field sound emissions using the boundary element method and laser scanning vibrometry*, in *Acoustics*, MDPI, vol. 6, **2024**, pp. 65–82.



1-WAY FSI SIMULATION APPROACH TO ASSESS LOW-PRESSURE AXIAL FAN AERODYNAMIC AND AEROACOUSTICS PERFORMANCE VARIATION

Juan David LAGUNA[1], Evangelos ANTONIOU[1] ,
Fabian QUINTERO[1] , Mario PESCE[1], Felix CZWIELONG[2],
Stefan SCHODER[3]

[1] *Dassault Systemes Deutschland GmbH, Meitnerstr. 8, 70563 Stuttgart, Germany*

[2] *Institute of Fluid Mechanics, FAU Erlangen-Nürnberg, Cauenstr. 4, 91058 Erlangen, Germany*

[3] *Institute of Fundamentals and Theory in Electrical Engineering, TU Graz, Inffeldgasse 18, 8010 Graz, Austria*

SUMMARY

Low-pressure axial fans are widely used for cooling purposes in the automotive industry. Despite their efficiency, these fans face high structural loads, which can degrade performance and increase noise due to changing operating conditions. Accurate predictions of these effects can be achieved through a Fluid-Structure Interaction (FSI) simulation. This paper introduces a one-way FSI using a high-fidelity LBM solver to predict the unsteady flow, with validation data from the European Acoustics Association (EAA). The surface pressure results are coupled with a Finite Elements Analysis (FEA) software to evaluate deformation and stress levels. The deformed fan geometry is re-simulated to analyze changes in aerodynamic and acoustic performance.

INTRODUCTION

Low-pressure axial fans are essential in several industrial sectors, finding extensive utilization in the aeronautical, high-tech, agricultural, and automotive fields. In the latter, low-pressure axial fans have been intensively used for cooling purposes not only of internal combustion engines but also recently to guarantee a safe and reliable temperature operation range of battery racks on electric vehicles.

While solidly providing the required mass flow for cooling, low-pressure fans are highly structurally loaded and produce undesirable noise. High-structural loading has a negative effect on the fan performance - torque and pressure variations – and hence on the noise radiation, because of changeable fan operating conditions. To timely assess the variation in fan performance as a result of structural and acoustic phenomena, reliable and accurate predictions can be achieved through simulation methods, including Fluid-Structure Interaction (FSI) and computational aeroacoustics (CAA).

Numerical solutions offer significant advantages by providing valuable information on axial fan performance when considering complex aeroacoustical and structural phenomena, thus reducing the time and cost associated with development. This is key to rapidly achieving compliance with certification standards and to be able to cope with a competitive market that demands high-quality products.

Within the scope of this publication, a one-way FSI simulation approach is presented, in which a high-fidelity Lattice-Boltzmann (LBM) based solver, PowerFLOW®, is employed to predict unsteady flow physics and flow-induced noise generation of a low-pressure axial fan. The recorded unsteady and time-averaged fan surface pressure results are subsequently transferred to a Finite Element Analysis (FEA) software, ABAQUS/CAE®, to quantify the levels of deformation and mechanical stress in the fan as a result of aerodynamic load. A new fan geometry model is generated with the predicted deformation. The model is simulated again with the LBM solver in order to assess the variation in the aerodynamic and acoustical performance of the fan. Initial aerodynamic and aeroacoustic performance measurements are provided by the European Acoustics Association (EAA) benchmark platform and are used for validation purposes [1], [2].

This paper is organized as follows: Section 1 provides a general overview of the Fluid Structure Interaction (FSI) simulation and methodology, including a short overview of the LBM and the Structural Solver numerical approaches. Section 2 introduces the EAA benchmark. Section 3 introduces the employed numerical setup for the aeroacoustic and the structural simulations, including aspects such as the resolution strategy and boundary conditions. In Section 4, a comparison of experimental and computational results for the fan's aeroacoustic performance is conducted, preceded by Section 5, where the 1-way FSI results are presented. To finalize, Section 6 addresses the conclusions and future perspectives concerned with the present study.

FLUID-STRUCTURE INTERACTION (FSI)

Fluid–structure interaction (FSI) refers to the interplay between a fluid flow and a rigid or flexible structure, whether the fluid is within or surrounding the structure [3]. It is an application which intrinsically combines fluid and structural physics. For the present case study, a sequential (one-way) FSI technique has been applied. In general, the results from an upstream simulation are mapped onto a downstream simulation. The upstream simulation relates in this case to the fluid domain, the downstream simulation comprises the structural domain. This technique is particularly suitable for uncoupled problems, where the deformation of the structure is expected to be small as a result of the impact of the flow on it.

In particular, for this case, the recorded surface pressure measurements from the transient LBM fluid simulation are mapped onto a separate FEA solver. Surface pressure measurements are recorded on the low-pressure fan blades using the geometry of the EAA benchmark test rig model. The mapping is performed by PowerEXPORT®, a software application of the PowerFLOW® suite that is used to interpolate surface measurements onto a finite element mesh. The structural model processed by the FEA software is based on Abaqus/Standard solver. The structural solver calculates the deformations resulting from the aerodynamic loading and, subsequently, the analyzed geometry is updated via script (the deformed fan blades) and simulated again with the LBM solver to account for variations on the aeroacoustical performance of the analyzed low-pressure fan.

The simulation workflow is outlined in Figure 1. A general overview of both fluid and structural solvers is presented in the following subsections.

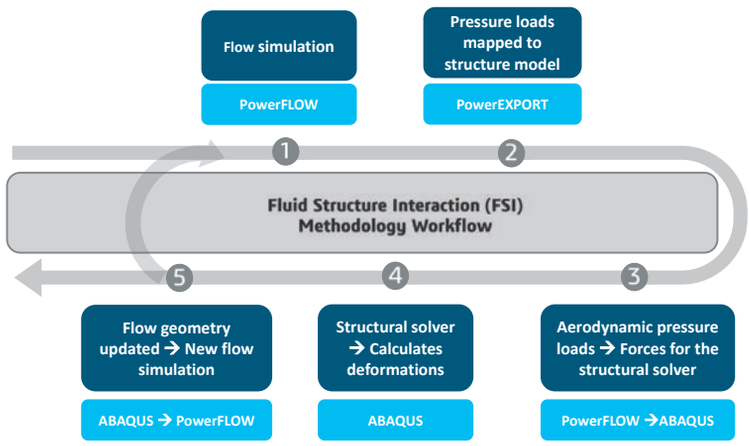


Figure 1: Fluid Structure Interaction (FSI) Methodology

Lattice-Boltzmann Method

This work utilizes the Lattice-Boltzmann Method (LBM), combined with a wall-modeled Very Large Eddy Simulation (VLES) approach, as implemented in the commercial CFD/CAA solver SIMULIA PowerFLOW®. This approach is employed to compute the unsteady flow around the fan and its resulting far-field noise radiation, without relying on coupling with an acoustic analogy-based solver.

The LBM scheme operates on a Cartesian mesh composed of cubic volume elements (voxels) arranged across various Variable Resolution (VR) regions. Solid surfaces are discretized within voxels intersecting the wall geometry using planar surface elements, known as surfels. No-slip and slip wall boundary conditions on each surfel are implemented using a boundary scheme based on particle bounce-back and specular reflection processes, respectively [4]. Due to its inherently unsteady and compressible nature, combined with its very low dispersive and dissipative properties [5], the LBM is particularly well-suited for aeroacoustic simulations. This allows Direct Noise Computations (DNC) to be performed without requiring coupling with an acoustic analogy.

Standard Structural Solver

The Abaqus / Standard solver uses finite element analysis (FEA) to simulate structural problems by discretizing the geometry into finite elements with defined material properties, boundary conditions and loading scenarios [6]. The solver effectively handles non-linearities, including material plasticity, large deformations, and complex contact interactions. Implicit time integration schemes are utilized to ensure stability and accuracy in static and dynamic analyses. Post-processing capabilities allow for detailed visualization and interpretation of results, such as stresses, strains, and displacements, facilitating in-depth analysis of structural behavior under various conditions [7].

EAA BENCHMARK TEST RIG

This section provides a brief overview of the EAA axial fan benchmark. The acoustic validation data were recorded in an upstream test chamber in compliance with the ISO-5801 [8] standard (see Figure 2). The test chamber resembles an anechoic environment with sound-absorbing walls. The test setup featured a 9-blade axial fan manufactured with the Vacuum casting polyurethane resin PX 223 HT (black) [9].

The fan has a diameter of 495 mm, with a tip clearance of 2.5 mm between the fan blades and the duct. At its design operating point, the fan operates at 1486 rpm, achieving a volumetric flow rate of 1.4 m³/s and a pressure difference of 125.6 Pa.

The measurement data analyzed in this study, including precise information about the microphone positioning are detailed in [1], include time signals recorded by seven 1/2-inch free-field microphones (type 4189-L-001, Brüel & Kjaer). These microphones were positioned horizontally in a semicircular arrangement with a radius of 1 m, located upstream of the fan's inlet nozzle. The microphone signals were recorded at a sampling frequency of 48 kHz over a measurement duration of 30 seconds.

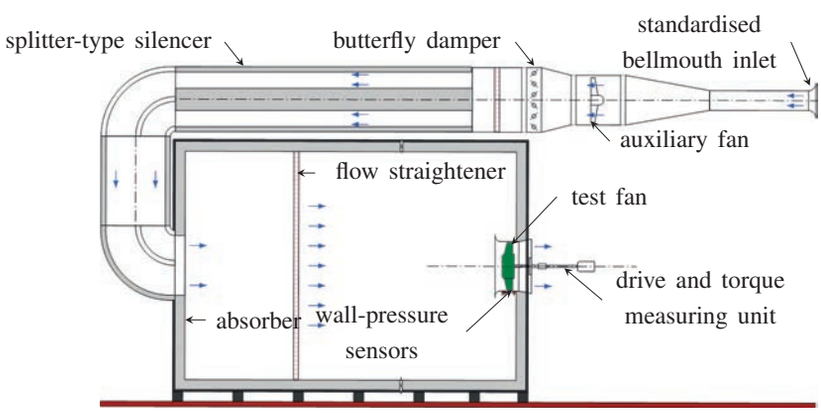


Figure 2: Experimental setup of the test chamber, adapted from [10].

NUMERICAL SETUP

Fluid Simulation

The computational setup replicates the experimental configuration and includes an upstream chamber, the 9-blade axial fan, a duct, a shaft with struts at the duct outlet, and a drive motor. To minimize acoustic reflections, large damping zones with progressively increasing viscosity were implemented between the settling chamber and the simulation boundaries. The computational domain was discretized using 11 Variable Resolution (VR) zones, each with a resolution doubling that of the adjacent area (see Figure 3). The finest grid resolution, 0.3125 mm, was applied to the tip gap and blade area on the suction side. The simulation was run for a total time of 0.8 seconds, corresponding to 20 fan revolutions, with 5 revolutions allocated to allow the fan's airflow performance to stabilize.

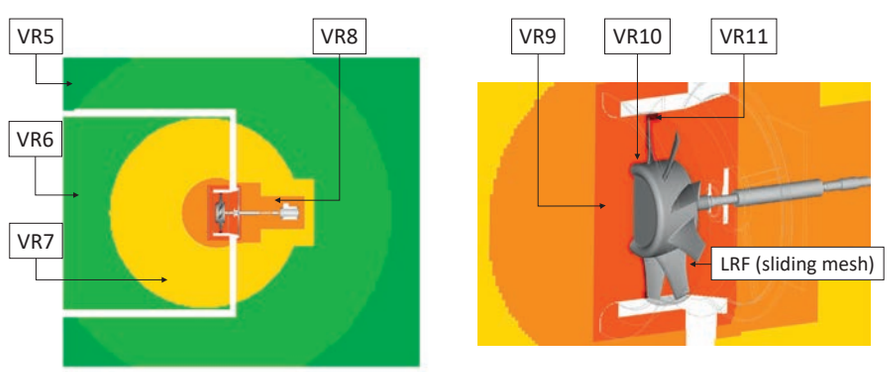


Figure 3: Variable Resolution (VR) regions, adapted from [11]

The recorded surface pressure measurements from the transient LBM fluid simulation have to be first mapped onto a suitable target mesh before being analyzed by the FEA solver. This is performed by PowerEXPORT®. Once both the CFD and the FEA meshes have been geometrically aligned, an interpolation takes place. The time-averaged values of the surface blade pressure are computed from the original transient results. The time-averaged surface measurements are subsequently transferred to the exterior faces of the volumetric elements of the FEA target mesh. The interpolation process generates an interpolation map for computing the values at the target element face centroids by spatially averaging, i.e., smoothing the LBM data measurements.

Structural Simulation

The tetrahedral volumetric mesh is imported. A Young's Modulus of 2300 MPa and a density of 1120 kg/m³ are specified on the FEA solver for the blade's material (polyurethane resin). The boundary conditions restrict the fan displacement in all cartesian directions and the previously interpolated time-averaged surface pressure results on the target FEA mesh are now used as input for the structural simulation. A single simulation step and time increment is configured. The deciding outputs for the FSI simulation are the mechanical deformations caused by the aerodynamic loading on the fan blades.

AEROACOUSTIC VALIDATION RESULTS

This section presents a comparison of experimental and computational results regarding aeroacoustic performance of the axial fan. This section serves the purpose of demonstrating the validity and accuracy of the simulation results when compared to the available experimental data of the EAA test rig. The microphones installed on the test-rig as well as on the simulation setup are placed upstream. These microphones provide valuable insights into sound generation and propagation phenomena. A total of seven microphones are symmetrically positioned with respect to the fan axis.

For microphone 1 (see Figure 4a) , a notable offset is observed in the sub-harmonics, both in amplitude and frequency. However, a better agreement is found for the second and third sub-harmonics, particularly for microphones closer to the fan axis. The proximity of microphone 1 to the wall is likely responsible for the larger discrepancies in the sub-harmonic humps.

For microphone 2 (see Figure 4b), while the frequency of the first sub-harmonic is under-predicted, its amplitude matches the experimental BPF well. Microphones 3 and 4 (see Figures 4c-d), located nearer to the axis of rotation, show good agreement with the experiment in both broadband and tonal components.

However, for all microphones - most notably for microphones 3 and 4 - the predicted first sub-harmonic hump (below 200 Hz) deviates from the experimental results in both frequency and amplitude. This discrepancy could be due to insufficient resolution, differences between the numerical setup and the experimental configuration, or inadequate simulation time to statistically capture low-frequency components. In general, the simulation and measurement results are consistent.

FSI RESULTS

The FEA solver predicted a maximum deformation of 0.2 mm at the tip of the fan blade under the specified loading conditions. This result was obtained using a mapping algorithm to interpolate the fluid forces, derived from the LBM simulation, onto the finite element mesh. The mapping process ensured an accurate transfer of surface pressures from the CFD model to the structural model, preserving the spatial resolution and fidelity of the original data. The spatial deformation on the low-pressure fan is displayed in Figure 5.

FAN 2025
Antibes - Juan-les-Pins (France), 9 - 10 April 2025

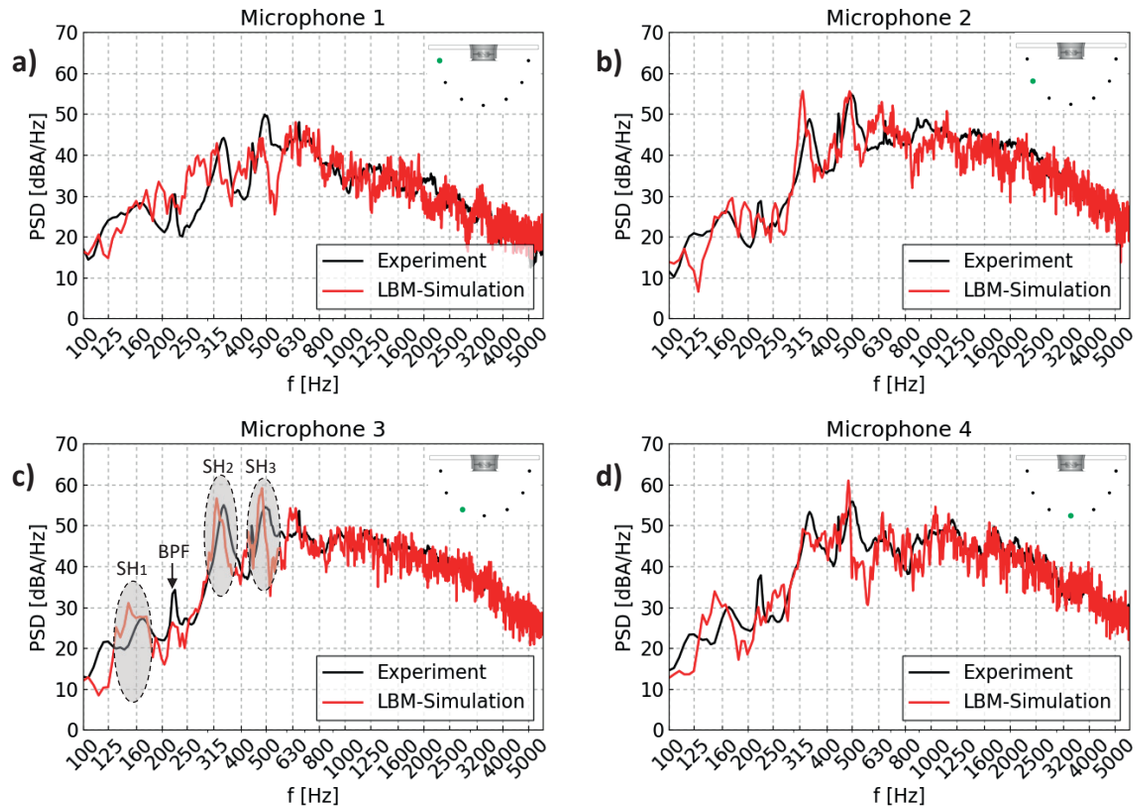


Figure 4: Comparison between numerical and experimental far-field noise power spectral density (PSD) at the microphones 1 (a), 2 (b), 3 (c) and 4 (d), adapted from [11]

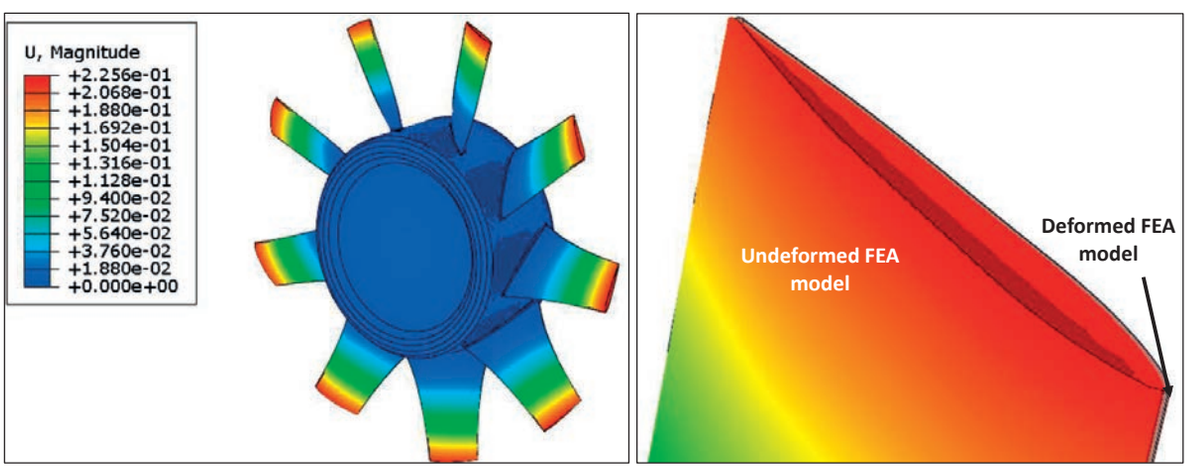


Figure 5: Displacement visualization as a result of aerodynamic loading on the low-pressure fan

The predicted deformation from the FEA computation is transferred to a deformed CFD mesh by using a mapping algorithm, in which the displacements of the FEA mesh nodes are assigned onto a CFD mesh suitable for the LBM solver. This mapping process ensures that the CFD mesh accurately reflects the structural deformations predicted by the FEA solver, thereby enabling the analysis of fluid-structure interaction (FSI). By aligning the CFD setup with the deformed geometry, the aerodynamic performance and flow characteristics can be reassessed under the influence of structural deformation by launching a new LBM run with the deformed CFD mesh.

This iterative approach provides a comprehensive understanding of how deformation affects fluid behavior. In this case and to specifically investigate the impact of fluid-structure interaction (FSI) on aerodynamic and acoustic performance, the deformed CFD mesh, which incorporates the structural deformations predicted by the FEA solver, was used to compute the resulting flow field and associated noise characteristics. The analysis mainly focused on comparing the resulting aerodynamic performance and the far-field noise power spectral density at selected microphones from both non-deformed and deformed fan geometries.

As before indicated, the structural deformations of the fan blade were minimal, with a maximum deformation of only 0.2 mm at the blade tip. The influence of these small deformations on the flow field and subsequent acoustic propagation are small but not negligible. Regarding the aerodynamic performance, the predicted pressure rise and fan efficiency for the deformed fan resulted in a slight relative deviation of 3% compared with the baseline non-deformed fan. The absolute values for the pressure rise and fan efficiency are presented in Table 1.

Table 1: Pressure rise and efficiency prediction for non-deformed and deformed fan

	Δp [Pa]	η [-]
Non-Deformed Fan	124.1	0.519
Deformed Fan	128.6	0.536

The computed far-field noise power spectral density at the installed microphone locations displays slight differences as well when compared to the baseline results obtained from the undeformed CFD mesh, especially on the low-frequency range, specifically below 250 Hz. The results as shown in Figure 6 on next page. This fact is relevant, since the blade passing frequency (BPF=225 Hz) is within this range, and although this frequency is not clearly captured by the simulation, it could be affected by the blades' deformation as a result of the aerodynamic loading. The position of the analyzed microphone plays a role as well on the results. The more exposed microphones, in this case microphones 3 and 4, display slightly higher deviations in the PSD for the specified low-frequency range when compared with the less exposed microphones 1 and 2. In general, both narrow and broadband components slightly differ over the whole frequency range, this is confirmed by the overall sound pressure level OSPL (100-6000 Hz) results in Table 2, which shows only a small absolute discrepancy between both data sets.

Table 2: OSPL (dBA) comparison (100-6000 Hz) at the indicated microphones.

Microphone	1	2	3	4
Non-Deformed Fan	71.8	78.4	80.1	80.5
Deformed Fan	71.4	78.7	79.8	79.8
Abs. Dev. (dBA)	-0.4	0.3	-0.3	-0.7

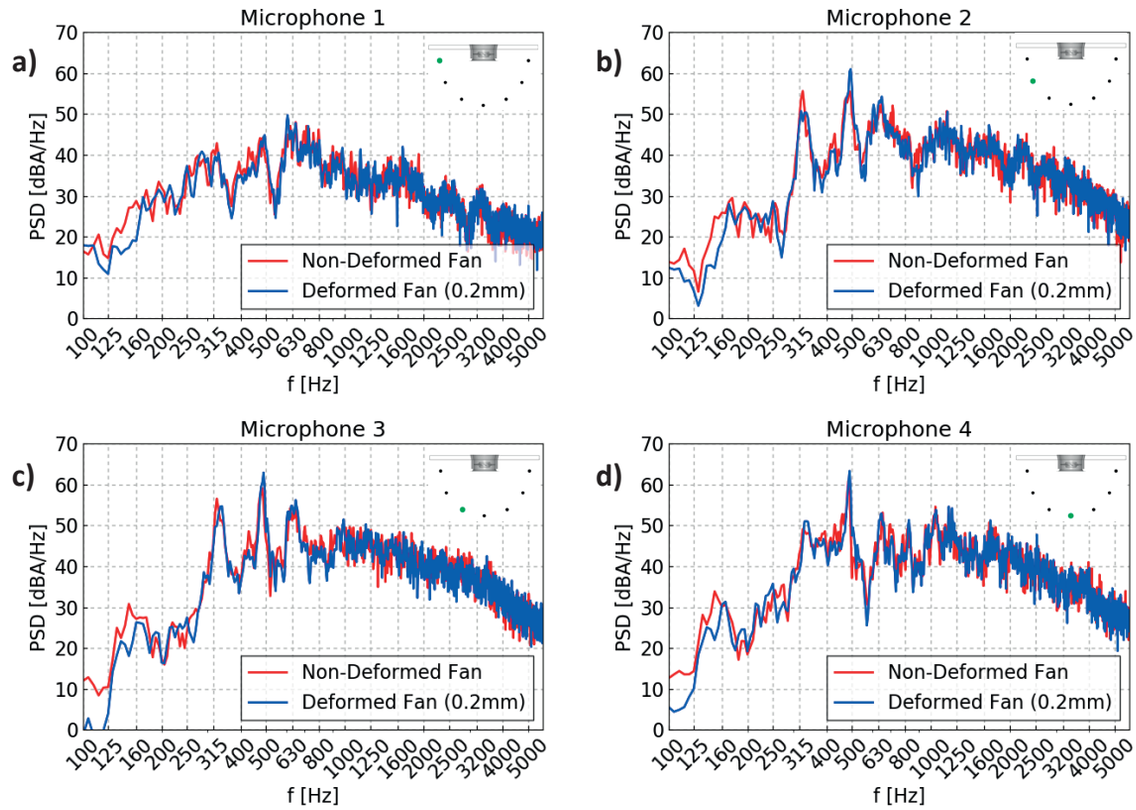


Figure 6: Far-field noise power spectral density (PSD) comparison for the non-deformed and the deformed fan at the microphones 1 (a), 2 (b), 3 (c) and 4 (d)

To summarize, the subtle variations in the microphone results underscore the relatively minor impact of the observed deformations on the aerodynamic and aeroacoustic performance of the fan, suggesting that, for this specific configuration, the structural integrity of the fan blade design is sufficient to maintain consistent acoustic characteristics under operational loads.

To further investigate the potential impact of structural deformation on the acoustic performance of the fan, additional analyses were conducted. These studies included a sensitivity analysis on the FEA mesh to ensure the accuracy and convergence of the computational results, particularly in capturing the interaction between deformation and fluid flow. Additionally, the influence of different material properties on the structural response were examined. By varying the material composition of the fan blade, the relationship between stiffness, deformation, and aeroacoustic performance can be better understood. These additional analyses aim to provide a more comprehensive assessment of how deformation characteristics affect the overall sound pressure level, enabling a deeper understanding of the role of FSI in acoustic optimization and design improvements.

A mesh independence study was carried out with three different seed markers on the structural solver. The non-deformed fan geometry was meshed with three different mesh densities, dictated by the separation of the seed markers. The seed markers were set to the values of 2 mm, 5 mm and 10 mm. Once meshed, the surface pressure from the CFD simulation was mapped to all three mesh qualities of the structural target mesh geometry. Finally, a structural simulation with particular attention to deformation as output variable was performed. The results indicated a maximal variation of 8% for the maximal local deformation, representing an absolute deviation just below 0.02 mm for the coarser mesh quality. Taking into account the minimal variation, no further LBM simulation was performed.

FAN 2025
Antibes - Juan-les-Pins (France), 9 - 10 April 2025

A last further analysis was performed, in which the influence of different material properties on the structural response of the blades was examined. For this specific case, a Young's Modulus of 230 MPa (an order of magnitude lower when compared with the original case) and the original density of 1120 kg/m³ were specified on the FEA solver for the blade's material. The computed maximal deformation is 10 times larger when compared with the original deformed fan geometry (2.0 mm vs. 0.2 mm). To complement, the computed far-field noise power spectral density from the LBM simulation at the different microphone locations is displayed in Figure 7 as follows.

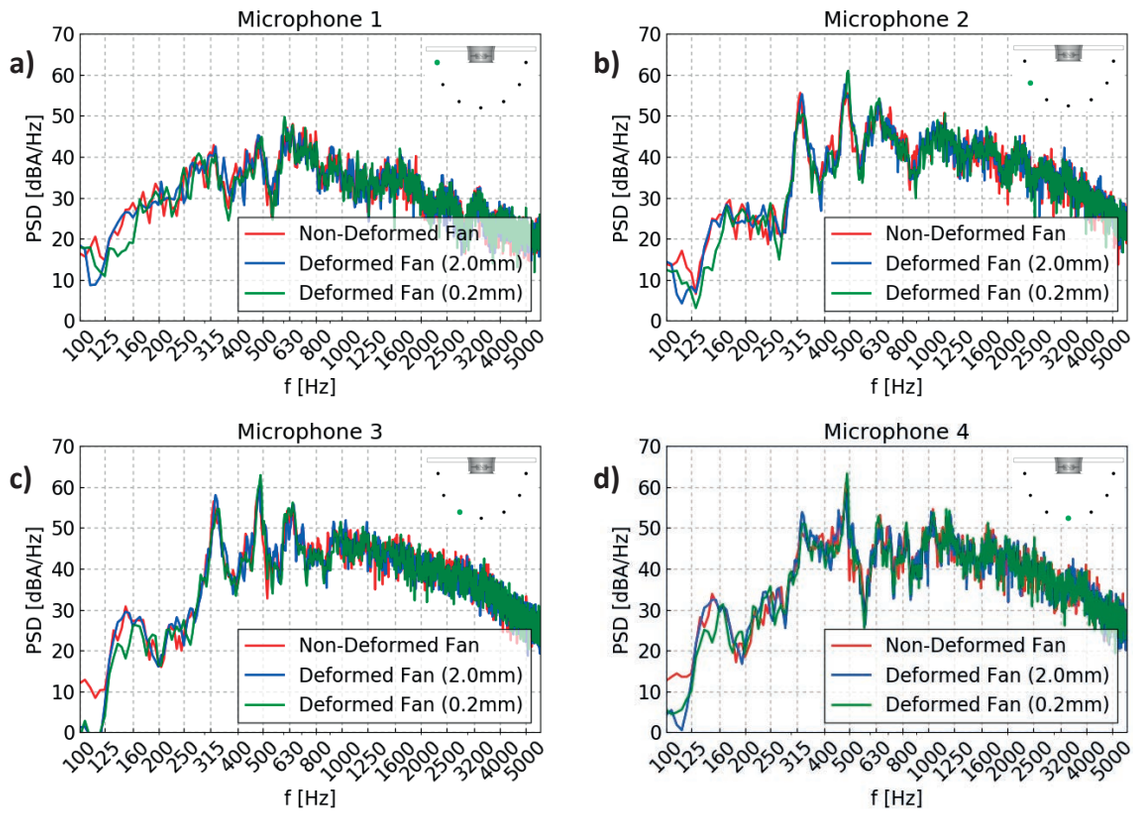


Figure 7: Far-field noise power spectral density (PSD) comparison for the non-deformed and deformed fan variants at the microphones 1 (a), 2 (b), 3 (c) and 4 (d)

Interestingly, although the given elastic material properties greatly differ from the original data sheet properties, the spectral variation repeatedly takes place for the low-frequency region of the PSD results, but with OSPL absolute variations not higher than 0.9%, very similar to the initial reported deformation of 0.2 mm.

CONCLUSIONS

This study demonstrated the integration of fluid-structure interaction (FSI) analysis into the evaluation of the aeroacoustic performance of a low-pressure fan. By mapping structural deformations predicted by finite element analysis (FEA) onto a computational fluid dynamics (CFD) mesh, the effects of deformation on the Power Spectral Density (PSD) of selected microphones were assessed. The results indicated that the small deformations observed in this specific configuration had a limited impact on acoustic performance, with only slight variations in the PSD at the installed microphone locations. These findings highlight the robustness of the current fan blade design under operational conditions.

However, the subtle influence of deformation observed here warrants a base for further analyses in order to understand its full implications across a wider range of conditions. In this regard, the mesh sensitivity study ensures an establishment of an optimal mesh resolution ranges for the FSI coupling process and its impact on aeroacoustic predictions. Additionally, the effect of varying material properties on structural response and noise generation could help to identify potential design improvements for enhanced performance.

In general, the integration of structural deformations into a CFD model enabled a more realistic representation of the fan's aeroacoustic behavior, as changes in blade geometry due to deformation can significantly influence the generation and propagation of noise. The presented results provided insights into the variation of the fan's acoustic signature caused by the coupled effects of fluid flow and structural deformation, highlighting the relevance of FSI modeling in accurately predicting noise levels for optimized design and noise mitigation strategies.

REFERENCES

[1] F. Zenger, C. Junger, M. Kaltenbacher, and S. Becker, *A benchmark case for aerodynamics and aeroacoustics of a low pressure axial fan*, SAE Technical Paper, **2016**.

[2] S. Schoder and F. Czwielong, *Dataset FAN-01: Revisiting the EAA Benchmark for a low-pressure axial fan*, **2022**.

[3] A. de Vaucorbeil, V. P. Nguyen, S. Sinaie, and J. Y. Wu, *Material point method after 25 years: Theory, implementation, and applications*, Advances in Applied Mechanics vol. 53, pp. 185–398, **2020**.

[4] H. Chen, C. M. Teixeira, and K. Molvig, *Realization of Fluid Boundary Conditions via Discrete Boltzmann Dynamics*, International Journal of Modern Physics C vol. **9**, no. 8, pp. 1281–1292, **1998**.

[5] G. A. Brès, F. Pèrot, and D. M. Freed, *Properties of the Lattice-Boltzmann Method for Acoustics*, in *Proceedings of the 15th AIAA/CEAS Aeroacoustics Conference (30th AIAA Aeroacoustics Conference)*, **2009**.

[6] L. Börgesson, *ABAQUS, in Developments in Geotechnical Engineering*. **1996**, vol. **79**.

[7] A. Khennane, *Introduction to Finite Element Analysis using MATLAB and Abaqus*. **2013**.

[8] *Fans-Performance testing using standardized airways*, ISO 5801:2017, **2017**.

[9] *Technical Data Sheet PX 223 HT Polyurethane Casting/Vacuum Casting System*, Axson Technologies, **2012**.

[10] E. Antoniou, A. Jantzen, G. Romani, S. Schoder, and F. Czwielong, *Numerical flow noise simulation of an axial fan with a Lattice-Boltzmann solver*, Aachen Acoustics Colloquium 2022, **2022**.

[11] E. Antoniou, G. Romani, A. Jantzen, F. Czwielong, and S. Schoder, *Numerical flow noise simulation of an axial fan with a Lattice-Boltzmann solver*, Acta Acustica vol. **7**, no. 65, **2023**.

H1 Fan Integration and Noise Prediction

11 April - 11:30 - Auditorium

Chairman: Andreas Lucius

List of papers

HVAC Noise Prediction Combining Power and Wave Based Methods

- Mats ÅBOM – KTH-Royal Inst. of Technology (Sweden)
- Mina Wagih NASHED – Ain Shams University (Egypt)
- Tamer ELNADY – Ain Shams University (Egypt)
- Ahmed KHAMIS – Ain Shams University (Egypt)

Aeroacoustics Analysis of Radiator Installation Effects in a Pulling Engine Cooling Module

- Francesco BELLELLI – Politecnico di Torino (Italy)
- Renzo ARINA – Politecnico di Torino (Italy)
- Stéphane MOREAU – Université de Sherbrooke (Canada)
- Francesco AVALLONE – Politecnico di Torino (Italy)

Aeroacoustic Investigation of a Charging Cabinet for Electrical Vehicles

- Safouane TEBIB – Université de Sherbrooke (Canada)
- Stéphane MOREAU – Université de Sherbrooke (Canada)
- Charles LUZZATO – Dassault Systemes Simulia Corp (USA)

Evaluation of Hybrid Computational Aeroacoustic Methods Applied to Automotive Cooling-Fans

- Debarshee GHOSH – Chalmers University of Technology (Sweden)
- Michail VOURAKIS – Chalmers University of Technology (Sweden)
- Alexander BOSTRÖM – Chalmers University of Technology (Sweden)
- Niklas ANDERSSON – Chalmers University of Technology (Sweden)
- Ashik ROY – Volvo Group Trucks Technology (Sweden)
- Sassan ETEMAD – Volvo Group Trucks Technology (Sweden)

HVAC NOISE PREDICTION COMBINING POWER AND WAVE BASED METHODS

Mats ÅBOM[1], Mina Wagih NASHED[2], Tamer ELNADY[2], Ahmed KHAMIS[2]

[1] *KTH-Dept. of Mechanics/MWL, 100 44 Stockholm, Sweden*

[3] *Ain Shams University, Faculty of Engineering, 11517 Cairo*

SUMMARY

This paper suggests a general formalism based on two-port networks. In the low frequency plane wave range a wave based formulation is used which is changed to a power based formulation in the mid- to high frequency range. The wave and power based models created for a given HVAC system are then used to compute the radiated sound power. By plotting the results from both wave and power based models together one can estimate the effect of low frequency system resonances on the radiated noise. This is an aspect overlooked in standard power based approaches and can be important to identify risks for low frequency noise issues. This paper will describe the background and theory behind the proposed method and present case studies.

INTRODUCTION

The nature of how acoustic waves propagate in a duct depends on the frequency with respect to the cross dimension of the duct [1]. Depending on the source and the duct network, the frequency range of interest is determined and a suitable modeling technique is selected. In general, the frequency range is divided into three regions [2], where each region has different wave propagation nature (low, mid and high frequency regions). The low-frequency (**LF**) region starts from zero frequency to the cut-on frequency of the first higher order mode. Only plane waves propagate in this region which makes the acoustic pressure constant over the cross section of the duct and makes the use of 1D modeling techniques possible. Nevertheless, due to the strong coupling between the source and the duct network in this region, small changes can have a large effect on the output acoustic power. In this region, a full wave-based description of the sound field is required for accurate wave propagation analysis [1].

The mid-frequency region starts after the low-frequency region and ends at (say) 2-3 times the cut-on frequency of the first higher order mode. Non-plane waves (or modes) start to propagate in this region which makes it more complicated to analyze. There is still a strong coupling between the source and the duct network requiring wave-based models including all propagating modes. By increasing the frequency, more modes start to propagate, and the wavelength becomes shorter. When the propagating modes are more than (say) ten, the wavelength becomes short compared to the duct cross section and modes well above their cut-on can be seen as plane waves or rays. This is where the high-frequency (**HF**) region begins. The coupling between the source and duct network is weak in this region and therefore it is suitable to use a power-based method [3,4]. A full modal description is not needed in this region, where the sound field is assumed to be composed of many rays

propagating in all directions over a half-sphere ("semi-diffuse field"). This makes ray tracing and statistical methods possible for the analysis [5].

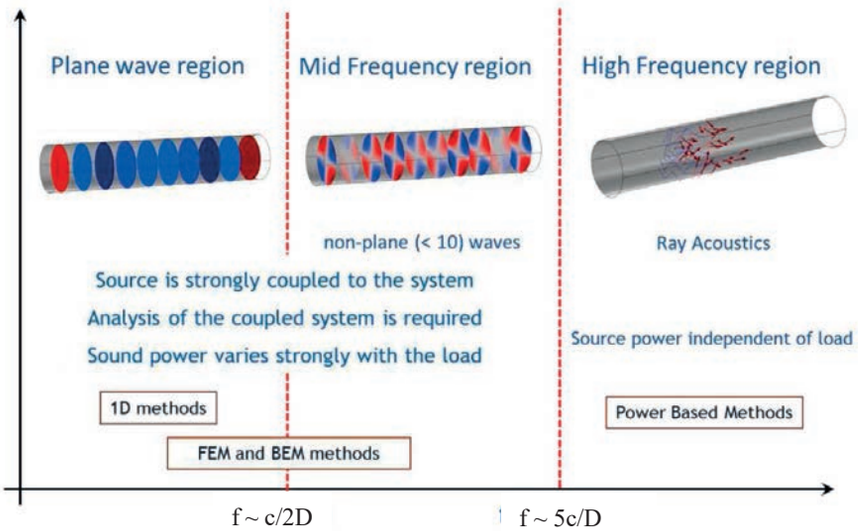


Figure 1. Frequency regions, c is the speed of sound and D is the duct diameter.

One important duct network is the HVAC system. Over the years the usage of HVAC systems has become common in private and public places as well as in vehicles. Regulations and standards have been formulated [3,4,6,7] to restrict noise levels in different spaces, indoor and outdoor and to ensure a comfortable acoustic environment. Moreover, standards may provide guidelines and calculation methods to be used in the design phase to achieve this goal. The standards define the background noise with respect to the activity and size of the space [6]. Regarding the HVAC systems design, the standards use the well-known approach called the Source-Path-Receiver method [8]. This method assumes that the cross dimension of the duct is much larger than the minimum propagating wavelength and is a power-based model.

THEORY

Sound transmission in complex duct networks can, assuming linear and time-invariant systems, be described using multi-port theory [9]. In the frequency domain this implies a matrix formulation where the size of the matrices is determined by the number of modes in the model. The matrices operate on state vectors that describe the acoustic state at duct cross-sections. Common choice of state variables are modal pressure and modal velocity along the duct axis, which leads to impedance or mobility based formalisms. A more general formulation is to use up- and downstream acoustic modal pressure amplitudes as state vectors, leading to a so called scattering-matrix formulation. An important advantage of the scattering-matrix formulation is that it is causal, i.e., it is never a problem to transfer data back to the time domain. In the low frequency plane wave range only one mode is propagating and the scattering-matrix order is 2x2 also called a two-port. A general formalism for analyzing complex two-port works, including sources anywhere in the system, has been presented by Glav and Åbom [10]. That paper demonstrated that a scattering-matrix formulation can be computationally the most efficient for large two-port networks.

In conclusion the multi-port method based on a scattering-matrix formulation is an efficient approach for creating wave-based models of complex duct networks. However, the method will in practice be limited to the plane wave and mid-frequency range up to (say) a maximum of ten propagating modes, see e.g., Refs. [11,12]. As in other areas of acoustics, e.g. room acoustics, it will make sense as the frequency increases to switch to power based methods. This implies using a frequency band average of the wave-fields to smooth out the effect of wave interference. The acoustic power in a duct cross-section W can be seen as the difference between up- (+) and downstream (-) propagating fields, i.e., $W = W_+ - W_-$. In analogy with the plane wave range where there are two state variables, e.g., propagating pressure amplitudes p_+, p_-, one can chose to define W_+, W_-, as

"state variables". In this way it could be possible to use two-port methods for the high frequency power based models. This topic will be investigated in the next sub-section.

Power based Two-Ports

To extend the frequency range of the two-port method to also cover the high-frequency region where many waves (modes) are cut-on, the two-port method needs to be reformulated. In the high-frequency region the coupling between the source and a system is weak and can be neglected, which makes it convenient to use the acoustic power (W) as state variable instead of acoustic pressure (p) [2,5]. In this section, starting from the multi-port model for a ducted element [9], a derivation of the power-based two-port formulation will be presented.

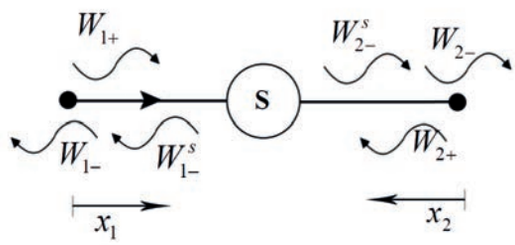


Figure 2. Power based two-port element.

Assuming a multi-port element with one inlet and one outlet, where the inlet and outlet are numbered 1 and 2 respectively (see Figure 2). The multi-port can be described in the frequency domain using Equation 1

$$\begin{pmatrix} \mathbf{P}_{1-} \\ \mathbf{P}_{2-} \end{pmatrix} = \underbrace{\begin{bmatrix} \mathbf{R}_{11} & \mathbf{T}_{12} \\ \mathbf{T}_{21} & \mathbf{R}_{22} \end{bmatrix}}_{\mathbf{S}} \begin{pmatrix} \mathbf{P}_{1+} \\ \mathbf{P}_{2+} \end{pmatrix} + \begin{pmatrix} \mathbf{P}_{1-}^{s} \\ \mathbf{P}_{2-}^{s} \end{pmatrix}, \tag{1}$$

where $\mathbf{P}_{n+/-}$ is a vector of complex modal acoustic pressure amplitudes (n =1,2), **S** is a scattering-matrix (**R** and **T** are reflection & transmission matrices, respectively), the sub-scripts +/- denote waves moving in/out from the system and the super-script s denotes a source. As the first step in the derivation of a power-based model new state variables related to acoustic power [13] are introduced

$$\Pi_{n\pm,i} = \sqrt{\frac{\alpha_n}{Z_n}} \left(\frac{1-M_n^2}{1 \mp \alpha_{n,i} M_n} \right) P_{n\pm,i}, \tag{2}$$

where Z_n is the duct plane wave impedance, M_n is the Mach number, $P_{n\pm,i}$ is the complex pressure amplitude (RMS-value) for the i:th mode and

$$\alpha_{n,i} = \sqrt{1 - \left(k_{n,i} c_n / \omega \right)^2 \left(1 - M_n^2 \right)}, \tag{3}$$

where $k_{n,i}$ is the transverse wave number of the i:th mode, c_n is speed of sound and ω the angular frequency. Note that it is assumed that only cut-on or propagating modes [1] are included in the formulas above. The incident and reflected acoustic power for the i:th mode can finally be calculated using the relation

$$W_{n\pm} = \mathbf{\Pi}_{n\pm}^{\dagger} \mathbf{\Pi}_{n\pm}, \tag{4}$$

where $(...)^{\dagger}$ is the complex conjugate transpose, and it is assumed that the modes form an orthonormal system.

The multi-port in Eq. 1 can now be transformed into the new power-based state variables

$$\begin{pmatrix} \mathbf{\Pi}_{1-} \\ \mathbf{\Pi}_{2-} \end{pmatrix} = \begin{bmatrix} \mathbf{R}_{11}^{\Pi} & \mathbf{T}_{12}^{\Pi} \\ \mathbf{T}_{21}^{\Pi} & \mathbf{R}_{22}^{\Pi} \end{bmatrix} \begin{pmatrix} \mathbf{\Pi}_{1+} \\ \mathbf{\Pi}_{2+} \end{pmatrix}, \tag{5}$$

where $\mathbf{R}_{mn}^{\Pi}$ and $\mathbf{T}_{mn}^{\Pi}$ are reflection & transmission matrices relative the new state variables.

Equation 5 implies that

$$\mathbf{\Pi}_{1-} = \mathbf{R}_{11}\mathbf{\Pi}_{1+} + \mathbf{T}_{12}\mathbf{\Pi}_{2+}, \tag{6}$$

where from now on the superscript Π is dropped on **R** and **T**. Using Equation 4 the power propagating out from side 1 is

$$\begin{aligned} W_{1-} &= \mathbf{\Pi}_{1-}^{\dagger}\mathbf{\Pi}_{1-} = \left(\mathbf{R}_{11}\mathbf{\Pi}_{1+} + \mathbf{T}_{12}\mathbf{\Pi}_{2+}\right)^{\dagger}\left(\mathbf{R}_{11}\mathbf{\Pi}_{1+} + \mathbf{T}_{12}\mathbf{\Pi}_{2+}\right) = \\ &= \mathbf{\Pi}_{1+}^{\dagger}\mathbf{R}_{11}^{\dagger}\mathbf{R}_{11}\mathbf{\Pi}_{1+} + \mathbf{\Pi}_{1+}^{\dagger}\mathbf{R}_{11}^{\dagger}\mathbf{T}_{12}\mathbf{\Pi}_{2+} + \mathbf{\Pi}_{2+}^{\dagger}\mathbf{T}_{12}^{\dagger}\mathbf{R}_{11}\mathbf{\Pi}_{1+} + \mathbf{\Pi}_{2+}^{\dagger}\mathbf{T}_{12}^{\dagger}\mathbf{T}_{12}\mathbf{\Pi}_{2+}. \end{aligned} \tag{7}$$

When power-based methods are used in other areas such as room acoustics [2], the equations are applied in frequency bands (1/3 octave or 1/1 octave). Here Equation (7) will be used similarly in frequency bands. The first and last terms are real-valued and positive (>=0), while the second and third (cross-terms) are complex valued. Since the phase for the second and third terms will vary with frequency, these terms will tend to zero when added over a band. This implies that the frequency band version of Equation (7) is

$$W_{1-,b} \approx \left\langle \mathbf{\Pi}_{1+}^{\dagger}\mathbf{R}_{11}^{\dagger}\mathbf{R}_{11}\mathbf{\Pi}_{1+} \right\rangle_b + \left\langle \mathbf{\Pi}_{2+}^{\dagger}\mathbf{T}_{12}^{\dagger}\mathbf{T}_{12}\mathbf{\Pi}_{2+} \right\rangle_b, \tag{8}$$

where the subscript b denotes a sum over the frequencies in the band and it is assumed that: $\left\langle \mathbf{\Pi}_{1+}^{\dagger}\mathbf{R}_{11}^{\dagger}\mathbf{T}_{12}\mathbf{\Pi}_{2+} \right\rangle_b \approx \left\langle \mathbf{\Pi}_{2+}^{\dagger}\mathbf{T}_{12}^{\dagger}\mathbf{R}_{11}\mathbf{\Pi}_{1+} \right\rangle_b \approx 0$.

The power reflection and transmission factors are now introduced based on

$$\begin{cases} R_{11}^{W} = \dfrac{\left\langle \mathbf{\Pi}_{1+}^{\dagger}\mathbf{R}_{11}^{\dagger}\mathbf{R}_{11}\mathbf{\Pi}_{1+} \right\rangle_b}{\left\langle \mathbf{\Pi}_{1+}^{\dagger}\mathbf{\Pi}_{1+} \right\rangle_b} \\ T_{12}^{W} = \dfrac{\left\langle \mathbf{\Pi}_{2+}^{\dagger}\mathbf{T}_{12}^{\dagger}\mathbf{T}_{12}\mathbf{\Pi}_{2+} \right\rangle_b}{\left\langle \mathbf{\Pi}_{2+}^{\dagger}\mathbf{\Pi}_{2+} \right\rangle_b} \end{cases}. \tag{9}$$

The reflection and transmission factors defined in the above equation will depend on the modal distribution. The assumption of equal modal energy for the propagating waves in the same band is commonly used in duct acoustics [5]. Combining Equations (8) and (9) gives

$$W_{1-,b} \approx R_{11}^{W}\left\langle \mathbf{\Pi}_{1+}^{\dagger}\mathbf{\Pi}_{1+} \right\rangle_b + T_{12}^{W}\left\langle \mathbf{\Pi}_{2+}^{\dagger}\mathbf{\Pi}_{2+} \right\rangle_b = R_{11}^{W}W_{1+,b} + T_{12}^{W}W_{2+,b}. \tag{10}$$

Similarly, an equation for $W_{2-,b}$ can be deduced and then together with $W_{1-,b}$ formulated in matrix form

$$\begin{pmatrix} W_{1-} \\ W_{2-} \end{pmatrix}_b = \begin{bmatrix} R_{11}^{W} & T_{12}^{\Pi} \\ T_{21}^{W} & R_{22}^{W} \end{bmatrix}\begin{pmatrix} W_{1+} \\ W_{2+} \end{pmatrix}_b, \tag{11}$$

where R_{ij}^{W} and T_{ij}^{W} are the power-based transmission and reflection factors defined as shown in Equation (9). Formally Equation (11) can be extended to also include sources in the two-port by adding an extra term

$$\underbrace{\begin{pmatrix} W_{1-} \\ W_{2-} \end{pmatrix}}_{\mathbf{W}_-} = \underbrace{\begin{bmatrix} R_{11}^{W} & T_{12}^{\Pi} \\ T_{21}^{W} & R_{22}^{W} \end{bmatrix}}_{\mathbf{S}}\underbrace{\begin{pmatrix} W_{1+} \\ W_{2+} \end{pmatrix}}_{\mathbf{W}_+} + \underbrace{\begin{pmatrix} W_{1-}^{s} \\ W_{2-}^{s} \end{pmatrix}}_{\mathbf{W}^s}. \tag{12}$$

Equation (12) is a general power-based two-port where **S** is the scattering matrix with reflection and transmission factors and $\mathbf{W}^s$ is a source vector. Note that here and from now on the sub-script b for band is

dropped. The two-port element can be used to simulate any element with two openings in a duct network, see Figure 2. Besides the two-port, a similar element with just one opening or a one-port is used to simulate network boundaries (terminations). The one-port is defined using a source strength and a reflection factor.

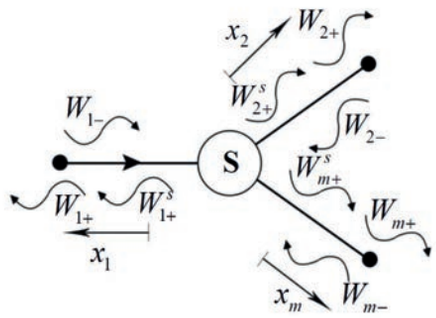


Figure 3. Power-based multi-port node, the number of ports corresponds to the number (m) of ducts connected. Note the positive direction is defined opposite to the two-ports

In a duct network the two-port elements are connected at branch points or nodes. These nodes can be seen as multi-ports scattering the incident sound power (see Figure 3). One can also include sound generation, e.g., from flow noise, at a node. In analogy to Equation (12) one can now define a power-based scattering-matrix also for a node (n).

$$\begin{pmatrix} W_{1+} \\ W_{2+} \\ . \\ . \\ W_{m+} \end{pmatrix} = \underbrace{\begin{bmatrix} S^n_{11} & S^n_{12} & . & . & S^n_{1m} \\ S^n_{21} & S^n_{22} & . & . & S^n_{2m} \\ . & & & & . \\ . & & & & . \\ S^n_{m1} & S^n_{m2} & . & . & S^n_{mm} \end{bmatrix}}_{\mathbf{S}^n} \begin{pmatrix} W_{1-} \\ W_{2-} \\ . \\ . \\ W_{m-} \end{pmatrix} + \begin{pmatrix} W^s_{1+} \\ W^s_{2+} \\ . \\ . \\ W^s_{m+} \end{pmatrix}. \tag{13}$$

Simple formulas for power based scattering-matrices $\mathbf{S}^n$ at nodes neglecting the effect of reflections as in ASHRAE and VDI standards can be found in Refs. [14]. By connecting two-ports and one-ports using multi-port nodes, the full network is constructed. A complete network equation can then be assembled using the formalism proposed by Glav and Åbom [9]. Equation (14) shows the network equation where $\mathbf{S}^c$ is a tridiagonal matrix containing all two-port, $\mathbf{S}^n$ are node matrices, $\mathbf{G}^n$ the projection matrices where each element selects (0/1) the two-ports connected to a certain node n and $\mathbf{W}^{c,s}_-$ & $\mathbf{W}^{s,n}_+$ represent the power radiated by all two-ports and nodes, respectively.

$$\left[\sum_n \left(\mathbf{G}^n - \mathbf{S}^n\mathbf{G}^n\mathbf{S}^c\right)\right]\mathbf{W}^c_+ = \left[\sum_n \mathbf{S}^n\mathbf{G}^n\right]\mathbf{W}^{c,s}_- + \sum_n \mathbf{W}^{s,n}_+. \tag{14}$$

The summation is over all the nodes (n) to assemble the system matrix from which the distribution of incident sound powers $\mathbf{W}^c_+$ can be solved. Once this is known, the outgoing sound powers are obtained from the two-port Equation (12) applied to all two-ports.

A COMPLETE TWO-PORT MODEL

The introduction of power based two-ports makes it possible to create network models that can capture the entire frequency range, i.e., from plane waves (LF) up to the range with many propagating modes (HF). The same two-port network is used and formally the complete network equation (Eq. 14) looks the same for both cases. The difference is the matrices used in the model, which are complex valued to describe the wave based plane wave range and real valued for the power based model.

FAN 2025
Antibes Juan-les-Pins (France), 9 – 11 April 2025

SIDLAB HF&LF

By extending the existing code SIDLAB HF [14] (power-based two-ports), including wave based models for all elements, a complete two-port code SIDLAB HF&LF has been created. SIDLAB HF is based on a combination of models from two standards (ASHRAE and VDI [3,4,7,8]) to capture as many cases as possible. As in the standards the effects of reflections are neglected and the analysis is done in octave bands. To create SIDLAB HF&LF wave based two-ports models from the LF code SIDLAB [15] have been added. Sources (fans & flow separation) are included based on sound power, either as user defined data or via models provided by the standards. For the LF range it is assumed that the sources correspond to dipoles and the sound power data is converted to a dipole force. Since the LF part of the analysis will be done in narrow band the HF source data is converted assuming a white noise spectrum.

To create a model a given system is first split into two-port elements and a network is constructed using SIDLAB. Based on the network two sets (LF & HF) of the network equation (Eq. 14) can be created and solved. The LF model is based on narrow band and is used up to the octave band where cut-on of a higher mode has occurred in all elements. The LF narrow band result is finally converted to octave bands and presented together with the HF result.

Two test cases

The complete two-port model is evaluated in two real cases. Case 1: a large industrial muffler; Case 2: HVAC duct network supplying two rooms in a building. These two cases are selected as the network includes both reflective and dissipative elements, and the duct dimensions and source frequency range increase the importance of LF range.

Case 1: Industrial muffler

The muffler is connected to a large diesel engine used for power generation. Large internal combustion engine noise contains low frequency components with high amplitudes. In addition, since modern high performance diesel engines are turbo-charged, there will also be significant high frequency noise. Unlike traditional exhaust silencers (e.g., on cars) the size of the machine and muffler for this case calls for an analysis including both LF and HF. Figure 4 shows the muffler drawing and the resulting two-port network with 11 elements. The muffler consists mainly of circular pipes at the inlet and outlet, two empty chambers that are treated as plenums, and a lined duct near to the exit pipe. The pipe diameters are between 200 mm to 540 mm, the diameter of chambers is about 950 mm and total length of the muffler is about 3500 mm. In Figure 5 the computed Insertion Loss (IL) is presented.

The results show that the plan wave limit is in 250 octave band, where the Insertion Loss (IL) of the low and high frequency modeling is the same. Moreover, the HF IL is lower than LF IL which is expected as the HF modeling ignores the reflections and resonances.

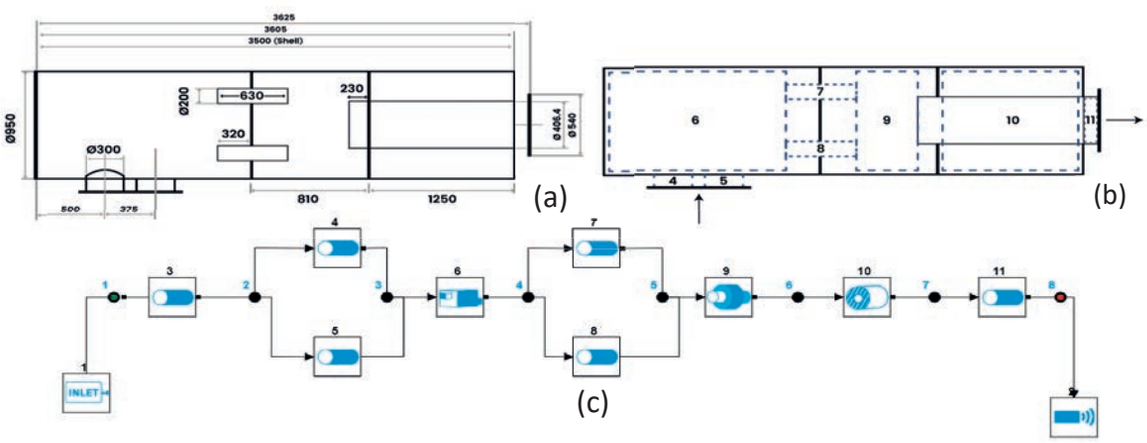


Figure 4. Industrial muffler, a) muffler drawing, b) muffler divided into two-port elements, and c) SIDLAB network.

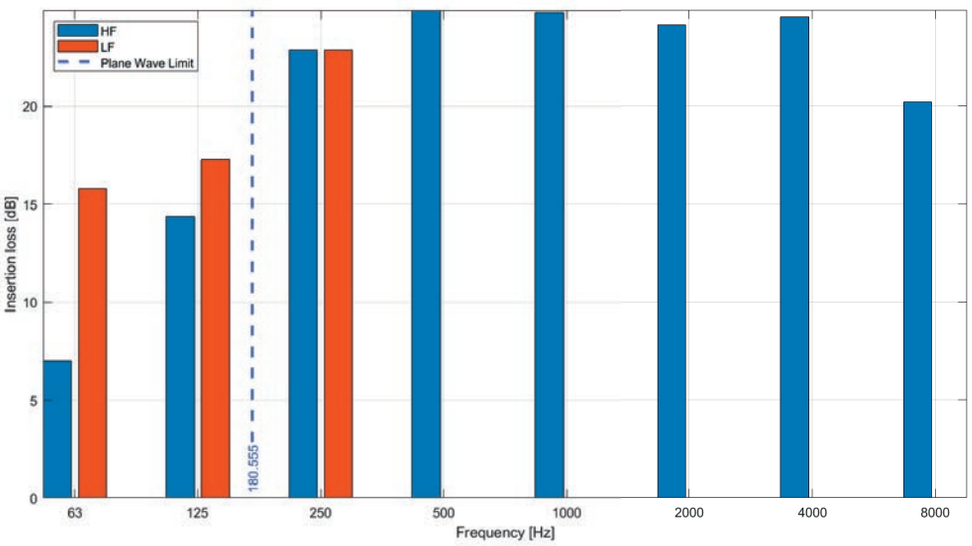


Figure 5. Case I: Insertion loss for industrial muffler.

Case 2: HVAC system

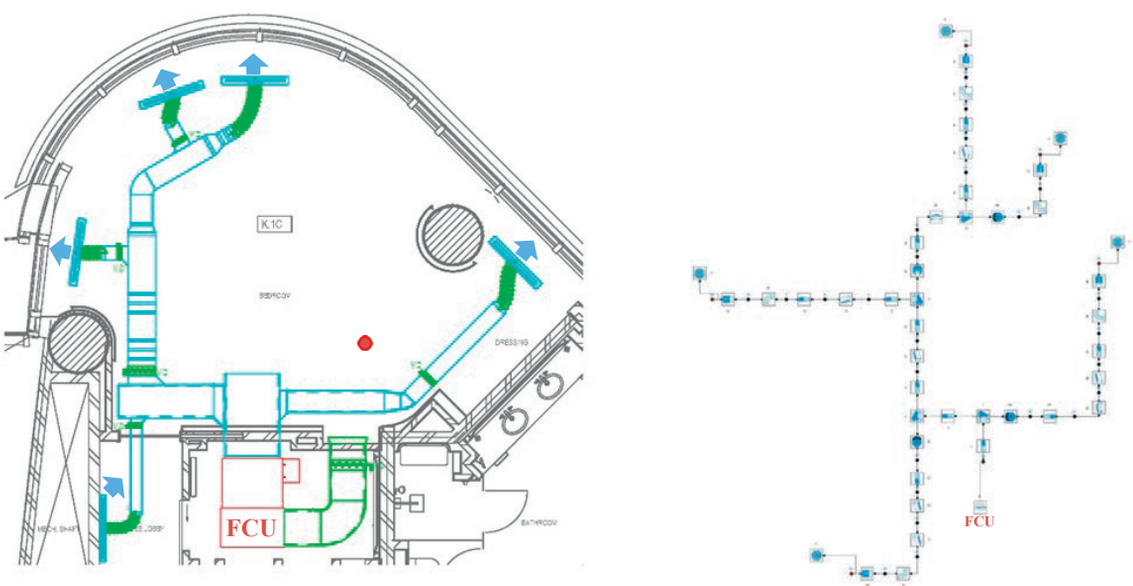


Figure 6. Drawing of the HVAC system analyzed and the corresponding SIDLAB two-port network. The red point marks the reference point where the SPL was measured.

The HVAC system analyzed here exists in apartments on the 59th floor in the iconic tower New Cairo. The system is supplied with a Fan Cooling Unit (FCU) that supplies two rooms. Figure 6 shows a drawing of the system in one of the rooms. The two-port network (see Figure 6) is built in SIDLAB and consists of 44 elements. The duct network starts with a fan source with octave band sound power levels based on manufacture data. The network splits into five branches where one branch supplies one room and four other branches supply another room. The network consists mainly of lined ducts, volume dampers, flexible ducts, branching and supplying grills. The average duct dimensions at the main branches are 400 x 200mm, while the supplying branch is 250 x 200mm. The lining is 1 inch in all ducts, the volume damper flow generated noise is from manufacture data, while the supplying grill flow noise is estimated based on standard models. Moreover, the room reverberation time is set based on the room furnishing at the measurement time. The SPL is predicted at

the red point shown in Figure 6 at 1.5 m above the floor. Then NC level [6] is calculated using only HF modeling and by using a combined LF&HF modeling. As shown in Figure 7 the plane wave limit is between the 125 and 250 Hz bands, therefore it is safer to assume the 125 Hz as the LF limit. The result shows that the NC level is 40 when using HF modeling for the entire frequency range, but the NC drops to 34 when using a mixed two-port modeling (HF&LF) technique. This result agrees much better with the on-site measurements of SPL performed in the room.

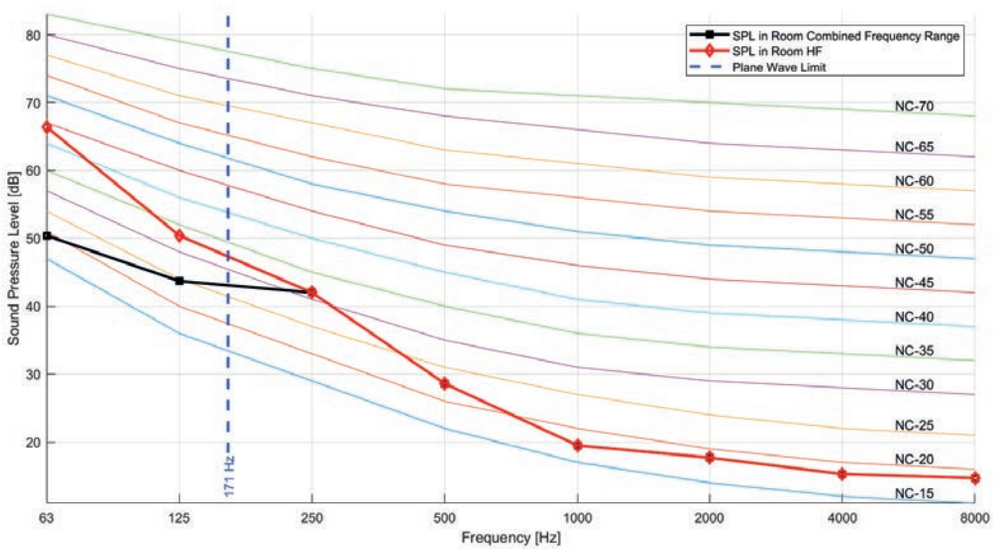


Figure 7. Case 2: NC level at the reference point (see Fig. 6) in the room using HF modelling only and combined LF&HF modelling.

SUMMARY AND CONLUSIONS

By using a power based formulation (Eq. 12) it is possible to extend the concept of acoustic two-ports to the HF range. The same two-port formalism (Eq. 14) for investigating complex duct networks can then be applied from the LF up to the HF range. As has been shown earlier it is also possible to formulate 1-D flow calculations using two-ports [16]. This means that after the corresponding two-port network of a system is built, both the acoustics for the entire frequency range as well as the flow distribution and pressure drops can be calculated.

To evaluate the proposed method two test cases are presented, see Figs. 4 to 7. As shown by these cases large deviations from power based standard models can occur in the low frequency range. The introduction of a mixed wave and power based analysis is an alternative to estimate these effects and reduce the risk for LF noise problems.

BIBLIOGRAPHY

[1] M.L. Munjal, *Acoustics of Ducts and Mufflers*, 2nd Edition, John Wiley & Sons, **2014**.

[2] H.P. Wallin, U. Carlsson, M. Åbom, H. Bodén, R. Glav, R. Hildebrand, *Sound and vibration*, **2010** ed., ISBN 9789174155532.

[3] D.D. Reynolds, J.M. Bledsoe, *Algorithms for HVAC Acoustic, American Society of Heating, Refrigeration and Air-Conditioning Engineers* (ASHRAE), Atlanta, GA, **1990**.

[4] VDI 2081 Part 1, *Noise generation and noise reduction in air conditioning systems*, Germany, **2001**.

[5] A. Cummings, *High frequency ray acoustics models for duct silencers*, J. Sound Vib. 221 (**1999**), 681–708. https://doi.org/10.1006/jsvi.1999.2030.

[6] ANSI/ASA, *Criteria for Evaluating Room Noise*, **2008**.

[7] ASHRAE, *A47 I-P: Sound and Vibration Control*, *in: 2007 ASHRAE Handbook—HVAC Appl*., **2007**.

[8] VDI 2081 Part 2, *Noise generation and noise reduction in air conditioning systems-Examples,* Germany, **2005**.

[9] H. Boden, M. Åbom, *Modelling of fluid machines as sources of sound in duct and pipe systems*, ACTA ACUSTICA-LES ULIS-3 (**1995**), 549–560.

[10] R. Glav, M. Åbom, *A General formalism for analysing acoustic 2-port networks*, J. Sound Vib. 202 (**1997**), 739–747. https://doi.org/10.1006/jsvi.1996.0808.

[11] S. Sack, M. Åbom, *Investigation of orifice aeroacoustics by means of multi-port methods*, J. Sound Vib. 407 (**2017**), 32-45. https://doi.org/10.1016/j.jsv.2017.06.026.

[12] S. Sack, M. Shur, M. Åbom, M. Strelets, A. Travin, *Numerical eduction of active multi-port data for in-duct obstructions*, J. Sound Vib. 411 (**2017**), 328-345. https://doi.org/10.1016/j.jsv.2017.09.012.

[13] Y. Aurégan, R. Starohinski, *Determination of the acoustical energy dissipation / production potentiality from the acoustical transfer functions of a multiport*, Acoustica. 85(6) (**1999**), 788–792.

[14] M.W. Nashed, T. Elnady, M. Åbom, *Modeling of duct acoustics in the high frequency range using two-ports*, Applied Acoustics 135 (**2018**), 37-47. https://doi.org/10.1016/j.apacoust.2018.01.009.

[15] T. Elnady, M. Åbom, *SIDLAB: new 1D sound propagation simulation software for complex duct networks* (**2013**), Proceedings of ICSV13, Vienna, Austria.

[16] T. Elnady, S. Elsaadany, M. Åbom, *Flow and pressure drop calculation using two-ports*, J. Vib. Acoust. Aug **2011**, 133(4): 041016. https://doi.org/10.1115/1.4003593.

AEROACOUSTIC ANALYSIS OF RADIATOR INSTALLATION EFFECTS IN A PULLING ENGINE COOLING MODULE

Francesco BELLELLI[1], Renzo ARINA[1],
Stéphane MOREAU[2], Francesco AVALLONE[1]

[1]*Department of Mechanical and Aerospace Engineering, Politecnico di Torino, Corso Duca degli Abruzzi 24, Torino, 10129, Italy*

[2] *Department of Mechanical Engineering, Université de Sherbrooke, 2500 Boulevard de l'Université, Sherbrooke, QC, J1K1R1, Canada*

SUMMARY

Fan noise is a critical issue for manufacturers, as they must balance aerodynamic and acoustic performance. Coupling a fan with a radiator in a pulling configuration, introduces significant challenges. Since it is challenging to perform scale resolved simulations of a radiator, an equivalent fluid approach is adopted. This study investigates the effects of an equivalent porous medium mimicking the radiator, and casing geometry on inflow and noise sources in an industrial cooling fan. Three configurations (Fan + Frame + Equivalent Porous Medium, Fan + Frame, Fan) are investigated using high-fidelity simulations. While aerodynamic performance remains consistent, the equivalent porous medium and casing geometry introduce inflow distortions, causing tonal noise variations, particularly in the full module configuration.

INTRODUCTION

With the increasing demand for electric vehicles, the need for high-performance cooling fans has intensified, particularly to manage heat during fast charging cycles. In practical applications, fans are usually paired with radiators, which affects the cooling module aerodynamic and acoustic performance making a challenge their performance prediction.

Sortor [1] stressed the sensitivity of both aerodynamic and acoustic performance to the installation effects of the radiator; it is essential to account for this coupling when installing different fans on the same radiator geometry. Therefore, a detailed description of the interaction between the fan and the radiator is essential to improve the overall efficiency and reduce noise of these systems.

Literature reports a wide variety of experimental studies on the effects of radiator-induced turbulence on fan aeroacoustic performance. Wagner et al. [2] examined the effect of the axial spacing between radiator outlet and fan inlet, highlighting its impact on noise levels at the blade passing frequency (BPF) and harmonics. Czwielong et al. [3] demonstrated that reducing the diameter of coolant tubes,

when large compared to the fan-radiator spacing, reduces the broadband noise, while the shape of the casing affects the tonal component. They also demonstrated the noise-reduction benefits of circular casing shapes compared to rectangular ones, due to a smoother casing-to-fan shape transition in the former case. However, their radiator technology might not be representative of industrial state of the art. Zarri et al. [4] showed that the thin coolant tubes are responsible for breaking down the turbulent eddies and increasing the non-homogeneity of the turbulence, while the presence of an upstream casing contributes to slightly shift turbulence towards anisotropy. This last aspect, although widely experimentally assessed in terms of turbulent energy spectra, still lacks a detailed three-dimensional flow description. Such a description can be obtained through numerical simulations, providing further insights into the rotor-inflow interaction. However, most numerical studies on isolated fans assume a uniform pressure drop, which does not adequately capture the complexities introduced by the radiator, as emphasized by Zhang et al. [5]. By adopting a porous medium model, Tebib et al. [6] showed that modelling the radiator as an equivalent porous medium produces sufficiently accurate numerical predictions of the aeroacoustic performance of the fan for industrial applications, and that including the tubes have no significant acoustic effect. However, the specific impact of this non-uniformity on the aerodynamic and acoustic properties of the system remains unclear.

The purpose of this paper is to address the impact of considering an equivalent porous medium, as opposed to a uniform pressure drop, and the transition in shape from square to round between the radiator casing and the fan on the upstream aerodynamics and, subsequently, on the noise sources of a realistic engine cooling module where the radiator is placed upstream of the fan. For this purpose, scale-resolved high-fidelity numerical simulations are carried out with the lattice-Boltzmann method (LBM) by means of the commercial software PowerFLOW by 3DS. Reference experimental data, acquired and provided by the manufacturer, are used to validate the numerical simulations.

The first section briefly summarizes the reference geometry, while the second section presents the numerical setup used to perform simulations. The grid convergence study and the validation of the numerical simulations against the experiments are discussed in the third section. The fourth section discusses the results, while the main conclusions are reported in the fifth section.

FAN AND RADIATOR GEOMETRIES

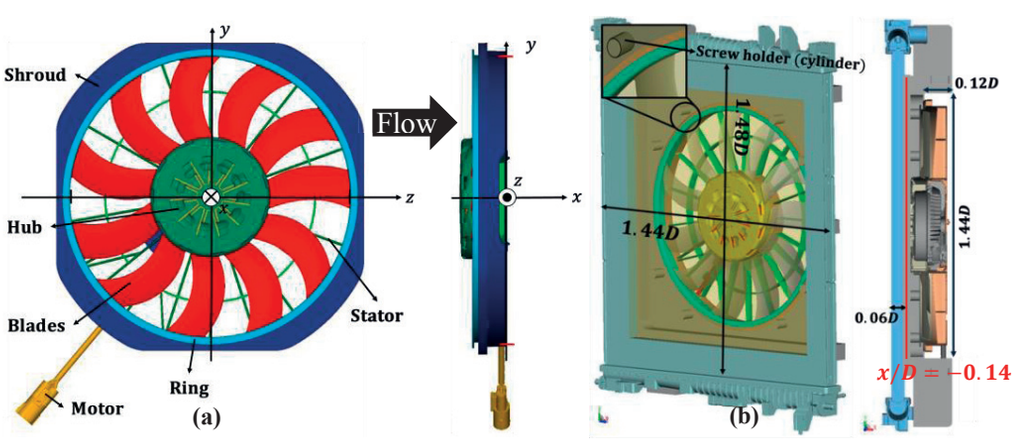


Figure 1: Tested engine cooling module parts. (a): Fan. (b): Radiator.

Fig. 1 shows the geometries of the fan and the radiator object of this study as well as the coordinate system that will be used to define the absolute position of planes and probes. The fan (Fig. 1a) consists of a 465 mm diameter (D) rotor with $B = 11$ unevenly spaced blades connected to a ring, a hub, a driving electrical motor, $V = 20$ unevenly spaced stator vanes, and a shroud. The fan tip clearance is equal to $0.009\ D$. The radiator (Fig. 1b) consists of a $1.48\ D \times 1.44\ D$ core placed $0.02\ D$ upstream of the fan hub and of a square casing that joins it to the fan through

FAN 2025
Antibes Juan-les-Pins (France), 9 – 11 April 2025

8 screws, covered by upstream protruding cylinders. The light blue solid part of the core joint with the square casing in grey will be referred as "Frame" in the rest of the paper.

Volume flow rate, torque and fan rotational speed are measured in an aerodynamic facility, while sound pressure level measurements are performed in a semi-anechoic room, in which the fan is placed at a distance $z/D = 3.23$ from the floor and a microphone is placed $2.15D$ upstream of the fan, aligned with its rotational axis. The module is described using non-dimensional parameters as it is an industrial product. Aerodynamic measurements are carried out along the full operating range for both the fan only and the complete cooling module, while acoustic measurements are carried out only at free blowing conditions for the complete cooling module, corresponding to load coefficient equal to $\psi = \frac{\text{pfs}}{\frac{1}{2}\rho v_{tip}^2} = 0$ and flow coefficient equal to $\varphi = \frac{qV}{\pi\left(R_{tip}^2 - R_{hub}^2\right)v_{tip}} = 0.13$, where pfs is the pressure rise through the cooling module, v_{tip} is the tip velocity, and qV is the volume flow rate through the fan. In both the air performance and acoustic measurements, the fan rotational speed is equal to $n = 3048\ rpm$.

NUMERICAL SETUP

The CAD geometries were provided by the. Three configurations are analysed: (i) the full cooling module (Fan + Frame + Porous Medium), (ii) the Fan + Frame, and (iii) the Fan.

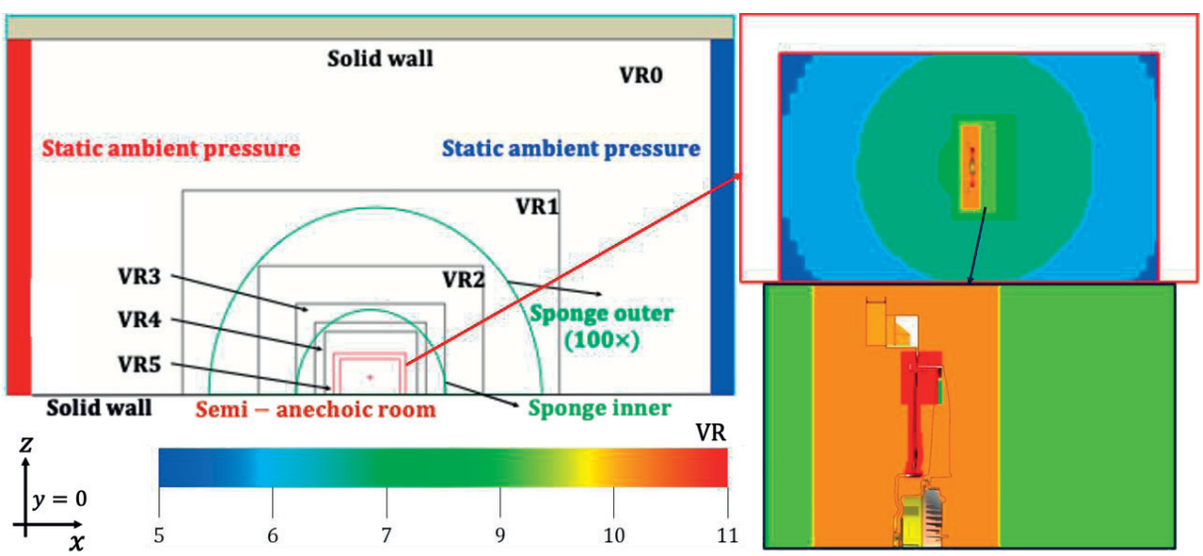


Figure 2: Sketch of the computational domain in the plane at $y/D = 0$.

The computational domain used to simulate all the configurations is shown in Fig. 2. The same numerical simulation setup was previously validated by Bellelli et al. [7]. A large fluid domain of $135\ D \times 135\ D \times 135\ D$ is built enclosing the semi-anechoic room. The room walls, of the same size as the experimental one, are modelled as an equivalent porous medium with viscous resistance equal to $50000\ 1/s$. The floor is modelled as a solid reflective wall. A discretization strategy, based on 11 Variable Resolution (VR) regions, is adopted. The regions with maximum resolution are set around the rotating blades and near the tip gap region, where for the most refined case there are 11 voxels in the tip clearance. In the VR3 region, a sponge region is defined by an artificial change of viscosity by a factor of 100 with an exponential function between the regions marked as “Sponge inner” and “Sponge outer” in Fig. 2. Inlet and outlet have a boundary condition equal to the static ambient pressure. In the full module configuration, the radiator is modelled as an equivalent porous medium [8]. In the Fan + Frame and Fan configurations, as the equivalent porous medium is removed, the fan is provided with a pressure rise that matches the pressure loss of the equivalent porous medium at the

same operating condition. To impose the matching pressure rise, a thin and acoustically absorbing wall, mimicking a wind tunnel aerodynamic facility is added. The pressure rise is imposed by initializing the flow on the suction side of the domain with a static pressure equal to the difference between the ambient pressure and the pressure rise. The inlet boundary condition is changed accordingly.

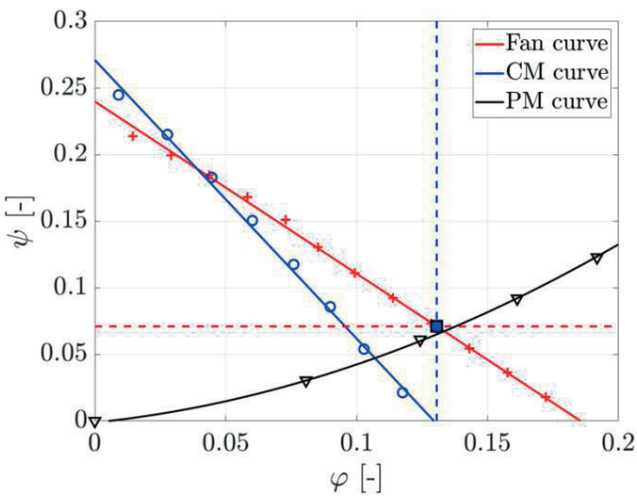


Figure 3: Experimental curves of fan alone (Fan), complete cooling module (CM), and radiator alone (PM).

The experimental aerodynamic curves of the complete module, fan alone, and radiator are shown in Fig. 3. The matching pressure rise is calculated as the pressure rise that the fan achieves at the same flow rate as the one at free discharge ($\psi = 0$) of the complete module i.e. $\varphi = 0.13$. A matching pressure rise of $\psi = 0.071$ is obtained. It is worth noting that the radiator pressure loss matches the pressure rise at $\varphi = 0.13$, resulting in almost no installation effect on the complete module.

60 revolutions are simulated for every case and time-averaged values are obtained by averaging over the last 10 revolutions. Simulations have been performed at three different resolutions of 300, 600, and 1200 voxels per diameter (vox/D) in the finest VR region. Far-field noise spectra are calculated using the Welch [9] averaging algorithm with 50% overlap and 8 Hamming windows directly from the simulation data, with a frequency resolution of 11.8 Hz and a sampling frequency of 48,000 Hz.

GRID CONVERGENCE STUDY

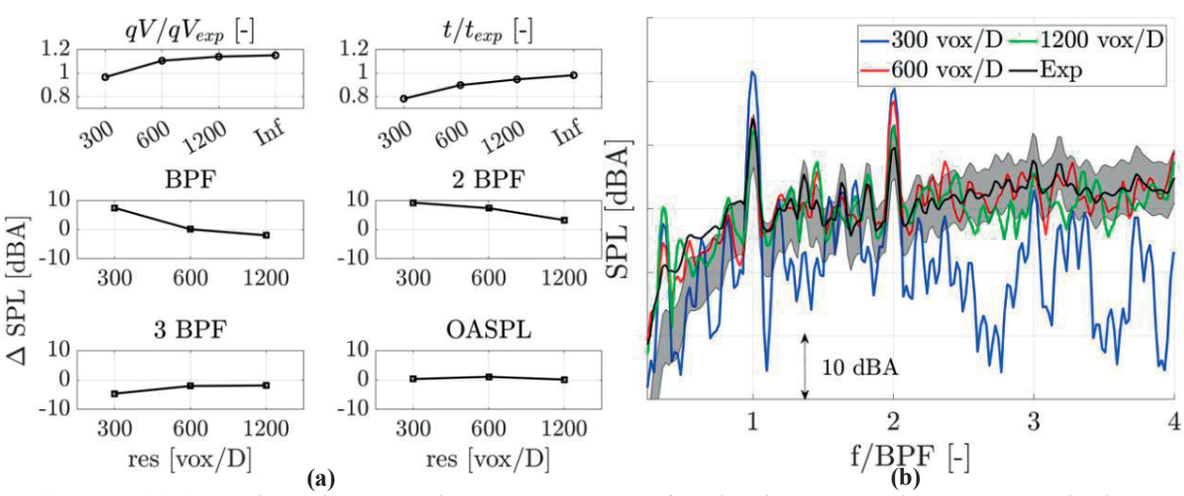


Figure 4. (a): Integral aerodynamic and acoustic quantities referred to the corresponding experimental values. (b): Sound Pressure Level in dBA obtained at x/D=-2.15 upstream of the fan (aligned with the fan rotation axis). The solid black line is the averaged experimental signal, while the grey shade is the variation in SPL each 10 revolutions.

The volume flow rate through the fan and aerodynamic torque obtained from the simulation of the complete cooling module configuration are shown in Fig. 4a made dimensionless by the corresponding experimental values. The "Inf" values are obtained through a Richardson extrapolation [10] with refinement ratio $r = 2$ and order of convergence $p = 2$ [11]. The figure shows that grid convergence is reached for the finest resolution case, as the extrapolated values are within 2% of the finest resolution. The volume flow rate exhibits a more evident convergence, although resulting in a slight overestimate of the experimental value. On the other hand, the torque is characterized by a steeper variation between resolutions and underestimates the corresponding experimental value. The differences in torque can be due to the difficulty in measuring a pure aerodynamic torque, while the differences in flow rate might be associated with the presence of complex flow phenomena in the casing as well, as shown by Moreau et al. [12]. These results are aligned with similar cases in the literature [13]. In addition, Fig. 4a shows the Sound Pressure Level (SPL) at the BPF and the first two harmonics as well as the Overall Sound Pressure Level (OASPL) in terms of discrepancies against the experimental values. Increasing the resolution the difference with respect to the experimental values is within 3 dB. In particular, the BPF and first harmonic are overestimated, while the second harmonic is underestimated; the OSPL instead shows drastically less sensitivity to the resolution.

To further investigate the impact of the grid resolution on far-field noise, the noise spectrum obtained with a direct probe at $x/D = -2.15, y/D = z/D = 0$ upstream of the fan at the three grid resolutions is compared against the experimental one in Fig. 4b. The probe is located $1.93D$ upstream of the radiator and is aligned with the fan rotation axis. A grey-shaded area has been superimposed on the plot, representing the variation in the SPL during the entire sampling time of the experimental values ($30\ s$) considering time-windows of 10 revolutions, i.e. the same number of revolutions sampled in the numerical simulations. One can note that the coarse resolution of $300\ vox/D$ is not sufficient to properly capture the broadband content, while the tones up to the first BPF harmonic are overestimated; this justifies why the OASPL is not different from the experiments. The medium ($600\ vox/D$) and fine ($1200\ vox/D$) resolutions are instead able to correctly predict the broadband levels and are characterized by a less prominent tonal content at BPF and harmonics. The $1200\ vox/D$ resolution shows better agreement at higher BPF harmonics; therefore, the results in the rest of this paper are shown only for the finest resolution.

RESULTS AND DISCUSSION

Table 1: Averaged aerodynamic integral quantities percentage variations with respect to the full cooling module configuration (Fan + Frame + PM). For each case, the quantities have been averaged over the last 10 revolutions.

	Fan + Frame + PM	**Fan + Frame**	**Fan**
ΔF	-	-14%	-5%
ΔqV	-	+2%	+1%
Δt	-	-5%	-6%

First, the impact of the different configurations on the overall aerodynamic performances is assessed. In Tab. 1 the average axial thrust force (F), volume flow rate through the fan (qV), and aerodynamic torque (t) are shown as percentage variations (Δ) with respect to the full cooling module configuration. Removing the equivalent porous medium (Fan + Frame) has a significant effect both on thrust and torque, which are reduced respectively by 14% and 5%, while keeping the flow rate mainly unaltered. It is also observed a similar trend in the torque and the volume flow rate when the Fan alone configuration is considered. However, it is interesting to note that the thrust has a lower decrease in this configuration rather than in the intermediate Fan + Frame configuration. The differences in the thrust and torque can be explained by looking at the different pressure patterns upstream of the fan.

FAN 2025
Antibes Juan-les-Pins (France), 9 – 11 April 2025

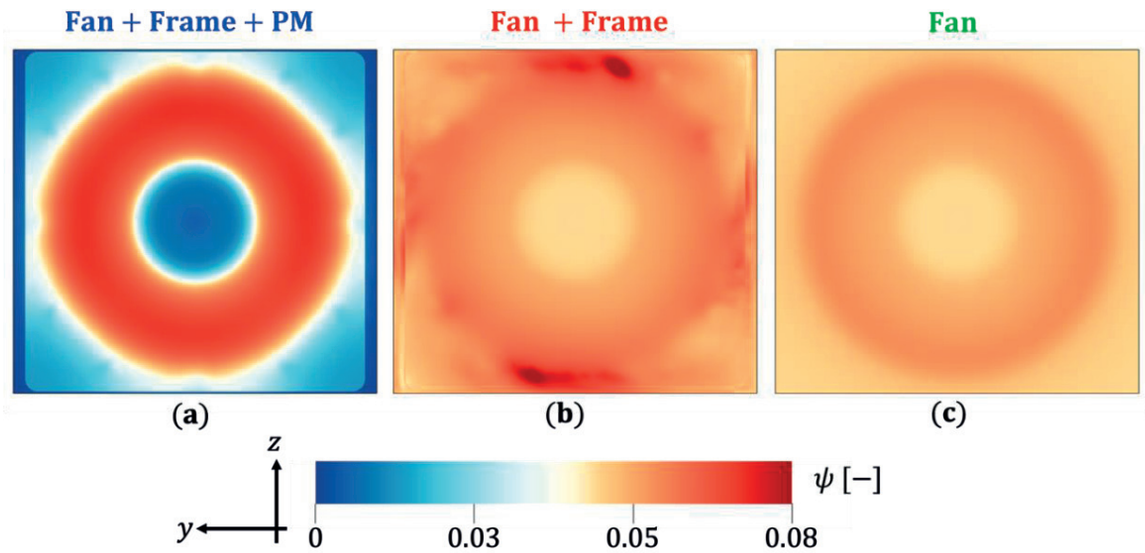


Figure 5: Mean pressure loss with respect to the ambient pressure in a plane located at x/D=-0.14, upstream of the fan. (a): Fan + Frame + PM. (b): Fan + Frame. (c): Fan.

In Fig. 5 the contour of the pressure rise with respect to the ambient pressure for all the simulated configurations in a plane located at $x/D = -0.14$ (see Fig. 1 for the plane location) are shown. The effect of the equivalent porous medium (Fig. 5a) is evident, as it concentrates the pressure loss mainly on the fan disk, unlike the Fan + Frame (Fig. 5b) and Fan (Fig. 5c) configurations, that show a more uniform distribution of ψ. This behavior is a direct consequence of the fact that the equivalent porous medium gives a pressure loss that depends on the inflow velocity. Therefore, it will result in higher pressure losses just on the region characterized by higher inflow velocities, such as the fan disk. Then, it can be noted that the square casing (Fig. 5b) is responsible for high ψ spots in the middle of each side. They can be attributed to the flow distortions caused by the square-to-round shape transition between the casing and the fan, that causes local stronger flow acceleration in the regions of shorter fan-frame distance. Finally, the Fan alone configuration (Fig. 5c) is characterized by a highly uniform distribution of ψ as the equivalent porous medium is removed, as well as any possible source of flow recirculation and inflow distortion.

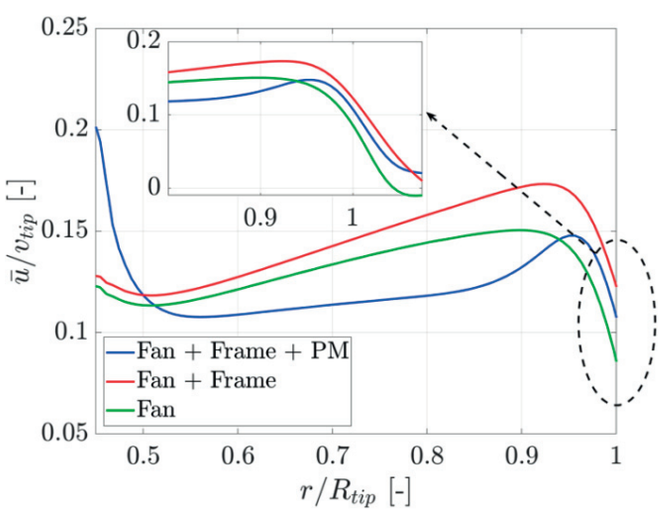


Figure 6: Mean axial velocity profile, azimuthally averaged, at x/D=-0.14. A zoom in the near tip region is shown in the top of the figure.

The azimuthally averaged axial velocity made dimensionless using v_{tip} at $x/D = -0.14$ is shown in Fig. 6. The full cooling module configuration shows the lowest values of $\bar{u}/v_{tip}$ for

$0.5 \leq r/R_{tip} \leq 0.95$ because of the greater pressure losses seen in Fig. 5. On the contrary, near the hub, at $r/R_{tip} \leq 0.5$, $\bar{u}/v_{tip}$ is the highest, as ψ is nearly equal to zero. Moreover, an increase in the axial velocity gradient for $0.9 \leq r/R_{tip} \leq 1$ is seen in the top of Fig. 6 because of the non-uniform ψ seen in Fig. 5. The Fan + Frame configuration shows a $\bar{u}/v_{tip}$increase for $0.7 \leq r/R_{tip} \leq 0.95$ due to the flow distortions seen in Fig. 5 while negligible differences in the near tip region are seen.

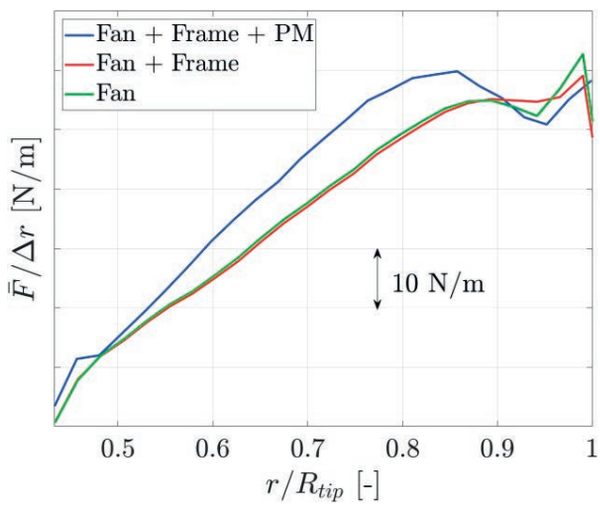


Figure 7: Mean thrust per unit length distribution on one blade, averaged on the last 10 revolutions.

The radial distribution of thrust per unit length is shown in Fig. 7. The full cooling module configuration is characterized by higher thrust per unit length up to $r/R_{tip} \leq 0.9$ due to higher ψ on the fan disk. The velocity decrease near the tip, seen in Fig. 6, results in lower thrust per unit length values for $r/R_{tip} \geq 0.9$. Moreover, the different flow topologies in the hub, shown in Fig. 6, is causing the thrust per unit length to experience a slight hump near $r/R_{tip} = 0.45$, which is also associated with flow recirculation in the hub. It is worth mentioning that the hub has several small slots to allow cooling of the driving electric motor; therefore, flow recirculation is present in those areas, especially in the presence of strong gradients such as when the equivalent porous medium is present. Finally, the effect of the frame is seen to be mainly located at the tip, where the distribution shows a higher drop. This is related to the presence of flow recirculation in the casing.

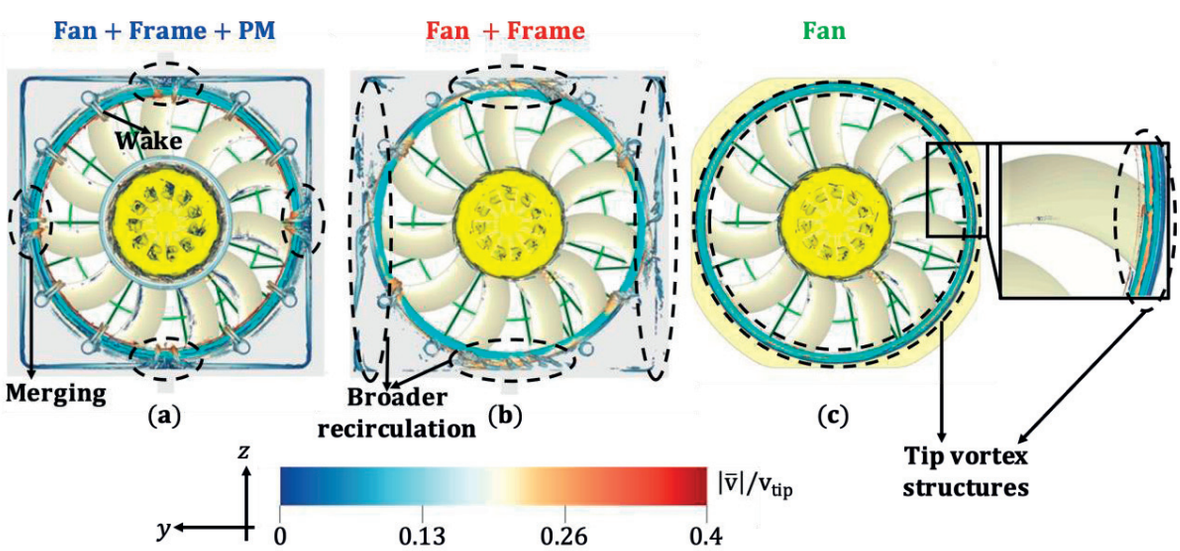


Figure 8: Mean $\Lambda_2 = -2.5 \cdot 10^5\ 1/s$ iso-surfaces coloured with velocity magnitude, in the casing upstream.

FAN 2025
Antibes Juan-les-Pins (France), 9 – 11 April 2025

The above analyses have highlighted the relevant role of the flow recirculation in the casing on the mean flow topology and on the blade loading distribution. Therefore, the $\Lambda_2 = -2.5 \cdot 10^5\ 1/s$ iso-surfaces coloured with the non-dimensional velocity magnitude are shown in Fig. 8. This quantity is obtained after averaging the flow field over the last 10 revolutions to identify only the coherent vortex structures that are steady in time. Only the coherent structures in the square casing area are shown. First, one can note that the full cooling module configuration (Fig. 8a) is characterized by almost steady coherent vortex structures along the four sides of the casing which strongly merge at the centre of each side. Moreover, wakes are shed by the 8 cylinders that house the fixing screws, which are then ingested by the fan in the tip region. The Fan + Frame configuration (Fig. 8b) is characterized by a broader recirculation, with less coherent steady vortex structures, because of the less strong velocity gradients. The vortex structures that are present in this case can be caused by the flow distortions due to the square-to-round shape transition between the casing and the fan. Finally, the Fan configuration (Fig. 8c) shows very small steady vortex structures only localized in the near tip region, wrapping around the rotating ring, which can be associated with tip leakage flow phenomena. In this case, these structures are not well visible because they are highly unsteady, and they are averaged out. The different vortex structures topology seen in Fig. 8 is expected to drastically influence the loading fluctuations of the blades, as the rotor will interact with a highly non-uniform flow field upstream in the configurations with the solid frame at certain azimuthal locations.

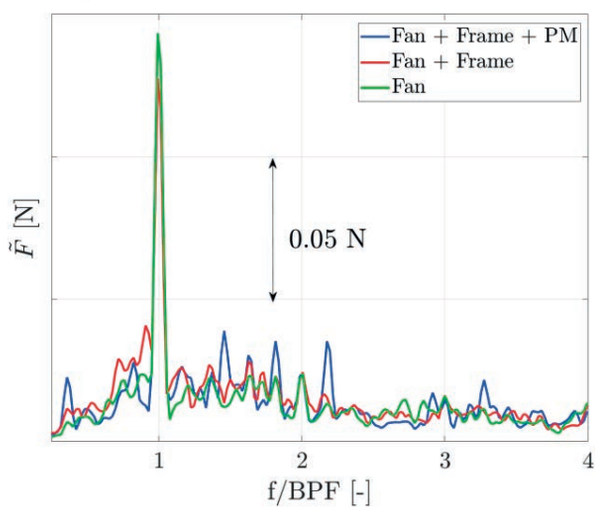


Figure 9: Spectra of the thrust given by all the 11 blades for the three configurations.

The spectral content of the unsteady thrust is shown in Fig. 9. The frequency axis is made dimensionless with respect to the BPF. The peak at the BPF is prominent in all the cases, with the Fan configuration showing the highest amplitude while the Fan + Frame configuration the lowest one. Furthermore, all the configurations show similar values at higher BPF harmonics. The cooling module configuration is characterized by several inter-harmonic narrow-band humps due to the periodic interaction of the blades with the vortices at the centre of each side of the casing and the wake of the 8 cylinders that hold the fixing screws. The Fan + Frame configuration is characterized by higher fluctuations for $0.5 < f/BPF < 1$ due to the stronger recirculation in the casing in this configuration. In contrast, the Fan alone case shows almost no inter-harmonic hump, except for a slight fluctuation at $f/BPF = 1.81$, which is associated with rotor-stator interaction phenomena, as both the blades and vanes are not equally spaced [10]. The blade loading fluctuations are subsequently expected to drive the acoustic footprint of the system, as typical in low-speed fan applications.

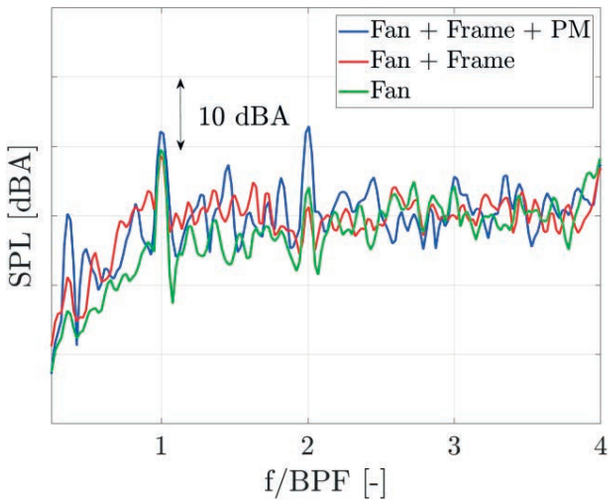


Figure 10: Far-field noise spectra at x=-2.15D upstream, along the fan axis.

Fig. 10 shows the spectra for the three configurations of the pressure fluctuations sampled at $x/D = -2.15$, $y/D = 0$, and $z/D = 0$, which corresponds to the upstream location on the fan axis. At the BPF and harmonics, the cooling module configuration is seen to have higher SPL. This can be associated both with the higher mean loading of this configuration, as shown in Fig. 7, and with the presence of recirculation in the semi-anechoic room, as pointed out in Refs. [7], [14], [15]. Furthermore, several inter-harmonic humps at frequencies $f/BPF = 4/11$ and harmonics are found. They are caused by the interaction between the rotor and the periodic inflow inhomogeneities due to the presence of the square casing and the 8 cylinders that house the screws, similarly to what is seen in Fig. 9. The broadband content of the spectra is characterized by a higher contribution of the Fan + Frame configuration at low and mid frequencies (approximately for $f/BPF < 2$), which can be attributed to the stronger recirculation pattern in the casing, as seen in Fig.5. The Fan configuration is then characterized by the absence of any inter-harmonic hump, as its inflow distribution is mostly uniform. Finally, the higher frequency broadband contribution (approximately for $f/BPF > 2$) shows almost the same levels for all four simulated configurations.

CONCLUSIONS

The impact of the radiator installation on the aerodynamic and aeroacoustics performance of a fan are analysed numerically considering three configurations: the full cooling module, where the radiator is replaced by an equivalent porous medium, the module without an equivalent porous medium but with the solid frame, and the fan alone. Simulations were performed at free blowing conditions. The latter two configurations have the same global pressure loss induced by the equivalent porous medium in the first configuration. Each of these factors plays a distinct role in modifying the fan performance and noise generation, particularly through their influence on upstream aerodynamics.

Removing the equivalent porous medium while maintaining the same pressure drop across the system results in a decrease in thrust and torque, slightly improving the aerodynamic efficiency. Moreover, the equivalent porous medium focuses the pressure losses on the fan disk, contributing to higher sectional blade loading in the axial direction. Removing the equivalent porous medium, pressure losses become more uniformly distributed across the system, affecting the distribution of aerodynamic loading along the blade and, therefore, the tonal noise of the fan at the BPF and harmonics. The increased inhomogeneity in the upstream flow amplifies the noise generated by interactions between the blades and the inflow distortions caused by the shape transition in the frame, particularly in the low frequency range. Furthermore, several inter-harmonic humps are present as a consequence of additional inflow distortions given by small cylindrical screw housings.

BIBLIOGRAPHY

[1] M. Sortor, «On-System Engine Cooling Fan Measurement as a Tool for Optimizing Cooling System Airflow Performance and Noise», *SAE Int. J. Mater. Manuf.*, vol. 4, fasc. 1, pp. 1221–1230, apr. **2011**, doi: 10.4271/2011-01-1169.

[2] S. Wagner e J. Rohlfing, «Effects of the fan - radiator interaction on the noise emissions of heat pumps: experimental and numerical studies», FAN2022, **2022**.

[3] F. Czwielong, J. Soldat, e S. Becker, «On the interactions of the induced flow field of radiators with axial fans», *Experimental Thermal and Fluid Science*, vol. 139, p. 110697, nov. **2022**, doi: 10.1016/j.expthermflusci.2022.110697.

[4] A. Zarri, M. B. Botana, J. Christophe, e C. Schram, «Aerodynamic investigation of the turbulent flow past a louvered-fin-and-tube automotive radiator», *Experimental Thermal and Fluid Science*, vol. 155, p. 111182, giu. **2024**, doi: 10.1016/j.expthermflusci.2024.111182.

[5] P. F. Zhang, M. T. Zhu, Z. J. Li, e K. Wang, «The Cooling Module Aerodynamic Noise Prediction Considering Porous Media», *AMM*, vol. 711, pp. 20–26, dic. **2014**, doi: 10.4028/www.scientific.net/AMM.711.20.

[6] S. Tebib *et al.*, «Detailed noise analysis of automotive engine cooling modules using the Lattice-Boltzmann Method», in *AIAA AVIATION 2023 Forum*, San Diego, CA and Online: American Institute of Aeronautics and Astronautics, giu. **2023**. doi: 10.2514/6.2023-3205.

[7] F. Bellelli, R. Arina, e F. Avallone, «On the impact of operating condition and testing environment on the noise sources in an industrial engine cooling fan», *Applied Acoustics*, vol. 227, p. 110252, gen. **2025**, doi: 10.1016/j.apacoust.2024.110252.

[8] M. Piellard, B. B. Coutty, V. Le Goff, V. Vidal, e F. Perot, «Direct aeroacoustics simulation of automotive engine cooling fan system: effect of upstream geometry on broadband noise», in *20th AIAA/CEAS Aeroacoustics Conference*, Atlanta, GA: American Institute of Aeronautics and Astronautics, giu. **2014**. doi: 10.2514/6.2014-2455.

[9] P. Welch, «The use of fast Fourier transform for the estimation of power spectra: A method based on time averaging over short, modified periodograms», *IEEE Trans. Audio Electroacoust.*, vol. 15, fasc. 2, pp. 70–73, giu. **1967**, doi: 10.1109/TAU.1967.1161901.

[10] L. F. Richardson, «The approximate arithmetical solution by finite differences of physical problems involving differential equations, with an application to the stresses in a masonry dam», *Phil. Trans. R. Soc. Lond. A*, vol. 210, fasc. 459–470, pp. 307–357, gen. **1911**, doi: 10.1098/rsta.1911.0009.

[11] F. Avallone, W. C. P. Van Der Velden, D. Ragni, e D. Casalino, «Noise reduction mechanisms of sawtooth and combed-sawtooth trailing-edge serrations», *J. Fluid Mech.*, vol. 848, pp. 560–591, ago. **2018**, doi: 10.1017/jfm.2018.377.

[12] S. Moreau e M. Sanjose, «Sub-harmonic broadband humps and tip noise in low-speed ring fans», *The Journal of the Acoustical Society of America*, vol. 139, fasc. 1, pp. 118–127, gen. **2016**, doi: 10.1121/1.4939493.

[13] D. Lallier-Daniels, S. Moreau, e M. Sanjose, «Aeroacoustics of a Low-Speed Free Tip Fan With a Complex Clearance Geometry», in *Volume 13: Vibration, Acoustics and Wave Propagation*, Montreal, Quebec, Canada: American Society of Mechanical Engineers, nov. **2014**, p. V013T16A004. doi: 10.1115/IMECE2014-39160.

[14] M. Sturm, M. Sanjosé, S. Moreau, e T. Carolus, «Aeroacoustic simulation of an axial fan including the full test rig by using the lattice boltzmann method», **2015**.

[15] S. Moreau, O. Marck, e M. Roger, «Aero-acoustic installation effects in cooling fan systems PART 2: near-field and ground effects», **2008**.

AEROACOUSTIC INVESTIGATION OF A CHARGING CABINET FOR ELECTRICAL VEHICLES

Safouane TEBIB[1], Stéphane MOREAU[1],
Charles LUZZATO[2]

[1] *Université de Sherbrooke, Sherbrooke, QC, J1K 2R1, Canada*

[2] *Dassault Systemes Simulia Corp, 3979 Freedom Circle, Suite 750, Santa Clara, CA 95054, USA*

SUMMARY

A first high-fidelity compressible simulation of a charging cabinet for electrical vehicles is achieved using the Lattice-Boltzmann Method. The cabinet is equipped with five fans in order to cool down the heating parts located at the bottom. This simulation provides the flow topology inside the cabinet and the heat transfer effect on the acoustic pressure computed directly in the far field. The dominant noise contributors are the two upper front fans, with a noise signature containing similar tonal and broadband noise components. Adding protective grids and heat transfer increases the loading on the fans and consequently the broadband noise levels.

INTRODUCTION

The last few years have seen an incredible rise in demands on electrical vehicles around the world. According to the Canadian federal government, one-fifth of all passenger cars, SUVs and trucks sold in Canada in 2026 will need to run on electricity. This percentage will increase by 2030 and will hit 60 per cent of all car sales to finally become a hundred percent in 2035. This exponential increase in a short period of time will put a great strain on electricity providers, such as Hydro-Québec, for the deployment of efficient charging cabinet. In order to achieve that, these cabinets have to comply, among other things, with noise regulations, as they will be deployed everywhere in urban areas to respond to the insatiable demand. One of the issues experienced until now with these cabinets is the noise generated by the several fans located inside that are aimed at cooling the electrical equipment. The operating conditions (flow, pressure) of these axial fans inside the charging cabinets can vary

according to their installation and the surrounding obstacles. They also depend on the power supply as some of the stations are destined to fast charging (where 80% of the vehicle battery charging occurs in under 20 minutes). Thus, the objective of this study is to provide first insights into the aerodynamic and acoustic characteristics of a charging cabinet during fast charging conditions, and to provide some noise evaluation.

To achieve this goal, numerical simulations with the Lattice-Boltzmann Method (LBM) for low Mach number applications [1, 2], can be a great help to reproduce the aeroacoustic phenomena that take place inside the cabinet and propagate to the surrounding environment. Previous studies numerically investigated low-speed fan noise [3, 4, 5, 6] and engine cooling module noise [7, 8, 6, 9], but none of them studied them in a charging cabinet context. However, as the Reynolds numbers based on the blade tip chord and relative velocity and the tip Mach numbers are similar, these studies will help model the flow in the charging cabinet, as it is equipped with five low-speed axial fans.

Therefore, in the present study, a numerical investigation of the aeroacoustic aspects of these charging cabinets is described, using an unsteady compressible LBM simulation [10, 11]. This work is a continuation of the studies of Tebib *et al.* [12] where two engine cooling modules meant for electrical vehicles were compared in terms of their aeroacoustic behavior. Leaning on previous works [13] that clearly showed that tip noise is dominant in such rotating machines, similar approaches are carried out in this work with respect to grid refinement used in LBM simulation to capture such phenomena.

The present work is organized as follows: the next section introduces the numerical model for the charging cabinet, and the fan design validation. The following section shows the aerodynamic and acoustic results for three different cabinet configurations. Conclusions and perspectives are finally drawn.

NUMERICAL SET-UP AND CONFIGURATIONS

The present Hydro-Québec charging station is mainly equipped with five fans. Two of them are disposed in the front, 2 in the back and one inside on top of the electric transformer as shown in Fig. 1 (left). Based on the drawings provided by the industrial partners, CAD models for the charging cabinet and the 5 blades axial fans have been developed with 3DS Solidworks. Most of the features on the electrical components, screws and washers and several cables have been omitted in the cabinet to simplify the model. The protective grills highlighted with yellow circles in Fig. 1 (left) are also taken into account by introducing equivalent porous media, as explained below. All five fan systems are identical and correspond to a production electronic cooling fan system shown in Fig. 1 (right), which has been reproduced based on detailed metrology of the fan. All marks have been removed and the electrical motor is modeled as a solid cylinder.

In order to reproduce the environment from an actual experiment in an anechoic chamber similar to that used for automotive engine cooling modules in [12] and provide valuable acoustic data, the cabinet assembled with the fans, is placed in a large simulation domain, as shown in Fig. 2. All of its outer surfaces have free-flow conditions (uniform pressure in the room) and the computational domain is mapped with an octree mesh. The grid consists of cubic elements called voxels. A Variable Resolution (VR) mesh strategy is used and the grid size changes by a factor of two for adjacent resolution regions. Different VR regions are shown in Fig. 2 as well as the position of the microphones that are represented as red crosses. The first VRs (up to VR3) with larger voxels are damping zones that mimic an anechoic chamber environment. VR3 to VR6 regions (top of Fig. 2) mesh the anechoic chamber around the cabinet. VR7 to VR10 zones (bottom of Fig. 2) are consecutive grid refinements around each fan. A final VR11 with a 0.25 mm resolution is a donut around the tip gap and the tip of the fan blades. A grid convergence has been achieved with the last three voxel refinements. A 0.5 mm voxel size yields grid independence, similarly to the previous LBM simulations reported by Moreau



Figure 1: Left: actual charging cabinet being simulated. Right: Axial fan systems.

and Sanjose [8] on automotive ring fans.

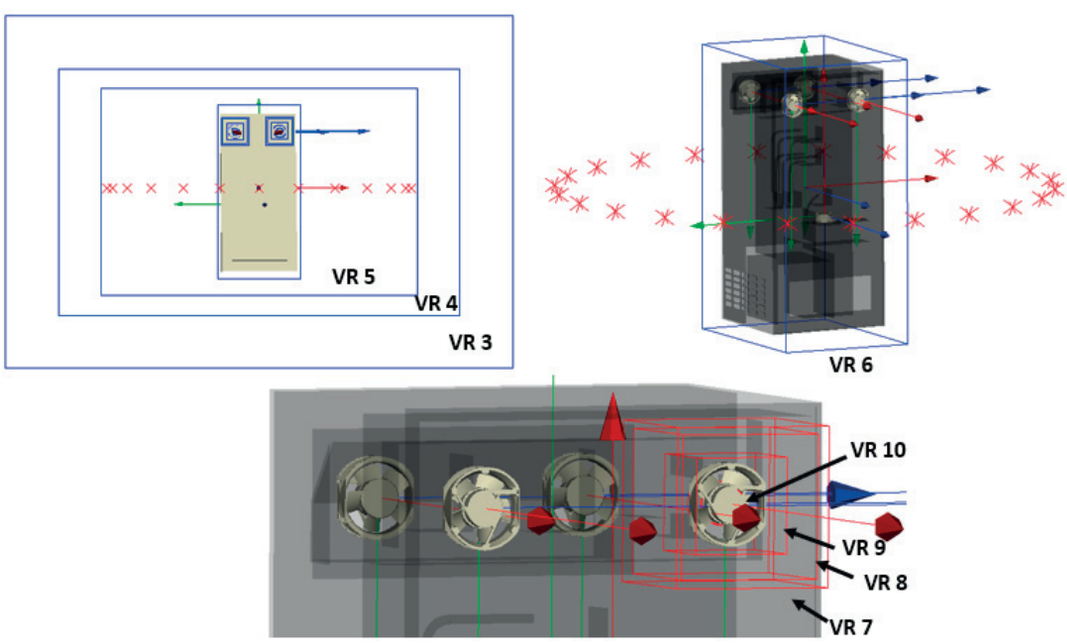


Figure 2: Numerical domain for the LBM simulation.

The operating conditions are representative of fast charging. The fan rotating speed is 3300 rpm. The grills located on the low side of the door as well in the electric transformer (circled in yellow in Fig. 1 (left)) are modeled as porous media in the simulations. Three configurations are investigated and compared in this paper. First, the cabinet with the fan alone is simulated. Then the porous media are added to the parameters. Lastly, heat transfer is taken into account by imposing the heat flux recorded on the electric transformer on the calculations. All simulations are performed with the LBM solver Powerflow version 6 from 3DS, in the Very Large Eddy Simulation mode to properly capture the largest turbulent structures. The LBM consists in solving the Boltzmann equation that describes the evolution of the probability density function for a particle to be at a given position with a given velocity for a finite number of directions in a voxel. The lattice used for the present application consists of 19 discrete velocities in three dimensions (D3Q19), involving a third-order truncation of the Chapman–Enskog expansion. This scheme was shown to accurately approximate

the Navier–Stokes equations for a perfect gas at low Mach numbers under isothermal conditions [14, 15, 16]. When heat transfer is considered, an additional energy equation is coupled with the D3Q19 lattice. 2 s were enough to converge the cold and porous cases, whereas about 10 seconds of physical time have been simulated in the heated case to capture the temperature ramp-up.

The designed 5-blade fan has been simulated separately in free flow with the above LBM method for its operating point at 3300 RPM using the above grids based on the same numerical configuration as presented by Tebib *et al.* [12]. The converged mass flow rate computed downstream of the fan is compared with the original fan data sheet specification and represented in Tab. 1. The free-flow mass flow rate is well reproduced and the two values compare well with a relative error of around 5 %.

Table 1: Fan mass flow rate comparison

	Real fan	**Designed fan**
Mass flow rate (kg/s)	0.135	0.142

In addition, a grill sample of the cabinet was provided from the industrial partner and resistivity measurements have been performed at Université de Sherbrooke. For several air velocities, pressure drop across the grill is recorded and fed to PowerCase in order to define the porous medium (defined as a box with the heat exchanger dimensions) in the streamwise direction. The other two directions are blocked to mimic the strong guidance of the heat-exchanger fin and louvers. In this work, two different anisotropic porous media are considered that are associated with the front door and electric transformer grills, respectively. The effect of these porous media as well as the different aeroacoustic aspects related to the different configurations simulated in this work are developed in the next section.

RESULTS

Three different configurations have been simulated and analyzed: a first one with no heat transfer and no porous media in front of the fans mounted on the doors, termed "cold case"; a second one in which these porous media have been added, termed "porous case"; and finally a third one that further includes heat transfer, termed "hot case". A comparison of the first two configurations will assess the effect of the finger guards in front of the fans and a comparison of the last two will assess the aero-acoustic modification introduced by heat transfer.

Cold case

Aerodynamic results

Fig. 3 shows the overall flow evolution inside and around the cabinet after 2 seconds of physical time using the coarse grid by representing an instantaneous velocity snapshot. Air can be seen flowing with low velocities (5-10 m/s) outside the cabinet to the surrounding environment from both top sides. These zones are associated with the four top fans. The latter are seen to have very axial wakes as expected close to optimal design conditions. Moreover, a portion of low speed air can be seen escaping the porous medium defined at the bottom of the front door in front of the electric transformer, which is mostly coming from the central fan that is directly blowing on top of the electric transformer at the bottom of the cabinet.

Details of the flow topology around the top fans are represented in Fig. 4 with iso-contours of the Λ_2 (second invariant of the velocity gradient) criteria for both coarse (up to VR9) and medium grids (up to VR10). A good consistency between both grids is observed in terms of turbulent structures

and vortices. The flow is mostly laminar and well attached to the blades. Big turbulent structures are observed to roll up around the tip gap region and in the wake where transition to turbulence has occurred. These thick turbulent eddies are typical of the low tip Reynolds number based on the chord of these fans. The minor difference noticed here when moving to the medium grid, is that the turbulent structures in between the fan blades are slightly better resolved due to the finer mesh. Further grid refinement up to VR11 yields no noticeable changes as mentioned above. Therefore, further results in this study are shown on VR10 (0.5 mm resolution).

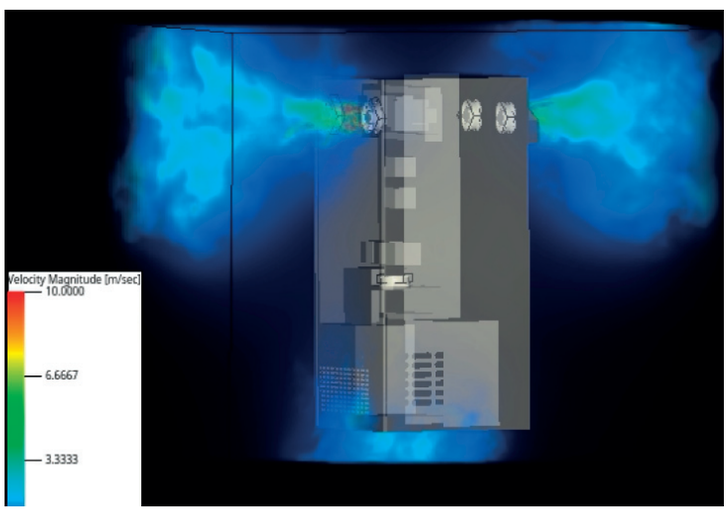


Figure 3: Instantenous velocity contours in and around the cabinet.

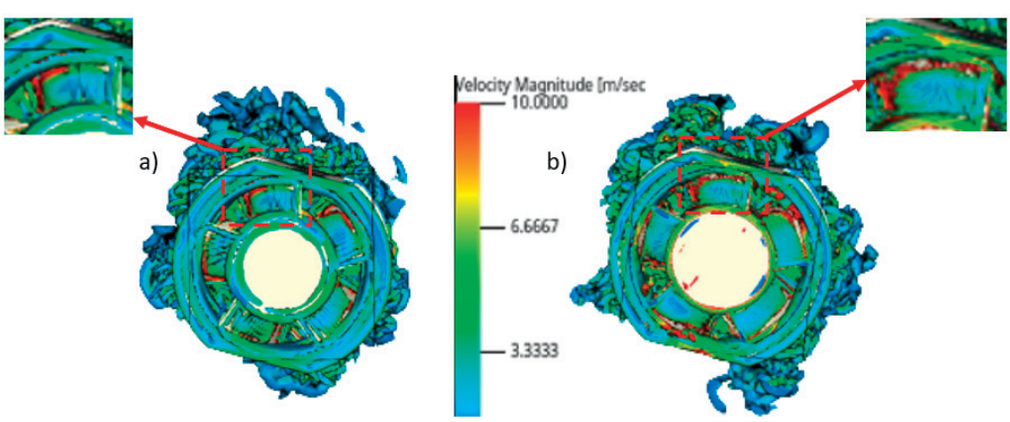


Figure 4: Λ_2 criteria in a front view of the top front right fan colored with tangential velocity. a) Coarse grid. b) medium grid.

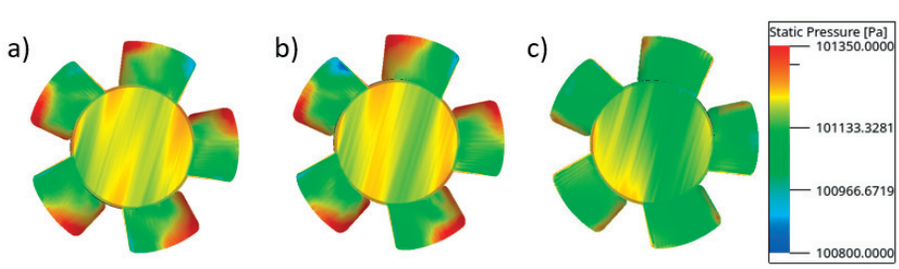
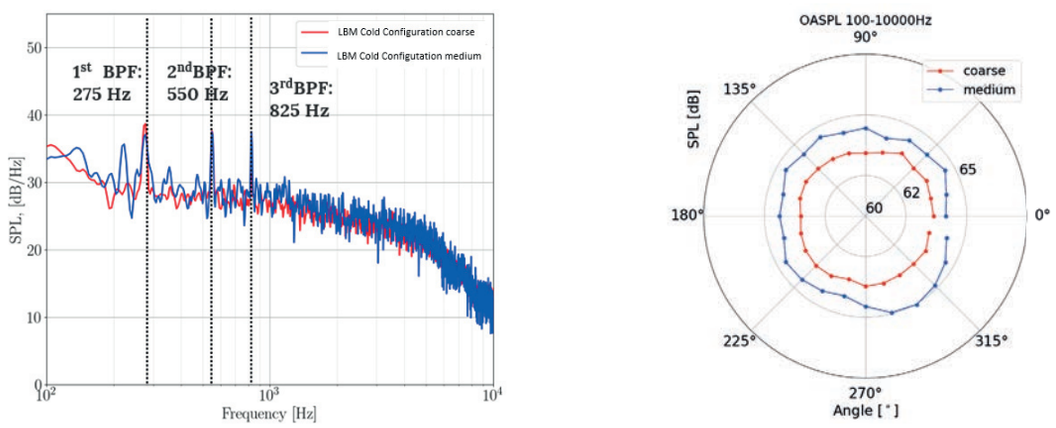


Figure 5: Averaged fan suction-side wall-pressure contours. a) Front fan. b) Back fan. c) Central fan.

Fig. 5 shows the iso-contours of mean wall pressure on the three fan locations (front, back and central). This describes the fan loading installed in the cabinet. Overall, similar loading can be seen for both the front and back fans. Only the central fan presents less loading caused by less resistance and thus may not contribute to the noise propagation as much as the top fans: as shown for example in Figs. 3 and 4 in [8], the overall sound power levels of a low-speed fan usually increases with decreasing flow rate and increasing blade loading. The stagnation point is close to the leading edge over the whole blade span, stressing the proper design of the fan for this application. The loading is also pretty uniform in the spanwise direction, emphasizing a proper radial equilibrium along the fan blade. Only the sections near the hub and the tip show differences, caused by the secondary flow features shown in Fig. 4. The overall pressure difference between the suction and pressure sides is also consistent with the fan data sheet.

Acoustic results

Direct acoustic results are computed at different locations around the cabinet. Fig 6a first shows the Sound Pressure Level (SPL) computed on a microphone located in the back of the cabinet. The recorded noise is both broadband and tonal, the latter being at the Blade Passing Frequency (BPF) and its first two harmonics. Overall, no significant differences are observed between the two grids in the mid- and high-frequency range. The first three BPFs are well captured at 275 Hz, 550 Hz and 825 Hz, respectively. However, at low frequencies (<200 Hz), a small peak emerges for the medium grid due to better resolution of turbulent structures in the fan region. Similar conclusions can be drawn at other locations.



(a) Spectra on a back probe. *(b) OASPL directivity*

Figure 6: Sound pressure level computed on the two grids.

The OverAll Sound Pressure Level (OASPL) directivity is then compared between the coarse and medium grids in Fig. 6b. The OASPL integration is achieved from 100 to 10000 Hz. An overall similar pattern of directivity is observed for both grids, and only a small increase of about 1 dB is found on the medium grid mainly caused by the higher low frequency levels seen in Fig. 6a. Slightly larger levels are observed in the front (between 270° and 315°), which will be the focus of the next spectra.

Filtered pressure fluctuations on the fan surface are then used for potential noise source localization. Fig. 7a shows the PSD of wall-pressure fluctuations for a frequency range centered around the first BPF at 275 Hz. The main areas of high-pressure fluctuations are located on the fan blades with generally more elevated levels near the tip region. The contribution from the tip region is increased when filtering the PSD around the second BPF at 550 Hz as shown by Fig. 7b. For both BPFs, high pressure-fluctuation regions can be seen at the leading edge as well as at the trailing edge that start

near the tip gap region and going all the way down to approximately the hub.

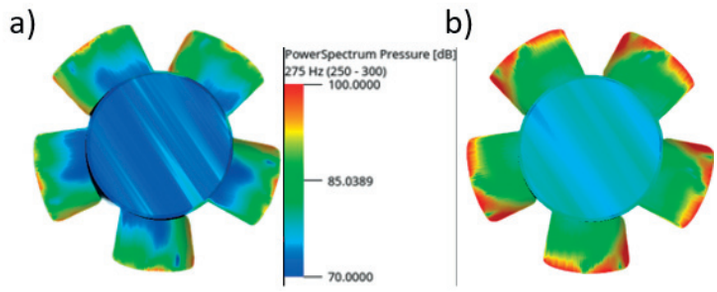


Figure 7: PSD of wall-pressure fluctuations on the top right fan. a) 1st BPF. b) 2nd BPF.

Porous case

Aerodynamic results

A porous medium is introduced to mimic the cabinet door grill as well as the electric transformer, as shown in Fig. 1. The overall flow topology is similar to Fig. 3. Mean surface pressure contours are represented in Fig. 8 for the front right fan. A clear shift on the blade loading is found compared to the cold case in Fig. 5, as expected from the additional restriction.

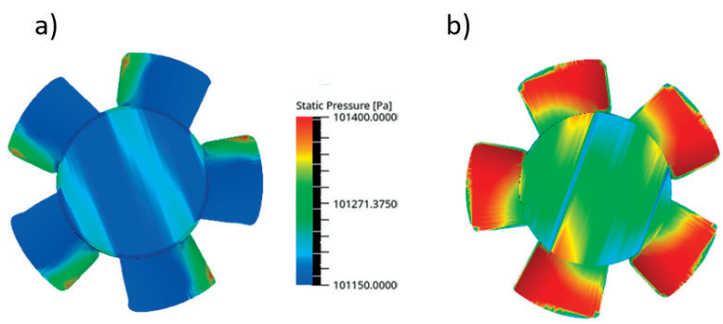


Figure 8: Averaged fan surface pressure contours. a) Pressure side. b) Suction side

Acoustic results

Only the front probes are investigated as they have been identified as the highest noise contributor to the far field. In Fig. 9, sound pressure levels computed on this front probe show that the main difference when adding the porous media lies in the low frequency region as well as on the amplitude of the BPFs. With the additional restriction, higher sound levels are recorded at lower frequencies with a faster frequency decay, and both BPF are much stronger. Indeed, higher wall-pressure fluctuations are found around the first two BPF in Fig. 10, compared with the cold case in Fig. 7.

Hot case

Aerodynamic results

Finally and in order to have a complete investigation, a heat source is added to the electric transformer to mimic the real fast charging conditions. A heat flux, provided by the industrial partner, is imposed on the porous medium representative of the electric transformer. As in the porous case, no change in the overall flow-field topology is seen. However, higher temperatures are recorded on the surface of the electric transformer by reaching approximately 355 K over the course of around 8 seconds of physical time. Hot air is then convected through the right side of the cabinet wall, due to the central

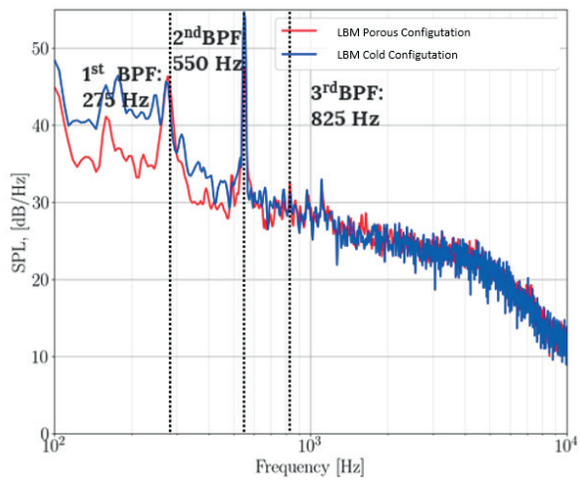


Figure 9: Sound pressure level computed for the front probe.

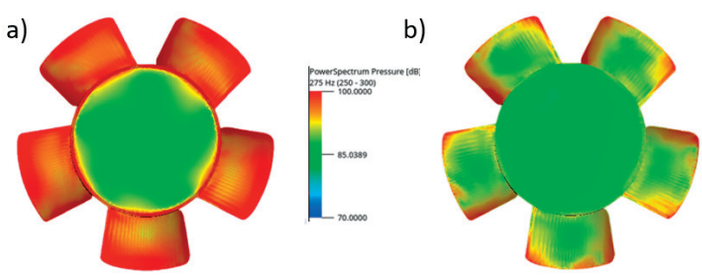


Figure 10: PSD of wall pressure fluctuation on the top right fan. a) 1st BPF. b) 2nd BPF

mid fan blowing and forcing air, and circulates upwards until it exits the unit from the two top fans. The overall load on the fans is increased compared to the cold and porous cases due to the added heat source. The temperature is stabilized at 335 K in the heat source region.

Mean wall-pressure contours in Fig. 11 show a further shift in the blade loading, with the stagnation point moving to the pressure side at the blade tip.

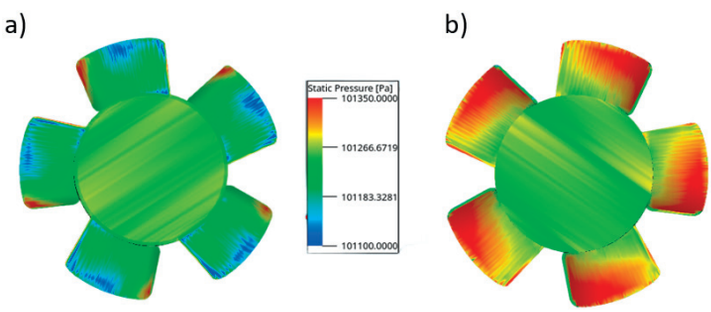


Figure 11: Averaged fan surface pressure contours. a) Pressure side. b) Suction side

Acoustic results

The acoustic effect of the heat source is investigated and compared to the cold and porous cases as shown in Fig. 12. Overall, higher broadband levels are captured for the hot case. However, a lower amplitude for the BPFs is displayed. This is consistent with a less adapted flow configuration on the fan corresponding to a higher incidence yielding larger adverse pressure gradient and consequently larger broadband noise levels with a smaller tonal emergence.

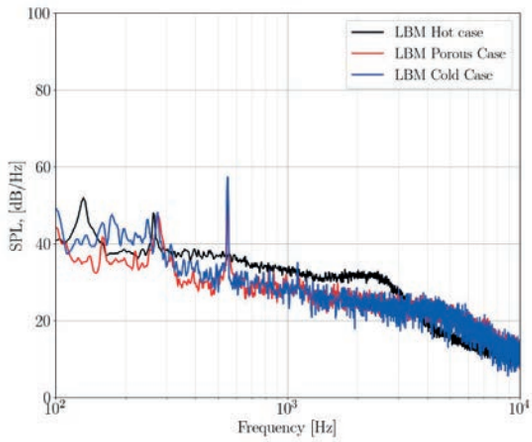


Figure 12: Sound pressure level computed for the front probe

This is further confirmed by the filtered pressure fluctuations on the fan surface shown in Fig. 13. No notable differences are seen on the first BPF at 275 Hz in terms of pressure fluctuation distribution except that the blade-tip contribution is more dominant in the hot case than in the porous one.

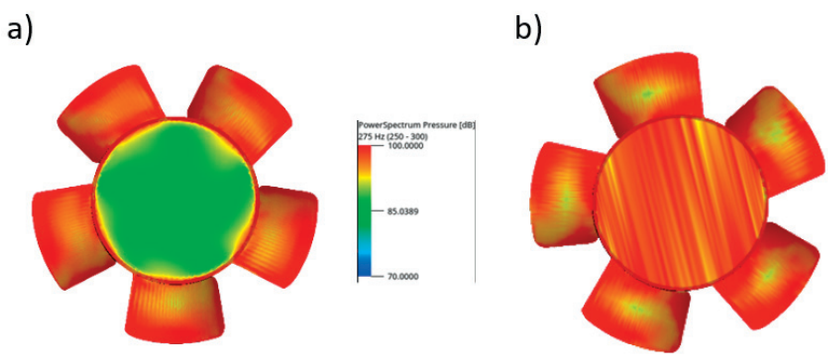


Figure 13: PSD of wall-pressure fluctuation on the top right fan: a) First BPF porous case; b) First BPF hot case.

CONCLUSIONS AND OUTLOOKS

The first high-fidelity compressible simulation of a complete fast charging cabinet configuration for electrical cars has been achieved using the Lattice-Boltzmann Method. The numerical configuration of the cabinet includes five fans that were designed from the drawings provided by the industrial partners. Three configurations have been investigated with increasing complexity added in order to get closer to the real cabinet setting. On the reference cold configuration, a mesh convergence has been performed, which shows that a minimum grid resolution of 0.5 mm is adequate for the present study. The three configurations show sound spectra around the cabinet combining both tonal and broadband noise components with similar amplitudes. The two upper front fans are the dominant noise contributors. Adding the protection grills and the heat source from the transformer alters the operating condition of the fans, with a stagnation point that moves to the blade pressure side in the hot case yielding an increase in broadband and overall noise.

Noise reduction could be achieved by adapting the fan design to the hot case better, and by choosing a blade design with less tonal noise content with forward sweep for instance. This will be the subject of future high-fidelity simulations of the charging cabinet.

REFERENCES

[1] Stéphane Moreau. Direct noise computation of low-speed ring fans. *Acta Acustica united with Acustica*, 105(1):30–42, 2019.

[2] Stéphane Moreau. The third golden age of aeroacoustics. *Physics of Fluids*, 34(3):031301:1–15, 2022.

[3] Jang-oh Mo and Jae-hyuk Choi. Numerical investigation of unsteady flow and aerodynamic noise characteristics of an automotive axial cooling fan. *Applied Sciences*, 10(16):5432, 2020.

[4] Marlène Sanjose and Stéphane Moreau. Direct noise prediction and control of an installed large low-speed radial fan. *European Journal of Mechanics-B/Fluids*, 61:235–243, 2017.

[5] M Sanjose, D Lallier-Daniels, and S Moreau. Aeroacoustic analysis of a low-subsonic axial fan. In *ASME Turbo Expo 2015: Turbine Technical Conference and Exposition*. American Society of Mechanical Engineers Digital Collection, 2015.

[6] Dominic Lallier-Daniels, Mélanie Piellard, Bruno Coutty, and Stéphane Moreau. Aeroacoustic study of an axial engine cooling module using lattice-boltzmann simulations and the ffowcs williams and hawkings' analogy. *European Journal of Mechanics-B/Fluids*, 61:244–254, 2017.

[7] Orestis Amoiridis, Alessandro Zarri, Riccardo Zamponi, Julien Christophe, Christophe F Schram, Gyuzel Yakhina, and Stephane Moreau. Experimental analysis of the sound radiated by an automotive cooling module working at different operational conditions. In *AIAA AVIATION 2020 FORUM*, page 2598, 2020.

[8] Stéphane Moreau and Marlène Sanjose. Sub-harmonic broadband humps and tip noise in low-speed ring fans. *The Journal of the Acoustical Society of America*, 139(1):118–127, 2016.

[9] Mélanie Piellard, Bruno B Coutty, Vincent Le Goff, Vincent Vidal, and Franck Pérot. Direct aeroacoustics simulation of automotive engine cooling fan system: effect of upstream geometry on broadband noise. In *20th AIAA/CEAS Aeroacoustics Conference*, page 2455, 2014.

[10] Simon Marié. *Etude de la méthode Boltzmann sur Réseau pour les simulations en aéroacoustique.* PhD thesis, Université Pierre et Marie Curie-Paris VI, 2008.

[11] Guillaume Bres, Franck Pérot, and David Freed. Properties of the lattice boltzmann method for acoustics. In *15th AIAA/CEAS Aeroacoustics Conference (30th AIAA Aeroacoustics Conference)*, page 3395, 2009.

[12] Safouane Tebib, Athreya Ballapur Jayasimha, Stephane Moreau, Bruno Desmory, Manuel Henner, Adrien Mann, and Charles Luzzato. Aeroacoustic investigation of automotive engine cooling modules using the lattice-boltzmann method. In *28th AIAA/CEAS Aeroacoustics 2022 Conference*, page 2859, 2022.

[13] F. Pérot, M.-S. Kim, S. Moreau, M. Henner, and D. Neal. Direct aeroacoustics prediction of a low-speed axial fan. In *16th AIAA/CEAS Aeroacoustics Conference*, AIAA2010–3887 paper, Stockholm, Sweden, June 2010.

[14] H. Chen, S. Chen, and W. Matthaeus. Recovery of the Navier–Stokes equations using a lattice-gas Boltzmann method. *Physics Review A: Statistical Mechanics and its Applications*, 45(8):5339–5342, 1992. Discrete Simulation of Fluid Dynamics - Proceedings of the 13th International Conference on Discrete Simulation of Fluid Dynamics.

[15] S. Chen and G. D. Doolen. Lattice Boltzmann method for fluid flows. *Annual review of fluid mechanics*, 30:329–364, 1998.

[16] H. Chen, S. A. Orszag, I. Staroselsky, and S. Succi. Expanded analogy between Boltzmann kinetic theory of fluids and turbulence. *Journal of Fluid Mechanics*, 519:301–314, November 2004.



EVALUATION OF HYBRID COMPUTATIONAL AEROACOUSTIC METHODS APPLIED TO AUTOMOTIVE COOLING-FANS

Debarshee GHOSH[1], Michail VOURAKIS [1], Alexander BOSTRÖM[1], Niklas ANDERSSON[1], Ashik ROY [2], Sassan ETEMAD [2]

[1] *Chalmers University of Technology, Fluid Dynamics Division, Hörsalsvägen 7A, 41296 Göteborg, Sweden*

[2] *Volvo Group Trucks Technology, Gropegårdsgatan 10, 41715 Göteborg, Sweden*

SUMMARY

In the absence of the internal combustion engine in electric vehicles, the noise produced by the cooling-fan becomes prominent. This study presents a comparison between experimentally and numerically obtained acoustic characteristic curves for three aerodynamic operating points of an in-service cooling-fan. An additional investigation is done for the aerodynamic best efficiency point, incorporating an upstream blockage which obstructs a 60° sector of the fan inlet. Three-dimensional, full-annulus, unsteady, scale-resolving simulations are done using the Delayed Detached Eddy Simulation (DDES) turbulence model and the permeable Ffowcs Williams-Hawkings (FWH) method, with the Farassat-1A formulation as the far-field acoustic analogy.

INTRODUCTION

Cooling-fans are integral to the thermal management systems of electric vehicles, facilitating heat exchange between the liquid coolant circulating in the heat-exchanger and the ambient air. The cooling-fan generates a pressure gradient that drives airflow in-between the channels of the heat-exchanger. Positioned downstream of the heat-exchanger, these cooling-fans enable forced convective cooling, using ambient air as a heat sink to dissipate heat from the liquid coolant. Cooling-fans are predominantly operational at low vehicle speeds ($< 30\ km/h$), where ram-air is insufficient to drive airflow in between the channels of the heat-exchanger [1]. At higher vehicle speeds, the increased ram-air velocity in the underhood region typically negates the need for a cooling-fan. Automotive cooling fans in most cases are low-pressure axial fans.

In the absence of internal combustion engines (ICEs) in electric vehicles, cooling-fans emerge as a notable source of noise, particularly at low vehicle speeds. Furthermore, these fans are often arranged in parallel configurations. The parallel arrangement of cooling-fans results in an amplification of the overall Sound poWer Level (SWL), with an upward scaling of the acoustic spectra in accordance to having strong uncorrelated sound sources [2], [3]. At higher vehicle speeds, wind-noise and tyre-road-interaction noise dominate [4], [5].

Cooling-fans in electric vehicles are installed in increasingly compact underhood spaces, where manufacturers seek greater flexibility to position the fan in areas that may partially or fully obstruct the fan inlet. This places significant importance on the need to quantify the change in the aerodynamic and acoustic behavior of cooling-fans when subjected to upstream blockages. Typically, the air entering the underhood region passes through the grill, charger cooler, and heat-exchanger before being ingested by the fan, often resulting in a spatially non-homogeneous and turbulent flow at the fan inlet. Several scientific studies have demonstrated that spatial inhomogeneity and increased turbulence at fan inlets can significantly deteriorate both the aerodynamic and aeroacoustic performance of cooling-fans.

While several numerical studies have investigated the aerodynamic and aeroacoustic performance of cooling-fans under clean inlet flow conditions, limited research has focused on the aeroacoustic performance of cooling-fans subjected to upstream blockages. The authors consider this an essential step towards the accurate prediction of the acoustic performance of cooling-fans when subjected to blockages. Furthermore, numerical aeroacoustic investigations are often restricted to the BEP. It is valuable to evaluate the aero-acoustic performance of these cooling-fans at aerodynamic operating points away from the BEP, as is often required in several of its operational scenarios.

In this work, three-dimensional, full-annulus, scale-resolving, unsteady simulations are performed using Delayed Detached Eddy Simulations (DDES) as the turbulence model for an in-service automotive cooling-fan with a rotating ring. Far-field noise is calculated using the Ffowcs-Williams and Hawkings (FW-H) analogy, with the Farassat-1A formulation. First, computational aeroacoustic investigations are conducted for three aerodynamic operating points, and the numerical results are compared against acoustic data obtained from experiments conducted at Volvo Group Trucks Technology (VGTT). Changes in the aerodynamic and aeroacoustic performance of cooling-fans as a result of change in the aerodynamic operating points is analyzed. Second, a solid, unperforated blockage in the shape of a 60° sector is positioned upstream of the fan. The numerical results for this inlet-blockage case is compared against experimental data at the aerodynamic BEP. Finally, the ability of the numerical setup to predict the aeroacoustic performance of cooling-fans with upstream blockages is evaluated.

NUMERICAL SETUP

Geometry

This study focuses on an automotive cooling fan with a rotating ring, which is currently in use in several heavy-duty trucks. Geometrically, the fan has a tip diameter (d_{fan}) of 300 *mm*, a hub diameter (d_{hub}) of 150 *mm*, and a casing diameter (d_{casing}) of 332 *mm*. The fan has seven rotor blades with a non-equidistant circumferential spacing, and 12 equally spaced outlet guide vanes (OGVs). An additional quarter-circle bell-mouth with a radius of 235 *mm* is positioned upstream of the fan, to ensure a clean undisturbed flow into the fan. For the inlet-blockage case, the 60° sector with a thickness of 2 *mm* is positioned at a distance of 80 *mm* upstream of the fan hub face, see Fig. 1.

The aerodynamic and aero-acoustic performance of the fan is experimentally obtained for a rotational speed of 4511 rpm for three different aerodynamic operating points, with inlet volume flowrates (Q)

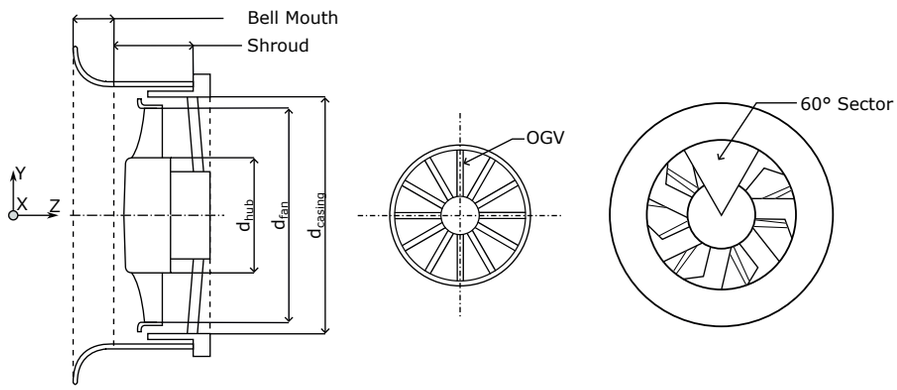


Figure 1: Schematic of geometry used in this work

of: 0.64, 0.9, and 1.17 m^3/s . The experimental BEP is obtained at an inlet volume flowrate equal to 0.64 m^3/s. The far-field sound is obtained using microphones positioned in a half-sphere at a radius of 103 *mm* upstream of the fan. The microphones are separated by an angle of 15° in the circumferential direction and 60° in the radial direction. The microphones used are half inch free-field type GRAS 46AE. The measurement uncertainty is tabulated in Tab. 1

The acoustic measurements were made for a total of 65 seconds with a sampling frequency ($f_{s,exp}$) of 50 kHz. A Fast Fourier Transform (FFT), with the Welch method, 2^{14} samples (N_{exp}), 50 % overlap factor, and the Hanning window is used, to obtain the Power Spectral Density (PSD) spectrum, which corresponds to a frequency resolution (Δf_{exp}) of 3 Hz for the experimental data. Additional details of the experimental test-rig used to obtain the measurement data at VGTT, is provided by Gullberg [6].

Table 1: Measurement Uncertainty

Parameter	**Uncertainty**
Volume flowrate	$\pm$ 1.5 %
Pressure	$\pm$ 3 *Pa*
Density	$\pm$ 0.3 %
PSD	$\pm$ 0.65 *dB*
Microphone position	$\pm$ 20 *mm*
Rotational speed	$\pm$ 1.8 *rpm*

Computational Setup

All numerical investigations presented in this work have been done using the commercially available software Star-CCM+ version 2310 [7]. Air as an ideal gas has been used as the fluid medium for all numerical investigations. All numerical investigations are performed for an ambient density (ρ_∞) of 1.17 kg/m^3. Compressible flow simulations are done using the segregated solver to obtain the flow-field. The governing equations are discretised in space, using the Bounded Central Differencing (BCD) scheme. The SIMPLE algorithm is used to couple pressure and velocity.

The numerical simulations aim to resolve frequencies up to 10 kHz in the acoustic spectra. A second-order temporal discretisation scheme is used to discretise the time-domain with a maximum of 10

inner iterations per time-step. A time-step of 5 μs, which corresponds to a rotation of 0.135° per time-step is used. A total physical time of 0.425 seconds corresponding to 32 full rotations of the fan is computationally simulated.

The far-field sound is obtained through a hybrid Computational Aeroacoustic (CAA) approach. To obtain the far-field noise, the permeable FW-H method is used, with the Farassat-1A formulation [8], [9]. A permeable FW-H surface is defined within the computational domain which encapsulates the noise source. For all regions encapsulated by the permeable FW-H surface, a Direct Noise Calculation (DNC) is done. Acoustic pressure fluctuations $p'(\vec{x},t)$ are recorded at the permeable FW-H surface, and propagated to the far-field using the Farassat-1A formulation.

Scale-resolving DDES is used as the turbulence model. The DDES turbulence model uses the Unsteady RANS (URANS) formulation in the near wall and irrotational flow regions, and the LES formulation in the mean flow region, see Fig. 2. The Spalart-Allmaras (SA) model is used in the URANS region.

The PSD spectrum is calculated using the $p'(\vec{x},t)$ signal from the fourth to the last simulated rotation, which corresponds to a total time-signal length of, 0.372 seconds. A FFT, with settings identical to those used for the experimental data is used to obtain the PSD spectrum, which corresponds to a frequency resolution (Δf_{CFD}) of 12 Hz for the numerical data.

Computational Domain and Grid

A cuboidal computational domain is implemented with cross-sectional area of $5d_{casing} \times 8d_{casing}$, perpendicular to the fan rotational axis. The inlet and outlet of the computational domain have been extended upstream and downstream of the bell-mouth inlet and fan outlet by $5d_{casing}$, respectively. The permeable FW-H surface is also a cuboid with cross-sectional area of 500 $mm \times 500$ mm, perpendicular to the fan rotational axis, and extends 250 mm in the axial direction, see Fig. 2. The inlet is prescribed as velocity inlet, and the outlet as a pressure outlet. The motion of the fan is modeled using the sliding grid approach [7]. All walls are modeled as no-slip walls. The computational domain is divided into a rotating region and two stationary regions. The rotating region extends 110 mm in the axial direction, starting from an axial position 60 mm upstream of the rotor hub.

A trimmed cell mesher is used to spatially discretize the computational domain. Prism layers are used to discretize the near-wall regions. Three different grids, labeled "coarse", "medium", and "fine" are generated to evaluate grid independence. The Grid Convergence Index (GCI) [10] method is used to evaluate grid independence [10]. For the coarse, medium, and fine grids a constant cell size of 3.5 mm, 2.0 mm, and 1.35 mm, respectively, is maintained everywhere within the FW-H surface, i.e., the DNC region. The cell size is increased in a homogeneous manner from the coarse to the fine grid. In the rotating region of the computational domain, four prism layers with the first cell wall distance of 20 μm, and a total thickness of 0.5 mm is used to discretize the near wall region. To ensure numerical damping of the acoustic waves incident on the outer extents of the computational domain, significantly large cells are used at the walls, to mimic an anechoic test-chamber.

The grid quality is evaluated using three parameters: cell skewness angle, cell volume change, and cell aspect ratio [7]. The solver requires the cell skewness angle to be below 85° and the cell volume change to be greater than 0.01. Although the solver does not prescribe a specific value for the cell aspect ratio, efforts have been made to ensure that all cells are as close as possible to the ideal value of 1.0. All grids used in this work adhere to the aforementioned grid quality criteria.

The grid independence is evaluated at the experimental BEP, i.e., inlet volume flowrate (Q) of 0.64 m^3/s. The total-to-static pressure (p_{ts}) rise, is used to evaluate the grid independence. The total-to-static pressure rise is defined as the difference between the area-averaged pressure at the outlet of

FAN 2025
Antibes - Juan-les-Pins (France), 9 - 11 April 2025

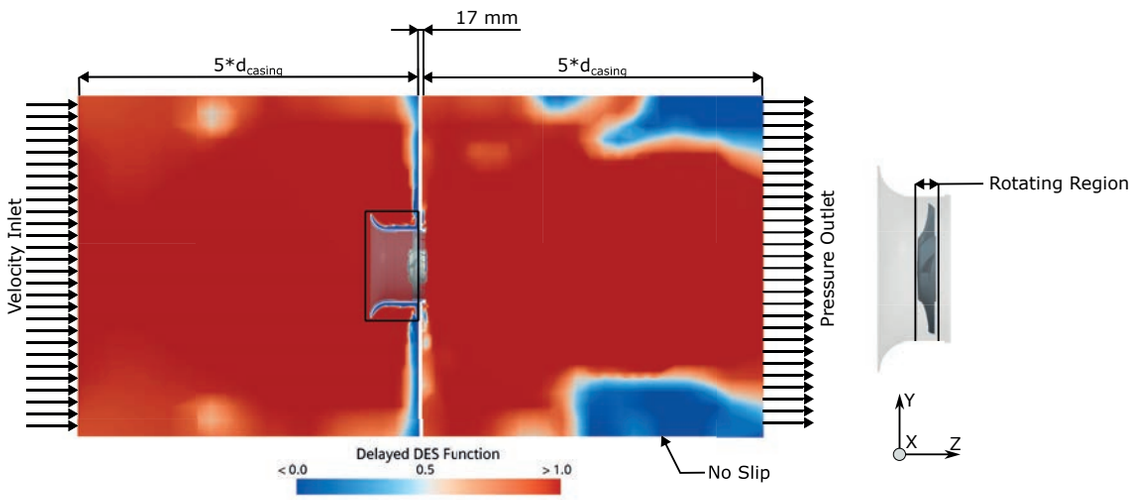


Figure 2: Cross-section of the CFD domain, illustrating the boundary conditions and the distribution of LES (DDES Function = 1.0) and URANS (DDES Function = 0.0) regions.

the computational domain and the massflow-averaged total pressure at the inlet of the computational domain. This total-to-static pressure was seen to vary by less than 1 % between the medium and fine grid according to the GCI method. The medium grid is used for all further investigations.

For the medium grid with a constant cell size of 2 *mm* in the DNC region, a minimum of 18 grid points are used to spatially resolve the highest frequency acoustic wave of interest (f_{max} = 10 kHz), which corresponds to the shortest wavelength ($\lambda_{min} = 34.5mm$). Additional details of the computational setup is detailed by Ghosh et al. [2].

RESULTS

Aerodynamic Performance Results

The change in aerodynamic performance as a result of changing the operating point of the fan, and introducing an upstream blockage is first briefly analyzed, and compared against experimental data. The effect of including the upstream blockage in the form of a 60° sector is evaluated only at the experimental BEP. The aerodynamic performance at a specified aerodynamic operating point, is quantified by the total-to-static pressure rise (p_{ts}), and the total-to-static efficiency (η_{ts}), according to Eq. 1. Specifically, the total-to-static pressure rise, is used to compare the numerical and experimental aerodynamic performance, as tabulated in Tab. 2. A positive value of deviation in Tab. 2, indicates an over-prediction by CFD compared to experimental data.

$$p_{ts} = (p_{s,outlet} - p_{t,inlet}) \qquad \eta_{ts} = \frac{Q\, p_{ts}}{P_{shaft}} \tag{1}$$

At the experimental BEP, corresponding to Q = 0.64 m^3/s, CFD marginally over-predicts the total-to-static pressure rise by 1.37 % compared to experimental data. Experimentally, the total-to-static pressure is observed to drop by 9.6 % when the upstream blockage is introduced. In comparison, the numerical results predict a smaller drop of 4.8 % in the total-to-static pressure as a result of incorporating the upstream blockage, i.e., the numerical setup under-predicts the effect of an upstream blockage compared to experiments. For the second investigated operating point, corresponding to an inlet volume flowrate of 0.90 m^3/s, CFD marginally under-predicts the total-to-static pressure rise by

1 % compared to experimental data. The largest inlet volume flowrate experimentally investigated, $Q = 1.17\ m^3/s$, corresponds to free-discharge conditions with a total-to-static pressure rise of 6.5 *Pa*. For this aerodynamic operating point, corresponding to the experimental free-discharge conditions, CFD substantially over-predicts the total-to-static pressure rise. However, here it is important to note that, close to the free-discharge point even small measurement uncertainties lead to substantial differences in aerodynamic operating point and the corresponding aerodynamic performance. With the measurement uncertainty tabulated in the Tab. 1, the inlet volume flowrate, can lie between 1.188 m^3/s to 1.152 m^3/s. At free-discharge conditions, the stagnation point moves to the suction surface and flow-separation occurs on the pressure side of the blade [11], i.e., significantly unsteady phenomenon occur at free-discharge operating conditions, limiting the ability of the numerical setup to accurately capture the aerodynamic performance.

Here, it is concluded that the numerical setup used in this work successfully predicts the aerodynamic performance of this in-service cooling fan at aerodynamic operating points away from the free-discharge conditions for clean inlet flow conditions. The used numerical setup, however, fails to accurately capture the free-discharge operating point compared to experiments, and under-predicts the effect of the blockage.

Table 2: Aerodynamic Performance Comparison

Volume flowrate	Experimental	Numerical	Deviation
0.64 m^3/s	528.93 Pa	536.20 Pa	+1.37 %
0.64 m^3/s **with blockage**	477.95 Pa	510.325 Pa	+6.77 %
0.90 m^3/s	313.29 Pa	310.04 Pa	-1.04 %
1.17 m^3/s	6.50 Pa	30.26 Pa	+365.54 %

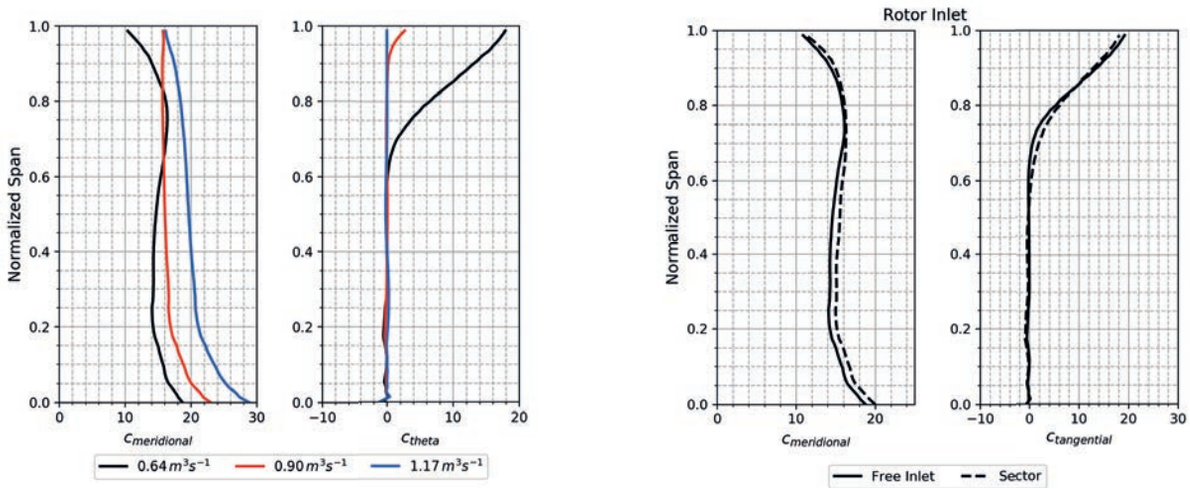
The radial profiles of meridional and circumferential velocity at the rotor inlet are presented, in Fig. 3. The radial profiles are obtained through massflow and time-averaging the velocity components at a plane is positioned 3 *mm* downstream of the fan hub face. No experimental data is available for the velocity components.

Predictably, an increase in the meridional velocity, is observed as result of increasing the inlet volume flowrate. An increase in the meridional velocity component correspondingly reduces the absolute inlet flow-angle for individual blade sections, which in turn leads the incidence angle, and ultimately to reduced work done by the rotor blade on the flow [12].

The presence of an inlet blockage is observed to have minimal effect on the inlet meridional and circumferential velocity components. The velocity profiles along the rotor blade span, for the experimental BEP for the free-inlet and blockage case is illustrated in Fig. 3. A marginal increase is observed at the rotor inlet in the meridional velocity for the blocked case. This is a direct result of section of the inlet area being blocked, accelerating the flow through the unblocked section of the fan inlet face to achieve the target inlet volume flowrate. This increased meridional velocity, as described previously, leads to reduced work done by the rotor blade, and consequently a reduced total-to-static pressure rise achieved by the fan. Here, it is reiterated that the numerical results under-predict the effect of the blockage compared to experimental data. No change is observed in the circumferential velocity component as a result of incorporating the upstream blockage.

Aeroacoustic Performance

The change in aeroacoustic performance of the fan as a result of changing the aerodynamic operating point, is first discussed. The PSD spectrum, for numerical and experimental data are compared for



(a) Rotor Upstream *(b) Rotor Upstream*

*Figure 3: **(a)**: Effect of changing aerodynamic operating point **(b)**: Effect of upstream blockage*

the three operating points in Figs. 4-5.

Both numerical and experimental data capture the upward scaling of the acoustic spectra as a result of decreasing the inlet volume flowrate, see Fig. 4. For all three operating points, the numerical setup accurately captures the base broadband noise levels, see Fig. 5. For all three operating points, the high frequency broadband noise region ($f > 5\ kHz$), which is typically dominated by trailing edge noise [13], is marginally under-predicted by CFD. This is predicted to be a result of grid-induced acoustic cut-off. The mid-frequency broadband noise spectra between 1-5 kHz compares well with experimental data for all three operating points. The low-frequency base broadband level is marginally over-predicted by CFD for all three investigated operating points.

The fan geometry used in this work has unequal blade spacing in the circumferential direction. A rotor with blades spaced equally in the circumferential direction, is expected to emit tonal noise only at the Blade Passing Frequency (f_{BPF}) and its subsequent harmonics. In comparison, a rotor with unequal circumferential blade spacing is expected to emit tonal noise both at the BPF and at shaft rotational frequencies (f_{SF}) [14], [15]. Consequently, as a result of having unequal blade spacing, a large number of tonal peaks at frequencies other than the BPF, can be expected in the acoustic spectrum. However, a properly chosen circumferential spacing may lower the magnitude of the tonal peaks, resulting in less perceivable tonal peaks due to the masking effect of broadband noise. This use of unequal rotor blade spacing is especially useful for low-solidity fans ($\sigma < 0.7$), where the circumferential spacing between rotor blades is high, i.e., the flow from one rotor blade is unlikely to be affected by the adjacent blade. Additionally, tonal peaks are expected to become more pronounced at higher volume flowrates [14]. For this particular fan geometry with unequal circumferential blade spacing, the BPF is at 526 Hz, and given a rotational speed of 4511 rpm, the shaft rotational frequency is at 75.16 Hz.

For all three operating points, the experimental PSD curve accurately captures the shaft rotational frequency at 75 Hz, BPF at 526 Hz, and its higher harmonics. The increased magnitude of the tonal peaks as a result of increase in inlet volume flowrate is also captured accurately by experimental data.

The numerical data accurately captures the BPF for all operating points at $f_{BPF} = 526\ Hz$. The base broadband noise level for the numerical data at low-frequency is higher compared to the experimental data, masking the lower harmonics of the shaft rotational frequency for the numerical data. But for all investigated operating points, the higher harmonics of the shaft rotational frequency also becomes

visible in the numerical data. This is especially notable in the highest investigated volume flowrate, Q = 1.17 m^3/s. The increase in the tonality with the increase in the inlet volume flowrate is also visible in numerical data, albeit not as severe as observed in the experimental data. A potential explanation for the increased tonal components observed in the experiments could be the elevated inflow turbulence levels, in contrast to the CFD simulations where ideal inflow conditions are enforced [16], [17]. However, due to the lack of direct turbulence level measurements during the experimental campaign, this assumption cannot be definitively confirmed by the authors.

For the experimental BEP, Q = 0.64 m^3/s, the fifth and sixth harmonic of the shaft rotational frequency ($5f_{SF}, 6f_{SF}$) is masked by a narrow-band hump associated with the sub-harmonic tip noise. Subharmonic tip-noise is generated as a result of coherent tip structures which originate from the rotor tip. These coherent tip structures rotate with an angular velocity lower than the rotational speed of the rotor and interact with the subsequent rotor blade. This narrow band hump is observed at frequencies lower than the BPF [18]–[21]. In this case, the sub-harmonic tip noise is observed at a frequency of 400 Hz for both numerical and experimental data.

Subharmonic tip noise is typically observed at lower flow rates. The reduced inlet volume flow rate, leads to a reduced meridional velocity at the rotor inlet, see Fig. 3, which consequently leads to an increased absolute flow angle at rotor inlet ($\alpha = tan^{-1}(c_\theta/c_m)$). An increased absolute flow angle, in turn leads to an increased angle of incidence at the tip region, $i = (\alpha - \alpha^{'})$, where $\alpha^{'}$ is the blade inlet angle. An increased angle of incidence (i), ultimately leads to a stronger suction peak on the blade suction side, which leads to stronger tip clearance flow and vortices. Therefore it follows, that the narrow band hump becomes less prominent at higher flowrates, with decreasing tip clearance flow. The reduced prominence of the sub-harmonic tip noise at higher inlet volume flowrates is visible for both the experimental and numerical data. The fifth and sixth harmonic of the shaft rotational frequency becomes visible at Q = 0.90 m^3/s, and Q = 1.17 m^3/s, as a result of the reduced prominence of the narrow-band hump associated with the subharmonic tip noise.

Lastly, the effect of the upstream blockage on the aero-acoustic performance is analyzed in Fig. 5. Experimentally, as a result of incorporating the blockage, the tonal components at f_{SF} and its harmonics is elevated. This is a consequence of the increased turbulence levels and flow non-uniformity incident on the rotor LE. The numerical data accurately captures the base broadband noise levels. However, it is unable to accurately capture the increase in the tonal peaks at shaft rotational frequency. This under-prediction in the tonal peaks by the numerical data is assumed to be a result of the numerical setup under-predicting the effect of the blockage, flow separation, and therefore spatial non-homogeneity, and turbulence levels.

CONCLUSIONS

Three-dimensional, full-annulus, scale-resolving, unsteady simulations are performed for an in-service automotive cooling-fan with a rotating ring. The change in the aerodynamic and aero-acoustic performance as a result of changing the operating point, and incorporating a blockage is evaluated. The numerical setup does a sufficient job predicting both the aerodynamic and aeroacoustic performance of the fan, when operating without an upstream blockage. Some limitations are observed in the ability of the numerical setup to accurately predict the tonal components at the shaft rotational frequency. The aerodynamic and aeroacoustic effect of the upstream blockage is under-predicted by CFD.

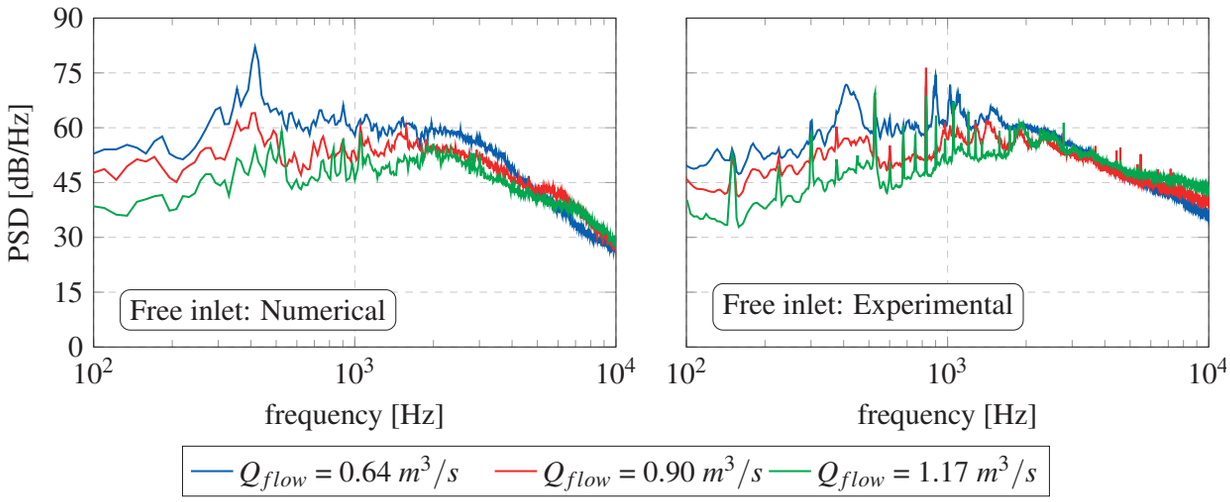


*Figure 4: PSD spectra for different aerodynamic operating points: **left**: Numerical and **right**: Experimental*

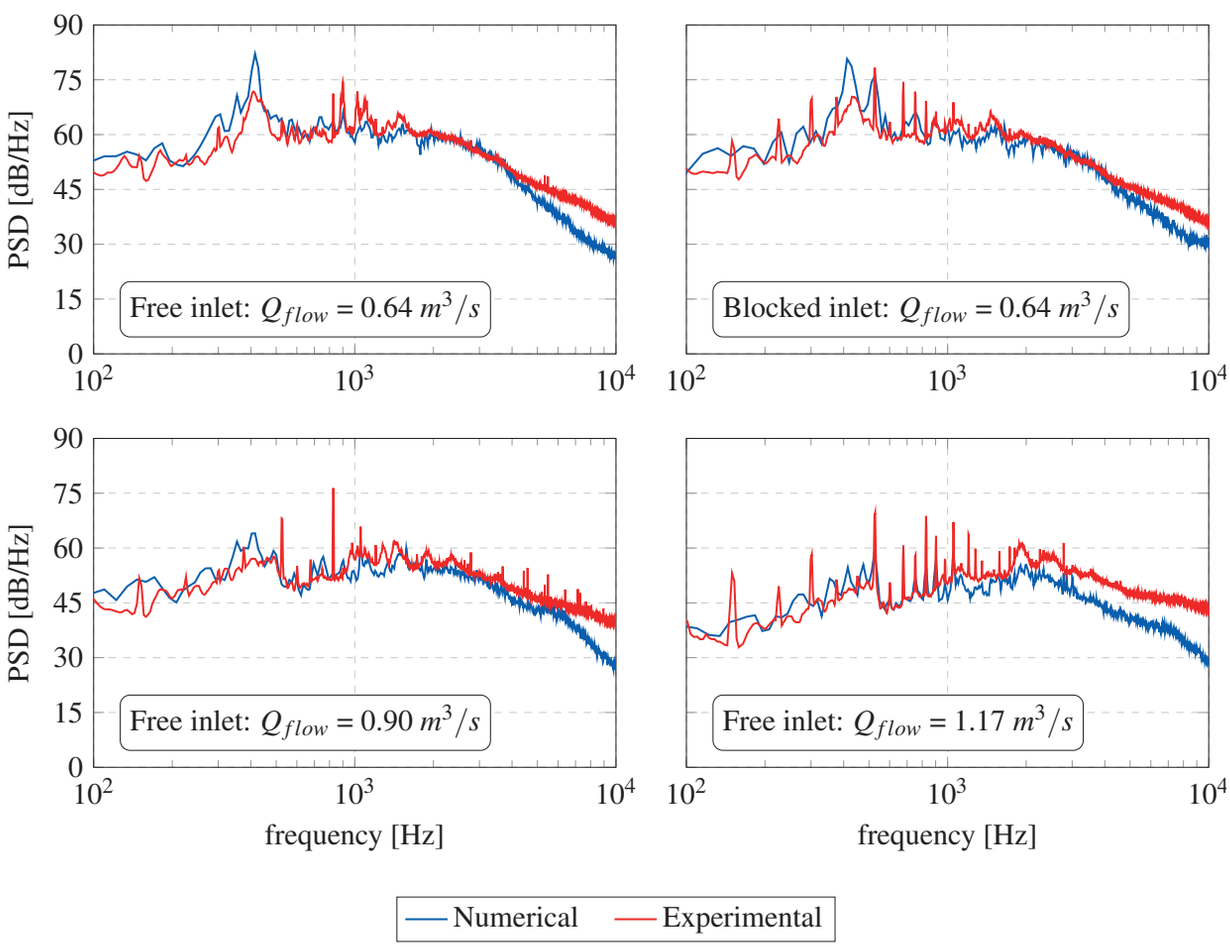


Figure 5: PSD spectra comparison between numerical data (Δf_{CFD} = 12 Hz) and experimental data (Δf_{exp} = 3 Hz)

ACKNOWLEDGMENTS

The Swedish Energy Agency, Volvo Group Truck Technology (VGTT), and Volvo Car Corporation (VCC) are acknowledged for financing this work. The Swedish Energy Agency is acknowledged for financing this work under the Grant Agreement No. 2018-018411. All the experiments, computations and data handling presented in this work were enabled by resources provided by VGTT and VCC.

REFERENCES

[1] M.-J. Park and D.-J. Lee, *Sources of broadband noise of an automotive cooling fan*, Applied Acoustics vol. 118, pp. 66–75, **2017**.

[2] D. Ghosh, M. Vourakis, N. Andersson, and S. Etemad, *Computational aeroacoustics of low-pressure axial fans installed in parallel*, Journal of Fluids Engineering vol. 147, no. 2, **2025**.

[3] M. Vourakis and M. Karlsson, *Aeroacoustic interaction effects between parallel low-pressure axial flow fans*, in *10th Convention of the European Acoustics Association, Forum Acusticum*, **2023**, pp. 10–15.

[4] A. Zeitler, *Psychoacoustic requirements for warning sounds of quiet cars*, SAE International journal of passenger cars-electronic and electrical systems vol. 5, no. 2012-01-1522, pp. 572–578, **2012**.

[5] X. Hua, A. Thomas, and K. Shultis, *Recent progress in battery electric vehicle noise, vibration, and harshness*, Science Progress vol. 104, no. 1, p. 00 368 504 211 005 224, **2021**.

[6] P. V. Gullberg, *Optimisation of the flow process in engine bays-3d modelling of cooling airflow*. Chalmers Tekniska Hogskola (Sweden), **2011**.

[7] Siemens Digital Industries Software, *Simcenter STAR-CCM+ User Guide v. 2310*, version 2310, **Siemens 2023**.

[8] J. Ffowcs Williams and D. Hawkings, *Sound generated by turbulence and surfaces in arbitrary motion*, Philosophical Transactions of the Royal Society vol. A264, no. 1151, pp. 321–342, **1969**.

[9] F. Farassat and M. Myers, *Extension of kirchhoff's formula to radiation from moving surfaces*, Journal of Sound and Vibration vol. 123, no. 3, pp. 451–461, **1999**.

[10] I. B. Celik, U. Ghia, P. J. Roache, and C. J. Freitas, *Procedure for Estimation and Reporting of Uncertainty Due to Discretization in CFD Applications*, Journal of Fluids Engineering vol. 130, no. 7, **2008**, 078001, ISSN: 0098-2202. DOI: 10.1115/1.2960953.

[11] E. J. Gunn and C. A. Hall, *Loss and deviation in windmilling fans*, Journal of Turbomachinery vol. 138, no. 10, p. 101 002, **2016**.

[12] B. S. Larry Dixon and C. Hall, *Fluid Mechanics and Thermodynamics of Turbomachinery*. Elsevier Science, **2013**, ISBN: 9780124159549. [Online]. Available: https://books.google.se/books?id=CEpipwAACAAJ.

[13] S. Wright, *The acoustic spectrum of axial flow machines*, Journal of Sound and Vibration vol. 45, no. 2, pp. 165–223, **1976**.

[14] A. Cattanei, F. Mazzocut Zecchin, A. Di Pasquali, and A. Lazari, *Effect of the uneven blade spacing on the noise annoyance of axial-flow fans and side channel blowers*, Applied Acoustics vol. 177, p. 107 924, **2021**, ISSN: 0003-682X. DOI: https://doi.org/10.1016/j.apacoust.2021.107924. [Online]. Available: https://www.sciencedirect.com/science/article/pii/S0003682X21000177.

[15] W. Neise and U. Michel, *Aerodynamic noise of turbomachines*, Deutsche Forschungsanstalt für Luft-und Raumfahrt, eV, DLR, Institut für Strömungsmechanik, Abt. Turbulenzforschung, Berlin vol. 5, **1994**.

[16] F. J. Zenger, A. Renz, M. Becher, and S. Becker, *Experimental investigation of the noise emission of axial fans under distorted inflow conditions*, Journal of Sound and Vibration vol. 383, pp. 124–145, **2016**.

[17] H. Reese, T. Carolus, and C. Kato, *Numerical prediction of the aeroacoustic sound sources in a low pressure axial fan with inflow distortion*, Fan noise vol. 9, 1–12P, **2007**.

[18] F. Kameier and W. Neise, *Experimental study of tip clearance losses and noise in axial turbomachines and their reduction*, **1997**.

[19] R. Mailach, I. Lehmann, and K. Vogeler, *Rotating instabilities in an axial compressor originating from the fluctuating blade tip vortex*, J. Turbomach. vol. 123, no. 3, pp. 453–460, **2001**.

[20] T. Zhu, D. Lallier-Daniels, M. Sanjosé, S. Moreau, and T. Carolus, *Rotating coherent flow structures as a source for narrowband tip clearance noise from axial fans*, Journal of Sound and Vibration vol. 417, pp. 198–215, **2018**.

[21] S. Magne, S. Moreau, and A. Berry, *Subharmonic tonal noise from backflow vortices radiated by a low-speed ring fan in uniform inlet flow*, The Journal of the Acoustical Society of America vol. 137, no. 1, pp. 228–237, **2015**.

Author Index

Åbom, Mats 167, 367, 368, 431, 479, 481, 482, 485, 489,
Ahuja, Amit 81, 109, 208
Akhtar, Tayyab 431, 445,
Aldi, Nicola 197, 199, 208,
Andersson, Niklas 255, 275, 479, 513, 522
Angelis, Walter 11, 347, 349
Antoniou, Evangelos 379, 443, 457, 469, 478,
Arina, Renzo xvi, 479, 491, 500
Arroyo, Ramo Andrea 221, 243, 244, 246, 253, 254, 428
Assaf, Samir 119, 147
Avallone, Francesco xvi, 311, 479, 491, 500,

Balla, Esztella157, 189, 195, 196, 510
Becker, Stefan 43, 119, 135, 144, 145, 284, 357, 359, 367, 380, 454, 455, 457, 459, 468, 478, 500, 523
Bellelli, Francesco 479, 491, 493, 500
Bennouna, Saad 255, 267, 273, 276, 284
Bierrenbach-Lima, Andre 287, 301, 326, 402
Bleiziffer, Mihai 350, 355, 431, 433, 442
Bode, Christoph 1, 13, 21, 22,
Boshoff, Francois 42, 81, 83, 84, 90, 93,
Boström, Alexander 479, 513
Bregolin, Edoardo 42, 403, 405, 419,
Breuer, Julius 81 97, 98, 102, 105, 106

Chouard, Nicolas 255, 267
Compain, Armand 255, 267, 274
Czwielong, Felix 119 135, 141, 144, 145, 276, 284, 368, 441, 443, 455, 457, 459, 467, 468, 469, 478, 491, 500

Danieli, Piero 1, 33, 42, 287, 403, 405, 419, 427
Dargel, Alrik 197, 211, 219
Delfs, Jan Werner 43, 62, 63, 71, 79
Demeulenaere, Alain xiii, 287, 289,
Demory, Bruno 431, 445, 454,
Dietrich, Philipp 43, 53, 62, 71, 74, 79
Drame, Ahmadou Bamba 157, 169, 178, 188,
Dsilva, Lionel 221, 223
Ebert, Christoph 197, 211, 219, 289,
Edwards, Sean 287,
Elnady, Tamer 43, 368, 479, 489,
Erbig, Lars 371, 373, 380, 381, 390, 391, 392
Ernst, Daniel 43, 63, 71, 73, 79
Etemad, Sassan 1, 255, 275, 457, 479, 513, 522

Facca, Massimo 81, 109,
Ferhat, Jacques 119, 147
Fritzsche, Marco 334, 457, 459

Geyer, Thomas 62, 144, 145, 221, 223, 224, 225, 232, 468
Ghosh, Debarshee 429, 479, 513, 517, 522
Godart, Alban 255, 267, 274
Goecke, David 313, 325,
Gras, Thibaut 119, 147,
Grützner, Dominik 119, 135
Gude Maik, 197, 211, 219,

Heidegger, Patrick 457, 459
Heigl, Christoph 457, 459
Herrlich, Ferdinand 1, 3, 221, 233
Hosoi, Takeru 221, 233
Huang, Yixin 313, 337,
Hub ,Sandra 11, 231,

Jacob, Stefan 81, 357, 359, 368,

Kaltenbacher, Manfred 390, 457, 459, 468, 478
Karlsson, Mikael 255, 275, 277, 284, 522
Khamis, Ahmed 479, 481
Kluger, Jonas 197, 211,
Koch, Lisa Danielle 119, 121, 131, 132, 133, 170, 177
Konig, Richard 197, 211, 219
Kovács, Kinga Andrea 157, 189, 195, 196
Kucukcoskun, Korcan 371, 373, 380, 381, 390, 391, 392
Kunze, Eckart 3, 197, 211, 219,

Laguna, Juan David 457, 469,
Lakamana, Uma Mahesh 81, 109,
Lauber, Manuel 457, 459
Laubscher, Ryno 81, 83, 86, 93,
Le Bras, Sophie 371, 381, 391
Le Roux, Tristan Oliver 1, 23
Li, Bin 313, 337
Liberson, Lev 43, 62, 63, 71, 79
Liu, Liyi 347, 349, 434,
Lörcher, Frieder 1, 3, 11, 313, 315, 371
Lucius, Andreas 62, 221, 223, 232, 323, 479
Luzzato, Charles 479, 501, 510

Mallu, Shivaprasad Reddy 43, 53, 55, 62, 71, 79
Masi, Massimo 33, 42, 347, 403, 405, 419,
Mees, Valentin 313, 325, 334, 335, 336
Merkel, Markus 119, 135, 144
Meyer, Chris 1, 23,
Minorikawa, Gaku 255, 257, 265
Moreau, Stéphane 11, 71, 79, 167, 177, 221, 231, 240, 243, 252, 253, 254, 310, 311, 313, 371, 393, 402, 431, 438, 443, 445, 454, 455, 479, 491, 495, 500, 501, 502, 510, 523

Nakano, Takefumi 255, 257, 265,
Nashed, Mina Wagih 368, 479, 489
Nyári, Bendegúz 157, 189

Ottersten, Martin 157, 159, 167,
Ouyang, Hua 284, 313, 337
Özenen İmge B Engisu 43, 45

Pargal, Saurabh 221, 243, 244, 245, 246, 247, 248, 250, 251, 252, 253
Pelat, Adrien 255, 267
Pelz, Peter F. 24, 31, 81, 97, 105, 106, 357
Pesce, Mario 457. 469,
Pinelli, Michele 197, 199, 208,
Piovan, Mattia 197, 199, 208,
Pompoli, Francesco 197, 199
Pott-Pollenske, Michael 43, 62, 63,
Pouhe Hiol, Ralph Kinte 71, 79
Pretorius, Johannes 81, 83, 93,

Quintero, Fabian 457, 469,

Ravi, Vinay 371, 381
Rech, Sergio 1, 33,
Rendón-Arredondo, Jose 371, 393
Reuschling, Fabian 43, 62, 63, 71, 73, 74, 79
Riedel, Jörg 351, 359, 368,
Roy, Ashik 479, 513

Sanjosé, Marlène 71, 157, 167, 169, 177, 178, 188, 221, 243, 244, 252, 253, 254, 287, 301, 310, 402, 443, 454, 455, 500, 503, 510, 523
Santamaria, Jorge 287, 301, 309, 310, 397, 402
Sasaki, Soichi 177, 221, 233
Schneider, Marc 43, 62, 71, 73, 221, 223, 232, 270, 274, 275, 284, 316, 323, 379
Schoder, Stefan 374, 379, 390, 443, 457, 459, 468, 469, 478,
Schroder, Leon 197, 211,
Schultheiß, Garvin 119, 135
Scouarnec, Denis 255, 267, 273, 276, 284
Sheard, Anthony Geoffrey 11, 60, 62, 208, 287, 289, 299,
Şimşek, Ekincan 43, 45
Sivaramkrishnan, Anand Sivaram 431
Spehr, Carsten 43, 71, 73
Spitzer, Sebastian 197, 211, 219,
Suman, Alessio 197, 199, 208,

Tebib, Safouane 431, 445, 446, 448, 451, 452, 455, 479, 492, 500, 501, 502, 504, 510

Van Der Spuy, Sybrand Johan
Van Der Spuy, Sybrand Johannes 1, 23, 42, 81, 83, 93, 284, 287
Verzè, Emilio 197, 199
Vicente, Thibault 255, 267
Vourakis,, Michail 255, 275, 277, 284, 479, 513, 522,

Wang, Peng 347, 349, 355,
Witte, Hauke 1, 13, 15, 21, 22
Wu, Yadong 156, 172, 284, 313, 337, 346, 478
Wurzinger, Andreas 457, 459, 468

Yang, Weigang 313, 337
Yu, Zerong 313, 337,
Yu, Peixang 313, 337,

Zangeneh, Mehrdad 347, 349, 350, 354, 355, 431, 433, 442, 443
Zanini, Nicola 197, 199, 208,
Zea, Elias 255, 275
Zhang, Mingding 347, 349, 442,
Zhao, Qian 347, 348
Zhoy, Z 221, 243